

Institute of Energy and Climate Research  
Plasma Physics IEK-4

# Laser Induced Desorption as Hydrogen Retention Diagnostic Method

*Mirosław Zlobinski*



**Laser Induced Desorption**  
**as**  
**Hydrogen Retention**  
**Diagnostic Method**

Inaugural-Dissertation

zur Erlangung des Doktorgrades  
der Mathematisch-Naturwissenschaftlichen Fakultät  
der Heinrich-Heine-Universität Düsseldorf

vorgelegt von

**Mirosław Zlobinski**  
aus Beuthen

Düsseldorf, Juni 2016

Aus dem Institut für Energie- und Klimaforschung - Plasmaphysik (IEK-4)  
der Forschungszentrum Jülich GmbH,  
für die Heinrich-Heine-Universität Düsseldorf

Gedruckt mit der Genehmigung der  
Mathematisch-Naturwissenschaftlichen Fakultät der  
Heinrich-Heine-Universität Düsseldorf

Referent: Prof. Dr. U. Samm

Korreferent: Prof. Dr. G. Pretzler

Betreuer: Dr. V. Philipps

Tag der mündlichen Prüfung: 15.7.2016

Kontakt zum Autor: [LID@GMX-TOPMAIL.DE](mailto:LID@GMX-TOPMAIL.DE)

# **Laser Induced Desorption as Hydrogen Retention Diagnostic Method**

*Mirosław Zlobinski*

Berichte des Forschungszentrums Jülich; 4396  
ISSN 0944-2952  
Institute of Energy and Climate Research  
Plasma Physics IEK-4  
Jül-4396

D 61 (Diss. Düsseldorf, Univ., 2016)

Vollständig frei verfügbar über das Publikationsportal des Forschungszentrums Jülich (JuSER)  
unter [www.fz-juelich.de/zb/openaccess](http://www.fz-juelich.de/zb/openaccess)

Forschungszentrum Jülich GmbH  
Zentralbibliothek, Verlag  
52425 Jülich  
Tel.: +49 2461 61-5220  
Fax: +49 2461 61-6103  
E-Mail: [zb-publication@fz-juelich.de](mailto:zb-publication@fz-juelich.de)  
[www.fz-juelich.de/zb](http://www.fz-juelich.de/zb)



This is an Open Access publication distributed under the terms of the [Creative Commons Attribution License 4.0](https://creativecommons.org/licenses/by/4.0/), which permits unrestricted use, distribution, and reproduction in any medium, provided the original work is properly cited.

# Abstract

Laser Induced Desorption Spectroscopy (LIDS) is a diagnostic method to measure the hydrogen content in the surface of a material exposed to a hydrogen isotope (H, D, T) plasma. It is developed mainly to monitor hydrogen retention in the walls of magnetic fusion devices that have to limit the amount of their fuel tritium mainly due to safety reasons. The development of fusion increasingly focusses on plasma-wall interactions for which in situ diagnostics like LIDS are required that work during plasma operation and without tile removal. The method has first been developed for thin amorphous hydrocarbon (a-C:H < 500 nm) layers successfully and is studied in the present work on thick (15  $\mu\text{m}$ ) layers, carbon fibre composites (CFCs), bulk tungsten (W), W fuzz and mixed C/W materials.

In LID a 3 ms Nd:YAG (1064 nm) laser pulse heats a spot of  $\varnothing 3$  mm with  $500 \text{ MW/m}^2$  on W to 1800 K at the surface and thus above 1300 K within ca. 0.2 mm depth. On C materials (graphite, CFC, a-C:H) this temperature guarantees a nearly complete (>95%) desorption already within 1.5 ms pulse duration. The retained hydrogen atoms are desorbed locally, recombine to molecules and migrate promptly to the surface via internal channels like pores and grain boundaries. Whereas, in W the retained hydrogen atoms have to diffuse through the bulk material, which is a relatively slow process also directed into the depth. The desorbed hydrogen fraction can thus be strongly reduced to 18-91% as observed here. This fraction is measured by melting the central part of a previously heated spot ca. 40  $\mu\text{m}$  deep with a  $\varnothing 2$  mm, 3 ms laser pulse, releasing the remaining hydrogen. W samples exposed to different plasmas in TEXTOR, Pilot-PSI, PSI-2, PADOS and PlaQ show that the desorption fraction of LID mainly decreases due to higher sample temperature during plasma exposure. The heat causes deeper hydrogen diffusion and/or stronger hydrogen trapping due to creation of traps with higher binding energy. Such effects can lead to the observed desorption fractions as simulations (TMAP7 code) of heat and H diffusion during the laser pulse show. These experiments are performed in a vacuum chamber outside the tokamak, where the desorbed gases are quantified by a quadrupole mass spectrometer, thus representing the ex situ method LID-QMS.

In the tokamak TEXTOR the in situ diagnostic method LIDS is used utilizing the same physics for heating, desorption and surface modifications. Understanding the latter becomes important to mitigate material release into the plasma. Here, the quantification of the desorbed hydrogen is done by passive spectroscopy of the Balmer  $H_\alpha$  and  $D_\alpha$  light (656 nm) observed coaxially to the laser beam as a double line by a spectrometer and from the side by a camera with gated image intensifier using a narrow-band H&D filter. A simplified data evaluation has been developed which determines the plasma radius of the light intensity maximum of the LIDS light, takes the electron density and temperature at this radius measured by edge plasma diagnostics and looks up the corresponding quotient of ionisation to excitation rate  $S/X_B$  ( $n_e$ ,  $T_e$ ) in a database (ADAS). A second factor takes into account the dominant plasma processes which yield only one atom from one hydrogen molecule for pure hydrogen release and even less for desorbed hydrocarbons. The combined light-to-particle conversion factor is ca. 30 H atoms/ $H_\alpha$  photons which agrees with simulations of the LIDS light (ERO code). While the simulated spatial light distribution is very sensitive to the details of the plasma edge profiles, the total photon amount stays very constant, thus justifying the simplified data evaluation. The experimental FWHM of the light in toroidal/poloidal direction is 30-40 mm and has an e-folding decay length of 15-20 mm in radial direction. Its intensity maximum is typically at  $n_e \approx 4 \cdot 10^{18} \text{ e}^-/\text{m}^3$  and  $k_B T_e \approx 60 \text{ eV}$  close to the last closed flux surface.

A measurement series shows good reproducibility of LIDS with a standard deviation of  $\pm 13\%$ , while the estimated uncertainty of a single LIDS measurement is  $-47\%$  to  $+43\%$ . LIDS measurements are also in agreement with results from LID-QMS, slow thermal desorption (TDS) or nuclear reaction analysis (NRA). The lower detection limit of LIDS is determined by the  $H_\alpha$  background fluctuations in TEXTOR to  $8 \cdot 10^{20} \text{ H/m}^2$  for ohmic and  $5 \cdot 10^{21} \text{ H/m}^2$  for neutral beam heated plasmas for a  $\varnothing 2.6$  mm laser spot. The upper measurement limit due to local plasma cooling by the cooler desorbed gas lies at ca.  $6 \cdot 10^{22} \text{ H/m}^2$  for TEXTOR conditions.

# Kurzfassung

Laserinduzierte Desorptions-Spektroskopie (LIDS) ist eine Diagnostikmethode zur Messung des Wasserstoffgehalts in Materialoberflächen, die einem Plasma aus Wasserstoffisotopen (H, D, T) ausgesetzt sind. Sie wird vorwiegend zur Überwachung der Wasserstoffrückhaltung in den Wänden von magnetischen Fusionsanlagen entwickelt, um den hauptsächlich aus Sicherheitsgründen eingeführten Tritiumgrenzwert einzuhalten. Die Fusionsforschung konzentriert sich zunehmend auf Plasma-Wand-Wechselwirkungen, wofür in situ Diagnostiken wie LIDS benötigt werden, die während des Plasmabetriebs arbeiten und keinen Ausbau von Wandelementen erfordern. Die Methode wurde ursprünglich für dünne amorphe Kohlenwasserstoffschichten ( $a\text{-C:H} < 500 \text{ nm}$ ) entwickelt und wird in dieser Arbeit an dicken ( $15 \mu\text{m}$ ) Schichten, Kohlefaserverbundstoffen (CFCs), Wolfram (W), W fuzz und gemischten C/W Materialien untersucht.

Bei der Laserdesorption heizt ein 3 ms Nd:YAG-Laserpuls ( $1064 \text{ nm}$ ) einen Fleck von  $\varnothing 3 \text{ mm}$  auf W mit  $500 \text{ MW/m}^2$  auf  $1800 \text{ K}$  an der Oberfläche und damit auf  $1300 \text{ K}$  bis in ca.  $0,2 \text{ mm}$  Tiefe auf. Auf C Materialien (Grafit, CFC,  $a\text{-C:H}$ ) garantiert diese Temperatur eine fast vollständige ( $>95\%$ ) Desorption schon bei  $1.5 \text{ ms}$  Pulsdauer. Die adsorbierten Wasserstoffatome desorbieren lokal, rekombinieren zu Molekülen und wandern durch interne Kanäle wie Poren und Korngrenzen rasch zur Oberfläche. Dagegen müssen in W die adsorbierten Wasserstoffatome in einem relativ langsamen Prozess durch das Volumenmaterial diffundieren, der auch in die Tiefe gerichtet ist. Der Desorptionsgrad kann daher stark sinken, hier auf gemessene  $18\text{-}91\%$ . Er wird gemessen, indem der innere Bereich eines bereits erhitzten Flecks ca.  $40 \mu\text{m}$  tief mit einem  $\varnothing 2 \text{ mm}$ ,  $3 \text{ ms}$  Laserpuls aufgeschmolzen wird, wodurch der verbliebene Wasserstoff freigesetzt wird. In TEXTOR, Pilot-PSI, PSI-2, PADOS und PlaQ exponierte W Proben zeigen, dass der Desorptionsgrad bei LID hauptsächlich durch eine Erhöhung der Exponierungstemperatur sinkt. Die erhöhte Temperatur führt zu tieferer Wasserstoffdiffusion und/oder stärkerer Wasserstoffbindung durch Erzeugung von Bindungen mit höherer Bindungsenergie. Solche Effekte können zu den beobachteten Desorptionsgraden führen, wie Simulationen (TMAP7-Code) der Wärme- und Wasserstoffdiffusion während des Laserpulses zeigen. Diese Experimente werden in einer Vakuumkammer außerhalb des Tokamaks durchgeführt, wo die desorbierten Gase mittels Quadrupolmassenspektrometer quantifiziert werden und stellen daher die ex situ Methode LID-QMS dar.

Im Tokamak TEXTOR wird die in situ Methode LIDS benutzt, die auf der gleichen Physik des Aufheizens, Desorbierens und der Oberflächenveränderungen beruht. Die Kenntnis der Letzteren wird wichtig um Materialfreisetzung ins Plasma zu vermeiden. Hier erfolgt die Quantifizierung des desorbierten Wasserstoffs mittels passiver Spektroskopie des Balmer  $H_\alpha$  und  $D_\alpha$ -Lichts ( $656 \text{ nm}$ ), das koaxial zum Laserstrahl mit einem Spektrometer als Doppellinie beobachtet und von der Seite mit einer bildverstärkten Kamera durch ein schmalbandiges H&D-Filter aufgenommen wird. Eine vereinfachte Datenauswertung wurde entwickelt, die den Plasmaradius des LIDS-Lichtmaximums bestimmt, die Elektronendichte und -temperatur dieses Radius aus Plasmaranddiagnostiken nimmt und deren zugehöriges Verhältnis von Ionisations- zu Anregungsrate  $S_{XB}(n_e, T_e)$  einer Datenbank (ADAS) entnimmt. Ein zweiter Faktor berücksichtigt die dominanten Plasmaprozesse, wonach ein Wasserstoffmolekül nur ein Atom hervorbringt bei reiner Wasserstofffreisetzung und noch weniger bei Kohlenwasserstofffreisetzung. Der gesamte Licht-zu-Teilchen Konversionsfaktor ist ca.  $30 \text{ H-Atome/H}_\alpha\text{-Photonen}$ , was mit Simulationen des LIDS-Lichts (ERO-Code) übereinstimmt. Während die simulierte Lichtverteilung sehr sensibel auf die Details der Plasmaprofile reagiert, bleibt die Gesamtphotonenzahl sehr konstant, was die vereinfachte Datenauswertung rechtfertigt. Die experimentell bestimmte Halbwertsbreite des Lichts ist  $30\text{-}40 \text{ mm}$  in toroidaler/poloidaler Richtung und hat eine Abfalllänge von  $15\text{-}20 \text{ mm}$  in radialer Richtung. Sein Intensitätsmaximum liegt typischerweise bei ca.  $n_e \approx 4 \cdot 10^{18} \text{ e}^-/\text{m}^3$  und  $k_B T_e \approx 60 \text{ eV}$  nahe der letzten geschlossenen Flussfläche (LCFS).



Eine Messreihe zeigt die gute Reproduzierbarkeit von LIDS mit einer Standardabweichung von  $\pm 13\%$ , während der abgeschätzte Fehler der Einzelmessung bei  $-47\%$  bis  $+43\%$  liegt.

Die LIDS-Messwerte sind auch im Einklang mit Ergebnissen von LID-QMS, langsamer thermischer Desorption (TDS) oder Kernreaktionsanalysen (NRA). Die untere Nachweisgrenze von LIDS wird von den  $H_{\alpha}$ -Untergrundfluktuationen in TEXTOR bestimmt zu  $8 \cdot 10^{20} \text{ H/m}^2$  für ohmsche und  $5 \cdot 10^{21} \text{ H/m}^2$  für neutralteilchengeheizte Plasmen bei einem  $\varnothing 2,6 \text{ mm}$  Laserfleck. Die obere Messgrenze, bedingt durch lokale Plasmakühlung aufgrund der kühleren desorbierten Gase, liegt bei ca.  $6 \cdot 10^{22} \text{ H/m}^2$  für TEXTOR-Bedingungen.

# Contents

<b>Abbreviations and Nomenclature</b>	<b>12</b>
<b>1. Introduction</b>	<b>15</b>
<b>2. Laser Heating of Different Materials</b>	<b>31</b>
2.1. Laser Induced Desorption Setup . . . . .	31
2.2. Laser Pulse Properties . . . . .	34
2.3. Laser Reflexion and Absorption . . . . .	42
2.4. Heat Propagation in Different Materials . . . . .	46
2.4.1. Isotropic and Homogeneous Materials (Tungsten and Graphite) . . . . .	49
2.4.2. Anisotropic Carbon Materials (CFCs) . . . . .	55
2.4.3. Amorphous Hydrocarbon Layers (a-C:H/D) . . . . .	59
2.4.4. Mixed C/W Layers . . . . .	65
<b>3. Surface Modifications due to Laser Heating</b>	<b>67</b>
3.1. Graphite and a-C:H Layers . . . . .	68
3.2. Mixed C/W Layers . . . . .	85
3.3. Bulk Tungsten . . . . .	90
3.4. Tungsten Fuzz . . . . .	103
3.5. Tungsten Coatings . . . . .	104
<b>4. Desorption Mechanism of Hydrogen</b>	<b>110</b>
4.1. Desorption from Tungsten . . . . .	110
4.2. Deuterium Diffusion Simulation with TMAP . . . . .	114
4.3. Desorption from Carbon and a-C:H Layers . . . . .	121
<b>5. Ex situ Laser Induced Desorption (LID-QMS)</b>	<b>125</b>
5.1. Experimental Setup and Measurement Procedure . . . . .	125
5.2. QMS Calibration . . . . .	129
5.3. QMS Spectra Evaluation . . . . .	132
5.4. Accuracy of the Ex situ Method . . . . .	134
<b>6. Applications of Laser Induced Desorption (LID-QMS)</b>	<b>138</b>
6.1. Laser Desorption from Mixed C/W Layers . . . . .	138
6.2. Laser Desorption from Bulk Tungsten . . . . .	143
6.3. Laser Desorption from Tungsten Fuzz . . . . .	154

<b>7. In situ Laser Induced Desorption Spectroscopy (LIDS)</b>	<b>157</b>
7.1. Tokamak TEXTOR . . . . .	158
7.2. Experimental Setup at TEXTOR and Measurement Procedure . . . . .	159
7.3. Temporal Evolution of the Light Emission . . . . .	164
7.4. Calibration of the Light Detection Systems . . . . .	168
7.5. Quantification of Released Particles . . . . .	170
7.5.1. Background Subtraction . . . . .	170
7.5.2. Atomic Yield Factor . . . . .	171
7.5.3. Light-to-Particle Conversion Factor . . . . .	174
7.5.4. Field of View Correction . . . . .	177
7.6. Simulation of the Light Emission with ERO . . . . .	180
7.7. Reproducibility and Stability . . . . .	185
7.8. Detection Limits . . . . .	190
7.9. Plasma Cooling Limit . . . . .	192
7.10. Accuracy of Laser Induced Desorption Spectroscopy . . . . .	195
<b>8. Applications of Laser Induced Desorption Spectroscopy</b>	<b>209</b>
8.1. Laser Desorption of a-C:H Layers . . . . .	210
8.2. Laser Desorption of a-C:D Layers . . . . .	221
<b>9. Summary</b>	<b>227</b>
<b>A. Appendix: Tungsten Grade Details</b>	<b>232</b>
<b>B. Appendix: TMAP7 Input File Example</b>	<b>233</b>
<b>List of Tables</b>	<b>236</b>
<b>List of Figures</b>	<b>244</b>
<b>Bibliography</b>	<b>245</b>
<b>Erklärung</b>	<b>256</b>
<b>Danksagung</b>	<b>258</b>

# Abbreviations and Nomenclature

$\lambda_T, \lambda_n$  e-folding decay length of the electron temperature and density along the minor plasma radius

$\nu_p$  laser pulse frequency in Hz

$\theta_L$  divergence half-angle of a laser beam in degree

$\Phi$  plasma flux in  $1/m^2s$

$B_{pp}, B_{pp,Gauss}$  Beam parameter product of a laser beam or of a Gaussian laser beam

$E_0$  laser pulse energy at laser output in J

$E_1$  laser pulse energy at the target in J

$F$  Fluence = number of particles per  $m^2$ ; also called dose;  $F = \Phi t$

$f_r$  fractional retention = retained fraction = retention fraction

$k_B = 1.38 \cdot 10^{-23} \text{ J/K}$  Boltzmann constant

$n, n_e, n_i, n_D$  density, electron density, ion density, Deuterium density in  $1/m^3$

$N_A = \sin(\text{half angle})$ ; Numerical Aperture

$n_{e,la}$  line averaged electron density (typically along a line through the plasma centre)

$T, T_{surf}, T_e, T_i$  Temperature, surface Temperature, electron and ion Temperature in K (or °C)

$t_p$  laser pulse duration in s

$U_{laser}$  laser flashlamp voltage in V

$w_0$  laser beam waist, i.e. half of the minimal beam diameter in m

## — Abbreviations —

a-C:H amorphous hydrocarbon; a-C:D the same but with deuterium instead of protium

A/D Analogue/Digital

ALT-II Advanced Limiter Test II

AR Anti-Reflexion

CCD Charge-Coupled Device, a type of camera chip

CFC Carbon Fibre Composite

CMSII Combined Magnetron Sputtering and Ion Implantation

CVD Chemical Vapour Deposition

cw continuous wave

DEMO DEMONstration Fusion Power Plant

DIC Differential Interference Contrast

DLC Diamond-Like Carbon

dpa displacements per atom; a unit for material damage

ECR Electron Cyclotron Resonance

EDS Electron Drift Side, direction in a plasma from where slightly more electrons arrive than ions due to the diamagnetic drift

EDX Energy-Dispersive X-ray spectroscopy

EPMA Electron Probe Micro-Analysis

ERO EROsion-Deposition simulation code

FIB Focussed Ion Beam

FoV Field of View

HFS High Field Side, direction towards the centre of a tokamak, where the magnetic field of the transformer coil is higher than further outside

IDS Ion Drift Side, direction in a plasma from where slightly more ions arrive than electrons due to the diamagnetic drift

ILW ITER-Like Wall

IR Infra-Red light range

JET Joint European Torus

LCFS Last Closed Flux Surface, the outermost plasma layer which still contains closed field lines

LFS Low Field Side, direction away from the centre of a tokamak, where the magnetic field of the transformer coil is lower than in the centre

LID-QMS Laser Induced Desorption - Quadrupole Mass Spectrometry

LIDS Laser Induced Desorption Spectroscopy

MCP MicroChannel Plate, part of an image intensifier

NBI Neutral Beam Injector

NI Neutral beam Injection

NRA Nuclear Reaction Analysis

PADOS glow discharge device in FZ Jülich for Plasma Assisted Deposition Of Surface layers

PFM Plasma-Facing Material

PK Periphere Komponente = peripheral component (of a vacuum device)

PMI Plasma-Material Interaction

PSI Plasma-Surface Interaction (also a name for plasma devices, e.g. Pilot-PSI, PSI-2)

RBE Relative Biological Effectiveness; the radiation weighting factor

RSP Rapid Solidification Process

SBR Signal to Background Ratio

SEM Scanning Electron Microscope

SEM Secondary Electron Multiplier

SHE Supersonic HELium beam

SIMS Secondary Ion Mass Spectrometry

SNR Signal to Noise Ration

SOL Scrape Off Layer

SRIM Stopping and Range of Ions in Matter

TDS Thermal Desorption Spectrometry = Thermal Desorption Spectroscopy

TEXTOR Tokamak EXperiment for Technology Oriented Research

TMAP Tritium Migration Analysis Program

tokamak Russian acronym: торайдальная камера в магнитных катушках,  
in English: toroidal chamber in magnetic coils

TRIM TRansport of Ions in Matter

UHP Ultra High Purity

UHV Ultra-High Vacuum

UV Ultra-Violet light range

VIS VISible light range

# 1. Introduction

Energy and electricity supply should not only be **reliable** and **affordable** but the technology used should also **minimise negative effects** on humans and nature. Although the best "energy source" is energy saving and improving energy efficiency on the provider and consumer side, new energy sources and technologies are developed. This is sensible as they could fulfil the mentioned requirements better than sources mainly used today. The latter might have been assumed or been optimal in the past, but new knowledge of their negative aspects, shrinking resources or a shift in priorities within the requirements motivate changes in the energy mix.

In the past, such changes occurred for example with the oil boom in the 20<sup>th</sup> century because of its easy use in transportation and heating due to its convenient use in fluid state. Oil and gas extraction was easier and thus cheaper than coal extraction, which therefore lost importance. The inverse development started with the "relative peak oil" turning point in the 1970s, when oil reached its maximum of 48% of the world primary energy consumption [BP14]. This fraction has then decreased to constant 39% in the 90s and to **32%** in 2013 [BP14]. Although oil is still the biggest energy source, coal is rising since 2002 and reached **30%** already in 2013, followed by natural gas at stagnating **23%** [BP14]. But the growing importance of the adverse effects of fossil fuel usage on the global climate degraded the assessment of **fossil fuels** drastically. Moreover, the strongly growing global energy demand and the inhomogeneous geographical distribution of oil led to a strong price increase despite production increase in absolute values.

These disadvantages are widely mitigated for nuclear power as its fuel has an **energy density** a million times higher than fossil fuels, which is valid both for nuclear fission and fusion. The fuel for fusion are lithium (<sup>6</sup>Li) and heavy hydrogen (<sup>2</sup>H) – mostly called deuterium (D = <sup>2</sup>H) because it contains two nucleons: a proton and a neutron. The energy content of 1000 litres of oil is equal to 0.0003 kg of **fusion fuel** contained in D from 2 litres of water and <sup>6</sup>Li from a handful of stones. Therefore, nuclear power plants need very small amounts of fuel compared to fossil power plants and thus are much less dependent on the price or geographical distribution of fuels and their abundance. Nevertheless, the fission fuel uranium and the fusion fuel lithium are also limited resources. As a fraction of the resources, the already verified and economically minable **reserves** are predicted to last only until ca. 2075 for uranium, which is just a bit longer than gas (2068) and oil (2049), while coal reserves could last 120-280 years [BMWi14]. These estimates simply assume that the global consumption will be the same as in 2007 every year, while it has increased by a factor of 1.17 already. Thus the reserves will probably be exhausted even earlier. The reserves of lithium (ca. 1 Mt <sup>6</sup>Li from 13 Mt Li [Jaskula14]) would last for ca. **700 years** of the energy consumption of 2013 (530 EJ), if half of the primary energy was supplied by fusion. Of course, this duration will reduce due to the growing energy consumption and the increasing use of Li for batteries. Including Li recycling, the total Li used until 2050 for all purposes excluding fusion, could amount to 4-9 Mt Li depending mainly on the number of electric cars with Li ion batteries [Angerer9]. Additionally, the increasing growth of renewable energies creates the need for huge energy buffers including large battery parks, which recently started operation in Germany. If renewables provide the other half of the energy in the future, these battery parks might also need a considerable amount of Li, decreasing the available fusion fuel.

In terms of **resources**, which additionally include assumed deposits or verified but today unprofitable deposits, a huge Li amount is predicted, three times larger than the reserves (i.e. ca. 3 Mt  ${}^6\text{Li}$  from 39 Mt Li [Jaskula14]). This amount makes fusion practically limitless, nearly like renewable energies, as it would last for more than **2000 years** with the above consumption assumptions (265 EJ/a from fusion). The other resources are estimated to last 150 years for oil, 280 years for uranium, 570 years for gas and roughly 1300 years for coal, assuming the present consumption [BMW14]. But resources beyond reserves are partially speculative. Using them will also be much more expensive than using the reserves as they partly exist in unconventional form, which requires doubtful mining technologies like fracking. However, if all the fossil resources were spent, this would be most probably catastrophic for the climate without effective carbon capture techniques. Moreover, it should be kept in mind, that surface **mining** destroys the landscape for decades, relocation of whole towns is often necessary and cracking of buildings and biosphere dehydration are evoked by the often required ground water lowering. Similar damages to buildings and permanent pumping of water often occurs for underground mining, too. In contrast to fossil fuels, fission fuel would be climate friendly, but the final safe storage as nuclear waste for nearly a **million years** or complete recycling is still – and could remain – an unsolved problem. Additionally, a permanent rest risk of an uncontrolled nuclear chain reaction leading to a meltdown of the reactor content with a breach of containment and severe nuclear contamination exists even during operation, not only during final waste storage.

Fusion power has the advantage that only components of the power plant become nuclear waste and no burned-up or used nuclear fuel is produced. Thus the material for these components can be chosen such that low-activation materials are used, which quickly reduce their radioactivity, e.g. martensitic steels or vanadium alloys. These materials have to be stored safely for less than a **hundred years** until their radioactivity is at a medium level which allows recycling of the material by remote handling. The main security aspect of fusion is that the fusion principle does not include a chain-reaction and thus no uncontrolled energy accumulation can occur. In laser induced fusion, also known as inertial confinement fusion, the amount of fuel used for one fusion cycle is limited to a harmless amount. In magnetic confinement fusion any failure of a system directly leads to the end of the fusion reaction by physical principles without human or technical intervention. This **passive safety** even holds for the case of a complete cooling failure with total loss of coolant, where the nuclear decay heat of the structure materials could heat parts of the reactor to 1200-1450 K within few days [Maisonier5, p.18]. "Detailed calculations, show that at no time does any component reach a temperature close to melting" [Maisonier5, p.17].

Although today's fusion devices of the tokamak type only operate in a pulsed mode, the stellarator type overcomes this intrinsically by its design. There are also promising, but partly unproven techniques to establish continuous operation of a tokamak. With these schemes or a synchronised, alternating sequence of several fusion devices, fusion power plants could provide constant and reliable energy suitable for the **base load** – in contrast to solar and wind power. The latter need huge energy buffers to achieve this, which increase their **space consumption** further, that already is a factor of  $10^6$  (for photovoltaic), 1000 (wind), 300 (solar thermal) and 200 (water reservoir) larger compared to nuclear power.

In a fair comparison in the energy mix, further negative aspects of some **renewable energies** should be taken into account. For example the consequences of the above mentioned enormous space consumption, which is unproblematic for solar cells on roofs and acceptable for solar cell farms and wind parks, if the occupied space is sensibly used e.g. by farming. But already onshore wind turbines are an aesthetic problem for some people, while others appreciate the continuous, majestic motion – a matter of taste, in the end. Wind turbines provoke



---

also ornithological problems especially at night, when the rotors are barely visible for birds, who additionally are attracted by the aviation safety lights. Passive radars which detect planes and illuminate the lights only when necessary are being installed to reduce the latter effect, at least. Still, some people see a problem e.g. in the permanent sound and infrasound, shadows and light reflexions in the vicinity of wind turbines.

Questionable is also the renewable biomass power, at least when food is converted to energy, which raises the price for food and thus aggravates the hunger problem in poor countries. Landscape destruction occurs not only in mining but also by controlled flooding to create water reservoirs for water power. Accumulating mud at the barrier is a huge problem for the reservoir and for the agriculture downstream, which is not provided with this natural fertiliser any more. Water power at rivers has to take special measures to allow the fish to bypass. Geothermal power has discredited itself in recent years by unforeseen geological reactions that lead to ground movements like swelling and caused damages in the buildings of whole towns.

But in the last decades the importance of these climate friendly energy technologies increased as the relevance of **greenhouse gas emissions** on the climate became more and more evident. These emissions occur during the construction, operation and recycling or disposal of a power plant. In this sense, even renewable energies and nuclear power emit greenhouse gases in the whole process, mainly before and after operation, while fossil fuels emit them predominantly during operation. A comparison of these emissions relative to the energy delivered during the whole operation time of a power plant shows that coal is worst with 1-1.8 kg CO<sub>2</sub>-equivalent emissions per kWh [PSI14]\*. Oil is similar, but has a larger span down to half of this value depending on the actual technology, location and conditions. Natural gas is slightly better, especially using modern combined cycle gas turbines and reaches at best 0.4 kg CO<sub>2</sub>-eq/kWh. The gap to the renewables is at least a factor of 2, where the least efficient onshore wind turbines are operating. Onshore wind and water power at reservoirs have the largest span, from these rather high emissions down by more than an order of magnitude to 0.01 kg CO<sub>2</sub>-eq/kWh depending mainly on location. Photovoltaic and geothermal power have average values of 0.06-0.09 kg CO<sub>2</sub>-eq/kWh with a smaller span reaching down to 0.025 kg CO<sub>2</sub>-eq/kWh for the thin film solar cells. The smallest – nearly negligible – variations of emission have nuclear power, offshore wind and water power at rivers as they have the lowest fluctuations and thus highest reliability. In absolute values, nuclear power and offshore wind emit ca. 0.015 kg CO<sub>2</sub>-eq/kWh and thus about two orders of magnitude less than coal and oil and at least a factor of 25 less than the best gas turbines. The winner in this category of greenhouse gas emissions is water power at rivers with 0.005 kg CO<sub>2</sub>-eq/kWh [PSI14].

This low climate impact of renewables seems to compensate their negative aspects mentioned above as the strong **growth rates** of renewables imply. Although in total all renewable energies contributed only 10% to the **world primary energy consumption** in 2013, this fraction increased by an annual factor of 1.052 on average in the last five years [BP14]\*. This is a mean growth of 5.2% every year. Especially solar power increased extraordinary with a factor of 1.6 and wind power with 1.2, while the smaller growth of water power (1.01) and other renewables (1.15) reduced the combined growth of all renewables. All these growth rates are higher than for the fraction of coal (1.009) on average in the same time period. Simultaneously, the fraction of natural gas lost slightly (by a factor of 0.997), oil likewise (0.986) and nuclear fission decreased strongest (0.96). For the latter it is surprising, that the advert sides of nuclear fission are accepted by many countries, although it only contributes about 4% to the total primary energy of the world [BP14].

A simple extrapolation implies, that the fraction of renewables could reach 50% of the world energy consumption in 2045, assuming a constant annual growth rate of 5.2%. If their rela-

---

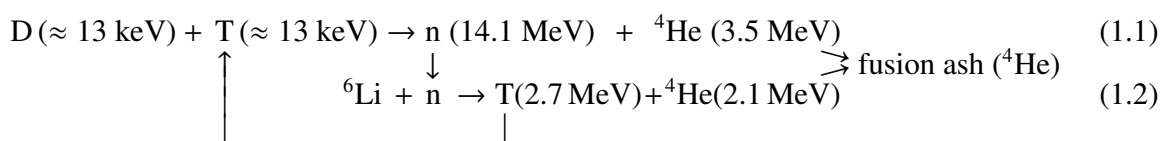
\*The following data up to the repetition of the same citation mark originate from the same source.

tive fraction rather grows linearly with the average growth rate of the last five years, then renewables would reach 50% supply in 2100.

However, from today's view, renewable energies are not suitable to serve the energy base load due to the natural fluctuations of sunshine, wind, water flux, ocean waves etc. Whether this could change with gigantic energy buffers like water reservoirs or accumulators and whether it will be economically sensible, is highly questionable. When rejecting fossil fuels to keep the climate stable as long as a feasible carbon capture technology is missing and rejecting fission to exclude the risk of a severe nuclear contamination and the unresolved waste disposal problem, then fusion power is the remaining option. It could be the perfect base load complement to renewables as it is also climate friendly and nearly limitless – although not renewable. The direct **costs of electricity** from fusion in the series production are estimated to be in the same range as for wind power and fission [Maisonnier5, p.210]. The external costs, i.e. those not included in the market price but paid by society for environmental pollution, accidents, health care etc. are also very low. For fusion, they are also comparable to wind power (below 3% of the direct costs) and 1-2 orders of magnitude lower than for fossil fuels [Maisonnier5, p.V,15,197].

### **Hydrogen fusion**

Fusing light elements (i.e. lighter than <sup>56</sup>Fe) releases energy like splitting heavy elements, but yields typically a several times larger energy output than a fission reaction. The fusion reaction with the highest output power density is at the same time the reaction which needs the lowest impact energies of the fusing nuclei and thus requires the least effort. Therefore this reaction is the easiest and most powerful and is thus the first choice for fusion power plants. It is the reaction of the heavy isotopes of hydrogen: **deuterium** (D) and **tritium** (T = <sup>3</sup>H) also called super heavy hydrogen as it consists of one proton and two neutrons in the core. D is stable and can be found as every 6420<sup>th</sup> hydrogen\* atom and is routinely extracted by isotope separation from water. T is unstable with a half-life period of 12.3 years, decaying to <sup>3</sup>He under emission of an electron and an antimatter electron neutrino. Due to its short half-life period, T is rare in nature, but can be bred artificially by nuclear reactions e.g. from <sup>6</sup>Li, which is therefore the other fusion fuel. In a fusion power plant both reactions are used mutually in the following way.



When the positively charged cores of D and T approach each other, they repel each other due to the Coulomb forces or fuse if they come so close that they are attracted due to the nuclear strong force. This strong interaction force dominates only within few femtometres around the cores, while the repelling Coulomb force dominates the whole range outside this area. Fortunately, the nuclei can tunnel through this potential barrier and thus do not need to reach the region where both forces are exactly equal. The tunnelling probability increases with smaller distance of the nuclei but this closer approach requires higher energies and thus the fusion probability has a maximum at some tens of femtometres distance. The corresponding maximum of the fusion power density occurs around 13 keV and is quite broad with a FWHM of 15 keV reducing by an order of magnitude at 2 and 80 keV. But even at the maximum, more than 10 Coulomb collisions occur before one fusion reaction takes place. The kinetic energy

\* The term "hydrogen" is used in the present work in general for all hydrogen isotopes. If a distinction is necessary, then the chemical symbols H, D and T or the terms protium, deuterium and tritium are used.

---

of all these unsuccessful collisions would be lost in a cold environment like an accelerator, where the kinetic energy is dissipated to the cold surrounding gas or wall, making efficient fusion impossible. In order to gain more energy from the fusion reactions than spending on the acceleration of the hydrogen atoms, the kinetic energy of the unsuccessful collisions must be preserved. This can be achieved in a **plasma** environment. Because of the high energies ( $k_B T = 13 \text{ keV} \hat{=} \mathbf{150 \text{ million K}}$ ) or temperatures – as referred to in a plasma – this environment is ten times hotter than the core of the sun, which uses less efficient fusion reactions. For magnetically confined plasmas, different plasma forms were tested and the best form seems to be a ring or – geometrically – a *torus* with a D-shaped cross-section in *poloidal* direction, i.e. parallel to the axis of rotation symmetry of the torus. This cross-section plane is spanned by the poloidal and *radial* direction, which is just pointing outwards from the centre of the torus. The third direction in a torus is perpendicular to the cross-section plane and runs circularly along the torus and is thus called *toroidal* direction.

The first reaction (1.1) has to take place in the plasma, while the T breeding (1.2) can be done in the surrounding wall, because the fast neutrons permeate the plasma and the first metre of the wall. They carry the main part of the fusion energy, which is transformed from the nuclear strong interaction into kinetic energy of the neutron and the helium core – also called alpha particle. The wall is therefore mainly heated by the neutrons, but the first wall directly at the plasma also by the hot plasma itself.

Beside the right impact energy or temperature of the D and T, the product of **plasma density**  $n$  and **energy confinement time**  $\tau_E$  must be as high as possible to achieve a high energy gain. In inertial confinement fusion the product  $n\tau_E$  is high due to a high density of  $10^{30}$ - $10^{31} / \text{m}^3$  achieved by laser induced compression of a small sphere of D-T ice. These are densities close to those in the core of the sun, while solid matter has a density of  $10^{28}$ - $10^{29} / \text{m}^3$ . But at the same time  $\tau_E < 1 \text{ ns}$  in inertial confinement fusion. Oppositely, in magnetic confinement fusion this product is high, because  $\tau_E$  is more than a billion times larger ( $\tau_E \approx 1 \text{ s}$ ), while  $n \approx 10^{20} / \text{m}^3$  only, which is a vacuum five orders of magnitude thinner than atmospheric air. As the plasma is confined by the magnetic field, the ions and electrons can hardly move outwards across the toroidal field lines, thus the plasma contact to the wall is reduced as far as possible. This hampered movement of the plasma particles establishes the high energy confinement time, as the particles carry the energy. Therefore the temperature, which is hottest in the plasma centre, reduces towards the wall down to 1-100 eV depending on the wall position and the kind of plasma. These are still more than 10000 K but the already small density of the core plasma also decreases towards the wall by typically 1-2 orders of magnitude. Thus, there are more than 5 orders of magnitude less particles impacting the first wall of a fusion reactor compared to atmospheric air particles touching a room wall. Therefore, the first wall does not heat up to the plasma temperature, even without active wall cooling.

In its outer parts, the colder and thinner edge plasma is in contact with the surrounding walls despite enormous progress in the confinement of the plasma by magnetic fields. Therefore, versatile **plasma-wall interactions** (PWI) occur, also called plasma-surface interactions (PSI) or plasma-material interactions (PMI). Some of these interactions represent a modification of the wall due to the plasma and others the opposite direction, resulting in a change of the plasma properties due to wall effects. In the latter category are plasma changes that can increase the plasma density due to released atoms, molecules, clusters or dust from the wall. This is often combined with cooling of the plasma due to the much colder wall particles and the light emission they cause in the plasma. The plasma composition is often changed, since the released particles are often not hydrogen isotopes, and thus called "plasma impurities". Conversely, the wall and the vacuum pumping system behind it absorb particles from the plasma like the He ash of the fusion reaction and thus purify the plasma.

In the other category are effects of the plasma on the wall. These are wall erosion by phys-

ical and chemical sputtering and chemical erosion by impinging plasma particles, desorption, sublimation, bubble and blister formation, roughening, melting and cracking mainly due to thermal effects. As a consequence, the thermal and mechanical properties of the wall can change and embrittlement, creep or fatigue can result. Conversely, modifications of the wall caused by the plasma can also be accumulating instead of destroying. In general, this is called material deposition, which includes not only hydrogen and helium from the pure plasma, but also wall elements like Be, C, W, Mo etc. that became part of the plasma due to previous erosion. While a fraction of the plasma particles are reflected from the wall, some stick to the wall surface (adsorption) or penetrate deeper inside, which is then called implantation. Thus, the chemical composition of the wall can be altered due to the implanted elements or due to nuclear transmutations caused by the neutrons from the fusion reaction. Deposition can lead to formation of layers on the wall, mainly consisting of the wall materials chosen for the first wall. If during this process also hydrogen isotopes are deposited simultaneously, the process is called co-deposition. Such layers can subsequently be re-eroded and re-deposited on a different wall position, which can repeat frequently.

### Hydrogen retention

An important plasma-wall interaction is the **retention** of the hydrogen isotopes (H, D and T) from the plasma in or on the wall materials. Here, two mechanisms from the list above are important for hydrogen retention: implantation and co-deposition. They will now be introduced in more detail:

**Implantation** is the process by which the hydrogen ions\* or atoms intrude into the solid wall due to their high kinetic energy. Adsorption, known from gas-wall interaction, is often skipped in the sorption process of hydrogen from plasma into the wall, because the impacting particles usually have a high enough kinetic energy to go beneath the surface directly. During the impact they collide with lattice atoms of the wall and thus reduce their energy, transferring it to the solid, until they have the same temperature as the surrounding matter where they stop. This stopping process is called thermalisation. Hydrogen can be implanted in any wall material, if it has an impact energy higher than the wall potential barrier of typically few eV (details for W cf. chapter 4.1). This can be hydrogen ions or atoms from the edge plasma region with energies of  $k_B T = 1-100$  eV. For the hydrogen ions this energy is increased typically by about a factor of 3-4 in the very vicinity of the wall called the sheath region due to acceleration by the sheath potential. Additionally, also fast hydrogen atoms with energies of inner plasma regions (up to some keV) can hit the wall due to recombination. These hydrogen atoms are called "charge-exchange particles" as they were fast ions in the hot inner plasma and grabbed an electron (the "charge") from a slow atom. Thus they became neutral and therefore could escape the magnetic field still having their high energy. The implantation depth and depth distribution depend on the impact energy and angle, projectile mass and the wall material and can be calculated by computer codes like TRIM/[SRIM] or [TriDyn]. For typical edge plasma temperatures, hydrogen has a very shallow implantation depth, e.g. in W all hydrogen isotopes with 100 eV lead to a hydrogen peak at 2-3 nm depth. The hydrogen concentration decreases to 10% of the maximum value at ca. **6 nm** (= "end of implantation depth"). For an impact energy of 1 keV the H concentration peak is at 10 nm and the end of implantation depth at **23 nm**, while for D and T these values are a factor of ca. 1.2 larger: for D below 1.2 and for T slightly above 1.2.

---

\* The terms "ion" and "atom" are differently defined by different authors (e.g. in [SRIM] "ion" is defined as "The moving atom, whether it is charged or neutral".) In the present work the term "ion" is used for a charged atom, while the term "atom" is used for a neutral, uncharged atom.

For lighter wall materials made of carbon the implantation depths are about twice as large due to the 10 times lower mass density – despite the atom density is twice as high as for W. For example for graphite the end of the implantation depth is at ca. **55 nm** for 1 keV/D and at 160 nm for 6 keV/D [Doyle80, Scherzer90].

In ion beam experiments with mono-energetic hydrogen ions it was found that for a small amount of impacting hydrogen per unit area – i.e. for a low hydrogen **fluence**  $F < 10^{21}/\text{m}^2$  – all the implanted hydrogen is retained. The implanted amount is nearly equal to the impinging amount except for a small material-dependent fraction of 5-10%, which is instantly reflected [Doyle80]. That means that the retention fraction, also called retained fraction or **fractional retention**  $f_r = 0.9-1$  independent of the fluence. The fluence threshold of  $F = 10^{21}/\text{m}^2$ , which marks the end of this regime of **complete retention**, was found for graphite bombarded with 400-800 eV/D<sup>+</sup> [Philipps87]. This threshold increases with increasing impact energy e.g. by a factor of 6 for 2 keV/D<sup>+</sup> [Philipps87]. On other wall materials this threshold occurs slightly later (e.g. on B<sub>4</sub>C and pure boron) or up to a factor of 4 earlier (e.g. on VB<sub>2</sub>, TiB<sub>2</sub>, TiC and Si) in comparison to graphite [Doyle80].

Above this threshold fluence the regime of **saturation** begins, where the retention does not increase linearly with time or fluence any more and thus  $f_r < 0.9-1$  and decreases with increasing  $t$  or  $F$ . In the early stages of this regime only local saturation occurs, i.e. in a specific depth below the surface the hydrogen concentration reaches a maximum. For graphite this maximal concentration occurs at a ratio of 0.3-0.63 D/C [Doyle80] depending on the exposure conditions and graphite grade (polycrystalline, amorphous, fine grain, porous, pyrolytic graphite etc.). Finally, for the so far discussed mono-energetic case a total saturation occurs, i.e. the total amount of retained hydrogen is constant with time and fluence at  $F \approx 2 \cdot 10^{21} \text{ D}/\text{m}^2$  for 1 keV/D [Haasz94]. This is especially true for (pseudo-)monocrystal graphite, while for more porous graphite grades, like pyrolytic and fine grain graphite, the retention is proportional to  $F^{0.1}$  or  $F^{0.14}$  [Haasz94]. The latter grades provide internal pathways for **diffusion** of hydrogen atoms along grain boundaries and crystallite boundaries into the depth, while a single crystal lacks such internal surfaces [Haasz94].

In a plasma, the angular distribution of the impinging particles is broader than in a mono-energetic beam – or even isotropic. Additionally, their energy distribution is much broader with typically a Maxwellian distribution or a shifted Maxwellian distribution after sheath acceleration. In this case, there are *few* much faster impactors from the high energy Maxwell tail that reach deeper implantation depths, which thus can *hardly* cause local saturation in those greater depths. Therefore, instead of a total saturation, an **asymptotic saturation** occurs, i.e. the total hydrogen retention  $R_H$  approaches a linear function of fluence or time in a double logarithmic scale with a slope below one:  $R_H \sim F^s \sim t^s$  with  $s < 1$ . For different graphite grades the slope of this asymptote varies slightly, but  $R_H$  is typically proportional to  $F^{0.2}$  up to  $F^{0.3}$ . In this quasi-saturation regime, the retention is then rather a function of the **impact energy** and thus of the plasma temperature and increases by an order of magnitude when  $kT_i$  rises from 10 to 1000 eV [Doyle80].

For W the retained amount starts orders of magnitude lower for small  $F$ . This is partly due to a much higher reflexion of hydrogen ions on W than on C, e.g. 36% of 200 eV D<sup>+</sup> ions are reflected on oxidised tungsten (WO<sub>3</sub>), 44% on tungsten carbide (WC) and even 56% on pure polycrystalline W [Ogorodnikova3] reducing to 42% for 3 keV D<sup>+</sup> [Ogorodnikova8]. But the retention in W increases stronger with increasing fluence, roughly proportional to  $F^{0.5}$  up to  $F^{0.7}$  (cf. figure 6.14 on page 153, [Lipschultz10]). Thus, there is a point at which the retention in W catches up with the retention in graphite and overtakes it. Due to the spread of retention results in different W experiments and C grades, the actual point is rather a region somewhere between  $10^{23} \text{ D}/\text{m}^2 < F < 10^{25} \text{ D}/\text{m}^2$ . The steep slope of retention in W is mainly due to the much more dominant hydrogen diffusion in W, while it plays a minor role in graphite, as dis-

cussed above. Therefore, for graphite the dependence of retention on time or fluence is nearly exchangeable, while for W there is a much stronger dependence on exposure time and wall temperature. Exposure time extends the diffusion length with a root dependence ( $t^{0.5}$ ) and the wall temperature increases the diffusion coefficient (details in chapter 4.1), which increases the diffusion length in the same extent. The hydrogen can be retained as atoms in a perfect bcc (body centred cubic) W lattice inbetween the W atoms on so called **interstitial sites** or shortly "interstitials". Further retention sites for hydrogen are defects of the regular W crystal like a missing W atom, dislocations, vacancies, voids, grain boundaries etc. Larger clusters of hydrogen mostly in molecular form can agglomerate at cavities between the W grains or cavities inside one grain. In general, all these places for hydrogen are called **traps** or trap sites. For a low hydrogen fluence such **intrinsic traps** that already exist in the material dominate the retention. This is diagnosed e.g. by heating a sample in vacuum and measuring the desorbed gases with a mass spectrometer, a method called TDS (Thermal Desorption Spectrometry\*) [Ihde1] or TPD (Temperature Programmed Desorption) [Manhard11b]. The desorption from such intrinsic traps leads to a desorption peak in the range of 400-600 K – the so called low-temperature peak – as their binding energy for hydrogen is relatively low, while desorption peaks at higher temperatures are often explained by migration and clustering of vacancies [tHoen, p.42f]. Due to the interaction with the plasma, additional traps can be created – the so called **plasma induced traps**. In the binary collision picture of one hydrogen ion removing one W atom from its lattice position, a threshold has to be overcome which is called displacement energy  $E_{dis}$  or damage threshold energy. A hydrogen ion needs 2 keV for H on W, 1 keV for D on W [Quastel6, p.9] and ca. 700 eV for T on W corresponding to  $E_{dis} = 44$  eV energy transfer during the collision. However, different values are stated in the literature in the range of  $E_{dis} = 40$ -250 eV with an average around 90 eV [tHoen14, p.38]. But plasma induced traps have also been generated by deuterium plasmas with a much lower ion impact energy down to a few eV. Therefore other mechanisms like thermo-mechanical stress or "retention stress", i.e. local super-saturation with hydrogen can create plasma induced traps, too, which is an active field of research. In the latter case, retention could create retention sites by itself by the accumulation of hydrogen or vacancies and would thus be a self-sustaining and a self-growing mechanism. Such vacancies, cavities or voids are called **bubbles** if they reach a certain size or **blisters** if they are located at the very surface. Although it was found that only few percent (3-5%) of the retained hydrogen is stored in blisters [Manhard11b], the sub-surface cavities might play an essential role in hydrogen retention.

The  $F^{0.5}$ - $F^{0.7}$  dependence of retention is often associated with the filling of the intrinsic traps governed mainly by diffusion and thus ceases at some fluence, determined by time and temperature distribution. For higher fluences, more and more plasma induced traps are generated and they dominate retention while the contribution of the intrinsic traps decreases. Finally, this trap creation also saturates at high fluences, e.g. experiments showed total saturation of retention for  $F > 4 \cdot 10^{26}$  D/m<sup>2</sup> in W and W alloys (at  $T_{surf} \leq 450$  K,  $\Phi = 8 \cdot 10^{23}$  D/m<sup>2</sup>s,  $k_B T_e = k_B T_i \approx 5$  eV,  $E_{D^+} = 50$  eV) [Zayachuk13, p.120-124]. The saturation level depends on the actual material and exposure conditions and can be as small as few  $10^{20}$  D/m<sup>2</sup> like in the case above or can reach  $10^{22}$  D/m<sup>2</sup> as few experiments and data extrapolation suggest (cf. figure 6.14 on page 153, [Lipschultz10]). The latter value is about one order of magnitude larger than the saturated retention in some graphite grades.

This is still not the end of retention, because after retention on intrinsic traps and plasma induced traps additionally retention on neutron induced traps occurs. Since in a D-T fusion reactor the first wall is exposed to the high-energy neutrons of the fusion reaction, they also cause material damage and can thus create retention sites. But neutron irradiated samples be-

---

\*In many publications the term "spectroscopy" is used although no spectroscopic detection is done. Instead, I use the term "spectrometry" to clearly distinguish it from spectroscopy which uses optical methods and light.

---

come highly activated, thus rare experiments are performed with real neutrons and even then mostly with low-energy neutrons instead of the required 14 MeV.

One real neutron experiment used 0.1 MeV neutrons to create a damage of 0.025 dpa (displacements per atom), which means that on average every 40<sup>th</sup> W atom was removed once from its original position. The damage was done at 323 K, while the subsequent plasma exposure with 100 eV deuterium was done at 473 K (with  $\Phi \approx 6 \cdot 10^{21}$  D/m<sup>2</sup>s,  $F \approx 6 \cdot 10^{25}$  D/m<sup>2</sup>). While the undamaged W showed a typical desorption spectrum from 400-700 K, the neutron damaged W had a very broad spectrum from 300-1050 K proving high damage with a variety of traps. In total, its retention was about a factor of 4 higher ( $R_D = 3 \cdot 10^{21}$  D/m<sup>2</sup>) than for the undamaged W [Shimada12].

To test even higher damage levels, but mitigate the even higher radioactivity of such samples, the neutron damage is usually "simulated" in experiments by high-energy ion irradiation. Most sensibly this is done with W ion bombardments in order not to introduce additional impurities. Then samples can be handled in any laboratory and plasma conditions can be used which are much more similar to those expected in fusion reactors, e.g. a high flux ( $\Phi = 1.1 \cdot 10^{24}$  D/m<sup>2</sup>s) low temperature ( $k_B T_e = k_B T_i = 0.7$  eV) plasma. For such conditions with  $F = 1.1 \cdot 10^{26}$  D/m<sup>2</sup> and  $T_{surf} = 520$  K, retention increases with increasing damage by nearly 2 orders of magnitude compared to undamaged W, but saturates at ca. 0.2 dpa [tHoen14, p.41]. For temperatures of  $T_{surf} = 800$ -1200 K as expected at the strike points\* and 5 times higher flux, the retention increases still by more than an order of magnitude compared to undamaged W (for  $k_B T_e = k_B T_i = 1.6$  eV,  $F = 4.4 \cdot 10^{26}$  D/m<sup>2</sup>) [tHoen14, p.53]. However, the damage caused by pre-plasma irradiation with W, Fe or H ions reaches only few  $\mu$ m deep below the surface, while real neutrons create damage throughout the whole bulk. Additionally, neutron induced damage has different characteristics and creates different trap sites as proved by TDS. Moreover, neutrons introduce new effects like transmutation as they slowly transform the first wall and parts of the surrounding blanket into other elements and thus change the properties of the material.

Despite these advert effects of **neutrons**, they play an important role for the harvesting of the fusion energy because they easily escape the magnetic fields and thus transport the fusion energy behind the first wall. There they are stopped and deposit their energy in form of heat relative homogeneously, which is convenient as it is spatially decoupled from the direct plasma contact and does not stress the heat convertor materials in a localised manner. Nevertheless, the disadvantages of the fusion neutrons are so large that ultimately neutron-free – also called "aneutronic" – fusion reactions might be the better choice despite lower effectiveness, lower energy output and higher required plasma temperatures. The best reaction could be the proton-boron reaction ( $p + {}^{11}\text{B}$ ) yielding three alpha particles and 8.7 MeV energy, which is only a factor of 2 less than from D-T fusion, but at one order of magnitude higher plasma temperature. Such a step in plasma temperature was already achieved more than twice in fusion history as the first tokamak T3 in Russia reached a few million degrees roughly 50 years ago, while modern tokamaks like JET<sup>†</sup> in Great Britain, JT 60-Upgrade in Japan, TFTR in the USA or ASDEX-Upgrade in Germany achieved 200-500 million degrees. Thus, a further improvement by one order of magnitude does not seem impossible. But the radiated losses due to bremsstrahlung would be too large at these temperatures – at least with today's knowledge. Another neutron-free reaction is  $p + {}^6\text{Li} \rightarrow {}^3\text{He} + {}^4\text{He} + 4$  MeV, which uses the same kind of lithium as D-T fusion. Its products can be used for a further reaction that is used by the sun  ${}^3\text{He} + {}^3\text{He} \rightarrow {}^4\text{He} + 2p + 12.9$  MeV. All these reactions are not only neutron-free but also tritium-free and thus avoid T retention problems. However, hydrogen retention in general

---

\*Strike point is the name for the wall area where the plasma has the strongest interaction with the wall and the magnetic field lines intersect the wall with a maximum angle.

<sup>†</sup> JET is today the most powerful fusion reactor of the tokamak type [see [www.efda.org/jet](http://www.efda.org/jet)]

is always present, as H or D are involved either in the main reaction or less probable side reactions.

Beside the just described retention by implantation, there is a second form of retention, that practically ruled out C as plasma-facing material (PFM). For C wall materials, namely, the main contribution to retention is not the implanted hydrogen but the build-up of thick hydrogen-rich layers on the wall surface. These hydrogenic layers are created in a process called **co-deposition**, as the hydrogen isotopes are deposited "together with" (= "co") the deposition of the wall element itself. Hydrogen co-deposition with C is extremely high, reaching concentrations up to  $D/C > 1$  at room temperature, which can even stay around 1 up to 520 K [Lipschultz10, p.7]. These high D/C ratios are reached because of the chemical likelihood of carbon and hydrogen to bind together, which is seen throughout nature. In a plasma where both exist as free particles they like to come together and build networks of C and H atoms that show no repetitive order and thus are called amorphous. These amorphous hydrocarbon layers – shortly named a-C:H layers – can consist of graphite-like  $sp^2$ -bondings that form rather planar ring-structures or diamond-like  $sp^3$ -bondings that create tetrahedral structures. Often both occur together in different ratios with further bonding types like the linear  $sp^1$ -bondings depending on the plasma and temperature conditions during their formation and further treatment. Thus, a-C:H layer can be "hard", if their hydrogen content is rather small (typically for  $H/C < 0.6$ ) or "soft", if they are very hydrogen-rich. Especially, the hard a-C:H layers are often called diamond-like carbon (DLC) and have a high density ( $1500\text{-}2500 \text{ kg/m}^3$ ) and high optical refraction index ( $n = 2\text{-}2.5$ ). The soft layers can be less dense than  $1000 \text{ kg/m}^3$  with  $n$  as low as 1.6 or slightly less. These properties of a-C:H layers are very sensitive to the plasma conditions like particle energies and fluxes, but also to temperature as heating leads to hydrogen desorption and thus a change of the layer composition. For higher temperatures the hydrogen-to-carbon ratio reduces continuously down to 0.03-0.07 D/C at 870 K deposition surface temperature [Lipschultz10, p.7]. The hydrogen co-deposition with W is nearly two orders of magnitude lower with 0.02 D/W at room temperature and 0.001 D/W already at a deposition temperature of 570 K [Lipschultz10, p.7]. Co-deposition with tungsten carbide (WC) or Be lies between the values for C and W.

### The tritium issue

In both forms – implantation and co-deposition – hydrogen retention can become a severe safety issue especially in the case of **tritium**, since it is a  $\beta^-$  radiator. In case of an accidental release of tritium from a fusion power plant into the environment, potential health hazards for the biosphere can result. Mainly, because the electrons emitted by tritium can damage organic tissue especially when incorporated in the organism [Bridges7]. There it can accumulate as tritiated water or organically bound tritium in organic molecules, where it continuously emits electrons. "Tritiated nucleic acid precursors can present a unique hazard because of the possibility of their incorporation in DNA." [Bridges7, p.4] Unlike  $\gamma$  radiation, the  $\beta^-$  radiation from T with an average electron energy of 5.7 keV has a very short absorption length. In air it is stopped after 6 mm, in water after 6  $\mu\text{m}$  and in organic tissue after few micrometres or even sub-micrometre ranges and thus has a high ionisation density there, unfortunately. As T behaves chemically like H or D, it is incorporated in the body when inhaled or ingested. "While many radionuclides are likely to be encountered in only a few common forms, tritium can become incorporated in many organic compounds with very different behaviour in both the environment and the human body." [Bridges7, p.8] A fraction of the tritium can not be exchanged with H or D quickly and washed out of the organism in the natural way but becomes 'buried'. "In such a fraction the 'buried tritium' in biomacromolecules, such as native proteins, is in bridge positions where the exchange rates are reduced from microseconds to days, months or even years as a consequence of the three-dimensional structure that arises upon



---

the 'folding' of these native biomacromolecules." [Bridges7, p.18] "There is an enrichment of tritium in the newly identified buried hydrogen bonds compared to the free water in the cell." [Bridges7, p.18] "Tritium that is incorporated into the DNA of oocytes is a special case since most of it is likely to remain there until fertilisation." [Bridges7, p.4]

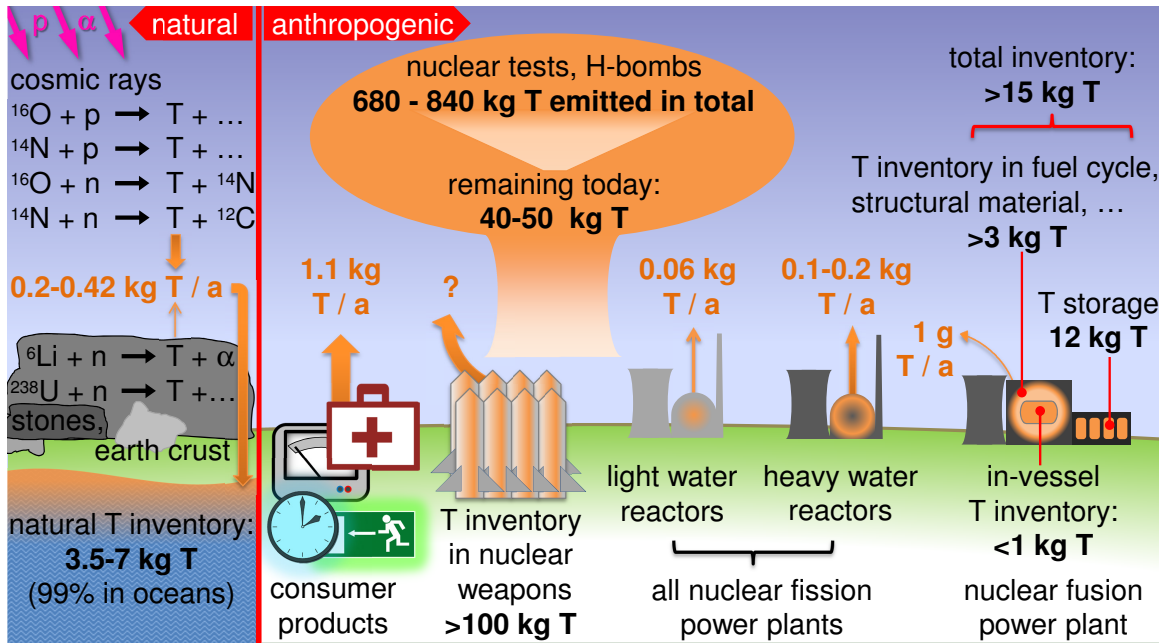
Additional biological issues arise from the  $^3\text{He}$  which is produced by the T decay. The relative biological effectiveness (RBE) of  $\beta$  and  $\gamma$  radiation, which is an empirical value used to determine the radiation weighting factor and thus the **equivalent dose** from the absorbed dose is usually  $1 \text{ Sv/Gy}$ . But due to the high ionization density,  $^3\text{He}$  production and T incorporation into the DNA, Bridges et al. expect it to be higher than 1 for T and list many publications with values of 1-3, but also with 5 and 8. In their conclusion, they plead to rather use an RBE of 2-3 for tritium compared to gamma radiation [Bridges7, p.29]. Thus the radiation doses due to T exposures from a fusion power plant mentioned further below would have to be increased by this factor to determine their real biological effect. The biological damage caused by T can partly be healed by the organism as it had always been exposed to ionising radiation and also natural T in the evolution history and thus is used to cope with it.

Tritium is produced naturally mainly by reactions in the stratosphere and atmosphere, where protons from cosmic radiation and secondary neutrons react with oxygen and nitrogen (cf. figure 1.1). It builds molecules like HT and water isotopes like HTO via photo-chemical reactions and thus becomes part of the water cycle. The second but much minor source of **natural T** are reactions in the earth crust, rock and stones which contain Li, U, B or D. The global natural *production rate* is reported to be  $0.2 \text{ kg T/a}$  [Sültenfuß98, p.7]\* or  $0.42 \text{ kg T/a}$  [Tanabe14]. The *reduction rate* due to the radioactive  $\beta^-$  decay is always 5.4% per year in relative terms, which results in a higher absolute loss, the higher the inventory. Therefore a self-stabilising equilibrium establishes for the natural T inventory, which reaches a constant value of  $3.5\text{-}7 \text{ kg T}$  depending on the assumed production rate. Some earlier publications cited in [Sültenfuß98, p.3] stated more extreme estimations of 0.9, 10 or even 20 kg. The distribution of the natural tritium inventory is stated there to be concentrated to 99% in the superficial ocean water.

Beside the natural tritium there is **anthropogenic tritium**, which is produced by human action. Its amount is far more than one order of magnitude larger than the naturally created tritium. The largest artificial release of T into the biosphere occurred due to the nuclear tests between the 1950s and the 1980s, mainly from hydrogen bombs, as they use the D-T fusion reaction. Despite the  $\beta^-$  decay, the remaining T amount from these bombs is still one order of magnitude larger than the natural T amount. Still many bombs containing T exist with an estimated T inventory of more than 100 kg [Sültenfuß98, p.5]. As hydrogen is one of the substances which are most difficult to contain, the release from such a huge amount to the environment is probably considerable. But there are also consumer products of the daily life that contain T like exit signs and other self-glowing things, electronics, measurement devices and medical products. The release from such sources to the environment is reported to be larger than  $1 \text{ kg T}$  per year, which is 2-5 times the natural T production rate. In comparison to this, the T release of all nuclear fission power plants together is much lower and roughly equal to the natural production rate. Release estimations for a nuclear fusion power plant are in the range of only  $1 \text{ g T/a}$  [Milch2, p.32], which would require more than 200 fusion power plants to approach the natural T production rate or 1000 to equal the consumer products release. A clear distinction has to be made between the T release (**orange** text in the figure) and the T inventory (**black** text) in these comparisons. Although the release is very small,

---

\*While the values and designations in the figure in [Sültenfuß98, p.7] are correct as they are in agreement with the text, there is a translation error in the German figure caption: The value given under (a) is not the annual production of natural tritium, but the natural T inventory.



**Figure 1.1.:** Tritium emission rates and amounts of natural and anthropogenic T sources on Earth [Sültenfuß98, p.1-7], [Milch2, p.31f], [Tanabe13]

the T inventory of a fusion power plant will probably be 2-4 times larger than the natural T inventory of the whole earth, or they could be equal when referring to the maximal natural estimates. Due to the low fusion efficiency or burning efficiency of a few percent (ca. 3%) of the input D and T, the fuel throughput of a fusion reactor must be very large [Tanabe14]. As the majority of the input fuel is pumped out of the vacuum chamber again and has to be separated, processed and recycled and additionally the T breeding ratio in the reactor blanket is rather low (<1.15), a large T storage is needed [Tanabe14]. About 12 kg T storage are estimated for a reactor with an electric output of 1 GW [Tanabe14]. All the T in a fusion power plant should remain contained during normal operation, which is achieved by several shielding stages and screenings, except for the very small released amount mentioned above. There are different categories of this inventory, which differ by the type of T binding. Often the most general distinction is "mobile (or dynamic) inventory" and "immobile (or static) inventory", which are characterised by a fast or slow release rate, respectively. The T in the storage and the fueling system is transported as gas in tubes to the reactor and thus belongs to the dynamic inventory. On the other hand, T can creep into the structural material of the reactor, support structure or the gas tubes and vessels of the fuel cycle, where it is rather immobile, unless it is heated. This immobile inventory grows slowly in time and is predicted to reach more than 3 kg T. However, the distinction is not always so clear, e.g. for the **in-vessel inventory**, which is defined as all T inside the vacuum vessel including T in and on the first wall (main chamber, divertor, dome), plasma facing components (including antennas, mirrors, probes and other diagnostics) and remote areas. Here, a diversity of T binding types lead to different release rates due to different retention mechanisms (hydrogenic layers, implantation), different wall temperatures, T energies, fluxes and erosion/deposition conditions. Despite this variety, the whole in-vessel inventory is commonly defined as mobile, because the low T release rate of some parts would increase in case of accidental strong heating. This could happen in off-normal events that can have internal or external reasons.

Internal reasons, called "in-plant accidents", could be for example the loss of cooling due to leaks or electricity blackout and the subsequent self-heating due to the **radioactive decay heat**. This heat generation which comes from the materials activated during operation would

---

heat the reactor, mainly the first wall and innermost blanket parts above 1200 K within few days [Maisonnier5, p.18]. This could occur, if a total loss of cooling and the total loss of coolant of one cooling loop occurred and no counter-measures could be performed. In the worst case of this scenario, numerical simulations predict peak temperatures of 1450 K after one month, depending on the actual size and shape of the reactor and the coolant used (water, He or LiPb). In either case, the increased temperature would increase the tritium release and diffusion rate and would probably lead to a nearly complete T release of the first wall as it would be the hottest part. Further outward parts of the wall, which are cooler, would probably still release considerable fractions of their T inventory. Not only T is mobilised but also H, D, O etc. and thus **oxyhydrogen gas** could form with residual and leaking oxygen, potentially creating detonation gas in case of an appropriate mixture. Additionally, large amounts of hydrogen can be produced by oxidation of the wall materials by the water or water vapour of a leaking cooling loop or external water influx. This chemical reaction is faster the hotter the surface and the more porous the wall material. Especially Be and even more its dust, but also W and C and their dust are highly reactive and could produce large amounts of hydrogen. Ignited by a spark or a hot surface an oxyhydrogen explosion could occur. To prevent this, the amount of in-vessel hydrogen is limited and has to stay below a critical value.

Beside tritium, also radioactive dust, gas and other activated materials would be mobilised which are contained by a pressure suppression system or an expansion volume in the simulations. However, there is always leakage in such systems (3% per day in the simulation) and a perfect containment thus impossible. The escaping radioactive material is most dangerous, when it is not distributed in the atmosphere broadly but concentrated in a small area around the fusion plant e.g. due to rain and weak wind. Therefore the calculation assumes such a worst case weather and estimates the **radioactive dose** at the fence of the power plant, which is most probably the place with the maximal dose. Again different values result depending on the reactor type, mainly on the containment system, with doses of 1.2-18 mSv, while the average annual dose is ca. 2 mSv from natural and 2 mSv from anthropogenic sources\*. The doses are comparable to a computer tomography examination which has doses of 2 to 10 mSv depending on the organ analysed. The population evacuation limit recommended internationally and applied in most countries is at 50 mSv. However, a larger leakage of the containment system or its failure due to hardware failure or due to external reasons like an extraordinary strong earthquake, plane crash, a rocket, a comet etc. are conceivable. The released tritium amount and overall dose would be much larger in such an event as not only the in-vessel inventory could be mobilised but also parts of the much larger inventories in the structural material, fuel cycle or the T storage. Estimations for such a case of damage predict the release of up to 1 kg T, which would result in a dose of up to 450 mSv per week through inhalation and radiation in a 2 km<sup>2</sup> sector in the wind direction, assuming constant wind from one direction [Milch2, p.33]. However, to mitigate accidents by in-plant energies with potential release of in-vessel T and the risk of an explosion of oxyhydrogen, the in-vessel inventory is limited to ca. 1 kg. Thus the total T inventory of a fusion power plant with 1 GW electric output is estimated to at least 15 kg, which is one order of magnitude less than other artificial T amounts e.g. in nuclear weapons or the T emitted in their tests.

Further issues which endanger plasma operation can be caused by hydrogen retention in general such as structural changes in the wall through hydrogen blister growth, enhanced wall erosion etc. Fuel retention also influences the fuel cycle, tritium breeding, plasma fuelling etc. and thus hampers the T cycle and diminishes the T self-sufficiency of the whole power plant. But the most serious safety issue for the "development of a fusion reactor is unacceptable long term retention of the fuel" itself [Z11].

---

\*data for Germany; The anthropogenic sources are nearly completely dominated by medical applications.

### **Retention monitoring**

The main aim is the **minimisation of tritium retention**. Thus "measurement and control of long term tritium retention is one of the most critical issues for ITER and future fusion devices." [Z11] Secondary aims are the reduction of hydrogen retention of all isotopes and mitigation of its effects. In order to achieve these goals, especially to obey the tritium limit, the measurement of the total retention alone may be insufficient. Such global measurements – the so called gas balance – can be done by exact detection of the tritium input at the fuelling valves and output at the vacuum pumps. But, additional knowledge of the spatial hydrogen distribution and its local growth or depletion rate would be optimal. Only this allows to identify the crucial retention areas as well as plasma scenarios and wall conditions with low retention. This also shortens time for tritium cleaning procedures, as they can be assessed by the local retention diagnostic and thus can be applied more efficiently. "In order to have a solid base for the tritium retention behaviour in the activated phase of ITER, a detailed analysis of fuel retention is needed already in the non-activated phase, to prove the predictions on retention and to qualify the tritium control schemes." [Z11] "As a prerequisite, a space-resolved diagnostic to **monitor fuel retention** is required", which at best can measure retention during plasma operation and without wall tile removal [Z11b]. "The vast majority of data on fuel retention in present devices is based on post-mortem analyses", i.e. "when tiles are taken out of fusion devices after a certain time of operation, averaging thus normally over a variety of wall and plasma conditions. These measurements become more and more difficult with actively cooled tiles, which are activated" by neutron radiation and tritium retention [Z11]. Beside the nuclear toxicity, there is also chemical toxicity due to beryllium dust and volatile tungsten oxides. Therefore tile removal for post-mortem analysis becomes difficult and time consuming.

Laser based methods like laser ablation and desorption [Miller98] can be combined with spectroscopic methods to overcome these problems. Laser Induced Ablation Spectroscopy (LIAS), Laser Induced Breakdown Spectroscopy (LIBS) and **Laser Induced Desorption Spectroscopy (LIDS)** are under development to provide an in situ diagnostic for fuel retention and the surface material composition [Huber11], [Gierse11, b][Gierse14, b], [Philipps13]. Such laser based methods give access to the wall characterisation inside the reactor. LIDS is directed to measure the fuel retention and has been developed in TEXTOR (Tokamak EXperiment for Technology Oriented Research)\* to provide a tool to monitor the hydrogen inventory of the first wall in situ. The terms "in situ" and "ex situ" are used in the present work from the viewpoint of fusion application. "In situ" methods are measurements inside the main plasma chamber during plasma operation. "Ex situ" methods usually require the removal of wall elements and consecutive analysis in a special laboratory or at least a plasma operation shutdown. Laser induced desorption can be used in both ways. In both cases the diagnostic is based on rapid laser heating of a small spot and consecutive detection of the thermally released hydrogen. The detection and quantification of the released hydrogen amount can then be done either by mass spectrometry (in case of the ex situ method **LID-QMS**) or by spectroscopic detection of hydrogen Balmer line emission in the plasma (in case of the in situ method **LIDS**). The present work concentrates on the processes occurring during Laser Induced Desorption and its utilisation as a hydrogen retention diagnostic. In earlier works ([Schweer4], [Schweer9], [Irrek4], [Irrek8]) first applications of this method in TEXTOR, JET and in laboratory experiments have been presented. Later, an improved laser system was used and the method has been explored qualitatively and quantitatively on thin ( $d < 500$  nm) a-C:H layers on graphite [Irrek8]. It was shown that the method is able to measure the hydrogen content of such layers on graphite in TEXTOR, which were in reasonable agreement with ex situ measurements by LID-QMS on the same samples.

---

\*TEXTOR was the main plasma device in FZ Jülich from 1983-2013 see [www.fz-juelich.de/fusion],[Samm5]

---

In the present work, the application of LID is extended to hydrogen retention of thick a-C:H layers, C and W bulk material and C/W mixed materials. The studied C materials are graphite or carbon-fibre-composites (CFCs). Moreover, a new observation system has been tested, in which the detection path is always coaxial with the laser beam path and thus LIDS can be applied from a single plasma access port. Additionally, curved metallic mirrors are used in this setup instead of lenses, which would degrade by the neutrons emitted by the fusion reaction. Due to these advantages, the principle of this new setup can be used to apply LIDS on fusion devices like ITER.

The first chapters discuss the processes involved in LID until the release of the hydrogen. In **chapter 2** first the general design of the laser beam path is shown, which is used in the LID-QMS and LIDS setups and how to obtain a homogeneous laser beam profile. The laser beam is characterised in space and time and the optimal laser pulse parameters are shown. Which materials can be heated and why, is discussed thereafter and how the laser light is absorbed and converted to heat is described including the underlying physical processes of laser absorption and heating. In the final section the heat propagation in different materials is elaborated by analytical calculations (in 1D) and numerical simulations (in 3D) in comparison to measured temperature evolutions during the laser pulse. First, the homogeneous and isotropic W bulk material and graphite are discussed, before anisotropic heat propagation in CFCs demonstrates how the laser pulse properties have to be adjusted for every material and even each material orientation. At the end, heating effects that have to be taken into account for a-C:H layers and C/W mixed layers are pointed out, where temperature measurements during LID can additionally provide detection and analysis of such layers.

Surface modification or even surface destruction are a direct consequence of heating and are thus depicted and explained in **chapter 3**. Which surface modifications are avoidable and which are unavoidable on the different materials is discussed. For thin a-C:H layers the D depletion is also shown already here as it is closely compared to C depletion. How heat propagation, desorption and surface modifications change for thick a-C:H layers is shown on representative examples already hinting to a limitation of LID capabilities in some cases. For W also a detailed characterisation of the melting process, crater formation and rapid solidification with their morphological consequences is included. Additionally, LID on a highly porous sponge-like tungsten material called fuzz is shown, as such a material could be formed in future fusion reactors. As tungsten is not only used in bulk form for the first wall but also as a thin layer on a C substrate, the impact of LID on such materials closes this chapter.

With the knowledge of the heating process and potential structural modifications, the most important physical processes of hydrogen diffusion and desorption can be treated in **chapter 4**. Here the rather theoretical background for the understanding of the experimental results is laid with the help of numerical simulations of the hydrogen dynamics during the applied laser pulses. Especially the qualitative differences between W and C materials are shown and the explanation, why on W laser heating without melting is often insufficient for complete desorption. Details for the much easier hydrogen desorption from graphite and a-C:H layers are discussed on an important example measurement of a real long-term tokamak sample from TEXTOR demonstrating how much LID agrees with TDS and other methods.

Then the ex situ method LID-QMS for quantification of the released gases is discussed in **chapter 5** with pointing to precautions that have to be obeyed for an undistorted measurement. How to calibrate the QMS in a way that is most similar to the subsequent measurement procedure and is therefore specially adapted to LID will be described. How the acquisition, interpretation and evaluation of the QMS spectra is performed and the accuracy of the ex situ method follow.

The application examples of this method in **chapter 6** go beyond the already shown and quite routine a-C:H/graphite examples towards W by analysing a TEXTOR-produced C/W mixed layer by several methods. The long second section concentrates on bulk W itself, starting with a study that shows, how the optimal laser parameters for W were found experimentally. To thoroughly test the method and the understanding of diffusion and desorption, bulk W samples were exposed under a large variety of exposure conditions. Five different plasma devices from a glow discharge (PADOS), ECR plasma (PlaQ), a linear plasma (PSI-2) to a tokamak plasma (TEXTOR) and even a linear plasma reaching ITER fluxes (Pilot-PSI) were used providing orders of magnitude difference in plasma flux and different conditions. How the experiments can be explained with the previously described theory and simulations is summed up in the end of this section. The third short section presents the retention measurement of the already known tungsten fuzz sample pointing rather to future applications of LID and still open questions in retention physics.

LID-QMS is a stand-alone diagnostic method for quantification of adsorbed gases in solids and has been used as prerequisite and supporting method during development and application of LIDS. This is the more important method for fusion applications, which detects the released hydrogen spectroscopically during plasma operation and is described in **chapter 7**. After an introduction of the conditions at TEXTOR, the LIDS setup and calibration, the measurement procedure and background issues are discussed. The temporal aspect of the LIDS light emission is discussed and the background of the deduction of the quantification factors is presented including a comparison of measured and numerically simulated LIDS light. The question how well reproducible the LIDS signal is, was estimated by a dedicated experiment with a homogeneously hydrogen loaded sample. What is the lower and upper limit of detection and what are their reasons will then be described and evaluated, closing with the estimated accuracy of LIDS.

Throughout the description and explanation of the physical processes involved in laser desorption, examples and experimental results are given for illustration. Further application examples that observed the LIDS light emission from several directions simultaneously are presented in **chapter 8**. Finally a summary with conclusions and discussion is given.

Details on the material grades and a commented listing of the input file for the numerical simulation of the hydrogen diffusion and desorption during LID on W are provided in appendix.

## 2. Laser Heating of Different Materials

For a well defined desorption of hydrogen isotopes by laser pulses, the heating process has to be known and controlled as good as possible to achieve a high degree of desorption, but minimise target surface modifications or even damage. Therefore, the origin of surface modifications (chapter 3) and the basis of the desorption process (chapter 4) is the temperature development derived in this chapter.

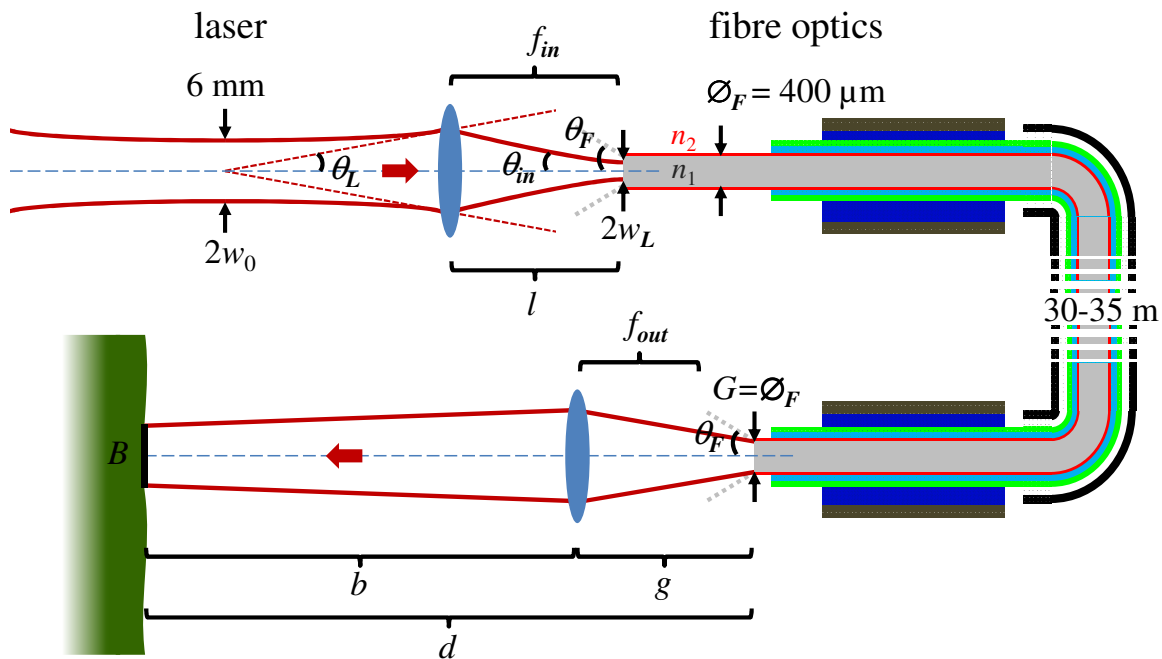
In the first section a description of the LID setup and technical aspects related to the guidance of the laser beam by fibre optics is given. Then the laser beam is characterised with special emphasis of the light intensity distribution and its temporal evolution on the target. In the third section the energy losses by reflexion on the target surface are discussed for many materials that have been studied by LID. Its knowledge is decisive for the calculation of the heating intensity and the initial laser power to be selected. In the fourth section the transformation of the remaining light energy into heat is depicted and the heat propagation in the material is discussed. Analytical calculations and numerical simulations are compared to the measured surface temperature development. Several heat diffusion examples are discussed, starting from homogeneous bulk material with isotropic heat properties (tungsten and graphite), proceeding with anisotropic carbon fibre composites and closing with hydrocarbon layers and mixed material layers of carbon and tungsten.

### 2.1. Laser Induced Desorption Setup

All laser desorption experiments described in the present work use the identical laser source. It is a commercial Nd:YAG laser from the LASAG company (FLS 352N-306) designed for cutting, welding and drilling applications. It produces a circular beam of 6 mm diameter at  $\lambda = 1064$  nm wavelength. The internal optical setup is a classical solid-state laser setup with only one additional aperture ( $\varnothing = 6$  mm) inside the resonator. The pumping source is a flashlamp, which is mounted on one focal axis of the cavity, that has an elliptical cross-section. The laser operates in pulsed mode with the pulse duration determined by the flashlight duration. It can be selected continuously via the laser control between  $t_p = 0.1$  and 20 ms. The repetition frequency ranges from  $\nu_p = 0.1$  to 1000 Hz. In addition, the voltage  $U_{laser}$  applied to the flashlamp can be varied. These three parameters ( $t_p, \nu_p, U_{laser}$ ) cannot be used in their full range simultaneously, because the laser control forbids potentially unsafe operation modes. Thus, they can only be chosen in such a combination, that none of the following thresholds is exceeded:

- The maximum energy of a single pulse is  $E_0 < 60$  J. This value is only reachable with new flashlamps and perfect optical alignment. Typically energies of 45-50 J were available.
- The single pulse power is limited to  $P_0 < 20$  kW and thus defines a lower limit for  $t_p$ . Therefore, maximum energy can only be obtained with longer pulses.
- The average power is limited to  $\bar{P} < 300$  W defining an upper limit for the repetition frequency.

The flashlight power is higher than these values because much of the broad light spectrum is unused for the electron excitation, thus, cavity, flashlamp, crystal etc. have to be cooled. The inner wall of the cavity is coated by gold for high reflectivity. Due to its elliptic geometry, the pumping light is focussed on the second focal axis, where the Nd doped YAG crystal (Yttrium aluminium garnet,  $Y_3Al_5O_{12}$ ) is mounted. The Nd atoms are the laser active medium, generating laser light at 1064 nm by electronic transitions in a 4-level system of energies. This infrared radiation is invisible, therefore a helium-neon (HeNe) pilot laser with visible red light at 630-640 nm is coupled into the resonator through the end mirror, which is the totally reflecting mirror for the IR light. It serves as alignment beam for all internal optical components during adjustment of the laser as well as for coupling into the fibre optics and targeting at the samples. After the light exits the resonator at the partly reflecting mirror, a small fraction is coupled out by a beam splitter into a small integrating sphere, from where it is guided via a fibre to a fast photodiode. This time resolved signal of the laser power is routinely recorded during the experiments for supervision of the lasing process (cf. chapter 2.2). Its time integral is a measure of the laser pulse energy. As an alternative to the flashlamp voltage, the pulse energy can be used directly as laser parameter. In this energy-controlled mode the voltage is automatically adjusted, hence the pulse energy stays inside a tolerance range around a preset energy value. This mode has not been used in the later stages of the work, because of the quite large tolerance range and a long adjustment time of the automatic control. Much better energy control is achieved by adjusting the capacitor voltage manually. There is also an automatic supervision of temperature to prevent overheating and damage of components. Further details on the internal laser setup can be found in [Irrek8].

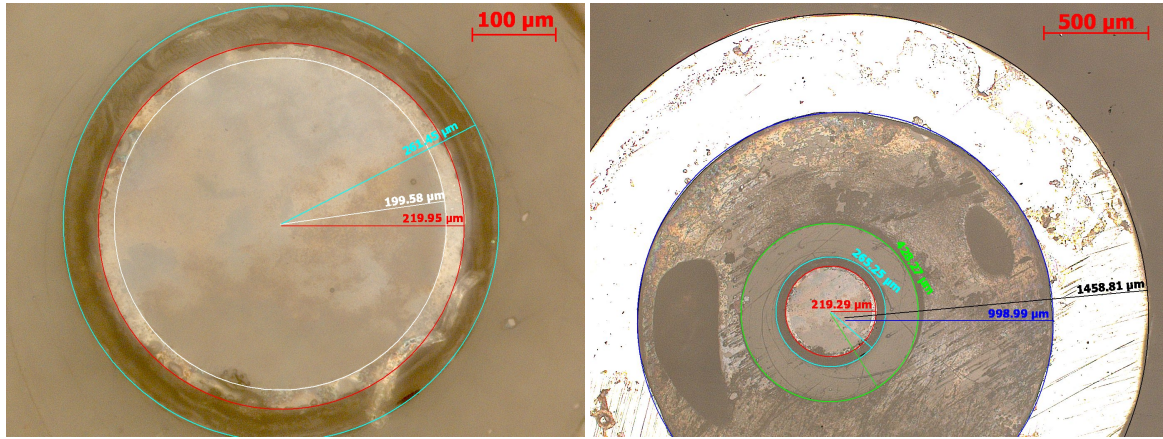


**Figure 2.1.:** General optical setup of the LID experiments; detailed setups for LID-QMS in figure 5.1 on page 126 and for LIDS in figures 7.1, 7.2 on pages 161–162

### Coupling into the fibre optics

The laser system has a small beam parameter product in the range of  $B_{pp} = 15\text{-}29$  mm mrad, in terms of the full-angle aperture and beam diameter notation. More common is the use of the half-angle  $\theta_L$  as the aperture angle and the beam radius  $w_0$  instead of the diameter (cf. figure 2.1). This definition will be used for the rest of the work. In this notation the beam parameter





**Figure 2.2.:** Cross-section of the laser fibre optics (Ceramoptec® WF 400/440 T); white: inner fibre core ( $n_1$ , silica,  $\varnothing 400 \mu\text{m}$ ); red: cladding ( $n_2$ , fluorine silica,  $\varnothing 440 \mu\text{m}$ ); Only these 2 parts of the fibre are remaining for the coupling-in of the laser light. cyan: silicone buffer ( $\varnothing 530 \mu\text{m}$ ); green: Tefzel coating ( $\varnothing 850 \mu\text{m}$ ); fibre embedded in two-component glue (dark blue circle, with air enclosures) and steel cylinder ( $\varnothing 3 \text{ mm}$ );  $N_A = 0.22$ ; attenuation  $< 1 \text{ dB/km @ } 1064 \text{ nm}$

product is defined as

$$B_{pp} = \theta_L w_0 = M^2 \frac{\lambda}{\pi} . \quad (2.1)$$

$\theta_L$  ... divergence half-angle of the laser beam in degree

$w_0$  ... beam waist, i.e. half of the minimal beam diameter in m

$M^2 = B_{pp}/B_{pp,Gauss}$  ... quality of the beam compared to an ideal Gaussian beam

In these terms the  $B_{pp} = 3.75\text{-}7.25 \text{ mm mrad}$ . A small  $B_{pp}$  is important for the setup of LID used in the present work, because the laser beam is coupled by a lens into an optical fibre shortly after the laser output and guided to the LID experiments. For a complete coupling of the laser pulse energy into an optical fibre, the  $B_{pp}$  must not exceed a certain value, determined by the properties of the fibre. The reason is, that a lens cannot focus a laser beam to an ideal point as assumed in geometrical optic approximation, but only to a finite circle with radius  $w_L$  with

$$w_L = 2 \frac{B_{pp}}{\tan \theta_{in}} . \quad (2.2)$$

where  $\theta_{in}$  is the half-angle of the light focussed by the lens into the fibre. The minimal beam diameter  $2w_L$  has to be smaller than the diameter of the inner core of the fibre  $\varnothing_F = 400 \mu\text{m}$  (cf. figure 2.2) in order to achieve complete coupling. Therefore the beam parameter product has to be smaller than the threshold

$$B_{pp} \leq \frac{1}{4} \varnothing_F \tan \theta_{in} . \quad (2.3)$$

The fibre diameter could be increased slightly, but not much, because the spot size on the target is limited in order to obtain the necessary power densities. A compensation by a lower magnification for the imaging of the fibre to the target would need extremely large lenses or mirrors in diameter and focal length, which is expensive and difficult. The maximum value for  $\theta_{in}$  is limited by the acceptance angle that the fibre allows without energy loss. The laser fibre used in the present work has a numerical aperture of  $N_{A,F} = \sin(\theta_F) = 0.22$ . This is equivalent to the acceptance or aperture half-angle  $\theta_F = 12.7^\circ$  (cf. table 2.1). Light with a larger angle of

incidence cannot be coupled into the fibre. For  $\theta_{in} = \theta_F$  the maximal  $B_{pp}$  of the laser beam is therefore **22.6 mm mrad** = 22.6  $\mu\text{m}$ .

In order to realise the angle of  $12.7^\circ$ , a focal length of the lens of  $f_{in} = 13.3$  mm would be needed, which directly follows from the laser beam radius of 3 mm. However this is operation with maximal  $B_{pp}$  which is shown below to lead to strongly inhomogeneous energy distributions in the laser spot. An optimised coupling discussed in the next section shows that a much more homogeneous energy distribution is achieved with  $f_{in} = 30$  mm, which corresponds to an angle of incidence of  $\theta_{in} = 5.7^\circ$  ( $N_{A,in} = 0.10$ ). This allows – according to equation 2.3 – a maximum beam  $B_{pp}$  of **10 mm mrad**.

Therefore the choice of a laser system with a small beam parameter product is important. This has been taken into account already for the choice of the laser wavelength for the LID applications, leading to the choice of a relatively short laser wavelength. According to equation 2.1, the  $B_{pp}$  increases linearly with  $\lambda$  and would be one order of magnitude larger e.g. for CO<sub>2</sub> lasers, at the same beam quality  $M^2$ . Exceeding both threshold values discussed above, it would be impossible to couple a beam with 10 times larger  $B_{pp}$  into the same fibre without significant energy loss. The disadvantages of a larger fibre diameter and coupling angle have already been mentioned. With the best beam quality achievable with the laser system ( $M^2 = 11$ ), the maximum wavelength for lossless coupling would be  $\lambda = 6.4$   $\mu\text{m}$  and 2.8  $\mu\text{m}$ , if the preferred coupling for a homogeneous energy distribution is used.

The divergence  $\theta_L$  itself is only important, if the light is propagating a long way as a beam, e.g. when guided by mirrors. But in all setups no long free beam path exists due to the use of fibre optics and thus no far field effects like beam divergence are relevant.

### Coupling out of the fibre optics

In many other fibre optics applications the light propagation out of the fibre is governed by the numerical aperture of the fibre, because there the light uses the full aperture at the fibre exit. In the LID experiments the light divergence at the fibre output is not determined fully by the fibre properties. The main parameter is the coupling half-angle  $\theta_{in}$  at the coupling of the light *into* the fibre (coupling convergence). It is determined by the focal length  $f_{in}$  of the lens which couples the beam into the fibre. Therefore the numerical aperture of the laser light at the fibre output is e.g. for  $f_{in} = 30$  mm,  $N_{A,out} = 0.126$  and thus significantly smaller than the numerical aperture of the fibre ( $N_{A,F} = 0.22$ ) (cf. table 2.1). In terms of the corresponding divergence half-angles, the light enters the fibre at  $5.7^\circ$  and exits with  $7.2^\circ$  not using the full  $12.7^\circ$  provided by the fibre optics.

These values have been measured with burn patterns of the laser light onto a photosensitive paper a few centimetres after the fibre output. The divergence at the end of the fibre is a few degrees larger than the beam convergence into the fibre and depends on that. It is significantly lower than the fibre aperture and thus not limited by it. This property is best explained by the low amount of reflexions inside the fibre, which has two reasons: 1<sup>st</sup> the relatively short fibre lengths of 30-35 m and 2<sup>nd</sup> a fibre path layout with long straight parts and curves of large radii.

## 2.2. Laser Pulse Properties

The properties of the laser pulse at the target have to obey certain conditions in order to heat the material in a defined way. Ideally, the desired heating would be heating of a simple geometric fraction (e.g. a cube or a cylinder) of the target to a defined, homogeneous temperature in a linear time trace. A freely defined time duration of constant temperature would follow. The cooling phase after the laser pulse would ideally be the same as the heating phase, but

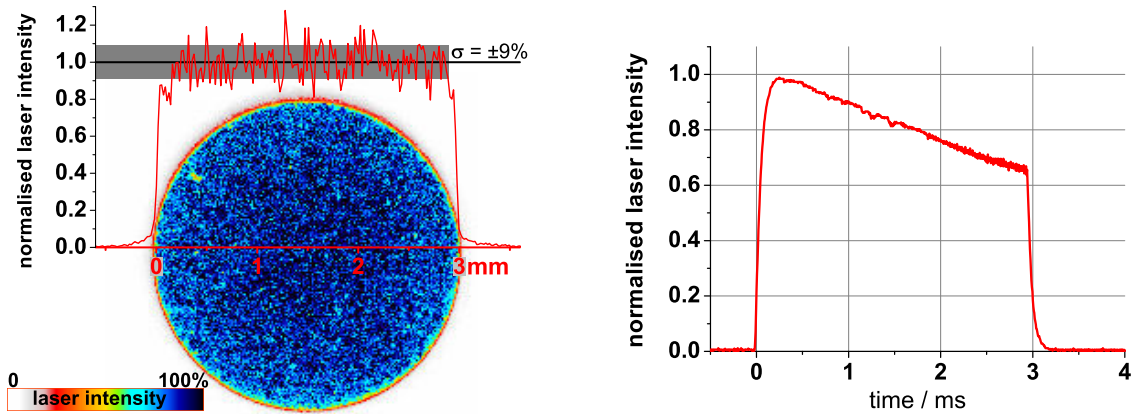
a) coupling in			b) coupling out		
$f_{in}$	$N_{A,in}$	$\theta_{in}$	$f_{in}$	$N_{A,out}$	$\theta_{out}$
mm		degree	mm		degree
13.3	0.22	12.7			
20	0.15	8.5			
25	0.12	6.8			
27	0.11	6.3			
<b>30</b>	<b>0.10</b>	<b>5.7</b>	<b>30</b>	<b>0.126</b>	<b>7.2</b>
40	0.075	4.3			
60	0.050	2.9	60	0.05-0.075*	2.9-4.3*
80	0.037	2.1	80	0.082	4.7

**Table 2.1.:** a) Beam convergence for coupling into fibre (geometrical optic approximation) and b) measured beam divergence for coupling out of the fibre for different focal lengths of the lens before the fibre; the corresponding numerical aperture and half-angle are given accordingly; \* = values from [Irrek8, p.69]

inverse, returning to the initial temperature. This simple scenario would have the advantages of a known heated area on the surface and a known heated volume inside the material. Additionally, the temperature increase and decrease would be described by simple functions and no temperature gradients would occur within the heated part of the sample. Although this scenario is not realistic, it helps to define the conditions, which the laser pulse has to fulfil to realise a heating as close as possible to this ideal scenario. Some laser properties have no significant importance for the purpose of heating the material. Nevertheless they can have influence on the laser heating process in some cases and are therefore shortly mentioned:

- The spatial and temporal coherence of the light and the resulting constant phase relationship are neither beneficial nor disturbing.
- Polarisation is not needed and does not have to be taken into account, if the laser beam is perpendicular to the surface. But if it is polarised and the angle of incidence substantially differs from  $90^\circ$ , then polarisation may be in some cases important for the amount of reflected light. In this case the reflectivity has to be known for the parallel and perpendicular light component. The laser used in the present work has been investigated for any remaining linear polarisation component after the transmission through the fibre optics and lenses. No significant deviations from the average light intensity was found in any direction and therefore polarisation effects are not considered further.
- In principle also the wavelength and the monochromatic properties are unimportant for the heat generation, but the wavelength together with the optical properties of the material determines the laser absorption depth. It would be desirable to extend this energy deposition depth beyond the hydrogen retention depth. However, the latter can vary between nanometres and centimetres depending on the retention conditions. An adaptation of the energy deposition depth is hardly feasible, but this is not a strong drawback, since the heat source can be shallow as long as heat conduction is good enough to heat the hydrogen retaining volume sufficiently. This is the case for the materials studied in the present work.

The important properties of the laser beam can be divided into two categories: spatial and temporal.



**Figure 2.3.:** Optimised spatial distribution (left) and temporal development (right) of the intensity of a 3 ms,  $\varnothing$ 3 mm Nd:YAG laser pulse after transmission through a 35 m long optical fibre of 400  $\mu$ m core diameter, imaged by a lens onto a CCD camera chip; The spatial distribution is normalised to the average value of the plateau region. figure already published in [Z13]

### **Spatial laser intensity distribution**

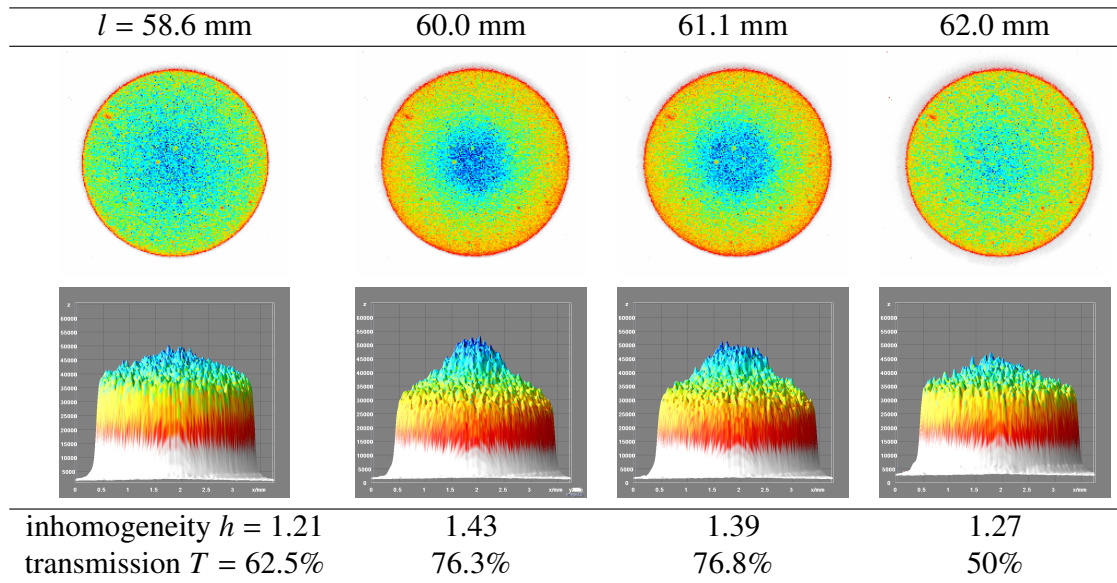
To heat a defined volume in a controlled way, the ideal spatial light intensity distribution on the heated surface should have a top-hat shape. This distribution is zero outside the circular or elliptic footprint of the laser and constant inside. With the fibre based setup described above, a top-hat profile can be approximated very well due to the intrinsic properties of fibre optics. Due to the internal total reflexion at the fibre cladding and multiple reflexions inside the fibre, a sharp border of the light distribution is realised. However, this fibre effect is not strong enough to generate the top-hat distribution at the fibre end for any arbitrary intensity distribution injected into the fibre. A particular coupling of the light into the fibre is necessary, as will be shown below. With this, a nearly top-hat like laser intensity distribution is achieved, which is confirmed by imaging the fibre end with a lens onto a CCD camera chip (cf. figure 2.3). This is exactly the setup as used for LID in the ex situ version (cf. chapter 5). Thus the light intensity distribution on the CCD detector is identical to the one which is incident on a desorption sample. The only difference is, that the power density has been attenuated by neutral density filters in front of the CCD detector. The overlaid profile (red line) in figure 2.3 represents the unsmoothed profile with a vertical width of 1 pixel ( $\cong 17.7 \mu$ m) along the horizontal diameter as marked by the x-axis. The same is valid for the 1D profiles in the following figures in this section. The sharp edges are excellent for the purpose of LID. The standard deviation  $\sigma$  of the light intensity inside the laser spot is only 9% of the average value. This homogeneous distribution is well suited for controlled heating. The small intensity variation leads to a surface temperature variation of only ca. 150 K at 2000 K final temperature, which is insignificant for most applications.

The general profile, i.e. the sharpness of the edges and larger-scale deviations do not change significantly for different pulse durations and energies. Only the spike positions change to some extent on a shot-to-shot basis, apart from some structures which originate from the fibre optics itself. E.g. the intensity reduction at the upper left (yellow-red area in figure 2.3) is immobile because it is due to a tiny damage of the fibre end surface, which can be seen under magnification. The intensity excursions discussed here are small – rather a noise on a constant intensity. With other laser systems excursions by a factor of 4 or more can occur, an example can be seen in the first row of figure 2.7 on page 40, which displays the light distribution of

the pilot laser (a cw HeNe laser). Although the spike positions change during the laser pulse, no sufficient homogenisation of the incident energy by this effect is reached. Such inhomogeneous laser energy distributions do not allow controlled, homogeneous heating, since some areas are not heated enough and others may be overheated leading to evaporation and even plasma formation [Schweer4]. Thus the choice of a laser with low spiking is decisive. Such spatial spikes do not appear with the laser system used in the present work, but the optical path and optical components on it also change the light intensity distribution. Especially fibre optics have many potential influences. Several influences have been tested therefore by changing only one parameter in the light path from laser to target (in this case the CCD detector) including the

- laser pulse energy
- laser pulse duration
- rotation of the lens along the optical axis
- form of the lens (plan-convex, biconvex, achromatic) and orientation
- winding direction and curvature of the first 3 m and last 2 m of the fibre, staying above the minimum curvature.

All these factors had hardly any measurable effect on the light intensity distribution.



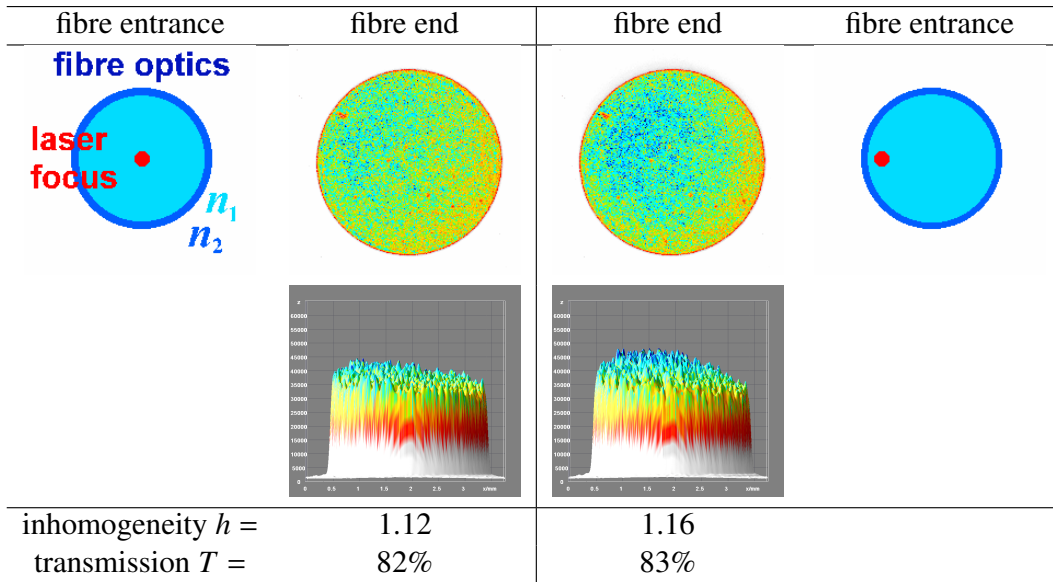
**Figure 2.4.:** Dependence of normalised spatial laser profile on lens-fibre distance  $l$ , CCD data (2D images) and smoothed 3D side views,  $h = \overline{I_{peak}} / \overline{I_{total}}$ ,  $T = E_{target} / E_{laser} = E_1 / E_0$ ,  $f_{in} = 60 \text{ mm}$  achromatic lens optimised for HeNe+Nd:YAG with AR 0.5%

In order to measure the quality of the laser light distribution, 2D images have been taken and normalised to the intensity maximum  $I_{max}$ . In addition a side view of the intensity in a 3D image with a weak smoothing will be displayed below the 2D image which helps in the interpretation of the homogeneity. The smoothing is identical in all data.

For quantification of the inhomogeneity, a peak intensity  $\overline{I_{peak}}$  has been defined as the average intensity on a circle of 8% of the total spot area. The position of the circle was located such, that the average value was maximal. The inhomogeneity  $h$  has been defined as the ratio of this peak intensity and the average value of the whole laser spot  $\overline{I_{total}}$  (truncated below 10% of  $I_{max}$ ). For the ideal top-hat distribution the inhomogeneity would be  $h = 1.00$ . The following aspects have an influence on the spatial laser profile:

## 2. Laser Heating of Different Materials

- The focal point size at the entrance of the fibre has a strong influence on the distribution (cf. figure 2.4). The focal point size has been varied changing the distance  $l$  between the focussing lens and fibre. The measurements were done with an  $f_{in} = 60$  mm coupling lens. This peaking effect can be avoided, if an optimised focal length is used, i.e. a lens that yields a top-hat profile ( $f_{in} = 30$  mm, see below).
- A change of the position of the focal point at the fibre entrance (varied by lateral movement of the fibre mounting and/or lens mounting) results in a slight shift of the intensity maximum (cf. figure 2.5).

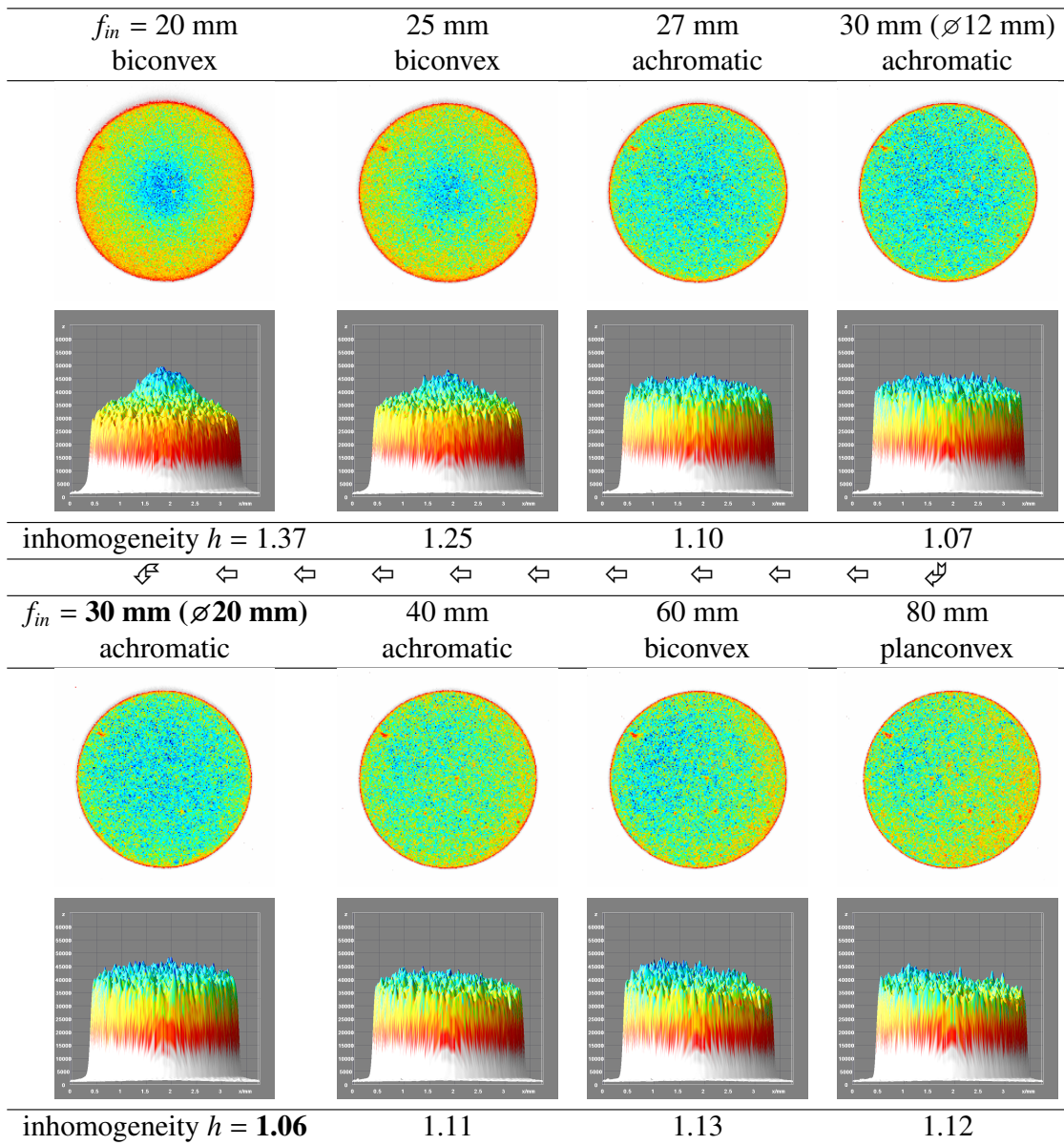


**Figure 2.5.:** Spatial laser profile optimisation, dependence on focal position at the fibre entrance, coupling lens with  $f_{in} = 80$  mm; legend: cf. figure 2.4

- These effects can be excluded by the choice of a lens without peaking effect and positioning of the laser focus in the centre of the fibre. For the fibre used in the present work, the peaking effect disappears for a focal length of  $f_{in} = 30$  mm (cf. figure 2.6). For this optimal focal length, achromatic 2-lens combinations and single biconvex lenses have been tested without significant differences. The achromatic lens with a larger diameter  $\varnothing = 20$  mm results in a slightly better homogeneity than a smaller achromatic lens with  $\varnothing = 12$  mm due to lower incident angles of the outer beam rays on the lens.

The overall result of the optimisation of the spatial profile is, that the focal length of the coupling lens must be fitted to the properties of the fibre optics used, which is a 30 mm focal length here. Other lengths result in a peaked intensity distribution (cf. figure 2.6), whose position is sensitive to the position of the focal point and its size (cf. figures 2.5, 2.4).

Using the optimal lens ( $f = 30$  mm achromat,  $\varnothing 20$  mm) with a low inhomogeneity of  $h = 1.06$ , the depth of focus has been studied (cf. figure 2.7). This demonstrates possible errors due to uncertainties of the distance to the target. The sharpness  $S$  has been defined as the slope of the spot border on the 1D radial profiles (bottom row). The focal depth is extremely short and thus the sharpness already decreases by a factor of 2.5, when the target is only 5 mm out of focus. The optimal distances to get a sharp image for the 3 mm and the 2 mm diameter spot are listed in table 2.2. It can be concluded, that an optimal focal length for coupling the light into the fibre, results in a top-hat laser profile which is robust against moderate changes of focal position and size on the fibre entrance.

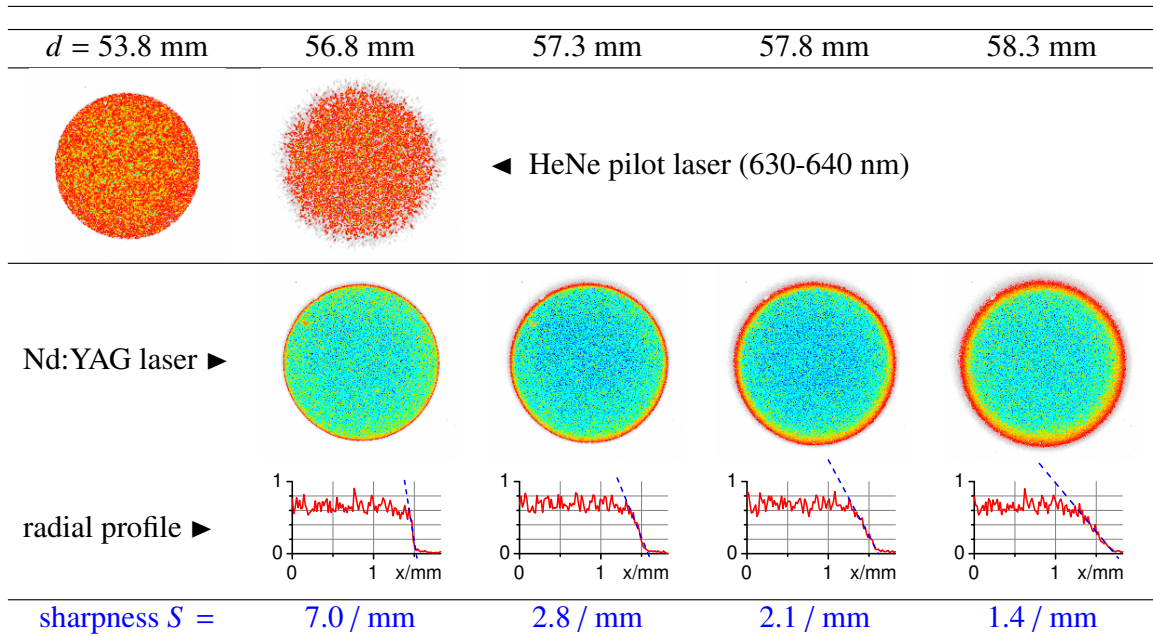


**Figure 2.6.:** Spatial laser profile optimisation, dependence on focal length of the coupling lens  $f_{in}$ , legend: cf. figure 2.4

image size $B$	magnification	object distance $g_{Nd}$	image distance $b_{Nd}$	$d_{Nd}$ $= g_{Nd} + b_{Nd}$	$d_{HeNe}$
2.0 mm	5×	7.2 cm	36.1 cm	43.3 cm	41.6 cm
3.0 mm	7.5×	6.7 cm	50.1 cm	56.8 cm	53.8 cm

**Table 2.2.:** Optical distances for imaging the fibre end (object size  $G = 400 \mu\text{m}$ ) with an achromatic lens of  $f_{out} = 60$  mm to the image size  $B$  on the target;  $d$ : fibre-target distance for the heating laser (Nd:YAG) and the pilot laser (HeNe)

## 2. Laser Heating of Different Materials



**Figure 2.7.:** Dependence of spatial laser profile on fibre-target distance  $d$ ; achromatic lens  $f_{in} = 30$  mm,  $\varnothing 20$  mm; colour scale like in previous figure; legend: cf. figure 2.4

Figure 2.7 also shows that the achromaticity of the in-coupling lens is not optimised for the wavelengths of the pilot beam (630-640 nm) and the Nd:YAG beam (1064 nm). The sharp image occurs 3 cm closer to the lens for the pilot beam than for the IR beam, because shorter wavelengths are refracted stronger. Therefore, focussing with the pilot laser at such distances is impracticable, except chromatically corrected lenses for these wavelengths (like the  $f_{out} = 60$  mm lens) are used for the whole light path. Moreover, the pilot beam is slightly smaller than the Nd:YAG beam by a factor of 1.09. Nevertheless, the pilot beam is very helpful for aligning purposes.

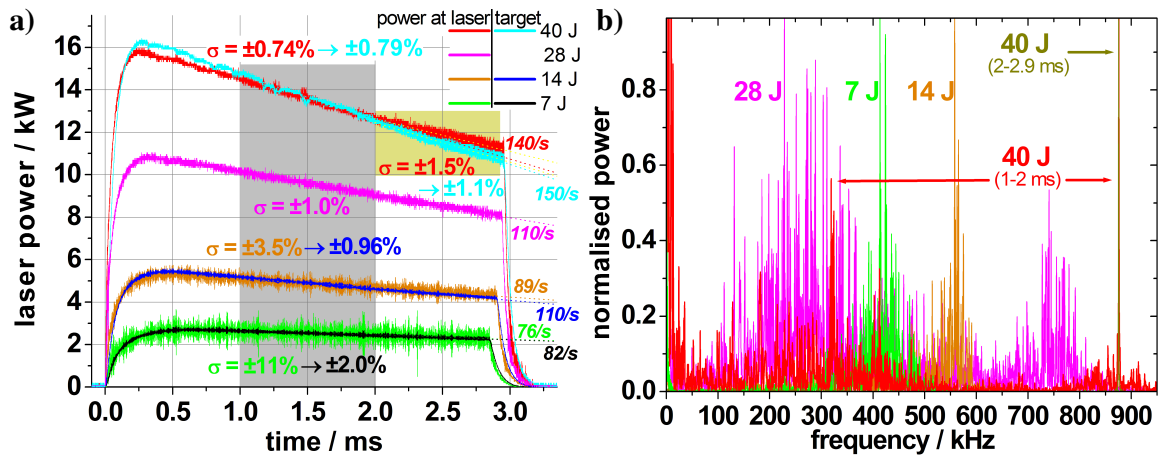
The reason for the inhomogeneities, the peaking effect and the tilted intensities for the long focal lengths is the relatively low number of reflexions inside the fibre. Increasing its length and more bends would probably yield a more homogeneous profile.

### Temporal laser intensity development

Of equal importance as the spatial light distribution is the temporal evolution of the laser pulse. Many lasers have a spiking output that consists of sharp peaks. For example, desorption has been first attempted at TEXTOR and JET with strongly spiking lasers with very similar mean pulse powers as used here (e.g.  $460 \text{ MW/m}^2$ ), but with temporal spikes up to  $6.6 \text{ GW/m}^2$  [Schweer4]. This led to the use of a laser with a smooth temporal waveform as most important property for its choice for desorption applications. Nevertheless, the temporal fluctuations have been analysed by monitoring the light intensity of a small fraction of the laser beam, which is reflected out of the main laser beam by a beam splitter, homogenised in an Ulbricht sphere and guided by a fibre to a diode. This calibrated signal is automatically integrated by the laser control unit and displayed as the laser pulse energy. In addition, a second photodiode with a fast time response has been installed on the other side of the fibre, measuring the light intensity of the beam after reflexion on a window (cf. figure 2.8), which represents the waveform at the target. It has been scaled to match the integral of the signal at the laser.

Both photodiodes have a time response fast enough to resolve the laser spikes and are sampled with 50 MHz. The relative spike amplitude is highest for low laser powers ( $\sigma > 10\%$  of the average power), but reduces quickly to 1% at about half of the maximum power,





**Figure 2.8.:** a) Temporal laser pulse form at the laser and target (up-scaled) for energies of  $E_0 = 7\text{-}40$  J. In the marked regions the standard deviation  $\sigma$  of the fluctuations, the slopes (normalised to the laser power) and Fourier transformations (b) are calculated.

where it is practically spike-free. For powers close to the maximum the remaining oscillations tend to increase towards the end of the laser pulse (cf. yellow marked area in the figure). Sporadically slight sudden increases of the oscillation amplitude occur for short time durations (ca. 0.1 ms). Comparisons of the waveforms before and after the optical fibre show that they are identical in shape, only shifted slightly in time due to the runtime of the light and electrical signals. The oscillation amplitude is significantly reduced by the fibre transmission. This effect is especially present for high initial oscillations and vanishing for already smooth waveforms.

Since the signals before and after the fibre have the same form except for the different spike amplitudes and a small shift in time, their Fourier transformations are identical. Only slight differences occur in the very low Hz region due to the differences described. Therefore only the Fourier transformations of the signals at the laser output are shown (cf. figure 2.8b). The signals have a bandwidth of  $\Delta\nu \approx 50$  kHz for low and medium laser power, increasing to several hundred kHz for high laser power. While at low power one main frequency region in the range of 400-600 kHz occurs, it splits into two main regions above and below this range for medium powers. At the same time the bandwidth of the low frequency hill increases. At the end of the laser pulse with the highest energy a transition to a single-mode oscillation of 876 kHz prevails.

The pulses have a rise time of roughly half a millisecond, after which a linear plateau starts. With increasing laser power the slope of the plateau region increases in absolute values and also if normalised to the laser power (cf. numbers in the figure). The normalised slopes increase only by a factor of roughly 2 from low to high pulse energy. The final decay of the laser pulse power has a similar time constant as the rise. The pulse rise and decay is also independent of the pulse duration. For longer pulses the slope in the plateau phase is just continued, following a linear function.

Two standard pulse lengths are used for desorption in the present work. For LID on graphite with thin a-C:H layers, a pulse length of 1.5 ms was chosen as optimum, after [Irrek8]. This choice was based on the wish to have the highest temperature gradient across the laser spot edge at the maximum temperature necessary for desorption, i.e. the 900 K isotherm. With this condition, the desorption process is optimised for spatial sharpness. The standard laser pulse ( $700 \text{ MW}/\text{m}^2$  absorbed intensity for 1.5 ms) results for graphite in a final temperature of  $(1500 \pm 200)$  K. The range in the laser intensity is due to different laser reflexion values on

different surfaces and different layer thicknesses (cf. next section).

Due to significantly increased reflexion on tungsten surfaces and due to the qualitatively different desorption behaviour of hydrogen from W (cf. chapter 4), higher pulse energies have been used for W.

For tungsten materials a pulse duration of 3 ms has been selected because the laser delivers the highest heat flux factor  $I\sqrt{t}$  and hence the strongest heating at 3 ms pulse length. Beside this technical reason, the desorbed deuterium fraction is highest at this pulse length (cf. chapter 2.4.1). The maximum intensity is also determined by the laser spot size, which had to be large enough to release enough hydrogen to be detected. This trade-off between high laser intensity and large spot size resulted in a 3 mm diameter spot. Therefore the standard heating pulse for W has been chosen to be **500 MW/m<sup>2</sup> absorbed intensity for 3 ms**, yielding a temperature increase of  $\Delta T = 1600\text{-}1700$  K. To reach even melting of W, the spot size has been reduced and pulse energy increased further. For W melting, the full laser power has been used, reaching absorbed intensities of 1.6-1.8 GW/m<sup>2</sup> on a 2 mm diameter spot.

### 2.3. Laser Reflexion and Absorption

Before the laser light can heat the target, it is diminished by several mechanisms. The energy losses in the optical path will be described in chapter 5. The final energy loss is due to reflexion of the laser light on the target, which is crucial to know, if a desired surface temperature has to be reached accurately. This is for example important for thick hydrogenic layers, because a certain temperature should not be exceeded to avoid sublimation and layer disintegration. The total reflectivity  $R_{tot}$  of a surface is the sum of the specular reflectivity  $R_{sp}$  and the diffuse reflectivity  $R_{dif}$ :

$$R_{tot} = R_{sp} + R_{dif} \quad (2.4)$$

The measurement of the total reflectivity also provides a direct measurement of the emissivity  $\varepsilon$ , because for materials without light transmission at the rear side, the following holds:

$$\varepsilon = 1 - R_{tot}. \quad (2.5)$$

For the materials studied, all three reflectivity components have been determined with a spectrophotometer (Lambda 950 from PerkinElmer company) in the wavelength range of 250-2500 nm. This two-beam device (one measurement beam and one reference beam) measures the total reflectivity of a sample by integrating the reflected light in a nearly fully closed Ulbricht sphere. By removing the wall fraction of the integrating sphere where the specular reflected beam impinges, the diffuse reflectivity can also be measured. The specular reflectivity is calculated from these two by subtraction. Although the only laser wavelength used in the present work is the fundamental Nd wavelength at 1064 nm, the full accessible spectral range has been scanned, since this information is useful e.g. for the application of the second (532 nm) and third harmonic (355 nm) or other laser types. The diffuse reflectivities are not shown here, since only the total reflectivity is necessary for the heating process. Nevertheless, materials with negligible diffuse reflectivity have been separated in figure 2.9 from those whose diffuse reflectivity is significant or even dominant. For the polished surfaces the values at 1  $\mu\text{m}$  wavelength agree very well with literature data from [Samsonov68, p.383ff] except for silicon, which is listed with constant 28% at 1-10  $\mu\text{m}$ . The value for polished W also agrees very well with [Lide94, p.12/137]. Further reflectivities for W, Al, Ag, Ni and Fe in the range of 0.04-10  $\mu\text{m}$  can be found in [Hartwig78, p.10]. In order to determine the reproducibility of these measurements, the very same polished W sample has been measured several times within several years. The maximum deviation of the measured value for the total reflectivity

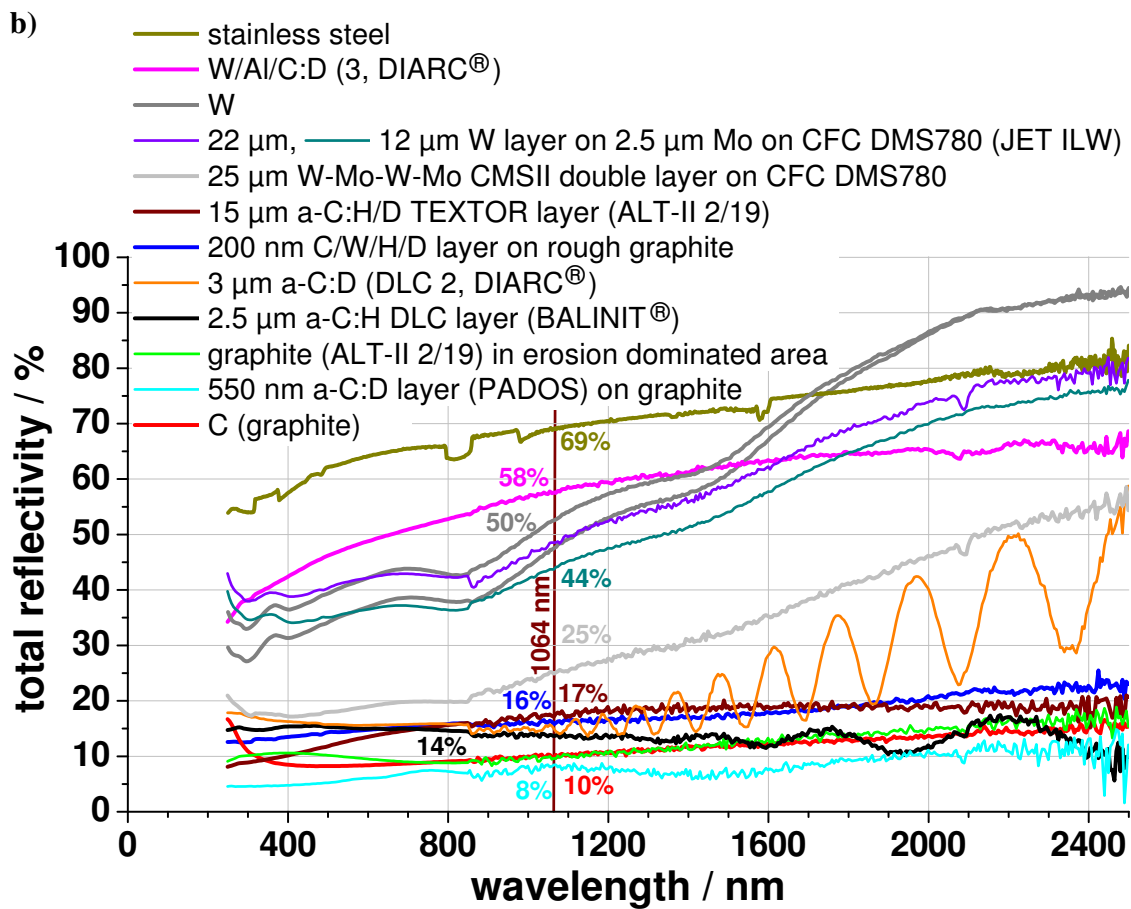
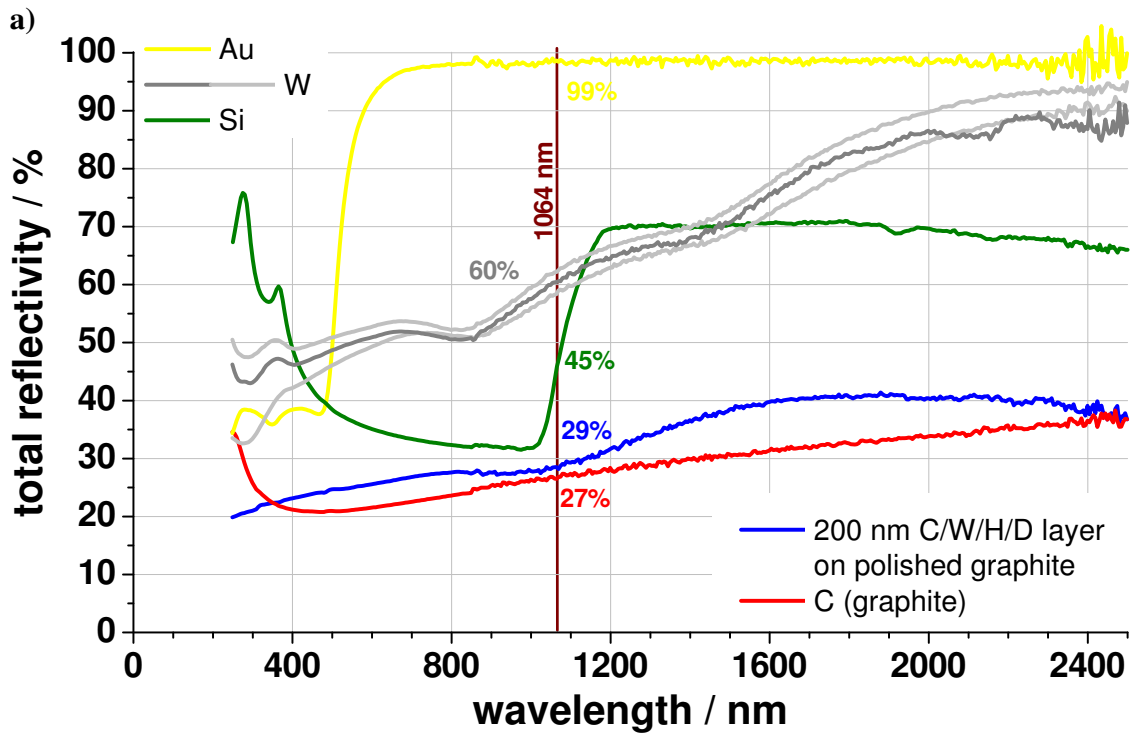


Figure 2.9.: Reflectivity of materials used for LID; measured with a spectrophotometer; a) polished surfaces; b) rough surfaces with considerable fraction of diffuse reflectivity; different W grades have been measured

at the laser wavelength varied only by 1.5 percentage points (i.e. by a factor of less than 1.03). In general, the materials can be separated by their total reflectivity into 3 classes: those with a low (< 30%), medium (40-70%) and high reflectivity (> 80%).

### **High reflectivity materials**

These materials are not suited for laser heating with IR laser pulses on the millisecond time scale, unless the spot size is decreased into the sub-millimetre range. This is due to the limited pulse energy with today's technology. Shorter wavelengths or much shorter pulse lengths have to be selected for these materials. The noble metals like Au and Ag with 95-99% reflectivity around 1  $\mu\text{m}$  and also Al with 85-95% belong to this class.

### **Medium reflectivity materials**

The medium reflectivity class, where roughly half of the light is reflected, contains metals like W, Fe, Ni and their alloys like stainless steel, as well as mixed layers that contain a high metallic fraction. Several pure ( $\geq 99.95$  wt%) W grades have been used, yielding values between  $58\% < R_{tot} < 62\%$  for polished surfaces (at 1064 nm). The arithmetic mean roughness  $R_a$  measured on 1 mm long profiles (cf. definition in equation 3.1 on page 90) is in the range of  $R_a = 20$ -50 nm on the polished surfaces. Taking into account the device stability (1.5%, see above) and that the polishing procedures were performed in different companies by different machines, this is a very small scatter (factor 1.07). Rough W surfaces used in the present work with a roughness of  $R_a \approx 1$   $\mu\text{m}$  have a 10 percentage points reduced total reflectivity than polished W, having approximately the same scatter for different W grades. Concluding on bulk tungsten, a value of  $R_{tot} = 60\%$  for polished and  $50\%$  for rough W surfaces has to be applied. This difference is also seen on samples from the same plate and, it is most likely to be explained by multiple reflexions inside the valleys of the rough surface.

In fusion also W layers on graphite or carbon fibre composite (CFC) materials are used as PFMs. Within the frame of the present work, a W coating on CFC with a Mo interlayer of 2-3  $\mu\text{m}$  has been produced with the same procedure as for the ITER-like wall (ILW) in JET, installed in 2012. The coating procedure was Combined Magnetron Sputtering and Ion Implantation (CMSII). A thin W layer (10-15  $\mu\text{m}$ ) and a thick W layer (20-25  $\mu\text{m}$ ) have been used. The CFC substrate (JET Dunlop CFC DMS780) is very rough  $R_a \approx 4$   $\mu\text{m}$  on the smoothest parts, but exhibiting many holes of tens to hundreds of micrometres in depth. The reflectivity is fully diffuse. The reflectivity is on average slightly (factor 1.09) lower than for rough bulk W. The similarity of the reflectivity is an indication for a nearly complete coating of the layer.

The thinner layer has a 4 percentage points lower reflectivity. A previous version of this coating, which has been produced with a double layer structure (W-Mo-W-Mo) on CFC only had a reflectivity of 25%, which is only half of the value of the finally applied coating. Also a mixed layer of W, Al, C and D has been produced by arc discharge deposition (DIARC® [Diarc12], pink line), showing slightly higher total reflectivity as polished W but also a considerable diffuse fraction of 22%. Half of the atoms in the layer are carbon atoms, but the reflectivity is very high, unlike carbon. This shows that the reflectivity cannot be easily deduced from the composition of a mixed layer. This kind of materials with medium reflectivity will probably be found in a fusion power plant.

### **Low reflectivity materials**

The lowest reflectivities occur for carbon dominated materials with 8-10% for amorphous hydrocarbon layers (cyan line) and rough graphite (red line). The values for an ALT-II limiter tile [Finken5] (N° 2/19) exposed in erosion dominated conditions in TEXTOR for several years (ca. 7000 discharges, 33200 s, green line) shows that the plasma does not have any significant impact on the reflectivity – except in the UV range. This is of course only valid

in erosion dominated areas. The unchanged reflectivity is not obvious, since these areas also contain considerable quantities of H and D (cf. figure 4.9 on page 123), which could in principle change the optical properties. In the deposition dominated area (brown line) the reflexion characteristic does not differ much from that of a 200 nm thin mixed C/W/H/D layer with about 10 at% ( $\approx 76$  wt%) W, which was grown on rough graphite in TEXTOR (dark blue line). Its reflectivity is twice as high as for the 550 nm thick a-C:D layer grown in a glow discharge (PADOS, cyan line).

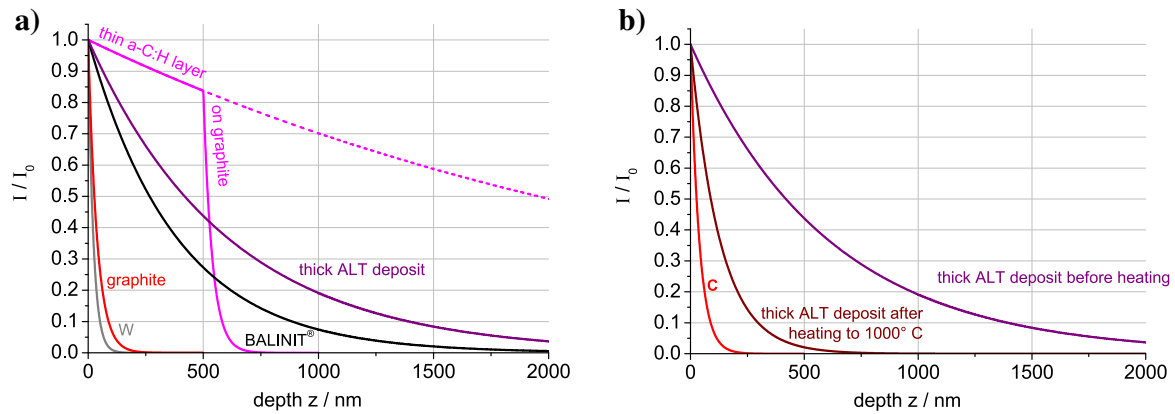
Two thick commercial C layers have been investigated by LID, both produced on tungsten substrates. The Balinit<sup>®</sup> layer was generated by chemical vapour deposition (CVD) by œrlikon balzers [Balzers12] and consists of a ca. 2.5  $\mu\text{m}$  DLC layer with protium on a 0.6  $\mu\text{m}$  Cr based interlayer (black line). Its reflectivity has a different wavelength dependence than the TEXTOR layers, but there is not much difference at the laser wavelength. The same is valid for the even thicker ( $d > 3 \mu\text{m}$ ) deuterated DLC layer from DIARC<sup>®</sup> [Diarc12] produced by an arc discharge (orange line). Both layers show characteristic oscillations in the spectral reflectivity, which are due to interference effects. This is a strong indication for the homogeneity of the layers.

The characteristic of the laser energy absorption is in principle important for the modeling of the heat propagation, because the volume of the laser absorption is the source of the heating process. The absorption volume is determined by the extinction coefficient  $k$ , which is the imaginary part of the refraction index  $n + ik$ . The light intensity  $I$  decays exponentially from its initial value  $I_0$  at the surface of the material (at  $z = 0$ ), according to Lambert-Beer's law:

$$I(z) = I_0 e^{-\alpha z} \quad \text{with} \quad \alpha = \frac{4\pi k}{\lambda}. \quad (2.6)$$

The interference oscillations described above, already show weather significant amounts of light reach the substrate or not, i.e. if the layer is transparent. On the thin TEXTOR layer the pattern appears on the whole measurement range. This means that the layer is transparent for light in VIS and IR range. The DIARC<sup>®</sup> layer is transparent at least for  $\lambda > 1000$  nm and the Balinit<sup>®</sup> layer for  $\lambda > 1200$  nm. This is consistent with ellipsometric measurements of the extinction coefficient. For example the exponential light decay (with  $k = 0.22$ ) for the laser wavelength in the Balinit<sup>®</sup> layer is shown in figure 2.10 (black line). The light is practically absorbed after penetrating 2  $\mu\text{m}$  deep into the layer, the e-folding decay length is  $1/\alpha = 380$  nm. With a thickness of  $d \approx 2.5 \mu\text{m}$ , the laser light is hence absorbed fully in the layer. It does not reach the substrate and consequently also no interference pattern is visible at  $\lambda_0 = 1064$  nm in the spectral reflectivity discussed above. For longer wavelength this does not hold any more, since the longer the wavelength, the deeper the penetration.

However, for the materials studied by LID the laser light penetration is always small in comparison to the temperature decay length at the end of the laser pulse. Even for a highly transparent and thick a-C:H layer, the light decay length could hardly exceed few micrometres, while the temperature decay is about 300  $\mu\text{m}$  and more, depending on the pulse properties. Moreover, the materials with a low light extinction coefficient are hydrocarbon layers, which graphitise at about 900 K, leading to a rising extinction coefficient and shortening of the light penetration for the remaining duration of the laser pulse. This has been demonstrated on an ALT-II deposit (cf. figure 2.10b), for which the light decay length reduces from 590 nm to 130 nm by heating to 1273 K, while for bulk graphite a shallow penetration depth of only 38 nm holds. Considering this heat effect, the laser light is penetrating progressively less deep into the material during the laser pulse. It is concluded that for the investigated materials no important influence on the global temperature distribution arises from the different laser absorption depths.



**Figure 2.10.:** Laser light absorption (at  $\lambda_0 = 1064$  nm) according to Lambert-Beer's law based on measurements of the complex refractive index by ellipsometry (for carbon layers) and interpolated data from [Palik98, vol.1, p.366], [Palik98, vol.2, p.458], [Lide94, p.12/137] for bulk C and W.

## 2.4. Heat Propagation in Different Materials

In this section, the temperature distribution in the laser irradiated material will be calculated for the laser pulses characterised in the previous sections. In space the laser intensity distribution is spatially nearly constant on the irradiated laser spot (top-hat distribution). In time, the pulse shape deviates slightly from a square pulse of equal energy by a factor of up to 1.2 decreasing linearly throughout the pulse. In depth, the laser light absorption is very shallow, mostly in the sub-micrometre range. The main aim of this section is to determine for each material the heating intensity needed to reach a surface temperature of 1800-2000 K and the lateral and in-depth heat propagation. The analytically or numerically calculated temperature is compared to measured surface temperature and experimental data of heating, even until melting of W. First, the principles of laser heating by conversion of light into heat are briefly mentioned to justify the use of the following heat diffusion models. Then the analytical and numerical models for the heat diffusion calculation are introduced. They are applied to the different materials in the four subsections of the present chapter. A detailed analysis of the temporal and spatial temperature evolution is given for tungsten in the first subsection, outlining also parallels and differences to graphite. In the second subsection the special heating behaviour of CFC materials due to their anisotropy is emphasised. In the subsection on a-C:H layers the determination of their heat parameters especially measured for the present work is described. In this subsection it is also shown how to deal with material mixtures in layered form. Heating of mixed materials as homogeneous mixtures is described in the last subsection.

### Light to heat conversion

Before heat diffusion can start, the laser energy, has to be transformed into heat. For the laser intensities used in LID here (up to few  $\text{GW}/\text{m}^2$ ) the conversion of light to heat is understood as a two-step process [Ready71, p.68]:

1. The electrons of the solid-state body which are under the influence of the electromagnetic field of the laser, absorb the photons from the laser beam and thus are excited to higher energy levels. For metals this levels are usually in the conduction band.
2. These excited electrons collide with other electrons and lattice phonons. By the collisions they convey energy, thus increasing the energy of lattice oscillations and hence the temperature of the solid.

The first mechanism is weaker if the electrons are not strongly bound in the potential of the lattice. Then they can oscillate more freely, stimulated by the electromagnetic wave and cause an increased reflectivity of the laser light [Delone93, p.335f]. A weak binding of the electrons can be either a material property or the consequence of very strong laser intensities. The first effect occurs in LID on metal surfaces (e.g. on tungsten), because the electrons are more free in metals than in half-metals or non-metals. The second effect only occurs for laser intensities above  $10^{14}$ - $10^{15}$  W/m<sup>2</sup> several orders of magnitude higher than the intensities applied in LID here.

The second step of the conversion to heat has a characteristic time scale of the mentioned collisions, which is in the order of  $10^{-13}$  s. This time scale is 10 orders of magnitudes shorter than the laser pulse duration. Thus the light to heat conversion can be described as instantaneous. Therefore on microscopic scale a local thermal equilibrium is established immediately and thermodynamics can be used for the description of the heat propagation.

After the heat is generated in the surface of the solid, it spreads by heat conduction and radiation from the surface. In the cases of melting, also heat convection might play a role, but will not be treated here.

### Heat diffusion models

Common to all of the following three approaches is the assumption that the source of the heat, i.e. the laser energy deposition area, is a very thin surface layer of the material. Even for large light penetration depths of 1-2  $\mu\text{m}$  this is fully justified in case of the numeric simulations, because they usually had a spatial resolution of 10  $\mu\text{m}$ . However, all approaches show a temperature decay length two orders of magnitude larger than even those large light penetration depths, justifying this assumption.

The analytical solution to the heat diffusion equation is one dimensional in the coordinate  $z$ , corresponding to the depth of the material (at  $z \geq 0$ ) with the surface at  $z = 0$ . The model assumes a homogeneous, semi-infinite body, temperature independent, isotropic heat properties of the material and a square pulse of constant laser intensity  $I$ .

It will turn out, that the assumption of the semi-infinite body is justified for the ms-duration pulses used, if the total sample thickness is above 1.5-2 mm, which was nearly always the case. The use of temperature independent heat properties will be also shown to have minor effects on the calculated temperatures. But the assumption of a square pulse will lead to marked deviations from the results with the real pulse shape. Finally also anisotropic heat properties cannot be introduced into a one-dimensional model. The analytically determined temperature profile with these assumptions is [Carslaw59, p.75, eq.7]:

$$T = T_0 + \frac{2}{\sqrt{\pi}} \frac{\sqrt{k}}{K} I \sqrt{t} \left( e^{-Z^2} - \sqrt{\pi} Z \operatorname{erfc}(Z) \right) \text{ with } Z = \frac{z}{2\sqrt{kt}} . \quad (2.7)$$

$T_0$  ... initial homogeneous temperature of the whole sample in K or °C

$\kappa$  ... thermal diffusivity in m<sup>2</sup>/s

$K$  ... heat conductivity in W/mK

$I$  ... laser intensity in W/m<sup>2</sup>

$t$  ... time after begin of laser pulse in s

$z$  ... depth below the surface in m

This is a mathematical solution "except for a remaining integral" contained in the complementary error function  $\operatorname{erfc}(Z)$ , which is a tabulated function based on the integral of the Gaussian function.

## 2. Laser Heating of Different Materials

---

Equation 2.7 describes the temperature profile into the depth for every time  $t$  after the onset of the constant heating. For the time after the laser pulse the surface temperature can be described as [Carslaw59, p.76, eq.10]

$$T = T_0 + \frac{2}{\sqrt{\pi}} \frac{\sqrt{\kappa}}{K} I \left( \sqrt{t} - \sqrt{t-t_p} \right) . \quad (2.8)$$

The terms outside the brackets in equation 2.7 represent the surface temperature evolution, while the term inside the brackets describes the spatial profile in  $z$  direction. The material dependent term is

$$\frac{\sqrt{\kappa}}{K} = \frac{1}{\sqrt{Kc\rho}} \quad \text{with} \quad \kappa = \frac{K}{c\rho} . \quad (2.9)$$

$c$  ... heat capacity in  $\text{J}/\text{kg K}$

$\rho$  ... material density in  $\text{kg}/\text{m}^3$

It will be referred to as "material heat term" with the fundamental heat properties of the material:  $K, c, \rho$ .

Next to this material term stands the laser pulse term, which is called the heat flux factor HFF:

$$I \sqrt{t} = \frac{P}{A} \sqrt{t} = \frac{E_1}{A \sqrt{t}} . \quad (2.10)$$

$P$  ... absorbed laser power in W

$A$  ... laser spot area in  $\text{m}^2$

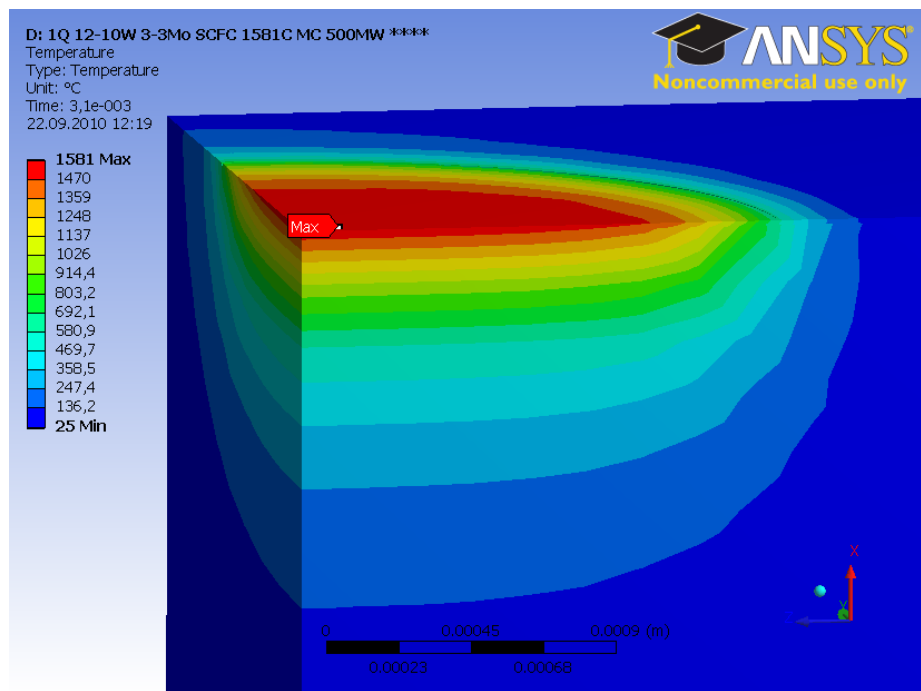
$E_1$  ... absorbed laser energy in J

The laser system used here can realistically reach heat flux factors of  $45 \text{ MW} \sqrt{\text{s}}/\text{m}^2$  for a  $\varnothing=3 \text{ mm}$  laser spot or  $100 \text{ MW} \sqrt{\text{s}}/\text{m}^2$  for a  $\varnothing=2 \text{ mm}$  laser spot (both tilted by  $22^\circ$ ) on unpolished tungsten.

Beside the analytical model also two numerical heat diffusion simulations have been used, in order to calculate the fully three dimensional temperature distribution. The first one is a two dimensional finite differences simulation developed in the Institute of Energy Research in Jülich. Details can be found in [Irrek8, p.31ff]. The simulation uses the cylindrical symmetry of the problem and thus only needs the depth coordinate  $z$  and a radial coordinate  $r$  on the surface, starting in the laser spot centre. It uses temperature independent heat properties and is restricted to isotropic materials. But it is capable of applying any spatial laser profile and temporal pulse form. However, in the following simulations the spatial laser profile has always been assumed as an ideal top-hat function due to the laser profile optimisation in the experiment (cf. chapter 2.2).

The second numerical simulation used was the transient thermal module of the commercial multi-physics solver ANSYS (Academic Research version) from the ANSYS, Inc. company [Ansys12]. It is a finite element calculation in fully three dimensional cartesian coordinates. Beside heat radiation it can calculate the heat diffusion in material combinations in any geometric form and arrangement with adjustable heat transfer coefficients. This capability was used here to calculate layered materials, e.g. W on CFC with a Mo interlayer. For every material the heat properties can be defined temperature dependent and anisotropic:  $K_x(T)$ ,  $K_y(T)$ ,  $K_z(T)$ ,  $c(T)$ ,  $\rho(T)$ . It turned out that the temperature dependence does not have a large effect on the temperature evolution, but that the anisotropy is necessary to simulate the heat diffusion in CFC materials correctly. The ANSYS simulation has significant advantages





**Figure 2.11.:** Temperature distribution at the end of the laser pulse; finite element calculation (ANSYS); one fourth of an LID laser spot is simulated to reduce calculation time; 3 mm laser spot diameter; 3 ms heating time;  $500 \text{ MW/m}^2$  absorbed laser intensity

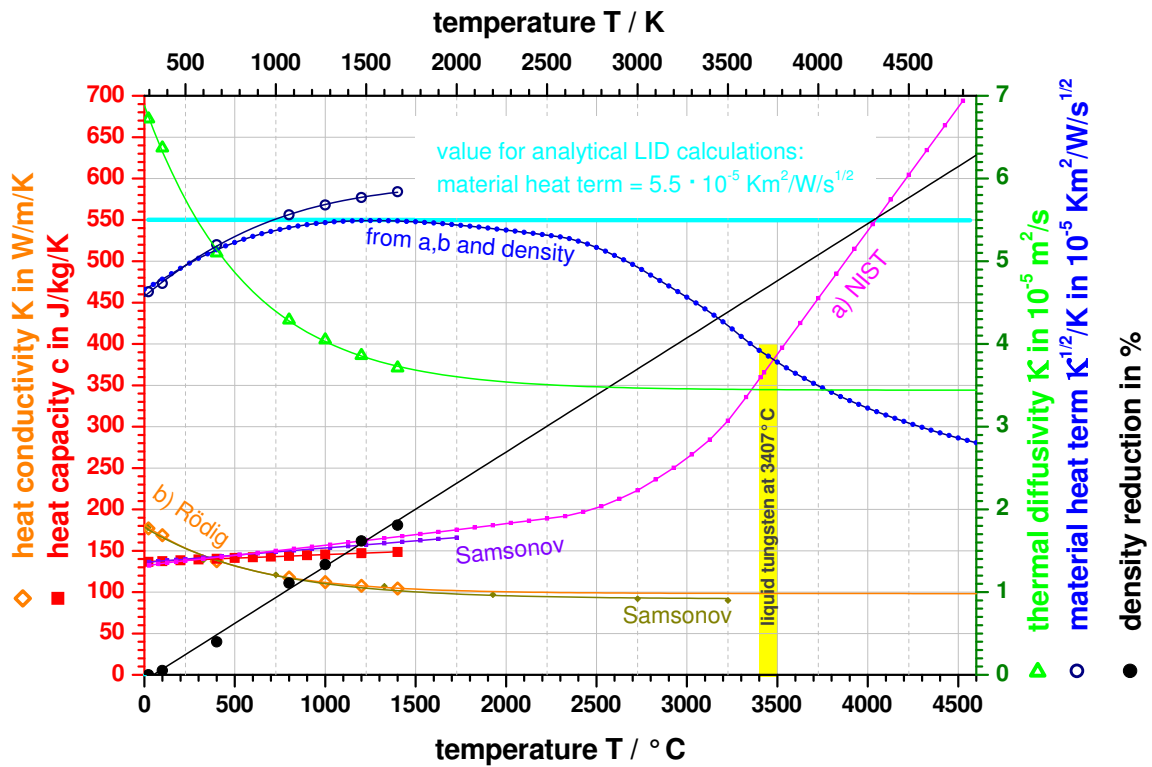
in computational speed, since an adaptive discretisation mesh is used with large steps at positions of small gradients and small steps at large gradients. The resolution of the mesh is even changed during the computation locally where necessary.

The analytic solution is very good for the inner part of the laser spot. In general up to the half of the laser spot radius the isotherms are nearly parallel to the surface. Here the analytical solution is valid because the heat propagates mainly into the depth and the surrounding cold material has no effect. In the outer half of the radius the direction of heat propagation gradually turns more and more into lateral direction the further away it is from the spot centre. Thus only on  $1/4$  of the spot area the analytical solution is valid. Therefore the numeric results are important, especially for longer laser pulses ( $t_p > 5 \text{ ms}$ ), small laser spots ( $\varnothing < 2 \text{ mm}$ ) or not perfectly top-hat laser profiles.

### 2.4.1. Isotropic and Homogeneous Materials (Tungsten and Graphite)

The heat properties, temperature calculations and measured temperatures will be described in more detail for W, more precisely polycrystalline W of high purity ( $> 99.95 \text{ wt\%}$ ). Figure 2.12 shows fundamental and deduced heat properties. The density reduces during heating linearly (black line) and shows only a decrease of 2% for the usual temperatures reached in the standard LID pulse and less than 5% at melting temperature when extrapolating linearly.

The heat capacity increases linearly with a moderate rate of roughly  $25 \text{ J/kg K}$  every 1000 K with increasing temperature until 2500 K, where it starts to increase rapidly to about 2.5 times of the RT value. Due to this increase, the melting of W needs much more energy than an analytical calculation with temperature independent values estimates. The heat conductivity decreases with rising temperature. The main decrease takes place for low temperatures and

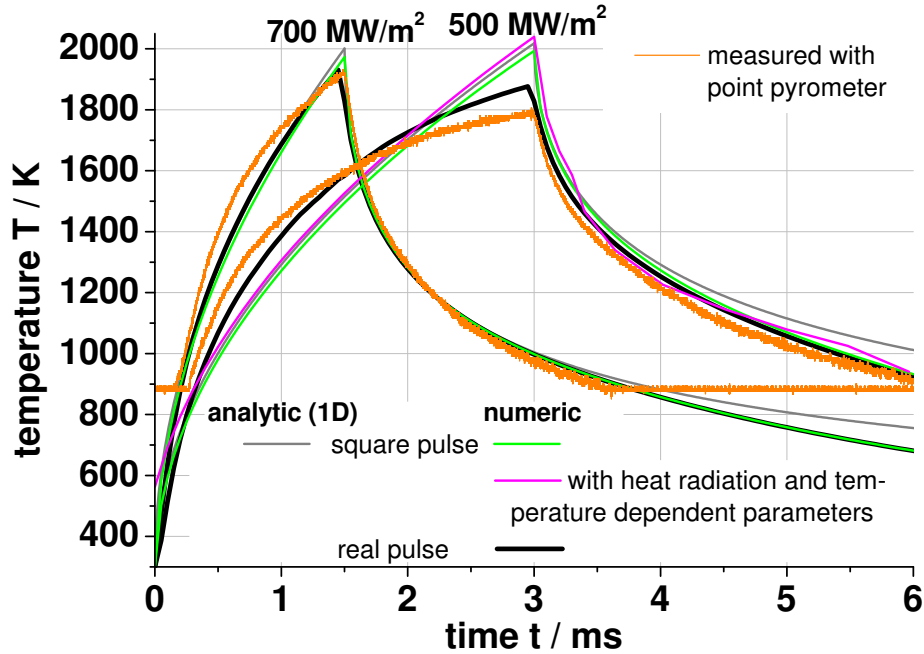


**Figure 2.12.:** Heat properties of tungsten with data from NIST [Chase98], [Samsonov68] and Institute of Energy Research Jülich [Rödigg3] (unlabeled data); lines are only guidelines

finishes at a value of factor 2 smaller than the initial value. This also leads to a decrease of the thermal diffusivity according to equation 2.9. However, the most decisive material property is the root of this value divided by the heat conductivity. Since both are decreasing it is easier to understand this quotient with the transformation in equation 2.9. This property – the material heat term – is shown by the blue lines and varies slightly depending on which literature data are used for the calculation. If the larger heat capacity from NIST is used together with the conductivity from [Rödigg3], then lower values with a maximum value of  $5.5 \cdot 10^{-5} K m^2/w \sqrt{s}$  result (shown as small blue dots). If only the values from [Rödigg3] are used, larger values result (open blue circles). Therefore this value, which is also marked by the horizontal light blue line, is a good compromise for the analytical calculations. From this value the material heat term decreases by a factor of 1.4 at melting temperature. This value at 3700 K underestimates the final temperature by more than 1200 K for a heating from RT to melting. Using the value at RT, which is only a factor of 1.2 too low, the final temperature is still underestimated by 550 K, that can decide whether melting occurs or not. This shows that the heat properties have to be known quite accurate since small deviations here already result in decisive final temperature differences.

The sensitivity has been studied further in the numeric heat diffusion calculations. In figure 2.13 the numeric calculations with temperature dependent heat properties (red line, ANSYS) are compared to calculations with constant heat properties (green line). Only a maximum deviation of 46 K at the final temperature occurs. The analytic solution (grey line) also fits very well to both curves, lying inbetween them during the laser pulse. Here the above mentioned optimal value for analytical calculations has been used for the material heat term. For the cooling phase increasingly larger deviations of the analytical solution occur, because in one dimension the heat cannot diffuse as fast as in three dimensions. In conclusion, the

sensitivity in the temperature dependence of the material heat term is not significant for the temperature range of LID, if an appropriate constant value is used. Therefore the temperature dependence of the heat properties is negligible and numeric calculations can disregard it. Much more influence on the heating has the decaying pulse form in contrast to the square pulse form. For the short 1.5 ms pulse this influence is small and the numeric simulations with square pulse and the real pulse are in good agreement.

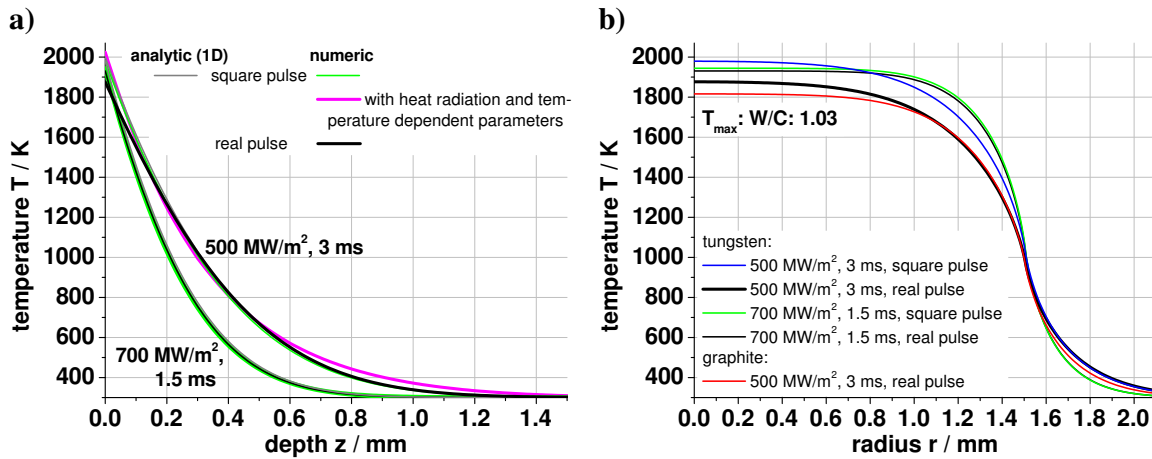


**Figure 2.13.:** Temporal development of the W surface temperature in the centre of the laser spot for 2 different laser pulses with the standard LID heat flux factor  $27 \text{ MW} \sqrt{\text{s}}/\text{m}^2$

The 3 ms pulse is affected stronger by the laser intensity decay in the real pulse form. The surface temperature at the end of the laser pulse deviates by about 150 K and the whole temporal development of the temperature is changed, being hotter first and colder later compared to the square pulse simulations and the analytical solution. For comparison with the experiment, the central part ( $\varnothing = 1\text{-}2 \text{ mm}$ ) of the laser spot is monitored with a fast pyrometer. The pyrometer has a measurement threshold of 873 K (horizontal orange line). The measured maximum temperature agrees well with the calculations (when using the real pulse form) with a deviation below 100 K. However, the measured temporal shape during the heating phase is even more bend in the sense just described. A nonlinearity of the pyrometer can be excluded, since it has been measured to be perfectly linear up to 1300 K. The deviation is already present below 1300 K, thus it is likely that in the whole temperature range a different effect is the reason. It might be speculated, that the laser intensity distribution changes during the laser pulse, since only the integrals of the laser profile over the whole pulse duration have been measured. The deviations in the later phase of the pulse probably originate from the spatial inhomogeneity of the temperature and the spatial integration of the pyrometer over it. Figure 2.14 shows the calculated spatial and depth distribution of the temperature, showing temperature variations starting at radii of 0.8-1 mm, which roughly correspond to the pyrometer detection size.

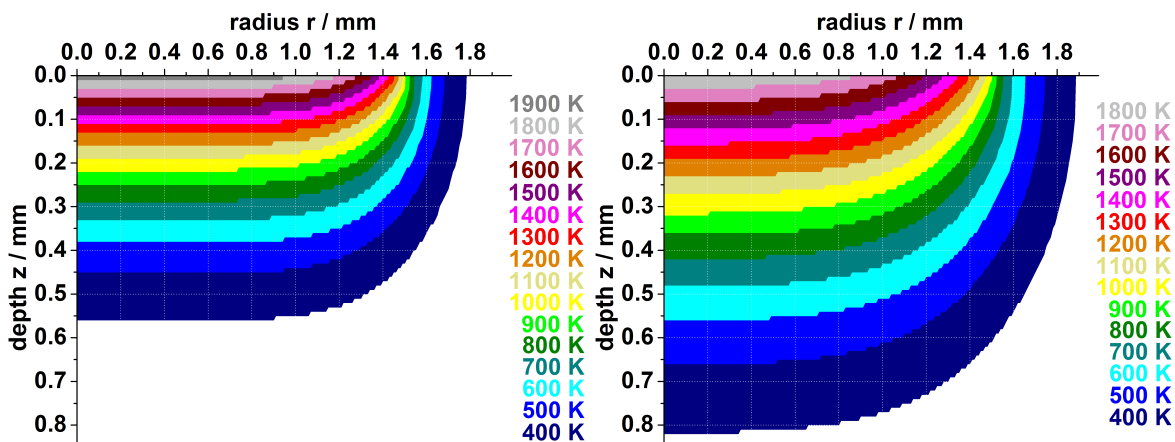
The radial temperature distributions also show another important effect. With the choice of a final temperature at 1800-2000 K, the largest derivative of the profile is at 1.5 mm, which is exactly the laser beam edge. At this radius always a temperature of 900 K is reached, which

## 2. Laser Heating of Different Materials



**Figure 2.14.:** Spatial temperature profiles in depth (a) and radial direction (b) at the end of the same laser pulses as in figure 2.13; 3.0 mm laser diameter

defines the desorbed area, that is then identical to the laser irradiated area. The fraction of desorbed deuterium depending on the surface temperature has been determined before [Irrek8, p.26] and applied to the radial temperature profile. There, it was found that the amount of undesorbed deuterium at the laser spot border but inside the spot equals approximately the desorbed D amount outside the spot in the case of 900 K at the spot edge. In general, the sharpness of the temperature gradient is better the shorter the laser pulse. The profile is already quite smooth for the 3 ms pulse. For longer pulses the profile becomes undesirably smooth and the central temperature reduces. An experiment and calculation series with a smaller spot size of 2.24 mm diameter has been done to demonstrate this, because this reduced area allows to compare different pulse lengths at a fixed heat flux factor ( $36 \text{ MW} \sqrt{s}/\text{m}^2$ ). Because of this, the analytically calculated temperature is always the same (2500 K), independent of the pulse duration, since the laser intensity was adapted accordingly. For pulse lengths of 0.5, 1.5 and 3 ms the final temperature in the numerical calculation is identical to the analytic result. But for a 6 ms pulse the maximum is reduced by 250 K and for a 12 ms pulse by 600 K compared to the analytical value. Additionally the partially desorbed area outside the spot becomes very large and an LID measurement integrates over larger areas. Hence, the distance between the LID measurements spots must be increased to more than 5 mm. Therefore a reasonable sharpness in temperature and desorption is not achievable for pulse durations above ca. 4 ms. For details of this LID series cf. figure 6.8 on page 144.



**Figure 2.15.:** Temperature distribution in W after two different laser pulses; 3.0 mm laser beam diameter; left:  $700 \text{ MW}/\text{m}^2$  for 1.5 ms; right:  $500 \text{ MW}/\text{m}^2$  for 3 ms

The just described effect is also illustrated very well by the temperature distributions in the cross-sections (figure 2.15). The area of validity of the analytical solution (i.e. horizontal isotherms) is much larger for the 1.5 ms pulse than for the 3 ms pulse. Consequently the whole temperature profile changes from a mainly depth dependent function to a more spherical shape of the isotherms. The cross-sections also allow an estimation of the desorption depth and volume. For the short pulse the potential desorption volume is smaller, reaching ca. 130  $\mu\text{m}$  deep referred to the 1300 K isotherm, while for the longer pulse it extends up to 190  $\mu\text{m}$ .

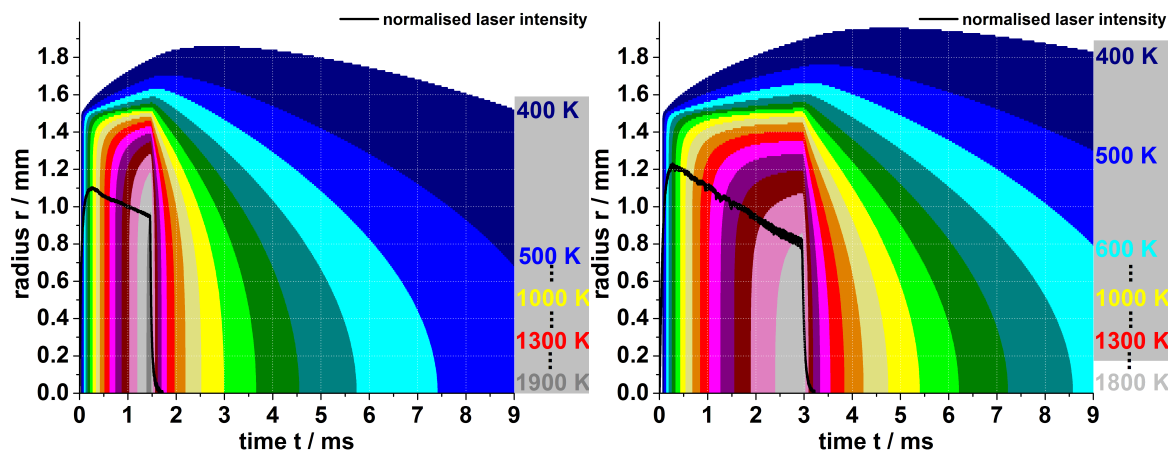
The desorption depth is identical for the analytic or numeric calculations and also for the real laser pulse form (cf. figure 2.14a). The described deviations of the surface temperatures, related to different pulse forms are restricted to a shallow surface region. For larger depths ( $z > 100 \mu\text{m}$ ) the temperature profiles for the square pulse and the real pulse are very similar. Only the temperature dependent calculation again shows some minor deviations for  $z > 600 \mu\text{m}$ .

After the laser pulse, the surface temperature decays immediately. However, a certain part of the heat continues to propagate and additional volumes become hotter after the laser pulse, compared to their temperature during the laser pulse. This is shown in figure 2.16. It shows the instantaneous occurrence of the isotherms during the laser pulse, their movement radially outwards, their stagnation and movement backwards to the spot centre.

All high-temperature isotherms collapse immediately at the end of the laser pulse and only temperatures below 500-600 K spread laterally outwards. Such low temperatures are of no importance for desorption, since for about 700 K a desorption fraction of 10% is reached e.g. for a-C:H layers. It can be concluded, that there is no relevant expansion of the desorption area.

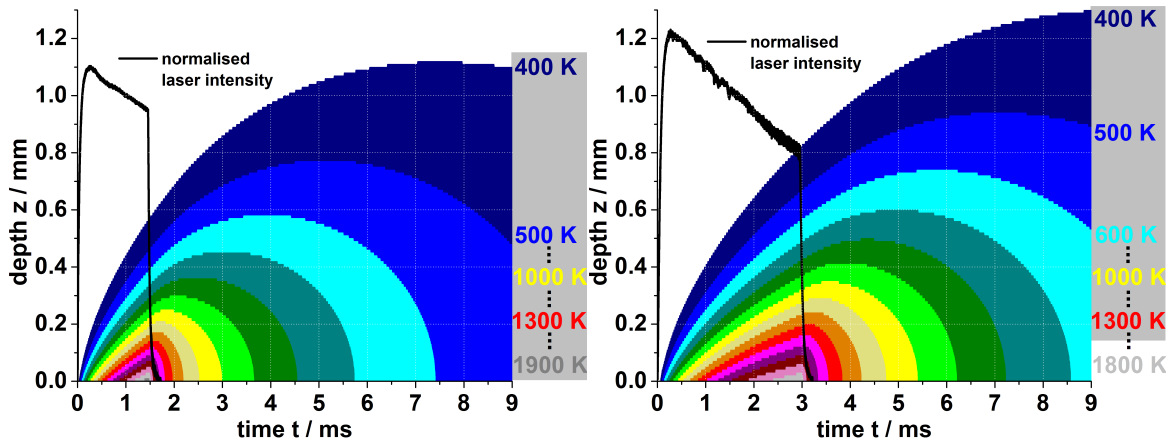
This is different for the direction into the depth (figure 2.17), since this is the main propagation direction of the heat. Here all isotherms for temperatures lower than 1100 K (for the 1.5 ms pulse) or 1200 K (for the 3 ms pulse) expand further into the material after the laser pulse. The additional propagation length is similar to the spatial temperature decay length at the end of the laser pulse, e.g. the 700 K isotherm moves an additional distance of ca. 100  $\mu\text{m}$  into the depth. In conclusion, the heat propagation in LID is preferentially directed into the depth despite a homogeneous material with isotropic heat conductivity is treated.

A comparison of the heating of tungsten and graphite shows that although these materials have very different fundamental heat properties, the heating process is nearly identical, especially regarding the surface temperatures. In table 2.3 the heat parameters for elevated



**Figure 2.16.:** Temporal development of isotherms on the W surface for two different laser pulses; left: 700  $\text{MW}/\text{m}^2$  for 1.5 ms; right: 500  $\text{MW}/\text{m}^2$  for 3 ms

## 2. Laser Heating of Different Materials



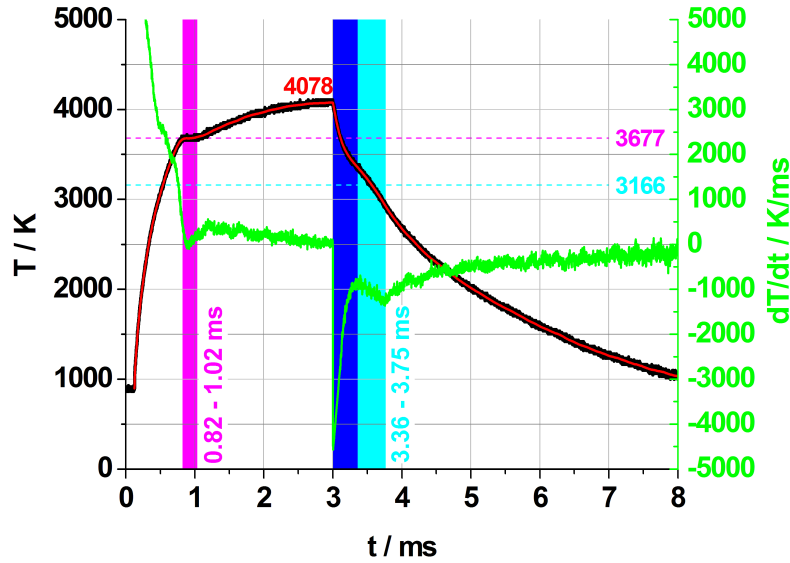
**Figure 2.17.:** Temporal development of isotherms on W in depth for two different laser pulses; left:  $700 \text{ MW/m}^2$  for 1.5 ms; right:  $500 \text{ MW/m}^2$  for 3 ms

temperatures are compared. The heat capacity of graphite is more than an order of magnitude larger than the one of tungsten. But this is compensated by the difference in material density. Together with the nearly equal heat conductivity, the material heat term in the analytical heating solution is practically the same for both materials. This means that all surface temperatures calculated for carbon will be only 3% higher for tungsten.

For tungsten much higher heating up to melting became necessary to desorb all retained hydrogen. Since no calculations of the heating of fluid tungsten have been done in the present work, only the experimental results will be shown here. Figure 2.18 shows the pyrometer data of the surface temperature. The melting temperature of W has been identified by the first plateau region at 1 ms and used to calibrate the pyrometer signals. It has been observed, that there is only a small temperature increase after the melt has formed. This increase is in reality even smaller than indicated by the pyrometer, because of the pyrometer detection spot diameter of 1-2 mm, compared to the laser spot diameter of 2 mm. The stunning feature is the resolidification process, which is identified by a bump in the cooling phase and a constant cooling rate of  $1000 \text{ K/ms}$ . This phase (light blue) appears about 500 K below the melting temperature, showing that the initial extreme cooling rates of up to  $5000 \text{ K/ms}$  generate an undercooled melt. This indicates a so called rapid solidification process (RSP) which will have a large effect on the surface structure as described in the next chapter.

	tungsten at 900 K	vs.	graphite ( $T < 1700 \text{ K}$ )
heat conductivity $\kappa / \frac{\text{W}}{\text{m K}}$	118	$\approx$	105
heat capacity $c / \frac{\text{J}}{\text{kg K}}$	144	$\ll$	1800
density $\rho / \frac{\text{kg}}{\text{m}^3}$	19079	$\gg$	1850
heat diffusivity $\kappa / \frac{\text{m}^2}{\text{s}}$	$4.3 \cdot 10^{-5}$	...	$3.2 \cdot 10^{-5}$
material heat term $\frac{1}{\sqrt{\kappa c \rho}} / \frac{\text{K m}^2}{\text{W} \sqrt{\text{s}}}$	$5.5 \cdot 10^{-5}$	$\approx$	$5.35 \cdot 10^{-5}$

**Table 2.3.:** Heat properties of tungsten and graphite at temperatures relevant for LID

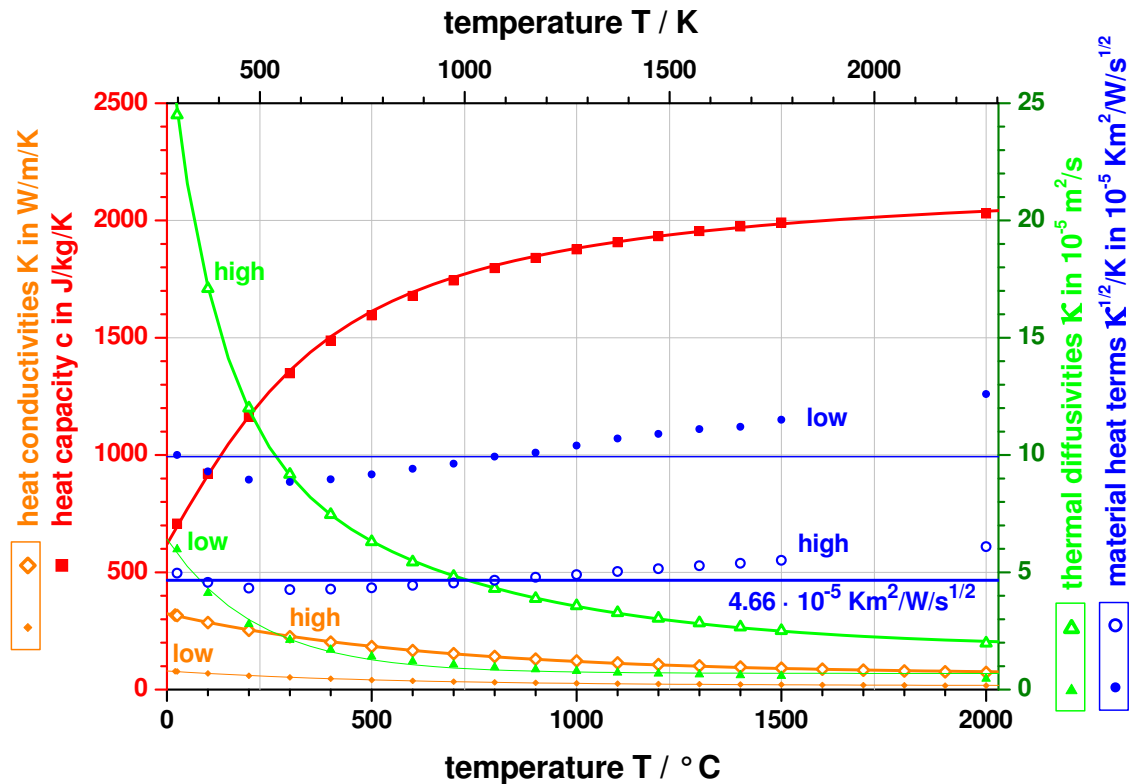


**Figure 2.18.:** Surface temperature and derivative during laser melting of pure tungsten with melting pulse ( $1.5 \text{ GW/m}^2$  absorbed intensity, 3 ms): rapid solidification processes appear due to the high cooling rate and temperature gradients

### 2.4.2. Anisotropic Carbon Materials (CFCs)

If the structure of a material is anisotropic on a scale larger than the atomic scale, then its heat conductivity is most probably anisotropic, too. This has consequences for the temperature distribution during LID, because it can influence the shape and size of the desorbed area and the surface temperatures. These effects will be discussed for a well known carbon fibre composite material with known thermal properties. Carbon fibre composites (CFCs) have been introduced as wall material in fusion because they combine the advantages of graphite with a much higher heat conductivity and mechanical strength [Pintsuk8]. They consist of carbon fibres with a high heat conductivity along the fibre (axial direction) and a low heat conductivity across the fibre (radial direction). There are two types of CFC structures: two-directional (2d) and three-directional (3d) CFCs. In 2d CFC a layer of fibres oriented in one direction (e.g. x-direction) alternates with a layer of fibres oriented perpendicular to the first one (y-direction). The two layers are separated by a layer of filler material – a felt layer, which has isotropic properties and a heat conductivity between the values for the axial and radial direction. For the CFCs used here, the distance between the fibre layers of orthogonal orientation is ca. 1 mm, thus the microstructure of the CFC repeats roughly every 2 mm. This two-directional structure leads to a material that macroscopically has a high heat conductivity  $K_{high}$  in two directions (x and y) and a lower value in the z direction:  $K_{low}$ . For the heat propagation and surface temperature the orientation of this anisotropic material is therefore decisive. If the low heat conductivity is directed into the depth of the material, then this orientation is called "parallel fibre orientation". If the low heat conductivity direction is perpendicular to the surface normal, then it is called "perpendicular fibre orientation" (cf. figure 2.20f). In 3d CFC an additional structure in z direction is introduced by a needling process, which causes full anisotropy with three different heat conductivities:  $K_x, K_y, K_z$ . In contrary to the 2d case, two of them are quite low and only one is higher (typically by a factor of 3-4). Examples of 3d CFC, namely N11, NB31 and NB41 from the SEPCARB<sup>®</sup> series produced by the SNECMA company, have been studied with LID in [Z9], where also their thermal properties have been shown in detail. Here the 2d DMS780 CFC, which is used in the JET tokamak will be discussed as an example for anisotropic materials.

Figure 2.19 shows its heat properties, where the open symbols and thick lines indicate the values for the directions of high heat conductivity, while the closed symbols and thin lines stand for the third direction. In the temperature range of interest, the low heat conductivity is always a factor of more than 4 lower than the high heat conductivities. In general the temperature dependence of the heat parameters is much stronger than for tungsten. The heat capacity is strongly increasing with temperature by nearly a factor of 3 until 2300 K, but saturates at high temperatures. At the same time, the heat conductivities reduce by a factor of 4. Both effects lead to a strong reduction of the thermal diffusivities according to equation 2.9 by an order of magnitude, while for W this reduction is only a factor of 2. On the contrary, for the material

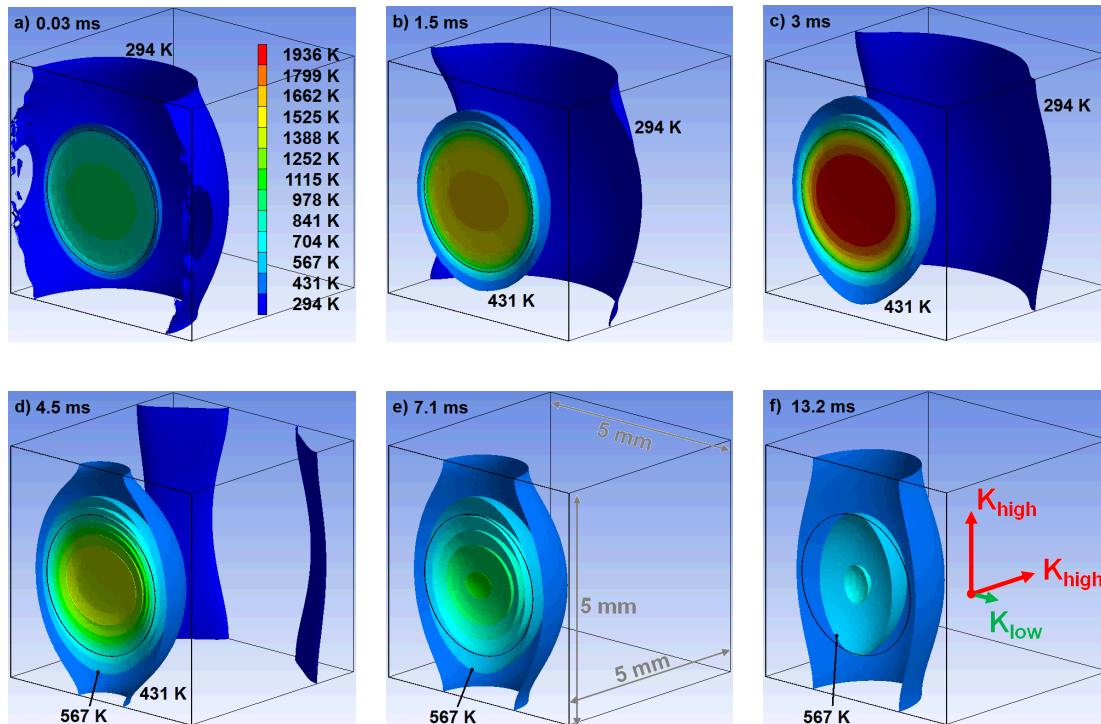


**Figure 2.19.:** Heat properties of the two-directional Dunlop DMS780 ("JET CFC"); lines are only guidelines; label "low" marks the direction of low heat conductivity; "high" marks the other two directions

heat term, which determines the temperature, the temperature dependence of the heat capacity and conductivity compensate each other, resulting in a nearly constant value as indicated by the blue horizontal lines. Therefore, the analytic calculation of the temperature and the numeric simulation with temperature independent heat properties does not introduce a large error. However, these approximations cannot take into account the anisotropy and give only an estimation of the lower limit for the temperature by using only  $K_{high}$ . The laser intensity which is deduced from this calculation guarantees the desired temperature, but can easily lead to overheating.

For a more accurate modeling of the heat propagation, the ANSYS simulation code was used. A cubic simulation volume of  $5 \times 5 \times 5 \text{ mm}^3$  was chosen (cf. figure 2.20e), on which a circular laser pulse of  $\varnothing 3 \text{ mm}$  with  $500 \text{ MW/m}^2$  absorbed intensity was applied for 3 ms. The CFC was oriented in the perpendicular fibre orientation with the low heat conductivity in horizontal direction (cf. figure f). The CFC was covered with a  $2.5 \text{ }\mu\text{m}$  thick Mo interlayer and finally a  $12 \text{ }\mu\text{m}$  thick W layer on the laser incident surface. Both material transitions were simulated





**Figure 2.20.:** Laser heating of a two-directional CFC (Dunlop DMS780) with  $2.5 \mu\text{m}$  Mo interlayer and  $12.5 \mu\text{m}$  W layer; perpendicular CFC fibre orientation;  $500 \text{ MW}/\text{m}^2$  absorbed intensity; 3 ms; circular  $\varnothing 3 \text{ mm}$  laser spot; numeric simulation with ANSYS

with ideal heat transmission. Although the layers have isotropic heat properties, effects due to the anisotropy of the substrate are clearly visible in the shape of the isotherms. Already at the very beginning of the laser pulse (figure a) the 294 K isotherm, which is just one degree above the initial temperature, reveals the anisotropy. While it has reached the boundary of the simulation volume in horizontal direction (direction of low heat conductivity), it has already extended over the boundary in vertical direction. Opposite to this elongation, the isotherms in the spot centre are elongated in the horizontal direction. The transition takes place in the region of the laser spot boundary, where the isotherms have a circular shape. After the first half of the laser pulse duration (figure b) also these isotherms start to become elongated vertically. Their eccentricity increases with time and is much more pronounced at the end of the laser pulse (figure c). Here the 431 K isotherm approaches a size of 5 mm in vertical direction, but is still close to the laser spot size in horizontal direction. In the cooling phase (figures d-f), this isotherm extends into the vertical direction, leaving the simulation volume, while stagnating in horizontal direction until it begins to shrink. The main effects of the anisotropy on the heating process are the following:

- For lower temperatures an elongation of the shape of isotherms on the surface in the direction of high heat conductivity occurs, which increases with time.
- For higher temperatures an elongation of the shape of isotherms on the surface in the direction of low heat conductivity occurs, which reduces in time.

With respect to the lateral expansion of the isotherms, the threshold isotherms are now a function of direction. For the horizontal direction, the 567 K isotherm stagnates, while all hotter isotherms shrink. In the vertical direction the stagnation temperature is higher, around 800 K. Despite the elongation effect, the stagnation position of this temperature is closer to the laser spot than for the 567 K isotherm in the horizontal direction.

The implications of the anisotropy on the desorption process can be judged by the fraction of desorbed deuterium at these temperatures. At 567 K typically less than 5% of the retained deuterium are desorbed from carbon, thus the heat propagation in horizontal direction does not lead to significant additional desorption. On the contrary, the isotherm for 50% desorption never reaches the laser spot border in horizontal direction and therefore small areas inside the spot remain undesorbed by more than half, while it extends over the border in vertical direction. At 800 K about one third of the retained deuterium in C is desorbed, thus the heat propagation in vertical direction leads to significant additional desorption outside the laser spot. Although the shape of the desorbed area changes, the size of the area is nearly the same as the circular laser spot area. For the later cooling phase beyond the stagnation, the anisotropic effects in the temperature distribution increase strongly (cf. figure e and f). In this phase the isotherms below 600 K even shrink in horizontal size, while still expanding in vertical size. However, these low temperatures are not important for desorption on the millisecond scale.

Beside this qualitatively different thermal behaviour than for isotropic materials, it is of much greater importance for the desorption process to know the laser intensity which is necessary to reach the desired surface temperature of 1800-2000 K. These calculations have to be done for both fibre orientations separately. For the analytic calculation according to equation 2.7, the two values marked by horizontal lines in figure 2.19 have been used. The heating intensities obtained from this equation were used as a first guess for the numeric calculation with ANSYS. Several simulation runs with 3 ms pulse duration have been done iteratively to reach the desired temperature range. For the DMS 780 CFC without any surface layer, the result was a laser pulse of 500 MW/m<sup>2</sup> absorbed intensity for the perpendicular, and 280 MW/m<sup>2</sup> for the parallel fibre orientation. These pulses were used for the retention analysis of this material after exposure in TEXTOR, which resulted in the deposition of a 280 nm thin a-C:H/D layer. The maximum temperature measured by the point pyrometer during ex situ LID has been averaged over the measurement positions and is compared to the theoretical temperatures in table 2.4.

CFC fibre orientation:	perpendicular	parallel
laser pulse:	500 MW/m <sup>2</sup> , 3 ms	280 MW/m <sup>2</sup> , 3 ms
measured temperature $T$ / K:	1910 ± 150	1982 ± 40
analytic $T$ / K:	1733	2024
material heat term $\frac{\sqrt{k}}{k} / 10^{-5} \frac{\text{K} \cdot \text{m}^2}{\text{W} \cdot \sqrt{\text{s}}}$ :	4.66	10
deviation factor to measurement:	1.10	1.02
numeric (ANSYS) $T$ / K :	1860	2011
deviation factor to measurement:	1.03	1.01

**Table 2.4.:** Maximum temperature for CFC (DMS 780): measured temperatures with statistical one-sigma deviation; analytic 1D calculation; numeric 3D calculation with temperature dependent, anisotropic heat parameters and heat radiation

The agreement between the measured and numerically simulated values with ANSYS is within 3%. The analytic values have a maximal deviation of 10%. The quite large scatter in the measured data for the perpendicular fibre orientation is a result of the inhomogeneous CFC microstructure. Spatially highly resolved thermography of such CFC materials shows this inhomogeneity [Herrmann4]. The inhomogeneity is pronounced for the perpendicular fibre orientation because all three CFC layers are visible on the surface, while for the parallel

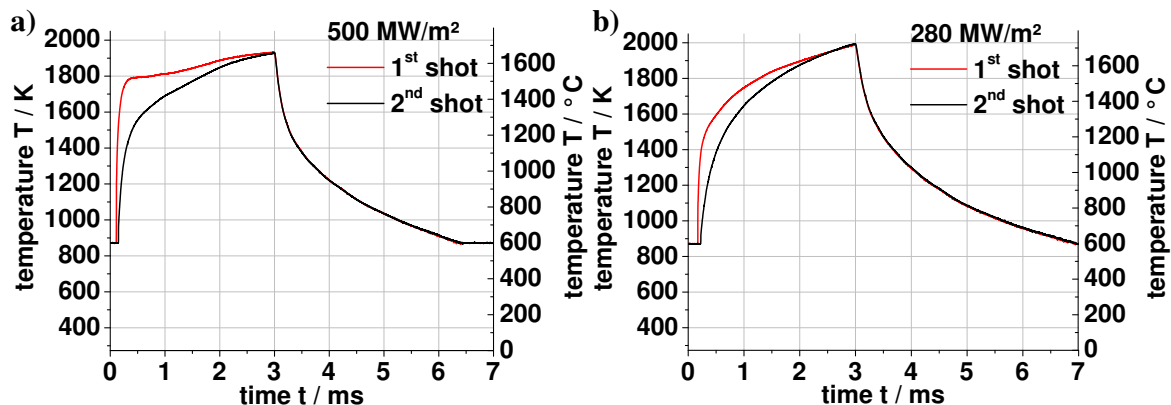
fibre orientation the surface consists of only one of the three layers. This inhomogeneity on the microscopic scale is not implemented in the numerical calculation with anisotropic heat conductivity, but its effects are strong and evident as will be shown in the next chapter on surface modifications.

### 2.4.3. Amorphous Hydrocarbon Layers (a-C:H/D)

Amorphous hydrocarbon layers are important in the field of hydrogen retention, as they contain the largest fraction of the total hydrogen retained in the plasma chamber, if they are formed. In this section it will be shown for which cases their temperature during LID can be calculated and how. For the other cases, the problematic effects and their consequences are described. Furthermore it will be demonstrated, how the analysis of the surface temperature during a laser pulse can give valuable information on the wall condition and the properties of a surface layer. The first part of this section deals with the heating of thin amorphous hydrocarbon layers, which are nearly transparent for the laser due to their optical properties and thickness. For the a-C:H/D layers studied here, this is the case for thicknesses below ca. 500 nm. The second part of the section deals with the heating of thick a-C:H layers, which absorb the laser energy within the layer.

For the thin layers the temperature of the layer can be equated with the temperature of the substrate. The heating of the substrates is described in the other sections of this chapter, but two additional thermal effects of thin amorphous hydrocarbon layers modify the heating process. These shall be discussed in this section and will be called "heat curvature effect" and "heat offset effect". The first effect appears for thin a-C:H/D layers on carbon substrates (graphite or CFC), while the second effect occurs for the same layers on tungsten substrates (bulk W or W layers).

The heat curvature effect can be seen on the CFC material introduced in the last section (pure DMS 780), which had a 280 nm a-C:H/D layer due to exposure in TEXTOR. In the ex situ LID analysis of this samples, repetitive laser shots on the same position were done for the two different fibre orientations with the adjusted laser intensities (cf. figure 2.21).



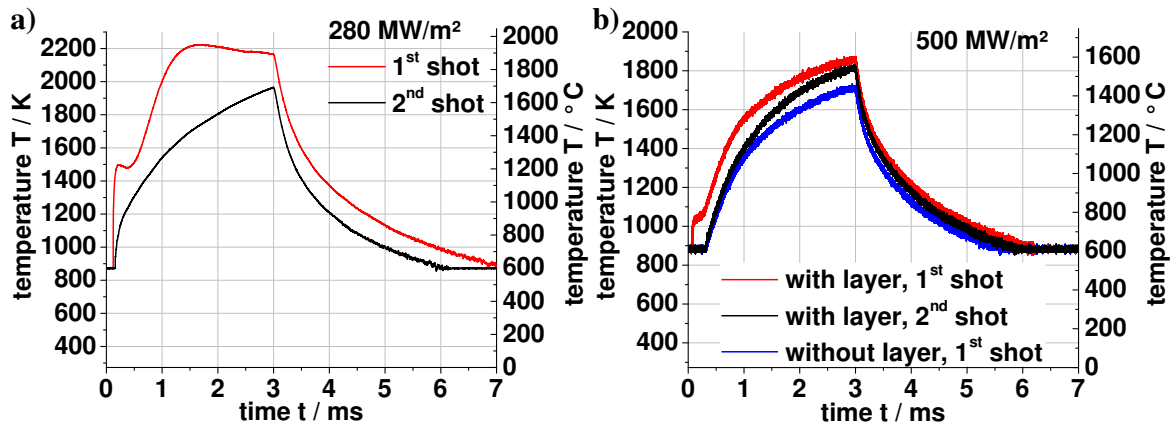
**Figure 2.21.:** Heat curvature effect: surface temperature evolution for CFC (DMS 780) in perpendicular (a) and parallel (b) fibre orientation; both covered with a thin a-C:H/D layer from TEXTOR; measured with a point pyrometer

The final surface temperatures deviates slightly from position to position, especially in the case of the perpendicular fibre orientation. But the maximum temperature is identical for all shots on the same spot. On the contrary, the surface temperature evolution is always different for the first shot than for the subsequent shots on the same spot. This is especially true

for the early stage of the pulse ( $t < 0.5$  ms) where the temperature rises much faster in the first laser pulse. The derivative of the first pulse falls below the derivatives of the subsequent shots already at 0.2-0.3 ms. During the whole temperature rise the heat curvature is therefore changed in the first laser pulse – steeper temperature rise first, flatter rise later. This heat curvature effect is an analogue to the faster charging of a capacitor with a lower capacitance. For thermal effects instead of electrical charge, it has been shown in simulations, that this characteristic shape change with equal final temperature is due to a lower product of density and heat capacity  $\rho c$ , especially for a layer on the surface [Herrmann7]. Therefore it is very probable that the thin a-C:H/D layer on the surface is responsible for this effect. Thus, the temperature development indicates that the heat capacity or density or both are higher in the subsequent shots. Apparently the laser heating induces this process already during the first laser pulse, since the temperature decay after all laser shots is identical. If  $\rho c$  was still low during the cooling phase of the first laser pulse, then the temperature would decay much faster, with a time constant comparable to the heating phase. This has also been shown in [Herrmann7]. Probably both components contribute to the effect, since it is known that the mass density of a-C:H layers increases when it contains less hydrogen but the same carbon content [Schwarz99]. It is also known that a-C:H layers restructure during heating from diamond-like  $sp^3$ -hybridised carbon bondings to graphite-like  $sp^2$ -hybridisation in the transition range of 700-900 K [Vietzke87]. This restructuring is combined with a heat capacity increase, since the heat capacity of graphite is considerably higher than that of diamond. Both processes are completed at ca. 900 K, while the temperature derivatives cross at 1100-1200 K, which fairly agrees, considering that this is a dynamic process, that needs some time to take effect. The heat curvature effect is not important for the desorption of carbon based materials, since the same final temperature is reached in any case. But the changed temperature development affects the duration of the hot phase, which becomes important for materials like W with a slow hydrogen diffusion. For W layers on CFC this will already become a considerable effect, which significantly increases the time available for hydrogen diffusion.

The second temperature effect of thin a-C:H layers is the heat offset effect, that appears when the a-C:H layer is on top of a tungsten material – either W bulk or a W layer. The characteristic feature of this effect is a sharp temperature jump in the early phase of the heating pulse. It is best visible on the ITER-like wall CFC, that is covered with a Mo interlayer (ca. 3  $\mu\text{m}$  thick), a W layer (ca. 12  $\mu\text{m}$ ) and the 280 nm thin a-C:H layer from TEXTOR exposure (figure 2.22 left). Both temperature developments are from the same position on the surface, measured with ca. 2 min temporal distance from each other. Subsequent pulses are again nearly identical to the 2<sup>nd</sup> shot only slightly reducing in temperature. The striking heat jump in the beginning of the 1<sup>st</sup> pulse and the surplus temperature are present in stronger or weaker extent for every sample with an a-C:H layer on W disregarding the substrate. It also appears on a bulk W sample exposed to the TEXTOR plasma, that was only partly covered with a 30-50 nm thin a-C:H/D layer, while a part at the plasma facing side has not been covered. The temperature offset is seen here as well (figure 2.22b), but with a much smaller temperature jump due to the reduced layer thickness. The jump does not appear on the part without layer and for any 2<sup>nd</sup> or further heat pulse. Since the a-C:H/D layer is very thin for this sample, the heat offset effect appears nearly alone without the curvature effect, since the heat capacity is negligible for such a thin layer. Therefore the red and blue curves are just shifted vertically by 150-200 K, excluding the initial jump. On the 280 nm a-C:H/D layer the heat curvature effect appears in addition to the heat offset effect, with the result that the curves do not run parallel to each other.

An offset in the temperature or heat flux in layered systems is usually attributed to a changed heat conductivity due to a good or bad heat contact between layer and substrate [Herrmann7]. The physical effect behind the heat offset effect must be due to the combination of materials

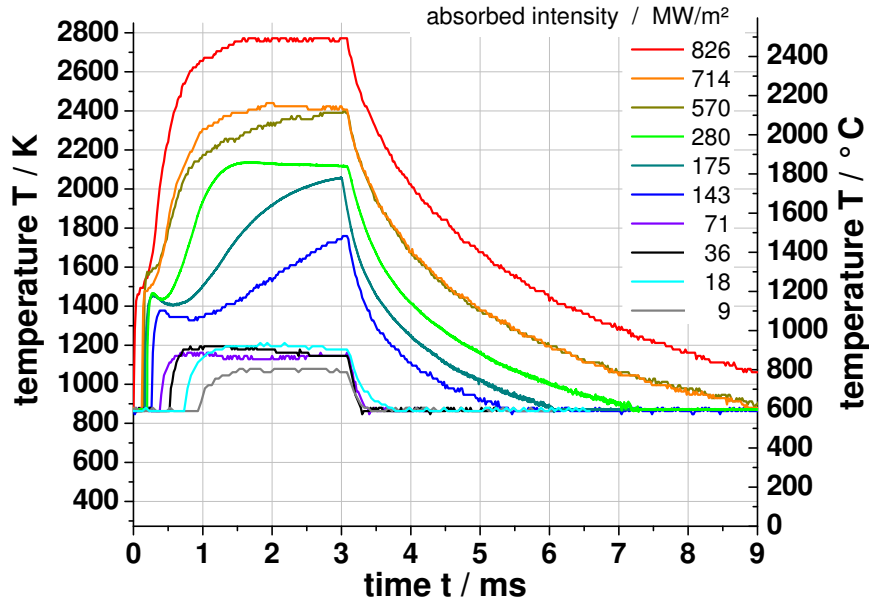


**Figure 2.22.:** Heat offset effect: surface temperature evolution for a) CFC (DMS 780) in parallel fibre orientation 3  $\mu\text{m}$  Mo, 12  $\mu\text{m}$  W and a 280 nm a-C:H/D layer; b) pure W with 40 nm a-C:H/D layer; both measured with a point pyrometer

of layer and substrate, because it only appears for carbon layers on tungsten but not on carbon materials. The interface between a carbon layer that starts to grow on carbon can adapt smoothly to the atomic structure of the substrate, due to their similarity. On the contrary, carbon and tungsten have very different density, heat properties, mechanical properties etc. Therefore, a large mismatch of these properties appears at the interface of layer and substrate. The experimental results clearly show that the heat contact strongly improves after a single laser heating pulse. It is therefore very probable that the mismatch in properties is removed. Additionally, it is known that the carbon content is unchanged in the laser spots after heating, which is known from NRA measurements (cf. figure 3.1 on page 69 and [Rubel12]). Therefore it must be concluded, that the carbon is bound stronger to the W substrate after the first heating pulse, probably due to the formation of tungsten carbide.

The stepwise temperature increase at the beginning of the pulse is heat flux-dependent as mentioned already in [Herrmann7]. This is also seen here in a power scan (figure 2.23) on the CFC sample described above. Below an absorbed laser intensity of ca.  $75 \text{ MW/m}^2$  the temperature quickly rises to a constant value of 1100-1200 K. The reason for the constant phase is not clear and cannot be explained with the heat parameters and their temperature dependence for CFC, Mo and W. The temperature jump which is characteristic when the heat offset effect occurs, is not visible for these lower laser intensities, in contrast to laser intensities of  $140 \text{ MW/m}^2$  and above. For these higher intensities, the temperature jump appears at temperatures of 1380 to 1580 K, slightly rising with laser intensity, except for the highest intensity. In some of the laser pulses above  $140 \text{ MW/m}^2$  a constant temperature phase occurs like for the low intensity pulses. The reason is unclear here, too, especially since the effect does not appear systematically in all of these laser pulses.

The final temperature value has also been calculated numerically with ANSYS, implementing the Mo interlayer and the W layer on top of the CFC. The heat parameters for all three materials were programmed temperature dependent and an ideal heat contact for both interfaces was used. Therefore the calculated temperatures represent a lower limit, since an imperfect heat contact increases the surface temperature. The results should rather be compared to the situation with improved heat contact in the experiment, which is reached in the second laser shot (cf. table 2.5). The agreement of measured and calculated values is worse than for the CFC without W/Mo layers (cf. chapter 2.4.2), especially for the perpendicular fibre orientation. This is again due to the more inhomogeneous surface, on which the fibres oriented parallel to the surface tend to overheat and thus artificially increase the measured value, since the pyrometer integrates over an area with inhomogeneous temperature. The high temperature



**Figure 2.23.:** Laser power scan on parallel CFC (DMS 780) with 3  $\mu\text{m}$  Mo, 12  $\mu\text{m}$  W and a thin a-C:H/D TEXTOR layer on top. The data show a power dependent temperature offset in the early phase of the heat pulse.

of these hot fibres increases the measured data above the mean temperature of the detection area. This pyrometric effect is due to the nonlinearity of heat radiation described by the Planck formula which has been explained for CFC materials in [Herrmann4].

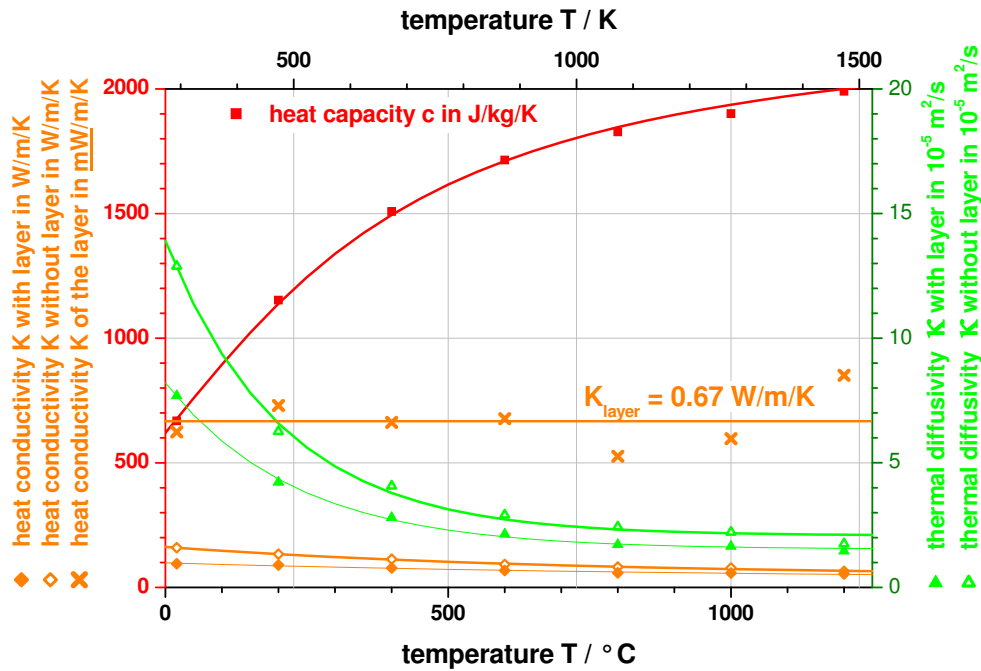
The table shows the average difference between the maximum temperature of the first and second laser pulse, which is 139 K for the perpendicular orientation with a low data spread, while it is on average 200 K for the parallel orientation with a maximum of 260 K.

CFC fibre orientation:	perpendicular	parallel
laser pulse:	500 $\text{MW}/\text{m}^2$ , 3 ms	280 $\text{MW}/\text{m}^2$ , 3 ms
measured temperature $T$ / K (1 <sup>st</sup> shot):	2270 $\pm$ 50	2070 $\pm$ 120
measured temperature $T$ / K (2 <sup>nd</sup> shot):	2130 $\pm$ 50	2000 $\pm$ 140
temperature difference $\Delta T$ / K (1 <sup>st</sup> -2 <sup>nd</sup> shot):	139 $\pm$ 8	200 $\pm$ 60
numeric (ANSYS) $T$ / K :	1854	1858
deviation factor to measurement (1 <sup>st</sup> shot):	1.22	1.11
deviation factor to measurement (2 <sup>nd</sup> shot):	1.15	1.08

**Table 2.5.:** Maximum temperature on CFC (DMS780) with 3  $\mu\text{m}$  Mo, 12  $\mu\text{m}$  W and a thin a-C:H/D TEXTOR layer on top: measured temperatures with statistical one-sigma deviation; numeric 3D calculation (CFC+Mo+W) with temperature dependent, anisotropic heat parameters and heat radiation

The heat propagation in thick a-C:H layers can be qualitatively different compared with thin layers or bulk materials. To illustrate this, the heat propagation in the deposited layer on an ALT-II limiter tile (N° 2/19) is discussed, that has grown in TEXTOR within an accumulated plasma time of 33200 s and a fluence of  $9.64 \cdot 10^{25}$   $\text{H\&D}/\text{m}^2$ . The heat conductivity of this thick hydrocarbon layer was measured by a laser-flash method. To fit into the device, a sample of  $9 \times 9 \text{ mm}^2$  was cut from the tile at the edge of the toroidal gap. A position has been chosen, where the layer did not flake when touched and had a homogeneous appearance. The thickness of the sample was reduced to 3 mm and a reference sample without layer was

cut from the graphite substrate below the sample with identical geometry. In the laser-flash device the front side of the sample is heated by laser pulses and the temperature on the rear side of the sample is recorded. A mathematical procedure evaluates the time duration needed for the temperature rise to the half of the temperature difference  $\Delta T/2$  and calculates from this the thermal diffusivity  $\kappa$  of the sample. This measurement is repeated at different base temperatures from 293 to 1473 K. Afterwards the same measurements were performed with the reference sample. The measured thermal diffusivities are shown in figure 2.24 in green triangles. With the layer, the thermal diffusivity is significantly reduced by a factor of nearly 1.7 at room temperature, reducing to 1.2 for the highest temperature measured.



**Figure 2.24.:** Measured thermal diffusivity of graphite with a thick a-C:H/D layer (TEXTOR ALT-II N° 2/19) and a reference sample without layer; deduced heat conductivities and used heat capacity; lines are only guidelines

From the thermal diffusivity the heat conductivity can be calculated according to equation 2.9 using the density of  $1850 \text{ kg/m}^3$  and the temperature dependent heat capacity of graphite, which is shown in red in the figure. They are used for the sample with layer and the reference sample, since the layer is thin compared to the substrate thickness. Therefore, the reduction factors for the heat conductivities remain the same for the combined system as for the substrate alone. The conductivity reduction is due to a very low heat conductivity of the layer itself. Its value can be calculated using the concept of thermal resistance

$$R_{th} = \frac{d}{K} \quad (2.11)$$

$d$  ... thickness of the material in m

$K$  ... heat conductivity in  $\text{W/mK}$

The total thermal resistance of the combined system is the sum of the resistances of the substrate and the layer.

$$R_{tot} = R_{sub} + R_{layer} \quad (2.12)$$

Inserting equation 2.11 into 2.12 and resolving for the heat conductivity of the layer yields

$$K_{layer} = d_{layer} \frac{K_{sub} K_{tot}}{d_{tot} K_{sub} - K_{tot} d_{sub}} \approx \frac{d_{layer}}{d_{tot}} \frac{K_{sub} K_{tot}}{K_{sub} - K_{tot}} \quad (2.13)$$

The approximation is valid, if the layer is very thin compared to the substrate thickness, which is the case here. The layer has a very inhomogeneous microstructure with thicknesses from 2 to 15  $\mu\text{m}$  as seen on cross-sections and a surface roughness of  $R_a = 6\text{-}10 \mu\text{m}$  measured by profilometry. A mean thickness of 8  $\mu\text{m}$  was evaluated and used for the calculation together with the heat conductivities already deduced from the measured thermal diffusivities for the substrate and the combined system. This results in a very low heat conductivity of the layer of 0.67  $\text{W/m K}$  on average with no clear temperature dependence (cf. crosses in figure 2.24).

The effect of this extremely low heat conductivity of a-C:H layers is negligible for thin layers below about 500 nm, since they are fairly transparent for the laser light, which is therefore mainly absorbed in the substrate as described in chapter 2.3 (cf. figure 2.10 on page 46). The heat propagates mainly perpendicular to the surface due to the good thermal conductivity of the substrate. The situation changes for the thick layers on the ALT-II limiter, where 90% of the laser light is absorbed in the first 1.5  $\mu\text{m}$  of the layer. The laser absorption volume has no direct contact to the substrate. No fast heat propagation into the depth is possible, thus a significant lateral heat propagation results, that increases the heated area on the surface. The layer was analysed by LID on the adjacent areas of the same ALT-II tile, where the samples had been cut from. The laser beam had a circular area of 4  $\text{mm}^2$ , but resulted in a heated and desorbed area of up to 8  $\text{mm}^2$  in the thickest parts of the layer directly at the edge of the ALT-II tile at the toroidal gap. The area was measured by optical microscopy, since a sharp border of the desorbed area is visible between the colourful unheated layer and the grey spot. With decreasing layer thickness the desorbed area decreases until it is finally identical to the laser beam size on areas without layer. The value of the laser intensity was calculated with the laser beam area of 5.4  $\text{mm}^2$ , but the heated area already doubled in size for 90  $\text{MW/m}^2$  in 1.2 ms pulses and reached up to 23  $\text{mm}^2$  for 520  $\text{MW/m}^2$  in 1.4 ms pulses. Further studies of this spot size change will be given in chapter 3.1 for a different ALT-II tile (N° 6/19).

The second effect of the low heat conductivity is a possible overheating of the surface to temperatures much above the desired values of 1800-2000 K. Temperature measurements during in situ LID by a fast IR camera on the ALT-II tile N° 6/19 have shown temperatures up to 5400-6700 K even for low laser intensities of 200  $\text{MW/m}^2$  in 1.3 ms laser pulses. For subsequent laser shots the maximum temperature decreases continuously by several hundred degrees per shot, which probably results from decreasing layer thickness due to evaporation.

The increase of the desorbed area only appeared for very thick layers like the ALT-II deposit and is concluded from post mortem microscopy of the target surfaces and infrared camera measurements during LIDS. A thinner layer of 2.5  $\mu\text{m}$  a-C:H on W (the Balinit® layer) has a similar, even shorter laser absorption length than the ALT-II layer, thus absorbing the laser light completely in the layer. But unlike the ALT-II deposits, the desorbed area is identical to the laser irradiated area on Balinit®. This sample has a Cr-based interlayer, which improves the thermal contact between a-C:H layer and substrate. However, similarly thick diamond like carbon (DLC) layers produced by arc plasma deposition without any interlayer did not show the effect, indication that other factors like the inner structure of the layers might play a role. The thick hydrocarbon layers, have a homogeneous structure, which is created in a single coating process, while on the ALT-II tile the layer consists of a multi-layer structure, which could promote the strong lateral and reduced perpendicular heat propagation.

For thick, light absorbing layers, care must be taken to evaluate the size of the heated area by close visual inspection or thermography, since the thermal properties and the thickness of the layer influence the desorbed area very sensitively.

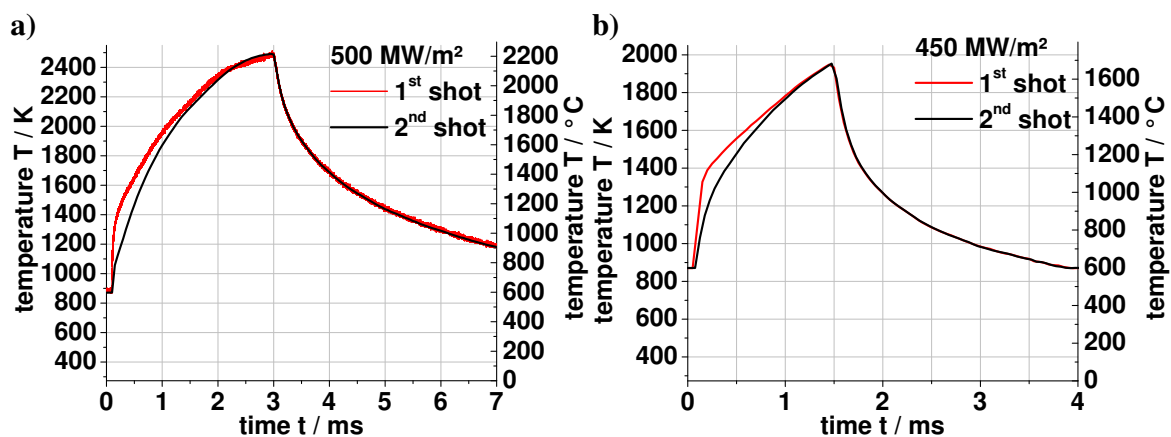


### 2.4.4. Mixed C/W Layers

Layered mixed materials like the JET W coatings for the ITER-like wall can also be called mixed material. But they have been treated in the previous section, since the surface temperature effects are dominated by the top layer. Due to exposure in TEXTOR, the deposited a-C:H/D layer governed the surface temperature effects and thus they have been described in the section on a-C:H layers. The mixed material discussed here is not layered but rather a homogeneous mixture. Here the temperature development of a hydrogen-rich mixed layer of carbon and tungsten will be discussed, to show that a material combination can have a response different from its constituents. This shows the necessity to study mixed materials and see them as a new material, because their behaviour cannot be deduced, even if the behaviour of all its constituents is known.

As will be described in chapter 6.1 on page 138 a C/W/H/D mixed layer was grown in TEXTOR by a special limiter geometry. It resulted in a 200 nm hydrocarbon layer with tungsten content (34 at% C, 25 at% D, 25 at% H, 10 at% W, 5 at% O and 1 at% B). For details see chapter 6.1, where its desorption is studied. Typical temperature evolutions of the surface during laser heating (figure 2.25) show a shape which is already known for thin a-C:H layers on graphite or CFC. The difference between the first and the second shot shows the heat curvature effect due to a change in the heat capacity like on layers without W content. The heat offset effect is missing, which shows that the W and C atoms are strongly bound to each other, without signs of discontinuity in the properties of the material or the attachment of the layer to the substrate. In this sense the thermal behaviour is like for a-C:H layers without W. But the final temperature does not agree with the theoretical calculations for pure graphite, that should reach 1950 K for a pulse of  $500 \text{ MW/m}^2$  during 3 ms. This temperature could be reached with an absorbed laser intensity of  $450 \text{ MW/m}^2$  in a 1.5 ms pulse (figure 2.25 right), which should theoretically reach only 1350 K. The final temperatures measured by the point pyrometer are always ca. 500-600 K higher than the calculated temperatures.

However, the measured temperature seems to be real, since the emissivity of the pyrometer was set to 0.8, which is correct according to the measured reflectivity (cf. fig 2.9 on page 43 C/W/H/D layer on rough graphite). Obviously the mixed material has significantly different heat properties than a-C:H layers, which are unknown at this point.



**Figure 2.25.:** Surface temperature evolution on a C/W/H/D mixed layer grown in TEXTOR on unpolished graphite; measured with a point pyrometer

The comparison of theoretically calculated temperatures with the measured temperatures and the study of the temperature evolution, as presented in this chapter, can be very helpful, if the target cannot be inspected by other methods. This is especially valuable, when the method

## *2. Laser Heating of Different Materials*

---

is applied in situ in large devices like ITER, where access to the wall is not easy. The heating process during laser induced desorption can then give answers to questions, whether a layer has grown on the surface, whether the material properties changed in comparison to the last LID analysis of this position or whether the layer and substrate are strongly connected or have a bad heat contact.

### 3. Surface Modifications due to Laser Heating

Surface modifications due to the laser heating are important for the application of laser induced desorption itself. For the evaluation of the areal concentration of hydrogen the size of the desorbed or heated area must be known, which is not always equal to the laser irradiated area. As spatially resolved thermography, which could directly measure this area, is not always available, surface analysis can often help to determine this important quantity. Moreover, the information about the modified surface is important, when LID is repeated on the same position. The surface can be changed such strongly by the first laser pulse that this has an influence on the heating process and surface modifications during subsequent pulses on the same spot.

In a wider view, the surface modification can influence the compatibility of LIDS with plasma operation as they can include the release of material in atomic or molecular form or larger fragments. This can have a direct influence on the plasma or can damage or weaken the wall material, which may lead to effects on the plasma operation in the future. This is a form of laser induced wall-plasma interaction which can be only assessed, when the extent and characteristic of the surface modifications are known. Inversely, the changed surface can lead to an altered plasma-wall interaction locally at the laser spot due to new surface properties. This chapter will not investigate all these consequences but it provides the necessary basis for such assessments as it investigates the laser induced modifications and the underlying processes.

The surface investigation begins with thin a-C:H layers as here connections to previous publications exist that are extended to thicker and very thick layers. Important questions that will be answered in chapter 3.1 are, whether significant C amounts are released during LID and how much the desorbed area increases depending on the layer thickness. Additionally, also the remaining hydrogen amount inside the laser spots studied by NRA will be discussed as it is a by-product of the specific surface analysis method. In the second section the probable future wall material tungsten is introduced. First, a mixed material layer of C and W is studied that has been grown in TEXTOR and can grow similarly wherever carbon and tungsten components are in contact with the same plasma. Then, the case of bulk tungsten is analysed, which introduces many new effects since it can melt in vacuum, in contrast to carbon. Looking further into the future, a special plasma modified W is studied, called W fuzz. It is a sponge-like W structure that can form in plasmas that contain He and thus might form in a fusion reactor because He is the product of the D-T fusion reaction. The behavior of such an exotic structure during LID heating is therefore very interesting. In the last section an alternative to bulk W is studied, namely the coating of other wall materials (here CFC) with a W layer. The analysed material is part of the ITER-like wall that is investigated in JET. The surface modifications that will be studied in the next 5 sections reach from the optical appearance like change of colour, brightness, reflectivity and transparency over local modifications like blistering, bubble formation, gas blister growth, cracking, layer slide, evaporation by sublimation and material redeposition, to large-scale modifications like surface roughening, smoothing, melting, rapid solidification patterns, crater formation, layer stiffening, layer folding, layer delamination, movement of grain boundaries and damage thresholds.

### 3.1. Graphite and a-C:H Layers

In previous studies of LID on thin a-C:H layers on graphite [Irrek8], the surface modifications were classified into unavoidable and avoidable effects. Unavoidable effects are those, which appear for surface temperatures below the necessary desorption temperature for complete desorption. Avoidable effects occur, when the surface temperature exceeds this temperature, which is called overheating. This distinction is not always strictly possible for a whole laser spot, because for some samples the spatial temperature distribution is strongly inhomogeneous due to material properties. Then local overheating on a microscopic scale coexists within a major area which is not overheated and only shows unavoidable surface modifications.

Unavoidable modifications for thin a-C:H layers on graphite are cracking of layer and substrate, layer blistering, slight blister sublimation and optical modifications such as colour and reflectivity change. Avoidable modifications are the complete sublimation of blisters or layer and the onset of the sublimation of the graphite substrate.

The main findings in the unavoidable category were that the cracks are always found in the layer and graphite at the same position. Hence, it was concluded that they always appear in parallel because the cracking of the substrate is the reason for the cracking of the layer. The typical width of the cracks was about 250 nm as deduced from SEM images [Irrek8, p.45f]. The blisters had different sizes from a few microns to the order of 10  $\mu\text{m}$ . Their shape was not necessarily circular but often irregular and they were formed already at low desorption temperatures below 850 K. With increasing layer thickness (already at 180 nm) few blisters even formed during the layer growth due to internal stresses in the layer. The laser heating enhanced the blistering process, especially by the increase of blister density rather than blister size.

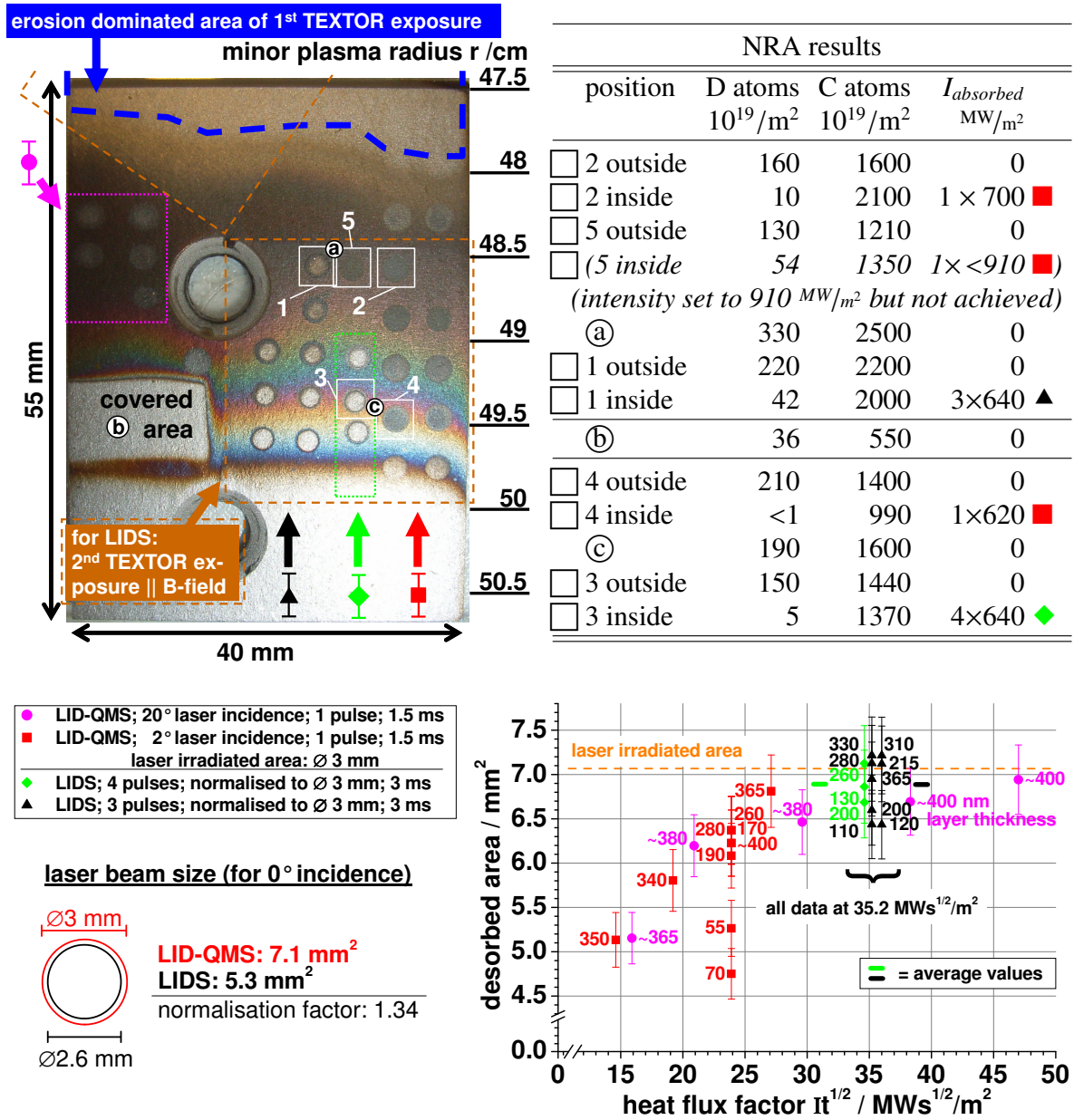
Both processes of cracking and blistering increase the surface roughness and lead to local detachment of the layer from the substrate. This also lowers the thermal contact and the total heat conductivity towards the substrate. Locally, this forces the heat flow parallel to the surface along the layer, as the heat cannot be conducted towards the substrate at the detached areas. Since the heat conductivity in the layer is about two orders of magnitude lower than in the substrate, this leads to an overheating of the detached parts compared to the attached layer. The heat cannot dissipate quickly, hence the blister caps and the crack edges start to sublime as they are the areas which are furthest away from the substrate.

Concerning the unavoidable optical changes, mainly four effects were discussed in the literature. The *reflectivity* of the laser light increases slightly and a colour change occurs, which is seen in the *colour angle* and *colour saturation* (details in [Irrek8, p.39ff]). At the same time the *transparency* of the layer is lost which is attributed to the internal restructuring of the layer from  $\text{sp}^3$  to  $\text{sp}^2$  bondings in the graphitisation process at ca. 800 K (cf. chapter 2.4.3).

The avoidable effects, that occur for heating over the necessary desorption temperature, are firstly a continuation of the already initiated sublimation process. This means that the blisters and other detached layer areas like crack edges can be sublimated completely. Then the whole layer sublimates and finally also the graphite substrate. It was found that these severe damages probably occur during a phase of nearly constant temperature at the end of the laser pulse, typically after 5 ms of heating [Irrek8, p.47f].

In the present work similar studies of thin a-C:H/D layers formed in the TEXTOR tokamak were performed. First, similarly thin layers are studied but on tungsten substrate, which opens a possibility to investigate whether the desorption of hydrogen can really be done without significant carbon sublimation.

Afterwards, the size of the laser modified area is studied as this aspect is very important since it is linked with the desorbed area, which is a crucial factor of LID. It is already studied for



**Figure 3.1.:** Bulk W with a-C:H/D layer grown in TEXTOR (1<sup>st</sup> exposure) and analyzed with LIDS (▲, ◆ in 2<sup>nd</sup> exposure by heating to ca. 2600 K), LID-QMS (■, ● at different temperatures between 570 and 2700 K), single-point NRA (@-©) and NRA inside and outside the laser spot (□1-5); NRA data and photography already published in [Rubel12] in simplified form; graph: laser spot size vs. HFF

### 3. Surface Modifications due to Laser Heating

---

the thin layers and a-C:H layers of several micrometres, but becomes more important with increasing layer thickness like on layers with more than 10  $\mu\text{m}$  thickness.

Then, known and new surface damage mechanisms are shown on the thicker layers like blistering and blister cap removal, cracking and delamination of the layer. They are important to know when assessing the release of material due to LID, which is important for the application in a plasma as it is a source of plasma impurities and dust.

Finally, the colour effects are discussed shortly as it gives further information on the heating characteristics.

Several of these topics are discussed on three samples which are now shortly introduced and the reader is encouraged to view the mentioned figures in advance to be acquainted with the samples.

- The thin a-C:H/D layer is studied on an annealed W plate of 2 mm thickness provided by Goodfellow GmbH (99.95 wt% pure, unpolished, further details in Appendix A on page 232) that was exposed on a double-roof limiter in the TEXTOR SOL. The limiter tip was at  $r = 47.5$  cm minor plasma radius for 30 NBI heated discharges (#111087-118) on the IDS\*. The inclination of the sample to the magnetic field lines was  $36^\circ$  which led to the deposition of a thin a-C:H/D layer over ca. 4 cm of the plate, which corresponds to  $r \approx 47.5\text{-}50$  cm. An image of the sample is shown in figure 3.1.
- The intermediate layer thickness is studied on a very homogeneous a-C:H layer provided by the company *œrlikon balzers* with a special Cr based interlayer between substrate and layer to improve the thermal contact. Details of this layered structure called *Balinit®* are shown in figure 3.7 on page 81 and an image of the sample in figure 3.2 on page 74. The W substrate was provided by Negele Hartmetall-Technik GmbH (99.95 wt% pure, unpolished, annealed, further details in appendix A on page 232). In contrast to the other two samples, the hydrogen in this layer is protium, while for the other samples deuterium prevails according to the plasma mixture in TEXTOR.
- The thickest a-C:H/D layers were studied on graphite tiles from the toroidal belt limiter ALT-II of TEXTOR, which were formed during several years of operation. A large part of the sample is shown in figure 3.3 on page 75. The layer, which is seen at the top, has a very inhomogeneous thickness from a few micrometres to ca. 15  $\mu\text{m}$  and therefore also a high roughness of several microns. In cross-sections of similarly exposed ALT-II tiles a layered structure can be seen due to the different operational conditions of the tokamak over the years. Thus, the layer is rather a combined layer of many thin hydrocarbon layers. This is supported by the fact that from the top the same interference colours can be seen under the microscope as on thin layers. That means that at least the topmost layer must be a thin layer, since the interference colours disappear for thicknesses above ca. 800 nm.

The first sample was exposed in two separate days in TEXTOR. In the first exposure only the a-C:H/D layer was grown at a fixed sample position and at the mentioned inclination to the plasma. To perform the LIDS measurements, in the second exposure the sample was mounted horizontally on a sample holder, that nearly hides the sample from further plasma impact. This is achieved by the lack of inclination between the W plate and the magnetic field lines and by retracting the sample by 5 mm from the top surface of the sample holder. Some parts of the sample were even hidden completely by the clamping plate of the sample holder. In figure 3.1 the dashed orange squares indicate where the sample was uncovered in the 2<sup>nd</sup> exposure and thus accessible to LIDS and plasma-wall interactions. Despite these two

---

\*IDS = Ion Drift Side, cf. Abbreviations on page 12. Side-note: An identical W sample on the EDS of the same limiter, which was exposed simultaneously, did not show any C deposition except in a very small area.

measures to mitigate plasma contact, these uncovered areas became slightly brighter than the surrounding areas covered by the holder. This is probably because during the second exposure the tip of the sample holder was not always in the deposition dominated region of  $r = 48$  cm and  $r = 49$  cm. For 3 TEXTOR discharges it was moved deeper into the plasma to  $r = 47.2$  cm, where erosion dominates and thus probably the stainless steel holder was eroded. Presumably, the eroded atoms were locally deposited then on the uncovered areas of the sample and added a slight silvery colour to its optical appearance. Additionally, a small area on the left side of the sample was covered by a metallic foil already in the first exposure to preserve a pristine surface without plasma-wall interactions for reference. This covered area was also covered during the second exposure by the clamping plate of the sample holder.

In comparison to previous studies of LID on thin a-C:H/D layers on graphite [Z9, Irrek8] the investigations here are performed on tungsten as substrate, while the layer is similar. The influence of the substitution of the substrate on the necessary laser pulse properties was treated in chapter 2.4.1 with the result that practically no changes in the laser parameters are necessary. Despite the difference in density and heat capacity for W and graphite, the combination of all thermal parameters results in nearly identical surface temperatures. Even the factor of 4 higher reflectivity does not have to be considered in its full extent, because only the first part of the laser pulse is reflected on the substrate. During the laser pulse the heated carbon layer becomes intransparent for the laser light and the reflexion position moves to the surface of the layer. However, the interface between the tungsten substrate and the carbon layer introduces some changes in the heating process due to the heat offset effect which was discussed in chapter 2.4.3. In general the interface between C and W leads to a faster heating in the beginning of the laser pulse and a higher final temperature of  $\Delta T \approx 200$  K. This effect only occurs in the first laser pulse on an unheated position and was attributed to a low heat conductivity in the first pulse. In subsequent pulses the heat conductivity is higher which was explained by a possible formation of tungsten carbide at the interface. Mainly due to the higher reflectivity, the standard absorbed laser intensity of  $700 \text{ MW/m}^2$  was probably not reached exactly in the LIDS pulses (marked in green and black in figure 3.1). Instead, an absorbed intensity of ca.  $640 \text{ MW/m}^2$  is estimated. But the pulse duration was with 3 ms twice as long as for the standard heating pulse for C. Thus, the heat flux factor for all these in situ measurements is ca.  $35 \text{ MW}\sqrt{\text{s}}/\text{m}^2$  as noted below the green/black data cloud in the graph, where the data points are artificially separated in horizontal direction for better readability. These LIDS data can also be seen as bright laser spots in the centre of the sample image and correspondingly in the NRA table as positions 1 and 3 again marked with green and black symbols. The ex situ data from LID-QMS are marked with red and pink symbols and are obtained with different laser intensities but all with the typical 1.5 ms pulse duration.

An important question of LID was whether the hydrogen desorption process can be decoupled from significant carbon release. In the previous studies on graphite only surface profilometry could give a weak hint, that this is possible, as typically no surface indentation could be found in the laser spots when the surface temperature remained in a suitable range. But element specific analyses were hindered by the fact that the layer and the substrate both consisted mainly of the same element – carbon. For example the use of NRA for the measurement of the C content of the layer was very difficult with a C substrate as it is hard to distinguish the C of the layer from the C of the substrate. The use of W as substrate opened new possibilities, as now the complete C signal in NRA can be unambiguously attributed to the layer. Simultaneously, the NRA method answers the question whether the D is desorbed completely.

The NRA method can quantify the D and C concentrations within its analysis depth of a few micrometres, which is more than sufficient for this sample as the layer is less than 400 nm

thick. The method has also a high spatial resolution, which makes it capable of measuring inside and outside the LID laser spots separately (cf. "inside" and "outside" in the table of figure 3.1). The carbon content in the vicinity of the laser spots on the original, unheated layer compared to the C content inside the laser spot is in general similar. But deviations up to a factor of 1.4 occur probably due to the layer thickness gradient and the choice on which side of the laser spot the "outside" measurement is done. However, the deviations of the five analysed spots cancel out when averaging over them and the ratio of the inside to outside C content exactly results in a factor of 1.00. Thus, in summary these deviations can be interpreted as statistical data scatter due to the NRA method itself and the choice of measurement positions on a layer with a strong thickness gradient. Apparently, the colour inside the laser spots changes to grey or silver, which could easily be misinterpreted as layer removal, because it partly has a very similar colour as the W substrate. But this is definitely not the case as the NRA measurements of the C content of the laser spots have proved.

The region named "covered area" in the figure, was indeed shielded from deposition as described above, which is also indicated by the colour fringes surrounding it. But NRA shows a small C content in this area, which still is ca.  $1/3$  of the layer C content at this plasma radius like in positions 3, c and 4 and a significant D content of  $3.6 \cdot 10^{20} \text{ D/m}^2$ . Two explanations are possible for these unexpected high values. Either the cover against the plasma was insufficient or the values are at the top of a very broad measurement uncertainty of the NRA method. Since the measured C content in the covered area is as large as the improbable increase of C in laser spot 2 compared to its outside value, the latter explanation is more likely. Even if the NRA measurement uncertainty would be as large as the values for the C and D content in the covered area, the D content is worth to analyse. Even then, the deuterium amount in the layer can clearly be discriminated from the background value in the covered area, because it is 4-6 times higher (cf. "outside" positions). Inside the laser spots the absolute D contents are nearly always below this background value except for laser spot 5. In principle, the "inside" value of this spot has to be excluded from the discussion due to incomplete heating caused by a failure of the fibre optics. Excluding this spot, the average remaining deuterium fraction inside the laser spots amounts to 7% of the values outside each respective spot, which is assumed as the undesorbed value. This is judged as a very satisfactory desorption fraction, as it is clearly above 90%, in some cases even above 95% and thus can be called nearly complete desorption. In summary, the NRA results show two important qualities of LID applied on thin a-C:H/D layers:

- **no significant C release** can be detected in the heated spots and
- more than 90% of the D is desorbed which is close to **complete hydrogen desorption**.

After these important findings, the size of the desorbed area shall be discussed as it is of great importance when areal D concentrations have to be obtained, which is the typical case. The desorbed area is not necessarily identical to the laser irradiated area due to the lateral heat conductivity in the layer and substrate. Even without a layer, the heat conductivity of the substrate leads to a temperature gradient at the laser spot edge, which shifts outwards for stronger laser pulses. Therefore, the standard laser parameters were chosen such that the desorbed area equals the laser irradiated area typically (cf. figure 2.14 on page 52 and its discussion). The influence of a thin a-C:H layer can be neglected, but with increasing layer thickness the heat flux into the substrate is hindered by the very low heat conductivity of the layer (cf. chapter 2.4.3). Thus more and more of the heat spreads parallel to the surface and thus the lateral heat conductivity becomes more important. As a consequence, the heated and desorbed area can become much larger than the laser irradiated area. Its size cannot be calculated easily due to the unknown local heat contact of the layer to the substrate that additionally changes during the heating due to the laser induced surface modifications. But



experimentally its size can be determined during the heating by thermography using an IR-camera and after the laser pulse by surface analysis. For the thin layers the colour change is a very good marker for the temperature and thus for the desorption of the layer. By microscopy or macro photography the border between the undesorbed layer which still shows colour and the grey desorbed area can be clearly detected. This is even the case for the several micrometre thick a-C:H/D layer on the ALT-II tile due to its mentioned constitution from several thin layers (cf. figure 3.9 on page 84). The image shows the edge of LID spots and the abrupt transition from coloured undesorbed layer, which remained below ca. 800 K and the desorbed laser spot. The right image even shows a very thin undesorbed area of less than 200  $\mu\text{m}$  width between two laser spots. Its colours prove that the laser spots did not overlap and thus their LID measurement are not influenced by each other.

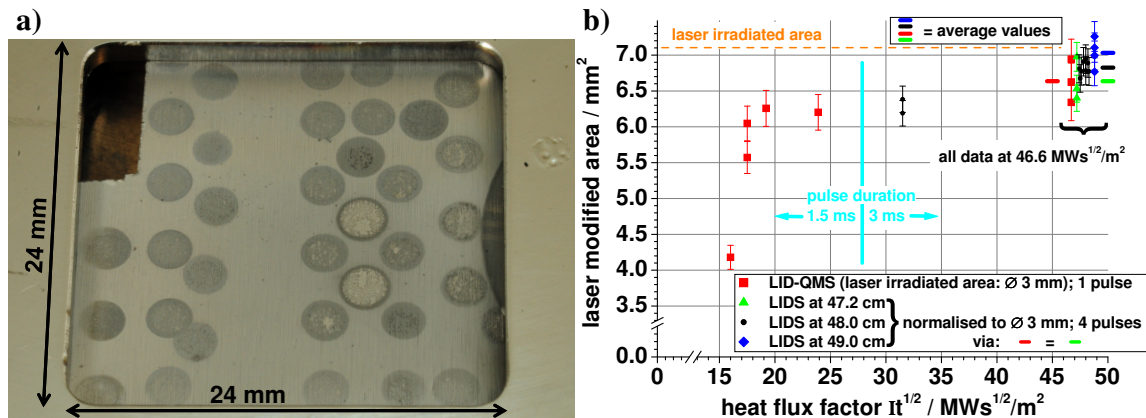
For the first sample the spot sizes were measured in the described way and first the variability of these values was analysed. As all LIDS data were obtained with the same laser pulse properties, the standard deviation of their desorbed area is a relevant quantity. It shows a very small data scatter of only 4.4% of the total value, which seems to be so low due to the long pulse duration. For the half as long LID-QMS pulses, the scatter is already larger with 9.6%, where 7 pulses with identical intensity of  $620 \text{ MW}/\text{m}^2$  were used, corresponding to  $\text{HFF} = 24 \text{ MW}\sqrt{\text{s}}/\text{m}^2$  (cf. graph). But even this variation of the desorbed area can be assumed as small. However, the largest spot at this laser energy is a factor of 1.3 larger than the smallest, which is mainly an effect of the different layer thickness. To correlate them, the layer thickness (in nanometres) as obtained by colorimetry is noted in the graph beside the data points. It can be seen that on the very thin layers below 100 nm the smallest spot sizes occur, while for the larger thicknesses above 150 nm up to roughly 400 nm the spots are largest.

The graph also shows a second correlation, namely between the spot size and the heat flux factor, i.e. the laser intensity and pulse duration. The higher the HFF, the larger the desorbed area. This can be seen for the near normal laser incidence (red data) on layer positions with 340-365 nm and for the series with  $20^\circ$  incidence (pink data) on thicknesses of 365-400 nm. A clear monotonous increase of the desorbed area can be seen with stronger laser pulses for nearly constant layer thicknesses. Also here a factor of 1.3 can be found between the smallest and largest spot sizes. In order to compare the LIDS data, which are obtained with a laser beam diameter of 3.0 mm and the LID-QMS data with 2.6 mm beam diameter, the LIDS data were scaled by the ratio of the two laser irradiated areas as depicted in the figure. The general trend of all data shows that a minimum HFF must be exceeded before the desorbed area equals the laser irradiated area. Within the error bars of the area determination method, this is the case for  $\text{HFF} \geq 27 \text{ MW}\sqrt{\text{s}}/\text{m}^2$ . Only the data point at  $29 \text{ MW}\sqrt{\text{s}}/\text{m}^2$  is an exception probably due to the  $20^\circ$  incidence, which is the largest of all data. For the data with this inclination (pink data) the increase of the desorbed area seems to be slower compared to the nearly normal incidence (red data). Also the average values of the LIDS data after 4 laser pulses on one position (green data) and 3 pulses (black data) marked by the horizontal lines are nearly reaching the size of the irradiated area. The data imply, that a repetition of several laser pulses on one position has no influence on the desorbed area which is measured after the last pulse. The first hint is the fact that the average of the LIDS data with 3 pulses is equal to the LIDS data with 4 pulses. A further supporting fact can be seen when comparing laser spots with 2 pulses to spots with only one pulse, with unchanged laser settings and similar layer thickness. This is e.g. possible for the spot position 4 with one pulse and the spot to its right with 2 pulses. The layer has nearly the same thickness in these two positions (ca. 190 nm) as can be seen by the interference colours and they have the same spot size. The two spots above them are also comparable in this way at a layer thickness of ca. 280 nm. Their spot sizes differ only by a factor of less than 1.05.

### 3. Surface Modifications due to Laser Heating

As expected, no value has exceeded the laser irradiated area clearly, i.e. no data point including its error bar is above the irradiated area. This shows that for thin a-C:H layers, the lateral heat flux parallel to the surface has no significant influence on the desorbed area. In contrary, the size of the irradiated area is the dominant factor and equals the desorbed area for a sufficiently strong laser pulse in the described heat flux range.

How does the spot size behave on thicker layers? The same spot size analysis was performed for the Balinit<sup>®</sup> layer with a homogeneous a-C:H layer of several micrometres (cf. figure 3.2). Also here the ex situ and in situ methods were used with the difference that for some LID-QMS pulses exactly the same HFF and pulse duration as in LIDS was chosen. Therefore, these data at  $46.6 \text{ MW} \sqrt{\text{s}}/\text{m}^2$  could be used for the compensation of the different sizes of the laser irradiated areas in the two methods. Hence, the average of the LIDS data at the closest approach to the plasma (green horizontal line) was set equal to the 3 LID-QMS data (red data) at the same HFF. The sample was also desorbed further away from the plasma at 48 cm minor plasma radius (black data) and 49 cm (blue data). The average values of the three series continuously increase because the laser beam diverges from its focal position at  $a \approx 47 \text{ cm}$ . Although this divergence is quite small as the image distance is more than 2 m, it causes this area increase of a factor of 1.06.

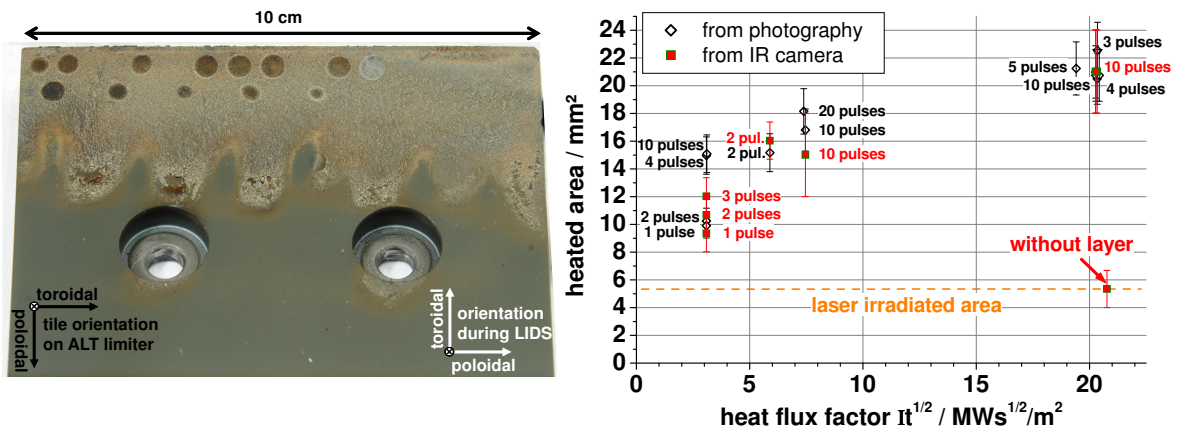


**Figure 3.2.:** a) LID on  $2.5 \mu\text{m}$  a-C:H layer (Balinit<sup>®</sup> 3a) with different laser pulse settings; b) laser desorbed area vs. heat flux factor on this and an identical sample

Even with this defocussing effect the laser modified area reaches the size of the irradiated area only for single spots but not for the average values like for the thin layers. However, they are again in relative good agreement for the strongest laser pulses. The general behaviour that the graph conveys is again an increase of the spot size with higher heat flux factor. The HFF is varied nearly in the same range of  $15\text{-}47 \text{ MW} \sqrt{\text{s}}/\text{m}^2$  as for the thin layer, but the area increases by a factor of 1.6 which is larger than before. Thus, a larger layer thickness seems to increase the effect of the laser strength on the spot size. This trend will finally be proved by the very thick layers on the ALT-II, in the following.

Up to now, samples have been discussed, where the laser modified area was smaller or equal to the laser irradiated area. This is the preferable situation for the application of LID because a strong enough laser pulse can be chosen, for which the irradiated area and heated area are equal. Both areas also equal the desorbed area and thus its value is known simply from the laser beam diameter. In the following, LIDS on the ALT-II tile N<sup>o</sup> 6/19 from the toroidal belt limiter of TEXTOR is discussed, where this advantage is no longer valid.

For the laser pulse duration a nominal value of 1.5 ms was set, which equals the real pulse duration only for high laser energies. For low energies, the real pulse duration is shorter due to the characteristics of the laser system. The smallest laser energy used here was  $E_0 = 1.0 \text{ J}$  at



**Figure 3.3.:** LIDS spots on ALT-II tile N° 6/19 and their size vs. HFF; The laser pulse parameters are shown in figure 3.4.


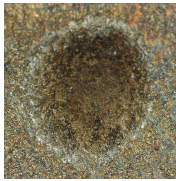

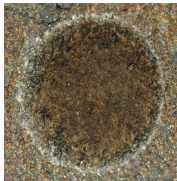

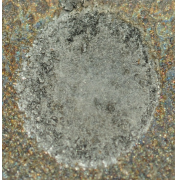
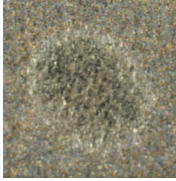
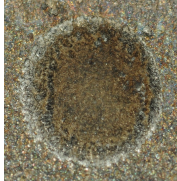
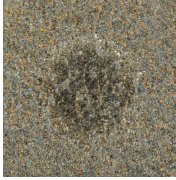
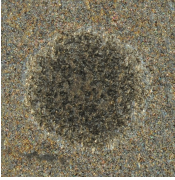



the laser, which corresponds to  $E_1 = 0.58 \text{ J}$  absorbed energy at the target. These pulses have therefore the shortest real pulse duration of nearly 1.2 ms (FWHM of the diode signal in the laser). This real pulse duration is used for the calculation of the corresponding laser power and intensity since it results in a power increase of up to a factor of 1.25 compared to the nominal values. Further laser parameters used in this study are given in figure 3.4.

The size of the modified area was measured on photographs of which the scale factor was determined by a simultaneously photographed ruler, the tile width or neighbouring laser spots. An outer spot diameter was defined at the transition from the grey spot border to the unmodified layer and an inner diameter for the dark brown inner spot area. These differently coloured areas can be seen in figure 3.4 in magnification. In the spot size analysis in figure 3.3 the outer diameter was used.

The laser irradiated area is always constant at  $5.3 \text{ mm}^2$  but the laser heated area is multiple times larger than the laser irradiated area. Even for very weak laser pulses with a HFF of only  $3 \text{ MW} \sqrt{\text{s}}/\text{m}^2$  the modified area is often twice as large as the laser irradiated area. The strongest pulses applied, had a HFF of  $20 \text{ MW} \sqrt{\text{s}}/\text{m}^2$ , which is at the lower end of the range used for the previous samples, but the heated area is more than 4 times the irradiated area. Hence, the factor between the smallest and largest spots sizes is 2.4 in this measurement series and thus larger than for the previous samples. It can be concluded, that the increase in spot size due to stronger laser pulses is larger the thicker the layer. The thick layer reduces the heat flux perpendicular to the surface due to its extremely low heat conductivity below  $1 \text{ W}/\text{m}\cdot\text{K}$  (cf. chapter 2.4.3). For a thin layer this effect is negligible as in the beginning of the laser pulse the laser light is mainly absorbed by the substrate and heats the layer from below. Even when the layer becomes intransparent and absorbs the rest of the laser pulse, obviously the heat can diffuse easily through a thin layer. Even for the Balinit<sup>®</sup> layer which is several micrometres thick and absorbs all the laser light (cf. figure 2.10 on page 46) the perpendicular heat conductivity is still good. This is probably due to the Cr interlayer that improves the heat contact. For the much thicker ALT-II layer, which additionally is not as homogeneous due to varying plasma conditions, the heat cannot be conducted to the substrate as efficient and spreads parallel to the surface. This lateral heat diffusion within the layer causes the large size of the heated area and therefore also a large desorbed area. The increase of the heated area with stronger laser pulses is common to all amorphous hydrocarbon layers regardless of their thicknesses, but it is most pronounced on the thick layers.

A second dependence can be found for the thick layers on the ALT-II tile, namely the dependence of the spot size on the amount of laser pulses on the same position. This effect did

### 3. Surface Modifications due to Laser Heating

number of laser pulses	absorbed laser intensity				
	90 MW/m <sup>2</sup>	160 MW/m <sup>2</sup>	200 MW/m <sup>2</sup>	520 MW/m <sup>2</sup>	540 MW/m <sup>2</sup>
10 pulses:				 laser beam Ø 2.6 mm	
5 pulses:	 laser beam Ø 2.6 mm				
4 pulses:					
2 pulses:					 5 mm
1 pulse:			 laser beam Ø 2.6 mm		
pulse duration:	1.17-1.20 ms	1.32 ms	1.32 ms	1.41 ms	1.41-1.43 ms
HFF / MW √s/m <sup>2</sup>	3.1	5.9	7.5	19.5	20.4

**Figure 3.4.:** Laser heating of a thick a-C:H/D layer from TEXTOR on graphite (ALT-II tile N° 6/19); 7° laser incidence; 1.5 ms nominal pulse duration, actual pulse duration and heat flux factor are given below the images; photography; all images adjusted to the same scale

not exist on thin layers as discussed above. But here it is very strong especially for the weak laser pulses. The difference in spot size between one and 10 pulses is a factor of 1.5 for the weakest laser pulses (cf. figure 3.3). For the intermediate pulse strength only one comparison is possible after 10 and 20 pulses, where the difference is already very small with a factor of 1.08. For the strongest laser pulses the effect disappears as no correlation can be seen between spot area and amount of pulses as even the value for 3 pulses is higher than that for 10 pulses. The explanation of this different behaviour for the weak and strong pulses will be possible with the additional information from IR data taken during the same LIDS pulses. The high-speed IR camera can temporally resolve the heating pulse as it records an image every 0.2-0.3 ms depending on the settings, while the active exposure time is only 3 or 4, sometimes up to 80 μs. In the IR images the heated area is defined as the area which is heated above a fixed, specified temperature.

Before turning to the effect of repetitive pulses, the IR camera was tested with LIDS pulses on the lower part of the ALT-II tile in the image of figure 3.3. In this erosion dominated

region of the tile, there is no thick layer. Only the uppermost surface is transformed by the hydrogen plasma into a similar structure like a thin a-C:H/D layer. The IR data show a much sharper edge of the heated area here compared to the heated spots on the thick layer, where the temperature gradient in the spot edge is smaller. By this sharp edge the heated area can clearly be distinguished from the colder surrounding. Its size is equal to the laser irradiated area (cf. arrow in figure 3.3), unlike in the region with the thick deposits. Hence, on rather homogeneous materials or even materials with a thin layer, the IR data confirm the already known fact that the heated area is smaller than or equal to the irradiated area.

For the study of the repetitive pulses the IR data add new possibilities as the spot size is measured for each laser pulse, not for accumulated pulses like with the post-mortem methods. But, in order to compare the heated areas determined from the photography and the IR camera, only the largest area from the IR data is shown in figure 3.3 for each position. It corresponds quite well to the values obtained from the photography, as a single heating pulse is sufficient to cause the colour change which is seen in the photographs and by eye. Thus, the differences in heating between laser pulses on the same position cannot be seen in the figure, but the IR data show, that not every laser pulse on the same position heats the same area.

On the thick ALT-II layer the IR data show a peculiar difference between the weak laser pulses below a HFF of ca.  $6 \text{ MW} \sqrt{s}/\text{m}^2$  and the strong laser pulses above this value. For the strong heating the first laser pulse yields the highest temperature, while the subsequent pulses on the same spot reach lower temperatures. In general, the next pulse reaches a lower temperature than the previous pulse, with only few exceptions. The drop is highest for the first pulses and becomes smaller then, but there is always still a clear decrease between the maximum temperature of e.g. the 3<sup>rd</sup> and 8<sup>th</sup> pulse. This is not only valid for the pixel with the maximum temperature but for nearly all pixels inside the laser spot and even in the surrounding of the spot. This observation can thus be summarised as a clear decrease of the maximum temperature with increasing amount of pulses on the same spot for the strong laser pulses.

The opposite behaviour is observed for the weak laser heating, where the maximum temperature is lower in the first laser pulse than in the subsequent 1 or 2 pulses. The heating in the 2<sup>nd</sup> and 3<sup>rd</sup> pulse is quite similar, with a very slight trend to decreasing temperature, that is much weaker than the temperature drop for the strong laser pulses. Like in the previous case, the temperature difference is observed for nearly all pixels inside the laser heated area, i.e. also outside the laser irradiated area.

These temperature trends also lead to a decrease of the heated area for strong pulses and an increase for weak pulses, with the above definition of the heated area by a fixed temperature. In relative numbers, the heated area increased by a factor of 1.3 for the weak laser pulses, which mainly occurred in the jump between the 1<sup>st</sup> and 2<sup>nd</sup> pulse. For the strong laser pulses, the area decreased by factors of 1.7-1.8 from the 1<sup>st</sup> to the 8<sup>th</sup> pulse. This coupling of maximum temperature and heated area shows once more that the lateral heat conductivity along the thick layer plays a major role in the heating process here.

Such temperature behaviours have not been observed on thin a-C:H layers, which were studied in the previous chapter. There, also a difference between subsequent laser pulses on the same position occurred, which was attributed to two effects. For thin a-C:H layers on carbon materials the heat curvature effect occurred but it leads to the the same maximum temperature, unlike here. For thin a-C:H layers on tungsten the heat offset effect was discussed, where the first heating pulse also reached higher temperatures than the second pulse. But subsequent pulses showed similar heating like the second shot, instead of a further temperature decrease, which is observed on the thick layer, here. Moreover, there is no W substrate here, which is essential for the heat offset effect. Only a very small amount of W is contained in the deposited layer on the ALT-II tile due to experiments in TEXTOR that caused W release into the plasma.

Similar temperature effects of a-C:H layers are often explained by the increase of the heat capacity or heat conductivity due to heating as discussed in chapter 2.4.3. But both would always lead to reduced final temperatures, while for the weak laser pulses an increase of the temperature is measured. Additionally, all these heat parameters change monotonously with increasing temperature and therefore cannot explain the opposite behaviour for weak and strong laser pulses. A possible explanation could be the evolution of the surface modifications on thick a-C:H/D layers in the following way:

- In a first phase, the blisters grow and lose their contact to the substrate or the remaining layer beneath it. As the thick layer consists of a stratified layer structure of many thin a-C:H/D layers, not necessarily the whole layer detaches from the substrate. It is conceivable that only the uppermost thin layer or few thin layers detach to form a blister, which leads to the same situation. This state is supposed to be reached at the end of the first weak laser pulse. Thus, for a long duration during the first pulse the layer is still attached and hence most of the heating energy reaches the lower parts of the layer and the substrate. The perpendicular heat conductivity is high compared to the lateral heat conductivity. But during the second and subsequent laser pulses the blisters are already formed and cannot conduct the heat into the depth. Only lateral heat conductivity remains locally at the blister, which is very slow in the layer and thus the blisters reach a much higher temperature than in the first laser pulse. Although the blisters are relatively small, with 5-25  $\mu\text{m}$  in diameter, the blister density can be quite high and the IR signal is sensitive, as the heat radiation grows with  $T^4$ . Therefore, even small hot spots can have a large influence on the IR signal, which then represents only an average temperature, as such small objects are not resolved spatially. Obviously, the low laser intensity is not high enough to sublime the blisters and therefore they are heated up to similar temperatures in the third laser pulse as well. In summary, the layer is locally detached by the first laser pulse due to blister and also crack formation, but it is not sublimed, i.e. only unavoidable damage occurred.
- The second phase of the surface evolution can only start with stronger heating, which is provided by the strong laser pulses. For these high laser intensities the blisters form much faster, overheat and their caps sublime already during the first laser pulse, which therefore shows very high IR radiation. Thus, at the beginning of the second pulse already the blister caps and other detached layer parts are partly gone. Hence, there is much less detached material than in the first pulse. Mainly the well attached parts of the layer are remaining, which do not heat up very strongly as they have good heat contact. Thus, the IR radiation is lower than in the first pulse. The further decrease of the IR radiation in the subsequent pulses can be explained with successive sublimation of the remaining layer parts that are poorly attached. Globally seen, the layer becomes thinner in this process. With every laser shot, less and less of this detached layer remains and thus the overheated areas become smaller and smaller, which reduces the IR radiation.

An alternative explanation could be based on the temperature dependent emissivity and reflectivity of the layer, which are coupled by equation 2.5 on page 42 at each wavelength. This material property is not changing monotonously like the heat properties, which was shown by previous measurements of the reflectivity of thin a-C:H layers at the laser wavelength (1064 nm). First it decreases until 700 K by a factor of 1.14, then increases, reaching the initial value again at 900 K and then rises by a factor of 1.3 of the initial reflectivity until 2300 K [Irrek8, p.40]. However, the changes in the maximum temperature induced by this reflectivity variation are rather small, when calculated with the heat properties of graphite. The largest possible temperature deviation towards higher temperatures in the second laser pulse would occur when a weak laser pulse reaches 700 K in the first pulse. The average

reflectivity of this first pulse would be the average of the initial value ( $R_{tot}=0.17$  cf. figure 2.9 on page 43 for the ALT-II layer) and the minimum of  $R_{tot}=0.15$ . Hence, for the first laser pulse a reflectivity of 0.16 would be valid. The subsequent laser pulses are reflected on the already modified and heated layer, thus for them the minimum reflectivity of 0.15 would be valid during the whole laser pulse. This is based on the assumption that the structure of the layer is changed during heating and that this leads to the changes in reflectivity. Hence, the reflectivity remains at the value which it reached for the maximum temperature in previous heating. This assumption leads to the consequence that only a further heating above this temperature can change the reflectivity again. The small difference of 0.01 in reflectivity leads to an insignificant temperature increase of 3 K for the weak laser pulses and 6 K for the pulses with  $7.5 \text{ MW } \sqrt{\text{s}}/\text{m}^2$  where the temperature already drops for subsequent pulses. For the strongest pulses applied here, this reflectivity effect would result in 17 K higher temperatures, but their temperatures are much higher and thus the above reflectivities do not apply for them, anyway. For these strong pulses, the largest possible discrepancy towards lower temperature in the second pulse would occur when the maximal reflectivity of 0.22 is reached at the end of the first pulse. During the first pulse the average reflectivity would lie somewhere between the initial value and this maximum. As the exact position is unknown the initial value is assumed for the first pulse to calculate an upper limit for the temperature difference. For the strongest laser pulses, the second pulse would lead to a 78 K lower maximum temperature, which is much less than observed. Moreover, this explanation cannot explain the further significant temperature decrease for the subsequent pulses.

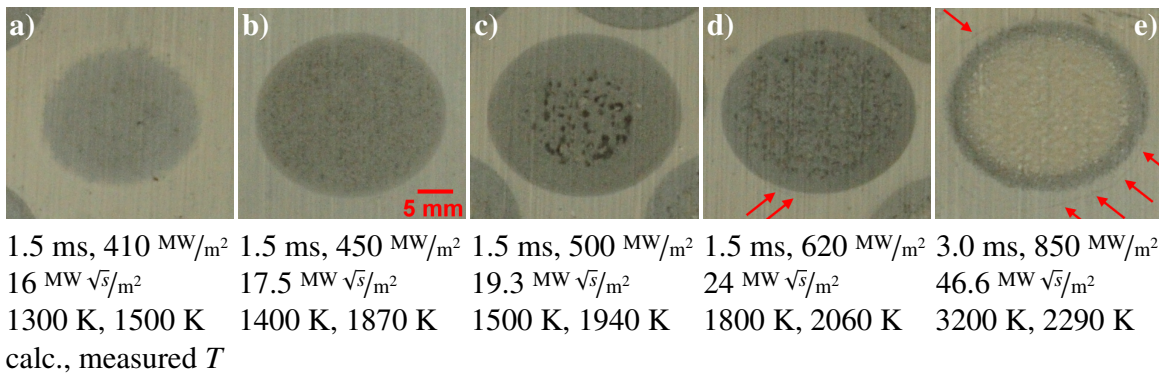
In the range of the IR measurements (3-5  $\mu\text{m}$ ) the emissivity could also have a temperature dependent behaviour which is not monotonous. As a change in emissivity is not accounted for in these measurements, such a behaviour could lead to an overestimation of lower and underestimation of higher temperatures. This would add to the small real variations of the temperature due to the reflectivity change at the laser wavelength discussed above. However, the extent of the emissivity variations due to heating is unknown in this wavelength range and thus cannot be discarded or verified as an explanation for the peculiar temperature behaviour. Like the reflectivity change, it also cannot explain the continued decrease of the maximum temperature for the pulses after the second pulse, as the emissivity would remain constant for them. In conclusion, the effects of reflectivity and emissivity change are quite small and cannot explain the temperature behaviour in subsequent laser pulses, hence the explanation based on surface modifications is preferred.

The previous spot size analysis shows, that the effects of blistering and cracking have a strong effect on the heating process and will therefore be analysed in detail now. The LID-QMS spots from the Balinit<sup>®</sup> sample (red data in figure 3.2) are shown in figure 3.5 with continuously increasing HFF from left to right. Not only the growth of the spot size can be seen, but also the increasing blistering and cracking.

Already in figure b) a slight roughening of the surface can be seen. In the next step, large blisters can be seen, which are rather in the spot centre and are very dark in colour. In figure d) the blisters appear in a larger area except an outer ring at the spot border. Here also one crack outside the laser spot can be seen as marked by the arrows. Crack widths up to 0.3  $\mu\text{m}$  were observed. For the strongest heating the colour in the spot centre changes to bright grey, which will be discussed at the end of this section. The cracking outside the spot increases as more and longer cracks can be found on different sides of the spot. These external cracks typically have a curved form running roughly circular around the spot because the tension during the cooling after a laser pulse is directed radially towards the spot centre.

Further details of the blistering process will now be studied by microscopy on the same layer after LIDS in TEXTOR. Two different heating intensities were used in situ with a HFF

### 3. Surface Modifications due to Laser Heating



**Figure 3.5.:** LID-QMS spots on 2.5 μm a-C:H layer (Balinit<sup>®</sup> 2a, 3a) show spot size growth, colour change, blistering, evaporation and cracking (red arrows); one laser pulse; pulse duration, absorbed laser intensity, HFF, calculated and measured maximal temperature are given; tilted photography; all in identical horizontal scale

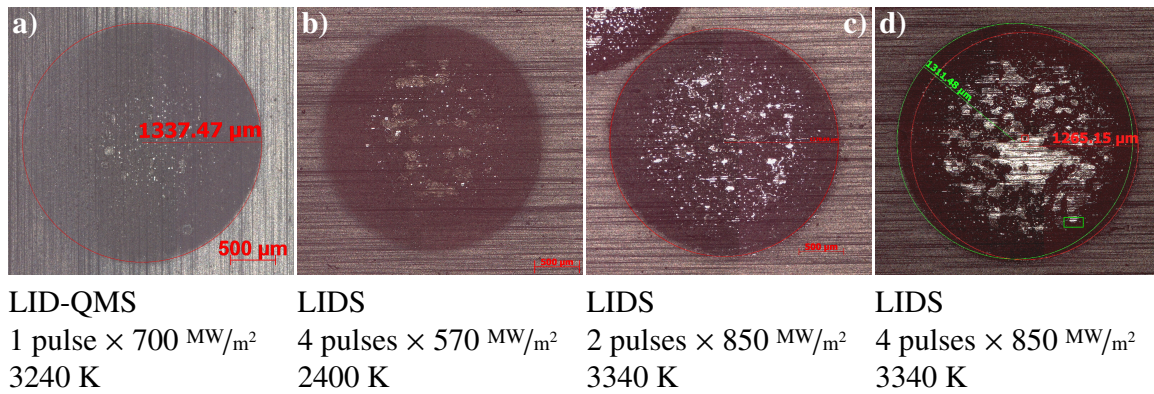
of 46.6 and 31 MW √s/m<sup>2</sup> as already seen in the spot size graph. They were achieved by the following laser settings. The highest laser energy was  $E_0 = 22.5$  J at the laser, resulting in  $E_1 = 13.5$  J of absorbed energy at the target, corresponding to  $I = 850$  MW/m<sup>2</sup> absorbed laser intensity during 3 ms. The lower initial laser energy was  $E_0 = 15$  J, corresponding to absorbed values of  $E_1 = 9$  J and  $I = 570$  MW/m<sup>2</sup> during 3 ms. With a typical base temperature of ca. 420 K for the TEXTOR limiter, the strong laser pulse should lead to a calculated maximal temperature of ca. 3340 K. However, the same laser intensity and pulse duration applied on the same sample in the ex situ method led to a measured maximal temperature of only 2290 K (cf. figure 3.5e). Nevertheless, both temperatures are high enough to cause "partial destruction and removal of the layer and interlayer (cf. figure 3.6). The lower energetic pulse with 15 J initial laser energy kept the layer widely attached to the substrate but unavoidable roughening of the layer due to thermal stresses occurred anyway" [Z11b] (cf. figure b). The brighter areas inside the spot are areas where the a-C:H layer is removed, while the much brighter small white dots are areas where additionally the interlayer is removed. This damage is even stronger for the high laser energy. The removal mechanism probably starts with blistering, which worsens the contact to the substrate and causes strong overheating of the detached areas. This leads to evaporation and delamination, which means that not necessarily the whole area is evaporated but may also lose its mechanical stability due to these modifications and fall off. This few examples already show two general trends.

1. A higher amount of pulses leads to larger areas that are removed, which can be seen comparing figure c) and d).
2. A higher intensity of the laser pulses leads to more starting positions, where removal occurs, i.e. to a higher density of destroyed positions and deeper destruction. This can be seen comparing figure b) to d) which have the same amounts of pulses.

Due to the interplay of both effects, the damage caused by one strong LID-QMS pulse in figure a) is very similar to the damage caused by 4 pulses of lower intensity in figure b). The choice of the high laser intensities was done in LIDS to be absolutely sure to desorb all the hydrogen. "On the one hand, this assures complete desorption, but causes partial removal of the layer and interlayer, which can be avoided by using lower laser energies." [Z11]

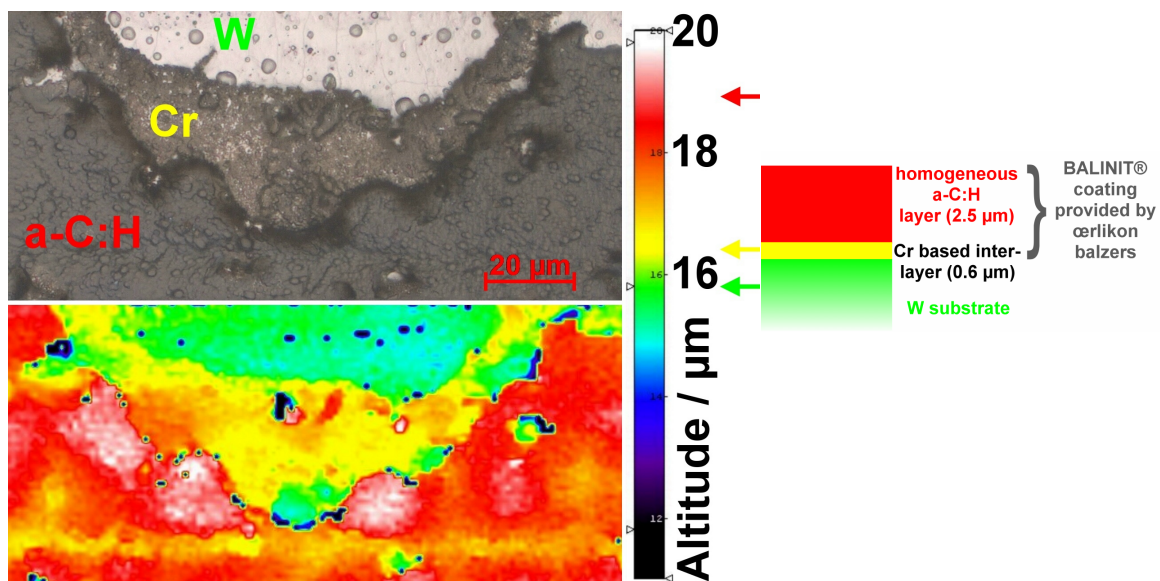
In figure d) the relative position of sample and laser beam have obviously slightly shifted once between the 4 pulses as indicated by the green and red circle. This is probably due to vibrations in the TEXTOR environment that inevitably occur during the plasma discharge. Although this shift is seldom, this sample is shown because two detailed microscopic inves-





**Figure 3.6.:** LID spots on 2.5  $\mu\text{m}$  a-C:H layer (Balinit<sup>®</sup> 3a) showing increasing layer removal from a) to d); each laser pulse with 3 ms pulse duration; the amount of laser pulses, absorbed laser intensity and calculated maximal surface temperature are given; optical bright field microscopy; all images in identical scale

tigations were performed in the positions that are marked with the red and green rectangles. In the latter position, high-resolution optical microscopy was done on the same position as surface profilometry in order to correlate the white and bright grey areas to substrate and interlayer.



**Figure 3.7.:** right: Balinit<sup>®</sup> layer scheme; left: surface after 4 laser pulses of 850 MW/m<sup>2</sup> absorbed power for 3 ms each; top: optical microscopy, zoom of green frame in figure 3.6d; bottom: confocal profilometry of the same position

It can clearly be seen that the areas that appear in white colour in optical microscopy like in figure 3.6 and in the upper image in figure 3.7 are the lowest in altitude. They correspond to the green colour in the colour-coded height of the 3-dimensional profilometry (lower image). Their altitude is roughly marked with a green arrow beside the altitude scale and represents the top surface of the tungsten substrate.

A bit higher lies the Cr interlayer, which appears as bright grey in the optical microscopy and in yellow in the height map, which means that its surface is ca. 0.6  $\mu\text{m}$  above the substrate. The dark grey area that covers most of the lower part of the image is the a-C:H layer, which is on average red in the height map but also shows some higher values (white) at its edges.

### 3. Surface Modifications due to Laser Heating

---

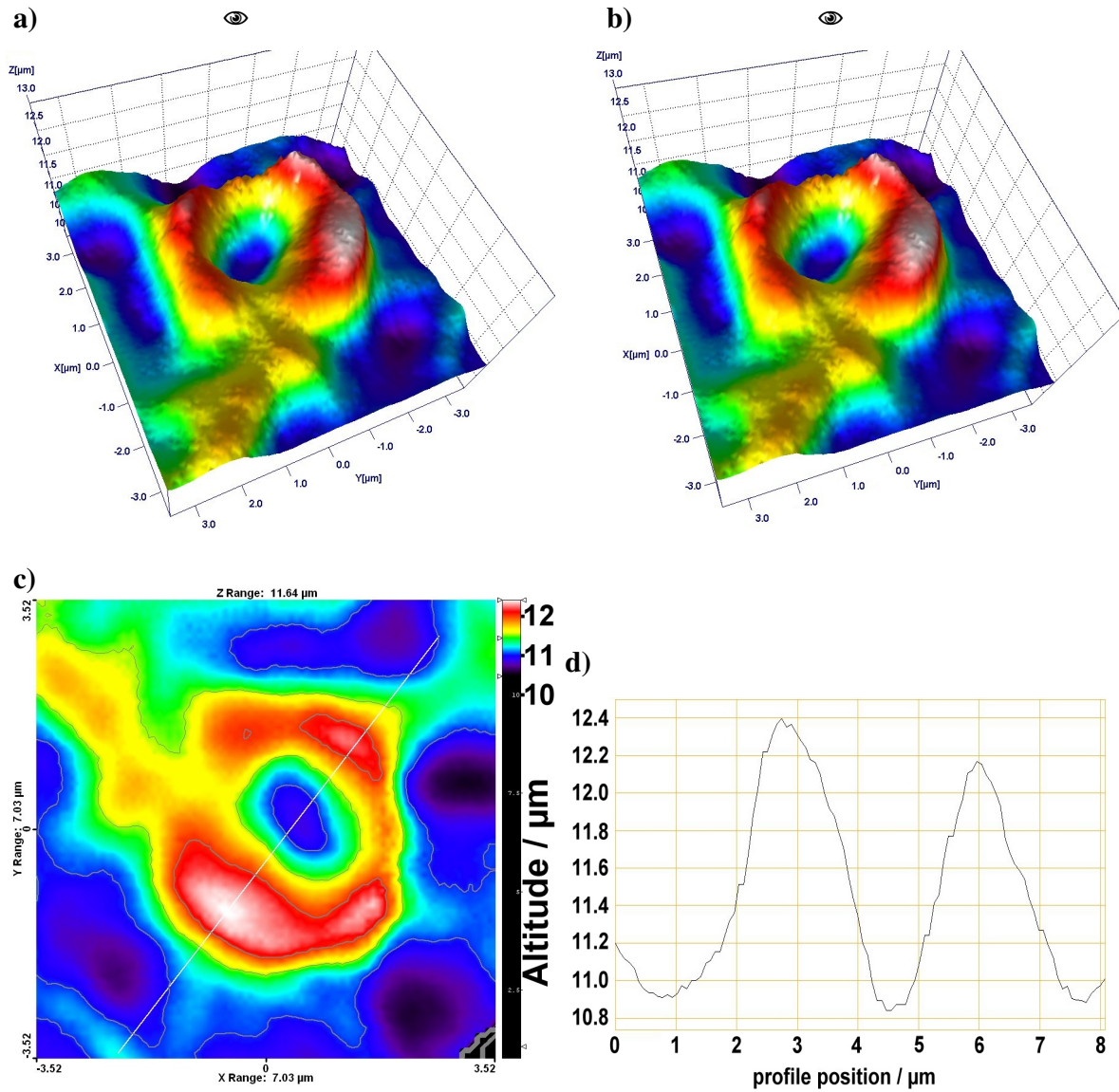
These show the process of detachment by delamination, where the layer is lifted on larger area scales than the blister size.

The horizontal yellow stripe that runs through the red part of the image is due to a scratch in the substrate of which many exist parallel to each other due to the W production process. They are especially visible in the previous figure 3.6. The blue and black dots in the profilometry are artefacts of the measurement process where the height information is lost due to too low light reflectivity of the sample. This can e.g. occur at steep slopes which do not reflect the light, which is emitted by the microscope, back into it for the height analysis. This can – but does not have to be – a sign for steep surface gradients. The blue and black signals that are seen between the red and yellow area are certainly such steep gradients and show that the a-C:H layer often has a steep edge. In contrast, the transition between the yellow and green area is rather free of this artefacts which indicates that the transition between the substrate and interlayer is rather smooth.

On the uncovered W substrate many thin cracks are seen that sometimes even build a crack network like in the upper image in figure 3.7. These cracks inside the laser spot do not show a preferential direction or shape in contrast to the cracks outside the spots. In the layer less cracks are found, which nearly always are connected to an evaporated blister or a delaminated area.

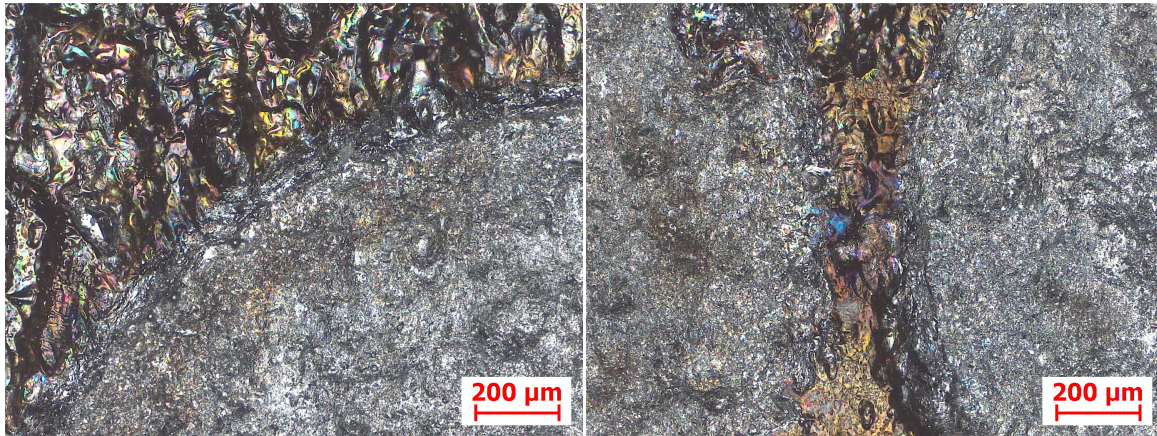
In the a-C:H layer many small blisters are visible on the upper image that are quite circular, while on the interlayer larger, irregularly formed blisters are observed. On the W substrate dots are visible, which turn out to be hills as closer profilometry reveals. Their origin is unknown, but they have a different characteristic than the carbon blisters, as they are larger and less dense. Therefore, it is improbable that these dots on the W substrate are the reason for or have any relation to the blisters in the a-C:H layer, although their height is similar with 1-2  $\mu\text{m}$ . For LID the blisters in the layer are more important and hence one of them, which is located in the centre of figure 3.6d in the red rectangle is shown in detail in figure 3.8. Since this position has already been exposed to 4 very strong laser pulses, the surface modification is in a late phase. The blister caps have already overheated several times and thus the blister caps are evaporated. Only one blister is shown in the figure from different perspectives. In figures a) and b) a 3-dimensional stereoscopic image of the blister is shown. The top-view in figure c) uses the same colour-coded altitude scale and additionally contour lines every 0.5  $\mu\text{m}$  height. The cap removal can be seen clearly, which gives the remaining blister edges the appearance of a volcanic crater. The line profile in figure d) shows a 1-dimensional cross-section across the highest hill and the deepest point in the centre of the blister. The width of the blister is largest in this direction with ca. 6  $\mu\text{m}$  and its height reaches up to 1.5  $\mu\text{m}$  from above the level of the undisturbed surface which is shown in blue. This level corresponds to the altitude of ca. 11  $\mu\text{m}$  in the scale and is found to the bottom, top and right side of the blister as well as inside the blister. This shows that the blister must have been rather empty when it was still closed and now that it is open, the material underneath it can be seen, from which the blister has detached. These small blisters have a high blister density, i.e. amount per unit area, and do not show the substrate even when they are open. This is senseful as their height is typically smaller than the layer thickness. But many larger blisters are found with sizes of 8-25  $\mu\text{m}$ , which typically show the white substrate if they are open. This means that their size before the cap removal must have been equal to the whole layer thickness. Thus, there seems to be a correlation between the width of a blister and its height and from a critical width of ca. 8  $\mu\text{m}$  the height equals the entire layer thickness. But this is a very rough estimate, which is not based on a thorough statistical analysis of the blisters.

At the end of this section the colour changes in the a-C:H layers due to the laser heating will be shortly discussed, although they are often misleading as shown for the first sample. The interference colours that occur for thin a-C:H layers have already been mentioned to be



**Figure 3.8.:** Blister cap removal on 2.5 μm a-C:H layer (Balinit<sup>®</sup> 3a) after 4 laser pulses of 850 MW/m<sup>2</sup> absorbed power for 3 ms each; zoom of red frame in figure 3.6d; confocal profilometry: a,b) stereoscopic\* 3D view, c) top view with contour lines every 0.5 μm in altitude, d) profile along the white line marked in c)

\* The same scene is shown from two slightly different view angles, which can be seen in 3D by squinting and thus completely overlapping the images. The eye symbols above the images help as they converge to one symbol, when the overlap is perfect.



**Figure 3.9.:** LID spots on ALT-II tile (N° 2/19) show sharp laser spot edges that clearly define the desorbed area (grey) in contrast to the ca. 15  $\mu\text{m}$  thick a-C:H/D layer (multi-coloured); left: edge of one laser spot; right: undersorbed area between two LID spots; optical bright field microscopy

good heat indicators like in figure 3.9, as they reliably show the 800 K isotherm. They lose their colour and transparency at this temperature due to the graphitisation of the a-C:H layer. During this process the fraction of  $\text{sp}^3$ -bondings (diamond-like structure) is transformed to  $\text{sp}^2$ -bondings (graphite-like structure) as described in chapter 2.4.3. Before this process only a fraction of the layer has the graphite-like structure, while afterwards nearly all the layer is transformed to it. This also causes the typical dark grey colour, which is similar to that of graphite. For the thin layers on the first sample (cf. figure 3.1) this can be seen for the LID-QMS spots (red and pink data points). But there are exceptions for very thin layers like for the first spots from the bottom, which look silvery. Here, the layer is less than 100 nm thin and therefore even after the graphitisation still transparent. With increasing layer thickness (upwards in the figure) the grey colour becomes darker as expected. On a graphite substrate these colour differences have never been visible in the past.

Further examples of this dark grey colour are the spots in figure 3.5a-d and figure 3.6 on the thicker layer. Also the very thick layer typically shows this dark colour, although it is rather dark brown for this layer as shown in figure 3.3 (except the very right spot) and figure 3.4 (except the spot with 5 pulses). Some spots have a bright circle at the spot edge, which occurs for small temperature gradients like on the very thick ALT-II layers and weak laser pulses on the Balinit<sup>®</sup> layer (cf. figure 3.5a). This might be an intermediate stage of graphitisation.

But sometimes the laser spots have a bright grey colour in the spot centre like the LIDS spots of the first sample (green and black data points). The same effect occurs on the thicker layer in figure 3.5e and on the very thick layer on the spot with 5 pulses. This colour is a second phase of colour change, which is deduced from two facts. The dark grey colour of the first colour change is typically still present for these cases as a dark grey circle around the bright grey centre. This already indicates that the second phase must be due to stronger heating, which is in fact supported by the used laser parameters. For the thin layer the bright grey spots were heated with longer laser pulses (3 ms instead of 1.5 ms) and more pulses (3 or 4 instead of 1 or 2 pulses). The difference in the calculated maximal temperature is 1800 K to 2600 K in every pulse. The same argument holds for the spot in figure 3.5e, which has been heated with the highest laser intensity and also twice as long pulse duration as the other spots. As all the spots in this figure were heated only once, the amount of pulses does not seem to be the decisive factor but rather the pulse length and intensity and therefore the final temperature. Here the highest measured temperature of the dark grey spots was 2060 K, while the temperature of the

bright grey spot was 2290 K. This is consistent with the previous difference in temperature for the thin layers. Hence the transition to the bright grey colour must occur in the temperature range of ca. 2100-2200 K.

Only for the bright grey ALT-II spot with 5 pulses no such explanation can be found as even spots with higher laser intensity, identical pulse duration and 10 pulses do not show the effect. Here an additional heating effect by the plasma might be possible as this spot was out of range of the IR camera view and thus could not be monitored. A second possibility could be some technical laser issue as after the 5 pulses the laser switched off automatically due to a laser cooling failure, which did not happen for all the other spots on this sample. A third explanation could just be the inhomogeneity of the thick layer, which may have different properties here than in the other positions.

However, the bright grey effect is a fact as it is observed on all these different samples and correlates with stronger heating. As the NRA results exclude a removal of the carbon layer in these bright grey spots the thin C layer is still present. Therefore, an explanation might be a specific change of the refraction index  $n$  and light extinction coefficient  $k$  that occurs at ca. 2100-2200 K. However, the nature of this process is unknown and no measurement of these quantities were performed in the bright grey spots. Nevertheless, it can be seen that this process is stronger for thin layers and weaker for thicker layers as the bright grey spot centre becomes darker with increasing layer thickness on the first sample.


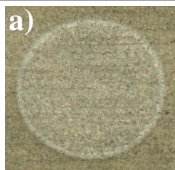
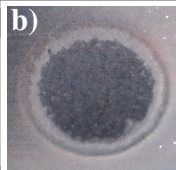
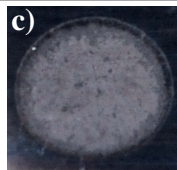
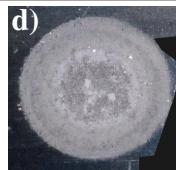

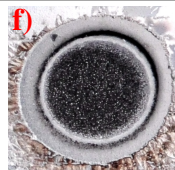

## 3.2. Mixed C/W Layers

To investigate the application of LID on mixed layers of carbon and tungsten, a ca. 200 nm thin C/W/H/D layer was grown on a special limiter in the SOL of TEXTOR. Details on the formation process and layer properties are given in chapter 6.1. The layer is hydrogen rich as half of its atoms are hydrogen isotopes, one third consists of C, while the fraction of W is 10 at%. The layer was grown on rough and polished graphite substrates simultaneously. The surface modifications of this layer due to laser heating are partly similar to those already known from carbon substrates and thin a-C:H layers, but also include new phenomena.

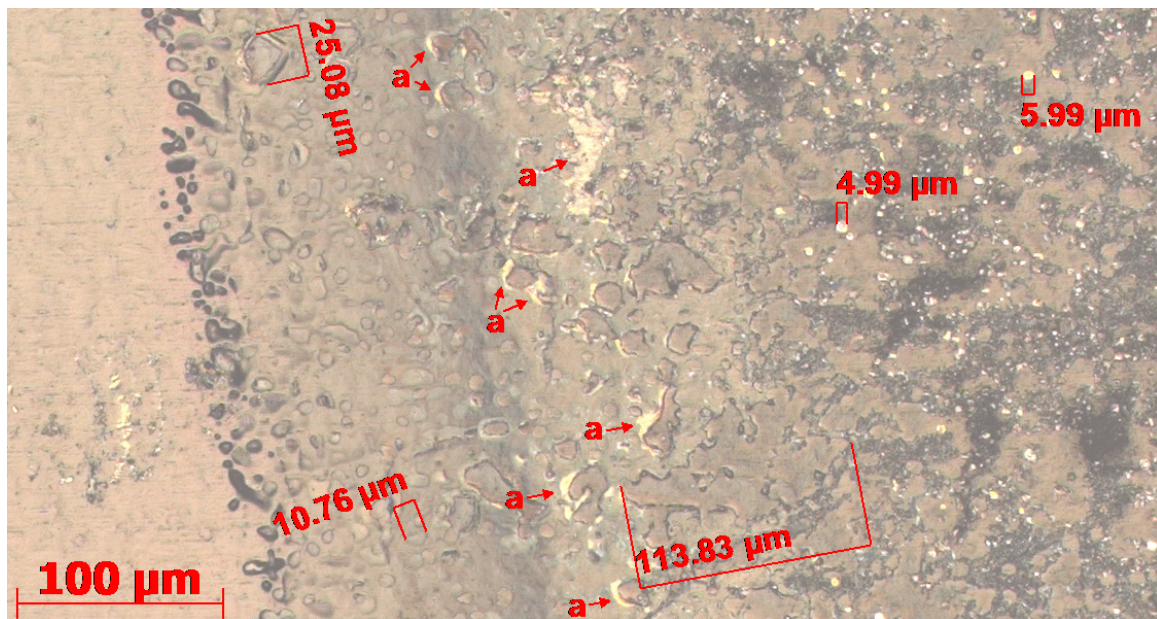
Primarily, a colour change to brighter or darker grey occurs, which is attributed to a similar graphitisation process as in pure a-C:H layers during the restructuring from  $sp^3$  to  $sp^2$  bondings. On the rough substrate, all laser spots appear very similar, independent of the chosen laser pulse duration (1.5 or 3.0 ms) and laser intensity (450 or 500  $MW/m^2$ ). Only slight variations in brightness are discernible. A representative laser spot for the rough substrate is shown in figure 3.10a). The whole sample is shown in figure 6.3 on page 139. In figure 3.10a) an LID pulse of 500  $MW/m^2$  absorbed laser intensity was applied for 3 ms on an elliptical area of 3.0 mm height and 3.2 mm width due to a laser incidence of  $23^\circ$ . The modified area extends nearly over the whole irradiated area and shows a height of 2.9 mm and a width of 3.0 mm. On the rough substrate only sometimes a structure can be seen in the modified area such as a very thin outer ring of different brightness (like in figure a) which is attributed to an intermediate graphitisation stage as mentioned in the previous chapter.

A much higher variety of modifications is visible on the polished substrate (figures b-f). The same laser pulse as in figure a) causes a colour change with 4 areas of different brightness after two identical pulses (cf. figure b). A faint bright outer ring, which is difficult to see without contrast enhancement is followed by a slightly brownish ring, a bright grey ring and a dark grey interior. A completely different image occurs after a 1.5 ms pulse of 700  $MW/m^2$  (figure c) in an area with similar layer properties. The layer similarity for identical toroidal positions as in the case of b) and c) is proved by toroidal EPMA scans (cf. figure 6.4 on page 140 and details

### 3. Surface Modifications due to Laser Heating

	rough substrate	polished substrate: b-f					
 3 mm ∅ 3 3 2							 2 mm
	3.0 ms, 500	3.0 ms, 500 3.0 ms, 500	1.5 ms, 700	1.5 ms, 700	1.5 ms, 700 3.0 ms, 2100	3.0 ms, 500 3.0 ms, 2100	

**Figure 3.10.:** Laser heating of a 200 nm mixed C/W/H/D layer from TEXTOR on polished graphite (except a: unpolished graphite); left column: laser spot diameter in mm; right value: absorbed laser intensity in  $\text{MW}/\text{m}^2$ ;  $23^\circ$  incidence; photography



**Figure 3.11.:** Laser spot edge on a 200 nm C/W/H/D layer from TEXTOR;  $\varnothing 3.0$  mm, 1.5 ms,  $700 \text{ MW}/\text{m}^2$  absorbed laser intensity, 2600 K; optical bright field microscopy

in that chapter). In figure c) a very thin but intense bright outer ring is followed by a dark bluish ring, a dark grey ring and a bright grey interior. These modifications can be attributed to light interference effects of the ambient light during observation or photography, similar to the interference colours in undesorbed a-C:H layers. Obviously, different temperature profiles during laser heating cause different structural changes. This interpretation is supported by the observation that the ring structure extends over a broader area for the long laser pulse, while the rings are thinner for the short laser pulse. This fits to the steeper temperature gradient for shorter laser pulses as shown in the previous chapter (figure 2.14 on page 52). The interference effect is obvious by the fact that the ring structures are hardly visible on the rough substrate, while they are distinct on the polished substrate. Typically, interference patterns are much more pronounced on polished graphite than on rough graphite.

Beside the laser pulse properties also the layer properties have a strong effect on the brightness changes, especially on the polished surface. This is demonstrated by the comparison of the spots in figure 3.10c) and d). The same laser pulse properties were used, but the laser spots were done on different toroidal positions on the limiter with different layer thickness and composition. Thus, a completely different structure in the brightness changes occurs.

The optical investigation shows that the macroscopic appearance of the laser spots, especially brightness and colour change on polished surfaces, sensitively depend on the laser and layer properties. However, to reveal a stringent dependence on such properties would require spatially resolved temperature measurements during LID. Nevertheless, these modifications are useful to identify the position of the desorbed spots and to estimate the desorbed area. In this way the macroscopic observations can answer, whether neighbouring laser spots overlap, whether a second laser pulse exactly irradiated the same area as the first pulse or which fraction of the laser beam hit the target in case of an obstacle in front of the target or if the spot is located at a tile edge.

A microscopic inspection of these laser spots shows similarities to those on pure thin amorphous hydrocarbon layers, but also new features (cf. figure 3.11). Like for the laser spots on pure a-C:H layers, blistering occurs. In the outer edge, blister sizes of up to 25  $\mu\text{m}$  occur. As described in chapter 2.4.4, the maximum temperature for the mixed layer is 500-600 K higher than expected for a pure a-C:H layer. For the example shown in figure 3.11 a maximum of 2600 K was measured. Therefore, the inner parts of the spot show more severe surface modifications. About 200  $\mu\text{m}$  from the edge, large areas of the layer are lifted from the substrate forming blister clusters of 100  $\mu\text{m}$  in size, as marked in the figure. Finally, on the right hand side of the image, some dark areas appear that hint at local C evaporation. In the same region small bright dots of ca. 5  $\mu\text{m}$  diameter occur. Probably, small blisters have lost their cap here and the substrate is visible through these holes in the layer, which appears as bright dots. This cap removal, which is also known from pure a-C:H layers, probably occurs due to extreme overheating and evaporation of the cap because of the loss of contact to the substrate.

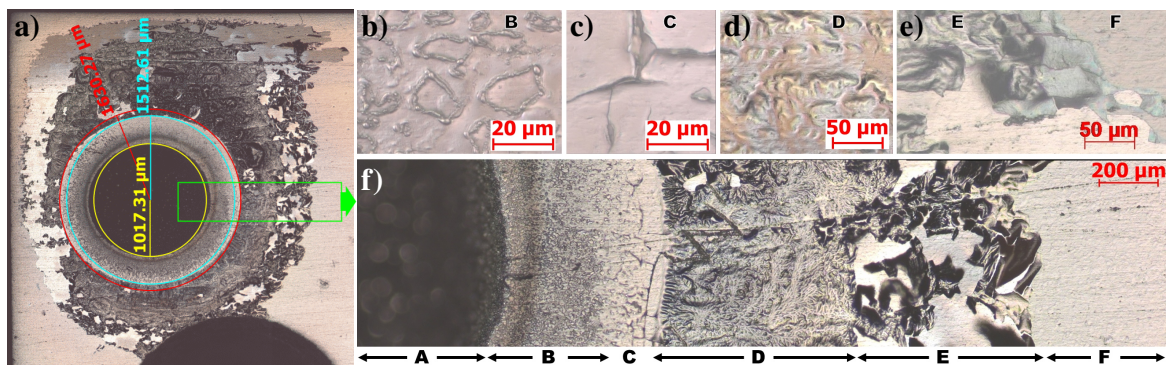
A new feature, which has not been observed for laser spots on pure a-C:H layers occurs in a region 130-230  $\mu\text{m}$  from the spot edge. Here, some areas close to blisters reveal the substrate, which can be identified by the same bright colour as in the dots discussed above. These areas are marked with "a" and arrows in the figure. The layer is removed only on the outer side of the blisters, i.e. on the side directed towards the spot edge. The shape of the uncovered areas often follows the shape of the blister. This effect cannot be explained by local overheating, as this would more likely occur on the blister cap or on the opposite side of the blister, which is closer to the spot centre. Additionally, this effect only occurs outside the central spot area with evaporation and cap removal effects. Therefore, the observations suggest that the layer has been torn apart on the outer blister side and the whole blister moved slightly towards the spot centre. This phenomenon of "layer slide" or "blister slide" indicates, that a thermo-mechanical force occurs that pulls on the layer and blisters in the direction of the spot centre. Its origin could be the temperature gradient or the evaporation of material further inside, which causes a contraction of the layer towards the spot centre. An explanation for the specific position of the slide effect could be that further outside and further inside of this position the layer is more firmly attached to the substrate. Further outside, i.e. in the outer 130  $\mu\text{m}$  of the spot edge, the surrounding original layer is still firmly attached and holds the layer in place. And further inside, i.e. more than ca. 230  $\mu\text{m}$  from the spot edge, the local overheating might cause an improved fixation of the layer to the substrate. Alternatively, if the temperature gradient is the driving force, the gradient is too small inside the spot. However, it will be shown soon, that this contracting force towards the spot centre exists and increases for more intense laser pulses, where it even affects areas far outside the laser irradiated spot area.

For the determination of the remaining fraction of hydrogen after a standard laser heating pulse, the inner part of the heated spot was exposed to the maximum laser intensity available (figures 3.10e, f). The standard laser pulse for carbon (700  $\text{MW}/\text{m}^2$  absorbed intensity for 1.5 ms) was applied on a spot of 3.0 mm diameter, yielding a maximum temperature of 2460 K (cf.

### 3. Surface Modifications due to Laser Heating

chapter 2.4.4). Then the maximum intensity pulse ( $2 \text{ GW/m}^2$  absorbed intensity for 3 ms) was applied on the inner 2.0 mm diameter of the first spot. The temperature was out of range in the pyrometric measurement, i.e. above 2620 K. In both cases, the angle of incidence was  $23^\circ$  which leads to a slightly elliptical spot shape in the horizontal direction, shown by the measurement circles in figure 3.12a).

The laser irradiated area of the second pulse (region A in figure 3.12f) was heated such strongly that carbon and tungsten evaporated, thus a crater of 2.0 mm diameter was formed. The crater has a sharp edge (between region A and B) and its interior consists of carbon and small W droplets. These droplets are the remnants of the molten and evaporated tungsten that was initially incorporated in the mixed C/W/H/D layer. They appear as blurred circles in region A since they are out of the focus of the microscope on the bottom of the crater but they still reflect light strongly. In the photography (figures 3.10e, f) the W droplets are visible sharply as small white dots on the whole inner 2.0 millimetres. Additionally, a strong modification of the whole area outside the first  $\varnothing 3.0$  mm spot can be seen that will be discussed in the following. Moreover, in figure 3.10f, brownish carbon redeposition of the evaporated carbon can be seen on the lower and left part of this strongly modified region outside the laser spot.



**Figure 3.12.:** Mixed C/W/H/D layer (10 at% W) on polished graphite; LID pulses: 1.5 ms with  $700 \text{ MW/m}^2$  on  $\varnothing 3.0$  mm and 3 ms with  $2 \text{ GW/m}^2$  on  $\varnothing 2.0$  mm; optical microscopy

The strong laser pulse of  $2 \text{ GW/m}^2$  has a large and peculiar effect on the surface, which affects areas up to 4 mm from the spot centre, where the mixed C/W/H/D layer is partly removed (cf. figure 3.12a). The removed areas are mainly located further away from the spot, while in the vicinity of the spot the layer still exists but in a modified type. It appears to be folded or crumpled. This behaviour repeated in a similar way in all four spots that were exposed to this strong laser pulse. Close microscopic inspection of the transition from the spot centre to the unchanged layer (cf. figure 3.12f) leads to the following interpretation.

The layer outside the first spot (region D, E) has been squeezed and contracted towards the spot centre and moved radially inwards. As a consequence, it was torn apart further away from the spot, because more than 4 mm away from the spot centre, the layer is still firmly attached to the substrate (region F). The reason for this contraction effect is probably a thermo-mechanical effect due to the strong lateral temperature gradients, as already indicated by the small "layer slides" inside the previous spot discussed above.

The contracted C/W/H/D layer can only be found in region D, i.e. exactly outside the area of the first laser spot. The boundary of this region (between C and D) is very sharp and therefore it is concluded, that the first laser pulse marks this boundary and prevents the layer from the contraction effect. This could have different reasons: During the standard heating of the first laser pulse the layer blisters and detaches locally as described above. As local detachment



releases stresses in the layer, this could lead to local improvement of attachment inbetween the blisters. A second explanation for the prevention of the contraction effect could be an improved lateral stiffness, i.e. mechanical strength of the layer parallel to the surface. This could be a consequence of the hydrogen desorption in the first pulse and formation of more C-C bondings during the change from  $sp^3$  to  $sp^2$  dominated structure.

These hypotheses are supported by the observations of two characteristic structures within the 3 mm diameter spot of the first pulse (region B and C, also shown in figure 3.13). Here, the layer showed most probably the same blistering after the first pulse as discussed above, since the same laser pulse was used. Additionally, the properties of the layer should be identical, since the two spots are only 6 mm separated (centre to centre distance) in poloidal direction, in which the layer properties are rather homogeneous.

In the inner part (region B) the surface is densely covered with annular structures of 10-20  $\mu\text{m}$  diameter, which can be described as deformed rings (cf. figure 3.12b). The shape and size of the rings exactly matches the blisters that appear after the first laser pulse. Inside the ring structures the layer has disappeared and the substrate is visible. These observations imply that the blisters grown by the first laser pulse collapse due to the strong second laser pulse. For the layer between the blisters an increased stiffness or attachment due to the first laser pulse is assumed, but the blister caps are weaker against the lateral contraction forces. Obviously the second laser pulse tears the cap apart somewhere in its centre and contracts the cap material to the blister borders forming these ring structures. Sometimes nearly spherical objects occur in the ring border which look like droplets. These are probably not molten W droplets, because they do not appear between the ring structures, where the temperature should be similar or even higher. Since the rings are found up to 0.3 mm away from the laser irradiated area of the 2<sup>nd</sup> pulse, they can only be heated by lateral heat conduction along layer and substrate and not by laser radiation. Thus, their temperature must be smaller or equal to the layer between them. The spherical objects are therefore rather areas, where more blister cap material has been contracted, which is likely as they often appear in the corners of the deformed rings.

The region with the ring structures gradually changes into a region at the edge of the first laser spot where cracks appear in the layer (region C). The crack edges are lifted from the substrate (cf. also figure 3.12c). In figure 3.13, a different part of the spot border with stronger cracking is shown. Some cracks are connected to the ring structures of region B. Few cracks also extend into region D of the squeezed layer. The mechanism of cracking in this area can be



**Figure 3.13.:** Magnification of laser spot border of figure 3.12a (optical bright field microscopy). The letters indicate the same regions as in figure 3.12f.

explained with the assumptions and interpretations discussed so far. Region B and C belong to the first laser spot and are therefore not contracted by the second laser pulse (except locally at the annular structures). In contrary, region D is strongly contracted by the second pulse. As region C is at the border between contracted and flat layer, it is likely that strong tension forces are established here, which are released by cracking.

The folded and squeezed layer in region D (cf. figures 3.12d and 3.13) shows hills and valleys with a typical scale length of 10-20  $\mu\text{m}$ . The layer is not split into fragments but is unseparated up to ca. 1.5 mm in some directions (cf. figures 3.12a). In other directions region D is very short or skipped completely like in the lower left of figure 3.12a.

Region E follows, which is the area from which the squeezed layer of region D originates. Therefore, parts of this area are uncovered substrate and partly it is covered with delaminated and loosely attached layer fragments (cf. figure 3.12e). The image shows the unchanged layer on the right hand side (reddish). Further to the left, slightly detached, but still flat layer (greenish) occurs and on the left hand side some loose and already squeezed layer fragments (dark) can be seen. Since region E extends up to 4 mm from the spot centre, the temperature gradient is much weaker here and unlikely the explanation for the layer rupture. It is assumed, that the contracting forces that are acting at least up to region D cause the layer contraction and as a consequence lead to the layer rupture in region E. Finally region F represents the flat, smooth and unchanged C/W/H/D layer.

In conclusion, mixed thin C/W/H/D layers show similar surface modifications like pure thin a-C:H layers. For standard temperature heating, colour and brightness change and blistering occur, while in the case of overheating, layer and blister evaporation are added. Additionally, the mixed layers show melting of W in form of small droplets in strongly heated cases and a layer contraction effect directed towards the spot centre. The contraction effect already slightly starts within the laser spot for temperatures around 2500 K, but can contract the surrounding 2-3 mm of the layer outside the spot in case of extreme heating. This leads to a sliding of the layer over the substrate toward the laser spot and thus uncovers the substrate at regions up to 4 mm away from the laser spot centre.

These severe layer detachment should basically be avoided in LID applications in fusion devices, since it is a possible source of dust. Already small amounts of dust can stop plasma operation [Rudakov9, p.9f], especially when the dust contains high-Z elements like tungsten. Layer detachment and dust generation can be avoided during LID by limiting the temperatures to about 2500 K, which is possible for thin layers by reducing the laser intensity. Indications were found, that a controlled heating can even have beneficial effects on the stability of the mixed layer improving its mechanical stiffness or its attachment to the substrate.

### 3.3. Bulk Tungsten

Laser induced heating of tungsten can mainly have two material effects, namely roughness increase and cracking. First the roughness increase is discussed, because it occurs always. Then heating above the melting temperature is discussed, where further effects like crater formation, bubble growth and surface stress patterns appear. Finally cracking is discussed as it occurs for intense laser pulses during heating and melting, but not always, since it depends on the material properties, which differ for different W grades.

The surface roughness is measured here in terms of the arithmetic mean roughness, defined as the average deviation of the surface altitude from a flat line (or plane in 2D):

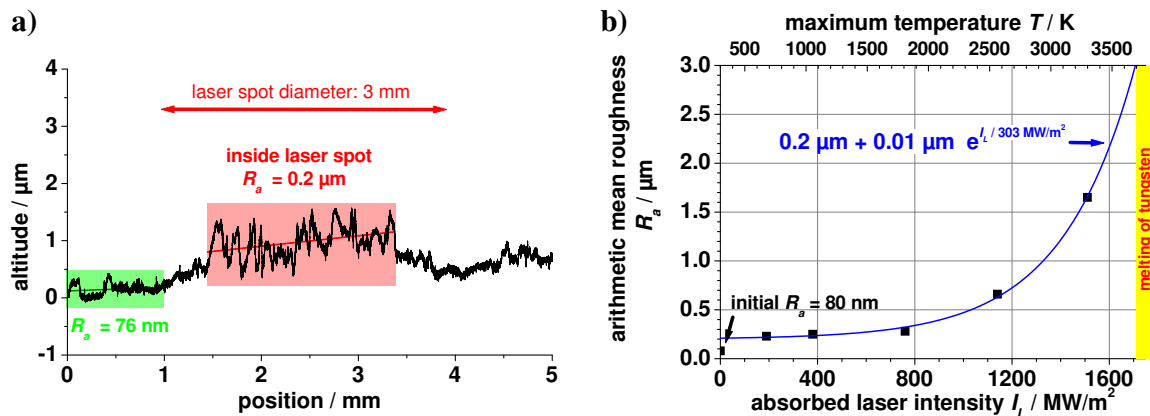
$$R_a = \frac{1}{L} \int_{x=0}^{x=L} |y| dx \quad . \quad (3.1)$$

$L$  ... length of the surface profile

$y$  ... altitude of the surface above the mean line

The mean line is the line which has the smallest deviations of the surface from it and is thus obtained by a linear regression fit to the profile. In the following example (figure 3.14a) the mean lines of two roughness measurements are indicated. This profile was measured by optical profilometry in a scanning confocal microscope (Micromesure 2 from Stil SA) which uses white light and avoids contact to the surface. Other surface profiles were also measured with laser profilometry and by a stylus profiler (Dektak 6M from Veeco Instruments Inc.), which uses a needle in mechanical contact with the sample.

The initial roughness of W surfaces after sample cutting by electric discharge wire erosion and surface cleaning by staining in nitric acid was  $R_a = 1.23 \mu\text{m} \pm 0.12 \mu\text{m}$ . Typically  $R_a$  is given without error range, since it already contains a deviation from an average. The error range here denotes the standard deviation of several roughness measurements on one sample. This roughness is already larger than the typical effect of roughening induced by laser heating and thus the roughening effect cannot be measured on rough surfaces. Therefore the laser induced effect is measured on polished surfaces. With mechanical grinding methods using diamond suspension, surfaces with mirror finish of  $R_a = 28\text{--}80 \text{ nm}$  were achieved. A typical surface profile through the centre of a laser heated spot is shown in figure 3.14a. Here a spot of 3 mm diameter has been heated with 100 laser pulses of 1 ms duration each and 2 s cool-down time between the pulses. The absorbed laser intensity ( $470 \text{ MW/m}^2$ ) is nearly as high as defined for the standard heating pulse for W in the previous chapter. The roughness of the W material (99.95 wt% pure W from MG Sanders) increased from 76 nm to  $0.2 \mu\text{m}$  in the inner 2 mm of the spot (red area). The outer regions of the spot do not show a roughness increase, but they are tilted conically towards the spot centre.



**Figure 3.14.:** Surface roughness increase of tungsten due to laser heating

a) surface profile across a laser spot (100 pulses of 1 ms,  $470 \text{ MW/m}^2$ )

b) roughness increase with laser intensity (each point: 100 pulses, 1 ms)

Roughening occurs due to thermal expansion of the grain structure of the polycrystalline material. When the W grains are heated, every grain expands and is lifting the surface locally. Globally the whole surface is swelling, but locally the offset is different for each grain. Thus the initially smooth surface shows steps at the grain boundaries. When the temperature reduces again, the misalignment of the grains remains. At the edge of the laser spot the roughening does not occur for two reasons: Firstly, the temperatures are already lower in this region (cf. figure 2.14 on page 52) due to heat conduction in the material and therefore the thermal expansion is smaller than in the spot centre. Secondly, for a grain in the centre, the mechanical

### 3. Surface Modifications due to Laser Heating

---

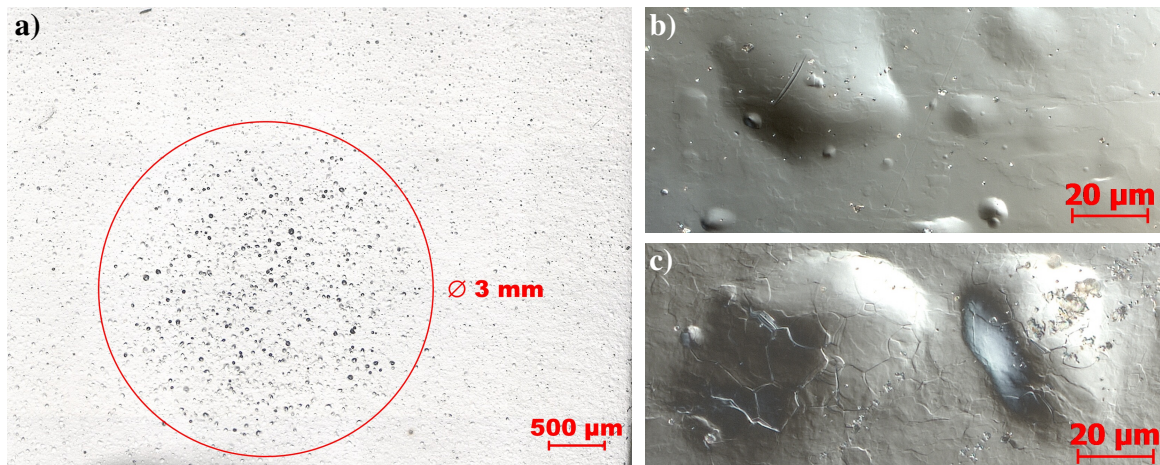
stresses impinge from all directions due to the expansion of the neighbouring grains. But at the spot edge the pressure from the cold surrounding material is small. Here, the grains can expand towards the cold material and thus the thermo-mechanical stresses are not as large as in the centre. Additionally, this asymmetric stresses on the grains in the spot edge lead to the conical tilting of the spot edge.

Due to the roughening, the grain borders become visible like after chemical etching, therefore the process is also called "thermal etching". In figure 3.19 on page 98 this effect can be seen in the heated area outside a molten spot. In the cold unheated area A the tungsten grains are not visible because the grain boundaries are filled with the eroded W material during polishing. The laser spot edge lies in area B, where the temperature increases from left to right until it reaches the melting temperature at the border to area C. Thus area B has been heated and the steps at the grain boundaries become visible. This example also shows that the roughening mechanism already appears at the first laser pulse, as this image was taken after one pulse.

A systematic study of the roughness increase as a function of the laser intensity, and thus temperature, was carried out with polished W of ultra high purity (99.9999 wt% W from Plansee). The initial surface roughness was 80 nm. The laser spot size was  $\varnothing 2$  mm. For every laser intensity 100 pulses of 1 ms duration each and 2 s cool-down time were applied. The roughness increases already for low laser intensities of  $190 \text{ MW/m}^2$  to  $0.2 \text{ }\mu\text{m}$  (cf. figure 3.14b) and increases first very slowly and then (above ca.  $1 \text{ GW/m}^2$ ) faster with increasing laser intensity. The roughness increase can be fitted very well with an initial offset of  $0.2 \text{ }\mu\text{m}$  and an exponential increase, which is shown in the figure. The highest roughness measured, was  $1.65 \text{ }\mu\text{m}$ , but the extrapolation according to the exponential increase indicates, that up to the melting temperature of W a maximum roughness of  $3 \text{ }\mu\text{m}$  could occur.

Beside roughening due to grain displacement, a second roughening mechanism occurs due to the growth of gas filled blisters. It only occurs on surfaces which already show blisters before laser heating. All W samples used in the present work, did not show blisters after plasma exposure in TEXTOR, PADOS, Pilot-PSI or PSI-2. Only a W sample exposed in an ECR-plasma in the PlaQ device (details on page 150) showed blisters that were filled by deuterium from the plasma, as found by TDS [Manhard11b]. The blisters are mainly responsible for the surface roughness, because the surface has been polished before plasma exposure. Before the laser heating, the blisters have lateral dimensions of up to ca.  $40 \text{ }\mu\text{m}$  (cf. figure 3.15b) and a height up to  $1 \text{ }\mu\text{m}$ . After laser heating they have a height of nearly  $4 \text{ }\mu\text{m}$  and appear as darker spots (figure 3.15a). Again the effect reduces in the edge area of the laser spot. In the magnification (figure 3.15c) it can be seen, that the displacement of grains is especially large on the blisters due to the strong swelling of the blister cap.

The blister swelling could be due to the expansion of the gas inside the blisters. Assuming an isobaric expansion due to the temperature increase of factor 6-7 (from 300 K to 1800-2100 K) a volume increase of the same factor is expected. Therefore the height increase by factor 4 seems to be plausible, considering that the volume increase could be smaller, if the process is not purely isobaric but the gas pressure also increases. The volume increase could also partly occur at the bulk side of the blister or laterally, thus the height increase at the surface would be also smaller than expected. When the temperature reduces, the grains which are shifted towards each other might remain in the lifted position. This fits well to the observation that the largest grain displacements are especially found on the blisters. The gas pressure inside the blister is then smaller than before laser heating. No open blisters due to rupture by the expanding gas could be found, while the rupture of blisters occurs during slow heating in TDS [Manhard11b]. Consequently, the deuterium gas could still be inside the blisters after LID, which could lead to an underestimation of the deuterium retention in the



**Figure 3.15.:** Growth of deuterium blisters due to laser heating: a) the blisters inside the laser spot (circle) appear darker after a single 3 ms LID pulse of  $555 \text{ MW/m}^2$  (optical microscopy, bright field); b) unheated blisters outside laser spot; c) blisters inside laser spot heated with  $2 \times 522 \text{ MW/m}^2$  (b and c: optical microscopy, DIC)

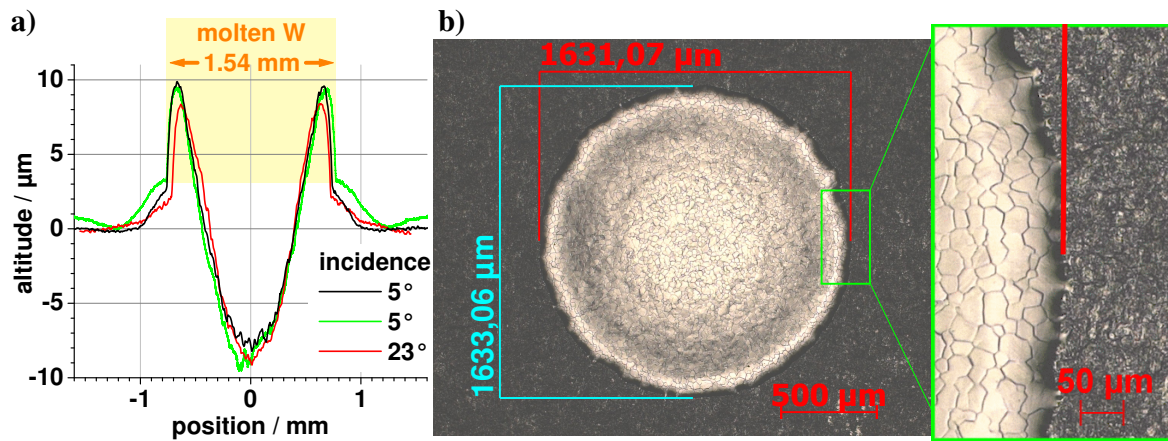
subsequent hydrogen quantification. But only 3-5% of the total D amount is retained in the blisters as found by TDS [Manhard11b], thus the effect could not be measured due to the larger measurement uncertainties. However, the possible underestimation would be negligible.

In some cases, laser induced heating is not sufficient to achieve complete desorption, then laser induced melting (LIM) is necessary. The molten area can easily be recognised in microscopic images of the surface, because the grain pattern is visible very well in the recrystallised material (cf. figure 3.16b or 3.19 region C and D). The size of the molten area does not reach the size of the laser beam (2.0 mm laser beam diameter). For the usually applied melting pulse of  $1.3 \text{ GW/m}^2$  absorbed laser intensity and a pulse duration of 3 ms, the average diameter of the molten spot is  $1.64 \text{ mm} \pm 0.09 \text{ mm}$ . The standard deviation expresses the deviation of the molten spot size on different W grades and surface finishes. On one sample, the differences in the molten spot size are much smaller. The molten spot is smaller than the laser spot size because of the temperature gradient at the spot edge due to the cooling by the surrounding cold material. This was proved on special samples of  $1.9 \times 2.5 \text{ mm}^2$  surface dimension. Here, the same melting pulse in the centre of the W block leads to melting of the whole width of 1.9 mm, since the heat cannot escape to the side and thus the surface temperatures are higher.

Back on large sample surfaces, for a shorter laser pulse of 1 ms duration at  $1.7 \text{ GW/m}^2$  the molten area is significantly smaller with  $1.32 \text{ mm} \pm 0.08 \text{ mm}$  than for the 3 ms pulse. This is due to the 2.2 times lower energy per pulse. The ratio of the molten areas is 1.5 and thus smaller than the ratio of the energies. The difference can be explained by an increased depth of melting for the longer laser pulses, which will be discussed later. In general, the total molten volume increases roughly according to the absorbed laser energy.

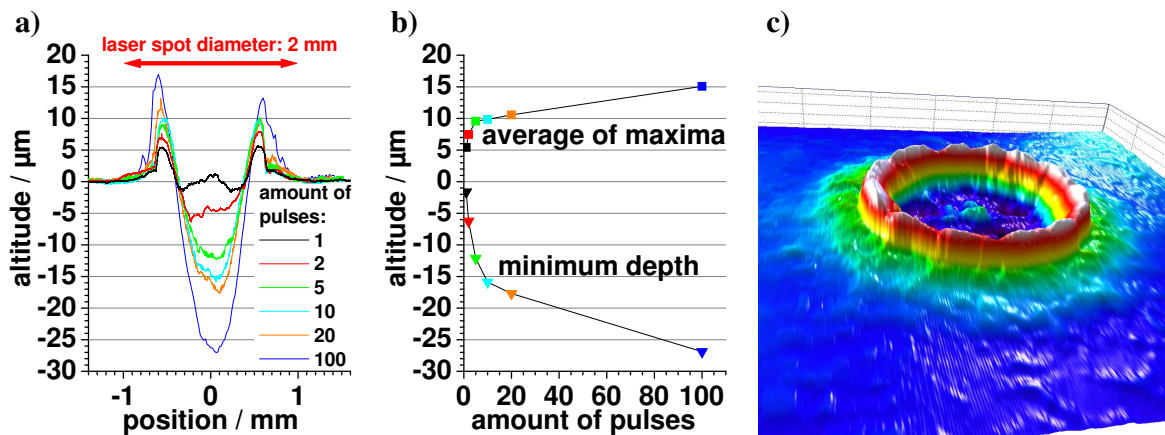
The surface deformations caused by melting are larger than by the roughening effects. After one standard 3 ms LIM pulse on a polished W surface with  $R_a = 30 \text{ nm}$ , the roughness in the centre of the molten spot increases to ca.  $1.2 \text{ μm}$  and to  $1.3 \text{ μm}$  in the heated, but not molten area around the molten spot. In comparison to these values, the global surface deformation is nearly one order of magnitude larger. The spot centre decreases by ca.  $8 \text{ μm}$  below the initial surface (figure 3.16a) and the spot edge is lifted by ca.  $9 \text{ μm}$ . The maximum altitude is reached close to the end of the molten area. Further outwards the surface is also raised several micrometres and returns to the initial altitude where the laser irradiated area ends or slightly further outside the laser beam. The end of the molten area is very sharp and can be

### 3. Surface Modifications due to Laser Heating



**Figure 3.16.:** Laser induced melting on W with  $1.3 \text{ GW/m}^2$ , 3 ms, laser  $\varnothing 2 \text{ mm}$ ; 1 laser pulse; a) 1D profiles on polished W (optical confocal profilometry); b) LIM with  $5^\circ$  incidence on rough W (optical microscopy)

identified in surface profiles and on microscopic images clearly by a sudden change of the surface characteristics (figure 3.16).



**Figure 3.17.:** Polished tungsten surface after laser induced melting with  $1.7 \text{ GW/m}^2$ , 1 ms pulses; optical confocal profilometry: a) 1D profiles; c) 3D view after 1 laser pulse; optical confocal profilometry

For the shorter 1 ms pulses described above, the valley in the spot centre is very small for one laser pulse (cf. figure 3.17a) comparable to the roughness increase in the centre. Therefore some parts of the spot centre lie even above the initial surface. The surrounding crater rim is with  $5 \mu\text{m}$  also lower than for the 3 ms pulse. A 3D-visualisation of the surface topology acquired by scanning confocal profilometry (cf. figure 3.17c) shows the cylindrical symmetry of the surface deformations. Since the crater rim is much higher than the valley in the centre, it is easily seen that an apparent volume increase occurred. This is also true for the 3 ms pulses shown above. Considering the cylindrical symmetry for integration of the surface profile, the void volume below the initial surface is  $2.2 \cdot 10^{-12} \text{ m}^3$ , while the material volume above the initial surface is  $9.4 \cdot 10^{-12} \text{ m}^3$ , i.e. factor 4 larger. For repetitive laser pulses on the same position (cf. figure 3.17a,b), the hill of the molten pool increases and the valley increases even faster. Thus the ratio of volumes above the initial surface and below decreases. But even after 100 pulses of 1 ms duration each, the volume above the initial surface is still a factor of 1.4 larger than the void volume of the valley. An explanation for this volume increase will be given below, when the cross-sections of the molten spots are discussed.

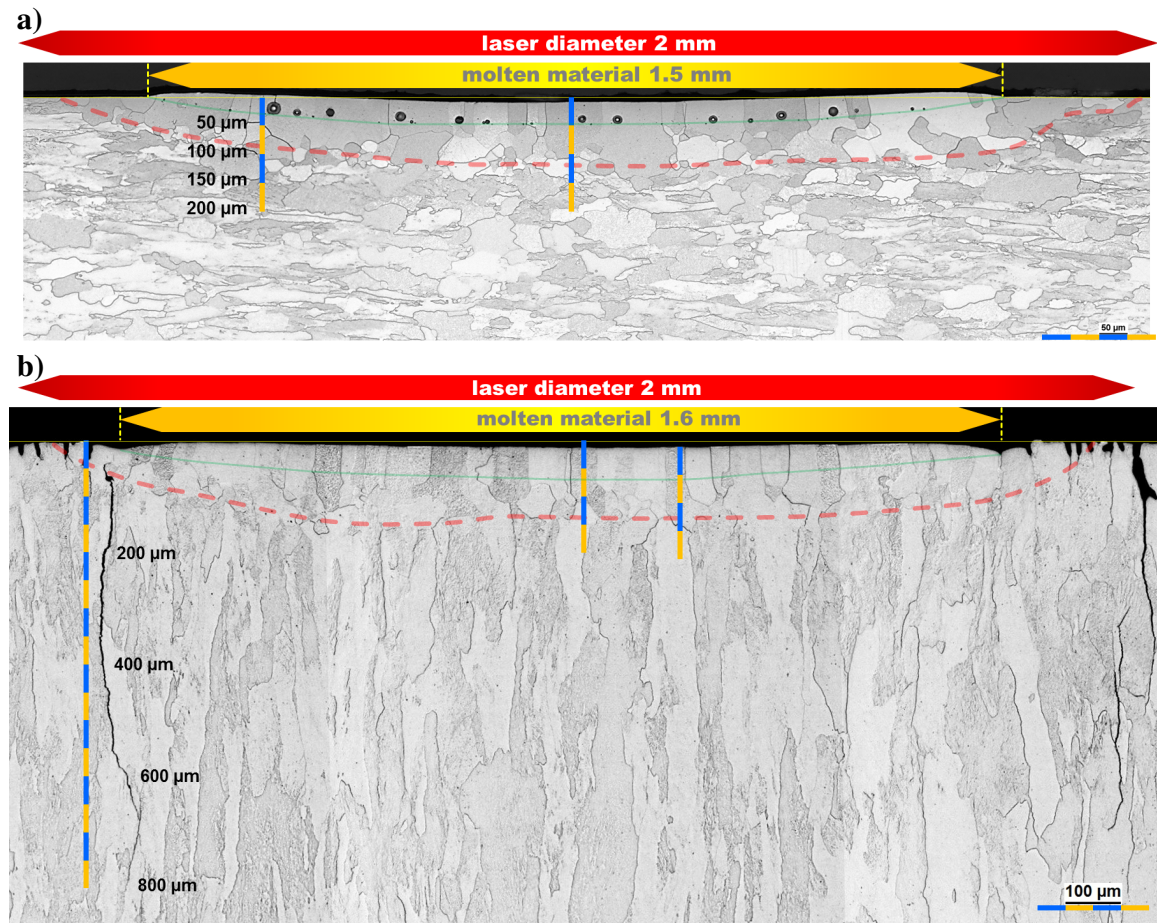
The surface changes due to the 3 ms pulse fit very well into the series with the 1 ms pulses between 2 and 5 laser pulses. Thus it is very probable that several pulses on one position yield the same profile as one laser pulse with a duration equal to the sum of the individual pulse durations. The diameter of the laser spots does not increase systematically after repetitive pulses. There are only maximal deviations of  $\pm 1.5\%$  in the diameter of the molten spots.

The form of the crater walls in the centre can be approximated with parabolic functions very well. This already hints at the formation mechanism for this shape, which is typical for craters formed by the vapour recoil pressure of the released particles [Sobol95, p.126]. The evaporated W atoms and the desorbed gases like CO, H<sub>2</sub>, H<sub>2</sub>O are ejected from the surface and thus impose a recoil pressure on the liquid W. This causes a repulsion of the viscous liquid to regions where the recoil pressure is lower, which is at the spot edge and outside of the melt. The resulting shape is a paraboloid of revolution [Sobol95, p.111f]. The vapor recoil must be mainly due to evaporating W because the other retained gases are desorbed after one melting pulse, but the crater growth is nearly undamped until the 5<sup>th</sup> laser pulse (i.e. 5 ms). The largest change in the profile happens in the first 5-10 ms of accumulated irradiation time, while from 10-100 ms the growth of the hills and valley slows down and seems to be linear (cf. figure 3.17b). For the highest pulse numbers of 20 and 100 pulses, the hill at the crater rim becomes asymmetric. Since the sample surface was oriented perpendicular to the ground and the higher peak is located at the bottom side of the sample, an effect of gravity is probable. For smaller hill altitudes this effect is not seen, since probably the surface tension force and vapour recoil force are dominant and the gravitational force has a minor effect. Theoretical considerations of the velocity of metal melts show that gravity becomes important for pulse durations in the order of milliseconds for 2 mm diameter spots [Sobol95, p.127]. Hence, an effect of gravity is very probable here.

The most important quantity of the LIM spots with respect to hydrogen desorption is the melting depth, which should be larger than the maximal depth of deuterium retention, which is typically less than 10  $\mu\text{m}$  (cf. chapter 4.1). This enables a mobilisation of the whole deuterium inventory and complete release of the retained deuterium. To measure the melting depth, metallographic cross-sections of the molten spots were done on different W grades and after different laser pulses. For the cross-sections, pieces of the material had to be cut out, in order to embed them into a transparent resin and polish the cross-sectional surface. The polishing was stopped in the centre of the spots and a grain-boundary etching (with H<sub>2</sub>O, H<sub>2</sub>O<sub>2</sub>, NH<sub>3</sub>) was performed to visualise the microstructure. Two examples after one standard melting pulse on two different W grades are shown in figure 3.18. The determination of the melting depth is easy for W grades with a purity of 99.95%, which is typical, but not "ultra pure" (see below). Large voids of various sizes up to 24  $\mu\text{m}$  were generated at the bottom of the melt pool. They also appear after the short 1 ms laser pulse and after many pulses (observed up to 100 pulses). The volume increase that was measured by surface profilometry originates most probably from the additional volume of these bubbles. The reduction of the volume ratio of hill to valley from 4 to 1.4 between 1 and 100 ms heating duration, is probably due to two effects: On the one hand, it is due to a general loss of W material due to evaporation. On the other hand, there is a tendency to less and smaller bubbles with increasing amount of laser pulses. But also for one spot a strict systematics in the size of the bubbles can be seen. The smallest voids, which are only a few micrometres in size, are located deepest (marked with a green line in the figure). With increasing bubble size, the centre of the bubbles is closer to the surface. In fact, there is a relationship between the size and position of the bubbles in such a way that the lowest part of the bubble touches the green line – the interface between resolidified melt and solid. This can be observed for the majority of the bubbles. Some bubbles are not touching this interface, but this is most probably only because they are not exactly cut across their maximal diameter. Thus they appear smaller since their full size is not visible in this particular section. Therefore

### 3. Surface Modifications due to Laser Heating

it can be concluded that the bottom of each bubble sticks to the melt-solid interface. The centre of the bubbles often exhibits a white dot, which is only an artefact due to the filling of the bubbles with the resin and the reflexion of the light of the microscope.



**Figure 3.18.:** Cross-section of a molten laser spot,  $1.3 \text{ GW/m}^2$  absorbed laser intensity, 3 ms pulse duration, 1 laser shot, optical microscopy  
a) polished tungsten 99.95 wt% pure W (from MG Sanders),  $6^\circ$  laser incidence  
b) rough tungsten 99.9999 wt% UHP W (from Plansee),  $23^\circ$  incidence

The melt-solid interface is always bent especially at the spot edges, where it reaches the surface exactly at the end of the surface hill. The position of the melt-solid transition, which is seen clearly at the surface (indicated with dashed yellow lines) coincides with the position, where the interface reaches the surface. If voids are present at the edge, this can clearly be seen by an extrapolation of the green line, like at the left spot edge in figure 3.18a.

One hypothesis explaining the formation of the bubbles is the presence of impurities in the material that serve as nucleation points for the vapour. Therefore cross-sections have been done also across melt spots on ultra high purity tungsten with 99.9999 wt% W (cf. figure 3.18b) which has virtually no impurities. In fact, no bubbles were found in the melt spots of this W grade, neither after 1 nor after 10 laser pulses. Thus it is very probable that the impurities are responsible for bubble formation during melting.

From the viewpoint of hydrogen retention, the filling of the bubbles is interesting, since they might contain hydrogen gas. However, this is not plausible, because the material with bubbles has been annealed and thus degassed and not exposed to plasma, while the ultra pure W grade has not been annealed and therefore contains protium from the fabrication. Thus hydrogen filled bubbles would be rather expected on the ultra pure W. This indicates strongly, that the voids are not filled with hydrogen. A detailed FIB cross-section in an SEM image



(figure 3.22 on page 101) shows that the bubbles have layered shells that exactly follow the shape of the bubble. An inner shell of ca. 600 nm thickness is followed by an outer shell of ca. 450 nm thickness. Both shells show several sub-shells evident by further darker lines following the curvature of the bubble in the same way. The inner shell shows "nano-crystals" or "nano-grains" of 100-200 nm in size in the direction perpendicular to the bubble wall and roughly half this size in the direction parallel to it. This ordered sequence of shells with constant thickness indicates a crystal growth due to condensation from the gas phase, because this process would be homogeneous along the bubble wall. Therefore there are indications, that the bubbles are filled with vapour of W and impurities, which then condense on the inner walls of the voids during recrystallisation.

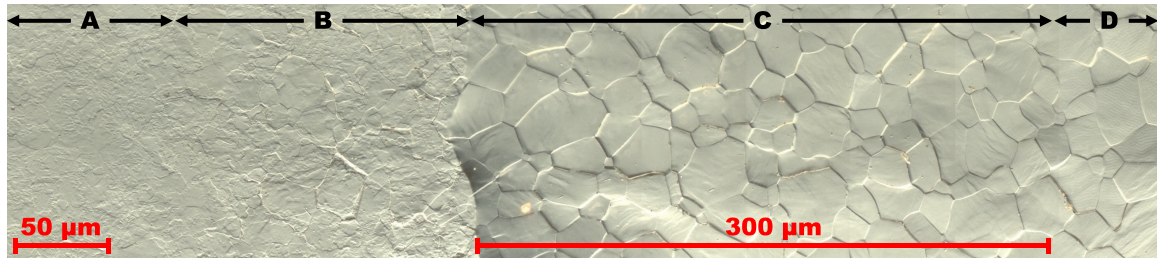
A second method of identifying the molten region is the orientation of grain boundaries perpendicular to the surface in resolidified melt. In figure 3.18 it can clearly be seen, that nearly all grain boundaries in the region above the green line have this orientation in contrast to arbitrary orientations in all other regions of the material. As a consequence, a grain boundary sometimes abruptly changes direction at the melt-solid interface and forms a kink. These kinks mark the interface in the same way like the small bubbles and are located on the green line as well. If no bubbles are present (like in figure 3.18b) the perpendicular grain boundaries and boundary kinks still allow to identify the melt region. In the central region of each molten spot, the melting depth is quite uniform. However, for different spots different melting depths occur even on the same sample and with the same pulse parameters. For the 3 ms standard melting pulse, the melting depth therefore lies between 30 and 55  $\mu\text{m}$ , which is deep enough for deuterium desorption purposes here. For the 1 ms laser pulses with  $1.7 \text{ GW}/\text{m}^2$  the melt depth is 20-25  $\mu\text{m}$  independent of the number of laser pulses (for 1-100 pulses). This difference explains the relatively low increase in molten area on the surface between the two laser pulse settings. The 2.2 times higher energy in the longer pulse is not only used for a lateral extension of the melt but also for a deeper melt pool.

The thin horizontal yellow line in figure 3.18a is drawn at the altitude of the initial surface based on the areas outside the spot. The surface deformations discussed above in detail can be roughly found here again with hills and a valley of ca. 10  $\mu\text{m}$  height. In figure 3.18b the surface shape is similar, but below the initial surface due to the absence of voids and the disappearance of the ca. 20  $\mu\text{m}$  deep groves on the initial surface. Outside the molten volume, a second modified area can be recognised (marked with the red dashed line). Inside this area, the grains are not elongated as strongly as outside this area. In figure 3.18a the grains of the unchanged material are elongated parallel to the surface, while in figure 3.18b they are elongated perpendicular to the surface. This preference does not fully vanish in the marked area, but the grain size in horizontal and vertical direction becomes much more similar. Moreover, especially in figure 3.18a, the sub-grain structure is very homogeneous and smooth in the marked area, while the unmodified grains show an inhomogeneous and coarse interior. A smooth grain texture shows that stresses inside the grains have been released. This indicates the first phases of a recrystallisation process where sub-grain boundaries are moved to the grain boundary and thus internal stresses and inhomogeneities are reduced. In figure b) this effect is not visible probably due to stronger etching, but should be present as well. However, strong recrystallisation does not occur, as the volume of a grain remains similar only changing the aspect ratio as discussed above. In the ultra pure material the grain volume even decreases in the marked area.

It can be concluded that the marked area corresponds to a strongly heated volume with initial phases of recrystallisation but no strong recrystallisation. As recrystallisation begins roughly at half of the melting temperature, the laser induced temperatures are high enough even for strong recrystallisation. But probably the short heating duration does not allow for further recrystallisation and significant grain growth.

### 3. Surface Modifications due to Laser Heating

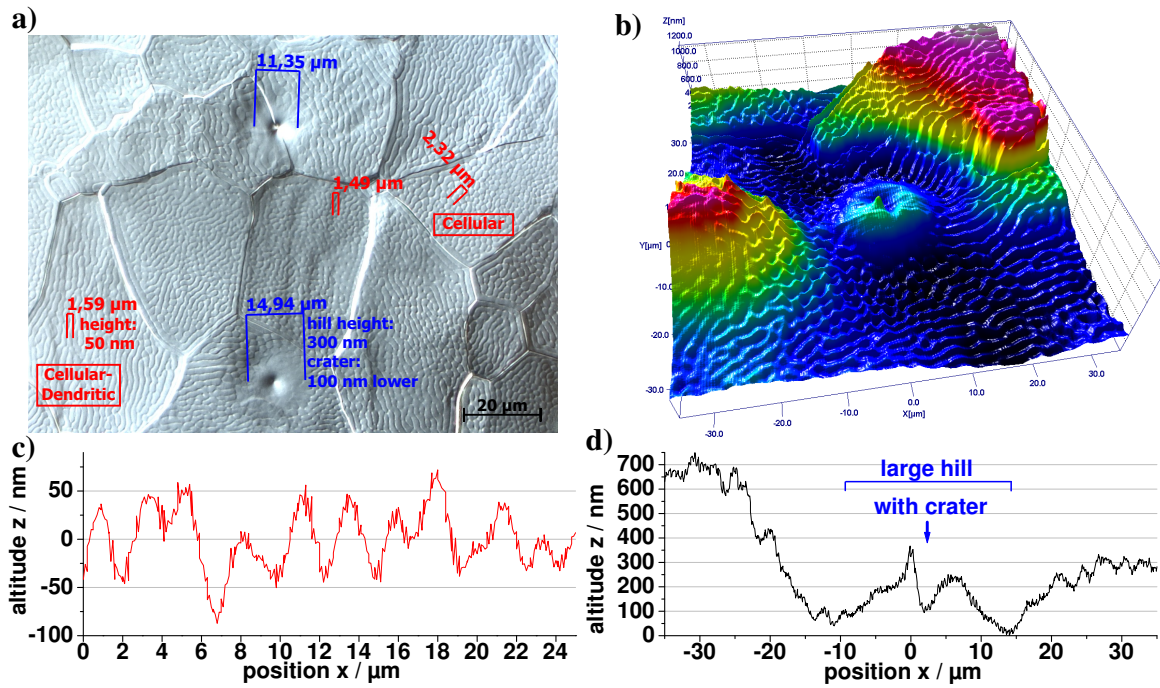
Close microscopic inspection of the surface of a melt spot summarise the three zones discussed so far (cf. figure 3.19): In region A the polished, flat initial surface of a typical tungsten sample can be seen outside the heated area of a laser spot. Further inside, a heated area (region B) with thermal etching due to laser heating is visible outside a sharp solid-melt border. The first ca. 300  $\mu\text{m}$  of the molten surface (region C) show vertical displacements of the resolidified grains with no special pattern within each grain. This changes inside the complete inner part of the molten spot (region D), where a characteristic sub-grain structure appears on all grains. This is due to surface stresses that occur due to the fast solidification and are therefore called Rapid Solidification Pattern (RSP). They are well known in welding [Clark88], in alloy metallurgy [Das85] and fabrication of amorphous metals [Matyja85].



**Figure 3.19.:** Edge of a laser melting spot of  $\varnothing 2$  mm,  $1.5 \text{ GW/m}^2$  absorbed intensity for 3 ms after one laser pulse on polished Goodfellow W; optical microscopy with DIC contrast

The RSP microstructure can hardly be seen with normal bright light microscopy, but very easy with the use of the differential interference contrast (DIC). It can show even faint surface changes by splitting the light of an optical microscope in two slightly shifted images and the interferometric combination of both. In this microscopic mode the RSP structure is clearly seen (cf. figure 3.20a) as a pattern within the W grains. It has a characteristic scale of ca. 2  $\mu\text{m}$  and can be disordered forming cellular structures or can form stripes like in the region named "cellular-dendritic". Confocal profilometry scans (cf. figure 3.20c) show that these structures have only an amplitude of 50-100 nm in height. Within this structure also hills appear (marked in blue in figure a) on which the RSP pattern vanishes. For lateral sizes above ca. 10  $\mu\text{m}$  they have a crater in the centre. Figure 3.20b shows a 3D scan of the surface around such a large hill with crater (in the scan centre). The higher red regions are neighbouring grains, that are vertically displaced by ca. 1  $\mu\text{m}$  compared to the dark-blue region. A one dimensional scan across the hill in X-direction (left to right) is shown in figure 3.20d. The hill height is a few hundred nanometres, in this case 200-300 nm and has a crater of 150-250 nm depth.

The reason for the formation of the RSP pattern are surface stresses that occur due to very fast cooling rates with typically  $\frac{dT}{dt} > 10^3 \text{ K/s}$  [Giamei85, p.204]. Then the cooling is faster than the atoms can arrange in their energetically preferred positions. Therefore stresses remain, which form the RSP surface pattern. The necessary cooling rate for this process depends on the material. The cooling rates in the first cooling phase (cf. figure 2.18 on page 55) here, are  $1 \cdot 10^6 \text{ K/s}$  and during solidification  $10^6 \text{ K/s}$ , which are obviously high enough for tungsten, although the necessary threshold is unknown. Due to the rapid cooling, the melt is undercooled and the effects are stronger, the larger the undercooling. From the temperature measurements done here, a significant undercooling of 500 K was deduced in the previous chapter. These thermal aspects and comparison of the observed sub-grain pattern with RSP patterns in the literature strongly indicate that rapid solidification is the reason for this phenomenon.

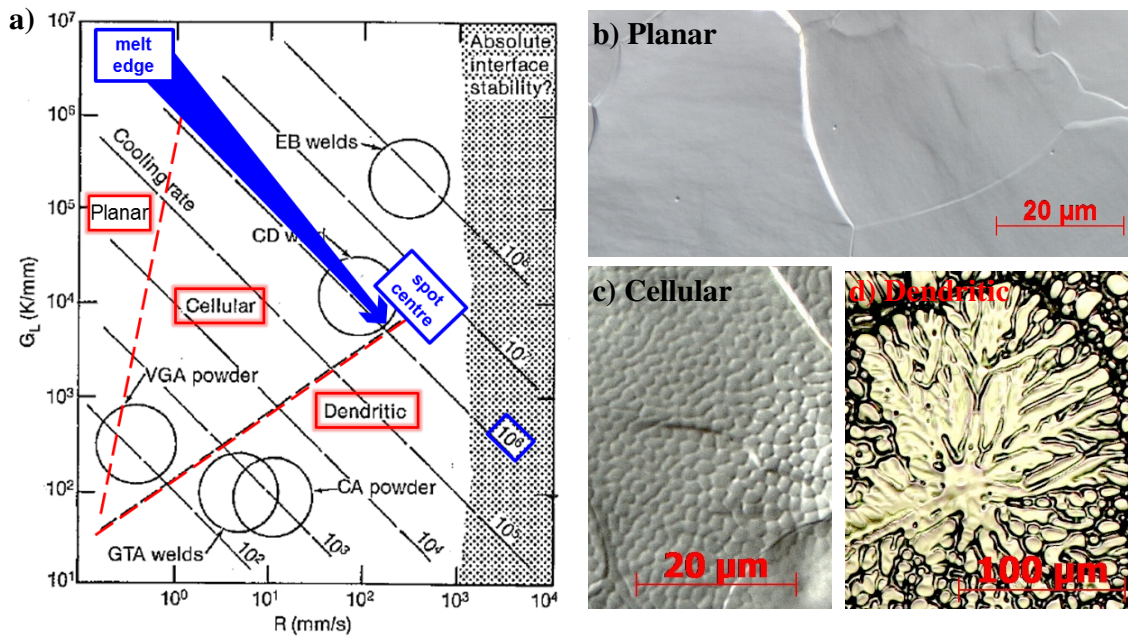


**Figure 3.20.:** a) RSP microstructure in molten tungsten (optical microscopy with DIC filter); b) 3D surface profile of area around a large hill; c) line profiles of RSP microstructure; d) line profile across large hill in b); (b-d: optical confocal profilometry)

The classification of RSP structures begins with planar surfaces, then cellular, cellular-dendritic and finally dendritic structures [Giamei85, p.205]. Examples are shown in figure 3.21b-d. Which pattern appears, depends on the temperature gradient  $G_L$  at the melt-solid transition during solidification and the velocity  $R$  of the solidification front (cf. figure 3.21a). These values are strongly related to the cooling rate by

$$\frac{dT}{dt} = R G_L \quad . \quad (3.2)$$

This is visualised in figure a by the diagonal lines, where the line labeled with  $10^6$  represents the cooling rate after laser melting here. Although the values in the figure are valid for stainless steel, the qualitative behaviour is plausible for tungsten, too, as described in the following. The cellular and cellular-dendritic structures observed in the centre of the laser melt spots imply that the cooling procedure takes place at the border of the cellular and dendritic regime. Most probably the solidification process starts at the melt edge, where the temperatures should decrease first due to the surrounding cold material. Moreover the temperature in the centre is probably higher than at the spot edge also during melting. Thus the solidification process should end in the spot centre. At this time, in the last phase of solidification, the cooling rate is  $10^6$  K/s as mentioned above. The spot centre is located in the diagram where the corresponding diagonal line in figure 3.21a intersects the border between the cellular and dendritic regions (marked by the arrow). The edge of the molten spot has a planar appearance and should be located in the upper left of the diagram at even higher cooling rates, which have been measured in the onset of cooling. This localisation of the melt edge and centre means that the temperature gradient at the spot edge is larger than at the centre at the time of solidification. This is plausible, because the gradients at the border are always larger than in the centre. Moreover the velocity of the solidification front would be slower at the edge than in the centre. This can be understood as well, because the temperature decrease stagnates in the second



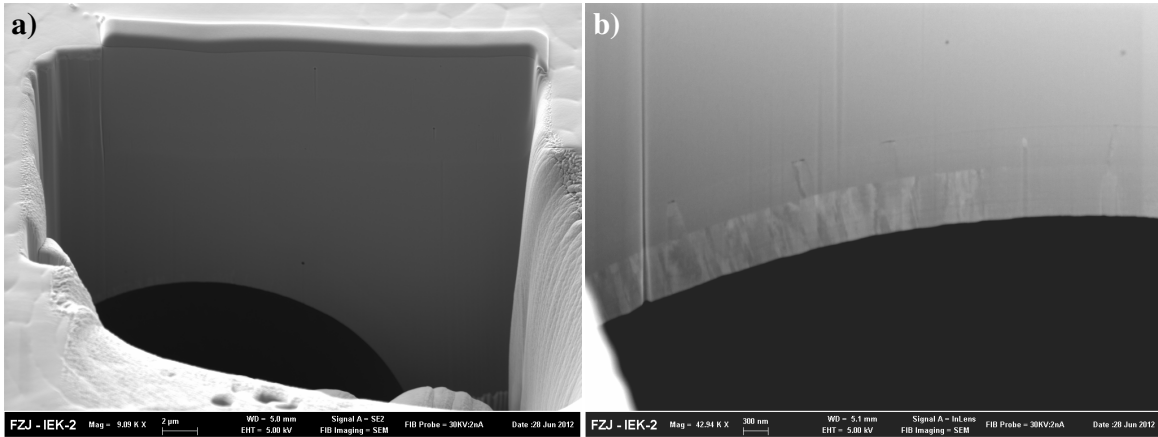
**Figure 3.21.:** a) Different RSP microstructures can form depending on:  $G_L$  = temperature gradient at solidification front,  $R$  = velocity of solidification front; combined information from [Clark88, p.15] and [Giamei85, p.205]; b-d) examples of these structures from the present work

cooling phase (cf. light blue are in figure 2.18) where solidification begins. The heat of fusion, which had to be applied additionally for melting, is released during solidification and thus retards solidification. The total amount of this heat for one laser melt spot is considerable: With a melt diameter of 1.6 mm and a depth of 40  $\mu\text{m}$ , a melt volume of  $8 \cdot 10^{-11} \text{ m}^3$  results, corresponding to a mass of  $1.5 \cdot 10^{-6} \text{ kg}$ . With the specific heat of fusion for W of 192 kJ/kg a total energy of 0.3 J is released by solidification, which corresponds to a temperature difference of  $\Delta T = 1300 \text{ K}$  assuming the same volume. The real temperature effect is much smaller, since this heat is distributed over a much larger volume due to heat conduction. To estimate a more realistic value, it is assumed that the released heat is applied on the melt surface of 1.6 mm diameter within a duration of 0.4 ms. This duration is the duration of the second cooling phase, which is the phase with increasing cooling rate (cf. light blue are in figure 2.18). With this assumptions  $\Delta T = 477 \text{ K}$  results, which is a more realistic temperature effect due to the release of the heat of fusion.

The amount of released heat is larger at the beginning of solidification, because the material volume in the spot edge, where solidification starts, is larger than in the centre due to the circular geometry. Therefore it is plausible, that the solidification rate at the edge is retarded more than in the centre and is thus lower than in the centre. The RSP pattern on the melt and its disappearance in the melt edge can be qualitatively explained in this way.

An explanation of the hill structures, which are about one order of magnitude larger and on which this pattern vanishes, has not been found in literature. But their size and their appearance lead to the hypothesis, that they are related to the bubbles at the melt-solid interface. They occur in different sizes but have a similar maximal sizes. Unfortunately the hills cannot be seen in the metallographic cross-sections, because the small hill altitude of a few hundred nanometres obviously cannot survive the cross sectioning. Therefore a more delicate way of cross-sectioning was applied using a focussed ion beam (FIB) to create a rectangular crater of 10-20  $\mu\text{m}$  under the SEM. With this technique a very clean cut can be made and surface struc-

tures are preserved especially when a protective layer (here Pt) is deposited before sputtering. Such a FIB cut with protective Pt layer has been done across a large hill with central crater (cf. figure 3.22a). On the top surface the cellular RSP pattern can be seen and the protective Pt



**Figure 3.22.:** FIB cross-section of a surface hill with crater after laser melting of W with  $1.3 \text{ GW/m}^2$ , 3 ms,  $6^\circ$  incidence; a) large bubble in  $13 \mu\text{m}$  depth below the surface hill; b) magnification of the bubble shell of the image a)

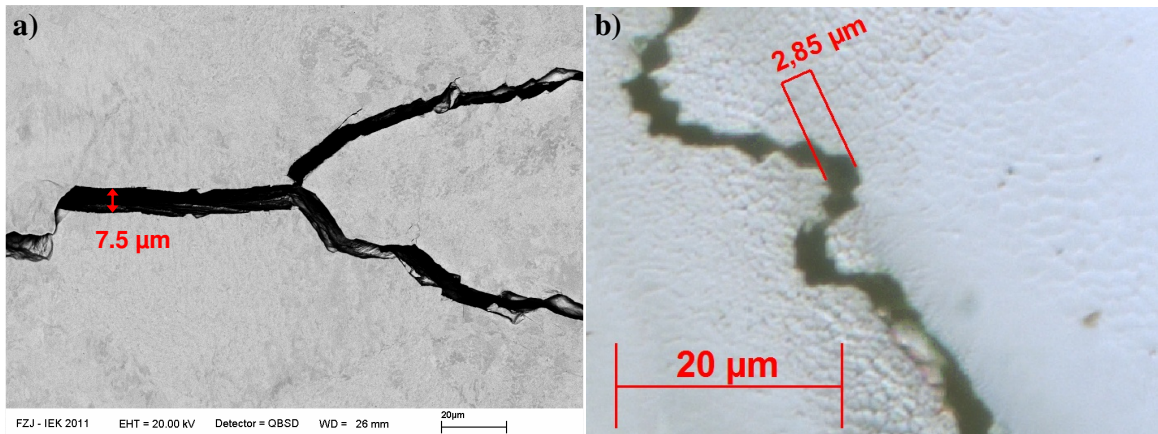
layer. Vertical lines, which appear especially in the unprotected left side and below the pores are artefacts of the FIB process, which will be explained in more detail in the next section. The horizontal line that separates the slightly brighter upper part from the slightly darker lower part of the inner crater wall is only an artefact as well. The image shows the surface hill with its central crater, already known from the surface profilometry. Here it appears very flat, since the z-axis is not exaggerated like in the profilometry, but it has also a height of ca. 300 nm with a crater of about 180 nm depth. The crater and thus the centre of the hill, is located exactly above a huge bubble, which starts  $13 \mu\text{m}$  below the surface. In few other positions similar cuts were done and below all large hills with craters, large voids have been found. Beneath small surface hills without a central crater no bubble could be found until a depth of  $15 \mu\text{m}$ . However, they are assumed to belong to smaller bubbles, which are located much deeper as described above. It is thus very probable that the surface hills are caused by the bubbles at the melt-solid interface. During solidification they seem to bend the surface, which forms the hill and flattens the surface waves of the RSP pattern that are trying to form. The explanation for the craters in the hills is more difficult. They could be formed because on large hills the surface forces that cause the RSP pattern finally overbalance the bending force from the bubble. Or during bubble growth, compression waves are emitted from the void and cause an oscillation of the surface similar to waves caused by a stone in a lake. These oscillations could then be frozen during solidification in a moment when the surface moves downwards again. However, these are only speculations.

A more important observation on the FIB cross-sections is that the RSP pattern is only present at the surface. Even with large SEM magnification no structure is visible, that would extend into the depth of the material. This excludes the hypothesis of epitaxial growth of the melt on the underlying solid, because in this case a structure starting at the bottom of the solid, reaching to the surface would be expected. Such epitaxial structures e.g. appear in laser melting of Ti-40W alloys [Baeslack86, p.105f] where the RSP pattern is seen throughout the whole melt.

A severe material modification, that is not only restricted to the surface, is the formation of cracks. They were not observed very often after LID or LIM pulses, since they are fatigue

### 3. Surface Modifications due to Laser Heating

cracks and thus rather appear after many heating cycles on the same position. But often several cracks run through the whole laser spot and form many junctions (cf. figure 3.23 left) resulting in a crack network, where practically all cracks are connected to each other. On the other hand,



**Figure 3.23.:** a) SEM image of a surface crack, 100 heating pulses,  $760 \text{ MW/m}^2$ , 1 ms per pulse; ultra high purity W from Plansee, unannealed  
b) surface crack after one melting pulse (optical microscopy),  $1.3 \text{ GW/m}^2$ , 3 ms, W from MG Sanders with elongated grains perpendicular to the surface, annealed, exposed to D plasma in PSI-2 (cf. chapter 6.2)

sometimes shorter local cracks are observed that are only present in a part of the laser spot and therefore mostly isolated from each other. A third kind of cracks was also found around LIM spots, which was running in bows around the spot often forming a semicircle. Large parts of this circular cracks were already outside the laser irradiated area. In some cases the formation of this circular cracks occurred not directly after laser melting, but when the material was cut close to the laser spot. It can be concluded that the melt spots cause permanent material stresses that are not always released immediately and totally by the formation of cracks.

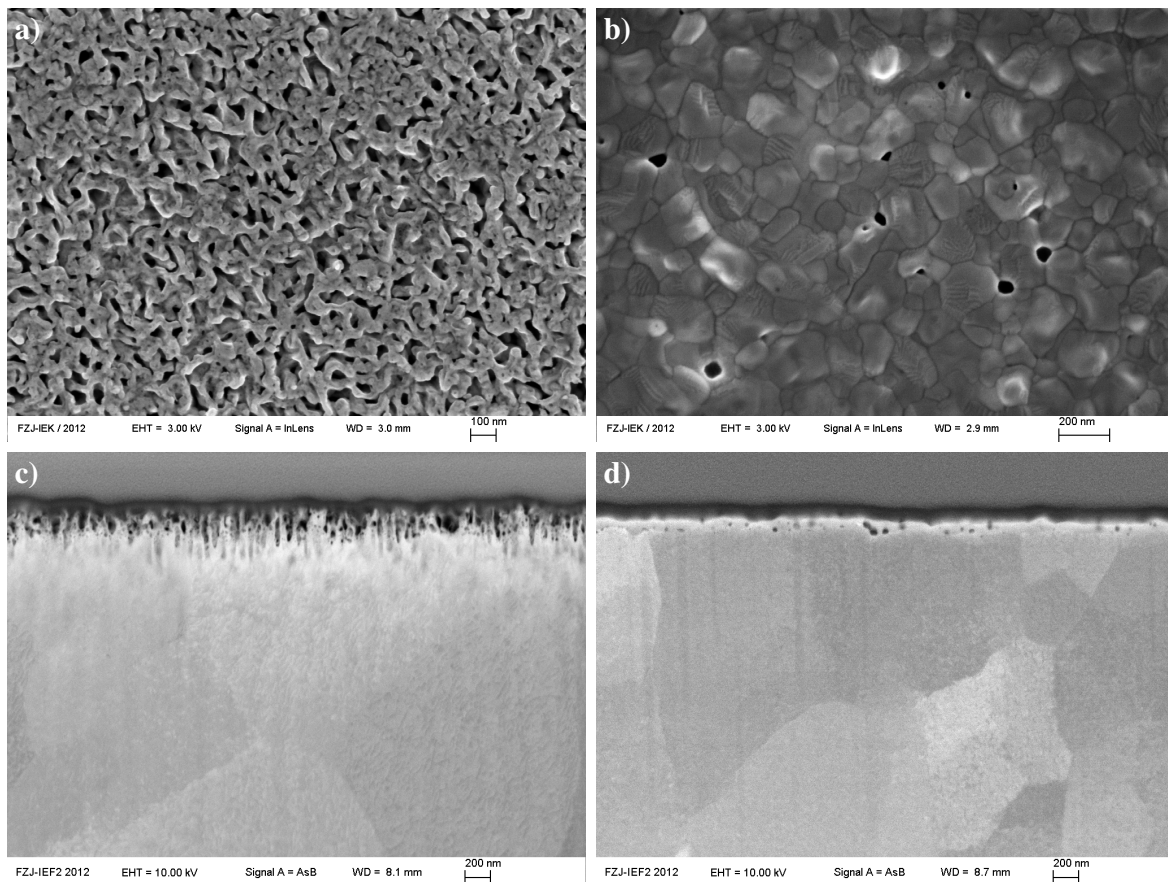
A systematic study of the crack pattern below the melting threshold was done on the ultra high purity tungsten for four different laser intensities up to  $1.5 \text{ GW/m}^2$  with 100 pulses of 1 ms duration [Wirtz12, p.79][Wirtz13]. Crack widths of up to  $10 \mu\text{m}$  were found and depths of up to 0.5 mm. After laser melting on the same tungsten grade, even deeper cracks of 0.8 mm were found (cf. figure 3.18b) after a single laser pulse. The long crack on the left side is located just outside the molten area, while the crack on the other side of the spot is at the end of the laser spot. A cross-section after 10 melting pulses showed similarly deep cracks in the centre of the laser spot and again one crack on each side of the spot even further outside the irradiated area.

The cracks are due to plastic deformations of the material during heating causing stresses during cool down which are larger than the strength of the material. The material properties differ for different W grades and therefore crack formation is different. On some grades cracks appear in every melt spot even after one pulse, while on others hardly any cracks occur. For example on the material shown in figure 3.18a ten cross-sections after different amounts of laser pulses were done and none of them shows a crack. Only the spot with 100 pulses shows a very shallow crack outside the spot, that runs parallel to the surface in  $20 \mu\text{m}$  depth. However, a spot with 50 pulses with the same settings on the same sample exhibits strong cracking on the surface, which even extends to areas outside the irradiated area. For this material the laser induced stresses seem to be slightly below the cracking threshold and thus only rarely cracks appear. This happens then probably in regions, where the material is weaker. Cracks were found on polished and rough surfaces and also the absence of cracks occurred on both after similar laser pulses.

### 3.4. Tungsten Fuzz

Under certain plasma exposure conditions and sample temperatures, impacting He ions can transform bulk W material into a sponge-like W structure called W fuzz. The presence of He in the plasma is the inevitable result of the fusion reaction or deliberately introduced He for plasma diagnostic, radiation cooling, disruption mitigation etc. The resulting nono-structure consists of "amorphous nanorods" [Baldwin8] with very high porosity. This can result in dust formation, arcing, enhanced erosion or hydrogen retention [Ueda11]. Here, the effect of laser heating on W fuzz during LID is analysed. The details of the production of the W fuzz used here, are given in chapter 6.3, where the effect of the fuzz structure on the hydrogen retention is discussed and further details of the experiment are described.

After exposure of the W fuzz under erosion dominated conditions in the TEXTOR plasma, its high porosity can still be seen on SEM images of the surface (cf. figure 3.24a) as dark areas. The rod-like structure is visible in the FIB cross-sections (cf. figure 3.24c), where the dark areas inbetween the bright W filaments shows the high porosity. The thin dark grey continuous layer above the fuzz and the larger light grey area at the top of the image do not belong to the sample itself. They belong to a platinum layer that is deposited onto the surface as a protection in the area where the focussed ion beam then sputters the W material to generate the cross-section.



**Figure 3.24.:** SEM images of W fuzz after TEXTOR exposure (left) and after one standard LID heating pulse (right); a, b) top view, a) and b) are in the same scale; c, d) FIB cross-section, c) and d) are in the same scale but different to a) and b)

The fuzz structure is very similar to unexposed W fuzz as shown e.g. in [Ueda11]. Only the thickness of the fuzz has been reduced due to erosion by the TEXTOR plasma to ca. 200 nm

(from initially 500-600 nm) as can be seen in the cross-section. The images on the right side show areas on the same sample after a single LID pulse (3 ms, 500 MW/m<sup>2</sup> absorbed laser intensity). The maximum temperature during this laser pulse was 2060 K as measured with a point pyrometer. The laser heating leads to a collapse of the W nanorods and thus a flattening of the fuzz layer to a 50-100 nm thin layer (white layer in figure d). The fuzz structure has disappeared and the porosity has been reduced strongly but is still present with pores up to 50 nm in size. Except of these pores the remaining layer appears rather homogeneous unlike the inhomogeneous fuzz structure. There is a clear interface between the new flat layer and the W bulk, which was not visible between fuzz and bulk. The darker vertical lines that appear below some of the pores in the cross-section, are an artefact of the FIB cutting procedure. The ion beam sputters deeper into the material below the pores, because it continues sputtering directly at the rear side of the pore when entering the pore. Therefore the sputtering front is ahead by the thickness of the pore compared to positions without a pore. This effect appears as vertical lines.

Below the new flat surface layer the W bulk begins with micrometre large areas of different grey intensity, which are grains or sub-grains. The pores are visible much better in the top view (figure b) due to the higher magnification. They are probably identical to the pores seen in the cross-section, since they are similar in size. The flattened nanorods do not show the spiky fuzz structure after heating, but generate a pattern similar to a usual grain boundary pattern of unexposed tungsten. However, these cannot be the W grains of the bulk or an imprint of the bulk W grains from below, since they are on average 100-200 nm in size and 50-100 nm thick and thus much smaller than the grain size. They rather appear similar to ice floes on freezing water and thus can be called "W floes".

The mechanism that causes the flattening of the fuzz is unclear. It can be speculated that the high temperatures of around 2000 K destabilise the static forces inside the nanorods. The weakened nanorods can deform and tend to transform into an energetically favourable structure probably by plastic deformation. The pores probably appear in positions, where the distance between nanorods was already large in the fuzz. The large distance cannot be closed by the flattened nanorods and remains a pore. This explanation for the pores is based on the observation that they are located predominantly at the borders of the W floes and not inside of them.

A further feature can be seen in the top view. On some of the W floes, areas with regular parallel lines or "waves" are present with a characteristic wavelength of ca. 20 nm. The reason for this effect is not known, but it seems to be a surface stress phenomena of a similar nature like the rapid solidification pattern after melting (cf. the previous section). It is improbable that these waves hint at melting, because they do not appear on the whole surface. They might occur in areas where too much material from the nanorods expands during flattening. The material from different nanorods presses against each other, surface tensions occur and some material is squeezed forming a wavy surface.

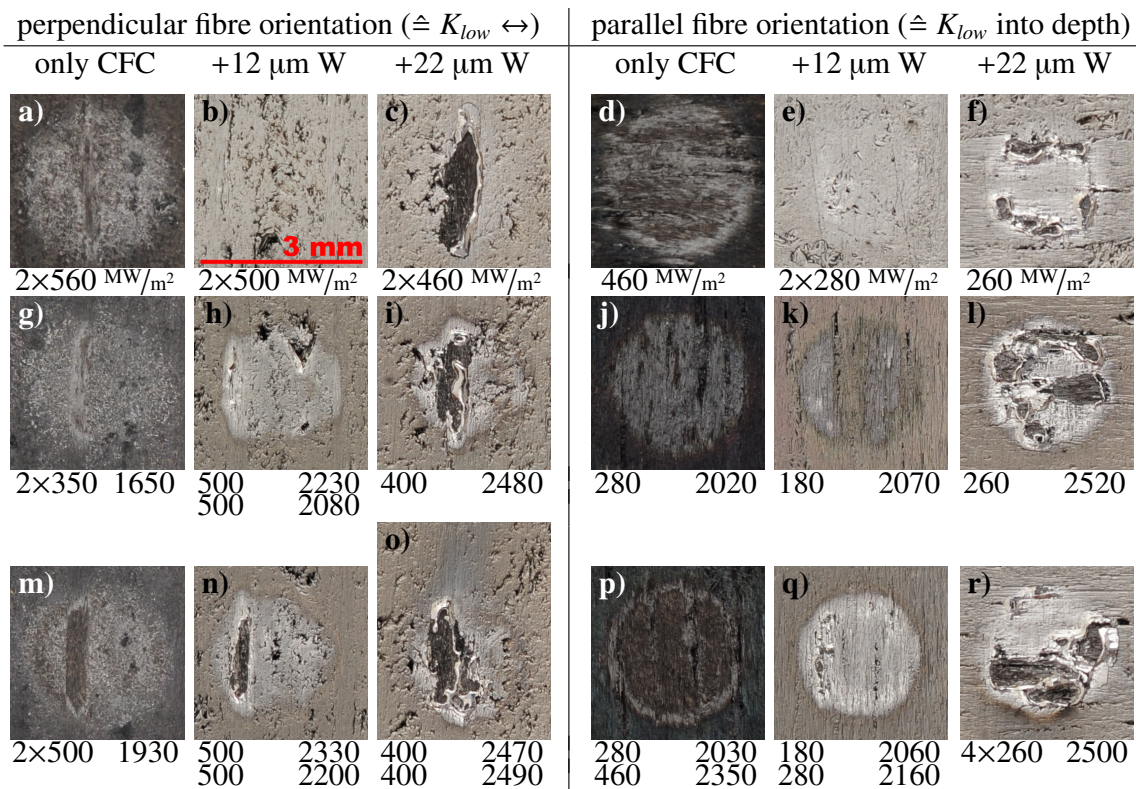
Cross-sections have also been done after two LID pulses on one position. No differences to the situation after one laser pulse was found. In conclusion, a single laser heating pulse destroys a W fuzz structure and a layer of flat tungsten floes with a thickness of less than half of the fuzz thickness remains, which still shows minor porosity.

## 3.5. Tungsten Coatings

The surface modifications due to the laser heating of anisotropic CFC material with and without a W coating will be discussed. The CFC samples with W coating of the ITER-like wall have been introduced in the discussion of reflectivity (cf. page 44) and with respect to



their structural and thermal properties in chapter 2.4.2 on page 55. Six different samples of this kind were investigated by LID-QMS (six columns in figure 3.25): three different layer types on two different CFC fibre orientations. The layer types were the CFC substrate (DMS780) alone, CFC with ca. 12  $\mu\text{m}$  W layer and CFC with ca. 22  $\mu\text{m}$  W layer. Between the CFC substrate and W layer a ca. 2.5  $\mu\text{m}$  thick Mo interlayer was applied. Each layer type was available in the perpendicular and parallel fibre orientation, where the direction of low heat conductivity  $K_{low}$  is either directed along the surface (horizontal in figure 3.25) or into the depth, respectively. After simultaneous exposure in the TEXTOR plasma, they were heated by LID laser pulses in vacuum on laser spots with 3 mm diameter and nearly normal laser beam incidence. The laser pulse duration was 3 ms. The first 1-2 cm of the samples, which were closest to the plasma, were exposed in erosion dominated conditions, where no carbon layers were formed on the W coatings. The surface of the CFC without W coating was transformed into hydrogen-implanted CFC, as hydrogen retention measurements show, leading to an amorphisation of the first nanometres of the material. The remaining part of the samples was covered by a thin a-C:H/D layer of several hundred nanometres thickness, deduced by colorimetry and the desorption characteristic (hydrocarbon fraction). The first row in the figure shows the effect of laser heating without the carbon layer, while the other two rows show surface effects with the carbon layer.



**Figure 3.25.:** LID on CFC (DMS780) after exposure in TEXTOR under erosion dominated conditions (a-f) and with 100-250 nm a-C:H/D layer (g-r); left value: absorbed laser intensity in  $\text{MW}/\text{m}^2$ ; right value: measured maximal temperature in K; the W layer is applied on a 2.5  $\mu\text{m}$  Mo interlayer; all images in identical scale

The first general effect that most often appears is a colour change of the surface, except cases like in image b), c) and e), where hardly any colour change is seen. Mostly a change to brighter colour of a light grey occurs. This is attributed to the structural changes in the a-C:H/D layer, which changes from a mostly diamond-like to graphitic structure typically in a transition range of 700-900 K [Vietzke87, p.453]. This graphitisation occurs for all surfaces

### 3. Surface Modifications due to Laser Heating

---

with an a-C:H/D layer on top and also for carbon based materials with implanted hydrogen like in the erosion dominated areas (images a, d). Under hydrogen ion impact the carbon structure is transformed into a more amorphous structure, because the impacting ions break the C-C bondings and build C:H bondings in order to be chemically integrated in the structure. This interpretation is strongly supported by laser heating of annealed but plasma unexposed graphite, where nearly no colour or brightness change can be seen. The change to light grey colour occurs until ca. 2000 K surface temperature.

Further heating increases the carbon evaporation that results in a second colour change to dark grey like in image p) and partially in image d). This is interpreted as evaporation or sublimation of the carbon layer and substrate. A proof of this interpretation can often be seen on the W coated samples with destroyed W layer. Then sometimes brown deposits are seen around the laser spot like in the lower part of image r) or in figure 3.26c). These deposits are most probably evaporated C atoms from the spot centre, that are redeposited around the spot.

A peculiar effect about the colour change is the difference in the size of the modified area. Different sizes occur, although the scale is the same in all images of the figure and the laser irradiated area was identical. The largest difference is seen between the carbon surface and the W coatings. The modified area is nearly equal to the laser irradiated area on the carbon surfaces, while it is considerably smaller on the W coatings, when spots with equal laser intensities or surface temperatures are compared (e.g. m and n, j and q). For example the diameter of the light grey spot surrounded by a brown border in image j) is 2.5 mm after one laser pulse with  $280 \text{ MW/m}^2$ . In contrast, after one pulse with  $180 \text{ MW/m}^2$  and a second pulse with  $280 \text{ MW/m}^2$  on the W coating in image q), the diameter of the brighter area is only 2.2 mm, resulting in a factor of 1.3 in the corresponding area. Even when a higher intensity was applied to the W coatings than to the C surface (e.g. g and h) this size effect occurs. The explanation for the different sizes cannot be due to different temperature distributions, since the W coated surfaces reach even higher temperatures at comparable heating intensities, but show smaller spot sizes. The radial temperature profiles are very similar for graphite and tungsten as shown in the previous chapter (cf. figure 2.14 on page 52). The anisotropic heat conductivity of the CFC also cannot be responsible for the different spot sizes, because the effect appears on both fibre orientations. Neither have the laser optics been changed between the samples.

Thus only the explanation remains, that much higher temperatures, at least 500 K more, are needed on W with a thin amorphous hydrocarbon layer to generate similar surface modifications as on a C surface. The closest agreement in spot size occurs on the thick W layer in parallel fibre orientation. For example image j) and l) have nearly identical modified areas: 2.5 vs. 2.4 mm and after 4 laser pulses (image r) the size is identical. But the surface temperatures are 500 K higher on the W layer. However, 500 K higher temperatures are not a sufficient condition for the perpendicular fibre orientation: In case i) and o) this condition is fulfilled compared to g) and m), but the spot sizes are only 2.1-2.2 mm, while on CFC it is 2.6-2.7 mm (both measured horizontally). For the perpendicular fibre orientation obviously a higher temperature difference is needed for the same apparent spot size as on CFC, while 500 K are nearly sufficient for the parallel fibre orientation.

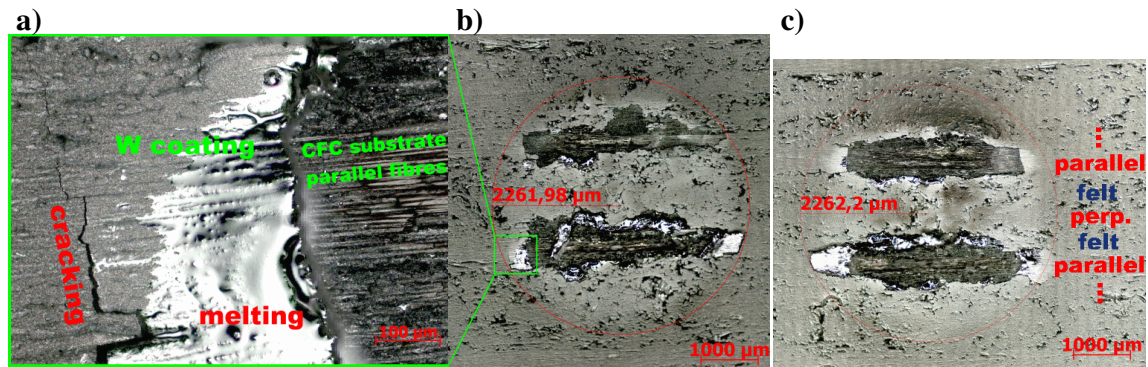
The following two assumptions concerning the temperature measurement should be kept in mind during this discussion. The values for the absorbed laser intensity are calculated with the reflectivities measured at room temperature at 1064 nm with a spectrophotometer (cf. chapter 2.3). In particular 10% reflectivity for pure CFC without a-C:H layer, 15-20% with the layer, 44% for the thin W coating and 49% for the thick W coating are used. Accordingly, the emissivity for the temperature measurement is set to the light absorption fraction at the wavelength of the pyrometer to 90% or 80% for CFC and 20% for the W coatings. Reflexion and emissivity depend on temperature, which is disregarded in the intensity calculation and

pyrometer measurement. But an even stronger influence on the real temperature and the temperature measurement results from the local melting or delamination of the W-Mo layer. Local melting probably leads to very inhomogeneous temperature distributions inside the  $\varnothing 2$  mm pyrometer spot, which results in measured temperatures higher than the average temperature in this area. The removal of the W-Mo layer strongly decreases the reflexion and thus a higher laser intensity is absorbed in these parts of the spot than expected. Thus the real temperature in the uncovered area is higher than on the W coating. At the same time the emissivity strongly increases according to the values above, because locally the carbon substrate is visible. This leads to an overestimation of the temperature by the pyrometric measurement, since it still assumes the low emissivity. Both effects lead to increased temperature values in the measurement, which are partly real due to the higher absorption and partly just an overestimation due to unadapted emissivity settings.

Due to the colour change, the anisotropy of the CFC heat conductivity can be demonstrated, especially for the thin W-Mo layer (images h and n). The low heat conductivity is oriented in horizontal direction and a strong elongation of the brighter area is observed in the same direction. This unexpected correlation can be explained with the above observation, that on the W surface much higher temperatures are needed to cause a brightness change than on the C surface. Together with the anisotropic temperature distribution that has been calculated and discussed in the previous chapter (cf. figure 2.20 on page 57) the effect can be explained. The high temperature isotherms (about ca. 1500 K) are elongated in the direction of the low heat conductivity, in contrast to the low temperature isotherms. Since the high temperatures are responsible for the colour change, the modified area has to be elongated in the same direction.

Beside colour changes, more severe surface modifications occur like delamination and melting of the W-Mo layer. These damages are much more severe on the thick W-Mo layer than on the thin layer, even for smaller laser intensities and independent of fibre orientation or the presence of the a-C:H/D layer. It has to be concluded that the W layer thickness strongly reduces the damage threshold. It is unclear whether the reason for this weakness is a thermal or mechanical effect. A thermal effect could lead to much higher temperatures and as a consequence to melting and delamination. Otherwise, mechanical weakness, e.g. mechanical stresses in the W layer that lead to an easy detachment from the substrate, could cause strong heating of the layer until melting. The temperature on both layer thicknesses develops synchronously until roughly 1.5 ms with typically ca. 100 K higher temperatures for the thick W layer. In the second half of the laser pulse this difference increases because the temperature on the thick layer increases monotonously, while on the thin W layer it saturates or slightly decreases. The 100 K offset indicates a lower heat conductivity of the thicker layer, which is unexpected, since the heat contact in the transitions of W-Mo and Mo-CFC should be independent of the W layer thickness. On the other hand, in some temperature developments on the thicker layer sudden temperature jumps are observed, which hint at sudden mechanical layer detachment. Thus both effect seem to be responsible for the delamination and melting of the thick W layer.

When the damage threshold is exceeded, three surface modifications can occur: cracking, melting and delamination of the W-Mo layer (cf. figure 3.26). Virtually always delamination and local layer removal is observed, while cracking and significant melting do not always occur. This already indicates that melting and cracking are a consequence of delamination. This is supported by the observation, that the molten areas are always located around the removed areas. This is also proved by a few cases, in which the delaminated W layer was not completely detached from the surface, but was still in contact in one position (cf. figure 3.27a). Here the W layer was delaminated and folded in such a way, that it was situated outside the laser irradiated area during the laser pulse. Therefore it did not melt, as it would have occurred with persistent laser heating.



**Figure 3.26.:** Laser heating of a 25  $\mu\text{m}$  thick W-Mo-W-Mo double layer on CFC (DMS780) with 100 pulses of  $610 \text{ MW}/\text{m}^2$ , 1 ms, 0.5 Hz,  $16 \text{ mm}^2$  laser irradiated area (red circle);  $2^\circ$  incidence; perpendicular fibre orientation  $K_{low} \downarrow$ ; optical bright field microscopy of the surface

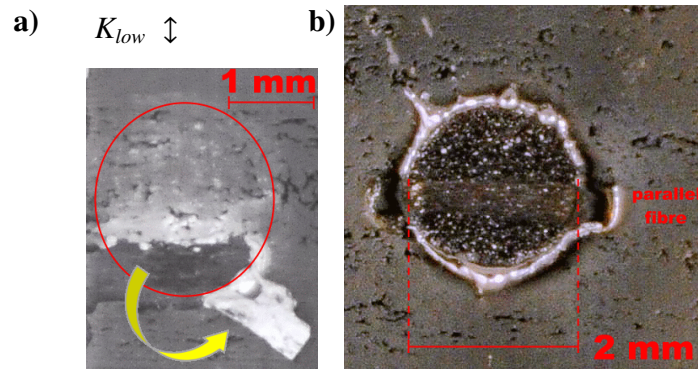
These damage mechanisms are distributed randomly within the laser spot (e.g. images 3.25f, l, r) in case of isotropic heat conductivity in the surface plane, i.e. in case of the parallel fibre orientation. In contrast, for perpendicular fibre orientation, the damage always starts at the position, where the fibres run parallel to the surface (cf. figure 3.25c, i, n, o and 3.26). This was also observed with other heat sources like electron beams [Thomser12], hence it is not a laser specific effect. The preference for the parallel fibre is explained in the literature by two effects: While the CFC fibres have a high heat conductivity in the axial direction along the fibre, it is very low in the radial direction across the fibre. Thus the surface temperature on a fibre, that runs parallel to the surface, is much higher due to reduced heat diffusion into the depth.

Secondly, the coefficient of thermal expansion was also used as an explanation for delamination, because of the mismatches of the expansion for W and parts of the CFC. While the coefficients for W and the felt layer are similar (ca.  $5 \cdot 10^{-6}/\text{K}$ ), and only a factor of 2 higher for the radial fibre direction, there is a huge mismatch for the axial direction. Along the fibre the coefficient is a factor of 50 lower than for W. Therefore the W layer expands 50 times stronger than the parallel fibre, which leads to mechanical stresses and finally delamination of the coating.

This damage preference on the parallel fibre is especially impressive in figure 3.26 on a sample with the same substrate, but where the thinner W-Mo coating was applied twice. Thus a W-Mo-W-Mo double layer covers the CFC. The laser irradiated area has been increased to  $16 \text{ mm}^2$  by increasing the distance of the laser fibre and imaging lens to the target. In contrast to the smaller laser spots shown above, now the laser spot comprises two parallel fibres (cf. annotations in figure 3.26c) instead of only one. On the other hand, also a reduction of the spot size to  $\varnothing 2.0 \text{ mm}$  has been done to increase the absorbed laser intensity to a maximum of ca.  $2.2 \text{ GW}/\text{m}^2$  (cf. figure 3.27b).

In this extreme case the coating is completely removed from the laser irradiated area and a circle of molten W and Mo is formed at the laser spot edge. Additionally, the evaporated metals are redeposited around the spot (grey-blue layer) already at lower laser intensities. But moreover, expulsion of molten metal in splashes and droplets is visible around the laser spot. The high heat conductivity of the parallel CFC fibre is shown here by repulsion of the melt much further outside the laser spot along the fibre.

Without the W coating, also strong surface damage by C evaporation occurs on the parallel fibre (images 3.25a, g, m). Here, also an expansion mismatches can be the reason due to the different expansion coefficients of the CFC components. However, also a thermal reason



**Figure 3.27.:** CFC (DMS780) with 25  $\mu\text{m}$  W-Mo-W-Mo double layer after deuterium plasma exposure in Pilot-PSI and LID-QMS, 3 ms laser pulse duration,  $22^\circ$  incidence; a)  $500 \text{ MW/m}^2$  on  $\varnothing 2 \text{ mm}$ ; b)  $500 \text{ MW/m}^2$  on  $\varnothing 3 \text{ mm}$  and  $2.2 \text{ GW/m}^2$  on  $\varnothing 2 \text{ mm}$

due to overheating of the fibres parallel to the surface is possible as it has a very low heat conductivity across the fibre. This observation and the above mentioned case of delamination without melting show that both effects – expansion mismatch and local overheating – can occur. In most cases both appear during laser heating above the damage threshold and lead to the described surface modifications: evaporation, redeposition, delamination, cracking and melting.

## 4. Desorption Mechanism of Hydrogen

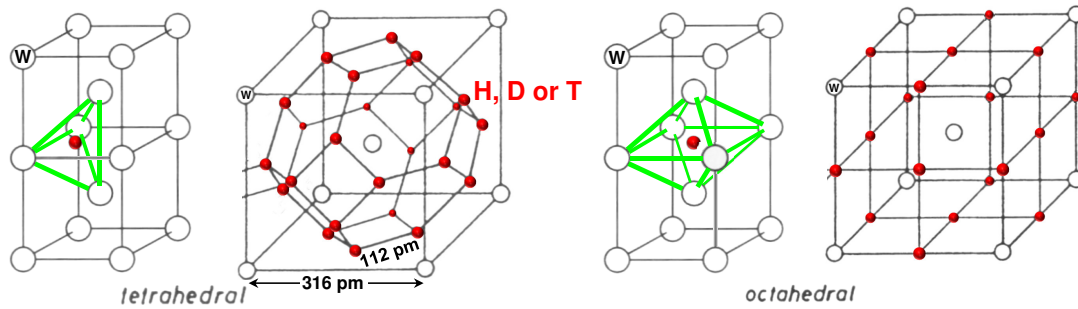
In order to use laser induced desorption as a quantitative method for hydrogen retention, "it is of fundamental interest to qualify and understand the desorption process during" laser heating [Z13]. In this chapter, the differences of desorption of hydrogen from tungsten and carbon based materials will be shown. In both materials, the thermal activation due to the heating by the laser is the origin of the desorption process. But the following transport of the hydrogen in the material is then qualitatively different. This has strong consequences for the desorption fraction – the ratio of desorbed to initially retained hydrogen amount. For carbon materials, the fraction is always close to 90-100%. For tungsten, the desorption fraction can be very low in some cases, which will be discussed and simulated numerically. The implications for tungsten are so strong, that the application of LID on W has to be extended to laser induced melting (LIM) due to the findings of this chapter. Experimental evidence and examples of the mechanisms described here, will shown in chapter 6.2 after the measurement procedure has been described in chapter 5.

### 4.1. Desorption from Tungsten

"Release of fuel from bulk W is based on diffusion, trapping and possible release by recombination of atoms on the W surface [Causey2]"[Z13]. The transport of hydrogen in W is determined by fast diffusion from one interstitial site (cf. figure 4.1) to the next and strong trapping in lattice defects, which hamper the transport. As a consequence, the rate of the transport is determined by the trap density and trap energy while the interstitial transport from one trap to the next is not rate determining. The general behaviour is a result of the low solubility of hydrogen in tungsten and will be described here in further detail.

If the tungsten lattice is undamaged, i.e. no vacancies, bubbles or voids exist, hydrogen (protium, deuterium or tritium) can only exist in atomic form inside the perfect W crystal. Thus a molecule has to dissociate, before it can be absorbed by an intact W lattice (cf. figure 4.1). Inside the material the W atoms repel the hydrogen atoms, thus the hydrogen experiences a three dimensional potential. Because it tends to minimise its energy, the hydrogen atoms occupy only certain places inside the bcc structured W lattice. In a perfect lattice these position are called interstitial sites, or shortly interstitials. There are two arrangements of interstitial sites for H in bcc metals reported in literature [Heitjans5, p.115f], namely the tetrahedral and octahedral sites (cf. figure 4.1).

In the tetrahedral arrangement the hydrogen atom is located in the centre of a tetrahedron consisting of 4 W atoms at its corners with a distance of 177 pm to each of the W atoms. In the unit cell of the W crystal the hydrogen interstitial sites are located in four positions on each of the six sides of the cube. Each interstitial site has 4 nearest neighbour sites with a distance of 112 pm. One unit cell of the W lattice contains 12 interstitial sites, because only half of each hydrogen atom is within the unit cell and there are 4 sites on each of the 6 cube sides. If they are fully occupied, interstitial saturation is reached with a hydrogen concentration of  $3.8 \cdot 10^{29} \text{ H/m}^3$ .



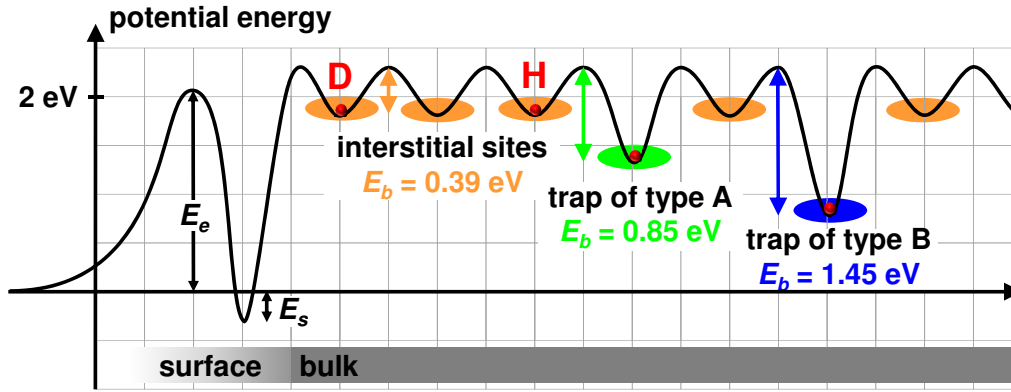
**Figure 4.1.:** Tetrahedral and octahedral interstitial sites for hydrogen in a bcc crystal like tungsten; adapted from [Heitjans5, p.23,116]

The octahedral sites are located in the centre of an octahedron of 6 W atoms with 158 pm and 223 pm distance to the W atoms of the octahedron. The interstitial sites have also 4 nearest neighbours, but at larger distance (158 pm) than in the tetrahedral case. One unit cell contains 6 interstitial sites: one interstitial site in the middle of each cube side, which contributes one half site and the remaining 12 sites located at the edges of the cube lie only with one quarter within the unit cell. Thus a full occupation in the octahedral arrangement yields half of the hydrogen concentration of the tetrahedral arrangement.

It might be speculated that for low hydrogen concentrations the octahedral positions are preferred and for increasing hydrogen concentrations a rearrangement into the more dense tetrahedral scheme occurs. It is reported, that ion-channeling experiments and recent first-principles calculations with ultrasoft pseudopotentials support the preference for tetrahedral sites of H in W [Johnson10, p.316].

The potential to which the hydrogen atom is exposed can be depicted along a one dimensional path (figure 4.2). Here the potential energy of the hydrogen outside the W lattice, i.e. in the vacuum or thin plasma is defined as zero energy. The first energy barrier at the surface of the material can have different heights depending on the grain orientation, but is usually around 2 eV as calculations by density-functional theory show [Johnson10]. For hydrogen that enters the material, i.e. for the inward direction, this barrier energy  $E_e$  is needed to reach the surface binding state, the first minimum of the potential. In the outward direction, this barrier must be overcome by the hydrogen to be released from the surface. In this direction, more energy is needed, because additionally the surface binding energy  $E_s$  has to be overcome. When a hydrogen atom is located in this first energy minimum, it is adsorbed at the material surface, where it can also find a partner to recombine into a molecule. When it moves further inward, it can only exist in atomic form, except in large voids or bubbles, where it can also be in molecular form. To reach the interstitial sites it has to overcome a second barrier which again has different heights depending on grain orientation and the actual path of the hydrogen atom. In W typically the second barrier is 0.1-0.4 eV higher than the first. This second step is called surface-to-subsurface diffusion, after which the hydrogen atom has finally reached the material bulk. The whole process of entering the bulk is endothermic for tungsten.

The hydrogen atoms sit on the interstitial sites and oscillate with a frequency at the order of  $10^{13}$  Hz in the potential minima. This frequency is called bounce frequency or test frequency and is determined by the local binding forces and the mass of the oscillating atom. The diffusion of hydrogen in W is realised by a random walk of the hydrogen atom by jumps of the distance  $d_{jump}$  from one interstitial site to a nearby site. The energy that is needed for one jump equals the amplitude of the potential energy between the two sites, which is called diffusion activation energy or binding energy  $E_b$  of the interstitial sites. The energy needed to overcome the binding potential comes from the temperature of the material, i.e. from phonons of the lattice vibration. The higher the temperature, the higher the thermal fluctuations and the more



**Figure 4.2.:** Sketch of energetic potential for hydrogen in the lattice of tungsten in the presence of deeper traps with two different binding energies

probable is a jump of a hydrogen atom to the next site. For a not perfect W lattice, which is already the case for the usually used polycrystalline W, additionally deeper traps are present. They can have different higher binding energies, depending on the type of imperfection of the crystal. A multitude of trap energies can be found in the literature, that were deduced e.g. from fits to TDS measurements by numeric simulations. For the D impact energies in the ranges used in the experiments here, often two trap types are discussed [Ogorodnikova8]:

- type A: Trapping of D at the grain boundaries of tungsten and in dislocations are associated with a trap energy of  $E_b = 0.85$  eV.
- type B: Trapping of  $D_2$  agglomerations in clusters and D in vacancies is associated with a binding energy of  $E_b = 1.45$  eV.

The diffusion mechanisms obey an Arrhenius-like equation for the diffusion coefficient:

$$D = D_0 e^{-\frac{E_b}{k_B T}} \quad (\text{Arrhenius equation}) \quad (4.1)$$

$D_0$  ... diffusion constant in  $\text{m}^2/\text{s}$

$E_b$  ... binding energy of a trap site for hydrogen in eV

$k_B$  ... Boltzmann constant in  $1/\text{K}$

$T$  ... temperature in K

The hydrogen diffusion coefficient in tungsten was measured and published several times. Today the values obtained by a series of  $H_2$  loading and fast degassing of a W cylinder [Frauenfelder69] are frequently used:

$$D_F = 4.1 \cdot 10^{-7} \frac{\text{m}^2}{\text{s}} e^{-\frac{0.39 \text{ eV}}{k_B T}} \quad (\text{H diffusion coefficient in W for interstitial sites}) \quad (4.2)$$

The diffusion coefficient increases strongly (by 4 orders of magnitude) from RT up to 800 K, but increases nearly linearly with temperature above ca. 1400 K (cf. figure 4.3). A very important property that directly follows, is the diffusion length  $L_D$ , which is determined by the diffusion coefficient, thus by temperature and the time duration  $t$  for which this temperature lasts:

$$L_D = \sqrt{2 D t} \quad (\text{diffusion length}) \quad (4.3)$$



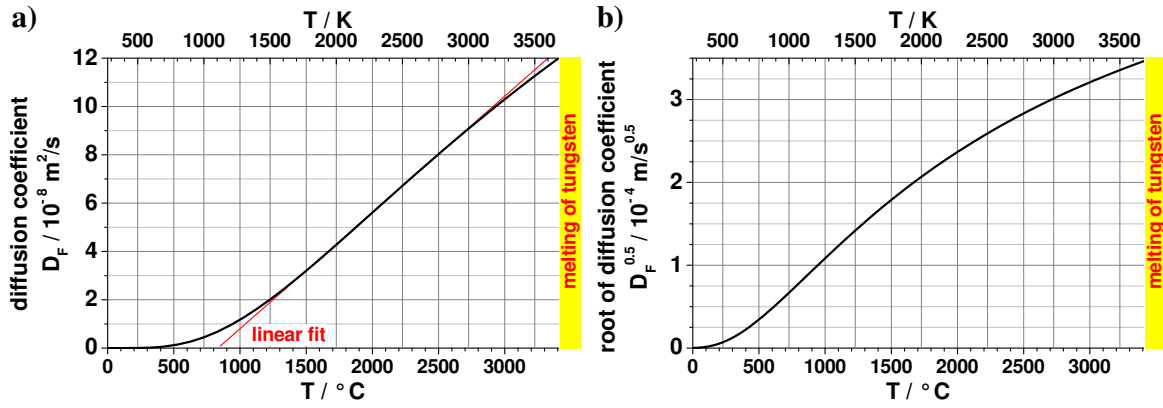


Figure 4.3.: Diffusion coefficient of hydrogen in tungsten according to [Frauenfelder69]

During plasma exposure this determines the depth that hydrogen can reach and during desorption the length the hydrogen can move. A necessary condition for complete desorption is that the diffusion length during desorption must be larger than the diffusion length during plasma exposure. For LID this means, that the temperatures during laser heating must be higher than during plasma exposure, because the duration of laser heating is usually orders of magnitude shorter than the exposure. But even if the short desorption duration is compensated by higher temperature, complete desorption is often not reached, because diffusion is omnidirectional and not only directed to the surface. This will be illustrated by diffusion simulations in the next section. Therefore a sufficient condition for complete desorption is, that the diffusion length during desorption must be larger than the size of the object, that retains the hydrogen. This is hard to achieve by temperature increase, because usually melting and even recrystallisation, which starts roughly at the half of melting temperature are undesired. The root of the diffusion coefficient only increases moderately with temperature (cf. figure 4.3b). For example the diffusion length for an exposure at 700 K can be increased by a factor of 14 maximally before melting occurs. The same extension of diffusion length can be achieved at 700 K by a desorption time that is ca. 200 times longer than the duration of plasma exposure. Since this is very time consuming, a combination of both factors is the best choice to accomplish complete desorption. This is usually done during heating of the whole sample in TDS measurements, which lasted for a minimum of 40 min in the experiments performed here. Compared to a few milliseconds during LID, the diffusion length in TDS is at least three orders of magnitude larger than in LID. Thus the hydrogen can diffuse far enough to be released fully.

Actually the hydrogen does not need to diffuse through the whole sample to all surfaces, since typically the diffusion out of the grain to the next grain boundary is the most important step. Further diffusion along the grain boundary, called grain boundary diffusion, is reported to be several orders of magnitude faster than diffusion inside the grain [Heitjans5, p.344]. Numerical calculations show that this can result in an overall effective diffusion constant of factor 5 higher than bulk diffusion alone [Toussaint11]. The effect of grain boundary diffusion becomes important, when the grain size is comparable to or smaller than the hydrogen diffusion length. This is typically not the case here, since the grains are at the order of 50-200  $\mu\text{m}$ , while the hydrogen diffusion depth due to plasma exposure is in the order of several micrometres.

For the description of the diffusion in the presence of traps, a release rate from the traps is needed. The release rate  $\alpha_r$  increases with higher temperature, approaching the bounce frequency for very high temperatures. It depends on the trap type and is therefore parametrised by the following two equations for each trap type separately.

$$\alpha_{r,A} = 10^{13} \text{ Hz } e^{-\frac{0.85 \text{ eV}}{k_B T}} \quad (4.4)$$

$$\alpha_{r,B} = 10^{13} \text{ Hz } e^{-\frac{1.45 \text{ eV}}{k_B T}} \quad (4.5)$$

The release rate can be used to calculate an effective diffusion coefficient for the diffusion only on the traps, with the approximation that the interstitial diffusion between two traps is negligible. [Johnson10, eq.5]

$$D_A = \frac{d_A^2}{6} \alpha_{r,A} \quad (4.6)$$

$$D_B = \frac{d_B^2}{6} \alpha_{r,B} \quad (4.7)$$

Here  $d_A$  is the average distances between traps of type A and  $d_B$  analogous for traps of type B. This approximation is especially true for low temperatures, where  $D_F$  is many orders of magnitude larger than  $D_B$ . Only above ca. 3000 K they are in the same order of magnitude.

In contrast to the release rate, the trapping rate  $\alpha_t$  does not depend on the trap type, but on the diffusing species and its diffusion characteristics. It is obtained from the diffusion coefficient  $D_F$  and the distance between two interstitial sites, which is the length of one jump of the hydrogen atom  $d_{jump}$ :

$$\alpha_t = \frac{D_F}{d_{jump}^2} \quad (4.8)$$

When e.g. D atoms reach the surface, they can predominantly only desorb as molecules of D<sub>2</sub> or HD. To form a molecule, the atoms at the surface must recombine. For the recombination coefficient  $K_r$  of two atoms at the surface of tungsten, very different values can be found in literature. No general conclusion on the recombination coefficient exists. Quantitative differences of more than 30 orders of magnitude ( $10^{-31} \text{ m}^4/\text{s} < K_r \leq 1 \text{ m}^4/\text{s}$ ) and qualitative differences from increasing  $K_r$  for higher temperatures to the opposite relationship are found. The recombination coefficient used here is taken from [Anderl92], because it does not reach extreme values:

$$K_r = 3.2 \cdot 10^{-15} \frac{\text{m}^4}{\text{s}} e^{\frac{-1.16 \text{ eV}}{k_B T}} \quad (4.9)$$

For low temperatures it is practically zero and increases to the order of  $10^{-18} \text{ m}^4/\text{s}$  for the final temperatures of the laser heating. Because of this extreme uncertainty of the appropriate recombination coefficient, in the next section a series of numerical calculations with different values is performed to assess the sensitivity of the main results on  $K_r$  and to justify this choice.

## 4.2. Deuterium Diffusion Simulation with TMAP

"Model calculations of hydrogen diffusion and trapping during laser induced heat pulses on tungsten using the one dimensional code TMAP7 [Longhurst8]"[Z13] were done for different initial D depth profiles, heating scenarios and assumptions on binding energies. The main aim was to find conditions that sensitively change the fraction of D desorbed by the laser induced heating.

TMAP stands for "Tritium Migration Analysis Program" and in principle solves the one dimensional diffusion equation for the deuterium concentration  $n$ :

$$\frac{\partial n}{\partial t} = D \frac{\partial^2 n}{\partial x^2} \quad (\text{Diffusion equation}) \quad (4.10)$$

But it can also simulate other processes like adsorption, trapping, recombination, desorption, radioactive decay (e.g. for tritium), heat conduction, heat convection, heat generation and up to 50 chemical reactions. All these processes can be simulated on up to 1000 finite elements

with 30 non-diffusing species and 10 diffusing species on maximal 3 different trap types beside the interstitial sites.

For the calculations here (cf. code in Appendix on page 233), two different trap types were used together with the normal interstitial diffusion, but not both trap types at the same time. One diffusing species, namely deuterium, was programmed and no non-diffusing species. All 1000 nodes were utilised for the discretisation of the problem in two different discretisations to resolve different regions. All desorption scenarios that have been simulated with both discretisations, show no difference in the results. The first spatial discretisation simulated a 10 mm thick W plate with 10  $\mu\text{m}$  resolution in the deep bulk and 1  $\mu\text{m}$  resolution in the first 10  $\mu\text{m}$  at the surface. The second discretisation focussed on the near surface region with a spatial resolution of 100 nm in the first 50  $\mu\text{m}$  and 10  $\mu\text{m}$  elsewhere, simulating roughly 5 mm thick W. Both thicknesses were sufficiently large to prevent permeation of the simulated fuel (deuterium) through the bulk material, i.e. in all cases the D flux at the back surface was zero.

The following common settings were used in the TMAP7 simulations. The initial temperature of the material was 300 K, initial partial pressure of  $\text{D}_2$  was set to zero. The heat parameters of W were input as temperature independent values. For the material boundary at the laser irradiated side, a surface heat flux is defined corresponding to the absorbed laser intensity. The heating intensity is defined as square wave pulse, starting instantly at  $t = 0$ , held constant for the pulse duration and set to zero 0.1 ms thereafter. The material boundary at the rear side is defined as thermally isolated without the possibility of heat transfer. All densities and concentrations calculated by TMAP7 base on the basic lattice number density, which is set to  $6.3 \cdot 10^{28} / \text{m}^3$  as the number density of the W atoms. Different initial D concentration profiles have been defined as tabular input, which are initially located only on the interstitial sites. In the cases where additionally traps were simulated, the trap concentration was always assumed as 1% of the lattice density and constant throughout the material. The traps are initially assumed empty.

For the interstitial diffusion, the Frauenfelder diffusion  $D_F$  (equation 4.2) is used. For the traps the release rate  $\alpha_r$  is input accordingly to equation 4.4 or 4.5, respectively and the trapping rate of all traps according to equation 4.8. The diffusion boundary conditions on both surfaces of the material are defined as rate dependent. Through this definition, the atomic D underlies the recombination rate at the surface and can form  $\text{D}_2$  molecules. Only this exchange reaction between atomic and molecular deuterium has been allowed. The other exchange direction, namely dissociation of  $\text{D}_2$  has been excluded, because re-absorption is not assumed. The recombination rate of atomic D on the surface of the material has been set according to equation 4.9.

The TMAP7 simulations calculate the diffusion processes for a time period of 1 s. The initial time step is set to 1  $\mu\text{s}$ , but the programme can reduce the time step by factors of 10 up to seven orders of magnitude, if needed for convergence of the algorithm. Regularly, it also tries to increase the time step in order to accelerate the calculation, which is done increasingly for the later stages of the calculation, when all values stabilise.

The TMAP7 code has been extensively validated and verified in comparison to theory and experiments in the literature [Ambrosek8]. However, a further validation of the code has been done against the PERI code (PERmeation, Recycling and Inventory), which was developed earlier for similar calculations. The PERI code [Wienhold83] is capable of calculating the permeation of hydrogen through metallic membranes, hydrogen release from metallic surfaces and the hydrogen inventory in metallic walls. Only the diffusion on the interstitial sites in W could be compared, because PERI cannot simulate traps. Hydrogen permeation was simulated with a hydrogen flux on the front surface of a 0.1 mm thin tungsten foil for 5 s at a temperature of 1473 K using the same diffusion and recombination coefficients.

TMAP7 and PERI were in very good agreement on the inventory with deviations of only few percent. For the flux leaving the front and rear surface, the agreement is similarly good except at the end of the loading phase at 5 s where deviations of 10% and 18% have been found, respectively. Since especially the important inventory is in very good agreement, the TMAP7 code was approved to be used for the simulation of diffusion and desorption during LID.

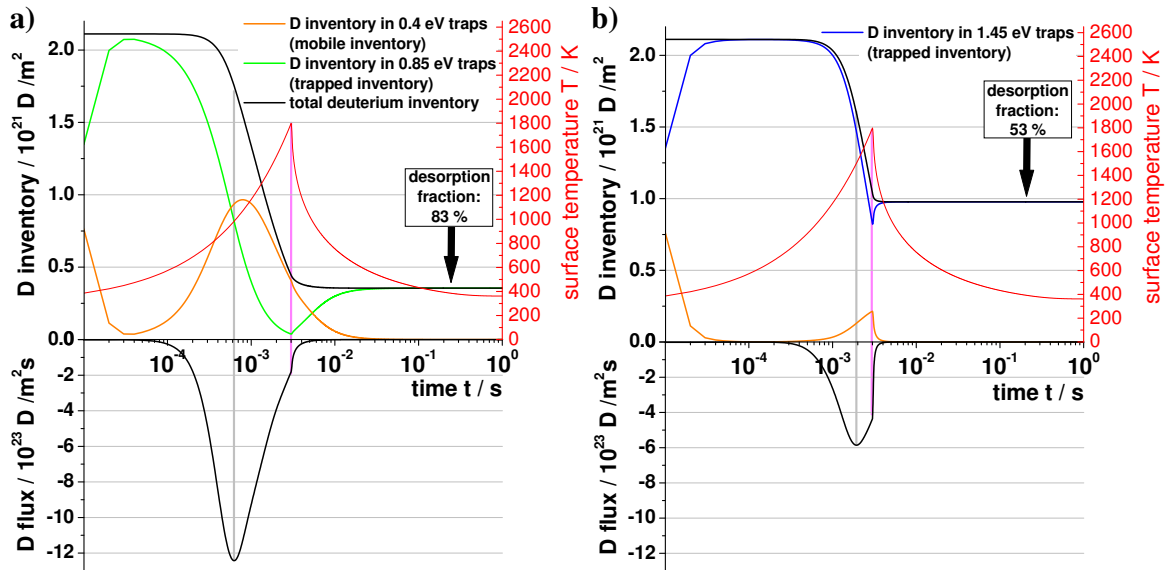
In a second study the sensitivity of the TMAP7 results against different recombination coefficients was tested, since very different values are reported as described in the previous section. A series of TMAP7 simulations of LID was done using six different constant values between  $10^{-35} \text{ m}^4/\text{s} \leq K_r \leq 1 \text{ m}^4/\text{s}$  and the temperature dependent  $K_r$  according to equation 4.9. For the lowest recombination coefficient the deuterium which reaches the surface by diffusion cannot recombine at the surface at all. In this case recombination is practically disabled, which leads to an enormous D density of  $10^{26} \text{ D}/\text{m}^2$  on the surface, but no desorption takes place.

With increasing recombination coefficient, the surface concentration at the end of the laser pulse continuously reduces down to  $10^{20} \text{ D}/\text{m}^2$  for  $K_r = 1 \text{ m}^4/\text{s}$ . However the influence on the desorption is not continuous, but a step like transition occurs. For  $K_r = 10^{-30} \text{ m}^4/\text{s}$  desorption starts, but only 18% of the initial D inventory are desorbed until the end of the laser pulse and the desorption process continues. This desorption is not supported by temperature any more, but by the high surface concentration which is nearly the same as in the case without desorption. After 0.5 s 25% of the initial D inventory is desorbed, but still desorption continues. This is definitely physically wrong, because it is known from time resolved QMS measurements on mass 4 ( $\text{D}_2$ ) during LID, that the desorption process including gas expansion and detection in the QMS is shorter than 2.5 ms for a 3 ms laser pulse. Between a recombination coefficient of  $10^{-30} \text{ m}^4/\text{s}$  and  $10^{-25} \text{ m}^4/\text{s}$ , an abrupt transition from recombination dominated desorption to diffusion dominated desorption occurs. For all cases with  $K_r \geq 10^{-25} \text{ m}^4/\text{s}$ , the recombination and desorption is faster than the diffusion to the surface. The desorption flux is identical for all these cases, the desorption fraction is always 87% and the inventory also reduces identically. The desorption is nearly completed at the end of the laser pulse. Such a desorption behaviour results also from the temperature dependent recombination coefficient (cf. equation 4.9).

It can be concluded, that for laser desorption, the experimentally observed desorption behaviour is simulated correctly for  $10^{-25} \text{ m}^4/\text{s} \leq K_r \leq 1 \text{ m}^4/\text{s}$ , but the exact value within this range is not important, since it does not influence desorption flux or desorption fraction. Other quantities like the surface concentration of deuterium are changed strongly by the choice of the recombination coefficient, but they are not discussed, since they have not been accessed experimentally.

In order to simulate LID, an exponentially decaying D concentration along the depth coordinate is assumed (cf. black line in figure 4.6a) and 0.85 eV traps with 1% of the lattice density. The temporal development of the D inventory under these conditions during an LID pulse is shown in figure 4.4a). The total D inventory is the sum of the inventories in the 0.85 eV traps and in the interstitial sites, also called "mobile inventory". At the very beginning of the calculation the whole D inventory is defined as mobile inventory. In the early calculation stages up to 0.03 ms nearly all D atoms leave this higher energetic state of  $-0.39 \text{ eV}$  (relative to the energy maximum) and quickly occupy the more favourable traps of  $-0.85 \text{ eV}$  due to their lower energy. For lower trap concentrations a correspondingly higher fraction of D atoms could remain in the interstitial sites, if the traps are already occupied fully. This initial distribution procedure of the atoms on the trap sites is a purely numerical effect, not occurring in reality, where the D atoms are already distributed on the different trap types.

With increasing temperature, the D atoms gain energy and more and more of them escape from their trap and can occupy an interstitial site from time to time. At 0.2 ms already more than 10% of the D atoms have changed from a deep trap to an interstitial site, thus decreasing



**Figure 4.4.:** Trapped and mobile deuterium inventory in tungsten and desorption flux during a standard LID pulse of  $500 \text{ MW/m}^2$  absorbed power for 3 ms; numerical simulation with TMAP7; a) traps of 0.85 eV; b) traps of 1.45 eV binding energy

the trapped inventory and increasing the mobile inventory. This "mobilisation process" is accompanied by desorption now, which did not start yet.

The diffusion of the atoms in the interstitial sites increases more and more, the atoms close to the surface can diffuse into the surface binding state and find a partner to recombine to  $\text{D}_2$  and desorb. The maximum desorption occurs at 0.6 ms and 987 K (marked by the grey vertical line). The desorption reduces both the trapped and mobile inventory. The processes of desorption and mobilisation both reduce the trapped inventory, but they counteract on the mobile inventory. While the mobilisation increases the mobile inventory, the desorption decreases it. This is the reason, why a maximum occurs in the mobile inventory at 0.8 ms.

At the end of the laser pulse ( $t = 3 \text{ ms}$  marked by the pink vertical line) the maximum temperature of 1800 K is reached, which leads to a minimum of the trapped inventory, because the atoms now have the highest energy. After the laser heating, the desorption process ceases more quickly than the temperature decay, thus only 4% of the initial inventory desorb in the cooling phase. This is not a speciality due to the presence of traps. The diffusion simulation which includes only interstitial sites shows that only 5% of the initial D content are desorbed during the cooling phase. In this phase, the decreasing temperature leads to a decrease of the energy of the atoms, which allows the D atoms to occupy the lower energetic traps again. In this "trapping phase" the mobile inventory decreases at the same rate as the trapped inventory increases until the mobile inventory vanishes. The trapping phase can be long compared to the laser pulse duration. In the case of 0.85 eV traps, it takes 9 ms until the mobile inventory decays below 10% of the final total inventory.

For the case of 1.45 eV traps instead of the 0.85 eV traps this trapping phase is negligibly short with 0.14 ms. The characteristic of the whole process changes (cf. figure 4.4b). The mobilisation effect is now very weak, as the mobile inventory maximum reaches only 10% of the initial D content in comparison to 46% for the previous weaker binding. For these conditions the trapped inventory is nearly equal to the total inventory, marginalising the mobile inventory. The opposite was true for the previous case, where nearly only mobile inventory is present at the end of the laser pulse. There the maxima of the desorption flux and the mobile inventory were only separated by 0.2 ms. In the case of strong binding, both processes occur at later

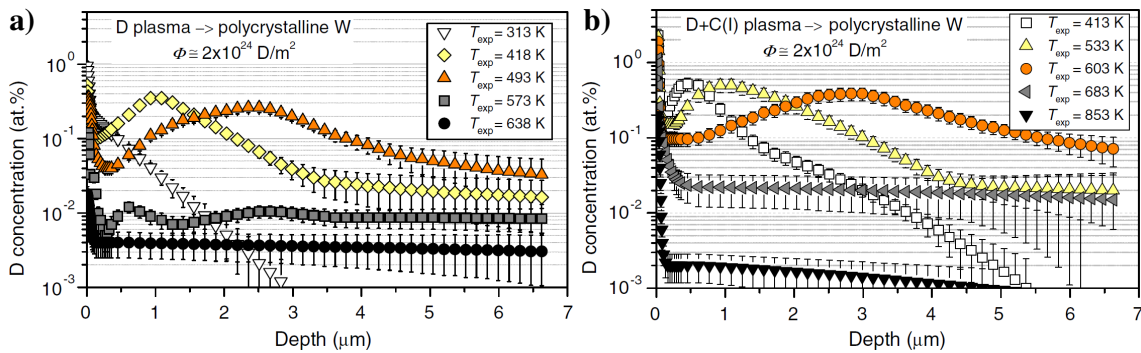
#### 4. Desorption Mechanism of Hydrogen

times and with a larger temporal distance to each other. The maximum of the desorption flux takes place at 2 ms (at 1500 K) and the maximum of the mobile inventory at 3 ms.

While the case of strong binding represents one extreme scenario, the opposite extreme scenario is the case, where no traps are present, only interstitial sites. In this fictive case, the D inventory develops very similar like the total inventory in the 0.85 eV case, reaching a desorption fraction of 86%. The maximum of the desorption flux is slightly higher ( $1.4 \cdot 10^{24}$  D/m<sup>2</sup>s) and occurs earlier, at 0.44 ms but at a similar temperature of 900 K.

The simulations by TMAP7 shown above, assumed an initial deuterium profile of 9 μm depth with 3 μm decay length, according to measured depth profiles reported in the literature under similar loading conditions (cf. figure 4.5)[Alimov8]. For low temperatures of 300-400 K (white symbols) during plasma exposure, such exponential decays are observed with different decay lengths. At the very surface sometimes a very narrow ( $d < 50$  nm) increase of the D concentration is measured and sometimes not. It was not included in the TMAP7 calculations here.

For this depth profile, the standard laser heating ( $500 \text{ MW/m}^2$  absorbed intensity for 3 ms) to 1800 K leads to a desorption of 86% of the deuterium inventory by a single laser pulse. The deuterium depth profile stabilises after ca. 20 ms, nevertheless the calculation runs until 1 s, to account also for some minor changes in the cooling phase. The desorption fraction increases only slightly to 91% for a stronger laser pulse of  $750 \text{ MW/m}^2$  for 3 ms that reaches 2500 K. This is due to the weak increase of diffusion coefficient and diffusion length for temperatures above 1400 K (cf. figure 4.3). Also an extension of the hot phase was simulated with a 12 ms laser pulse of  $250 \text{ MW/m}^2$  reaching the same temperature of 1800 K. The desorption fraction is nearly unchanged with 92%. However, in reality laser pulses longer than 4-5 ms are not favourable, since they lead to considerable lateral heat propagation. Consequently, the surface temperature of the one dimensional calculation is not reached, and unsharp desorption in the spot border occurs (details in chapter 6.2).



**Figure 4.5.:** Deuterium depth profiles from [Alimov8] measured by NRA in W exposed to a "clean" D plasma (a) and a D plasma with added C impurity (b) at different sample exposure temperatures; planar DC magnetron plasma;  $200 \text{ eV/D}$

The standard LID pulse reduces the deuterium concentration by more than two orders of magnitude in the surface region (figure 4.6a, orange line). At the same time a low concentration is formed throughout tens of micrometres in the bulk, where no deuterium was present before the laser pulse. This is due to inward diffusion driving the D to directions with lower D concentration, according to

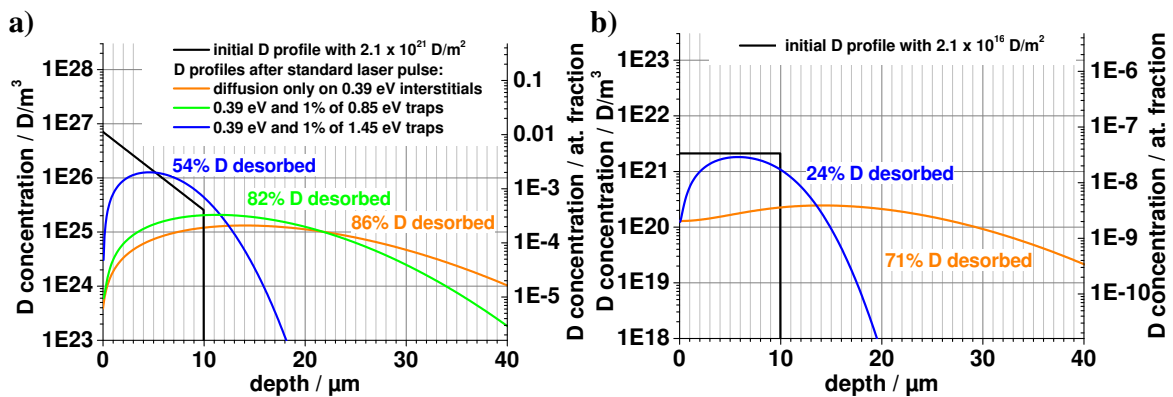
$$\vec{\Phi} = -D \nabla n \quad (\text{Fick's law}) \quad (4.11)$$

$\vec{\Phi}$  ... deuterium flux in  $1/\text{m}^2\text{s}$

$n$  ... deuterium concentration in  $1/\text{m}^3$

The initial concentration gradient extends from the vacuum towards the surface as well as from the deeper regions of the material toward the surface. Hence, during heating the deuterium flux is directed from the surface to the vacuum (desorption flux) as well as towards the depth of the material. After the heating pulse a D profile with a maximum at ca. 15  $\mu\text{m}$  depth results.

This high desorption fraction around 90% can be considerably decreased, if not only diffusion on interstitials is assumed but also deeper traps. If additionally 0.85 eV traps are assumed with a density of 1% of the lattice density, the desorption fraction reduces slightly to 82% and the D profile changes slightly in shape (figure 4.6a, green line). Its maximum shifts closer to the surface. Increasing the trap energy to 1.45 eV, reduces the hydrogen release to 54%. The maximum of the D profile is now much closer to the surface at a depth of 4-5  $\mu\text{m}$  and the whole profile is more narrow and compact (figure 4.6a, blue line). The reduction of the D concentration at the surface is only about one order of magnitude and in depths below 6  $\mu\text{m}$  the concentration is higher than before the laser pulse.



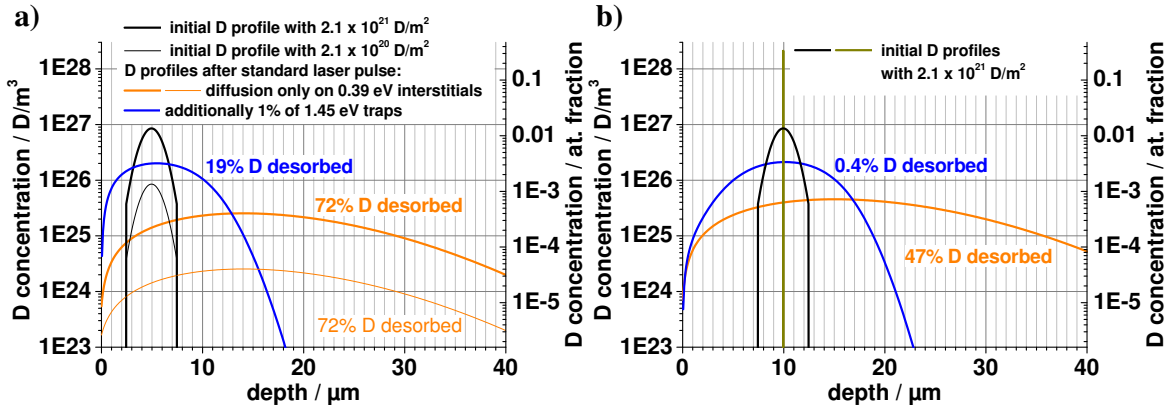
**Figure 4.6.:** Deuterium depth profiles in W before and after one 3 ms LID pulse to 1800 K with exponential (a) and constant (b) initial D profile; calculation by TMAP7; a) similarly published in [Z13]

A reduced desorption fraction can also have other reasons, like an increase of the trap density, which has not been simulated here. The most likely reason for a low desorption fraction, is the effect of a deeper deuterium depth profile. For elevated temperatures (400-600 K) the measured D depth profiles show a deuterium peak in a depth of several micrometres (cf. figure 4.5). Such peaked profiles have been modelled in TMAP7 with a Gaussian depth distribution with a FWHM of 2.4  $\mu\text{m}$  centred at different depths (cf. figure 4.7). If the peak is at a depth of 5  $\mu\text{m}$  (left figure), the desorbed fraction reduces to 72% if only diffusion on the interstitial sites is simulated.

A shift of the peak to a depth of 10  $\mu\text{m}$  (right figure) leads to a situation, where only 47% of the total deuterium is desorbed. In both cases the maximum value of the deuterium concentration is reduced by more than one order of magnitude, but the volume that contains the deuterium increases strongly. During the diffusion process the profile peak shifts into the depth and remains at ca. 15  $\mu\text{m}$  depth after the laser pulse. This is valid for all initial profiles: Gaussian, exponential, constant (cf. figure 4.6b). It can be concluded, that for initial profiles with a central depth\* smaller than 15  $\mu\text{m}$ , the final position of the D peak is mostly independent of the exact shape of the initial D profile. This is because the initial profile is smoothed out by the diffusion quickly. The final position of the peak is only at greater depths than 15  $\mu\text{m}$ , when

\*With "centre of mass" or "central depth", the depth is meant, at which the integral of the profile reaches one half of its total value.

#### 4. Desorption Mechanism of Hydrogen



**Figure 4.7.:** Deuterium depth profiles in W before and after one 3 ms LID pulse to 1800 K; effect of different initial D depths and trap binding energies; calculation by TMAP7

the initial profile was already centred at greater depths than 15  $\mu\text{m}$ . The final position of the D peak depends only on the trapping conditions. For stronger trapping, it is closer to the surface, because the mobility of the D atoms is smaller for higher binding energies. Thus the transport to the surface is hampered and steeper concentration gradients remain. For the 0.85 eV traps the final position of the profile maximum is at a depth of ca. 11  $\mu\text{m}$  and for the 1.45 eV traps at ca. 6  $\mu\text{m}$ . This is valid for all initial profiles that are centred at smaller depths than these corresponding final depths. This condition is e.g. not fulfilled for the Gaussian function in 10  $\mu\text{m}$  depth with 1.45 eV trapping, because the initial depth is larger than the final depth of 6  $\mu\text{m}$  for this binding energy. Consequently, the final position of the profile maximum is identical to its initial position (figure 4.7 right) and nearly no desorption can occur.

The influence of different absolute concentrations of D was tested with the Gaussian profile at 5  $\mu\text{m}$  depth (figure 4.7a). A reduction of the concentration by one order of magnitude (thin lines) showed no effect on the desorption fraction and only slight changes in the final D shape in the first micrometres below the surface.

Further variations of the initial D shape were done to test the sensitivity of the desorption fraction on the shape and width of the initial D distribution. Instead of a Gaussian function at 10  $\mu\text{m}$ , a delta function at 10  $\mu\text{m}$  depth with the same integral was used (figure 4.7 right). No change in the resulting D profile or desorption fraction occurred. A similar comparison was done for the peak in 5  $\mu\text{m}$  depth, assuming a broader Gaussian function with a FWHM of 4  $\mu\text{m}$  instead of 2.4  $\mu\text{m}$  but with the same integral. The resulting deuterium profiles after the laser pulse were very similar. The desorption fraction increased only slightly from 72% to 75% (cf. table 4.1) due to the shorter distance to the surface for the broader distribution. A last comparison can be done with the constant D distribution up to 10  $\mu\text{m}$  (cf. figure 4.6b), which has a central depth of 5  $\mu\text{m}$  like the Gaussian distributions. The desorption fraction for the diffusion only on interstitials is again nearly similar with 71%, although the shape of the final profile deviates up to one order of magnitude in the first micrometre below the surface. For the diffusion with additional traps of 1.45 eV, the final profiles are much more compact, thus small differences in the profile influence the desorption fraction from 19% in the Gaussian case to 24% in the constant case.

The results of the TMAP7 calculations concerning the desorption fraction are summarised in table 4.1. Desorption fractions between 20% and 90% have been found experimentally (cf. chapter 6), which can be reproduced in the calculations relatively arbitrary by assuming different combinations of trap energies and depth profiles. For a more exact simulation, the density, distribution and binding energy of the traps and the initial D profile would be necessary.



initial D profile :	exponential decay	const.	Gaussian peak FWHM: 4 $\mu\text{m}$	Gaussian 2.4 $\mu\text{m}$	Gaussian 2.4 $\mu\text{m}$	delta function
central depth =	2 $\mu\text{m}$	5 $\mu\text{m}$	5 $\mu\text{m}$	5 $\mu\text{m}$	10 $\mu\text{m}$	10 $\mu\text{m}$
<u>trap binding energy</u>						
0.39 eV	86%	71%	75%	72%	47%	47%
0.39 eV; 0.85 eV	82%	-	-	-	-	-
0.39 eV; 1.45 eV	54%	24%	-	19%	0.4%	-

**Table 4.1.:** Desorption fraction after an LID pulse ( $500 \text{ MW/m}^2$ , 3 ms, 1800 K) for different trap types and different initial deuterium profiles; calculated by TMAP7

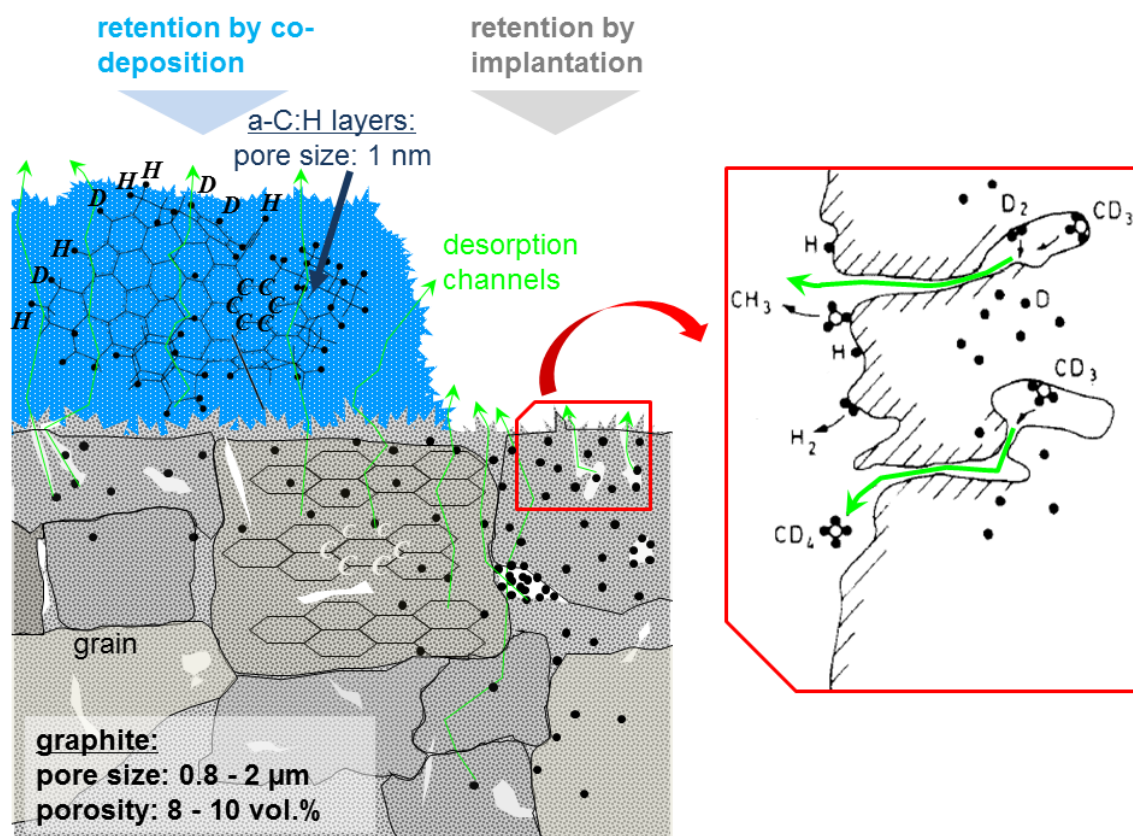
It can be concluded that the desorption fraction and final D profile are independent of the absolute D concentration, but depend on the type of traps, their concentration and the central depth of the deuterium profile rather than its actual shape. The deeper the fuel is retained and the stronger the binding energy, the lower is the desorbed fraction. On the other hand, it is rather insensitive to changes in the heating intensity or duration.

### 4.3. Desorption from Carbon and a-C:H Layers

Thermal desorption of hydrogen from carbon materials relies on "the model of local thermal detrapping of fuel from binding states with local recombination and rapid outward transport as molecule [Philipps87]."[Z13] This model of local recombination was proved with the local mixing model involving different hydrogen isotopes. This model achieved good agreement and interpretation of experimental results for implantation and thermal desorption in graphite [Möller87] and a-C:H layers [Vietzke87]. The local recombination has been demonstrated with a protium concentration in one depth and a deuterium concentration in a different depth with sufficient spatial separation. Similar experiments were done with deposited a-C:H on a-C:D layers. The fractions of H and D released in different gas species in such experiments excluded significant diffusion of hydrogen in atomic form through graphite and a-C:H/D layers. Therefore the transport of hydrogen isotopes must take place in molecular form. Although this was a surprising result, since molecules are too large to migrate through an atomic lattice of a solid usually, it turned out that the porosity of the graphite and a-C:H layers allows this.

The type of graphite used in the literature sources cited here and within the present work is a polycrystalline isostatically molded grade of pyrolytic fine-grain graphite (Ringsdorff\* EK98). It has an open porosity of 8% at  $1850 \text{ kg/m}^3$  with a pore size of 2  $\mu\text{m}$  while the grain size is 10-12  $\mu\text{m}$ . Additionally, a different but similar graphite grade was used (Kornmeyer R6650) with an open porosity of 10% at  $1840 \text{ kg/m}^3$ , average pore size of 0.8  $\mu\text{m}$  and average grain size of 7  $\mu\text{m}$  [Kornmeyer11]. Although a-C:H layers are much more compact compared to graphite, they also have pores e.g. build by carbon rings of 7 or more carbon atoms (cf. figure 4.8) or at areas where many hydrogen atoms come together. Since the hydrogen atoms only have one chemical bonding, which connect them only to C and not to other H or D, they locally terminate the carbon network. Therefore areas where hydrogen atoms agglomerate represent a pore. However, these are only micropores up to ca. 1 nm in size. Still they are responsible for a relatively high porosity like in graphite, which allows molecular transport through the material. The pores provide a direct connection of the thermally released molecules to the vacuum. Thus, the released molecules can desorb promptly without a significant delay. The

\*today part of SGL Group ([www.sglgroup.com](http://www.sglgroup.com))



**Figure 4.8.:** left: Scheme of hydrogen desorption from amorphous hydrocarbon layers and hydrogen-implanted graphite (a-C:H network adapted from [Küppers95, p.290]) right: local release of molecules and radicals (adapted from [Philipps87])

network or pores are often called "desorption channels" or "short circuits" for desorption, which are indicated as green lines in figure 4.8.

The hydrogen desorbs mainly molecularly as H<sub>2</sub>, HD or D<sub>2</sub> depending on the isotope concentration and a minor fraction of 10-20% as hydrocarbons CH<sub>4</sub>, CD<sub>4</sub>, C<sub>x</sub>D<sub>y</sub> (cf. figure 4.9c and figure 6.5 on page 141). In some cases, for example when thermal D<sup>+</sup> ions impinge on the wall, the release of radicals, i.e. unsaturated molecules like CD<sub>3</sub> occur during desorption [Philipps87]. This happens in situations, where the impinging particle is adsorbed at the very top surface e.g. due to low impact energy. In these cases the radical is thermally released so close to the surface that it cannot hit the graphite any more to collect a further H or D atom to saturate itself. In all other cases, the released radicals hit the walls of the pores frequently on their way to the surface and recombine with H or D atoms adsorbed at these walls to form saturated molecules. Radicals with one C atoms and less than three hydrogen atoms have not been released in notable amounts, since a successive formation (e.g. CD → CD<sub>2</sub> → CD<sub>3</sub> → ...) was "ruled out from the first order character of the desorption process" [Philipps87, p.295].

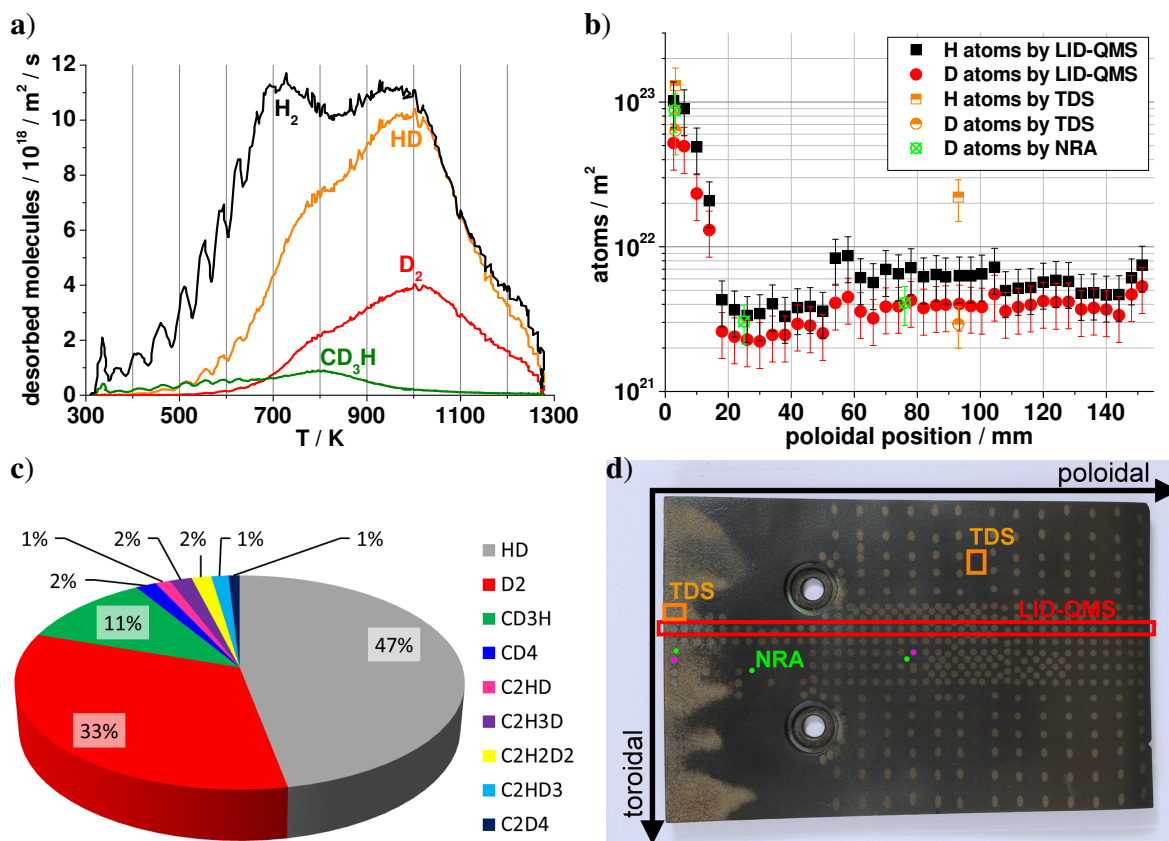
Larger carbon molecules with two or more carbon atoms also occur in the desorption spectrum, but contain only few percent of the total desorbed hydrogen amount (cf. figure 4.9c).

In [Vietzke87] it was also shown that hydrogen-implanted graphite is very similar to a-C:H layers in physical structure and thus similar in optical and electrical properties and chemical reactivity. It possesses some attributes of pure graphite and some of a-C:H layers and thus represents a material inbetween these two. For example the physical sputtering of hydrogen-

implanted graphite is similar to pure graphite, but its chemical sputtering is qualitatively similar to a-C:H layers. However, quantitatively the chemical reaction yield is about one magnitude higher for a-C:H layers.

Comparison of the temperature dependence of desorption by TDS and LID did not show large differences, indicating that the desorption is widely independent of the heating rate up to  $10^6$  K/s [Irrek8, p.52]. On the contrary, TDS with different heating rates usually lead to a shift of the desorption characteristic towards higher temperatures, e.g. [Manhard11b]. However, the similarity in temperature dependence, the equal total amount of desorbed hydrogen and a comparable molecule spectrum show that the short duration of laser heating has no significant influence on the desorption process. Only the hydrocarbon fraction is slightly smaller in LID typically (cf. figure 6.5 on page 141).

It can be concluded that the desorption process of hydrogen from carbon materials like graphite, a-C:H layers, CFC, DLC etc. is a prompt and complete release. The desorption rate is only determined by the thermal activation and not by diffusion, recombination or other processes. Therefore it is sufficient to reach the necessary temperature for complete desorption, which is known from TDS heating, to achieve nearly complete (i.e.  $> 90\%$ ) laser induced desorption.



**Figure 4.9.:** Retention in ALT-II (N° 2/19) graphite limiter of TEXTOR

- a) TDS delta-spectrum in the deposition dominated area; heating rate:  $0.136 \text{ K/s}$   
 b) spatially resolved H and D retention measured with 3 methods (positions in d)  
 c) molecular origin of desorbed D atoms during TDS of position a)  
 Figure b) and d) are similarly published in [Z11].

This necessary temperature is typically in the range of 1200-1400 K, which is deduced from TDS measurements during slow heating of the whole sample in an oven in vacuum. An

example of a TDS spectrum after background subtraction is shown in figure 4.9a. It was measured in the deposition dominated area of an ALT-II limiter tile of TEXTOR and shows that the desorption maxima are passed after 1000 K and desorption finishes between 1200-1300 K in this case. This temperature is usually sufficient for complete hydrogen desorption of carbon based materials and a-C:H/D layers. This example shall also demonstrate the mentioned desorption characteristics shortly in the following. Some of the following content has already been published in [Z11]. Literal citations are marked by quotation marks.

The ALT-II graphite limiter tile "has faced the plasma for about 33,200 s (accumulated time) during more than two years of tokamak operation. The limiter tile temperature during plasma exposure is typically between" 400-500 K but has also temporally increased due to transient heat loads. "An averaged fluence of  $10^{26}/\text{m}^2$  has been determined spectroscopically" from a diode signal by integration of the  $H_{\alpha}$  light on the ALT-II limiter. "The tile (cf. figure 4.9d) shows a large net-erosion zone and a smaller net-deposition zone," in which a thick (2-15  $\mu\text{m}$ ) "and rough a-C:H layer ( $R_a = 6-10 \mu\text{m}$ ) has grown, while the surface in the erosion dominated region is much smoother ( $R_a = 1.4-1.9 \mu\text{m}$ ). The two regions are separated by a sharp and meandering border ca. 1-3 cm from the left edge of the tile."

LID-QMS "shows a hydrogen retention of about  $5.5 \cdot 10^{21} \text{ H}/\text{m}^2$  in the erosion dominated area and a deuterium content of  $3.6 \cdot 10^{21} \text{ D}/\text{m}^2$ . In the deposition dominated area the hydrogenic retention is increased by factors up to 18 for H and 14 for D, reaching values of the order of  $10^{23}/\text{m}^2$ ." [Z11] Similar values also result from NRA measurements in the three positions indicated in figure 4.9d and from TDS measurements of two squares cut out of the tile. The agreement of the three different measurement methods shows that on bulk graphite and hydrocarbon layers the retained hydrogen is released nearly completely in a single laser pulse. This supports the general model of prompt hydrogen desorption, that is faster than the millisecond laser pulse duration.

In this comparison only larger deviations (i.e. by a factor of 1.5) to the NRA values occur in the area of thick deposition, which "can be due to the strong inhomogeneity of the layer. The deuterium values from TDS fit excellent to the LID-QMS results, but show a much higher H inventory (factor of 2.9) in the erosion dominated region which is due to" intrinsic hydrogen from tile fabrication, that is distributed "inside the whole volume of the tile". [Z11] While TDS desorbs this bulk hydrogen from the whole thickness of ca. 1 cm, the laser heating can only desorb a fraction of it at the surface (ca. 100  $\mu\text{m}$ ). Further LID-QMS results of this sample, e.g. the hydrogen retention on the tile side or around the mounting holes can be found in [Z9] and [Z11].

## 5. Ex situ Laser Induced Desorption (LID-QMS)

Historically the development of many laser based wall diagnostics like desorption (LIDS), ablation (LIAS) and break-down spectroscopy (LIBS) has been first developed under laboratory conditions before the application in the tokamak environment. This is mainly done because under better controllable laboratory conditions, better sample access and the absence of strong electromagnetic fields, the physical processes can be studied in more detail. The same is valid for LID, formerly also called LITD [Tagle83], i.e. Laser Induced Thermal Desorption in order to distinguish it from resonant laser desorption. It has been performed with many different laser types, e.g. with ruby laser [Pospieszczyk80], CO<sub>2</sub> [Hartwig78], Nd [Cowin78] etc. Usually these measurements were performed with laser pulses at the order of 1 J pulse energy, which made it necessary to use a very small spot size and/or short pulses in the nano- or microsecond range. The laser pulses in the millisecond range applied in the present work, require more than one order of magnitude higher energies per pulse in order to reach the same surface temperatures, which are needed for desorption. The laser energy has to be also large enough to heat a large area that releases a detectable amount of gas even for samples with very low hydrogen concentration. The laser pulse duration and therefore the heating duration is no longer comparable to time durations of surface effects and hydrogen bonding effects. The millisecond regime on the other hand offers the possibilities to investigate subsurface effects in micrometre to sub-millimetre scale, since considerably larger depths are accessible. These new techniques address the changing demand of hydrogen retention physics, with increasingly thicker layers and implantation depths. For long-term plasma-wall interaction the hydrogen can also penetrate a millimetre or more into the bulk under certain conditions. In this chapter, the laser desorption method is described, stressing mainly the changes for the setup and evaluation that are necessary for high energy pulses and long pulse duration. In order to distinguish this laboratory LID from the application in the tokamak, it is named LID-QMS. It is done with the same laser on samples reaching from bulk carbon and tungsten with implanted hydrogen to thin and thick hydrocarbon layers on different substrates. Also mixed carbon-tungsten layers and layers of tungsten on carbon have been analysed.

### 5.1. Experimental Setup and Measurement Procedure

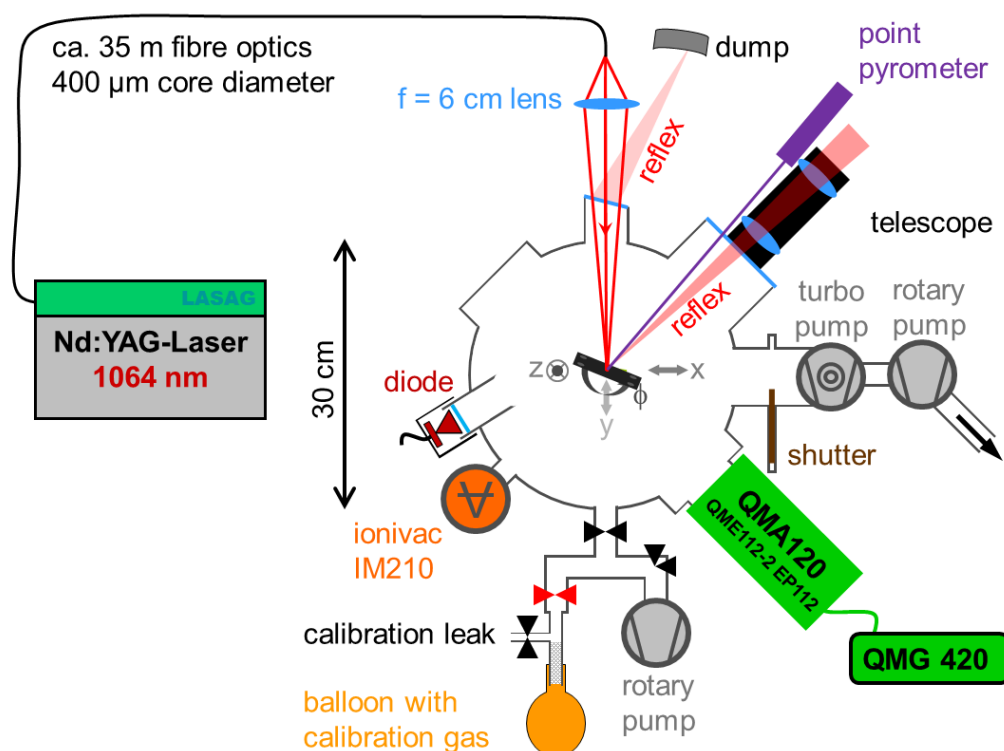
The laboratory method, called LID-QMS, was developed based on previous works in [Schweer7][Irrek8][Z9][Z11]. The quadrupole mass spectrometer (QMS) measurements have mainly been performed as residual gas analysis. In order to shield the QMS detector from carbon and W fragments ejected under extreme conditions, it is facing the rear side of the sample located in the centre of the vacuum chamber (cf. figure 5.1). This improves the stability and signal quality of the quadrupole, since no carbon layers disturb the currents at the analyser and the lifetime of the emission wire is extended.

Mainly an ionisation current of 160  $\mu\text{A}$  has been selected because then the signal linearity is maintained up to high pressure values, which are especially needed for hydrogen-rich samples.

## 5. Ex situ Laser Induced Desorption (LID-QMS)

Samples with lower gas inventory were investigated with higher sensitivity obtained with an emission current of 800  $\mu\text{A}$ , accepting a reduced linearity at higher pressures. The current must be extremely stable; fluctuations often indicate degradation of the filament or coverage with deposits.

The transfer of the axial QMS analyser head to the rear side of the sample did not reduce the initial pressure pulse of the desorbed gases [Irrek4, p.29] as expected, which has a duration of approximately 10 ms, but increased the lifetime of the filament and improved the signal stability. As filament material only rhenium seems to be suitable, since tungsten broke two times after short operation, which was probably due to the vibrations from the pump shutter and/or embrittlement by carbon. Rhenium, which is known to be more flexible and compatible with hydrocarbons, seems to be not influenced by this, while the more brittle tungsten breaks. The distance from ionisation to detection, thus the whole mass filter section, is screened by a cylinder of mu-metal to minimise the influence of external magnetic field e.g. during TEXTOR operation.



**Figure 5.1.:** Setup of the Laser Induced Desorption with Quadrupole Mass Spectrometry detection (LID-QMS) for hydrogen retention analysis

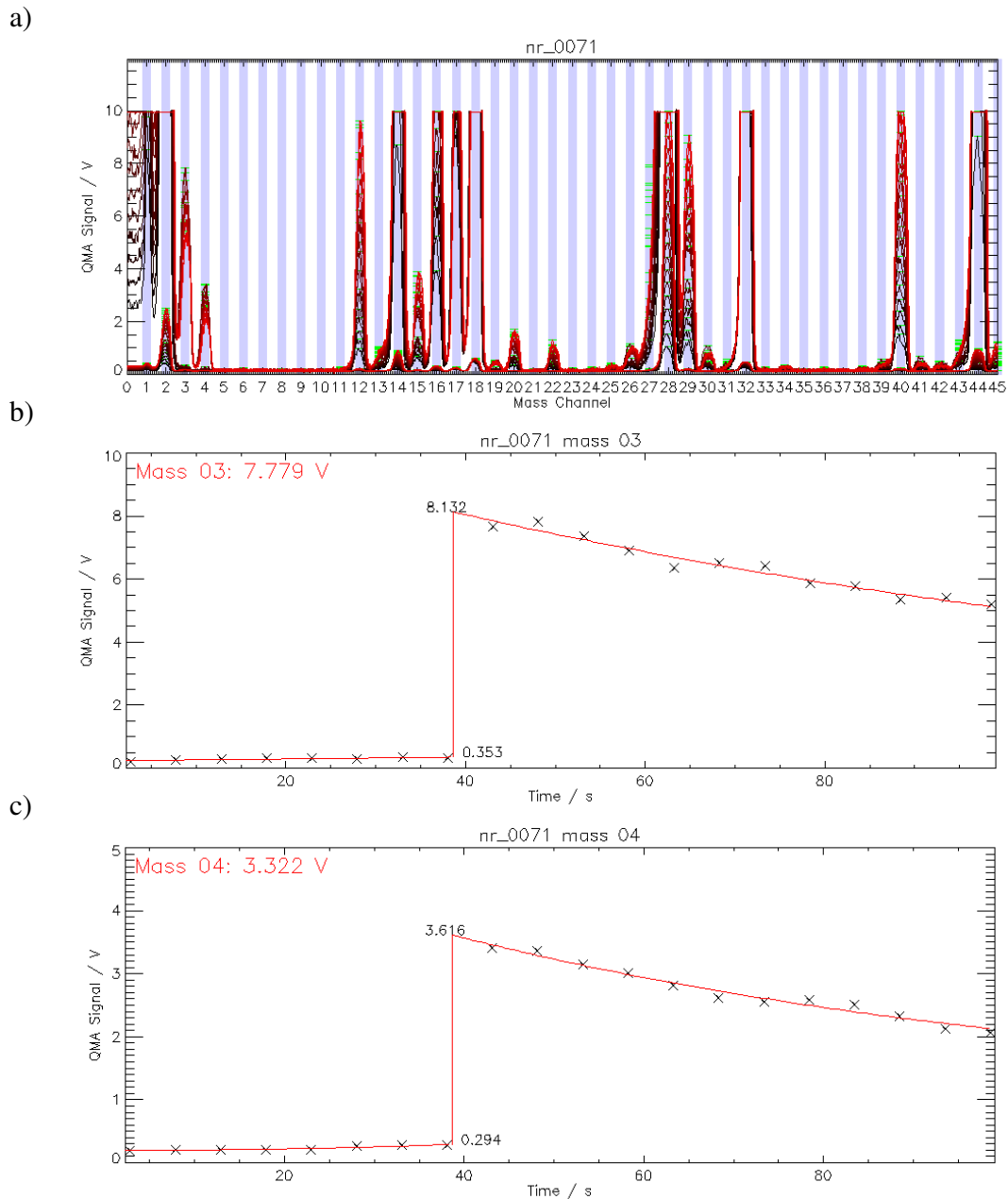
Of major importance for the optics safety at elevated laser energies ( $E_0 > 10 \text{ J}$ ) is the tilting of optical elements. The laser entrance window at the vacuum chamber (which can be made of quartz or normal glass without large transmission difference at 1064 nm) transmits 92% of the laser light at normal incidence and 90-91% at small angle incidence. For high laser energies, the reflected light fraction damages and destroys the fibre optics, if the light is passing the lens in reversed direction, since it is focussed back on the fibre and reaches high intensities there. An even stronger impact on the fibre output is induced by reflexion on the target. While the reflexion coefficient of the laser light on carbon surfaces is below 20% and mainly diffuse, for tungsten it is more than 50% at 1064 nm and even 60% for polished surfaces. There it is mainly reflected specularly in the image plane and therefore refocusses at the fibre output. This light can even burn the fibre if only a fraction of it is reaching the lens in reverse direction. For the window and target surface a tilting of few degrees preserves the integrity of the fibre. For

the window a solution with a vacuum bellow is implemented which turns the reflected beam on a dump that does not absorb it completely, but prevents further focussing. For the sample also a small angle of incidence can be realised either by vertical or horizontal tilting of the whole injection setup or by a rotation of the sample itself. Only few degrees are sufficient to direct the reflected light on the inner chamber wall instead of the laser entrance window. This preserves the fibre optics but has great disadvantages for measurements of samples with small hydrogen inventory, because this light desorbs the inner chamber wall and thus generates an irreproducible background. This is especially the case after experiments under special conditions, where material (mainly carbon) release from the target and redeposition on the chamber wall appears. As shown in the very same chamber, such release, which is comparable to ablation processes, results in wall deposits that incorporate considerable amounts of H and D, up to ratios of 0.05 D/C [Ivanova11]. Subsequent desorption experiments will then first desorb high and then descending amounts of this fuel at the wall. It is very difficult to determine a background for the measurement, since the hydrogen distribution on the wall is unknown. Moreover the light distribution after reflexion is mostly unknown and changes its characteristics from sample to sample and even drastically during the laser pulse due to roughening or melting of the sample. In the most extreme case the size of the illuminated wall area after reflexion on rough tungsten compared to polished tungsten can be two orders of magnitude larger. During a melting pulse on tungsten the area also shrinks considerable, since the molten surface reflects much more specular and confined. The thus obtained QMS signals may be totally dominated by this unknown background, instead by the signal from the sample itself, if the amount released from the sample is low. This mainly applies to tungsten samples with implanted H and D and less for a-C:H or a-C:D layers. In order to avoid this chamber background problems nearly completely, the reflected light has to exit the chamber with minimal absorption. Therefore the maximal possible light exit window of  $\varnothing 15$  cm diameter has been mounted and the sample is turned by approx.  $22^\circ$ , such that the laser light exits the chamber through the centre of the window. Other desorption chambers are made fully out of glass to decrease light absorption at the chamber walls even further [Neumann73, p.8f].

To minimise coating of the light exit window by particles that might leave the sample, the particle ejection path and the light exit path are decoupled. Any particles released are mainly ejected normal to the sample surface and are thus mainly deposited between entrance and exit window. Although the window may be also slightly covered with hydrocarbon layers, the light absorption in the layer is usually too small to induce significant desorption. Only if the laser is very well focussed after reflexion (e.g. by W mirrors), the light intensity can be high enough to destroy the thin carbon layer. This is clearly visible as the window has its usual transmission after such an event, while the surrounding of the laser exit spot has still reduced transmission. In case of heavy deposition the window was exchanged and cleaned.

A one-colour pyrometer (Kleiber 202/270B) integrating over 1.58-1.80  $\mu\text{m}$  wavelength monitors the surface temperature of the spot centre during the laser pulse. The temperature evolution of the millisecond pulse can be measured above a threshold of 873 K with good temporal resolution (maximal speed:  $5.7 \cdot 10^6$  K/s). The detection spot diameter of the pyrometer is around  $\varnothing = 1\text{-}2$  mm and measures the central part of the  $\varnothing = 3$  mm large laser spot.

The released species are detected by the quadrupole mass spectrometer. "To optimise the sensitivity and obtain a complete spectrum of released species, the valve to the pumps is closed" for the whole measurement duration (105 s). "Several mass spectra are recorded before and after the laser shot with typically 50 ms/u." [Z11] One mass spectrum, containing the masses 1-50  $\text{amu}/e$  is usually obtained within 2.5 s. Often the dynamic range is not sufficient to resolve all partial pressures. Then a multi-mode scan is used, where the QMS-electronics amplification is increased by a factor of 10 or 100 for the next scan. These two scan amplifications are alternated every 2.5 s.



**Figure 5.2.:** Illustration of evaluation procedure for one LID-QMS measurement spot on a deuterium loaded tungsten sample:

a) all QMS spectra in two alternating amplification ranges (highest sensitivity and factor 100 lower); time direction: black before red spectra; blue: peak search area

b) and c): time evolution of mass peak maxima for mass HD and D<sub>2</sub> (crosses); line: two automatically fitted exponential functions per mass are extrapolated to the time of the laser pulse (vertical line)



In a software evaluation, the analog mass spectra are cut into 50 slices, each one centred around every mass peak (cf. blue area in figure 5.2a). Because the peak value is not always exactly in the channel centre and also sometimes some noise is present, the spectra are slightly smoothed and then the maximum of each mass channel is searched. This is then the QMS value for the particular mass. Effectively for every mass a signal is acquired every 5 s (after two scans), because every second value is either saturated or in the background due to inadequate amplification. The further evaluation is only performed on the data with the adequate amplification. "Exponential fits are then applied to the temporal evolution of each mass peak before and after the desorption, from which the step of each mass signal at the desorption time is determined with high accuracy." (cf. figure 5.2) [Z11]. The mass spectrum during the laser exposure is often omitted in the analysis, since the dynamic over-pressure peak often saturates the mass signal which is measured directly after the laser pulse. This signal excursion would lead to a wrong exponential fit for this particular mass. The exponential fit is performed by an algorithm for minimisation of the squared deviations ( $\chi^2$ ) by the Levenberg-Marquardt technique [Markwardt9]. The three parameters ( $p_0, p_1, p_2$ ) of a simple exponential function

$$p(t) = p_0 + p_1 e^{p_2 t} \quad (5.1)$$

in time ( $t$ ) are used as degrees of freedom in this model for the partial pressure  $p$ . They are assumed to model adsorption and desorption processes, as well as chemical reactions of the desorbed gases at the chamber walls, since these kind of processes usually result in exponential density changes. For large desorbed amounts of H and D from hydrocarbon layers, which result in a pressure in the order of several  $10^{-6}$  hPa, a temporal decay of the  $D_2$  pressure and the simultaneous increase of the HD pressure after the laser pulse have been interpreted [Irrek8, p.72] as isotope exchange. However in case of low desorption (in the range of  $10^{-7}$  hPa) both pressures show an explicit decay (figure 5.2b and c) while the slope in the monotonic increase of the  $H_2$  pressure reduces.

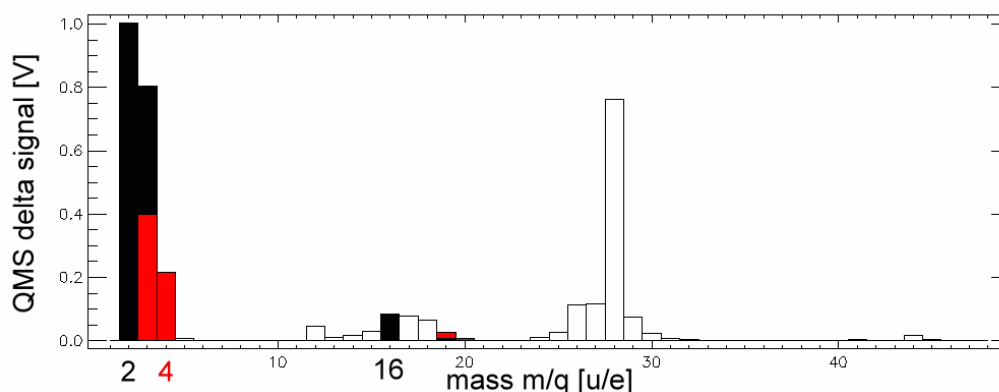
"The mass spectrometer is regularly calibrated with a calibration leak for  $H_2, D_2, CH_4, CD_4$ ", while also checking the calibration leak itself with He and the slope of calibration factors for the whole mass range by a heavy mass like Ar (details in chapter 5.2). "A typical desorption spectrum from a thick tokamak" a-C:H/D layer on an ALT-II limiter tile "is shown in figure 5.3, where the evaluated masses for protium and deuterium are marked" in black and red, respectively [Z11].

The total amount of desorbed gases, which is directly obtained after application of the calibration factors, is then evaluated with respect to H and D by summation of all masses, which are identified as fuel relevant (details in chapter 5.3). During the summation, the multiplication of the corresponding content factors has to be applied correctly, e.g. 4 for  $CD_4$ , 2 for  $D_2$  or 3 for  $CD_3H$  with respect to deuterium and 1 with respect to protium.

Finally the areal concentration of hydrogen is evaluated by taking the ratio of the absolute atom amounts and the desorption area, which is determined according to the considerations of the previous chapters 2 and 3.

## 5.2. QMS Calibration

The quadrupole mass spectrometer has been calibrated for the LID-QMS measurements by means of calibration leaks (Leybold TL4, TL6). Each gas that shall be quantified, requires its own calibration, since different quadrupoles and some quadrupole settings lead to a change of the ratios of the calibration factors for different mass channels. Therefore the change of detection modes has been checked not to introduce any instability. It has been found that the change of the SEM voltage (Secondary Electron Multiplier) leads to drifts of the intensity



**Figure 5.3.:** LID-QMS spectrum of a typical 15  $\mu\text{m}$  ALT-II layer after subtraction of chamber rest gas background; unambiguously identified masses are marked in red (D containing: 3, 4, 19, 20) and black (H containing: 2, 3, 16, 19); already published in [Z11]

signal for several minutes. Therefore it has been fixed to 1800 V in the early stage of the work. The measurement range has thereafter only been adjusted by the QMS-electronics amplification. The sacrifice for this is, that amplification is only possible in steps of factor 10, while the SEM amplification allows any factor. As a consequence some masses were out of measurement range, while weak signals on other masses were just above the detection limit for a specific setting. Therefore the measurement mode of the QMS had to be change from a single-scan mode with constant amplification to a multi-mode, in which two amplification factors alternate: First a scan is running at low amplification for detection of strong signals (mainly  $\text{H}_2$ ,  $\text{CO}$ , sometimes  $\text{HD}$  or  $\text{Ar}$ ) and then a scan is taken with 10 or 100 times higher amplification factors for weak signals. This multi-mode operation was necessary especially for the investigation of tungsten samples with very low deuterium inventory. An advanced control device (QMG420 or higher) is necessary for the multi-mode, replacing the QMG120, while the quadrupole electronics and analyser remained unchanged. The superior stability of the amplification by the QMS-electronics instead of SEM, has been clearly observed several times during calibration.

The factor between neighbouring amplification ranges of the QMS-electronics was regularly compared and was always 10, even for fast (20 ms) switching between two amplification ranges. Despite this stability, it is advisable to calibrate the QMS in the same or similar pressure ranges as those used in the measurements, to exclude further differences between calibration and measurement. By this, any chamber specific effects and interactions between different mass channels (e.g. adsorption and desorption on the wall, interaction with water vapor etc.) can be included into the calibration. Such chemical processes at the wall have been seen in the low pressure range, but not investigated in detail. In order to access the pressure regions of the experiment, two different calibration leaks have been used with leak rates of  $4.7 \cdot 10^{-5}$  and  $3.3 \cdot 10^{-7} \text{ Pa m}^3/\text{s}$ . These values are valid for helium and have an uncertainty of  $\pm 11\%$ . They are valid for inlet pressures of  $1000 \pm 20 \text{ hPa}$  and outlet pressures below 1 hPa. The pressure at the inlet side has been established by a balloon filled with the gas species to be calibrated (cf. figure 5.1). During the preparatory flushing of the calibration leak capillary with the gas, the QMS signal is monitored until it approaches steady-state. Then the air masses ( $\text{N}_2$ ,  $\text{O}_2$  etc.) do not decrease after further flushing, the calibration mass does not increase any more and the optimal inlet pressure is reached. If the flushing is done too long or too often, the inadequate inlet pressure is seen by a drop of the mass which is calibrated. In this case a calibration yields too low calibration values and the balloon has to be refilled. The calibration

procedure itself is carried out as similar as possible to the measurement procedure. This approach is in-line with the calibration of mass spectrometers in similar measurement tasks like the TDS device. While the QMS measurements during TDS are acquired with pumping and analogously the calibration is done under pumping also, in LID-QMS both are carried out without pumping.

Before connecting the calibration balloon to the chamber, a background measurement is done. After closing the pump shutter several partial pressures increase. Those corresponding to the calibration gas are extracted from the scans as the maximum values of the peaks and their slopes are determined by linear regression. The slopes are the background measurement for the calibration. In case of the large calibration leak rate it is not important, except for masses with a large background rise (like H<sub>2</sub>). The background measurement should be performed at least as long as the calibration runs, but a longer measurement duration increases the accuracy of the regression slope for weaker signals.

After the flushed calibration leak is connected to the chamber a short time for steady-state establishment of the flow is needed. Subsequently the partial pressure rise after the closure of the pump shutter is recorded and the peak maximum slope is evaluated in the the same way as for the background measurement. The slopes also easily show where nonlinearity of the QMS starts and how large it is for the different masses. The calibration factor (in units of molecules/V) results from the ratio of the leak flow (molecules/s) to the signal slope (in V/s).

However, the flow of the calibration leak is given for helium and has to be either corrected for other masses or one-gas calibration leaks can be used. The correction of the flow is an easy task for molecular or laminar flows. "Molecular flow conditions can only be assumed for leaks  $\leq 10^{-8}$  mbar ltr/sec and laminar flow conditions for leaks  $\geq 10^{-4}$  mbar ltr/sec" [manual94, p.9]. The two limits correspond to  $10^{-9}$  Pa·m<sup>3</sup>/s  $\cong 2 \cdot 10^{11}$  molecules per sec and  $10^{-5}$  Pa·m<sup>3</sup>/s  $\cong 2 \cdot 10^{15}$  molecules per sec for room temperature and frame the more difficult area of mixed flows. One of the leaks used for calibration is in the laminar regime ( $Q = 4.7 \cdot 10^{-5}$  Pa·m<sup>3</sup>/s) and was used for high partial pressures from samples with large gas concentrations. The laminar correction factors  $k_4$  are in this case the ratios of the dynamic viscosity  $\eta$  at the same temperature:

$$k_4 = \frac{\eta_{He}}{\eta_{gas}}. \quad (\text{for values see table 5.1}) \quad (5.2)$$

flow rate:		low	medium	high	dynamic viscosity $\eta/ \mu\text{Pa s}$
flow type:		molecular flow $Q < 10^{-9}$ Pa·m <sup>3</sup> /s	mixed flow $Q = 3.3 \cdot 10^{-7}$ Pa·m <sup>3</sup> /s	laminar flow $Q > 10^{-5}$ Pa·m <sup>3</sup> /s	
mass	gas	$k_8$	$k_6$	$k_4$	293 K ... 300 K [vac] ... [Lide5]
2	H <sub>2</sub>	1.41	1.92	2.22	8.8 ... 9.0
4	D <sub>2</sub>	1.00	1.37	1.59	... 12.6
4	He	1.00	1.00	1.00	19.6 ... 20.0
16	CH <sub>4</sub>	0.50	1.31	1.79	... 11.2
20	CD <sub>4</sub>	0.45	1.30	1.79	... 11.2*
28	N <sub>2</sub>	0.38	0.84	1.12	17.5 ... 17.9
40	Ar	0.32	0.68	0.87	22.2 ... 22.9

**Table 5.1.:** Gas flow rates used for QMS calibration leaks in different flow regimes relative to helium; \*=The same viscosity was used for CD<sub>4</sub> as for CH<sub>4</sub> since no literature value has been found and the viscosity of C<sub>2</sub>H<sub>4</sub> and C<sub>2</sub>H<sub>2</sub> are similar (10.4  $\mu\text{Pa s}$ ).

For the molecular flow the flow rate relative to helium can be calculated even easier by the quotient

$$k_8 = \sqrt{\frac{m_{He}}{m_{gas}}} \quad (\text{for values see table 5.1}) \quad (5.3)$$

but no calibration leak in this regime was used, since pressure ranges accessible in acceptable time are only relevant in ultra-high vacuum (UHV). For the lower pressure ranges a calibration leak in the region between molecular and laminar flow had to be used ( $Q = 3.3 \cdot 10^{-7} \text{ Pa m}^3/\text{s}$ ). In this regime "the effective flow phenomena within a capillary are unknown. [...] Only an approximate correction factor can be achieved by assessing a factor between those indicated for laminar and for molecular flow" [manual94, p.9-10]. These values have been determined experimentally by calibrating the QMS with the high flow leak in laminar regime and directly afterwards with the medium flow leak in the mixed regime. The calibration factors obtained in the laminar regime are measured with two amplification stages lower than for the low flow. Since the QMS-electronics amplification yields a factor of 10 for every stage the calibration factors are easily known for the low pressure ranges. But due to the effects described at the beginning of this section, it is more accurate to calibrate in the pressure range of the later LID-QMS measurements than two orders of magnitude above. Comparison of this cross-calibrated values for the low flow rate against the high flow rate with calculated values by linear interpolation between the two regimes was satisfactory and thus the values (cf. table 5.1) are assumed to be quite accurate (see chapter 5.4 for accuracy considerations of LID-QMS).

The average value of the calibration factors for  $H_2$  and  $D_2$  is used for HD. In order to exclude any exchange effects of H and D or formation of HD in the balloon, capillary, or chamber, the order of calibration is usually: He,  $H_2$ , Ar,  $D_2$ , thus separating H and D by noble gases. The advantage of calibrating  $D_2$  as final gas is, that after LID-QMS the calibration leak can be opened at the end of the day to prove the stability of the QMS detection within the measurement, which nearly always was excellent. In contrast to these gases,  $CD_4$  and  $CH_4$  are not always included into the calibration. In these cases their calibration factors are scaled with the general sensitivity change obtained by the other gases. For mass 19 (interpreted as  $CD_3H$ ) the factor of  $CD_4$  is used as well as for  $C_2D_4$ , while the factor for  $CH_4$  is also used for  $C_2H_2$  (cf. table 5.2 on the facing page).

In steady-state the shortest scanning duration for the QMS can be found by decreasing it until the peak maximum begins to decrease. The signal scatter increases slightly for shorter scan durations, but the average value over the same period of time does not show significant deviations until a threshold is reached. For the QMS112 this threshold was 30 ms/amu. Therefore the next higher step of 50 ms/amu is usually used in LID-QMS measurements.

### 5.3. QMS Spectra Evaluation

The evaluation method for the LID-QMS spectra starts in the same way as already described in the calibration procedure. For newer QMS systems nearly all the first evaluation steps (peak separation, maximum search etc.) can be skipped, since this is already done by the QMS software itself. The interlaced measurement mode with different amplification stages is also done implicitly by the newer QMS generations. For the control unit QMG420 and its previous versions, the alternative to the recording of the analog spectra is the use of the native software (Quadstar). It is in deed capable of extracting the peak values, which are sufficient and necessary for the further evaluation, but the use of the software unfortunately limits the acquisition speed to values not fast enough for LID. Despite the larger amounts of data and the additional post-processing steps, the advantage of recording the whole analog spectrum is the possibility to check every QMS peak form during all measurements. In that way certain

changes of the QMS detection properties and sensitivity can sometimes be recognised (by double, triple or asymmetric peak structure). A certain minimum speed is necessary since the amount of the peak points measured for the exponential fit should not be reduced too much (minimum ca. 6) to achieve a good fit. This is critical for slow scans, because the measurement time cannot be extended much longer than now (105 s), since with closed pump shutter, the chamber leak rate (air and hydrogen) makes it difficult to return to the same pressures before each laser pulse in acceptable time.

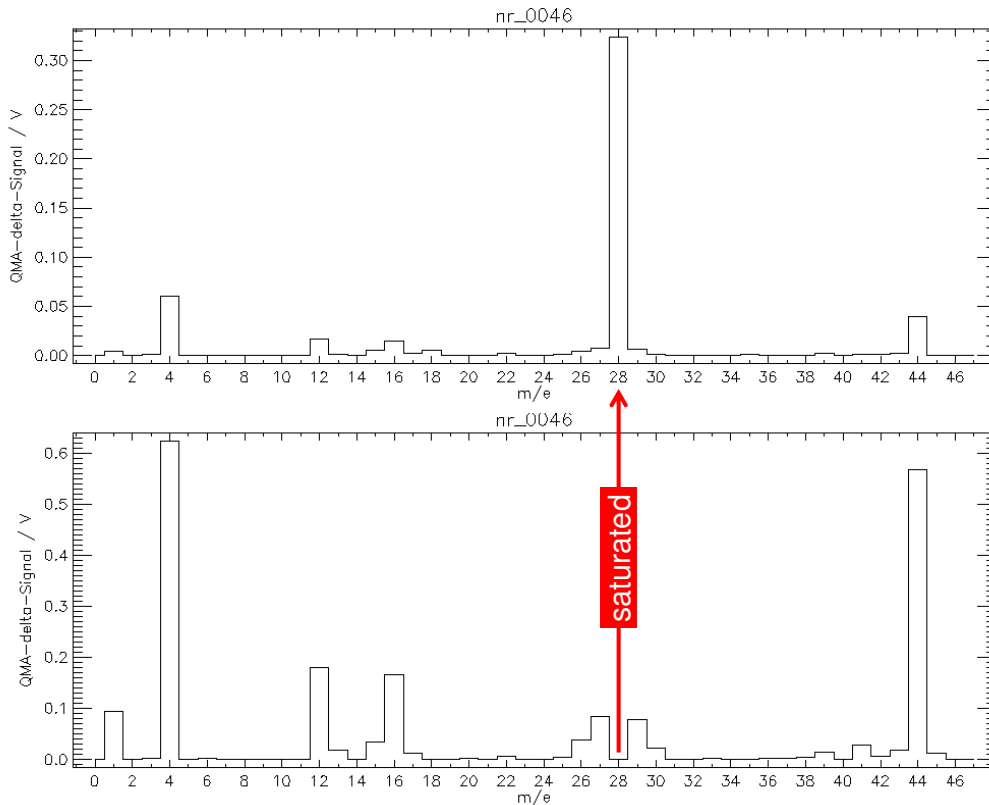
The identification of all QMS peaks could not be achieved, since for this task a complete cracking pattern deconvolution is needed. Detail on these problems with ambiguity in the interpretation of QMS spectra can be found in text books on mass spectrometry and device specific publications, e.g. [Umrath97, p.102ff]. In order to minimise these uncertainties, mainly QMS mass channels are included in the evaluation which are unambiguous (cf. table 5.2). For the fuel containing masses the interpretation is easiest on pure tungsten material because the fuel containing molecules are only H<sub>2</sub>, HD and D<sub>2</sub> (cf. figure 5.4). Many other masses appear in the raw measurement. Some come from desorption of the chamber wall by the reflected light (mainly only in case of W) if the laser escape path is not designed properly as discussed above. Others are leaking into the chamber from the outside (N<sub>2</sub>, O<sub>2</sub>, ...) or originate from continuous chamber outgassing (H<sub>2</sub>, CO, ...). In the QMS-difference signal for the case of W the solution of the qualitative peak analysis is easier than for carbon materials, which introduce a multitude of hydrocarbons with complicated spectra.

m/q amu/e	gas species	$k_{QMS}$ hPa/V	cracking from	source and characteristic
2	<b>H<sub>2</sub></b> H <sub>2</sub>	$9.84 \cdot 10^{-6}$	H <sub>2</sub> O	sample, chamber; large; large rise sample, chamber
3	<b>HD</b>	$1.46 \cdot 10^{-5}$		only with mass 4; sample, chamber
4	<b>D<sub>2</sub></b>	$1.94 \cdot 10^{-5}$		main mass in desorption from sample or chamber
16	<b>O</b> <b>CH<sub>4</sub></b> NH <sub>2</sub>	$1.14 \cdot 10^{-5}$	H <sub>2</sub> O, O <sub>2</sub> , CO <sub>x</sub> NH <sub>3</sub>	minor contributions during desorption desorption of a-C:H layers improbable occurrence
19	<b>CD<sub>3</sub>H</b> H <sub>3</sub> O	$1.46 \cdot 10^{-5}$		desorption of a-C:H/D layers improbable occurrence
20	<b>CD<sub>4</sub></b>	$1.46 \cdot 10^{-5}$		desorption of a-C:D layers
26	<b>C<sub>2</sub>H<sub>2</sub></b> C <sub>2</sub> D	$1.14 \cdot 10^{-5}$		desorption of a-C:H layers
30	<b>C<sub>2</sub>D<sub>3</sub></b> C <sub>2</sub> H <sub>2</sub> D <sub>2</sub>	$1.46 \cdot 10^{-5}$	C <sub>2</sub> D <sub>4</sub> , C <sub>2</sub> D <sub>3</sub> H	desorption of a-C:H/D layers desorption of a-C:H/D layers
32	O <sub>2</sub> <b>C<sub>2</sub>D<sub>4</sub></b>	$1.46 \cdot 10^{-5}$	CO <sub>2</sub>	sample, chamber desorption of a-C:D layers

**Table 5.2.:** Masses included in the evaluation of LID-QMS spectra (**in bold type**) and their corresponding gas species, cracking origin and sources;  $k_{QMS}$ : example values of calibration factors

Concerning the hydrogen-free masses, 99.95 wt%-pure unannealed W releases mainly CO<sub>2</sub> (since mass 44 (CO<sub>2</sub>), 28 (CO), 16 (O), 12 (C) and 22 (CO<sub>2</sub><sup>++</sup>) are present with mass 44 as main peak). Since the mass 28 peak is several times larger than the mass 44 peak (cf. figure 5.4), it is very probable that also CO is desorbed (mass 28, 16, 12). Mass 28 could also hint at nitrogen, but this is not desorbing since mass 14 (N) is not present, which always occurs

with a signal strength of 5-10% of the strength of mass 28 during nitrogen presence. Since some masses are very high their low-neighbour peaks cannot be resolved: e.g. often mass 27 is invisible due to a large mass 28 and mass 43 not visible due to a large mass 44. In the first place the temporal evolution of the partial pressures is not important for the quantification of the pressure increase induced by the laser heating at least for well-behaving sequences. Well-behaving here means a pressure sequence which can be fitted by simple exponential functions before and after the laser pulse, like the examples in figure 5.2.



**Figure 5.4.:** Example spectrum of an annealed 99.95 wt% W loaded with D in an erosion dominated area of TEXTOR; desorption with  $500 \text{ MW/m}^2$  in 3 ms; top: weak amplification only necessary for evaluation of masses 2 and 28; bottom: the same desorption with 10× higher QMS-electronics amplification for better accuracy in the low partial pressures

## 5.4. Accuracy of the Ex situ Method

In this chapter the uncertainties of the ex situ LID-QMS measurements are discussed. The phrases "error" and "uncertainty" are rather identical in this context. They are typically given in percentage of the measured value in the present work, e.g.  $\pm 13\%$ . For a value  $M$  this represents an error of the factor 1.13, i.e. the measurement result is  $M \pm 0.13 M$ . Beside such two-sided errors also one-sided errors, sometime called upper and lower error, can occur, e.g.  $+13\%$  or  $-13\%$ . Systematic and statistical errors of the same physical quantity are summed arithmetically while errors that potentially partially compensate each other are summed according to Gaussian error propagation. The latter can be different statistical errors of the same physical quantity or different systematic errors of the same physical quantity or the total errors of different physical quantities contributing to a new physical quantity.

Uncertainties due to physical or rather technical reasons are discussed for the laser illuminated and desorbed area, the heating process, the QMS calibration and the LID-QMS measurement itself.

**Laser spot size:** The measurement of the desorbed area is directly obtainable on the thin a-C:H layers, since their colour change in hue and contrast (cf. [Irrek8, p.40]) marks the area with temperatures sufficient for complete desorption. A microscopic determination of the spot size is also possible for certain types of thick a-C:H layers, like those on the ALT-II limiter of TEXTOR, because they show interference colours as well. Other thick a-C:H layers, that are more homogeneous do not show interference colours, but still the graphitisation due to the laser heating is optically visible by a local reflectivity change. For other samples (like W) and for adjustment of the optics alternative methods were necessary. Much better than the inaccurate spot size measurement by photosensitive paper is the use of a camera chip at the sample position (cf. chapter 2.2). The accuracy of the spot size is then defined by the spatial sharpness  $S$  of the laser profile. For the optimally focussed laser beam the gradient of the normalised profile has been determined in chapter 2.2 as  $S=7.0/\text{mm}$ , thus rising from zero to full laser intensity within 0.14 mm. For the standard laser spot of 3 mm diameter the increased spot area is hence a factor of 1.20 larger, thus introducing an uncertainty of  $\pm 10\%$ . For the laser spot size of 2 mm diameter the extended area is a factor of 1.30 larger, corresponding to an uncertainty of the desorbed area of  $\pm 15\%$ .

**Sample temperature:** If no surface temperature monitoring during the laser pulse is done, some uncertainties about the laser heating arise: The sample temperature can then only be calculated based on the laser power, energy losses on the light path, light reflexion at the sample and the heat properties of the sample. For a well known material like bulk carbon or tungsten this is analytically calculable and for anisotropic materials like CFC it is numerically calculable. But, as described in chapter 2, layers and stratified materials with a certain thickness introduce heat transitions which are unknown ab inito. The heat properties of the layer itself are also unknown very often and quite inhomogeneous on tokamak layers. Nevertheless, unknown heat transfer coefficients can only lead to higher surface temperatures than calculated. Additionally, carbon layers are characterised by much lower heat conductivities than the substrate, hence this uncertainty can also only lead to underestimation of the temperature. For hydrogen desorption from carbon materials (graphite, a-C:H, CFC etc.) the temperature for full desorption ( $\approx 1200\text{-}1300\text{ K}$ ) is known, thus a temperature around 1800 K is chosen for LID in order to assure full desorption, while staying below significant sublimation. Any of the previously mentioned uncertainties due to material changes results in higher temperatures, thus complete hydrogen desorption is guaranteed. Potential sublimation and material destruction could occur, but have no effect on the LID-QMS measurement. For unknown materials or strongly mixed or stratified materials it is more difficult to estimate the heat properties and heat transfer coefficients. Therefore a temperature monitoring of the laser pulse either by pyrometer or IR-camera is desirable. All uncertainties connected to the laser energy, energy losses, reflexion and material properties can be neglected, if the temperature is monitored. The correct setting of the emissivity for the one-colour pyrometer used, is known by the reflectivity measurement of the sample at the pyrometer wavelength. Since in the final LID-QMS setup the temperature evolution during LID is monitored, no error due to insufficient sample temperature is taken into account for the error estimation of LID-QMS.

**QMS sensitivity:** The calibration of the QMS has uncertainties that arise from the flow through the calibration leak, which is specified by the manufacturer with  $\pm 11\%$  for helium. This is a systematic error, since always the same calibration leaks are used, which therefore always have the same deviation from the nominal leak rate. Additionally, for other gases the conversion of the flow rate has to be done (as described in chapter 5.2). This is quite

accurate for the laminar flows, since the dynamic viscosities for the gases of interest from three literature sources result in a deviation of few percent (for H<sub>2</sub>, D<sub>2</sub>, CH<sub>4</sub>, ...) or maximal factor 1.11 (for Ar) for the corrected flow rate. The calibration in pressure ranges two orders of magnitude below the laminar regime, which is sometimes necessary, has somewhat higher inaccuracy due to the mixed flow regime. To estimate it, the differences of the flow correction factor for the mixed flow to the other two flow regimes is calculated, i.e.  $k_4 - k_6$  and  $k_6 - k_8$ . These two values are then averaged and weighted with the same factors as in the interpolation of the correction factor itself:

$$\left( (k_4 - k_6) \lg \frac{3.3 \cdot 10^{-7}}{10^{-9}} + (k_6 - k_8) \lg \frac{10^{-5}}{3.3 \cdot 10^{-7}} \right) / \lg \frac{10^{-5}}{10^{-9}} \quad . \quad (5.4)$$

One third of this value is estimated as the uncertainty because there are three flow regimes on which the error is equal shared in this way. This average deviation value for the four species that are used in the quantification of the LID-QMS measurements (H<sub>2</sub>, D<sub>2</sub>, CH<sub>4</sub> and CD<sub>4</sub>) is 0.158, i.e. a deviation of **±16%** from the value 1.0 for He. As this systematic error due to the correction of the He leak rate could partly compensate the systematic error of the calibration leak rate, – since they are independent – the errors are summed in the Gaussian way. Thus, in total the corrected flow rate is estimated to have a possible systematic error of **±20%**.

The statistical deviations during QMS calibration have been determined by a series of calibrations within few days resulting in deviations of around **±8-11%**. The long-term (10 months) stability of the calibration factors is within a factor of 1.24. From these calibrations a change of the sensitivity by **2-3%** per month can be deduced roughly, which is the longest duration between calibration and measurement.

Large sensitivity jumps can be detected by monitoring the pressure slopes of a long-term leak and frequent calibrations. In summary, the combined statistical error according to the Gaussian error propagation is **±12%** with an estimated systematic error of **±20%**. Thus, the total QMS uncertainty for a single measurement is **±32%**.

origin of uncertainty	importance for LID-QMS	timescale	relative error
QMS sensitivity	quantification of desorbed gas		<b><u>±32%</u></b>
consists of ...			
... total systematic error		permanent	<b><u>±20%</u></b>
... He calibration leak rate	QMS calibration	permanent	<b><u>±11%</u></b>
... species specific leak rate	calibration of species except He	permanent	<b><u>±16%</u></b>
... total statistical error			<b><u>±12%</u></b>
... daily statistical error	measurement and calibration	1 day	<b><u>±11%</u></b>
... monthly statistical error	QMS measurement	1 month	<b><u>±3%</u></b>
desorbed area (for ø2 mm)	for areal H concentration	permanent	<b><u>±15%</u></b>
desorbed area (for ø3 mm)	for areal H concentration	permanent	<b><u>±10%</u></b>
total measurement uncertainty (for ø2 mm)			<b><u>±36%</u></b>
total measurement uncertainty (for ø3 mm)			<b><u>±34%</u></b>

**Table 5.3.:** Error estimations for LID-QMS: determination of the average error of desorbed H (or D or CD<sub>4</sub> etc.) per unit area for a single measurement. Systematic errors are underlined. For the QMS it is added to its statistical error. The total errors for QMS and desorbed area are combined by Gaussian error propagation.

Sometimes the ratio of two LID measurements regarding one gas species is discussed. In this case the systematic error is not taken into account in the error calculation, because it has the same direction and size for both measurements and cancels out. The same is valid



for the uncertainty in the desorbed area. Moreover these measurements are usually done few minutes after each other, therefore also the monthly statistical error is disregarded. Most of the remaining statistical error is probably attributed to the gas filling procedure or flushing of the calibration leak and not to the QMS itself. Therefore the QMS deviations during LID are probably even smaller than during calibration, but this separation of the error sources could not be done. Thus, only a total uncertainty of  $\pm 9\%$  is assumed for a single measurement due to the short-time statistical deviations of the QMS that occur within a day. This results in a total error of  $\pm 13\%$  for the quotient of two LID measurements of one gas species.

In total, the uncertainties due to the QMS measurement and the desorbed area add quadratically to a final total error of  $\pm 36\%$  for the small laser spot of 2 mm in diameter and  $\pm 34\%$  for the 3 mm spot. Both are dominated by systematic errors and can thus be assumed to be mainly of systematic nature.

Sometimes two areal hydrogen densities on the same position are summed for a combined measurement result. In this case, the uncertainties of both measurements could compensate each other partly, but also add. Usually this is done for an LID spot of  $\varnothing 3$  mm and a melting LIM spot of  $\varnothing 2$  mm inside it. Both errors are combined by Gaussian error propagation to a total error of  $\pm 50\%$ .

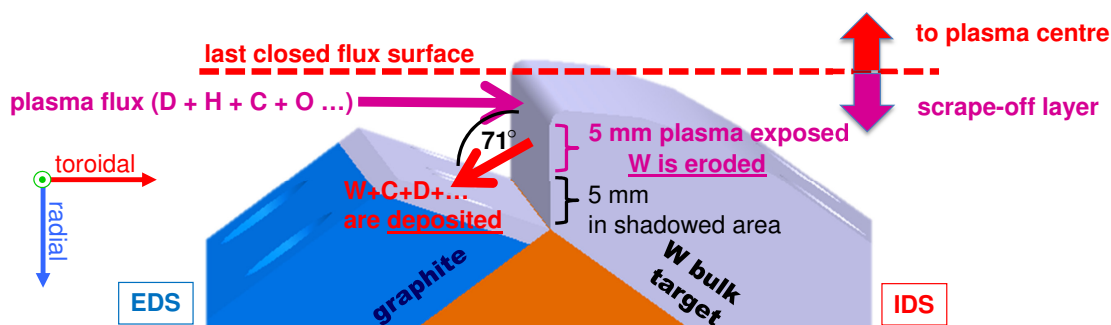
Until now the error estimation for a single measurement has been discussed, i.e. for the case when it cannot be repeated under the same conditions and circumstances. The estimated errors are applicable e.g. for inhomogeneous samples, where no sure assumption can be made that several measurement positions are virtually identical with respect to the measured quantity. These error estimations also have to be used for cases when several positions can be assumed identical but the measurement conditions like choice of laser spot size, inclination, pulse parameters etc. or relevant conditions of the QMS are changed.

If this can be excluded and several places on a sample can be assumed identical with high certainty, then a measurement series is possible. Then, the statistical errors do not have to be estimated in the way above, but can be calculated statistically and added to the total systematic error, which is  $\pm 25\%$  (for  $\varnothing 2$  mm) and  $\pm 23\%$  (for  $\varnothing 3$  mm). For a measurement series, the same quantity as above, namely the *average error of a single measurement* can be calculated by the standard deviation as the statistical error and added to the systematic error. But it is not very interesting for a series as it does not decrease the uncertainty significantly and thus makes not much use of the measurement repetitions. To narrow down the uncertainty of the real hydrogen concentration and thus push the boundaries closer to the real value, the *average error of the average value* is calculated. It is also known as confidence interval (with 68.3% confidence level) and is used instead of the average error of a single measurement in the present work when measurement series are performed.

# 6. Applications of Laser Induced Desorption (LID-QMS)

## 6.1. Laser Desorption from Mixed C/W Layers

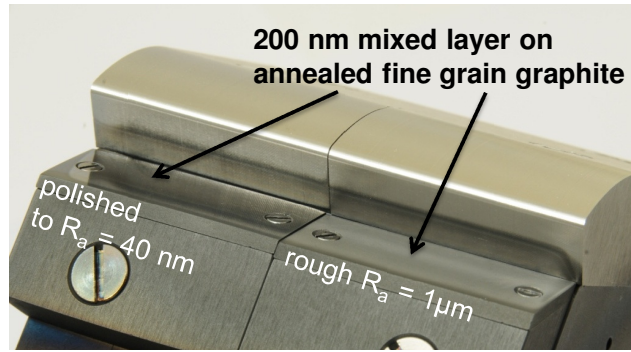
Since a mix of Be/W/C or Be/W alone is favoured as first wall material for ITER, the growth and analysis of mixed layers of these materials comes into the focus of research. In TEXTOR, the plasma usually does not contain W or Be as the PFCs are mainly made of carbon. Mixed C/W layers have already been formed in tokamaks and plasma devices by injection of W in gaseous form (e.g.  $WF_6$ ,  $W(CO)_6$ ) [Kirschner11][Krieger99][Geier2]. By gas puffing a stratified structure in the depth profile of the mixed layer is often obtained due to different gas puff rates and phases without gas puff. The layers are usually deposited around the gas inlet and therefore they are inhomogeneous also in lateral direction. In order to generate a more homogeneous mixed C/W layer, a dedicated limiter has been designed (figure 6.1).



**Figure 6.1.:** Limiter designed for growth of mixed material layers in TEXTOR

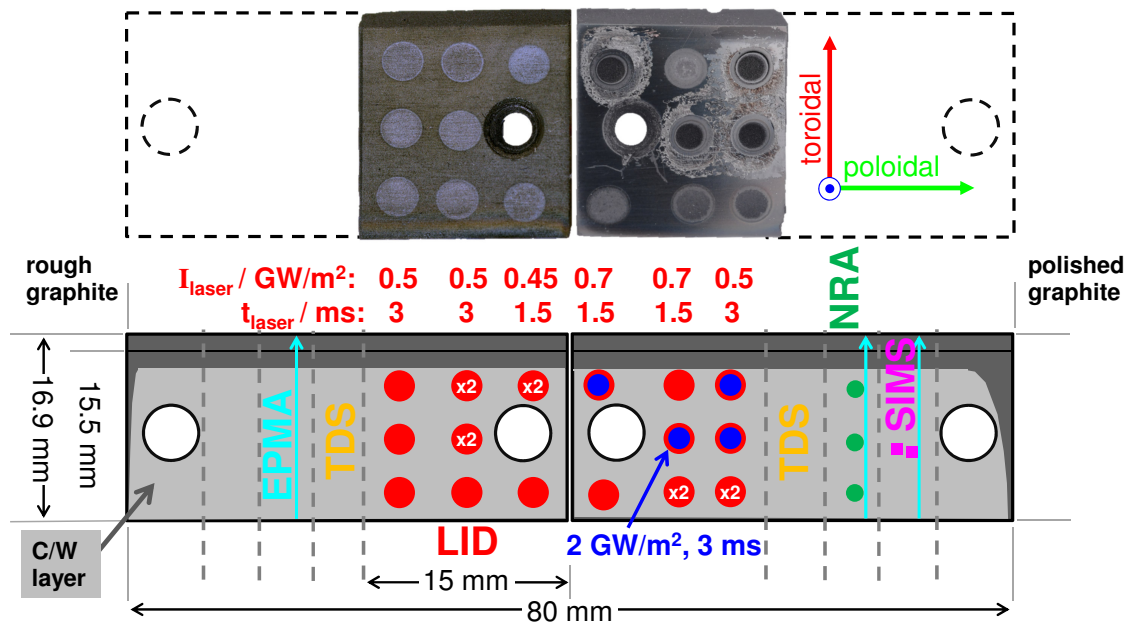
The plasma flux sputters the bulk W target. The sputtering surface has been oriented vertically to achieve the maximum plasma influx. The W atoms are sputtered over a radial distance of 5 mm from the limiter tip and the smoothed top edge. A fraction of them is entering the shadowed volume in the lower 5 mm of the vertical surface, which forms a wide open gap of 71° with the collector plate. The remaining 19° angle between the collector plate and the magnetic field lines allow the background plasma to enter the shadowed region and introduce a permanent carbon impurity flux into the gap volume. Together with the sputtered W both are deposited on the collector plate, which is not exposed to the main plasma flux (except its short side surface) and therefore should have very low or no erosion, thus the mixed layer can grow fast. As can be seen on the limiter after exposure (figure 6.2) the shadowed 5 mm of the sputter target are covered with carbon due to the carbon impurity flux from the plasma, while the exposed area is an erosion dominated area. H and D from the main plasma are co-deposited with the carbon and tungsten to form a hydrogen rich mixed layer.

The limiter has been exposed in limiter lock 3 at the top of TEXTOR. The limiter tip was at 47-47.5 cm radial plasma position for 3 discharges, 46.3 cm for 12 discharges and finally at 46.0 cm for 18 discharges exposed to identical ohmic plasmas ( $I_p = 355$  kA,  $B_t = 2.26$  T,



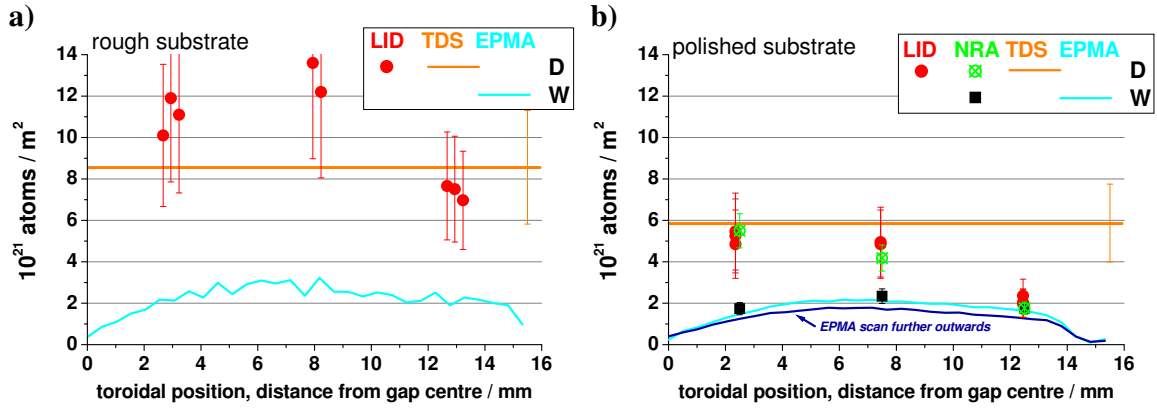
**Figure 6.2.:** "Mixed material limiter" or "big-gap limiter" after 3 min exposure to TEXTOR plasma, a 200 nm fuel enriched C/W layer has grown

$\bar{n}_e = 2 \cdot 10^{19} / \text{m}^3$ ). In total, the time during plasma exposure was 180 s (FWHM of  $I_p$ ). The bulk temperature 2 mm below the surface of the limiter block (orange object in figure 6.1) reached 410 K in the outward position and 460 K for the inward position, while the maximum surface temperature measured by a pyrometer was 640 K and 970 K, respectively. The mixed layer was deposited on two exchangeable collector samples of fine grain graphite, which had been annealed at 1273 K in a different vacuum chamber. One of the graphite surfaces has been mechanically polished prior to annealing, in order to compare the layer growth on polished and rough surfaces and to obtain better depth information in the later SIMS analysis.



**Figure 6.3.:** Allocation of different diagnostic applications on a mixed C/W/H/D layer grown in TEXTOR: LID for surface H and D contents; TDS for total H and D contents; NRA for surface D and W; EPMA for surface B, C, O and W; SIMS for depth profiles of all mentioned elements

The layer composition and material distribution has been determined by analysing the electron induced x-ray emission (EPMA-technique = Electron Probe Micro-Analysis, identical to quantitative EDX) of all the components except H and D. The linescans were done in toroidal direction along the collector plate (cf. figure 6.3). On the polished collector plate, the maximum of the W concentration occurs 5-9 mm from the gap centre and reaches 1.8-



**Figure 6.4.:** Deuterium and tungsten concentrations in a C/W/H/D mixed material layer grown in TEXTOR; result comparison of LID, NRA, TDS and EPMA;  
 a) deposition on rough graphite; b) simultaneous deposition on polished graphite

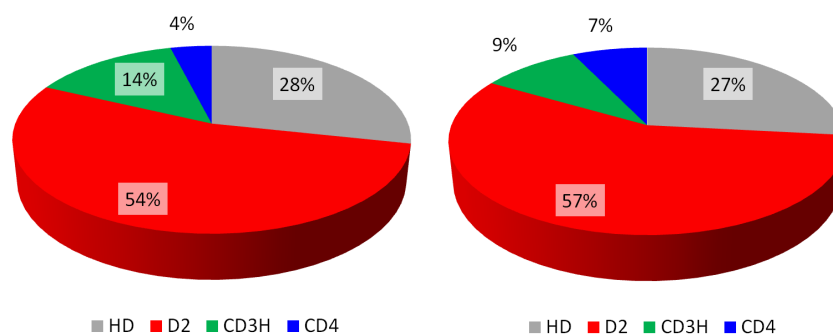
$2.1 \cdot 10^{21}$  W-atoms/ $m^2$  depending slightly on the poloidal position (cf. figure 6.4b). These values agree very well with NRA results in 3 spots on the same sample. The rough surface has a higher effective sticking probability, thus  $2.7 \cdot 10^{21}$  W-atoms/ $m^2$  is reached (figure 6.4a). All EPMA scans on the rough surface have a much higher signal scatter, indicating that the layer deposition is more inhomogeneous than on the polished samples. Clearly, W concentrations were also detected by SIMS and EPMA on the 2 mm thin plasma facing side of both samples, but a factor of 5 lower than the values on the main surface. In the EPMA analysis also oxygen ( $1.5 \cdot 10^{21}$  O/ $m^2$  on the rough surfaces and  $0.5$ - $0.8 \cdot 10^{21}$  O/ $m^2$  on the polished surfaces, corresponding to about 4-5 at%) and traces of boron (ca. 1 at%) were found.

The D retention was measured spatially resolved by LID-QMS. Two different LID pulse parameters with  $700$  MW/ $m^2$  for 1.5 ms and  $500$  MW/ $m^2$  for 3 ms were used, resulting in the same amounts of desorbed D. The retention profile shows a maximum in the sample centre for the rough substrate with values up to  $1.3 \cdot 10^{22}$  D/ $m^2$ , while on the polished sample the maximal retention is found closer to the gap centre, reaching only  $5 \cdot 10^{21}$  D/ $m^2$ . The shifted D maximum in comparison to the W maximum in the sample centre indicates that the deposition processes of different elements are decoupled from each other. In 4 LID spots (● blue dots in figure 6.3) on the polished substrate, the maximum laser intensity achievable for graphite was applied in a second laser pulse, to prove complete desorption by the first pulse. With a reduction of the spot size to 2 mm diameter the spots fit into the 3 mm spots of the first laser pulse and  $2$  GW/ $m^2$  absorbed intensity are reached for 3 ms. The material overheats and strong C sublimation occurs, which results in a very dark spot (cf. top image in the figure). The evaporated material was deposited on the inner wall of the desorption chamber and the laser entrance window, which decreased the laser beam transmission considerably. After only 14 of this strong C evaporation events, the window absorbed enough power from the laser beam, that it burned from the inside of the chamber. On the sample this strong heating leads to a contraction of the thin layer from regions up to 2 mm outside the spot border into the direction of the spot (details in chapter 3). The D released in these hot shots was always below 1% of the D released in the first laser pulse except in one spot, where it was 4%. Therefore laser induced desorption from a-C:H layers even with minor addition of W is complete in the first laser pulse.

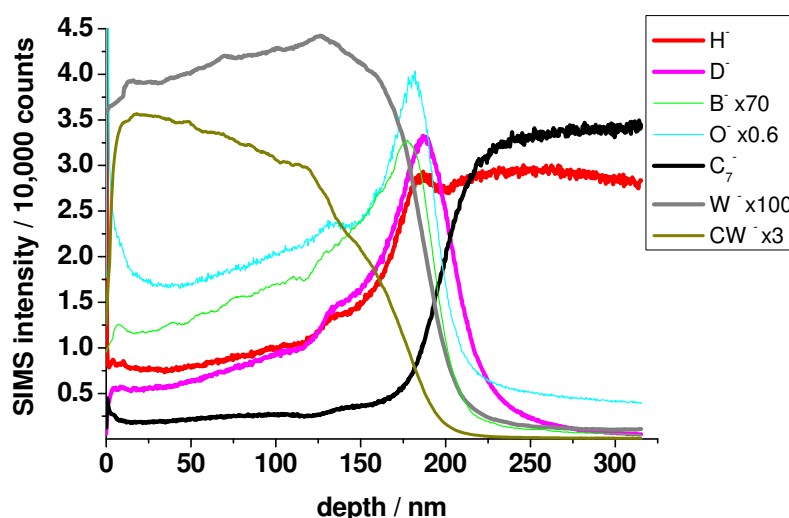
NRA detects up to  $5.5 \cdot 10^{22}$  D/ $m^2$  in perfect agreement with the LID-QMS results and confirms the LID data in all three measurement positions very well. From the same NRA measurements also the W concentration has been evaluated, which confirms the results from EPMA measured in the same poloidal position.

The total H and D content has been measured on 5 mm broad slices of each central part of the two samples by TDS (cf. figure 6.3). Also here the sticking of D seems to be slightly higher on the rough surface, which results in  $8.6 \cdot 10^{21} \text{ D/m}^2$  compared to  $5.9 \cdot 10^{21} \text{ D/m}^2$  on the polished surface. Compared to the integrated D retention measured by LID-QMS, TDS underestimates the total D amount in the rough sample by a factor of 1.2 and overestimates the D retention on the polished substrate by a factor of 1.4 compared to LID-QMS and NRA.

In LID and TDS the deuterium desorbs mainly as  $\text{D}_2$  and HD (cf. figure 6.5), while a smaller fraction of 11-23% desorbs as hydrocarbon molecules. This fraction is also typical for the desorption of pure a-C:H/D layers without W, indicating that the mixed layer here is very similar to a W-free a-C:H/D layer concerning its desorption characteristics.



**Figure 6.5.:** Fraction of deuterium retained in different desorbing molecules during desorption of a mixed C/W/H/D layer grown in TEXTOR; left: TDS; right: LID-QMS



**Figure 6.6.:** SIMS depth profile of the mixed material layer in its thickest part (cf. marking "SIMS" in figure 6.3); some signals are scaled to fit the range (see legend)

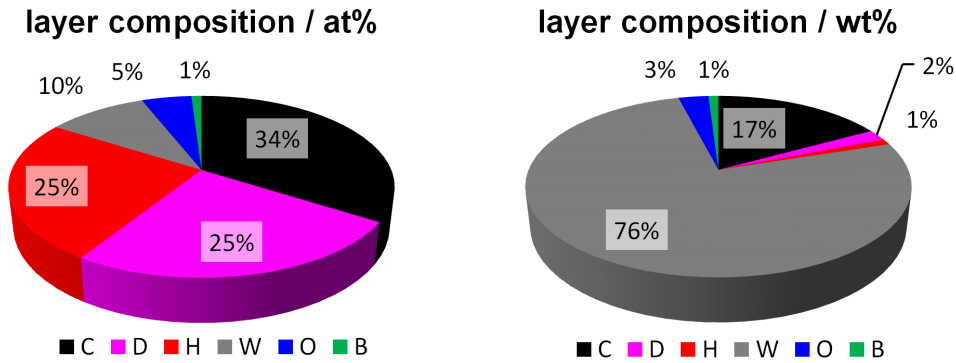
The SIMS profile (figure 6.6) shows nearly identical depth distributions of H and D in the layer. Both slopes increase from the surface to the peak at the interface to the substrate. The D signal then drops abruptly, while the H signal stays constant in the substrate on a level which is about a factor of 3 higher than in the layer. The H/D ratio in the layer is therefore nearly 1. It is slightly higher than 1 at the surface and slightly lower than 1 in the deeper part of the layer.

Combining the EPMA results (for surface content of C, W, O, B), TDS (for total H, D), SIMS (for H/D ratio in the layer), NRA (for the W, C and D content) and LID-QMS (for H, D

in the surface), the average composition of the layer can be deduced (cf. figure 6.7):

34 at% C, 25 at% D, 25 at% H, 10 at% W, 5 at% O and 1 at% B  
 17 wt% C, 2 wt% D, 1 wt% H, 76 wt% W, 3 wt% O and 1 wt% B.

Concerning the atomic fractions, the layer is dominated by carbon and hydrogen, while concerning the mass fractions it is a W dominated layer.



**Figure 6.7.:** Composition of a mixed material layer grown in TEXTOR on a dedicated limiter

The thickness of the layer has been determined by a combination of SIMS and mechanical profilometry, i.e. beside the measurement of the sample composition in a deep SIMS crater ranging far into the substrate, a second crater is created for the calibration of the depth. This calibration crater is placed in a position of nearly identical sample properties few millimetres from the first crater in poloidal direction. In this direction the layer properties do not change significantly according to EPMA and LID. The calibration crater has been created with the same sputter properties. To achieve identical sputter speed, not only the sputtering beam (in this case  $\text{Cs}^-$ , 1 keV on  $0.3 \times 0.3 \mu\text{m}^2$ ) but also the analysis beam ( $\text{Bi}_3^+$ , 25 keV,  $0.1 \times 0.1 \mu\text{m}^2$ ) have been used with the same currents as for the deep crater, although the sputter speed of the analysis beam is usually negligible with a monolayer in some hours. The production of this calibration crater is stopped, when the signal of the substrate (here carbon, viewed with good contrast on  $\text{C}_7^-$  clusters) has reached half of the value that is measured in the pure substrate. Both craters are measured at the same day with a small time delay of ca. 1 hour to each other. Within this time period the probability for instabilities in the SIMS processes (e.g. in the speed or intensity of sputtering due to beam source changes) is de facto excluded. The time for stopping the excavation of the calibration crater is already known from the measurement of the deep crater. In the present case, the calibration crater at the maximum of the layer thickness needed nearly half an hour to dig a crater of 200 nm. This value has been used to convert the sputter time into depth in figure 6.6. The described procedure is applicable without large distortion of the x-axis only for layers with a quite homogeneous depth profile, because every element has a different sputter speed. Thus the depth is not a linear function of time for highly stratified layers. Fortunately the C/W mixed layer is quite homogeneous in depth. The problem of sputtering bulk W can already be assessed here to be critical in terms of measurement time, since this layer only consists to 10 at% of W and already has such a low sputter speed. An analysis in bulk W is therefore an extremely time consuming task. Besides this, an extremely long time also introduces problems with the machine stability, which limits the maximal analysis time and therefore the depth.

For bulk W it is therefore difficult to sputter much larger depths than a few hundreds of nanometres. The sputtering speed in the C substrate is much faster than in tungsten, therefore an exact stopping of the sputter process is more difficult, but essential for a good depth calibration by surface profilometry.

This experiment showed that an a-C:H/D layer with additional content of W up to 10 at% generated by simultaneous deposition of C from the plasma and W from sputtering behaves like a pure a-C:H/D layer with respect to the hydrogen retention. The composition, depth profile and desorption characteristics are very similar, however the unexpected high surface temperatures in laser heating (cf. chapter 2.4.4) show differences in the thermal properties. To explain this, the heat conductivity and capacity of this layer should be measured, e.g. as described in chapter 2.4.3. Further progress in this field should pursue to generate mixed materials with higher metallic content to identify material concentrations, where the desorption changes qualitatively from the C-like prompt desorption to W-like diffusion dominated desorption. The characteristics of the latter will be studied in the next sections.

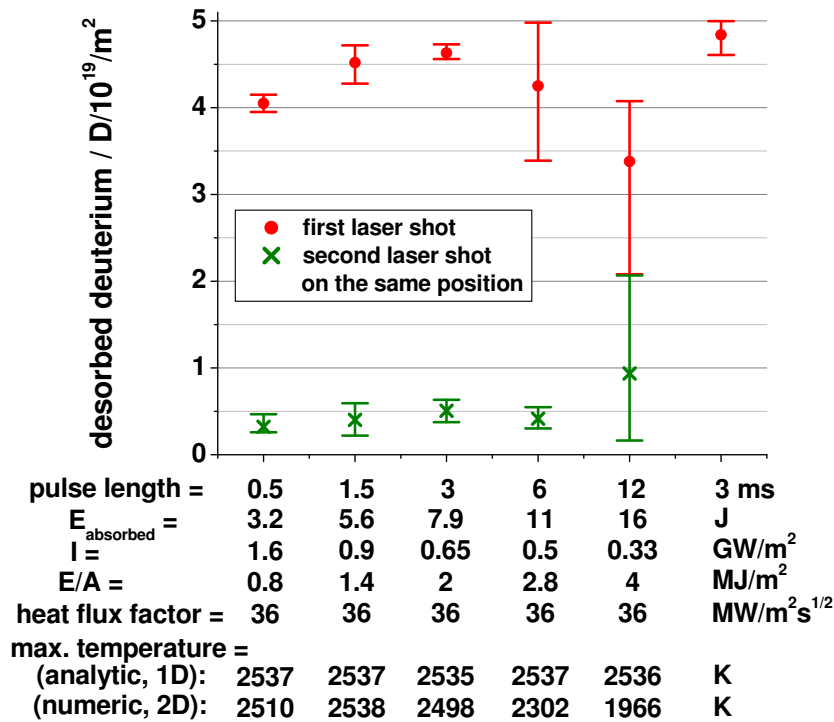
## 6.2. Laser Desorption from Bulk Tungsten

In order to extend the operational space of Laser Induced Desorption (LID) to tungsten materials, bulk W samples have been exposed in different deuterium plasmas with very different exposure conditions. The scope ranges from small laboratory plasma devices with glow discharges and low fluxes in the order of  $10^{19}$  D/m<sup>2</sup>s up to tokamak plasma in TEXTOR and linear plasma devices that simulate divertor conditions of ITER with fluxes in the order of  $10^{24}$  D/m<sup>2</sup>s. Five examples will be discussed here to show the main effects occurring in LID on W, some of which are also published in [Z13]. Since the main focus was to study different exposure conditions rather than the influence of material properties, the same material was used wherever possible and all samples have been annealed at 1273 K for at least one hour under high vacuum.

Two unpolished ( $R_a = 1.2$  μm) W samples of  $40 \times 55 \times 2$  mm<sup>3</sup> (polycrystalline, rolled W with 99.95 wt% purity\* provided by Goodfellow GmbH) were exposed to a deuterium plasma in an RF glow discharge in the PADOS facility. The plasma flux was  $2.8 \cdot 10^{19}$  D/m<sup>2</sup>s and the exposure time 2 hours, which results in a fluence of  $2 \cdot 10^{23}$  D/m<sup>2</sup>. In order to reach D impact energies like in the TEXTOR edge plasma, the samples were biased negatively with 500 V. Since roughly 2/3 of the bias are utilised for the D<sub>2</sub><sup>+</sup> ion acceleration and the impact energy is shared on both deuterons, this results in ca. 170 eV per D. A heater, which was integrated in the sample holder, kept the sample temperature constant at ca. 533 K during the exposure. The D loading of both samples and within each sample is homogeneous, since the sample holder, which also serves as the cathode of the discharge, is 129 mm in diameter and thus larger than the samples. The homogeneity was also proved by a line scan with LID with constant laser parameters.

The aim of the study was to investigate the influence of the laser parameters, especially the pulse duration for the desorption of D from bulk W. The pulse duration was varied between 0.5 and 12 ms. With each setting 4-8 different spots in a row on the sample were desorbed. The heat flux factor was kept constant, thus the analytically calculated surface temperature reaches always the same maximal value of ca. 2500 K. Figure 6.8 shows the amount of desorbed deuterium as an average of each row of laser spots. The bars represent the minimal and maximal value for each row. The average values show a maximum desorption for a 3 ms pulse duration. Shorter pulses induce lower desorption, because the time of the hot phase is shorter and therefore the time for the diffusion of D in the W bulk is shorter. Longer pulses of 6 and 12 ms have more time for diffusion, but on average also a lower desorption, because of increased lateral heat diffusion. These are general effects, which are obvious from the temperature distribution calculated by the two dimensional temperature simulation.

\*see Appendix A for details on the W material



**Figure 6.8.:** Optimisation of laser pulse duration on homogeneously D loaded bulk tungsten; LID-QMS with constant heat flux factor; The bars show the minimal and maximal values of a series of 4-8 desorbed positions. The values show their average.

1. The real maximum temperature is already lowered for such long pulses (cf. table in figure 6.8) due to longer contact to the cold surrounding bulk. While always the same temperature is reached by the shorter pulses up to 3 ms, it already reduces by 200 K for 6 ms pulses and by more than 500 K for 12 ms pulses.
2. The temperature profile on the surface is smoothed out for longer pulse durations, when compared at the end of the laser pulse. This leads to large areas inside the laser irradiated spot which are only partly desorbed and to partly desorbed regions outside the laser spot. Thus for the long pulses the neighbouring desorption volumes start to overlap even for a distance of 4-5 mm between the spot centres. The spot size of the laser irradiated area on this sample was  $\varnothing 2.25$  mm in diameter.

Due to these effects the average desorbed amount reduces and the scatter of the desorption values increases to an unacceptable extent. Thus for LID the pulse duration for the standard desorption pulse is chosen as 3 ms. The numeric temperature calculations were done with a rectangular wave pulse in time, to show that these effects appear for an ideal temporal laser wave form, since they are due to the nature of heat diffusion. For the real laser pulses, the effects described above are even stronger. The short pulses do not reach full power instantly (cf. chapter 2.2) and therefore the hot phase is even shorter. The long pulses decay in intensity slightly (cf. chapter 2.2) after the intensity maximum and therefore lead to even lower lateral temperature gradients.

For every measurement position a second laser pulse with the same settings was applied to the same position. For all pulse durations except 12 ms the second pulse yields about 10% of the desorption of the first pulse. The average values and also the individual pulses show a tendency that the second pulse signal is proportional to the first pulse signal. This is the typical behaviour, found on many other samples. On the contrary, for the 12 ms pulses this behaviour is turned to the opposite, since the second pulse signal is high when the first pulse



signal was low and vice versa. Obviously for these extremely long pulses the second pulse continues the desorption of the first pulse, which might be due to the increase in the heating depth. However the badly defined desorption area, the large signal variations and especially the lower desorption of the first laser pulse make this settings unpractical. Particularly for the spectroscopic detection a high desorption per single laser pulse is essential due to the increased signal background.

The 3 ms pulse settings were repeated at the end of the measurement series (last data point in the figure) to exclude the influence of systematic effects like sample inhomogeneity, degradation of laser power, fibre transmission or QMS sensitivity change. The data scatter again decreased to typical ranges for the short pulses and the average value of desorbed D even slightly increased compared to the previous 3 ms series, proving that the performance of the long laser pulses was a real effect based on desorption physics.

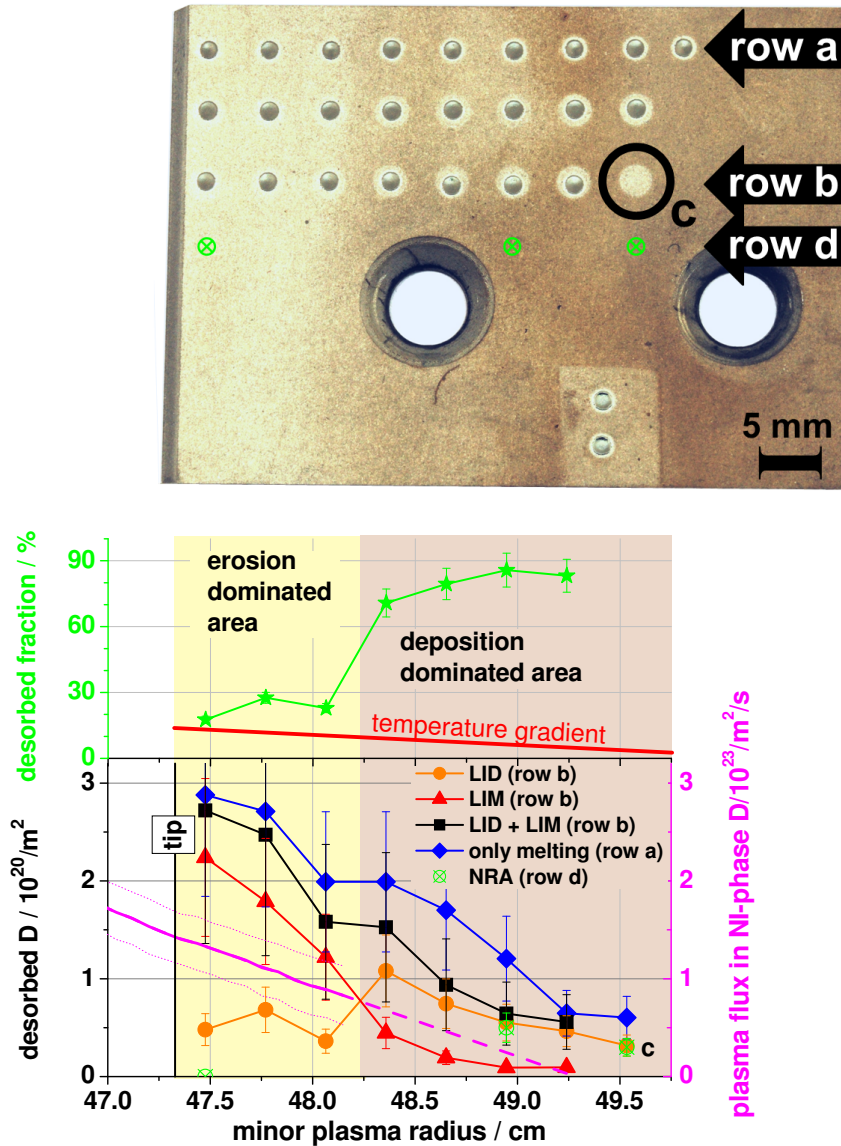
On average all LID measurements with 3 ms pulse duration result in a desorption of " $4.7 \cdot 10^{19}$  D/m<sup>2</sup> in the first laser pulse and  $0.5 \cdot 10^{19}$  D/m<sup>2</sup> in the second pulse." [Z13] The TDS measurement of the second bulk W plate exposed simultaneously shows  $7.4 \cdot 10^{19}$  D/m<sup>2</sup>, thus only 65% of the retained D was released and detected by LID. Although the flux and fluence on this sample are very low compared to the following samples, LID could not desorb all the retained deuterium. The main reason for this low desorption fraction will become clear in comparison to the other exposures. The increased sample temperature during deuterium loading will be shown to be the main parameter that determines the desorption fraction released by LID due to deeper diffusion and population of traps by the deuterium. "As a consequence less D can be desorbed by LID compared to LIM and TDS." [Z13]

With the optimal LID desorption duration of 3 ms, the retention and desorption characteristics of the following samples will be discussed, which represent different exposure conditions. The first sample was exposed in TEXTOR and had the highest surface temperature during plasma exposure. The sample loaded in the linear plasma in Pilot-PSI experienced the highest plasma flux. An exposure in an ECR plasma in the PlaQ device [Manhard11a] had the longest exposure time and lowest surface temperature and a sample in the linear plasma of PSI-2 received the highest plasma fluence of all studied bulk W samples. An overview of the samples discussed here with their exposure conditions and desorption results is given in table 6.1 on page 154. The following studies are partly published in [Z13].

In the TEXTOR tokamak, an unpolished ( $R_a = 1.2 \mu\text{m}$ ) bulk tungsten plate of  $40 \times 55 \times 2 \text{ mm}^3$  (polycrystalline, rolled W with 99.95 wt% purity provided by Goodfellow GmbH) was mounted on a roof limiter towards the electron drift side of the plasma. The sample surface was "tilted  $36^\circ$  with respect to the toroidal B-field. The limiter was transferred into the main plasma chamber from the bottom and the tip was positioned 1.3 cm behind the last closed" flux surface (LCFS). The sample "was exposed to a maximal fluence of  $1.7 \cdot 10^{25}$  D/m<sup>2</sup> at the tip" [Z13] and to  $1.5 \cdot 10^{25}$  D/m<sup>2</sup> at the closest analysis position to the tip. The total accumulated plasma exposure time was 110 s. The fluence had a spatial dependence along the sample according to the radial decay of the flux as shown in figure 6.9 (right magenta scale). This distribution is valid for the typically 3 s long duration of plasma heating with Neutral beam Injection (NI-phase) during every discharge. The flux is calculated from the  $n_e$ ,  $T_e$  measurements by the supersonic helium beam diagnostic. The dotted lines show the statistical error based on these data and the dashed line is a linear extrapolation. Thermocouple measurements 2 mm below the surface of the sample holder and 22 mm from the tip showed maximum temperature excursions of 400-700 K. The sample temperature certainly exceeded these values due to bad heat contact between sample and holder. Especially the tip of the sample reached temperatures above 700 K as images of the 2 mm thin sample side show, which were recorded during the discharges by a CCD camera with a filter for 656 nm light (with 3 nm spectral FWHM). A

## 6. Applications of Laser Induced Desorption (LID-QMS)

strong thermal radiation signal corresponding to  $T > 700$  K at the tip was observed, which was later cross-checked with a sample of the same material by heating it in the same position with an internal heater. The upper limit of the temperature can be roughly estimated to ca. 1000 K. In radial direction the temperature gradient is very strong, which is visible on the camera images that show a strong decay of the heat radiation after ca. 7 mm in radial direction. In poloidal direction the temperature is assumed to be constant. "The electron temperature of 30 eV at the limiter tip results in deuterium impact energies of up to 140-180 eV due to sheath acceleration." [Z13]



**Figure 6.9.:** Left axis: Laser Induced Desorption (LID) and Melting (LIM) on bulk W after deuterium plasma exposure in TEXTOR; Nuclear Reaction Analysis (NRA) data of retained D for comparison; right axis: plasma flux during exposure; figure similarly published in [Z13]

"Figure 6.9 shows a picture of the tungsten plate after LID measurements. A spot of 3 mm diameter was heated up to 1800 K by a laser pulse with 10 J absorbed energy in 3 ms corresponding to 500 MW/m<sup>2</sup> (standard LID pulse). To assess fuel which possibly was not released in

these pulses, the central area of the spot was molten by reducing the spot size to 2 mm diameter and increasing the energy to 15 J corresponding to  $1.6 \text{ GW/m}^2$ . [Z13] It has been verified previously by TDS after LIM that this melting procedure releases the retained D completely. Two different measurement series were performed on this sample. In row (a) only LIM was applied, while in row (b) first laser heating (LID) and then melting (LIM) in the heated spot centre were performed. In spot (c) only LID was done. The following LID and LIM results are normalised to the corresponding laser heated or molten area, respectively and are presented in figure 6.9. The D desorption without melting in row (b, ●) is always lower than the release from the spots in row (a, ◆). This is a first hint, that laser heating to 1800 K is not sufficient for complete desorption although this fact alone might still be explained by small-scale poloidal inhomogeneities. The proof of this hypothesis is given by melting of the already heated spots of row (b, ▲). The D amount, which is only released by melting is especially high for the first three measurement positions from the sample tip. For the other positions, it is lower than the D amount desorbed in the first pulse and it quickly reduces almost to zero.

"Generally the inventory decreases with increasing plasma radius and decreasing particle fluence, as expected" [Z13] for the erosion dominated area. On the contrary, the LID signal increases again at 48.4 cm, which is at the same position where the LIM signal becomes lower than the LID signal. "This is correlated with the start of the deposition of a ca. 30-50 nm thin carbon layer at larger plasma radii, visible also in" the image of the sample in brown colour. "The ratio of the amount desorbed until 1800 K to the total amount of D is" [Z13] shown as the *desorbed fraction* in the upper part of the figure and is often called desorption fraction. Although the total D inventory is best released by only melting once, here the sum of the LID pulse and LIM pulse on the same position (row b, ■) has been used as reference. This is done, because the sum does not equal fully to the LIM data of row (a, ◆), although they are expected to agree. The agreement is good in the erosion dominated area especially for the first two measurement positions, but deviations start as the hydrocarbon layer begins to build up. At the last measurement point they again agree well. The mismatch is attributed to poloidal inhomogeneities in the layer, since row (a) and (b) are already about 1 cm shifted in poloidal direction. Such poloidal inhomogeneities are known from many other exposures, where they are more obvious due to colour fringes, when the a-C:D layer is thicker. Therefore, the best approximation to the total D inventory at row (b) is the sum of LID and LIM pulse in the same row.

In the erosion dominated area, the LID-desorbed fraction of the total inventory is only 18-28% and jumps to nearly 90% in the deposition dominated area. Here, the nearly complete desorption by LID is very similar to the results for "a-C:D layers deposited on carbon materials. In the deposition zone the majority of D is retained in the carbon layer acting as a barrier for further penetration of D atoms into the W bulk. The carbon layer retains larger amounts of hydrogen when exposure time and fluence increase, but acts also as a protection barrier for deuterium diffusing into the W material." [Z13] This is proved by the fact that the LIM pulse on an LID spot releases nearly no further deuterium. If the deuterium was not only in the C layer, but also diffused into the tungsten, then the LIM signal would be as dominant as in the erosion dominated area. The existence of a diffusion barrier is very plausible, since the implantation depth of deuterium is less than 20 nm (cf. the introduction) and thus smaller than the layer thickness, that has been measured by ellipsometry in several positions. The implantation zone is therefore completely inside the hydrocarbon layer, in which the D atoms are chemically bound strongly to the C atoms and cannot move to reach the W substrate.

In the erosion dominated area, impinging C atoms, which are deposited here shortly, are eroded again. Therefore the impinging D atom is implanted directly into the tungsten, where it starts to diffuse and can reach depths of several micrometres due to a high diffusion coefficient

at the high temperatures. A further proof of this interpretation are the measurements of the D inventory by Nuclear Reaction Analysis (NRA). The NRA measurements were done in three positions on the sample in row (d, ⊗) as shown in the figure. The two values in the deposition dominated area agree very well with the LID values, which are practically equal to the sum of LID and LIM in this area. But in the area close to the tip, NRA could not detect any deuterium. Although the measurement was done for about half an hour on one position, not a single D count could be detected. This can only be explained by a very low D concentration at the sample surface, in the detection depth of NRA. The NRA method uses  $^3\text{He}$  with 2.35 MeV penetrating tungsten up to ca.  $3\ \mu\text{m}$  depth. Consequently, the D inventory in the first  $3\ \mu\text{m}$  must be lower than the detection limit of NRA (ca.  $10^{19}\ \text{D}/\text{m}^2$ ) and the main fraction of the inventory must be deeper in the material. Since the depth of the laser melting pulse is 30-50  $\mu\text{m}$  as shown in chapter 3.3, the deuterium must mainly be retained in depths between 3 and 50  $\mu\text{m}$ .

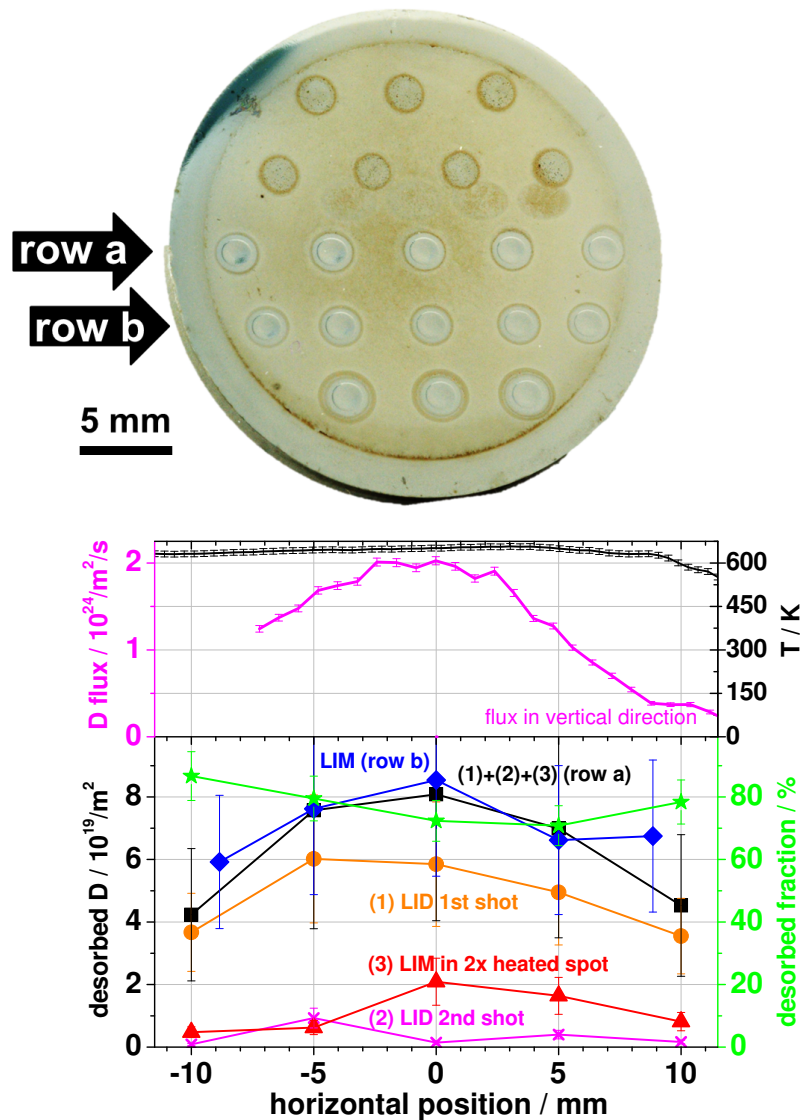
The same attempt to measure the D inventory by NRA was done on an identical W sample with the difference, that it had been polished to an arithmetic mean roughness of  $R_a = 30\ \text{nm}$  before annealing. A second difference was, that it was exposed only once, while the rough sample had already been used for exposure to a glow discharge deuterium plasma and heated to 1273 K afterwards a second time. The polished sample was exposed simultaneously with the rough sample in TEXTOR but on the ion drift side of the limiter. It has similar absolute D retention and desorption behaviour, with two modifications mentioned later. On the polished sample two NRA measurements were done at analogous positions at the first and sixth laser spot position from the tip, without being able to measure a single deuterium count. In contrast to the rough sample, both positions were in areas with no hydrocarbon layer, since the layer was localised to a smaller poloidal region on the polished sample, which is a well known effect of lower sticking probability for carbon on polished surfaces.

It should be stressed here that LID and LIM have a huge advantage over NRA in retention analysis, when deuterium is located deep in high-Z materials, since the LIM analysis depth is one order of magnitude larger. This is also shown for a W sample exposed to an ECR plasma, where even a 6 MeV NRA beam that reaches up to 12  $\mu\text{m}$  deep, could only detect 80% of the deuterium desorbed by TDS (details follow after the discussion of the next sample). However, with respect to analysis depth, TDS is superior to all methods, because the whole sample is heated.

The main effect of deep D diffusion and thus strongly reduced LID desorption fraction and low D signals in NRA is typical for TEXTOR samples, but in reduced extent as shown here. Since this sample had the highest exposure temperature, the effect is strongly emphasised here. More typical for TEXTOR exposed samples is not a monotonously decreasing total retention with plasma radius like here, but a clear increase where the a-C:D layer starts. Usually the sample is exposed further outside the plasma and thus the erosion dominated area is smaller and the layer thickness is several hundreds of nanometres. Then the total retention in the deposition dominated area is larger than in the erosion dominated area. At the same time, the desorbed fraction in the erosion dominated area increases due to lower sample temperatures than here and the effect is not as clearly visible as in the sample presented here. To a lesser extent this is also the case for the mentioned polished twin sample of the sample in figure 6.9. It has a slightly higher desorption fraction at the tip, which is sensible since the temperature of this sample was lower as seen on the camera images. Thus the deuterium did not diffuse as deep as in the rough, hotter sample.

In order to study the influence of even higher plasma flux, that is as high as expected in maximum in the ITER divertor, bulk tungsten was exposed in the Pilot-PSI facility. For the best comparison to the TEXTOR case, the same tungsten grade was used with polished surface, but circular in shape. Also the fluence was chosen similar to TEXTOR, which was achieved

with fluxes of up to  $2 \cdot 10^{24} \text{ D/m}^2\text{s}$  during 10 s and "an energy of 1.2 eV additionally accelerated by a negative biasing voltage of 55 V. These fluence and particle energy are comparable with those in the erosion zone of the TEXTOR sample." [Z13] The sample was actively cooled by a water flow at its rear side, which could cool the sample effectively due to a good heat contact established by brass foil and grafoil. Thus, the plasma exposed surface reached 655 K in the centre and 620 K at the edge, according to the peaked shape of the flux in the plasma centre. "Flux measurements were performed in vertical direction by Thomson scattering whereas an LID profile of retained D was obtained in horizontal direction. The data indicate a small deviation between the plasma beam and sample centre, which is also observed by the IR camera measurements." [Z13] It occurred when the biasing was applied to the sample, probably due to asymmetric radial components of the electric field. The measured fluence distribution and the LID results obtained in the orthogonal direction are shown in figure 6.10.



**Figure 6.10.:** Radial profile of exposure conditions and LID-QMS results on a tungsten sample exposed to deuterium plasma in Pilot-PSI; data partly published in [Z13]

"With the standard laser" heating "pulse (1, ●) a maximum of  $6 \cdot 10^{19} \text{ D/m}^2$  was desorbed in the first pulse. This is nearly identical with the value observed in the erosion zone of the TEXTOR sample, applying the standard laser heating pulse. Figure 6.10 shows in addition the profile of desorbed deuterium in a second laser pulse on the same spots (2, ×), which was

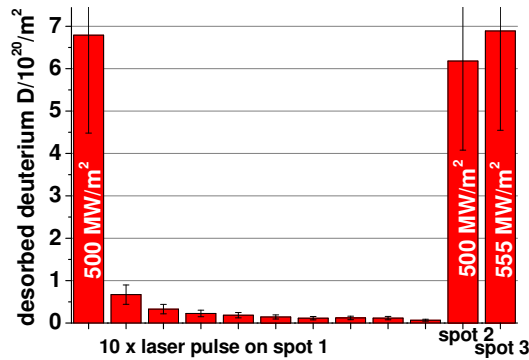
always below 10% of the amount in the first pulse." [Z13] There is only one exception at the position of  $-5$  mm. This second LID pulse has not been done on the TEXTOR sample, but on many other bulk W samples, showing that further heating pulses can never release significant amounts of the remaining deuterium.

In a third series (3, ▲), the inner part of the same spots was molten to release D which might still remain in the material. This Laser Induced Melting (LIM) pulse indeed releases considerable amounts of deuterium, that have not been desorbed by the two heating pulses. While the heating pulses have their maximum left of the sample centre, the melting pulse maximum is shifted more to the right side. This is well explained with the sample temperature, that is also shifted to the right and therefore caused deeper deuterium diffusion, while the deuterium is closer to the surface on the left side. The spot sum of all three desorptions (4, ■) shows a quite symmetric profile, which is nearly identical to the inventory measured by a single melting pulse in row (b) 4 mm below (◆). Only in the outer positions there are larger deviations, therefore the sum of the three pulses in row (a) is taken as reference for its total D inventory. The ratio of the desorbed D in the first LID pulse to this total inventory is shown in green stars (★). It decreases from 87% at the sample edge down to 71% in the minimum right of the sample centre, where the temperature is maximal. "This is consistent with the results in the TEXTOR experiment indicating an inverse dependence of the desorbed" fraction "on the target temperature." [Z13] In comparison to the TEXTOR case, the decrease of exposure time by one order of magnitude and the lower sample temperature decrease the D diffusion and thus lead to a higher desorption fraction. Beside this result for the heating pulse, the total D inventory, which is a factor of 3 lower than in the TEXTOR sample, indicates that long exposure time is more important for high D retention than higher plasma flux.

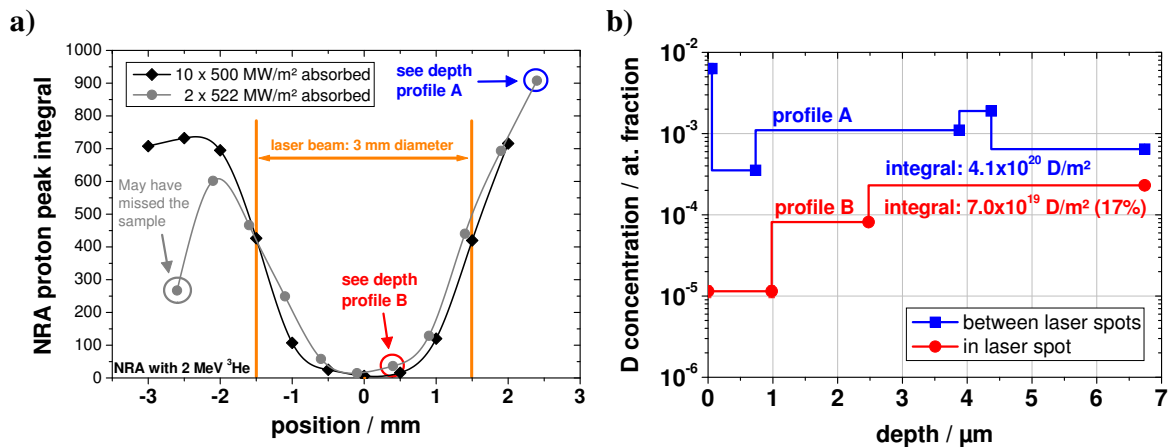
The importance of the factor time during plasma exposure is demonstrated by the longest exposure presented here: 18 hours in the device PlaQ [Manhard11a] but at four orders of magnitude reduced plasma flux to reach again similar fluence ( $6 \cdot 10^{24}$  D/m<sup>2</sup>). A polished tungsten sample ( $12 \times 15 \times 0.7$  mm<sup>3</sup>, "polycrystalline, hot-rolled, 99.97 wt% W provided by Plansee GmbH) was exposed in an ECR deuterium discharge with  $38$  eV/D and a flux of  $1 \cdot 10^{20}$  D/m<sup>2</sup>s." The sample temperature, which "was held constant at 370 K during exposure", is the lowest of all samples discussed in this section. "LID measurements were performed with standard laser parameters showing a D retention of  $6.8 \cdot 10^{20}$  D/m<sup>2</sup> in the first pulse as shown in figure 6.11. With consecutive laser pulses on the same spot, the LID signal decays from 10% of this value in the second pulse to about 1% after 10 laser pulses. The additional release and slow decrease of these values is attributed to lateral and perpendicular D diffusion into the desorption volume." [Z13] The sample is loaded quite homogeneously with deuterium as LID measurements at other positions with similar laser intensity show.

"In order to determine the fraction of desorbed D atoms by the 1<sup>st</sup> pulse of LID measurements in relation to the total amount, not only laser induced melting, but also TDS and NRA were applied. In TDS measurements [Manhard11b] with heating rates of 0.3-600 K/min up to 1273 K, an integrated amount of desorbed deuterium of  $(7.5 \pm 0.4) \cdot 10^{20}$  D/m<sup>2</sup> was found, corresponding to 91% of the deuterium measured by LID within the 1<sup>st</sup> laser exposure.

In addition, the D concentration was measured with NRA [Mayer9] at two energies (6 MeV <sup>3</sup>He with 12 μm penetration depth and 2 MeV <sup>3</sup>He with 7 μm penetration depth) and the D profile reconstructed by the code NRADC [Schmid12], delivering  $5.5 \cdot 10^{20}$  D/m<sup>2</sup> and  $4.1 \cdot 10^{20}$  D/m<sup>2</sup>, respectively." [Z13] This shows the insufficient analysis depth of NRA in case of high-Z materials, while TDS and LIM cover the whole deuterium retention depth. Since NRA is a localised measurement technique with higher spatial resolution than LID, lateral NRA scans across the LID spots have been done, that show the D depletion impressively (cf. figure 6.12a). However, the data of the lateral scans are only qualitative, since a deconvolution of the depth profile, necessary for the determination of the D amount, has only been done for the marked positions A



**Figure 6.11.:** Repetitive LID pulses for 3 ms each on a W sample exposed to an ECR D plasma illustrate D diffusion into the laser heated volume; the values are absorbed laser intensities; figure similarly published in [Z13]



**Figure 6.12.:** NRA profiles of D concentration in a W sample exposed in an ECR discharge; a) qualitative D depletion after LID; b) (already published in [Z13]): quantitative depth profiles inside and outside the LID spot as marked in figure a)

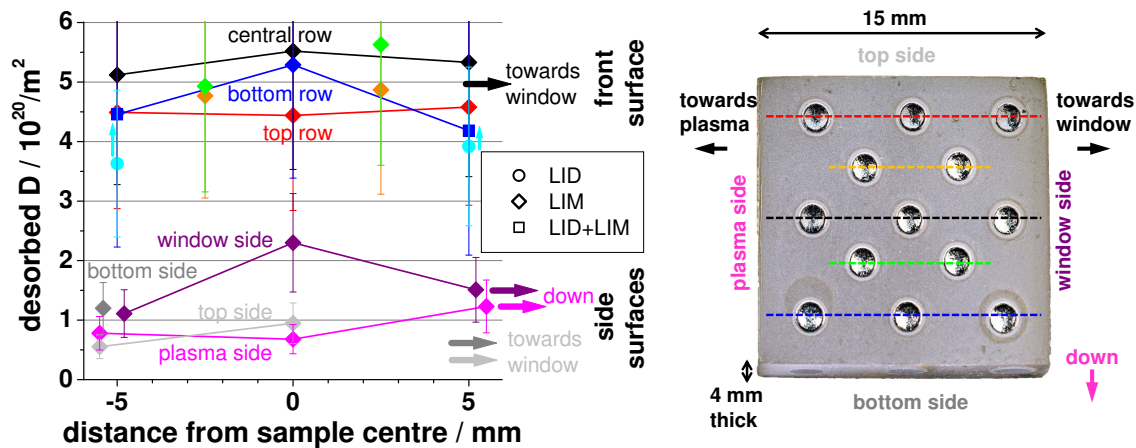
and B, outside and inside one LID spot (cf. figure b). "Inside the laser spot about  $0.7 \cdot 10^{20} \text{ D/m}^2$  was measured in the first  $7 \mu\text{m}$  (cf. figure 6.12, **profile B**). This corresponds to about 17% of the deuterium retention in the sample outside the spot (**profile A**). Inside the laser spot, the NRA" measurements prove a strong reduction of the D concentration by three orders of magnitude at the surface as the simulations by the TMAP7 model typically show (cf. chapter 4.2). "The high fraction of released deuterium by LID in this case indicates again the increase of the released fraction with decreasing temperature." [Z13] The low flux cannot be a reason for the high desorption fraction as the sample exposed to even lower flux in the RF glow discharge had a much lower desorption fraction.

Comparing the three samples from TEXTOR, Pilot-PSI and the ECR plasma, which all have fluences in the order of  $10^{25} \text{ D/m}^2$ , but up to 4 orders of magnitude different fluxes, strongly indicates that a high flux is not important for high retention, since their retention is decreasing with higher flux. Their total retention does not show a clear correlation with sample temperature, plasma temperature or ion impact energy (cf. table 6.1), thus they strongly indicate that exposure time plays the main role when fluence is similar. The sample with the shortest exposure time (Pilot-PSI) has a factor of 9 lower total retention than the sample with the longest exposure time (ECR). The TEXTOR data lie inbetween.

In order to study high fluence effects a different plasma device had to be used, since the devices used up to now either had a low flux (glow and ECR plasma) or were unsuited for

## 6. Applications of Laser Induced Desorption (LID-QMS)

accumulation of long exposure time (TEXTOR, Pilot-PSI). A steady state device with significantly higher flux than the glow and ECR plasmas was needed. Such conditions are realised in the linear plasma device PSI-2 [Koch4]. On the methodological side, this simultaneously offers an opportunity to demonstrate the advantage of localised measurements by LID and LIM in contrast to TDS. The high fluence in this exposure is comparable to expected values in the ITER divertor at the end of one standard discharge. Therefore, for this study a special W grade provided by MG Sanders was used, that fulfills the ITER material requirements, especially the orientation of elongated grains perpendicular to the surface. With metallographic cross-sections in all three directions, grain sizes up to 0.3 mm were found parallel to the surface and up to 0.6 mm perpendicular to the surface. The plasma exposed part of the sample was  $15 \times 15 \times 4 \text{ mm}^3$  large, which was held on a pin on its rear side by a cooled holder. The bulk W sample has been exposed to the deuterium plasma in PSI-2 for 4.5 hours with the quadratic front surface perpendicular to the main plasma flux along the axial direction of the linear plasma. The radial position was chosen such that the sample was in the flux maximum with maximum plasma temperature and density in ca. 2-2.5 cm distance from the plasma centre. The plasma flux as deduced by the current to the sample, which was biased negatively, was  $0.9\text{-}2.3 \cdot 10^{22} \text{ D/m}^2\text{s}$  depending whether the plasma wetted area is defined as the front surface with the four side surfaces or only the front surface. The flux measured by a Langmuir probe during the exposure results in  $1.6 \cdot 10^{22} \text{ D/m}^2\text{s}$  in the flux maximum, where the sample has been placed. Since this value lies well inside the previous range, it is plausible and used for the evaluation of the plasma fluence, that results in  $2.6 \cdot 10^{26} \text{ D/m}^2$ . In the calculation of the plasma wetted area certainly more than just the front surface of the sample has to be included, because the LID-QMS results show that the side surfaces have a deuterium retention of 23% of the front surface. Here, the average values of the front surface and the side surfaces were used (cf. figure 6.13). Such localised retention measurements are only possible with accurate and time-consuming sample cutting, that prevents heating, if the retention shall be measured by TDS.



**Figure 6.13.:** Laser Induced Desorption (LID) and Melting (LIM) on a bulk W sample exposed to deuterium plasma in PSI-2

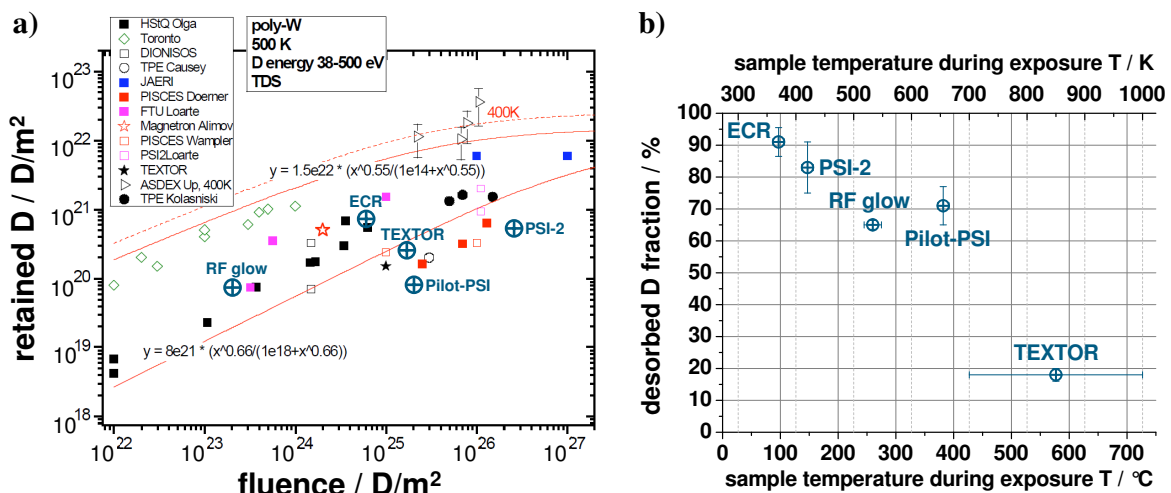
Taking into account the area of the side surfaces and front surface, then 20% of the total deuterium is retained in the four side surfaces and 80% in the front surface. The deuterium retention is rather homogeneous on the front surface, as the standard deviation of the measured values is only 8% of the average value. The sample surface temperature is quite homogeneous as IR-camera images show. The coldest temperature is in the centre with 390 K increasing radially outwards to the sample edges (ca. 410 K) and up to 420 K at the LID spots at the



corners. This outward radial increase is due to a circular pin of 4 mm diameter and 8 mm length that belongs to the sample and is located in its centre on the rear side. It is the main cooling contact to the sample holder, which embraces this pin. The variations of retained D in the side surfaces are much higher with a standard deviation of 46%, which could be due to considerably higher temperature variations. During the exposure only one side surface could be captured by the IR-camera, showing differences of 80 K in the LIM analysis positions.

The deuterium that is desorbed by laser heating without melting utilising the standard pulse ( $500 \text{ MW/m}^2$  absorbed intensity, 3 ms, 2000 K) was measured in the two corner spots of the bottom line (●). The one closer to the plasma has to be disregarded, since the sample has moved before the melting shot was applied and therefore they are not concentric. For the other LID spot the melting (LIM) was done directly after desorption resulting in perfect concentricity. Taking the ratio of LID pulse to the sum of LID + LIM, a desorbed fraction of 94% results, but some of the deuterium might have diffused out of reach of LIM by the first shot. Thus the ratio of the values by the two LID pulses and the average value in the other two corners measured only by LIM is more accurate: 80-86%. This value for the desorbed fraction fits well into the comparison of the other exposures at different temperatures (cf. figure 6.14b). It is the second highest desorption fraction and the second lowest exposure temperature.

In the overall comparison of absolute D retention (cf. figure 6.14a) however, the data point is clearly below the main band of data. But this is also valid for the data of other linear devices like PISCES and Pilot-PSI, to which it fits quite well.



**Figure 6.14.:** a) D retention overview after [Lipschultz10] with added results from this chapter (⊕); b) desorbed D fraction of discussed samples by LID at 1800-2000 K depending on the sample surface temperature during plasma exposure

The left overview figure compares the total retention of the discussed samples to each other and literature data. The primary factor for a high retention is obviously a high fluence with an exponent below one. For samples at similar fluence a longer exposure time is the secondary factor that leads to high retention. For LID the sample temperature during plasma exposure mainly determines the desorbed D fraction (cf. figure 6.14b). The lower the surface temperature of a sample during plasma exposure, the higher the desorption fraction of LID. "For W samples exposed at temperatures below 400 K" during plasma exposure "a good agreement is found between NRA, TDS and LID. With increasing surface temperature, TDS and LIM found systematically larger amounts of deuterium retention compared" to NRA and "LID under standard conditions (heating up to 1800 K). The results can be explained by the fact that with higher surface temperature and exposure time the deuterium diffuses deeper into

## 6. Applications of Laser Induced Desorption (LID-QMS)

plasma type and device	ECR plasma PlaQ	linear pl. PSI-2	RF glow PADOS	linear pl. Pilot-PSI	tokamak TEXTOR
<b>exposure conditions:</b>					
flux / $\text{D}/\text{m}^2\text{s}$	$1 \cdot 10^{20}$	$1.6 \cdot 10^{22}$	$2.8 \cdot 10^{19}$	$2 \cdot 10^{24}$	$1.3 \cdot 10^{23}$
plasma temperature / eV	$\approx 5$	9.4	$<0.1$	1.2	27
plasma density / $1/\text{m}^3$	?	$2.2 \cdot 10^{18}$	?	$3.7 \cdot 10^{20}$	$4.3 \cdot 10^{18}$
exposure time / s	64800	16200	7200	10	110
fluence / $\text{D}/\text{m}^2$	$6 \cdot 10^{24}$	$2.6 \cdot 10^{26}$	$2 \cdot 10^{23}$	$2 \cdot 10^{25}$	$1.5 \cdot 10^{25}$
sample temperature / K	370	390...420	533	620...655	400...>700
ion energy / eV	38	80	350	55	60-180
<b>desorption:</b>					
max. desorbed D / $\text{D}/\text{m}^2$	$7.5 \cdot 10^{20}$	$5.0 \cdot 10^{20}$	$7.4 \cdot 10^{19}$	$8.5 \cdot 10^{19}$	$2.9 \cdot 10^{20}$
method	TDS	LIM	TDS	LIM	LIM
retained D fraction:	$1.3 \cdot 10^{-4}$	$2 \cdot 10^{-6}$	$3.7 \cdot 10^{-4}$	$4 \cdot 10^{-6}$	$2 \cdot 10^{-5}$
LID desorbed fraction	91%	80-86%	65%	71-87%	18-86%

**Table 6.1.:** Overview of exposure conditions and D retention results for the position of highest retention in each discussed example; the order is according to surface temperature; parts of the table are published in [Z13]

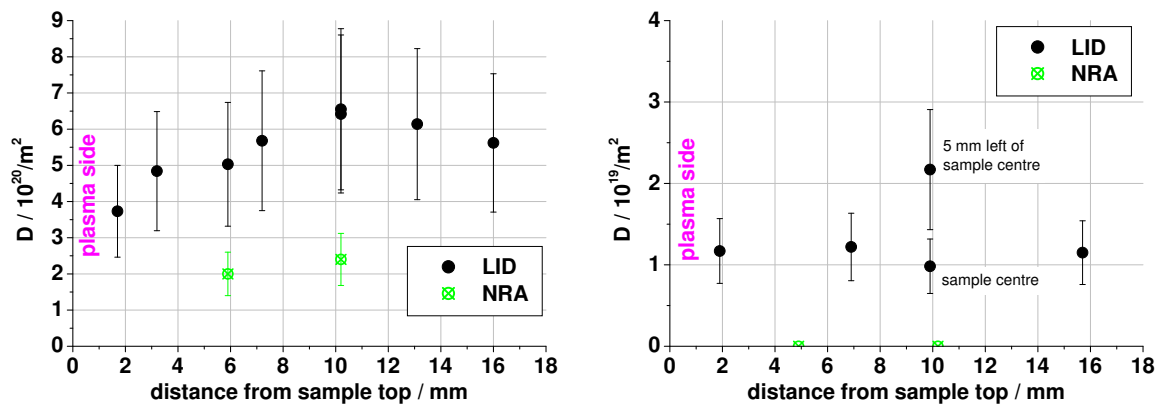
the W bulk and/or is stored in traps with higher binding energy. For both cases some of the retained deuterium is not accessible anymore for the desorption by the standard LID laser pulse heating." [Z13] The fact that the deuterium is completely undetectable by NRA in some of these high temperature cases shows that the deeper D diffusion is most probably the main mechanism and not the creation of stronger traps in shallow depths. The deuterium diffuses into the depth and thus migrates out of the analysis volumes of NRA and LID partly or completely. "This behaviour is in line with results from the TMAP modelling (cf. chapter 4.1). This effect must be considered for the application of these methods for W-bulk retention on erosion dominated areas. It has been found that Laser Induced Melting desorbs all the retained D (under the above conditions) and can be an alternative for complete desorption of hydrogen from W." [Z13] Under all plasma exposure conditions studied here, melting of the first 30-50  $\mu\text{m}$  of the sample comprises the whole retention depth. For an in situ application of LIM the important guideline can be deduced from these findings that LIM should be performed regularly, i.e. repetitively on the same spots. The time interval between the desorptions should be shorter than the hydrogen needs to diffuse deeper than the laser melting depth of the laser pulse. For an estimation of this time interval the temporal and spatial temperature distribution in the wall element as well as the hydrogen flux on the surface are the minimal requirements.

### 6.3. Laser Desorption from Tungsten Fuzz

When tungsten is exposed to a helium plasma or a plasma containing a certain fraction of He a so called tungsten fuzz can form at certain sample temperatures and He fluences. The bulk W is transformed into a sponge-like W structure with very high porosity. Example images of the W fuzz used here before and after laser heating are given in figure 3.24 on page 103. Two circular tungsten samples (18 mm diameter, 4 mm thick, polycrystalline, single forged tungsten with 99.97 wt% purity provided by A.L.M.T. Corp.) were mechanically polished and annealed at 1173 K for half an hour in flowing  $\text{H}_2$  atmosphere. Afterward one sample was exposed to a He flux of  $10^{22} \text{ He}/\text{m}^2\text{s}$  for 700 s at ca. 1070 K in NAGDIS [Ohno1] to generate a fuzz structure of 500-600 nm thickness. Both samples were exposed simultaneously to the

TEXTOR SOL plasma at the bottom of the machine to 23 standard ohmic PWW discharges (plasma current  $I_p = 350$  kA, magnetic field  $B_t = 2.25$  T, density  $\bar{n}_e = 2.5 \cdot 10^{19} / \text{m}^3$ ) under  $20^\circ$  incidence. One of the W samples had a W fuzz structure while the other was a polished reference sample of the same material grade without fuzz. Both were exposed at the same minor plasma radius, shifted by 2.5 cm in poloidal direction. Since they were moved 5 mm further inside the plasma after half of the exposure, their minor plasma radius was mainly within the range of 46.6-47.7 cm. The thermocouple inside the sample holder measured 470-510 K, with an increase of  $\Delta T = 20$  K by the discharge, while the IR camera showed surface temperatures of 770-820 K on the samples.

The samples were then desorbed by LID with  $\varnothing 3$  mm laser spots in a line scan along the direction of the minor plasma radius, close to the sample centre, and in additional positions shifted up to 5 mm in poloidal direction. On the W fuzz desorption values of  $4\text{-}7 \cdot 10^{20} \text{ D}/\text{m}^2$  were found with a maximum roughly in the middle of the sample. The reference W showed more than one order of magnitude lower desorption of  $1\text{-}2 \cdot 10^{19} \text{ D}/\text{m}^2$  (cf. figure 6.15).



**Figure 6.15.:** Deuterium desorbed by LID-QMS on a simultaneously exposed W fuzz (left) and a polished W reference sample (right) in the erosion dominated area of the TEXTOR SOL plasma; D content detected by NRA is shown for comparison

The maximum temperature during laser heating reached with 1980-2170 K slightly higher values than expected for  $500 \text{ MW}/\text{m}^2$  absorbed intensity. On the reference sample much lower values of 1400-1500 K were reached. Therefore, for several measurements on the reference sample the maximal laser power was used, delivering  $560 \text{ MW}/\text{m}^2$ , which increased the temperature to 1500-1600 K without an increase of the desorbed D amount. The remaining difference of ca. 500 K in maximum temperature, however, can usually account for a deviation of less than factor 2 in the desorbed amount: e.g. the sample discussed in the previous section, which was loaded homogeneously in a glow discharge, showed only a factor of 1.4 lower LID-QMS signal for 600 K lower desorption temperatures (cf. figure 6.8 on page 144).

To further confirm the much higher D retention in the W fuzz, two NRA measurements per sample were done ca. 5 mm beside the corresponding LID spots in poloidal direction. As already shown in the previous section, the deuterium can diffuse deep into the bulk if no diffusion barrier like a-C:H layers are present. Then NRA cannot detect the whole D content, since it is limited to ca.  $3 \mu\text{m}$  analysis depth at the energies of  $^3\text{He}$  used here. Therefore the D retention values measured by NRA are more than a factor of 2 lower than the LID-QMS values. On the reference sample no proton count representing deuterium could be measured by NRA despite long measurement time. For the reference sample the deuterium amount measured by LID-QMS is nearly at the limit of NRA detection and with additional reduction due to the diffusion of D into the depth, the zero NRA result can be explained.

Further NRA measurements were done in LID spots that were desorbed by one or two laser pulses on both samples. No D signal could be measured inside the laser spot, which shows that LID can deplete the surface region from deuterium at least in the first few micrometres below the surface.

The factor 20-30 higher retention values for the W fuzz are also not due to a-C:D layers that might form locally even in erosion dominated areas, due to surface roughness, especially in the fuzz structure. NRA measured a factor of roughly 2 higher C content on the W fuzz compared to the reference sample, but the absolute amount of  $1\text{-}2\cdot 10^{21}$  C/m<sup>2</sup> cannot account for a significant contribution of D from local a-C:D structures. The LID-QMS spectra support this interpretation, because only 3% of the total D content originates from molecules other than HD and D<sub>2</sub> for the W fuzz sample. With the presence of a-C:D layers this fraction should be 15-20%.

After the plasma exposure, microscopic cross-sections by a focussed ion beam (FIB) were done (cf. figure 3.24 on page 103) showing that ca. 200 nm of the fuzz structure are still present on the surface, which have not been eroded by the plasma. Therefore the fuzz is assumed to be the cause for the higher retention. The real deuterium retention might be even higher than measured by LID, since the desorption might be incomplete and no melting or TDS were done. With the knowledge of the desorption fraction of LID to LIM presented in the last chapter (cf. figure 6.14b), an exposure with the surface temperatures around 800 K could lead to a desorption fraction of 20-50% in LID and thus a factor of 2-5 higher real retention.

The explanation of the much higher retention of the W fuzz is out of the scope of the present work, but might be due to internal material changes in the fuzz region, like additional D traps created during fuzz formation. Another explanation might be a purely geometrical effect. The impinging D ions can penetrate deeper into the material through the high porosity of the fuzz and cannot directly escape like on a polished surface.

## 7. In situ Laser Induced Desorption Spectroscopy (LIDS)

This chapter deals with the physical processes after absorption of the laser energy, its conversion to heat and the release of the incorporated gases. These steps have been described in the previous chapters. Also the quantification of the desorbed gases by means of mass spectrometry has been presented as the LID-QMS method. But it cannot be applied during plasma operation in a tokamak because the released gases are ionised and confined and cannot reach the QMS. Even without the presence of the plasma, mass spectrometry is hardly feasible, because the amount of the gas released is too small to be detected in the usually large plasma chambers. One attempt of LID-QMS in TEXTOR has been done with a 400-500 nm thick, fuel rich a-C:D layer. Although the pump shutters were closed before the laser pulse, the QMS could not detect the pressure increase of the desorption, despite the relatively small chamber volume ( $7 \text{ m}^3$ ) compared to other tokamaks. In order to quantify the released amount of hydrogen in situ during plasma operation, spectroscopic methods can be used.

The general working principle of the spectroscopic quantification of the desorbed hydrogen is based on the heating of a small wall area or sample surface with a millisecond infrared laser beam. Like in LID-QMS, carbon or tungsten surfaces absorbing this laser light, are heated to surface temperatures of 1800-2000 K at the end of the laser pulse. In the depth of ca. 0.2 mm the temperatures then are still above 1300 K, which is sufficient for complete hydrogen release from carbon materials. For tungsten, often melting is necessary for complete desorption, depending on the plasma exposure conditions (cf. chapter 6.2). After the material dependent hydrogen migration from the heated volume to the surface, the hydrogen is set free mainly as  $\text{H}_2$ , HD and  $\text{D}_2$ . These molecules are first ionised and then dissociated by the impact of the electrons from the tokamak plasma. Roughly half of the hydrogen is already in ionised form after the dissociation of the molecules. The remaining hydrogen atoms are ionised and/or excited into higher electronic states mainly by impact of the electrons from the plasma. The subsequent decay into lower electronic states produces a spectrum of hydrogen light, of which mainly the strong  $\text{H}_\alpha$  line in the Balmer series are measured spectroscopically. The light-to-particle conversion factor can be calculated from the knowledge of the cross-sections of the molecular ionisation, dissociation, atomic excitation, ionisation and desorbed hydrocarbon fraction, if the electron temperature and density of the plasma are known. In this way an absolute quantification of the released hydrogen is obtained in the "forward direction" without the need of calibration samples. Oppositely, "backwards" the conversion factor can be determined experimentally as the ratio of detected photons to the desorbed hydrogen amount. In this case, calibration samples with known hydrogen retention have to be introduced into the plasma chamber.

In the beginning of this chapter the tokamak TEXTOR is briefly introduced concentrating on the conditions at the position of LIDS. Then, the setup of the laser injection systems is described, also comparing and evaluating different setups, that have been used at the same position. Further, the spectroscopic systems of TEXTOR that are used for the detection and recording of the LIDS light are presented including calibration, synchronisation and gated operation of the detection system. The adjustment of the integration time of the detectors to the

duration of the light emission is discussed, whose knowledge is a prerequisite for the optimal settings of the detection systems (cf. chapter 7.3).

The main part of this chapter describes the quantification of the spectroscopic signals in order to obtain absolute atom numbers for the desorbed hydrogen amount (cf. chapter 7.5). Since LIDS was only done in hydrogen plasmas (D main plasma, H from NBI) at TEXTOR, the background subtraction of the spectroscopic signals is a major issue (cf. chapter 7.5.1). It also plays a major role in the reproducibility and stability of LIDS measurements (cf. chapter 7.7) and determines the lower detection limits (cf. chapter 7.8).

In the sections 7.5.2 and 7.5.3 the processes in the plasma are described, that are most important for the correct quantification of the LIDS signals. In chapter 7.5.4, the often limited access and visibility of the area of the LIDS light is mentioned, that sometimes make a correction of the total conversion factor necessary for the light outside the detection volume. The total amount of LIDS light and its spatial distribution are compared to numerical simulations with the ERO code including all the previously mentioned processes (cf. chapter 7.6).

The light-to-particle conversion is only possible in the way as described here, if the plasma is not perturbed too much by the injected gas due to cooling of the plasma (cf. chapter 7.9). This represents an upper detection limit for LIDS which is deduced from earlier gas puffing experiments at the same position in TEXTOR and demonstrated experimentally. The chapter is closed with a detailed discussion of the uncertainties and accuracy of LIDS.

### 7.1. Tokamak TEXTOR

TEXTOR is a plasma device of the tokamak type with a major radius of  $R = 1.75$  m, a circular cross-section of  $r = 46.5$ - $46.7$  cm minor plasma radius, where the last closed flux surface (LCFS) is located. The TEXTOR plasma is limited by the toroidal belt limiter – the ALT-II (Advanced Limiter Test II) limiter [Finken5] – where all main vacuum pumping ducts of the TEXTOR pumping system end. A detailed description of TEXTOR can be found in [Neubauer5]. A test limiter or sample holder can be introduced from the bottom without vacuum break via a lock system [Schweer5] quite close ( $137$  cm or  $\Delta\varphi_{\text{TEXTOR}} = 45^\circ$ ) to the poloidal limiters.

The phrase "main plasma" is used in the present work for the entire volume inside the LCFS. For TEXTOR this are all positions with the minor plasma radius  $r < 46.5$ - $46.7$  cm. The term "edge plasma" is used by authors for different areas of the plasma sometimes. In the present work the expression edge plasma at TEXTOR refers to the outer part of the main plasma with temperatures below ca.  $100$  eV, which is followed by the scrape-off layer (SOL) outside the LCFS.

For the LIDS measurements in TEXTOR the plasma conditions at the plasma edge are important in two regions. Whenever a limiter or sample holder is used that has a non zero inclination to the magnetic field lines, the plasma flux and ion impact energy at the radial position of the samples and the surface temperature is needed to characterise the exposure conditions. In order not to rise the surface temperature too high ( $T < 400^\circ$  C) this region is outside the LCFS, usually at a minor plasma radius of  $r > 47$  cm. The second region of interest is at the position of the LIDS light. Here the electron density and temperature are the important values, which are needed for the conversion of the LIDS light signal into the hydrogen amount. Most of the LIDS measurements, that could be done in the dedicated experimental programme, have been carried out at a set of standard parameters, which are called PWW parameters (explained below). Setting of the same global plasma parameters leads to similar local plasma parameters. This is not ideally true since some plasma parameters like the impurity levels cannot be controlled directly and plasma shifts are sometimes not compensated in the same way. Although

TEXTOR can reach plasma currents of 0.8 MA and the 16 toroidal field coils can establish a toroidal magnetic field of up to 2.4 T on the centreline of the torus, these maximum values are usually not used for the experiments on plasma-wall interaction. These record values namely can only be achieved at the expense of more important conditions like a long plasma phase with constant plasma density and temperature, the so called "flat top phase". On the other side of the operational spectrum a maximum of 10 s discharge duration can be reached, but again only with reduced plasma parameters compared to the above mentioned parameters. For the plasma-wall interaction experiments a standard discharge in the middle of the parameter range has been defined already since years, which has the advantage to improve comparability in general. Nevertheless, density scans or additional heating are applied in dedicated experiments to investigate the sensitivity of the studied processes, like LIDS with different plasma parameters. The just mentioned standard global plasma parameters for the plasma-wall interaction experiments are referred to as "PWW plasma parameters" in the present work and are a plasma current of  $I_p = 350$  kA, toroidal magnetic field of  $B_t = 2.25$  T and  $\bar{n}_e = 2.5 \cdot 10^{19}$  /m<sup>3</sup> line-integrated electron density on the central vertical line at  $R = 1.75$  m. "The parameters at the plasma edge and SOL (measured by the thermal or supersonic helium beam diagnostic) at the position of the maximum of the LIDS light at around 46 cm minor radius" in ohmic plasma are usually as follows (cf. figure 7.17 on page 189): "the electron temperature  $T_e$  around 55 eV and the density  $\bar{n}_e \approx 4 \cdot 10^{18}$  /m<sup>3</sup>." [Z11b] If the plasma is additionally heated by NBI1, the LIDS light maximum shifts to ca. 46.7 cm, where a temperature of 60 eV and a density of  $4.5 \cdot 10^{18}$  /m<sup>3</sup> are measured, while the gradients become steeper in radial direction.

While these parameters will be decisive for the quantification of LIDS, the plasma flux, deduced from the same measurements at the radial position of the limiter is important for the processes during fuel retention. The plasma flux together with the exposed material type, geometry and heat contact to the limiter influences the temperature distribution in the sample, which is together with the flux and exposure time one of the most decisive parameters for retention. Moreover the impact energy of the hydrogen and deuterium atoms from the plasma is also important. On the test limiter, which is grounded on the experimental ground (TEXTOR earth), quickly a negative bias establishes due to the advanced electron mobility. The built-up sheath potential close to the surface of the limiter of typically ca. 3 kT accelerates the hydrogen ions, which already are ca. 1.5-2 times hotter than the electrons in this region. Depending on the plasma radius and chosen plasma conditions impact energies of 140-250 eV are reached.

## 7.2. Experimental Setup at TEXTOR and Measurement Procedure

The Laser Induced Desorption Spectroscopy in the present work has been performed at the limiter lock system (N° 1) at the TEXTOR tokamak. The laser setup and the coupling of the laser light into the fibre optics have already been described in chapter 2.1. In the same way as described there, the laser light is guided also to TEXTOR for the LIDS measurements. The general setup of TEXTOR has already been described earlier, thus the focus here lies on the laser injection and light detection systems for LIDS, located in section 10-11 of the tokamak. A poloidal cross-section of TEXTOR at this position and the schematic setup of the LIDS systems is presented in figure 7.1. The detailed description of LIDS starts at the point, where the laser light exits the fibre at TEXTOR. The opening angle of the laser light cone coupling out of the fibre has a numerical aperture of  $N_A = 0.126$  (cf. table 2.1 on page 35). The end of the fibre is imaged to the target at the bottom of the TEXTOR tokamak. The target is

introduced into the vacuum vessel from the bottom without vacuum break via the limiter lock system [Schweer5]. In the present work the targets have not been introduced deeper into the plasma than to a minor radius of 47 cm, still at least 3-5 mm behind the LCFS.

The poloidal position of the target is at the lowest point of the poloidal plasma cross-section, while the laser beam enters the plasma through a duct at the top of the torus, which is in the same toroidal position. This duct is not exactly opposite the lock system, but with a  $7^\circ$  angle to the vertical direction (cf. figure 7.1). It enters the vacuum chamber via a 10 cm diameter window that has a transmission of  $91\% \pm 1.5\%$  for light at the laser wavelength of 1064 nm. The laser beam has a diameter of ca. 6 cm on the window with a circular shape. For the typical target position at  $r = 48$  cm the distance from window to target is 220 cm. The laser beam passes through a 92 cm long tube with 100 mm inner diameter until it enters the open vessel of the torus. With the detection cone tip 10 cm above the window, this limits the scanning width of the laser and the FoV for the coaxial observation to a maximum opening angle of  $5.7^\circ$  ( $N_A = 0.05$ ). This allows to implement a maximal observation with circular Filed of View (FoV) of 23 cm diameter at the sample position. The liner is located 22 cm below the end of the duct and has an opening of 12 cm in diameter, which would allow for a full opening angle of  $6.0^\circ$  ( $N_A = 0.052$ ). Therefore it is not limiting the maximal observation aperture.

During the present work the setup of the LIDS experiment has been upgraded twice with respect to the laser injection and the observation system.

1. The first setup for the injection can be found in [Irrek8, p.70,75]. It used a  $f_{in} = 60$  mm lens ( $N_A = 0.05$ ) for coupling the laser light into the fibre, to achieve a small beam aperture of ca.  $N_A = 0.050-0.075^{**}$  after the fibre. It was a chromatically corrected doublet lens for 634 and 1064 nm wavelength, hence the focal lengths for the red pilot laser and the Nd:YAG light were exactly the same. Additionally it was coated with an anti-reflexion layer (AR), reducing reflexion to  $< 0.5\%$  and thus reducing energy losses. The  $f = 31$  cm focussing lens after the optical fibre was also AR-coated, but without chromatic correction. Therefore the focus for the Nd:YAG light had to be checked either by burn patterns on a photo paper, but preferentially by a CCD camera. This was also necessary because the focussing in a distance of more than two metres is hard to see by eye without a telescope. The imaging lens was positioned approximately 33 cm away from the fibre end. Both optical elements were centred on the  $7^\circ$  tilted optical axis defined by the centre axis of the duct. The whole injection system and the fibre to lens distance left only a small freedom to change the spot size. Usually a small spot setup was used with the lens 5-10 cm above the window, resulting in a spot diameter of 2.4-2.6 mm, depending on the actual setup. This yields a magnification of the fibre cross-section by a factor of 6.
2. The first change of this setup was the motorisation of the two-directional scanning stage. The manual adjustment by screws had been replaced by two step motors (Newport 850F actuator), which were mounted orthogonal to each other: one in toroidal direction and the other in poloidal direction. This was a major improvement, because the previous orientation of the axes was not aligned with the toroidal and poloidal torus axes. Moreover the desorption position could be controlled remotely via software from the control room. Nevertheless, experiences with this remote control showed that monitoring via cameras is by far not as accurate as the direct view by eye. Only an extensive positioning of every analysis position by eye before the experiment led to the same results as with the manual control. Additionally any vibration and displacement inbetween position changes had to be mitigated more thoroughly than for the manual system.

---

\*values from [Irrek8, p.69]



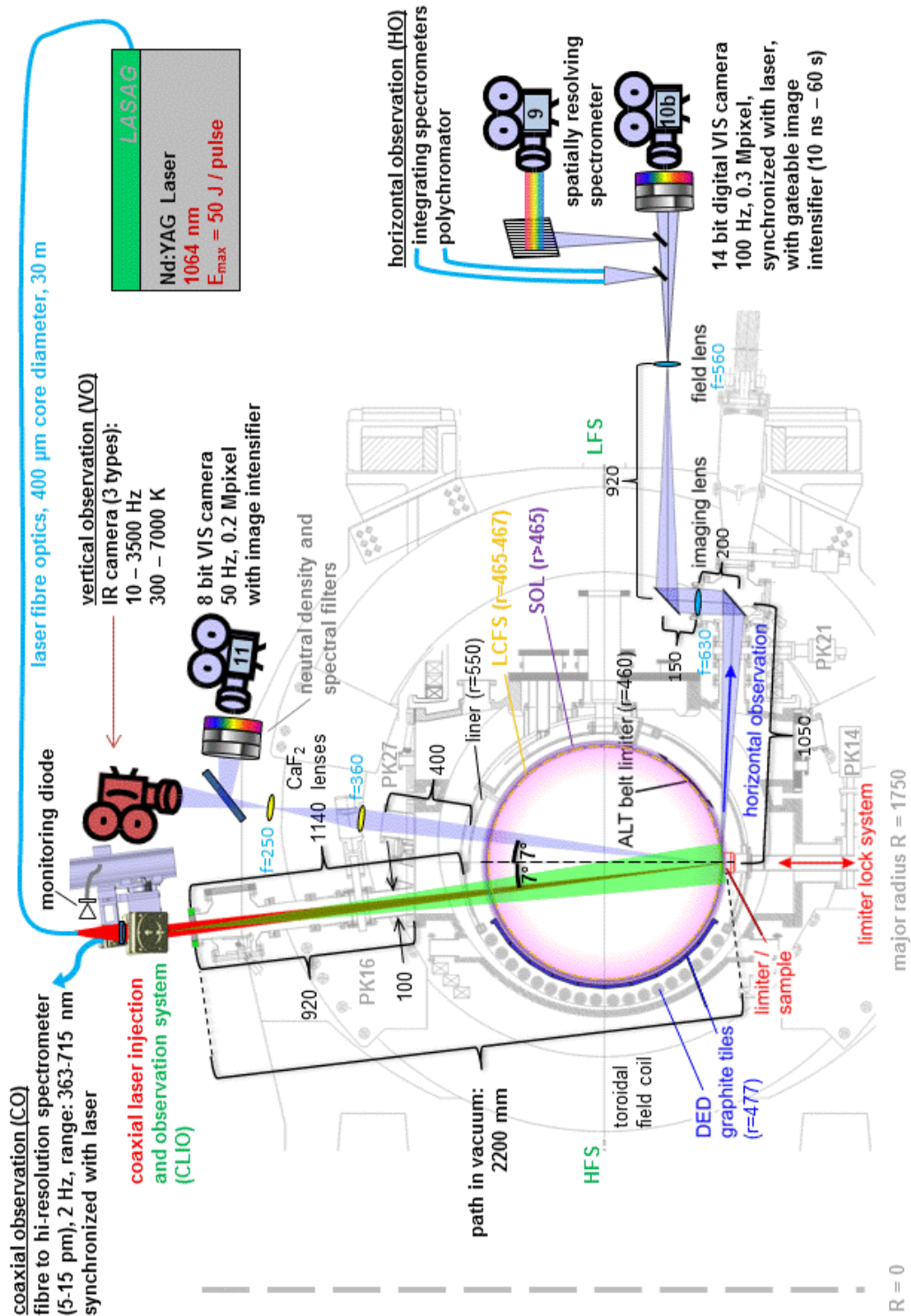
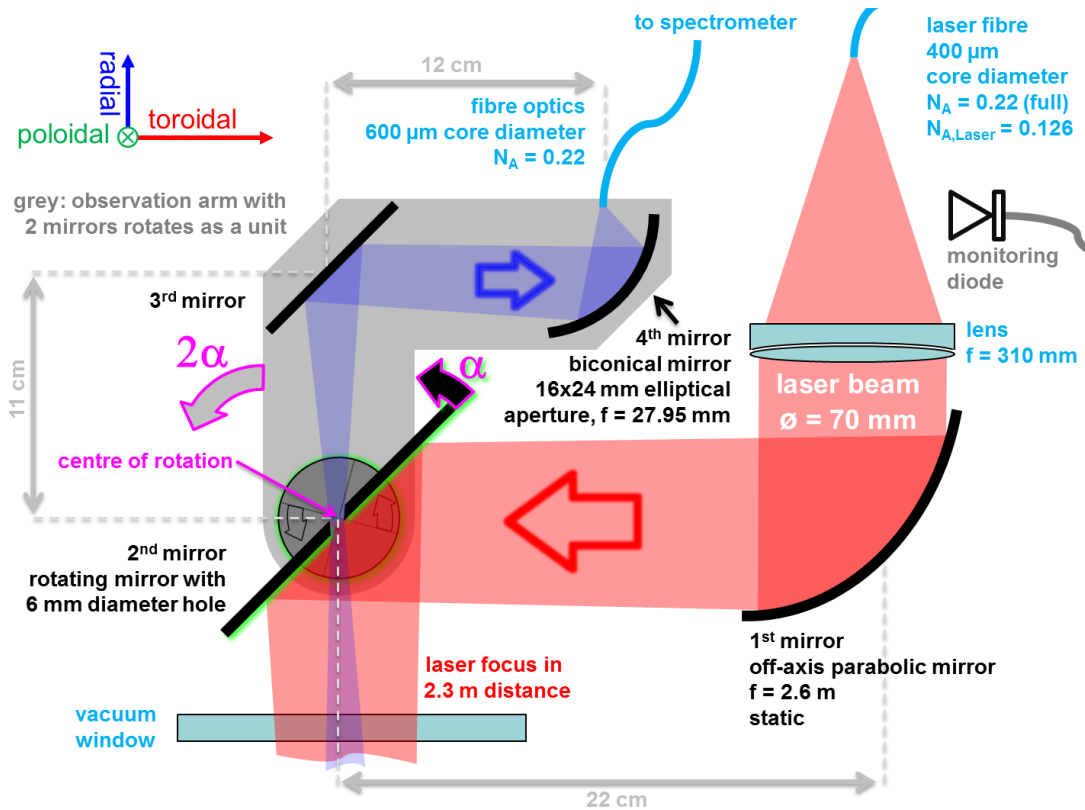


Figure 7.1.: Poloidal cross-section of TEXTOR with the LIDS setup in the coaxial version; for a 3D view of this position with an earlier laser setup cf. [Brezinsek5, Fig. 16]

3. The third setup design is guided by artificially high restrictions as expected in ITER. The final injection stage was implemented without glass components replacing lenses by reflective metallic optics, since glass is expected to become intransparent due to the neutron impact in the ITER environment. The main goal of this system is to combine the laser injection and spectral observation in one system, in order to apply it from a single port instead of two. A further main advantage is that the laser beam path and the detection path are coaxial and always move together. A schematic drawing of this Coaxial Laser Injection and Observation system (CLIO) is presented in figure 7.2.



**Figure 7.2.:** Scheme of the coaxial laser injection and observation system CLIO

In the CLIO setup the laser beam enters as a wide parallel beam with a diameter below 70 mm. In TEXTOR this is realised by using the  $f = 31$  cm focussing lens mentioned above in a distance close to its focal length creating a beam of 70 mm diameter. The image of the fibre can be focussed sharply on the target by small changes of the distance between fibre and lens. Few centimetres behind the lens the 1<sup>st</sup> mirror follows. This curved mirror has an off-axis parabolic shape in order to allow a beam deflection of 90°. Its diameter is 100 mm in order to guide a beam of 70 mm maximal diameter. Because of the small distance of the lens and the 1<sup>st</sup> mirror they represent a combined optical system with an image distance of 255 cm (from the centre of this combined system). Thus in a distance of 22 cm the laser beam diameter is reduced by less than 10%. Here it is reflected by nearly 90° into the vacuum vessel by the 2<sup>nd</sup> mirror. It has a plane surface with also 100 mm diameter. In order to observe the LIDS light through the same port, a 6 mm diameter hole was drilled into the 2<sup>nd</sup> mirror under a 45° angle to the surface. The walls of this channel are not fully parallel, but adapt to the observation path, thus they are slightly conical. The light, which is collected through the aperture in the rotating mirror, is deflected by a flat 90° mirror (3<sup>rd</sup> mirror) simulating the situation in the ITER port (cf. [Huber11]). Thus the 3<sup>rd</sup> mirror could be omitted in TEXTOR.

The focussing of the light into the fibre optics with a 600  $\mu\text{m}$  core diameter and 0.22 numerical aperture is done by the 4<sup>th</sup> mirror. It has a biconical shape with an elliptical aperture of 16×24 mm and a focal length of ca. 28 mm. All four mirrors are made of copper with a quartz protected Al layer.

A main feature of CLIO is the " $\theta/2\theta$  principle" which ensures that the observation path follows the injection path. A rotation of the 2<sup>nd</sup> mirror by an angle of  $\theta$  induces a deflection of the laser beam of  $2\theta$ . The observation arm (grey area in the figure) has to adapt by rotating  $2\theta$  around the same centre of rotation as the 2<sup>nd</sup> mirror. The observation arm moves as a unit, thus all distances and angles between the 3<sup>rd</sup> and 4<sup>th</sup> mirror and the spectrometer fibre remain constant during movement. The rotation is initiated by a piezo-electric motor pushing the upper part of the observation arm. The rotation is conveyed to the 2<sup>nd</sup> mirror by a gear system of 4 rollers and 2 vee belts with a reduction of exactly two. The laser beam can be tilted by  $2.44^\circ$  in toroidal direction with this system, which corresponds to a scanning length of 100 mm for a target at a minor plasma radius of 50 cm. The reproducibility of the same position is  $\pm 0.5$  mm and the drift less than 1 mm per day. The poloidal direction can be adjusted manually in a range of about 8 cm on the target.

In order to determine the size of the detection area on the samples, the observation path was illuminated backwards through the spectrometer fibre. Using a visible laser beam a circular observation area of approximately 14 cm in diameter ( $\hat{=} 154 \text{ cm}^2$ ) was seen on the target. However, this is not the full detection area, since the laser does not use the full aperture of the spectrometer fibre. Therefore back illumination was done with uncollimated light of a strong lamp. Because the light is too weak at the target, its size was measured in 28 cm distance below the lower edge of the CLIO system. In this position the light is elliptic in shape in contrast to a nearly spherical shape at the target position. The area is  $10.2 \text{ cm}^2$  in comparison to  $3.6 \text{ cm}^2$  for the laser, thus a factor of 2.8 larger. It is assumed that the observation area at the position of the sample is also 2.8 times larger than measured with the laser beam, thus reaching a size of ca.  $420 \text{ cm}^2$  ( $\hat{=} 23 \text{ cm}$  diameter). This is identical to the maximum allowed FoV due to the TEXTOR duct, as shown above. This means that the maximum possible FoV is used by CLIO, if it is centred on the duct centre and aligned on the optical axis. For any movement to the side or rotation of the mirror, some parts of the observation path are blocked by the duct.

This "setup with coaxial light paths" has been developed for the application of "LIDS in fusion reactors in order to reach the main plasma-wall interaction areas" [Z11, Huber11].

Beside the coaxial observation, a new vertical observation (VO) tilted by  $14^\circ$  to the LFS with respect to the laser injection was used (cf. figure 7.1). With a beam splitter a camera observation in the VIS and in the IR became available. Three different IR-cameras with full frame rates from 10 Hz to 3500 Hz (even up to 30 kHz with reduced frame size) have been used for either temperature control during sample exposure or for LIDS temperature measurements. The camera in the visible range was equipped with neutral density filters and spectral filters in the same way as the horizontal observation. It gives additional information on the LIDS light extent in poloidal direction.

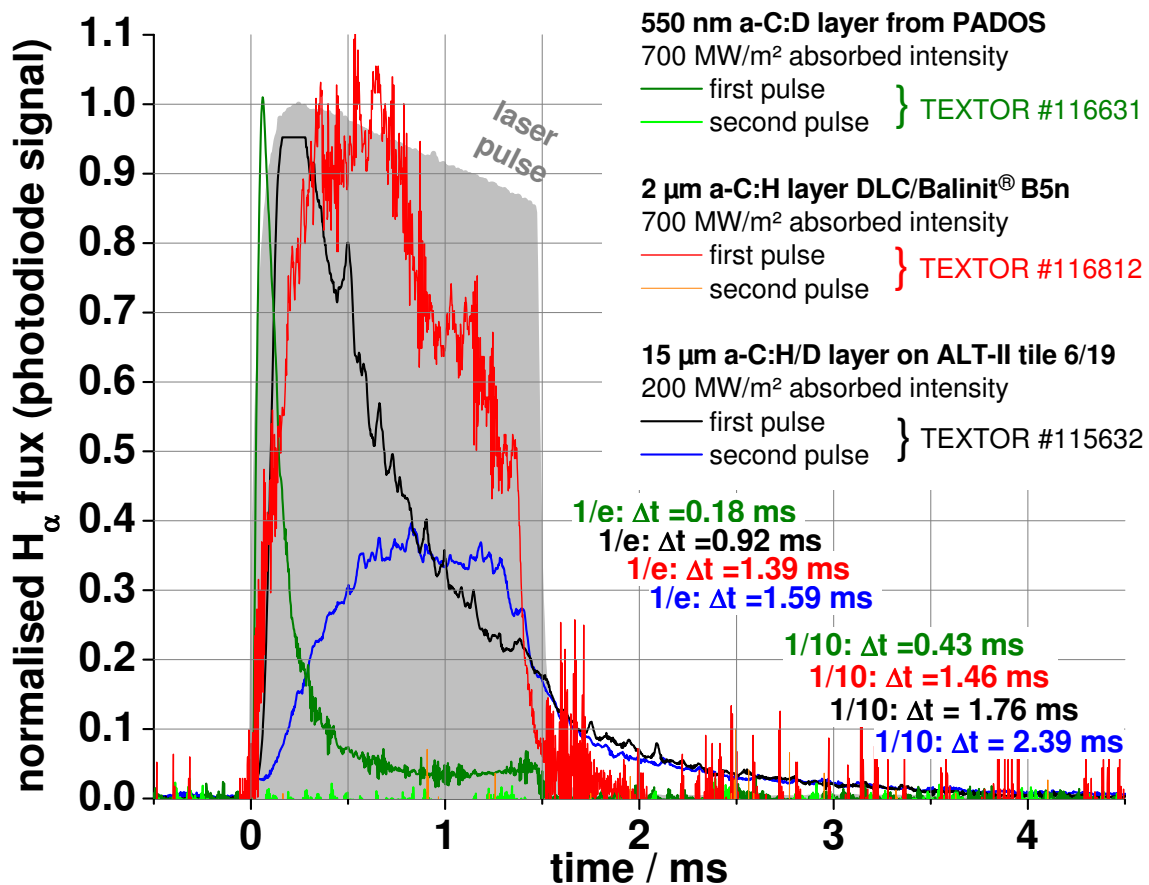
"The multiple reflexions inside the fibre produce a nearly" homogeneous "spatial intensity distribution", if a  $f_{in} = 30 \text{ mm}$  lens is used for coupling into the fibre (cf. chapter 2.2). "The reflexion of the laser light from the sample (14-18% for graphite or a-C:H layers, cf. chapter 2.3) is measured beforehand" in a spectrophotometer and taken into account. The energy "losses from reflexions at the lenses and fibre (24%) and the vacuum window (8%)" are measured with an energy meter inserted at different positions of the laser beam path [Z11].

For the camera observation, "a narrow-band  $H_{\alpha}$  filter is used with a FWHM of 3 nm, so that hydrogen and deuterium are detected simultaneously due to their small spectral separation of 0.18 nm. The light is recorded by a 2D digital camera (Allied Vision Technology PIKE F032B) with 0.3 MPixel, 14-bit depth resolution, 100 Hz frame rate and an image intensifier." [Z11] As camera objective a 'Canon Lens FD 135 mm 1:2' was used. "The camera and laser are synchronised via a common clock" at the horizontal observation (HO) [Z11]. This synchronisation is done in such a way that the laser pulse is started after a short time delay of ca. 300  $\mu$ s after a new camera frame acquisition has begun. At the same time when the frame acquisition starts, a gate signal for the image intensifier of the camera is generated, which can be chosen freely in its length. This timing procedure assures that the laser induced processes are recorded in only one camera frame. The image before and after the laser pulse are free of any laser influence and therefore can be used as background images (details in chapter 7.3). After background subtraction (see chapter 7.5.1) the "desorption image" is obtained. Then the absolute photon amount of the desorption image or difference spectra – in case of the spectrometer – are evaluated with the calibration factor of the respective detection system (cf. next chapter). Then the desorbed hydrogen amount is determined by the light-to-particle conversion factors (cf. chapters 7.5.2 and 7.5.3) and a field of view correction is applied, if necessary (cf. chapter 7.5.4). In the evaluation sequence of the camera images, usually the background subtraction is processed before the photon quantification, since only the signal difference is necessary for evaluation. Constant offsets, e.g. ambient light in the detection path, cancel out in background subtraction, since they are usually present in the same intensity on the LIDS frame and the background frame. If first the photon quantification is done to determine the absolute value of photons in the background signal, then special care has to be taken that no additional signals appear causing an offset.

### 7.3. Temporal Evolution of the Light Emission

For an optimised signal-to-background ratio (SBR) the exposure time and duration of the spectrometers and cameras have to be adjusted to the LIDS light onset and duration. This is only important for such detectors, whose frame rate is so small that they cannot resolve the light emission in time. Therefore one of the first goals in the study of LIDS was the determination of the light evolution in time with fast detectors, that could record the light emission on several acquisition frames. This is an important prerequisite in order to acquire the complete LIDS signal on detectors with a small repetition rate or detectors with a dead time. Already in the application of LIDS for analysis of thin a-C:D layers, such experiments have been done with a fast (2500 Hz), analog 32 $\times$ 32 pixel camera [Irrek8, p.88f]. There the desorption of a 200 nm thick a-C:D layer grown from  $CD_4$  precursor gas in the PADOS glow discharge was analysed by LIDS in TEXTOR. The same laser system was used as in the present work. The laser pulse was chosen longer than in the standard LIDS application: 5 ms (with 400  $MW/m^2$ ) instead of 1.5 ms (for C) or 3 ms (for W). This was done in order to resolve the desorption process in more detail. With this frequency the camera acquired a frame every 0.4 ms and the laser pulse was resolved on 12 images. The surface temperature at the end of the laser pulse is very similar to the standard heating pulses (ca. 1800 K). The deuterium and protium from this thin hydrocarbon layer emitted the highest Balmer photon flux at 1.2-1.6 ms after the start of the laser pulse, decaying within 0.4 ms to the  $1/e$  value and within 2.5 ms to 10% of the maximum value. The photon flux is closely related to the desorption rate, since the physical processes between hydrogen release and light emission take place on a much faster time scale (tens of  $\mu$ s) than the pulse duration.

In the present work also thick ( $> 500$  nm) hydrocarbon layers of 550 nm, 2  $\mu\text{m}$  and up to 15  $\mu\text{m}$  have been desorbed. The evolution of the LIDS signal has been recorded by a fast photodiode (time resolution  $< 2$   $\mu\text{s}$ ) with photomultiplier equipped with a narrow-band  $\text{H}_\alpha$  interference filter (3 nm FWHM) that transmits the  $\text{H}_\alpha$  and  $\text{D}_\alpha$  line radiation. This detection system is called polychromator and is indicated in figure 7.1 on page 161 as part of the horizontal observation. The temporal shape of the light emission is not only important for the optimisation of the integration duration of the slow cameras and spectrometers, but also gives insight into the desorption process itself. For the standard LID pulse for carbon materials ( $700 \text{ MW/m}^2$  absorbed laser intensity for 1.5 ms) three representative examples of the light evolution are presented in figure 7.3. For an easier comparison, the signals of the first laser pulses have been normalised and the signals of the second pulses have been scaled with the same factor as the corresponding first pulse. Thus the relative magnitude between the first and second pulse is preserved. The second pulses are performed in the same TEXTOR discharge one second after the first ones on the same position.



**Figure 7.3.:** Temporal evolution of the LIDS signal at horizontal observation; recorded by a fast diode equipped with an  $\text{H}_\alpha$  filter, that integrates the LIDS signal in space

The fastest desorption characteristic is seen for thin hydrocarbon layers. As an example a 550 nm thick a-C:D layer was desorbed in TEXTOR, that has been produced in the PADOS glow discharge plasma from  $\text{CD}_4$  precursor gas on rough graphite. The desorption peak is reached extremely fast (after ca. 0.1 ms) and is very thin, hence it drops to  $1/e$  in the same time as it needed to rise and it falls below 10% of the maximum value after only 0.4 ms. Then it stays on a very low but non-zero level of about 4% of the maximum until the end of the laser pulse and then quickly drops to zero within 80  $\mu\text{s}$ . This very fast desorption characteristic is due to the small thickness, but high porosity of the layer. Therefore the released deuterium

can easily and fast escape the carbon network via the pores (cf. chapter 4.3) and deuterium diffusion does not play a role. In the interpretation of the second half of the desorption signal three aspects should be mentioned:

1. The low, but constant desorption level after the sharp desorption peak is most probably due to the lateral heat expansion. The longer the laser is present on the target the larger is the area that is heated above the desorption temperature.
2. An alternative interpretation, namely the diffusion of hydrogen from the graphite substrate during the propagation of the heat wave into the depth of the material, can most probably be excluded as a reason for this behaviour. This is because the substrate has been annealed and outgassed before layer growth. Therefore no significant hydrogen should be present in the substrate. However the adsorption of protium from water vapor and air might occur between annealing and layer growth due to contact of the substrate with the atmosphere, but this effect has not been studied systematically.
3. Except the protium and deuterium line radiation at 656 nm, also C<sup>+</sup> lines (CII lines 657.8, 658.3, 658.4 nm) are transmitted with a low but non-zero transmission due to the spectral width of the H<sub>α</sub> filter (cf. figure 7.21 on page 197). Due to the 5° tilted surface of the interference filter with respect to the detection path, its central wavelength is slightly shifted to the blue, helping in the suppression of these parasitic lines. Nevertheless a strong carbon evaporation could contribute to the LIDS signal at this diode. However, this can also be nearly excluded, since the increasing temperature during laser heating would yield a strongly increasing carbon flux due to the nearly exponential dependence of the evaporation on the temperature. Instead a nearly constant signal is observed in the second half of the heating process. A second argument also speaks against carbon evaporation; namely the fact that the second and following laser pulses on the same spot do not show any signal at all. Carbon evaporation would occur similarly in every laser pulse, since the heating is always the same.

The last consideration about carbon evaporation can explain the other example. A very thick (ca. 15 μm) a-C:H/D layer on an ALT tile of TEXTOR has been grown for more than 3 years without cleaning on tile N°19 at ALT-II blade 6. It was dismantled, cut and installed in the limiter lock like all other samples for LIDS investigations. The example shows a desorption with very small pulse energy, since all higher energies yielded an extremely saturated signal, while this one is only slightly saturated in the peak. The normalisation was done with an estimation of the peak value by comparison of its shape to the just discussed curve. This is justified because both desorption evolutions are very similar in shape at the beginning, just stretched in time. The desorption peak appears slightly later (at ca. 0.22 ms) and the 1/e decay time approaches 1 ms. The characteristic of the further decay differs from the thin layer by the lack of a plateau region. Instead a continuous decay of the signal even after the laser pulse is observed. In fact, it decreases below 10% only after the laser pulse ended. The reason for this general extension in time is the much worse heat conductivity due to the thickness of the layer and its bad heat contact to the substrate (cf. chapter 2.4.3). Therefore both, the vertical and lateral heating is slower. Moreover the bad heat contact to the substrate induces a strong lateral heat propagation in the layer. That increases the heated area considerably (ca. factor 3) as the comparison between laser beam diameter and visible surface modifications showed. Despite a strong reduction of the pulse energy even below the 200 MW/m<sup>2</sup> used here, desorption of hydrogen could not be decoupled from massive carbon evaporation. This is due to the highly porous structure of the layer and therefore its mechanical instability and bad adhesion to the substrate. However this porosity still allows the hydrogen to desorb instantaneously after its local release from the sample. This is why the general shape of both "tokamak-like" layers is very similar, only stretched in time due to heat diffusion. The biggest difference between them

is the behaviour of the second and following pulses. Only in the case of very thick layers with such properties as just described for the ALT-II layer, further laser pulses yield a signal at all. The integral of this signal is about the half of the first pulse and its decay follows the one of the first pulse. Further pulses yield a similar shape, reducing in intensity slowly from shot to shot. This indicates that the origin of these signals and the second half of the first signal is due to carbon evaporation. This is also supported by the surface temperatures above 5000 K measured during LID on this ALT-II layer. Although the filter transmission is low for the CII wavelengths and the central wavelength is even slightly shifted to the blue, such temperatures yield a very high carbon flux due to the nearly exponential dependence.

In conclusion, for tokamak-like hydrocarbon layers the temporal desorption behaviour can be described as a very quick rise and a decay that depends on the further heat wave propagation. This can be a slower decay due to the layer thickness and its heat properties or it can be slower due to slower heating by a longer laser pulse. The latter effect has to be taken into account when comparing the here presented 1.5 ms heating with the 5 ms heating in the reference above. Although the layer is thin there, the peak appeared at 25% of the heating duration, while it is much earlier occurring here. This is probably due to a much slower rising temperature for the long laser pulses used there.

The third example is a DLC layer, which is not a "tokamak-like" layer, but an industrial layer used e.g. for hardening of tools. Although it is thick, it does not tend to overheat like the thick tokamak layers. This is due to a special Cr based interlayer between the DLC and the W substrate that establishes a good mechanical adhesion and thermal contact of the layer. The temperature evolution follows the calculated one like on the thin layers or the pure C or W substrates and therefore no significant C sublimation occurs. The diode signal can therefore be interpreted as the pure hydrogen signal without carbon contribution. The desorption behaviour of such DLC layers is different from the just described characteristic: Although the layers are much thinner than the ALT-II layers, the maximum of desorption occurs much later, usually close to the half of the heating duration. The layers with good heat conductivity do not show any signal after the laser pulse ended and often finish desorption before the heating stops, like in the example in the figure (red data). These layers are produced in a CVD process. Other DLC layers (produced by arc discharge without interlayer) tend to overheat and evaporation like the thick tokamak layers and have a similar decay of the signal. However the desorption maximum is reached always much later than on the tokamak layers. This is maybe due to the much larger hardness and reduced porosity of these layers, which obviously cause a delayed desorption due to diffusion of the hydrogen through the more dense and hard material. Depending on the layer structure they sometimes also show jumps and steps in the LIDS signal in the second half of the heating process, which is attributed to partial layer removal by delamination of big layer fragments.

In any desorption case the LIDS signal has decayed completely after 4-5 ms. Hence, the integration time of the image intensifiers for the cameras was usually set to 5 ms, while the laser pulse started 0.3 ms after the intensifier switched on. This was done as a safety margin for the timing. The fast spectrometer was operated at 10 ms integration time, due to uncertainties in the speed of its mechanical shutter, in order to be on the safe side. In this way the LIDS detection systems certainly recorded the full LIDS signal on a single frame or spectrum, respectively.

## 7.4. Calibration of the Light Detection Systems

Any kind of light detector that is used for the measurement of the light emitted by LIDS has to be calibrated properly to be able to convert the measured signal into the amount of photons. This is valid for any kind of light detector, may it be a camera, spectrometer, diode, etc. Although the specific procedure for the calibration differs from device to device, the general procedure that was applied within the present work, is always the same: A light source of well known spectral radiance is recorded by the detector that shall be calibrated. The detector signal is then calibrated against the known amount of photons emitted by this light source.

For the LIDS calibrations a certified Ulbricht sphere was used as a light standard with known photon emission for the whole VIS and near IR spectral range. The size of the sphere is larger ( $\varnothing \approx 0.2$  m) than the maximal inner diameter of the TEXTOR lock system, hence it has been placed in the tokamak only during operational breaks with venting. This first version of the sphere had a spectral radiance of  $L_{656} = 7.47 \text{ mW/cm}^2 \text{ sr}_{\mu\text{m}} (\hat{=} 6.3 \cdot 10^{15} \text{ photons/nm s} = U_{656}$  into the full solid angle of  $4\pi$ ) at 656 nm. It has to be taken into account that such light standards degrade with time, especially when frequently used in not dust free and vibration free environments. Therefore the second light standard, which was used, was a two-source standard, utilising one large static Ulbricht sphere (labsphere USS600,  $\varnothing \approx 0.4$  m) and a smaller, mobile one like the one previously described. Before and after calibration of the detection systems with the mobile sphere, it has been cross calibrated against the static sphere as the real light standard. The photon emission at the  $H_{\alpha}$  wavelength was  $3.0 \cdot 10^{15} \text{ photons/nm s}$  into the full solid angle and did not change after approximately half a year. This shows the improved stability of the two source light standard. The smaller, mobile version of the Ulbricht sphere "could be placed at the same position where the desorption light appears during LIDS", because the calibration was "carried out during a tokamak shut-down" with access to the torus. "In this way, the same optical path was used during calibration and experiment"[Z11b], which has the advantage that the total optical transmission of the observation system is taken into account. This contains not only transmission reduction of windows by carbon deposition, but also all obstacles (like the liner edges, lens diameters, vacuum ducts etc.) resulting in reduced optical aperture. Moreover no correction for the solid angle has to be applied.

On the other hand the calibration of some detectors like the high-resolution spectrometer could not be performed in this way, since the vessel was not accessible. In such a case the whole optical setup can be rebuilt outside the vacuum for calibration and the transmission of the last window has to be measured separately. For the high-resolution spectrometer, the setup is easily rebuilt outside the vacuum, since it was used at the coaxial observation, which has no optical component inside the vacuum except the vacuum window itself. The CLIO could be moved easily because all optical elements are combined in one compact system. Since the light is guided by fibre optics, no spatial resolution can be obtained from this detector. Therefore extreme care has to be taken in order to include the whole opening ( $d = 5.1$  cm,  $A = 20.4 \text{ cm}^2$ ) of the Ulbricht sphere in the detection path. This was ensured by back illuminating the spectrometer fibre with a laser. The detection cone of the diagnostic is at least as big as the laser illuminated volume, but usually larger because laser light does not necessarily use the full aperture of the fibre. Multiplication of the open area of the Ulbricht sphere with its radiance at the  $H_{\alpha}$  wavelength and multiplication by the full solid angle of  $4\pi$  yield the total number of photons emitted by the sphere opening. If the distance between sphere and detector cannot be rebuilt outside the vacuum (like in this case), a correction of the solid angle is necessary. Here the distance between the 2<sup>nd</sup> mirror of the CLIO setup, which is the effective aperture, to the sphere was 152.5 cm compared to a distance of ca. 229 cm to the LIDS light in the experiment. Therefore a factor of 2.25 arises as correction factor for the solid angle, when the square of the ratio is calculated.



For the camera observation, the emission of the sphere  $U_{656}$  has to be multiplied with the FWHM of the filter transmission (3 nm), which corresponds to the integral of the filter transmission (cf. figure 7.21 on page 197). When calibrating a spectrometer, the dispersion of the spectrometer at the wavelength of interest has to be taken instead.

For the calibration of the camera no special means have to be taken to ensure, that the Ulbricht sphere opening is in the FoV, since this is easily seen on the image. Not the full area of the opening is used for the integration, but only a central part within. This is more accurate, since in the area of interest inside the opening the light intensity is more homogeneous than at the edges of the opening. For any system also the effective integration time has to be taken into account. For the camera the time of the open gate of the image intensifier during calibration has to be used, which was chosen as in most experiments (5 ms). For the high-resolution spectrometer the integration time of the spectrometer camera is the important time. It had to be longer (500 ms) than during the experiment (10 ms in the LIDS measurements), to obtain a good signal. In both devices great care has to be taken, to set all parameters to the same settings as during experiment: record mode, image size, repetition rate, time base, signal amplification by software (brightness, contrast, gamma value, software gain, pre-amplifier gain, electron multiplier gain etc.), noise level (chip cooling, ambient light), readout speeds (pixel shift, effective integration time etc.). If a quantification not only of the background subtracted signals is desired, but also a quantification of a single frame, then also a dark frame has to be recorded without the light source on the day of calibration and measurement. For detectors with inhomogeneous detection on different parts of the detector like damaged pixels on cameras or dark areas due to taper optics on a CCD chip, also the acquisition of a white image is necessary to compensate for the sensitivity gradients. This is also necessary to detect vignetting of the optical path itself. In order to acquire the white frame, the Ulbricht sphere can be moved lateral in order to cover all areas of the FoV subsequently. The obtained sensitivity map can be used to perform the non-uniformity correction by software.

The wavelength calibration of the spectrometer has been done by several spectral lines of deuterium and halogen lamps. It has been found that the high-resolution spectrometer is very sensitive to ambient temperature changes and transport. A minor re-calibration to eliminate spectral shifts (in the sub nm range) and alignment shifts (by not more than 1 or 2 pixels in vertical direction) became necessary after such events.

The calibration of infrared detectors (IR cameras and pyrometers) for the sample temperature during exposure of LID heating, has to obey similar considerations as the calibration of VIS cameras. As a temperature reference several devices have been used depending on the measurement situation:

- For graphite surfaces a stripe of pyrolytic graphite has been heated in vacuum by the Joule effect to known temperatures at given current densities.
- For tungsten surfaces a tungsten lamp with a thick, flat wire (Osram PA 83299, certified as temperature standard (N° 576)) has been used.
- For mixed materials (like CFC with W coating) a TEXTOR test limiter with internal heater equipped with the materials to be measured, has been heated. The measurement by a thermocouple few millimetres below the surface has been used as reference for the surface temperature calibration after a steady state temperature was established (after ca. 30 min).
- Occasionally also the melting temperature of W or stainless steel has been utilised for calibration, when the transition into the fluid phase was visible in time (plateau region) or space (material transport), while applying a laser melting pulse.

## 7.5. Quantification of Released Particles

After the desorbed gases are released from the surface due to thermal heating by the laser, the main aim of the LIDS diagnostic is to quantify the amount of desorbed hydrogen. For a satisfying quantification, the technical boundary conditions and physical processes involved from the release to the loss of the particles from the observation volume have to be known. In the following sections first the more technical aspects of the background subtraction for the LIDS signal are described, since all LIDS measurements are measurements of differences. They measure the additional  $H_\alpha$  light, which is added to the  $H_\alpha$  line radiation already present in the plasma. This background light is dominant in case of desorption of small hydrogen amounts, e.g. hydrogen from the material bulk and becomes less important for higher amounts, e.g. from thick a-C:H layers. On the physics side, the processes involved in the decay of the  $H_2$  or  $D_2$  molecule into spectroscopically invisible ions and visible atoms is described and possible other decay mechanisms excluded. By knowledge of these processes the proper light-to-particle conversion factors are explained. The evaluation procedure – here with the example of a camera detector – can be summarised in the following way:

"The  $H_\alpha$  light emission due to the decay of the H atom after excitation by plasma electron impact is recorded by a digital CCD camera. The background subtraction is done by subtraction of half of the intensity of the previous and following image" for each pixel. The image obtained is called '*desorption image*'. "This image is then integrated by summing" the intensity of all pixels. "The result is converted to the absolute  $H_\alpha$  photon number via the calibration factor that is previously obtained during the camera calibration"[Z11b] (cf. previous section). Finally the amount of desorbed hydrogen is obtained from the number of photons with the light-to-particle conversion factor  $C$  that consists of the atomic yield factor  $1/\gamma$  (chapter 7.5.2) and the  $S/XB$  value (chapter 7.5.3).

### 7.5.1. Background Subtraction

**$H_\alpha$  background subtraction:** The first aim of the background subtraction method is the calculation of a background that approximates the situation at the time of desorption as it would occur without the laser shot. In the standard implementation of the LIDS detection with a 100 Hz image recording, the temporal image separation is already relatively large (10 ms) compared to the desorption duration. Therefore it seems sensible to take the background frames that are closest to the LID frame in time for this reconstruction. In order to obtain a situation at the time of LID, it also seems to be sensible to take a symmetric choice of images before and after the desorption. These two images just before and after the laser pulse are halved in intensity on every pixel and subtracted from the image during the laser pulse pixel by pixel. This means that the arithmetic average of the images before and after the LID frame represents the reconstructed background image for the time of the laser pulse.

It has to be assured that the next image after the desorption frame is free of influences from the desorption process. This was verified by high speed camera measurements or the use of a fast diode during LIDS: The case of the longest LIDS light duration observed by photodiode measurements occurred for the case of very thick (20  $\mu\text{m}$ ) a-C:H layers. Even in this case the  $H_\alpha$  intensity is back to the background level after 5 ms latest.

**Thermal background subtraction:** In the case that the observation system can see the heated laser spot, Planck radiation adds a false signal to the recorded intensity. In an observation setup, in which the laser irradiated spot cannot be seen, this aspect can be skipped completely. This is e.g. valid in the case of the horizontal view at TEXTOR, when flat surface limiters are used. Their plasma exposed surfaces, which are analysed by LIDS, are oriented in toroidal or radial direction and thus usually are not directly seen. For differently shaped test

limiters like the spherical test limiters this is no longer valid because one half of the surface is visible in the horizontal view. In that situation a thermal background subtraction is required. Such geometries have not been used in the present study. But regardless of the limiter geometry a thermal background subtraction has to be always applied for the vertical observation at TEXTOR and in principle also for the coaxial view.

The Planck radiation from the laser heated spot is detected in addition to the  $H_\alpha$  light from the desorption process. In case of a camera or photodiode view utilising a narrow band spectral filter at 656 nm the filter transmits not only the line radiation from the hydrogen atoms but also this Planck radiation from the heated spot. If a wall area with similar thermal properties is available in the vicinity of the LIDS spot, the amount of Planck radiation in the desorption signal can be subtracted by repeating the same laser pulse on this alternative position but in the absence of plasma. In this way only the thermal radiation is recorded. But for thick, inhomogeneous layers the short scale variation in thermal properties and contact to the substrate can foil this procedure, since one cannot be sure to reproduce the same surface temperature and lateral heat extend on a second position. For mixed layers it was also observed, that a consecutive laser shot on the same position can lead to significantly different heat generation due to a supposed transformation of the layer with obviously changed thermal properties. In such cases a different subtraction mechanism has to be applied as described in the following. In the case that such a thermal comparison cannot be used, a different subtraction procedure is needed. It depends on the kind of  $H_\alpha$  detector that is used. In a high sensitivity spectrometer signal the Planck radiation is visible as a background on all wavelengths and can thus be removed by using the signal close to – but outside – the  $H_\alpha$  line profile. This is done before evaluation of the  $H_\alpha$  line by a linear interconnection of this thermal background across the spectral line. However this thermal background has not been observed in the high-resolution spectrometer viewing the laser spot in the coaxial detection path.

For cameras that record the Planck radiation from the heated spot, like in the vertical observation, the thermal background can be distinguished spatially from the  $H_\alpha$  light. At the position of the laser spot a much larger signal appears compared to the surrounding of the spot. In this case, the signal in the spot area is substituted by values from the surrounding, thus interpolating the laser spot position. This leads to a slight underestimation of the photon amount, but due to the small size of the laser spot compared to the extent of the LIDS light, this difference is not significant.

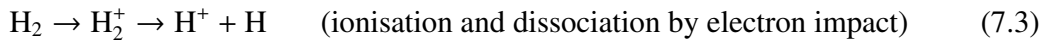
### 7.5.2. Atomic Yield Factor

"The amount of desorbed H and D atoms is determined quantitatively in TEXTOR by local spectroscopy of the  $H_\alpha$  light at 656 nm. By integration" of the  $H_\alpha$  light "and multiplication of a calibration factor that accounts for the detector sensitivity, the amount of photons of each frame is calculated." It is then "transformed into the total amount of hydrogen and deuterium via" the light-to-particle conversion factor that consists of "the  $S/X_B$  value (see next section) and the atomic yield factor" of the molecules [Z11]. The latter will be introduced in this section.

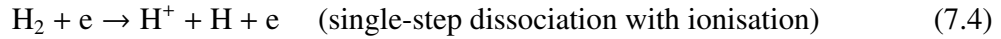
The atomic yield factor takes into account that during dissociation in the plasma, molecules often do not yield the exact amount of atoms they contain. Hydrogen molecules predominantly yield only one hydrogen atom instead of two in the edge plasma. "This is due to the electron induced ionisation and subsequent dissociation processes in the TEXTOR edge plasma that are summarised by the following reactions" [Z11]:



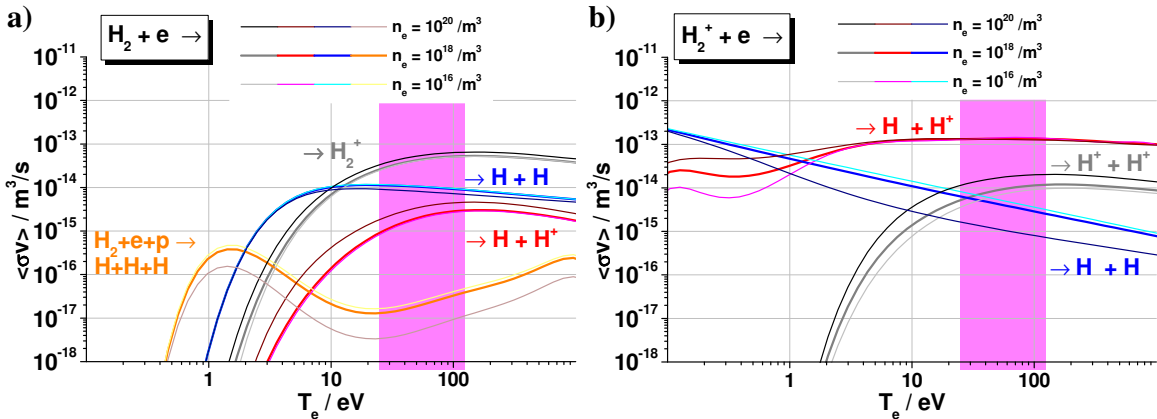
These two processes are dominant in the temperature range ( $25 \text{ eV} < k_B T_e < 120 \text{ eV}$ ) of the TEXTOR edge plasma. The highest reaction cross-section in that regime has the dissociation of hydrogen ions by electron impact (reaction 7.2) with a rate coefficient of  $\langle \sigma v_e \rangle \approx 10^{-13} \text{ m}^3/\text{s}$  (cf. figure 7.4b). The ionisation of the hydrogen molecule by electron impact (reaction 7.1) is the second highest with about a factor of 2-3 lower (cf. figure 7.4a) [Stangeby0, p.35] [Janev3, p.42]. A high reaction cross-section does not necessarily imply a high reaction rate, since the density  $n$  of the "input" species (here  $\text{H}_2^+$  for reaction 7.2) has to be high to realise a high reaction rate  $n \langle \sigma v_e \rangle$ . Nevertheless, the comparison of the cross-section rates is worthwhile, since it shows that these two reactions belong together as subsequent reactions. They can be seen as a single combined reaction because the "output" of reaction 7.1 (or its product) is the "input" (or educt) of reaction 7.2 and because the 2<sup>nd</sup> step reaction has a significantly higher cross-section than the 1<sup>st</sup> step reaction. Thus the life path of the hydrogen due to these two reactions can be summarised as



disregarding the electrons in the notation. Other reactions have much lower cross-section rates. For example the process that combines the upper two steps in just one single combined reaction:



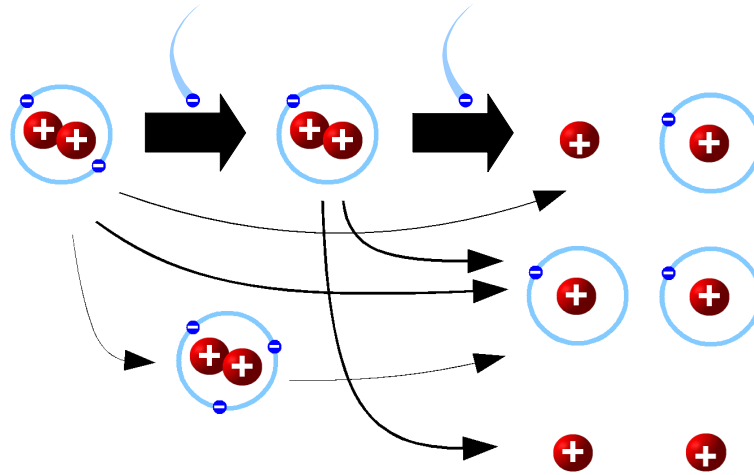
without intermediate step of a molecular ion. The rate coefficient of this reaction is more than an order of magnitude lower even far outside the temperature range under consideration (cf. figure 7.4a and [Stangeby0, p.35][Janev3, p.50]).



**Figure 7.4.:** Reactions of the hydrogen molecule by electron impact; reaction coefficients for proton impact are at least one order of magnitude lower; marked area shows the  $T_e$  range for the desorption spectroscopy in the edge plasma of TEXTOR (data source: [AMJuel12])

A slightly higher rate coefficient is valid for the single-step dissociation into two atoms (blue lines in figure 7.4a). For lower electron temperatures it increases but is still at least a factor of 2 lower than the two-step ionisation/dissociation. There are also other dissociation channels for  $\text{H}_2$  via an intermediate, negatively charged molecule: e.g. the generation of two hydrogen ions via intermediate steps like  $\text{H}_2^-$  [Janev3, p.77], but all have much lower reaction cross-sections than the dominant two-step dissociative ionisation reaction channel.

Because of this characteristic of ionisation and dissociation, each desorbed  $\text{H}_2$  molecule yields only one neutral H atom as source for  $\text{H}_\alpha$  radiation in the temperature regime discussed here ( $k_B T_e = 25\text{-}120 \text{ eV}$ ). The amount of H atoms that emerges from the dissociation of one molecule is the **atomic efficiency**  $\eta$ . For the above example of a pure  $\text{H}_2$  desorption  $\eta_{\text{H}_2}^{\text{H}} = 1$



**Figure 7.5.:**  $H_2$  break-up reactions due to ionisation and dissociation processes by electron impact in a plasma of  $k_B T_e = 25\text{-}120$  eV. Arrow thickness indicates cross-section rate: the two-step ionisation/dissociation into  $H^+$  and  $H$  is the dominant reaction channel.

holds. In order to determine the amount of all desorbed hydrogen particles, the ions have to be taken into account as well. Therefore the amount of hydrogen derived from the LIDS signal has to be multiplied by a factor of 2 in the case of pure  $H_2$  desorption. This compensation factor is called **inverse atomic yield factor**  $Y$  [Irrek8, p.60]. The atomic yield factor  $1/Y$  is then  $1/2$ , expressing that the amount of atoms that remains from the desorbed molecule is halved.

In the case of desorbing  $H$  atoms instead of molecules (which is not the usual case),  $\eta_H^H = 1$  and the atomic yield factor would be 1. In the cases discussed in the present work, the usual case of desorption is the molecular desorption. This molecular release is proved by the radial profile of the LIDS light, since for an atomic source the maximum of the light intensity would be much closer or nearly directly at the wall (details in chapter 7.6). For the case of only  $CH_4$  desorption the atomic yield factor  $1/Y = 0.2$  [Brezinsek7, p.1123]\*. Thus the determined hydrogen amount has to be multiplied by the factor  $Y = 5$ , and thus  $\eta_{CH_4}^H = 0.8$ . For the usual desorption of an a-C:H layer the inverse atomic yield factor is in the range of  $Y = 2.0\text{-}2.6$ . In general, when the atomic efficiencies of all desorbing species are taken into account, the atomic yield factor  $1/Y$  for protium takes the following form:

$$\frac{1}{Y_H} = \frac{\sum_m \eta_m^H N_m}{\sum_m n_m^H N_m} = \frac{N_H + N_{H_2} + 0.5N_{HD} + 0.8N_{CH_4} + 0.2N_{CD_3H} + \dots}{N_H + 2N_{H_2} + N_{HD} + 4N_{CH_4} + N_{CD_3H} + \dots} \quad (7.5)$$

$\eta_m^H$  ... amount of hydrogen atoms after dissociation of one molecule of type  $m$  in the plasma

$n_m^H$  ... amount of hydrogen atoms in the molecule of type  $m$

$N_m$  ... amount of desorbed molecules of type  $m$

On the right hand side of this equation beside the main desorption species  $H_2$  and  $HD$  only a few hydrocarbons are considered, namely those which are unambiguously identified in a mass spectrum of a QMS. Contributions by further species may still exist, but must be small, since on many samples good agreement between LID-QMS and NRA is found (e.g. in chapter

\*In [Brezinsek7] the atomic yield factor  $Y^{-1}$  is called  $\eta$ .

6.1), which detects all H atoms, independent of chemical composition. The atomic yield for deuterium reads in analogy

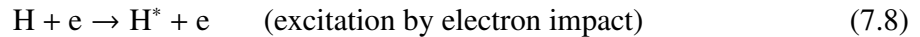
$$\frac{1}{Y_D} = \frac{\sum_m \eta_m^D N_m}{\sum_m n_m^D N_m} = \frac{N_D + N_{D_2} + 0.5N_{HD} + 0.8N_{CD_4} + 0.6N_{CD_3H} + \dots}{N_D + 2N_{D_2} + N_{HD} + 4N_{CD_4} + 3N_{CD_3H} + \dots} \quad (7.6)$$

The more hydrogen (or deuterium) is contained in other species than H<sub>2</sub>, D<sub>2</sub> or HD, the higher this factor is rising above the value of 2. It could only decrease below 2 if a significant amount of hydrogen is desorbed as atoms instead of molecules, which has not been observed. Mathematically it could also become smaller than 1 or even equal to 0 if the break-up of hydrogen would not produce atoms but only ions. Such reaction channels exist, but they are not important at least under the plasma conditions which are considered here. The two atomic yield factors mentioned above can be determined by LID-QMS. When a spectral filter is used in LIDS for example in front of a camera, then the narrow band transmission of the filter is too broad to distinguish the isotopes. In this case the combined atomic yield factor is suitable:

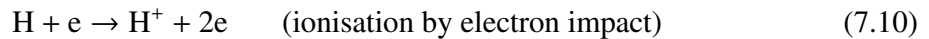
$$\frac{1}{Y_{H+D}} = \frac{N_H + N_D + N_{H_2} + N_{HD} + N_{D_2} + 0.8N_{CH_4} + 0.8N_{CD_4} + 0.8N_{CD_3H} + \dots}{N_H + N_D + 2N_{H_2} + 2N_{HD} + 2N_{D_2} + 4N_{CH_4} + 4N_{CD_4} + 4N_{CD_3H} + \dots} \quad (7.7)$$

### 7.5.3. Light-to-Particle Conversion Factor

The amount of photons emitted in the main plasma by the desorbed particles can be converted into the amount of particles desorbed. In particular the H<sub>α</sub> light is converted into the amount of desorbed hydrogen atoms. This is done by applying the light-to-particle conversion factor, which mainly consists of the atomic yield factor discussed in the previous section and the so called *S*/*X<sub>B</sub>* value. The *S*/*X<sub>B</sub>* value is based on the reaction cross-sections of the excitation and ionisation of the hydrogen atom. These processes take place after the dissociation reactions of the hydrogen molecule, which were discussed in the previous section. The dissociation is, figuratively said, the "birthpoint" of the hydrogen atom, when it can start to emit light until its "death", which is the ionisation into a proton or deuteron. While the other half of the hydrogen atoms (or usually slightly more than a half according to the just discussed atomic yield factor) are already ions after the dissociation of the molecules. They are therefore invisible or – to stay in the picture – "dead" for any line spectroscopy. The hydrogen atoms are exposed to two competing processes: electronic **excitation** mainly by electron impact (7.8) with subsequent decay (7.9) generates light emission:

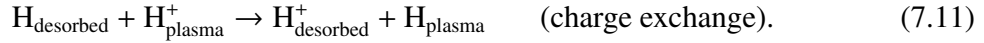


The excitation by proton impact is negligible, since the cross-sections are roughly two orders of magnitude lower for excitation from the ground state or the first excited state [Janev3, p.163, 165f.]. The excited hydrogen atom radiates on different electron transitions, but in the visible range most strongly on the Balmer- $\alpha$  transition (7.9). This is the reason for mainly choosing this spectral line for the LIDS diagnostic. The excitation and spontaneous emission continue until the atom is ionised. Again the ionisation by electron impact



is much more likely (more than 3 orders of magnitude in the cross-section higher) than ionisation by proton impact [Janev3, p.164,166].

There is also another process for ionisation, which has an even higher reaction rate coefficient than the electron impact, namely the charge exchange reaction



For a single hydrogen atom which originates from desorption, charge exchange also terminates its emission, but it is substituted by an ion from the plasma, which is neutralised. Thus this atom then takes over the production of light emission. In total the amount of hydrogen atoms stays constant. Therefore also the amount of emitted photons should stay constant, which allows to neglect this reaction for the determination of the absolute photon amount. The only effect that charge exchange introduces, is a broadening of the spatial extent of the light pattern. The hot protons from the plasma are faster than the hydrogen atoms from the desorption process, because they have the plasma temperature, while the hydrogen atoms from desorption can in maximum have an energy of 1.5 eV. This value is estimated by considering one half of the thermal energy according to the surface temperature at the release of the molecule (usually 800 K, max. 3300 K  $\cong$  0.28 eV) and additionally half of the dissociation energy of the molecular ion (max. 2.65 eV [Janev3, p.140]). Earlier measurements of the temperature of hydrogen atoms, that were not desorbed by LID but during the usual wall recycling on a 1200 K hot graphite limiter in TEXTOR have been performed by laser induced fluorescence. The results showed that most hydrogen atoms have energies below 1.2 eV [Brezinsek2, p.124]. The hydrogen atoms that are generated by charge exchange are much faster, thus their ionisation length is longer. On their way they emit light at similar rates as the cold hydrogen atoms from the desorption process. Thus, the light intensity they emit is lower, but on a longer distance. Therefore the total amount of emitted photons stays constant. On a camera image the  $\text{H}_\alpha$  light pattern is then weaker, but extended more in all directions than the light from the cold atoms.

In order to convert the detected amount of photons  $N_{Ph}$  into the number of desorbed hydrogen atoms  $N_{H+D}$ , a conversion factor  $C$  is needed:

$$N_{H+D} = C N_{Ph} \quad (7.12)$$

$C$  can be determined experimentally, by desorbing pre-characterised samples with known hydrogen content, but it is then valid only for particular experimental settings and circumstances. But it was found during earlier works on laser desorption [Irrek8] and confirmed also in the course of the present work, that in combination with the inverse atomic yield, the theoretically calculated inverse photon efficiency – the so called  $S/XB$  value – gives the correct hydrogen amounts without the need to use calibration samples. This value is also called Johnson-Hinnov factor and represents the number of H ionisations per emitted  $\text{H}_\alpha$  photons. This factor has also been used for the absolute quantification of wall recycling fluxes and hydrogen amounts of gas injection experiments, which are in many ways very similar to laser desorption. The value of this conversion factor is dependent on the plasma properties. It is based on the following relation between the number of atoms and photons (adapted from [Brezinsek2, p.16])

$$N_{H+D} = Y_{H+D} \frac{A_{32} + A_{31}}{A_{32}} \frac{\int_0^\infty n_e n_{H+D} \langle \sigma_S v_e \rangle dr}{\int_0^\infty n_e n_{H+D} \langle \sigma_X v_e \rangle dr} N_{Ph} \quad (7.13)$$

$A_{xy}$  ... rate of spontaneous emission from  $n=x \rightarrow y$ , Einstein-A coefficient in  $1/s$

$n_{H+D}(r)$  ... density of hydrogen atoms (both isotopes combined) in  $1/m^3$

$\sigma_S, \sigma_X$  ... cross-section of ionisation and of excitation in  $m^2$

$v_e$  ... electron velocity in  $m/s$

$\langle f \rangle$  ... =  $\int_0^\infty f b 4\pi v^2 dv$  integration over Maxwell-Boltzmann velocity distribution  $b(v)$

It is important to note that this relation is valid under the following assumptions:

- Although the edge plasma where it is applied is neither thin enough to be in corona equilibrium, nor thick enough to be in local (not to mention full) thermodynamic equilibrium, a complex balance of different collisional and radiative processes is established. Important for the quantitative  $H_\alpha$  spectroscopy is that a balance between the process of excitation by electron impact (7.8) and the spontaneous photon emission with decay into the two lower electronic states ( $n=1$  and  $n=2$ ) is approximately reached.
- In the excitation process (7.8) only excitation from the ground state to the  $n=3$  state is taken into account, neglecting higher excitation.
- The electron velocity distribution is assumed to be a Maxwell-Boltzmann distribution.
- After the first ionisation process the hydrogen ion is assumed to be lost for the spectroscopy with no chance to return by recombination or reemission. The first part is not a strong approximation since recombination is only important in the energy range of few eV but not in the temperature range of 30-100 eV where the  $H_\alpha$  light emission and ionisation take place. On the other hand a return of a part (ca. 20%) of the hydrogen atoms (in molecular or atomic form) to the wall with subsequent reflexion/reemission is observed in ERO simulations.
- The  $n=3$  state is assumed to decay spontaneously. Stimulated emission is neglected.

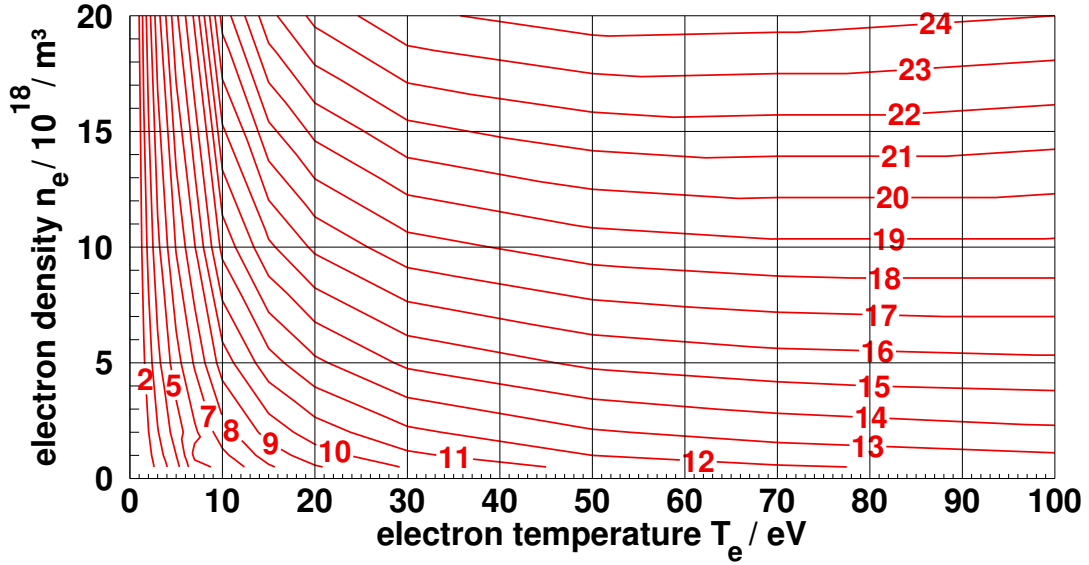
The first factor in 7.13 is the inverse atomic yield. The next factor, which describes the ratio of the decay rate of the observed transition  $A_{32}$  to the total decay rate from the excited state ( $n=3$ ), is called **Branching ratio**  $B$ . The upper integral integrates the ionisation rate  $n_{H+D} \langle \sigma_S v_e \rangle$  over the ionisation length. Including the multiplication with the electron density the integral represents the desorbed flux of hydrogen atoms in units of  $1/m^2 s$ . The integrand of the integral is commonly abbreviated as  $S$  (which stands for the  $S$  in **ioniSation**) in a simplified notation.

The lower integral is very similar and integrates in the same way the cross-section for excitation. Its integrand is commonly abbreviated as  $X$  (which stands for the  $X$  in **eXcitation**). With these three abbreviations the short form of the equation is often written as

$$N_{H+D} = Y_{H+D} \frac{1}{B} \frac{S}{X} N_{Ph} = Y_{H+D} \frac{S}{XB} N_{Ph} \quad (7.14)$$

where  $S$  and  $X$  are dependent on  $n_e$  and  $T_e$  and the combined conversion factor is called the  $S/XB$  value. Its physical meaning can be interpreted as the competition between the excitation, which in the subsequent decay emits light and the ionisation that terminates light emission. The gradients of  $S$  and  $X$  are quite high in the low temperature range below 15 eV, hence the application of this conversion factor might be difficult. Fortunately, in the temperature range of interest both values are only weak functions of temperature and their quotient is only weakly dependent on density (cf. figure 7.6), which is a desired property of good conversion factors. Due to the slightly different dependencies on  $n_e$  and  $T_e$  either the excitation or the ionisation is more pronounced depending on the plasma parameters. The same amount of desorbed hydrogen emits less light if ionisation is stronger. Then the  $S/XB$  is higher. This is valid in hot and dense plasmas, where also intuitively the dominance of the ionisation is expected. On the opposite side, in cooler and thinner plasma regions, where ionisation is less dominant, the excitation and the subsequent emission are relatively stronger than in the previous case. Here the LIDS signal increases, thus the  $S/XB$  value has to decrease. In general its value is – for  $k_B T_e > 15$  eV – more a function of density than temperature. The  $S/XB$  value has been measured in many previous experiments and calculated theoretically. The calculated values are available in the ADAS database (Atomic Data Analysis Structure) [ADAS].





**Figure 7.6.:**  $S/XB$  value dependence on electron temperature and density in the plasma for conditions of the edge plasma, theoretical calculations from [ADAS]

For the decision which  $S/XB$  value to apply a radially resolved  $H_\alpha$  measurement is necessary. Mainly the 2D camera image of the horizontal observation is used. The maximum of the  $H_\alpha$  light on the desorption image is determined. For the case of an automatic search, the images are smoothed by convolution with a gauss function prior to a simple maximum search. (The camera image information stamp – called SIS in the AVT camera – in the first 24 pixels of the first row has to be deleted before this procedure.) After the position of the maximum is found, it is converted to the minor plasma radius position. As position reference the reading of the limiter lock position together with a characteristic edge or line of the limiter on the image is used, which is often very good illuminated at the end of a discharge or in a disruption.

"The electron density and temperature at the radial position of this light maximum are then taken"[Z11b] from edge diagnostics: He- or Li-beams, Langmuir probes, etc, mainly from the supersonic He-beam (SHE) [Stoschus11] in the present work. These two values are then taken "to look up the corresponding  $S/XB$  value from the ADAS database." [Z11b] (cf. figure 7.6)

In combination with the previously introduced atomic yield factor the combined light-to-particle conversion factor is the  $S^Y/XB$  value:

$$N_{H+D} = \frac{SY}{XB} N_{Ph} , \quad \text{thus the conversion factor } C = \frac{SY}{XB}. \quad (7.15)$$

#### 7.5.4. Field of View Correction

In a static setup, like the horizontal and vertical observation at TEXTOR, "also a correction for the estimated light fraction outside the field of view has to be applied" for desorptions far away from the LCFS, "since the cameras do not follow the laser spot." [Z11] In principle this should not be necessary in a coaxial ITER-like setup (see setup 3 in chapter 7.2). But the prototype which was evaluated at TEXTOR does not overcome this problem of light loss for desorption positions which are more than 30 mm behind the LCFS. To investigate the light loss at the horizontal observation (HO) a dedicated experiment was optimised in order to reduce losses outside the collection optics. For this purpose "the sample was mounted in the centre of the holder and thus in the centre of the observation volume. Profiles of the desorption images show that the fraction of uncaptured light is" less than 30% at the HO [Z11b] (cf.

figure 7.8 and chapter 7.10 section "uncaptured light"). According to the desorption images and toroidal profiles the maximal distance without strong light loss is between 30 and 40 mm from the LCFS. For larger distances from the LCFS, the loss of light is similar in the vertical and horizontal observation and unfortunately also in the coaxial observation, which should in principle overcome this. For the HO and VO the limiting factor is the port duct of TEXTOR, that hides significant parts of the LIDS light when it extends toroidally and poloidally for desorptions with larger distances from the LCFS.

A second aspect is the light collection by fibre optics in case of the coaxial observation (CLIO), which is not as homogeneous as by cameras in the HO and VO. Two problems arise by the use of fibre optics:

- If the focal plane of the optics is in the position of the light emission and thus the light collection is done by imaging this position to the fibre end, then the image is sharp. Therefore no losses at the fibre edge occur, but a change of position of the light source or its distribution leads to a change in the output position at the other end of the fibre. This is critical, if spectrometers are used to analyse this light, since they usually have a very thin entrance slit, that lets only pass the fraction of the light, that is within the slit. Usually this is not a serious problem, since the light distribution is homogenised by long fibres and a lateral change of the observed light results in a radial movement of the light in the fibre cross-section. Thus, still reaching the spectrometer. If the fibres are shorter with only few reflexions, then the inhomogeneity at the fibre exit might cause unexpected changes in the intensity of the observed spectrum.
- This effect is diminished or even mitigated if the focal plane of the optical system is not in the position of the emitted light – like in the coaxial observation system at TEXTOR. In this case the image is not sharp, but vignetted and light homogeneity at the fibre exit is improved. On the other hand, light collected at the edges of the detection cone has a worse transmission through the fibre than light collected in the centre of the cone in this setup. Thus, a lateral change in the position or shape of the light source will lead to a change in the homogeneous light intensity at the output of the fibre. These effects can be decreased by using a shorter fibre without large differences in beam path length for light beams with a large angle to the fibre axis compared to beams with a small angle.

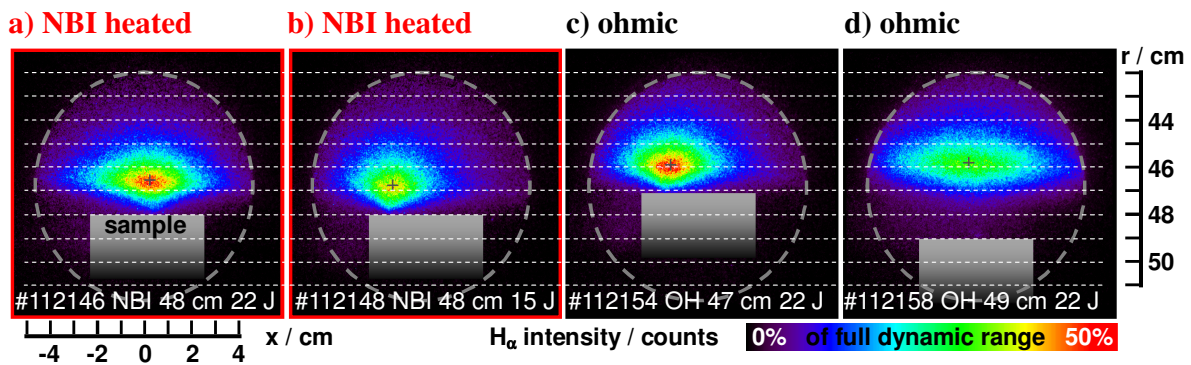
In order to omit these effects, cameras in combination with spectral filters are preferred as light detectors, where vignetting and inhomogeneities as well as loss of light can directly be seen. For the cases of light loss a Field of View (FoV) correction  $V$  has to be applied, which is the ratio of captured to total  $H_{\alpha}$  light which is emitted during LIDS. Its determination depends on the boundary conditions in different ways: Often one half of the image is complete, thus cutting of the camera image in the symmetry plane can be done. The contribution of the signal on the incomplete part of the image is ignored, while the one on the complete part of the image is doubled. When parts of the  $H_{\alpha}$  light are lost in both toroidal directions, a more complicated calculation of the  $V$  factor has to be performed either by using similar experimental desorption shapes in comparable conditions or by taking simulated shapes from numeric calculations like ERO or EIRENE. For the first solution a complete light distribution measured under similar conditions can serve as a template. By shifting it toroidally or radially to the current desorption position the missing photon amount can be determined. For the other case, the reproduction of the shape of the desorption cloud by the simulations is not completely satisfactory (detail in chapter 7.6 on page 180). Thus, the worth of the deduction of  $V$  from the comparison with simulations is limited and doubtful.

In total, the conversion factor can be extended by the geometric FoV factor in the following way:

$$N_{H+D} = N_{Ph} \frac{S}{XB} (n_e, T_e) Y_{H+D}(C_x H_y D_z\text{-fraction}) V(\text{relative positions}). \quad (7.16)$$

Typical values for the  $S/XB$  value are in the range of 13-17, usually 15; for the atomic yield factor for a-C:H layers 2.0-2.6, usually 2.4. This is rather a lower limit, because not all hydrocarbons could be unambiguously identified in the QMS spectra. For desorption of implanted hydrogen from tungsten it would be 2.0. The FoV correction often is  $V = 1$ , when the desorption position is close enough to the LCFS and in the centre of the observation. In other cases it can easily reached values as high as 4 and slightly higher.

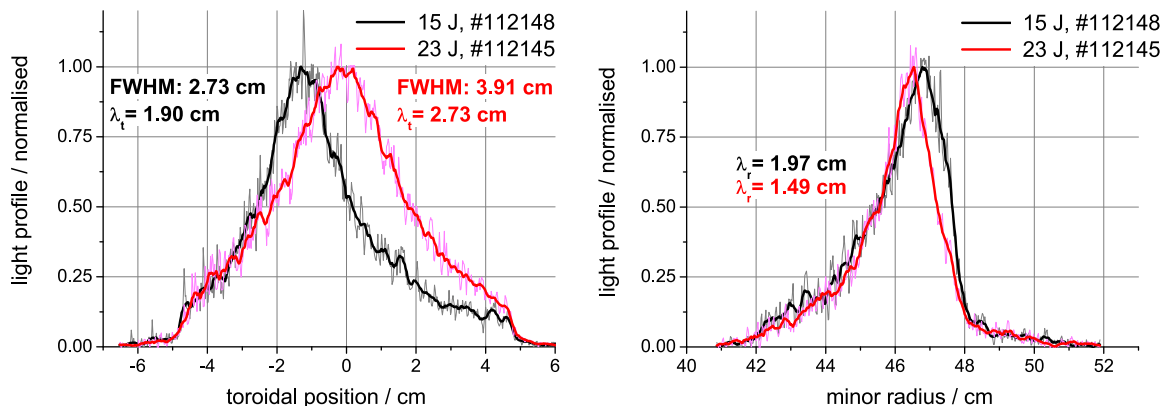
"Finally, the obtained amount of desorbed H atoms is normalised to the desorption area, which for layers with good attachment and heat contact to the substrate, is equal to the size of the nearly top-hat like laser beam." [Z11b] For increased lateral heat conductivity the area of desorption has to be estimated from temperature simulations or measurements or from visible changes of the sample surface in post-mortem analysis.



**Figure 7.7.:** LIDS on 2.5  $\mu\text{m}$  thick a-C:H layers (Balinit<sup>®</sup> B3a); background-free H $\alpha$  images, all in the same colour scale; effect of laser power, wall-to-plasma distance and plasma heating effect; already published in [Z11b]

"The change of the distance" of the desorption spot "to the LCFS has a significant effect on the shape of the H $\alpha$  light." [Z11b] For desorptions further away from the plasma, the plasma region, where excitation can take place, is further away from the desorption position and thus the atoms can spread much more in toroidal direction before they are excited and emit light (cf. figure 7.7d). This results in a broader light pattern in toroidal and poloidal direction. "But the image integral does not change, as long as all the light is collected by the detection optics." [Z11b]

For desorption conditions, in which the surface of the carbon material is not overheated and thus the carbon release by evaporation or layer delamination is small, the LIDS light pattern has a different shape than with a significant C release. One example is shown in figure 7.7, which is also published and discussed in [Z11b]. The only differences between image a and b is the higher laser energy in case a (and a toroidally shifted desorption position because always a fresh undepleted sample position with the same hydrogen content was used in this series of measurements). The plasma conditions and sample distance to the plasma were kept constant. The higher laser energy leads to a calculated surface temperature of around 3300 K, which is about 1000 K hotter than for case b. (For details of these temperature estimations cf. chapter 2.4.3.) The effect of this overheating is a partial layer removal (cf. optical microscopy and confocal profilometry in chapter 3.2). This carbon release broadens the shape of the LIDS



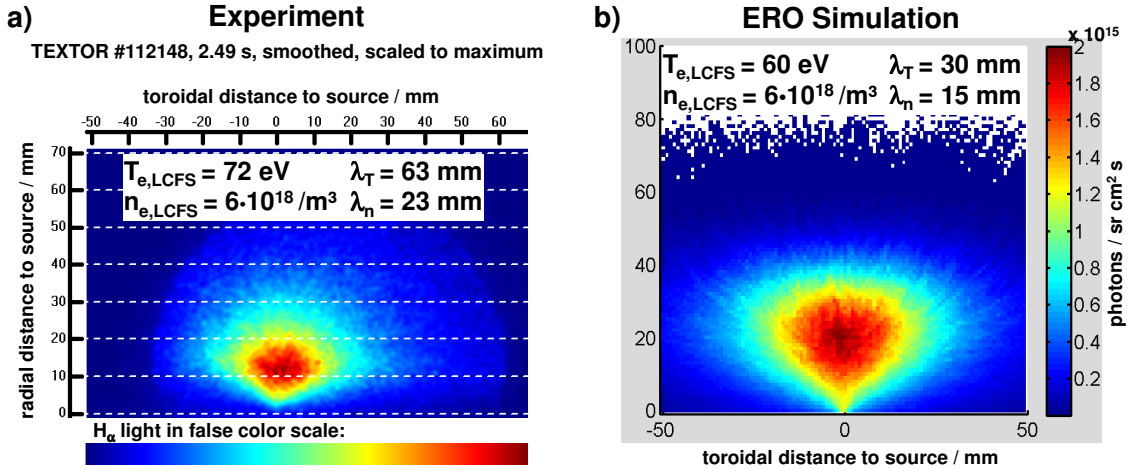
**Figure 7.8.:** LIDS on 2.5  $\mu\text{m}$  thick a-C:H layers (Balinit<sup>®</sup> B3a), profile through light maximum of background free  $\text{H}_\alpha$  camera images, desorption at 48 cm minor radius

light pattern in toroidal direction, as this is light from a  $\text{C}^+$  ion. This is already visible on the colour coded  $\text{H}_\alpha$  images. For a more detailed analysis the toroidal profiles of both cases are confronted with each other in figure 7.8. The radial position chosen for this comparison is the one of the light intensity maximum in the individual image, which is determined on a 2D-gaussian smoothed image. Although the unsmoothed original data (shown as thin lines in grey and pink colour) are not very spiking, they have been smoothed (shown in bold black and red) because for a shape comparison a normalisation should be done, which is hindered even by a single high spike. Thus, the normalisation is done on the 1D-nearest-neighbour smoothed curves and the unsmoothed data are scaled accordingly. The spiking data in grey and pink colour show the original values of one single row of the image, but scaled by a factor, such that the bold black and red colour curves are normalised.

## 7.6. Simulation of the Light Emission with ERO

In order to gain certainty, that all relevant physical processes are included in the understanding and evaluation of the processes involved in LIDS, numerical simulations have been done to verify the correctness of the conversion factors and gain more insight into the significance of the LIDS light shape.

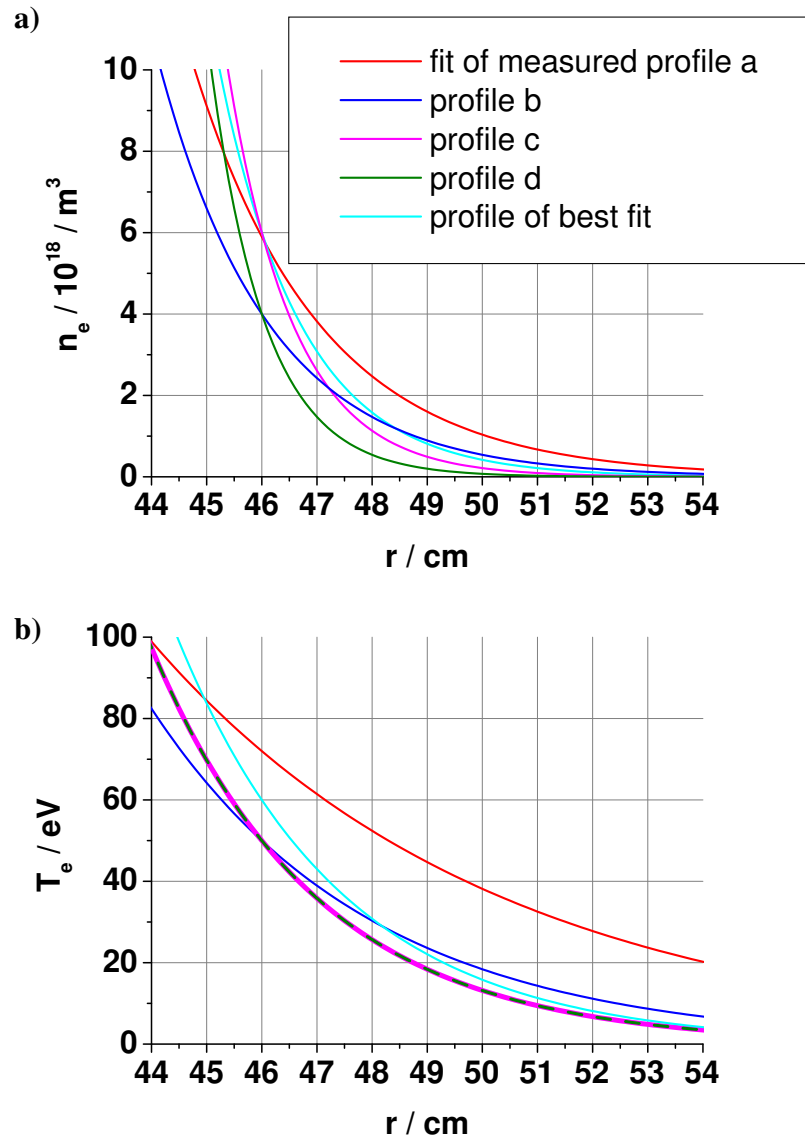
The amount of  $\text{H}_\alpha$  light measured in the LIDS experiments and the light distribution can be modeled in numerical simulations of the processes during desorption. In earlier works [Irrek8] such comparisons have been done with the Monte Carlo code EIRENE [Reiter92] for neutral particles. Here the Monte Carlo code ERO is used, which is frequently utilised for gas injection simulations and is suited to take into account many physical processes in the plasma and effects which result from the close presence of a solid limiter. The ERO code had mainly been used to calculate the transport and recycling of plasma impurities, but has recently been extended [vanHoey11] by a hydrogen tracking module, to take into account hydrogen transport and recycling. Besides this new feature, the ERO code includes a variety of relevant, surface related plasma-wall interaction processes such as adsorption, desorption, erosion and deposition mechanisms, particle reflexion etc. For some processes it relies on calculations by other programmes such as TRIM/[SRIM] or molecular dynamic codes. The desorbed particles are followed by the Monte Carlo procedure using the atomic physics database [ADAS], taking into account the interaction with the background plasma by collisions, friction and electromagnetic forces. The calculations are carried out in the presence of a given background plasma, which



**Figure 7.9.:** Comparison of (a) measured LIDS H $\alpha$  light distribution from a 3  $\mu\text{m}$  a-C:H layer and (b) numerical simulation of a comparable hydrogen gas puff with adapted NBI heated plasma conditions (plasma profile for "best fit")

is characterised by the electron temperature and density. In the calculations described here these two parameters are chosen to be exponential decay functions and are specified by the values at the LCFS ( $T_{e,LCFS}$  and  $n_{e,LCFS}$ ) and the e-folding decay lengths ( $\lambda_T$  and  $\lambda_n$ ). The calculations are done for a desorption position at  $r = 48 \text{ cm}$  with a circular limiter of 11 cm diameter at the same minor plasma radius. In the ERO results the position of the laser spot corresponds in radial and toroidal direction to the coordinates 0 and 0 – the origin of the ERO coordinate system. In this coordinate system the LCFS is at the radial position of 20 mm. The coordinates of the experimental data have been adapted to the ERO coordinates for better comparison. Although the gas injection into the plasma due to the laser induced desorption in the experiment is in the millisecond range, for the ERO calculations an injection of 1 s duration with a constant particle rate of  $10^{19} / \text{s}$  was programmed. This is justified, because the simulation result scales linearly with injection time and source rate. For every run a total simulation duration of 1 s was chosen. The desorbing molecules or atoms are programmed to leave the surface with an initial energy of 0.2 eV. In analogy to the sample holder of the experiments, a flat and horizontal wall surface was chosen, that is parallel to the magnetic field lines. The code calculates the particle transport and atomic processes and via the ADAS conversion factors the H $\alpha$  light distribution. For the comparison with the experiment this light distribution is line integrated in poloidal direction in the same way as the camera at the horizontal view is doing it in the experiment. The code delivers the total number of emitted photons and also the H $\alpha$  light distribution in radial and toroidal direction, which can then be compared to the experimental LIDS images (cf. figure 7.9). The spatial resolution in the ERO calculations is 1 mm.

At first the plasma parameters as measured by the supersonic He beam during the LIDS experiment in an NBI heated plasma have been used:  $k_B T_{e,LCFS} = 72 \text{ eV}$  with a decay length of 63 mm and  $n_{e,LCFS} = 6 \cdot 10^{18} / \text{m}^3$  with a decay length of 23 mm. The experimental LIDS image (figure 7.9a) differs significantly from the calculated light distribution (figure 7.11a). In the calculation the maximum of the light intensity is at the injection position, while it is 1.5–2 cm above the surface in the experiment. Also the toroidal extent of the calculated pattern is smaller than in the experiment. Nevertheless, the total number of photons in the simulation volume agrees very well with the measured photon amount of roughly  $10^{16}$  when the calculated photon number is scaled with the amount of injected molecules. Further studies with

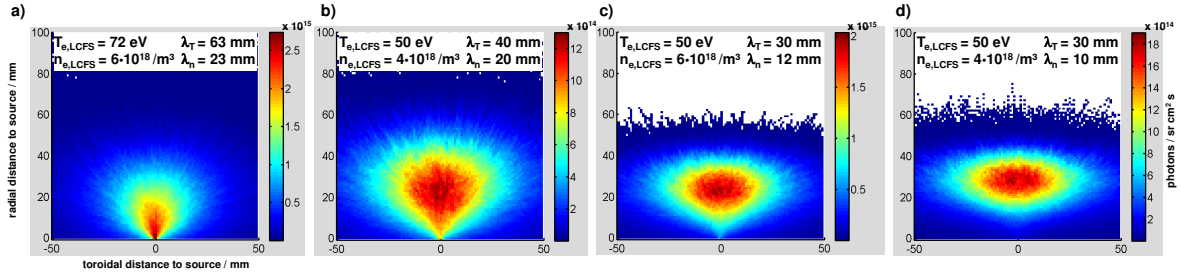


**Figure 7.10.:** Plasma profiles used in the ERO simulations; LCFS at  $r = 46$  cm

the same hydrogen injection but changed local plasma conditions have been done (see figure 7.11b-d). The study shows that the light pattern is extremely sensitive to plasma variations, even when the changes are small ( $< \text{factor } 1.5$ ) in the absolute values. The plasma parameter variations have mainly been done for the density, since the  $H_\alpha$  light emission is much more sensitive on the density than temperature for two reasons:

- As described in the previous section, the  $H_\alpha$  light emission efficiency is more a function of  $n_e$  than  $T_e$  above ca. 20 eV.
- The temperature decay length is a factor of 2-3 larger than the density decay length in the edge plasma, thus the effect of the temperature gradient on the light pattern is further reduced.

Two different  $n_e$  values have been chosen (cf. figure 7.10a): 4 and  $6 \cdot 10^{18} / \text{m}^3$  at the LCFS. The temperature was varied between 50 and 72 eV. The variation of the decay lengths had to be chosen larger (ca. factor 2) in order to obtain a simulation result that agrees with the experimental observation to a satisfactory degree. The series of plasma conditions in figure 7.11 has been chosen such that the light moves more and more away from the desorption position (from image a to d).



**Figure 7.11.:** Strong variation of  $H_\alpha$  light pattern for the identical  $D_2$  gas release under modest variations of plasma temperature, density and their decay lengths, while the total amount of  $H_\alpha$  photons is nearly constant (numerical simulations with ERO);  
a): plasma parameters as measured for figure 7.9a, 7.7a and 7.7b  
b), c), d): plasma parameters as shown in figure 7.10 for profile b, c and d

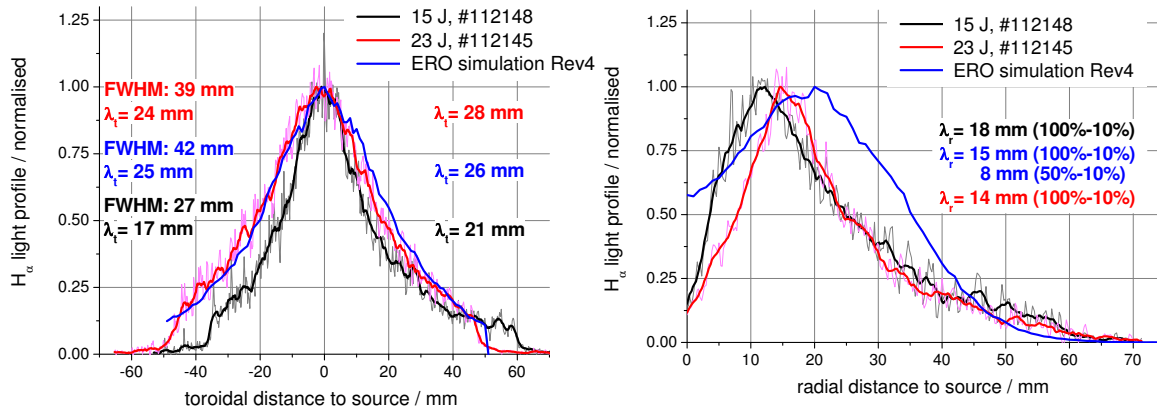
When changing the plasma parameters in the calculation, the light intensity distribution adapts to the variation of the plasma conditions such, that preferentially the emission takes place at similar light-to-particle conversion factors:  $14.5 < C/2 < 16$  (cf. table 7.1). The same behaviour is also observed in the experiments (cf. figure 7.7 on page 179 and discussion). In the experiment the conversion factor at the position of the light maximum was only changing by a factor of 1.04 between ohmic and NBI heated plasmas. In the simulations the conversion factor  $C$  is easily calculated as the quotient of the total photon number and the injected particles. Although the light pattern changes significantly, the total photon number and therefore the conversion factors vary only within a factor of 1.06 from the mean value. Based on experiment and simulation the conclusion can be drawn, that the light shape is very sensitive to the plasma conditions while the total amount of photons is very stable.

plasma profile:	a (fit to exper.)	b	c	d	best fit by shape	LIDS experiment
$n_e / m^{-3}$ at LCFS	$6 \cdot 10^{18}$	$4 \cdot 10^{18}$	$6 \cdot 10^{18}$	$4 \cdot 10^{18}$	$6 \cdot 10^{18}$	$6 \cdot 10^{18}$
$\lambda_n / mm$	23	20	12	10	15	23
$k_B T_e / eV$ at LCFS	72	50	50	50	60	72
$\lambda_T / mm$	63	40	30	30	30	63
$C$ from ERO	$14.5 \times 2$	$15.0 \times 2$	$15.0 \times 2$	$16.0 \times 2$	$14.5 \times 2$	—
radial position $r$ of						
LIDS maximum / cm	47.8	45.6	45.6	45.1	45.9	46.7
$n_e / m^{-3}$ at maximum	$2.7 \cdot 10^{18}$	$4.9 \cdot 10^{18}$	$8.4 \cdot 10^{18}$	$9.8 \cdot 10^{18}$	$6.4 \cdot 10^{18}$	$4.4 \cdot 10^{18}$
$k_B T_e / eV$ at maximum	54	57	57	81	51	64
$s/X_B \times Y$ for maximum						
from ADAS	$13.5 \times 2$	$15.3 \times 2$	$17.6 \times 2$	$18.7 \times 2$	$16.1 \times 2$	$15.0 \times 2.4$

**Table 7.1.:** Plasma profile parameters and light-to-particle conversion factor  $C$  calculated by ERO simulations of the LIDS light and corresponding values from ADAS for  $n_e$ ,  $T_e$  and  $s/X_B$  at light intensity maximum and in experiment; source at  $r = 48.0$  cm

Due to the high sensitivity it is a challenging and computational-time consuming task to find the plasma parameters that reproduce the shape of the  $H_\alpha$  light exactly. The best approximation of the experimental and simulated light shape, which could be found, is shown in figure 7.9b). The corresponding profiles through the intensity maxima of the experimental and simulated light patterns are shown in figure 7.12. The plasma parameters of this "best fit" scenario

have the same electron density and only a slightly reduced (factor of 1.2) temperature at the LCFS compared with the experimental data of the helium beam, but a factor of 2.1 stronger temperature decay and 1.5 faster density decay.

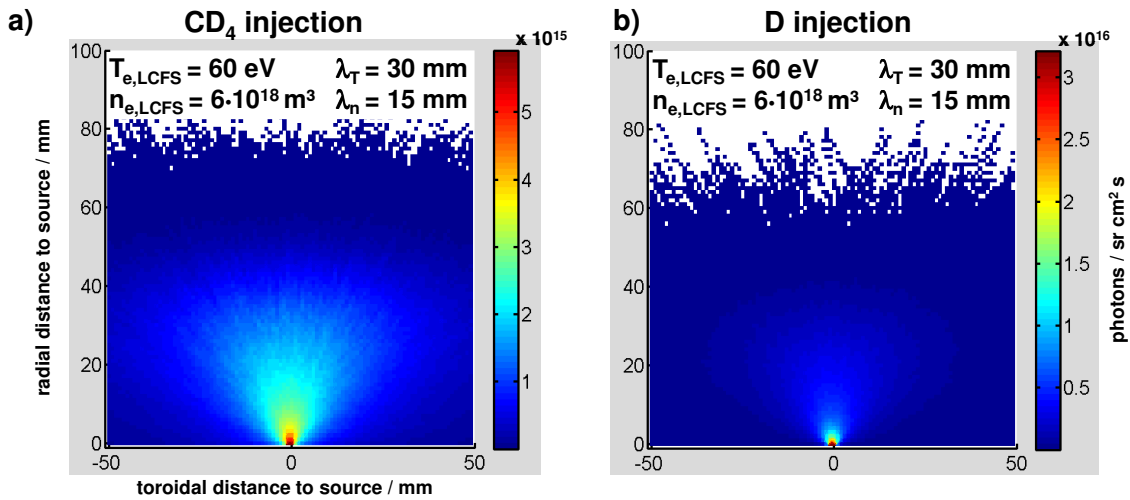


**Figure 7.12.:** Comparison of measured LIDS profiles with numerical calculations for the images in figure 7.9 on page 181

The toroidal extent is reproduced very well by the simulation. The FWHM value and the e-folding decay length on both sides of the maximum fit best to the high energy desorption case of the experiment. The radial light distribution shows a maximum slightly further inside the plasma compared with the experiment and has larger radial extent. The inward radial decay length of the light intensity, which is defined as the e-folding decay length from the intensity maximum into the plasma is 15 mm in the "best fit" scenario. This value is true for an estimated exponential decay from the maximum value to 10% of the maximum value. However, qualitatively the radial decay in the ERO data is not described very well by an exponential decay from 100%-50% of the maximum value. Only for lower values an exponential decay with 8 mm decay length fits. In contrast, the experimental data are fitted very well by an exponential decay with decay lengths of 18 mm and 14 mm, for the low and high energy case, respectively. A faster radial decay of simulated profiles and a light maximum further inside the plasma than in the experiment has already been observed in the work of [Irrek8] when the experimental data had been compared with EIRENE code simulations. This deviations of the light shape in experiments and simulation indicate that the plasma parameters at the position of laser desorption differ from those measured by the helium beam diagnostics. Since these diagnostics measure at different toroidal and poloidal positions, the reason for this deviation could be different magnetic connection lengths or local plasma cooling and distortion effects by the desorbed gases. A more unlikely explanation for the deviations could also be an unknown systematic effect, that might not be considered in the numerics.

For the plasma conditions with the best match between experimental and theoretical light distribution further ERO simulations have been performed in order to study the effect of hydrocarbons and atomic deuterium on the light distribution. In figure 7.13a the  $H_\alpha$  light emitted by a pure  $CD_4$  injection with the same puffing rate as for  $D_2$  has been simulated. The same calculation has been carried out for a purely atomic deuterium release (cf. figure 7.13b). In both cases the light distribution is qualitatively completely different from the  $D_2$  injection. The intensity maximum is directly at the wall and the radial and toroidal extent is much smaller than for molecular deuterium. This confirms the conclusion obtained by LID-QMS and theoretical considerations, that the hydrocarbon fraction is small and the hydrogen desorbs predominantly as a molecule from the surface, because such light patterns have never been observed experimentally.





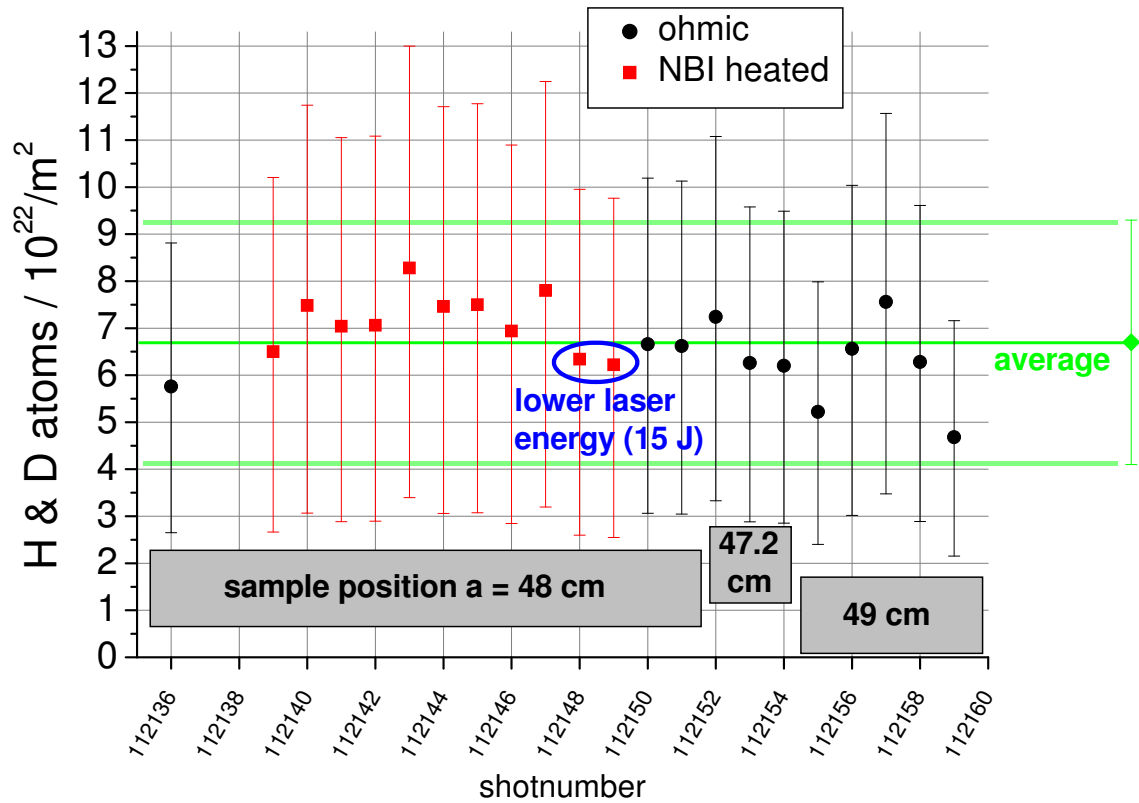
**Figure 7.13.:** Numerical ERO simulation of  $H_\alpha$  light from (a) pure  $CD_4$  injection and (b) pure atomic deuterium injection under the same plasma conditions as in figure 7.9b

## 7.7. Reproducibility and Stability

In order to obtain the statistical variation of the hydrogen release and detection processes of laser induced desorption spectroscopy in the setup used, an experiment was performed that minimised uncertainties in the LIDS measurement.

"For this study the a-C:H layers formed in situ in the scrape-off layer (SOL) of TEXTOR would not have been a good choice because of their inhomogeneous layer thickness and hydrogen content mainly in radial plasma direction. Moreover, they change due to their growth and also due to varying C impurities in the plasma. To overcome these problems and to obtain a high LIDS signal well above the plasma background light, a thick, homogeneous a-C:H layer was used. In order to exclude hydrogen desorption from the 2 mm-thick tungsten substrate, it was heated in vacuum ( $p < 10^{-3}$  Pa) to  $1000^\circ$  C and kept at this temperature for several hours. The further production was carried out by Oerlikon Balzers Coating Germany GmbH using plasma-assisted chemical vapour deposition. Firstly, a Cr-based interlayer of around  $0.6 \mu\text{m}$  was generated for better adhesion of the a-C:H layer. The a-C:H layer on top had a thickness of around  $2.5 \mu\text{m}$ . This two-layer system is commercially sold as the Balinit<sup>®</sup> DLC layer. This sample was introduced into TEXTOR from the bottom in the material test facility. It was mounted horizontally on a stainless-steel holder and retracted by 2 mm from its top surface. Thus, the sample surface was parallel to the magnetic field lines and exposed as little as possible to the plasma. This was done in order to prevent the sample from any change of hydrogen amount by layer build-up or hydrogen depletion due to plasma heating. The distance between the desorption position and the LCFS was changed between discharges as indicated in figure 7.7. [Z11b] The two missing discharges (#112137-8) in the overview figure 7.14 are omitted because no data were recorded by the camera due to a technical failure. For the other data together "the reproducibility of the LIDS signal is good with a standard deviation of  $\pm 13\%$ . The LIDS measurement is insensitive to moderate plasma parameter changes because the main light emission region follows the plasma (for details cf. figure 7.22 on page 202 and its discussion). The distance of the desorption spot from the LCFS is unimportant as long as all the desorption-induced  $H_\alpha$  light is collected.

Overheating of the wall by the laser does not alter the LIDS signal much, so that a big temperature margin towards higher temperatures can be selected to be sure of total desorption in the first laser pulse. A cross-check of the absolute value of the hydrogen content of the

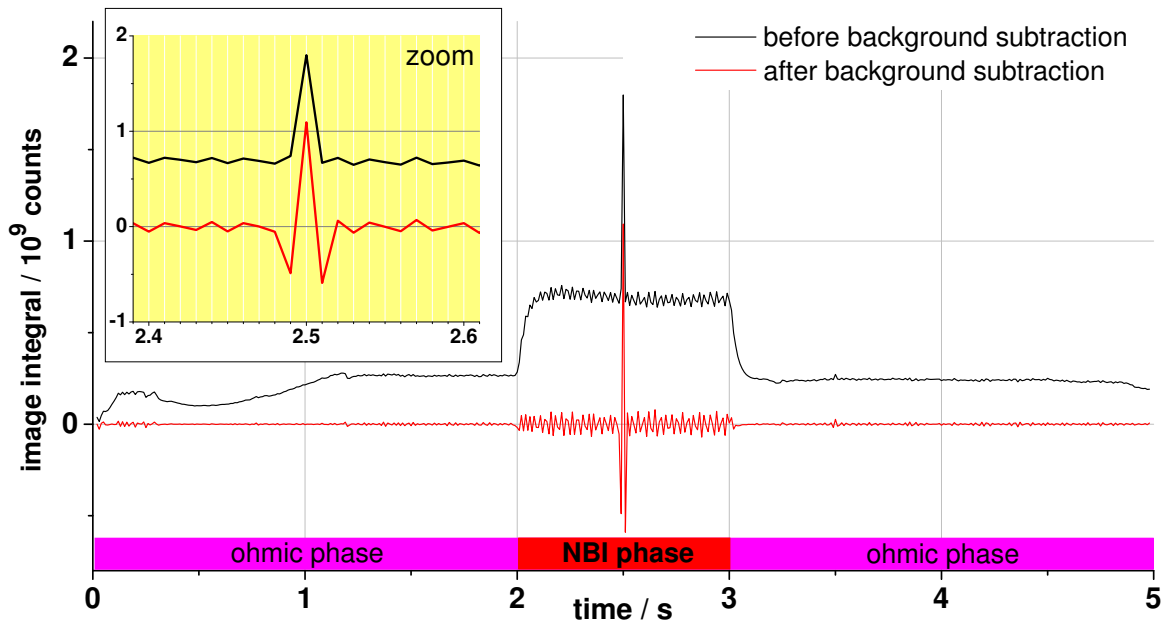


**Figure 7.14.:** LIDS on a sample with homogeneous hydrogen content (Balinit<sup>®</sup> B3a) with variation of plasma properties, laser energy and desorption position shows small standard deviations:  $\pm 13\%$  (for all data),  $\pm 9\%$  (only NBI heated plasmas) and  $\pm 7.2\%$  (for NBI except low laser energy); black/red error bars = errors of a single LIDS measurement; green error bars = error of the measurement series; similarly published in [Z11b]

sample with ex situ laser desorption showed" good agreement [Z11b]. The average values of the in situ and ex situ method differ only by a factor of 1.03.

The standard PWW plasma conditions "were used in 11 ohmic discharges. The other 11 discharges were additionally heated by a neutral beam injector (NBI) to vary plasma conditions and compare the performance of LIDS in conditions" with higher background fluctuations. The NBI beam 1 was used with  $H_2$ , 50 kV and a V-target opening of 150 mm for 1 s duration. "The NBI heating raised the  $H_\alpha$  background light in the measurement position by a factor of 3 and increased its fluctuation amplitude by a factor of 8 (see figure 7.15) on the timescale of the light integration of 10 ms." [Z11b] The increased  $H_\alpha$  level is the consequence of the increased flux on the first wall, due to increased densities and temperatures at the plasma edge.

"The hydrogen content of the 22 desorbed positions evaluated according to the procedure in the previous section is shown in figure 7.14. The overall standard deviation from the average value is  $\pm 13\%$ , which is seen as satisfactory, when the change of plasma conditions, the change of distance to the LCFS and the energy change of the laser pulse are kept in mind." The increasing amplitude of the  $H_\alpha$  fluctuations and the higher "level of the background light in the NBI-heated discharges do not lead to a significant change of the resulting value. It is only a factor of 1.1 higher compared to the average in the ohmic discharges. Also the scatter of the values does not increase but is even smaller than in the ohmic case due to the constant sample position. The change of laser energy does not affect the LIDS value as long as total desorption is achieved in the first pulse. The second laser pulse proves that more than 90%



**Figure 7.15.:** Typical  $H_{\alpha}$  light trace of the LIDS diagnostic recorded by the 14-bit digital AVT camera and integrated on the whole image; desorption of a  $2.5 \mu\text{m}$  thick a-C:H layer (Balinit<sup>®</sup> B3a); laser pulses at 2.5, 3.5, 4.5 s; TEXTOR discharge #112139; for zoom cf. figure 7.19 on page 191; similarly published in [Z11b]

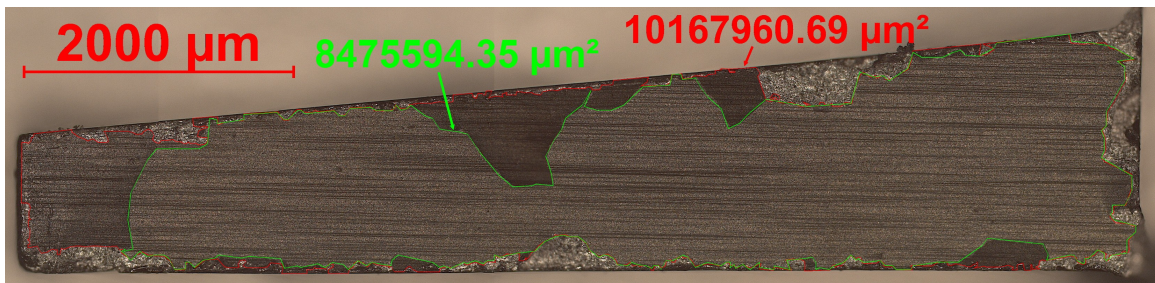
of the hydrogen is desorbed. Usually, the signal in the second desorption is below 3% of the first one and always below 6%. Consecutive pulses yield much less, if anything at all." [Z11b] It should be noted that a small signal in the second pulse is only a good proof of complete desorption for hydrocarbon layers but not for W and probably other metals.

This measurement is a measurement series since always the same homogeneously H loaded sample is desorbed under similar conditions. Thus, for the final result the average error of the average value reduces with the number of measurements and therefore becomes much lower than the standard deviation of  $\pm 13\%$ , which is the statistical error of a single measurement. Strictly identical conditions can only be assumed for the NBI plasmas excluding the last two measurements with lowered laser energy. But these 9 data points result in an average error of the average value of  $\pm 2.54\%$ , with the two low energy shots  $\pm 2.83\%$  and all data of the series yield  $\pm 2.77\%$ . Thus, they are anyway all rounded up to  $\pm 3\%$  and this strict discrimination of identical measurement conditions is unnecessary here. Conversely, this means that the variation of measurement conditions performed in this series, practically have nearly no influence on the statistical variation of the LIDS result. For the final result of this measurement series this very small statistical error has to be added to the much larger systematic error for the horizontal observation of  $\pm 35\%$ , which will be discussed in chapter 7.10. This results in a total uncertainty for this series measurement of  $\pm 38\%$  and thus in the final LIDS result of  $(6.7 \pm 2.6) \cdot 10^{22} \text{ H\&D/m}^2$ .

A comparison to a LID-QMS measurement series on the identical sample after LIDS, which resulted in  $(6.8 \pm 2.8) \cdot 10^{22} \text{ H\&D/m}^2$  shows a remarkable agreement. However, the comparison with TDS is not as easy as it required careful cutting of the 2 mm thick tungsten substrate without damaging the hydrogen containing carbon layer. The TDS analysis of a  $10.2 \text{ mm}^2$  large piece (cf. red area in figure 7.16), which was cut out of the same sample, only showed  $(4.5 \pm 1.5) \cdot 10^{22} \text{ H/m}^2$  and  $(6.5 \pm 2.1) \cdot 10^{20} \text{ D/m}^2$ . The discrepancy to LID is probably due to the difficult cutting of tungsten as it is very hard, which causes heating at the cutting edges due to the friction between saw and sample. Therefore, a very slow cutting method with a low

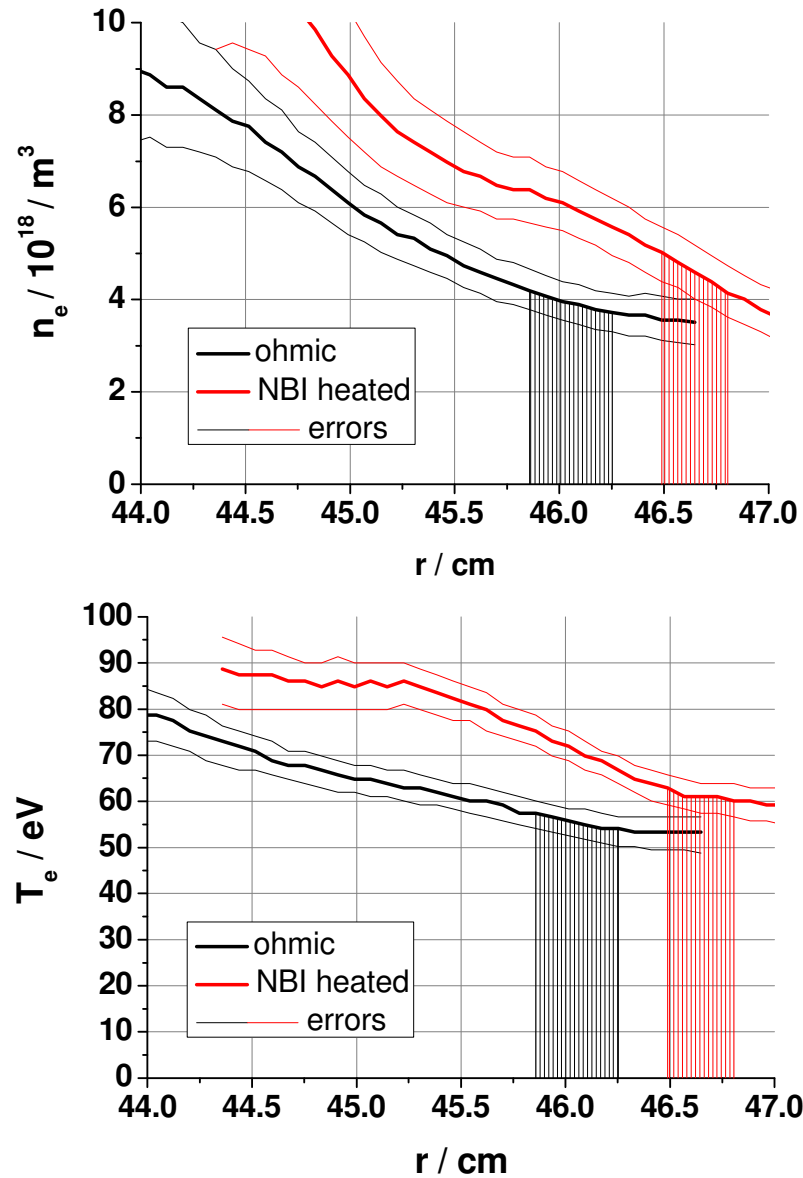
## 7. In situ Laser Induced Desorption Spectroscopy (LIDS)

weight and thus little force was used and hence the cutting procedure took days. Nevertheless, temperatures up to 370 K at the cutting edge could be measured by an IR camera. Additionally, the a-C:H layer was partly removed at the cutting edges (parts outside the red area in the figure) and partly lifted from the substrate (dark parts outside the green area) due to the sawing process. The layer removal outside the red area was compensated in the TDS result by a thorough determination of the remaining layer area under the microscope (red area in figure 7.16). However, the temperature effect was not compensated but might have had a significant effect due to the long cutting duration and the small size and elongated shape (8.3 mm) of the sample. Assuming, that the interpretation of the partly lifted layer is wrong, those much darker regions inside the red area, which are clearly distinguishable from the pristine layer may also have to be excluded. Then an area of  $8.48 \text{ mm}^2$  remains as completely unchanged area without macroscopic surface modifications (cf. green area in figure 7.16). The TDS result then increases to  $(5.5 \pm 1.8) \cdot 10^{22} \text{ H\&D/m}^2$ , which now includes the LIDS and LID-QMS values in its error range. Conversely, their error bars also include the TDS value for both choices of the desorbed area. In conclusion, the TDS and LID results agree within the measurement uncertainties with a remaining discrepancy of a factor of 1.22.



**Figure 7.16.:** 2 mm thick W with a  $2.5 \mu\text{m}$  a-C:H layer on a Cr interlayer (Balinit<sup>®</sup> B3a) after TDS with two possible choices for the attached layer area (red or green area); optical bright field microscopy (mosaic mode)

Finally, the variations of the experimental conditions during LIDS shall be discussed. The variation of the laser energy by a factor of 1.5 demonstrates that the hydrogen desorption process is rather insensitive to energy variations in this range. "The energy insensitivity also shows that an overheating with destruction of a major fraction of the layer, which is also accompanied with carbon release into the plasma, does not alter the results significantly. The LIDS method also seems not to be very sensitive ( $\pm 13\%$ ) to moderate changes in local plasma parameters." [Z11b] In figure 7.17 on the next page the plasma profile changes between the ohmic and the NBI heated discharges are shown quantitatively. At the LCFS the density increases by a factor of ca. 1.5 and temperature by a factor of ca. 1.3. The bars mark the positions of the LIDS light maximum in both cases. Also in figure 7.7 on page 179, "the position change of the light emission maxima is marked with a cross." In both figures there is an obvious trend of the light maximum to follow "the colder and thinner areas of the plasma. Thus, the corresponding values of density and temperature and therefore of the  $S_{/XB}$  value do not vary much", although the plasma edge is hotter and denser during NBI heating. "In this case, the difference between the two plasma scenarios results in an  $S_{/XB}$  value that is only a factor of 1.04 higher for the NBI plasma. Its absolute value is 15.1" [Z11b]. The observation that the conversion factor is nearly unchanged in different plasma conditions is very valuable, because this means that the plasma parameters do not have to be known very exactly at the desorption position. Once a suitable conversion factor is determined, not even the position of the light maximum would have to be known accurately for plasma parameter changes within such a moderate range. (Parts of this section have already been published in [Z11b].)



**Figure 7.17.:** Plasma parameters during LIDS as measured by the supersonic helium beam diagnostic; #112136 at 2.38 s;  $I_p = 350$  kA,  $n_{e,la} = 2.5 \cdot 10^{19} / \text{m}^3$ ,  $B_t = 2.25$  T and #112142 at 2.78 s additionally with NBI( $\text{H}_2$ ) at 50 kV and 150 mm V-target. The marked regions are the positions of the LIDS light intensity maxima of the measurements in figure 7.14 which are also shown in figure 7.22 on page 202. The error bands of the SHE diagnostic show only its statistical errors; cf. chapter 7.10 for further details on these errors.

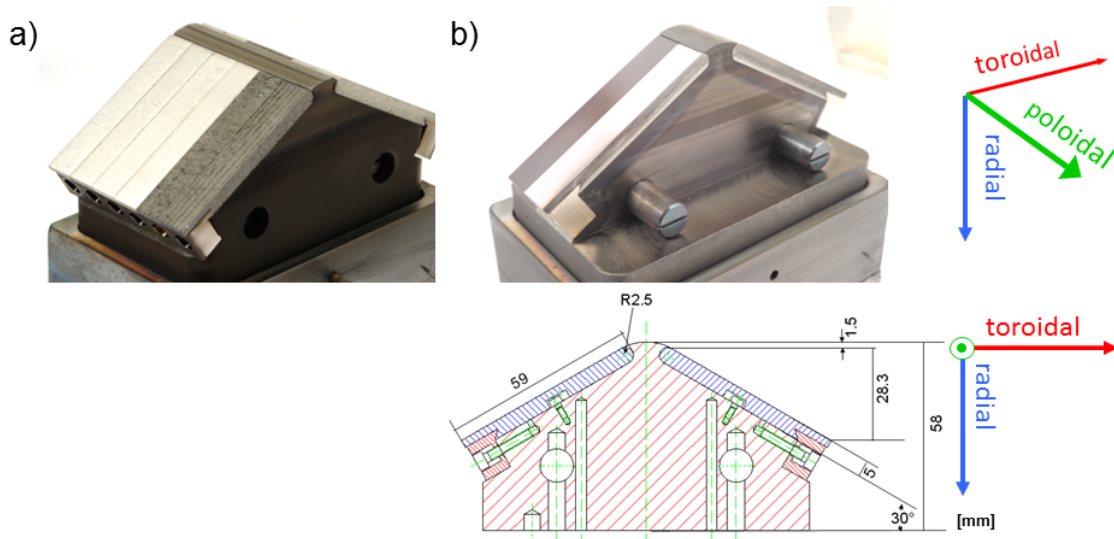
## 7.8. Detection Limits

The ratio of the LIDS light to background plasma light depends on various factors such as the integration time of the observation system, the line of sight, the plasma properties and sample characteristics:

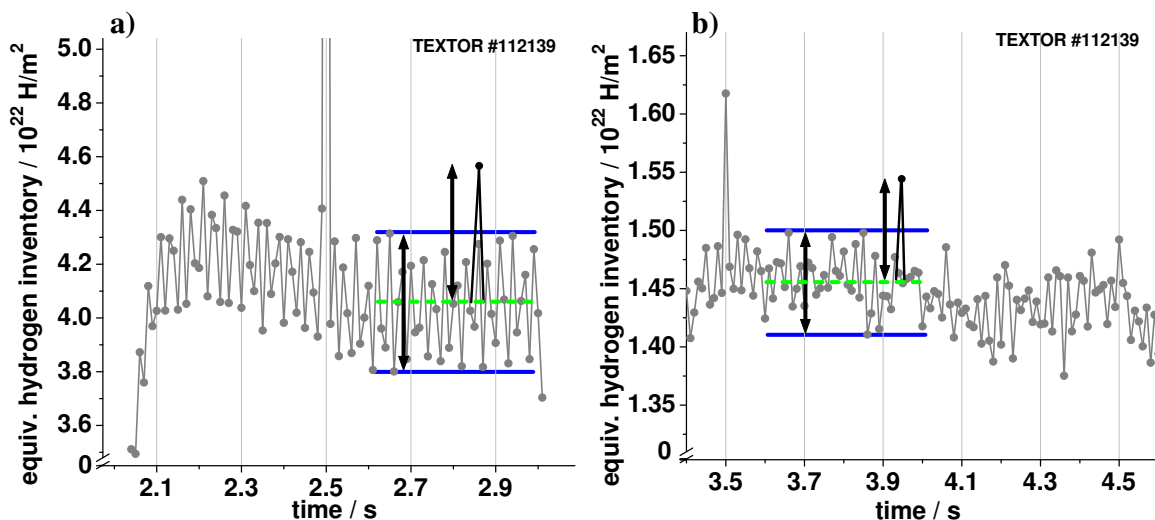
- The **effective integration time** of the AVT camera at TEXTOR is mainly determined by the duration, for which the image intensifier is switched on. The camera itself integrates light during the selected time of 9.917 ms after the frame trigger (as described in the measurement procedure in chapter 7.2). However, the light reaches the CCD chip only during the time for which the image intensifier is amplifying – so during the selected MCP gate duration. This effective integration time could also be reached in the opposite way with the intensifier MCP gate longer than the chosen camera integration time or permanently open and at the same time shortened camera integration time. In this setting the light reaches the CCD chip also outside the camera integration time, but the electronic shutter of the camera prevents this light from being recorded. Regardless of the actual realisation, it is possible by such technical means to shorten the effective integration time and to define also the start of the recording time. This effective integration time must be synchronised with the LIDS light emission to optimise the signal to background ratio. An optimal signal to noise ratio (SNR) can also be obtained by the use of a photodiode as detector or a camera with a high frame rate to resolve the LIDS light on several images. However these techniques suffer from a reduced signal strength per sample or image, respectively, because the LIDS light is split on more than one sample or image, respectively. This smaller signal per frame cannot be resolved as good as in the slow recording since fast detectors usually are fast because of reduced dynamic range or because of reduced spatial resolution. For example in the previous LIDS setups 8-bit A/D transformers have been used in the cameras. Due to the coarse graduation of the scale into 256 steps the SNR is much worse than with the present 14-bit A/D transformer that resolves 16384 steps. With a third camera setup a high frame rate up to 2500 Hz could be realised during LIDS measurements in earlier works [Irrek8] but only at the cost of significantly reduced field of view (factor 4.4) and a factor of 6 smaller spatial resolution.
- The **line of sight** of the detector, here the camera, affects in addition the SNR, since the detector does not only collect light in the depth of sharpness but also along the optical axis. Since the  $H_\alpha$  background light in a tokamak is mainly emitted in the edge plasma, where the hydrogen is not fully ionised and its energy level  $n = 3$  is populated, the horizontal observation integrates the light from the edge plasma at the bottom of the torus, which is viewed tangentially (cf. figure 7.1 on page 161). In case of the vertical observation or an ITER-like coaxial setup the edge plasma is viewed twice: at the bottom and top, which increases the background signal. On the other hand the tangential view path through the edge plasma also increases the background signal for shallow angles due to longer distances in the  $H_\alpha$  emitting edge plasma.
- The third parameter that determines the level of  $H_\alpha$  background are the plasma properties itself. In general a higher  $H_\alpha$  background intensity is observed for hotter and denser plasmas although the photon efficiency decreases. The  $S/X_B$  value for the  $H_\alpha$  light increases for higher  $n_e$  and  $T_e$  and thus less light is emitted by each hydrogen atom. This effect is small compared to the additional light due to the density increase itself. Even for doubling the density from  $5 \cdot 10^{18}$  to  $10^{19} / \text{m}^3$  the  $S/X_B$  factor only increases by a factor of about 1.2 (for  $k_B T_e > 30$  eV, cf. figure 7.6 on page 177). Therefore the higher density is not compensated by this moderate increase of the conversion factor and thus

the  $H_\alpha$  background light is enhanced according to the increased recycling flux. This effect reduces the SNR.

- Finally the geometry of the sample to be observed and desorbed influences the amount of  $H_\alpha$  background light. In general large objects or steep surfaces increase the edge plasma recycling and thus the background light because they receive and emit a higher flux. As an example two limiters are presented in figure 7.18. Limiter b) exposes only one third of the surface of limiter a) to the plasma flux in toroidal direction thus reducing the hydrogen recycling by about this factor locally. Thus a smaller poloidal extend, as well as other geometrical effects like a more shallow angle between limiter surface and flux surfaces reduce the background light.



**Figure 7.18.:** Two TEXTOR limiters with the identical toroidal cross-section (bottom) but with a factor of 3 difference in poloidal cross-section for reduction of hydrogen recycling fluxes in the SOL



**Figure 7.19.:** Zoom of figure 7.15 on page 187: The detection limit of LIDS is determined by the  $H_\alpha$  background fluctuation amplitude (blue lines). grey:  $H_\alpha$  signals converted to the equivalent hydrogen inventory which would yield this signal; **black**: definition of smallest detectable signal (fictitious data point); laser pulses at 2.5, 3.5, 4.5 s; a) NBI phase; b) ohmic phase

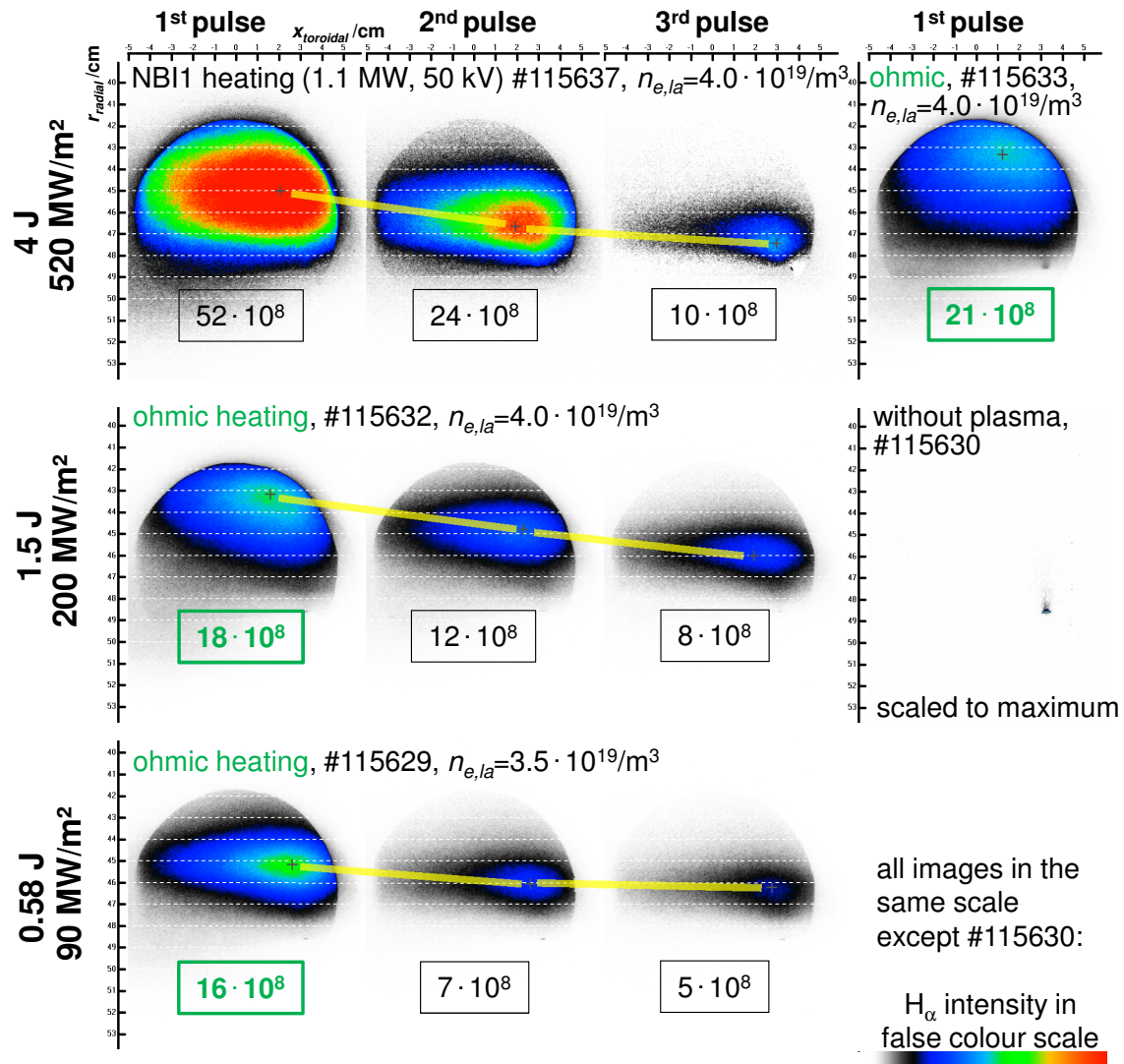
If the  $H_{\alpha}$  light of the whole visible area of the horizontal observation at the limiter at the bottom of TEXTOR is integrated a typical time trace like in figure 7.15 on page 187 is obtained. "The fluctuation amplitudes of the  $H_{\alpha}$  light dominate the detection limit of the LIDS system at least for the background subtraction method presented in section 7.5.1"[Z11b]. The detection limit can be defined as the smallest signal that can be distinguished from the background fluctuations. For the integrated camera images this can be defined as a signal that is twice as high as the upper fluctuation level (upper blue line in figure 7.19) with respect to the green line. The green line (dashed line) is the average fluctuation level, which is the average of the upper and lower fluctuation level within a certain time interval indicated by the length of the three lines. The smallest detectable signal is therefore equal to one fluctuation amplitude (black arrow) above the average fluctuation level. Thus, the detection limit is determined by the size of the fluctuation amplitude. For ohmic phases of TEXTOR discharges a value of  $8 \cdot 10^{20} \text{ H/m}^2$  can be determined and during NBI heating a lower limit of  $5 \cdot 10^{21} \text{ H/m}^2$ . These values are obtained for the integral of the full horizontal view ( $68 \text{ cm}^2$ ). But even if the integral of a LIDS image is within the fluctuation amplitude and thus is not recognisable as a desorption signal in this perspective, it is very often still distinguishable from the background light by its light distribution. Therefore an integration of a smaller area of interest centred at the position of the light intensity maximum raises the integrated signal above the background fluctuations. But this procedure comes only at the expense of the captured light, since an increasing number of photons is lost outside the reduced integration area.

### 7.9. Plasma Cooling Limit

The validity of the LIDS signal evaluation procedure described in the previous sections reaches a limit, if the plasma properties are influenced by the desorption process too much. The perturbation originates mainly in the cooling of the plasma by the injected species. The hydrogen molecules injected by LID into the plasma have approximately the temperature of the heated wall at the time of the gas release. As already described, this is at about 600-1000 K, corresponding to ca. 0.08 eV. Even taking into account the molecular dissociation energy, only few eV result (cf. chapter 7.5.3). This thermal gas cloud is colder than the plasma into which it is injected. Therefore in principle a cooling of the plasma can occur, especially when not only fuel, but also gaseous, liquid or solid impurities are injected. For bulk carbon and tungsten materials the impurity release is rather low, since the laser intensity needed for desorption is known and overheating and thus sublimation can nearly be mitigated. Nevertheless not only  $H_2$ , HD and  $D_2$  are desorbed, but also  $CO_2$ , CO, water and hydrocarbons as the QMS measurements show. This release of impurities, which is mainly due to previous sample storage in air or because the samples have not been outgassed after fabrication, nearly disappears when LID is used several times on the same spots inside a vacuum vessel without venting. For a-C:D layers on any substrate additionally a considerable amount (ca. 15-20%) of fuel is desorbed as hydrocarbons, mainly as  $CD_4$  and  $CD_3H$ . If melting is necessary to release the total inventory from tungsten, then also evaporation of W might occur, but this release has not been observed in LIDS at TEXTOR. For layers consisting of C, W or mixed materials with bad and especially unknown heat conductivity and/or low thermal coupling to the substrate, overheating of the spot nearly coincides with the hydrogen release. In these cases delamination of sub-millimetre small material parts appears due to high temperatures and thermo-mechanical stresses.

The kind of injected species is decisive for plasma cooling, since it is mainly due to "Energy losses by ionisation, charge exchange of neutrals, heating of generated charged particles and impurity radiation" [Tokar93, p.1120]. Thus on the one hand fuel needs higher energies for ionisation, but on the other hand impurities have a higher probability for radiation. While





**Figure 7.20.:** LIDS causes plasma cooling by fuel and impurity injection only for high desorption fluxes. Thick a-C:H layer on ALT-II (N $^{\circ}$  6/19) tile desorbed with 1.2-1.4 ms pulses, observed with an H $\alpha$  filter. Energy and intensity are absorbed values. Plasma heating by NBI reduces the cooling and the associated inward movement of the light. The numbers in boxes are the image integrals.

the plasma temperature drops, the density is increased by the same factor, thus conserving the plasma pressure. The cooling effect does not only depend on the kind of injected material, but mainly on the injection rate of the coolant. According to the released composition described above, LID on non-disintegrating wall elements usually releases mainly fuel species. Therefore the cooling effect due to fuel injection has to be considered. The maximum injected amount of fuel during LIDS on TEXTOR (except LIDS on the ALT-II) has been  $3 \cdot 10^{17}$  H&D with a 1.5 ms laser pulse. The duration of hydrogen release lasts for about 60-80% of the pulse duration (cf. chapter 7.3) and is not constant and steady-state as assumed in the theoretical calculations cited above. Instead, the release is largest at the temperature of hydrogen release from the specific material, shifted by the heat penetration delay and outgassing delay. On average the release rate is ca.  $3 \cdot 10^{20}/s$  for this maximal case. This puffing rate, when applied constantly in the TEXTOR edge, causes a reduction of the edge temperature from 50 to 35 eV and a corresponding density increase by the same plasma cooling factor of  $f_{pc} = 1.4$  as measured [Unterberg5, fig.3], and verified by the cited model. This is just the beginning of

the plasma cooling effect, which does not affect the  $S/X_B$  factor (cf. figure 7.6 on page 177), that is still 15. A higher LID release rate has to be prevented by

- reducing the laser spot size,
- reducing the maximum surface temperature during LID by reducing the laser pulse duration or energy (cf. example below), which then makes several laser pulses with increasing energy and/or pulse duration necessary to reach full hydrogen release from the analysed spot,
- perform LID during hotter plasma conditions (for example in NBI phase, cf. example below).

Otherwise, for example a cooling of factor 3 already leads to an  $S/X_B$  value of 18, introducing an error of 20%, if the local plasma parameters at the  $H_\alpha$  intensity maximum during LID cannot be measured or calculated. Fortunately, the occurrence of significant plasma cooling can easily be recognised on a radially resolving detector like the HO camera at TEXTOR by radial movement of the emission maximum (cf. figure 7.20). If the radial position of the  $H_\alpha$  maximum for a strong injection is the same as for a small amount well below cooling onset, then no significant plasma cooling appears. The further the maximum moves into the central plasma, the greater the plasma cooling is. This can be seen for the case of LID in the thick deposition layer of an ALT-II tile that has been installed in the limiter lock system for LIDS measurements. For laser intensities well below the ones needed to heat pure graphite, the  $H_\alpha$  light maximum moved more than 4 cm deeper into the plasma as for a normal desorption of small H amounts. It moved so far, that its main part was not in the detection volume any more. The light could be brought back into the volume by reducing the laser intensity (cf. bottom row in the image) or alternatively by heating the plasma with the NBI (cf. top row). The just described maximum shift criterion for plasma cooling detection is only applicable, if the maximum position for a small hydrogen amount is known under the considered plasma conditions. Because a shift of the maximum alone does not indicate plasma cooling, since a changed edge profile in density or temperature (e.g. due to plasma shifts or different heating etc.) will also move the  $H_\alpha$  intensity maximum. But this appears also for all release rates below the onset of significant plasma cooling in the same way and can therefore be checked.

The example illustrates the inward shift of the  $H_\alpha$  light during LIDS with significant carbon release from an ALT-II limiter tile (N° 6/19). Since the  $H_\alpha$  filter used at the camera also transmits  $C^+$  light, even the 2<sup>nd</sup> and 3<sup>rd</sup> laser pulse produce a signal although the hydrogen release is then below 10% according to the LID-QMS results. Therefore a quantification of the hydrogen amount is not sensible in this case; image integrals in pixel counts are hence given in figure 7.20. The camera views the poloidal gap side of the ALT-II tile. The area with the thick hydrocarbon layer is on the right hand side as can be seen on the image without plasma, where the Planck radiation due to the laser pulse has been intensified by image processing. The 2<sup>nd</sup> and 3<sup>rd</sup> laser pulses heat the same position of the sample as the 1<sup>st</sup> laser pulse. In each discharge the laser is moved to a new spot, which appears to be on the same position in the images, since the laser moves in poloidal direction, perpendicular to the plane of the image. This is done in order to stay in the area of the thick deposits at the very edge of the tile.

## 7.10. Accuracy of Laser Induced Desorption Spectroscopy

The different physical processes involved in laser induced desorption spectroscopy as well as the evaluation procedures have particular uncertainties due to physical or technical reasons. In this chapter the uncertainties of the in situ measurements in TEXTOR are discussed. Some of these uncertainties also occur during LID-QMS and are already discussed in chapter 5.4 on page 134. The uncertainties concerning the processes of laser heating and gas release that occur ex situ also occur in situ, but are not repeated here, unless they are different in strength or quality. In general, these effects are more pronounced when going from the ex situ to the in situ environment.

To classify the various uncertainties which can contribute to the overall measurement accuracy, one can distinguish between short-term and long-term uncertainties. The latter can be assumed constant during one day but may change on longer time scales e.g. degradation of detectors like the CCD cameras and image intensifiers or optical components. These uncertainties typically contribute to the systematic error. Other properties can vary on the time scale of a plasma discharge like heating up of samples due to plasma exposure. Finally there are even variations of important parameters on millisecond time scales and faster, e.g.  $H_{\alpha}$  light fluctuations at the detection position. Such errors are rather equally distributed around a central value and arbitrary or random and thus contribute to the statistical error. Below is a list of uncertainties that can contribute to the errors of LIDS measurements. Each aspect is categorised by its temporal domain, quantified as good as possible, its importance for LIDS is judged and countermeasures or situations when it is less pronounced are mentioned. They are summarised in table 7.2 on page 207.

### **First window, first mirror:**

In any optical detection of a plasma, the first optical element of the injection or detection system (window, mirror, fibre etc.) can be changed in its properties due to plasma-wall interactions. In the LIDS setup at TEXTOR three ports must be considered: the laser input port (PK16) which in the coaxial setup also serves as detection port, and the two other detection ports: for the horizontal observation (PK21) and for the vertical observation (PK27). The laser input port has a glass window as first optical component. It is retracted very far from the plasma (1.2 m to the LCFS in a 10 cm diameter port, cf. figure 7.1 on page 161) and therefore nearly unaffected by the plasma. Thus, its transmission of ca. 90-92% for 1064 nm light does not change due to plasma effects. No significant carbon transport has been observed, that would reduce its transmission. The window transmission has been measured with the LID laser beams during TEXTOR shutdown 2010 and 2011. Even slight carbon deposition would lead to visible surface changes (cf. chapter 5) when using the high power ablation lasers in TEXTOR, which have not occurred.

The horizontal observation uses a tilting mirror inside the vacuum (ca. 0.8 m away from the LCFS) as first optical element, such that the vacuum window itself has no direct line of sight to the plasma. Despite this long distance, a reduction in transmission is measured during operation breaks in the order of >15% reduction in UV, 8% in VIS, 2% in IR after 5 years. The vertical observation has a  $\text{CaF}_2$  window only 0.4 m from the LCFS. Due to its close distance, it should have the fastest degradation of the three, but no transmission measurement has been done, because it has never been exchanged after installation. The quantitative LIDS measurements were mainly done with the horizontal observation. The annual calibration of the detection system limit the effect of this error to a maximum of +5% underestimation of the light intensity. In the case of TEXTOR it is an effect on the timescale of years. For ITER or a steady state plasma the timescale will decrease significantly. Therefore, for ITER means like

local protective gas puffs, mirror heating or special duct geometries are investigated for the mitigation of such layer deposition or degradation by erosion effects [Litnovsky10].

### **Grey filter transmission:**

For the camera detection at horizontal observation, the linearity of the CCD detection might be an issue but is negligible based on camera specifications. However, linearity test performed with neutral density filters at TEXTOR (so called grey filters) at 656 nm show that they transmit more light than specified for the high transmission filters ( $T \geq 0.3$ ) and less for the low transmission filters. The average error is  $\pm 9\%$  determined on the basis of camera images which are reduced by the dark current, an offset in the detector. The deviations are probably due to an inhomogeneous spectral transmission of the grey filters and thus rather a systematic than a statistical error. However, the reason could as well be a non-linearity in the camera detector, as the deviation to the nominal filter values decreases nearly monotonously with decreasing transmission. This behaviour hints rather at a systematic deviation in the camera. Therefore, the nominal filter transmission values provided by the filter manufacturers are used and the measured deviations are included in the error calculation as "grey filter errors", which might as well be "detector errors", however.

For the coaxial observation only two types of grey filters were used and their transmission was measured during the spectrometer calibration. The deviation at the  $H_\alpha$  wavelength is  $-5\%$  and  $+13\%$  to the specified values and thus also an average error of  $\pm 9\%$  results for the grey filter error for CLIO. Again, it is not obvious whether the error source is the filter or the detector.

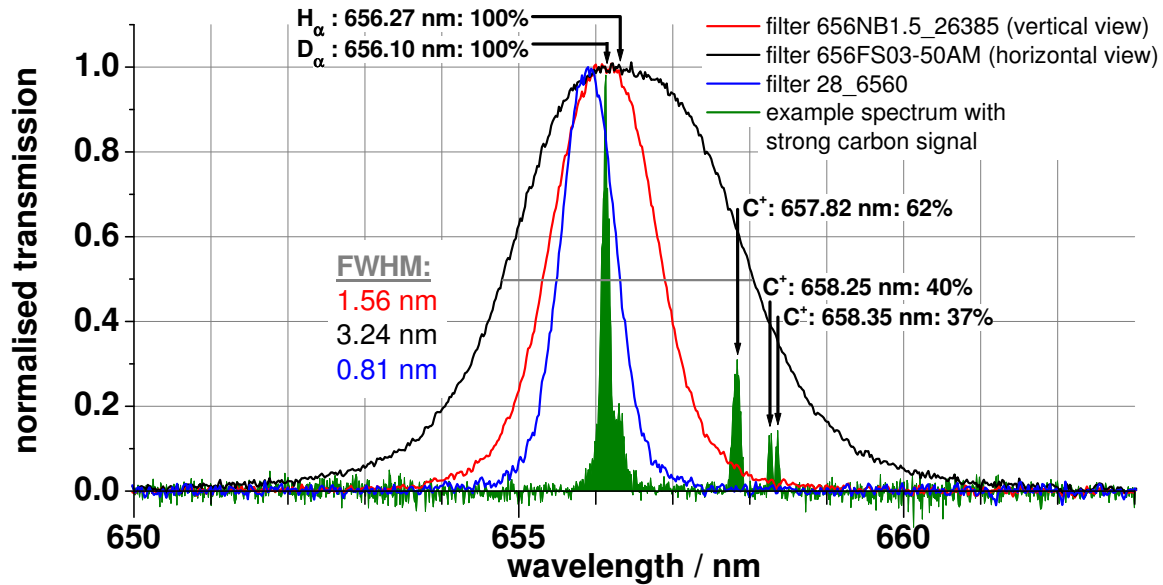
### **Spectral filter transmission at horizontal observation (HO):**

If a detector like a camera or diode is used to detect the LIDS light instead of a spectrometer, then a spectral filter is used in front of them to block all other wavelengths except the one of interest. In the present work mainly  $H_\alpha$  narrow-band filters have been used for this purpose. Their transmission properties have been tailored during production according to the spectroscopic needs by utilising the interference effects of dielectric layers. The bandwidth of the transmission window has to be narrow enough to transmit the desired line radiation while blocking all other wavelengths. The transmissions of three different  $H_\alpha$  interference filters are displayed in the range of interest in figure 7.21 as measured with a spectrophotometer. A sample LIDS spectrum recorded with the high-resolution spectrometer is given as an example for the position of different spectral lines. Here a desorption shot with overheating has been chosen, where C, W, Al, D and H have been released into the TEXTOR edge plasma. The CII carbon spectral lines from singly ionised carbon atoms, which are always seen during overheated laser desorption, are quite close to the  $H_\alpha$  transition and therefore not sufficiently blocked by some narrow-band filters. This parasitic light can lead to overestimation of the LIDS signal acquired by cameras or diodes.

This transmission of the carbon lines by the  $H_\alpha$  filter used is also the explanation for the apparent "after-glow" of the  $H_\alpha$  light in the previous work on LIDS\* [Irrek8, p.90-93]. The  $H_\alpha$  light decreased at first during the laser pulse, after the hydrogen of a thin a-C:H layer had been fully desorbed, but then again the high-speed camera recorded a significant amount of light. This effect only appeared at high laser intensities, when the surface temperature exceeded 2100 K. The amount of light was very similar each time, regardless of the hydrogen content of the sample – even for already desorbed positions this effect appeared in the same way. Several hypotheses had been drawn to explain the effect, in one of which the carbon sublimation has been considered to cool the plasma and therefore highly increase the  $H_\alpha$  signal of the wall recycling flux. But this "after-glow" can now be identified as the excitation of the

---

\*Laser Induced Desorption Spectroscopy was abbreviated as LDS in some previous works, but is identical to LIDS



**Figure 7.21.:** Three different spectral filter transmissions: Accurate tailoring of narrow-band interference filters adapted for exact selection of hydrogen spectroscopic lines, while excluding undesired line radiation, is essential for LIDS measurement when using a camera or diode.

sublimated carbon in the plasma itself, whose light emission passes through the  $H_{\alpha}$  filter\*. This explanation is also supported by the light shape of the after-glow, which is closer to the wall and thinner (ca. 1.5 cm) in radial direction than the real  $H_{\alpha}$  light (cf. figure 6.7 in [Irrek8, p.91]). This thin light pattern has also been observed for evaporated and delaminated carbon in the present work. The overestimation due to the after-glow can be overcome by one of the following methods:

1. Spectral separation: A narrow-band filter with a FWHM of less than 1 nm should be used (like filter N°3 in the figure). It has a smaller transmission at its central frequency (here 43%) than broader filters (here 67% and 70%, resp.), but this can be compensated easily if cameras or diodes with image intensifier are used like in the present setup. On the other hand, such narrow filters also do not block the full spectral range, like the filter N°1 (with FWHM=1.5 nm), which is transmissive for  $\lambda > 1.3 \mu\text{m}$  in contrary to the other two. Unfortunately, the standard  $H_{\alpha}$  filter at the horizontal observation has a transmission window of FWHM=3 nm, through which the carbon lines are transmitted with more than 60% and 40%, respectively. In contrast to the horizontal observation, at the vertical observation an  $H_{\alpha}$  filter with IR-transmission has been used so that the Planck radiation during laser heating is transmitted (cf. background subtraction in chapter 7.5). An improvement or exchange of these two filters or the adaptation of filter N°3 for the observation is highly advised.

The use of a spectrometer with high enough resolution is the best solution in the spectral domain.

2. Separation in the temporal domain: As shown in [Irrek8, p.89] at least for thin a-C:H layers the main desorption process is complete at about 50-80% of the laser pulse duration (depending on the pulse parameters), when a surface temperature of 1100-1300 K is reached. Since carbon sublimation occurs at higher temperatures, a fast LIDS detector can resolve the transition from hydrogen desorption to carbon sublimation. This

\*The same spectral  $H_{\alpha}$  filter with 3 nm FWHM has been used in previous LIDS experiments at TEXTOR ([Irrek8], [Z9]) and in the present work for the horizontal observation without exception.

is possible for bulk graphite and thin a-C:H layers, but not for thicker carbon layers or mixed layers with bad thermal contact to the substrate because hydrogen desorption is accompanied by carbon release in these cases. Thus, spectral separation is necessary in these cases.

3. For a well known material composition (like bulk carbon) the necessary desorption temperature is known and the necessary laser intensity can be calculated analytically or numerically (like described in chapter 2) to avoid overheating. The estimation of this laser intensity is complicated or even fails for layers that are badly attached and therefore can be delaminated easily or for layers with unknown heat properties.

Later, a high-resolution spectrometer was applied for LIDS detection and could resolve the carbon lines nearby the  $H_{\alpha}$  line and even  $D_{\alpha}$  and  $H_{\alpha}$  light to some extent. These measurements allow the quantification of the overestimation by the camera observation due to the broad spectral filter by taking the ratio of laser induced light from  $C^{+}$  to the  $H_{\alpha}$  light. For hydrogen-rich carbon layers this error is of course much lower and disappears nearly for desorptions without overheating. For a standard example of a 2-3  $\mu\text{m}$  thick hydrocarbon layer with the standard laser pulse for graphite (700  $\text{MW}/\text{m}^2$ , 1.5 ms) the parasitic light is usually in the range of 8-15%. Only sometimes it reaches up to 25-35% for layer-substrate systems with bad thermal conductivity. This overestimation due to the spectral filter is thus accounted with a systematic error of  $-15\%$ .

### **Notch filter transmission at coaxial observation (CLIO):**

To protect the spectrometer from the intense laser light, a notch filter for 1064 nm was inserted in the observation path. Unfortunately, its transmission is highly modulated in the visible range with ca. 4 nm wavelength in the  $H_{\alpha}$  region oscillating there between 21% transmission (at 658.5 nm) and 63% transmission (at 656.3 nm). An undesired tilting leads to a blueshift of the filter transmission curve. Spectrophotometer measurements showed that a small tilting of ca.  $4^{\circ}$  leads to a blue-shift of roughly half of a nanometre. Fortunately, this blueshift shifts the mentioned local maximum of the transmission curve towards the  $H_{\alpha}$  peak and over it. Thus, the potential error is only small with ca.  $\pm 4\%$ .

### **Camera/detection path errors at horizontal observation (HO):**

The detectors used for LIDS introduce uncertainties due to technical issues and uncertainties in the calibration, e.g. the stability of the reference light source used for calibration. The Ulbricht spheres used for calibration were certified and provided a wavelength resolved spectral radiance table. The newest Ulbricht sphere has been cross-calibrated with different spectrometers several times yielding slightly different values with a maximal deviation of only ca.  $\pm 4\%$  at the  $H_{\alpha}$  wavelength. The average deviation of repetitive calibrations during one calibration day was typically below  $\pm 5\%$ , similarly for the calibrations with a year or two inbetween. The image-to-image stability is below  $\pm 2\%$  and often below  $\pm 1\%$  but is negligible for calibration since averages over hundreds of images are used. But in the LIDS measurement it can occur because the LIDS light is only recorded on one image. The detector noise level can also be neglected due to the high dynamic range and since the LIDS measurement is a difference measurement it has to be concerned only during calibration. Also all possible electro-magnetic perturbations during signal transmission can be excluded due to the fibre cables used. However, some instabilities come from the gain factors of the image intensifier, which were mainly set by a manual potentiometer. Experimentally an average error of  $\pm 10\%$  was found for the image intensifier gain. Multiple reflexions on the various optical components, mainly the grey filters and narrow-band filters in front of the camera lens often lead to a maximum of 3 visible repetitions of the image especially during calibration. If all these reflexions overlap, they can increase the amount of photons by a factor of ca. 1.13 compared to the case when all reflexions are positioned outside the image. Due to undefined tilting of these components these reflex-

ions overlap each other differently after exchange of filters and re-mounting of the camera and thus lead to an uncorrected positive error. However, depending on whether the additional reflexions occur during calibration or during measurement the calculated photon amount can be increased or decreased, thus a two-sided error of  $\pm 13\%$  is estimated.

The tokamak environment itself with strong electric and magnetic fields, dust, stray light, high voltage device nearby the cameras and vibrations has certainly some effect on the cameras, but mostly during off-normal events that are recognised as such. Whether unrecognised influences remain also during normal operation and how strong they are, can hardly be judged. Adding all these rather independent statistical errors quadratically, an uncertainty for the camera detection of  $\pm 18\%$  is estimated.

#### **Spectrometer/fibre errors at coaxial observation (CLIO):**

As for the calibration of the spectrometer at the coaxial observation the same Ulbricht sphere was used as for the HO, the same Ulbricht sphere error of  $\pm 4\%$  at the  $H_\alpha$  wavelength is accounted. Inhomogeneous light distribution in the fibre transferring the light to the spectrometer might be a problem as discussed in chapter 7.5.4. However, as these problems are strongest for very long or very short fibres and here with ca. 30 m a medium long fibre is used, these fibre errors are assumed to be rather moderate with  $\pm 10\%$ . Since the internal amplifications and settings of the spectrometer were kept constant during the LIDS measurements and calibration (except integration time), no further error is assumed here. During calibration always 20 spectra are averaged for one measurement. The deviation between these calibrations within one calibration day is maximal  $\pm 9\%$  in the neighbourhood ( $\pm 1$  nm) of the  $H_\alpha$  wavelength on the recorded spectra. However, as the integration of spectral lines over ca. 55 data points is used in the evaluation of the photon amount, the recorded data should be smoothed with a nearest-neighbour smoothing of width 55 before such a comparison. The smoothed data only deviate less than  $\pm 1\%$  from each other in the same region around  $H_\alpha$  and less than  $\pm 4\%$  in the whole region with sufficient light intensity from the Ulbricht sphere i.e. above 550 nm. Since the LIDS measurements concentrate on evaluation of the  $H_\alpha$  light, only  $\pm 1\%$  is accounted for the calibration-to-calibration deviation. During the measurement no averaging of spectra is performed as the acquisition frequency is low with 2 spectra per second, each with 10 ms integration time only. Thus a spectrum-to-spectrum deviation probably occurs – as experienced also during calibration, where subsequent single spectra deviate and the average of 10 or 20 spectra also shows considerable differences to a single spectrum. These deviations amount to about  $\pm 6\%$  in the region around the  $H_\alpha$  wavelength. The quadratic sum of all these rather independent statistical uncertainties amounts to  $\pm 13\%$  for the combined spectrometer/fibre uncertainty.

#### **Background subtraction:**

The background subtraction as described in chapter 7.5.1 does not assume any advanced temporal pattern in the  $H_\alpha$  fluctuation time trace (cf. figure 7.19 on page 191). It simply performs a linear interpolation of the camera images (or spectrometer spectra) for the time of the laser pulse. This is the easiest way of a linear interpolation, because only one image (or spectrum) before the laser pulse and only one after the laser pulse is used. Therefore, the light intensity that would occur at the time of the laser pulse, if the laser was not fired, can be any value between the lower and upper fluctuation level. The largest error would occur, if the background at the laser time was at the upper fluctuation level and the two neighbouring data points were both at the lower fluctuation level – or exactly vice versa. Then the absolute error equals the fluctuation amplitude, which hence is the largest absolute error for the background estimation.

Conclusively, the background uncertainty equals the  $H_\alpha$  fluctuation amplitude with the typical values as given in chapter 7.8, i.e.  $8 \cdot 10^{20}$  H/m<sup>2</sup> for ohmic and  $5 \cdot 10^{21}$  H/m<sup>2</sup> for the NBI-heated plasma phases. It makes sense that these values are equal to the LIDS detection limits for

ohmic and NBI plasmas, which are also fully based on the  $H_\alpha$  fluctuations. The smallest LIDS value combined with the background uncertainty is thus  $(8 \pm 8) \cdot 10^{20} \text{ H/m}^2$  and  $(5 \pm 5) \cdot 10^{21} \text{ H/m}^2$  which is a value range starting at 0 as expected for a value at the lower detection limit. Hence, these definitions of the detection limit and the background uncertainty fit very well together in the ways they are defined here. In relative terms, the background uncertainty amounts to 100% at the lower detection limit and decreases with increasing LIDS values, as it is a constant absolute value independent of the desorbed amount of gas. For different discharge conditions the  $H_\alpha$  fluctuation amplitude differs, but the above mentioned typical values are assumed to be constant in the present work. A systematic analysis of the fluctuation amplitude with respect to different plasma parameters and scenarios is out of the scope of the present work. However, the actual  $H_\alpha$  fluctuation amplitude in the temporal vicinity of a LIDS measurement can always be determined from the data, if a sufficiently fast detector is used.

To quantify the background uncertainty in relative terms, the upper measurement limit of  $5.6 \cdot 10^{22} \text{ H/m}^2$  is used as determined in chapter 7.9 from the onset of plasma cooling. With respect to this value, the background uncertainty is only  $\pm 1.4\%$  for the ohmic case and  $\pm 9\%$  in the NBI case. As these are the lowest possible background errors it would be euphemistic to use them in the overall error calculation. Thus, the typical relative error is estimated with respect to half of the upper measurement limit yielding an average error of  $\pm 3\%$  for the ohmic and  $\pm 18\%$  for the NBI case.

**Photon amount  $N_{ph}$  at horizontal observation (HO):**

All uncertainties mentioned above contribute to the total uncertainty of the amount of  $H_\alpha$  photons emitted by LIDS. The total systematic error of the measured photon amount results in an error range of  $-18\%$  to  $+11\%$  and thus mainly overestimating the light intensity. The total statistical error has to be treated separately for the case of ohmic and NBI heated plasmas due to the large difference in the background  $H_\alpha$  fluctuations. For the ohmic case the total statistical error is  $\pm 19\%$ , while for the NBI case it amounts to  $\pm 26\%$ .

Hence, all systematic and statistical uncertainties together result in a total error of the measured photon amount in the range of  $-37\%$  to  $+30\%$  for ohmic and  $-44\%$  to  $+37\%$  for NBI plasmas. For the ohmic case the uncertainty is dominated rather by systematic errors while during NBI statistical errors prevail. Hence in the following, the combined error is treated as systematic error for the ohmic case and as statistical error for the NBI case.

**Photon amount  $N_{ph}$  at coaxial observation (CLIO):**

For the coaxial observation the dominance of the total statistical errors is clearer with  $\pm 14\%$  for the ohmic and  $\pm 23\%$  for the NBI case compared to the total systematic error of  $\pm 10\%$ . Thus, the total uncertainty of the photon measurement with the coaxial setup is  $\pm 24\%$  for purely ohmic plasmas and  $\pm 33\%$  for NBI heated plasmas.

**Local plasma parameters at LIDS position:**

**Measurement accuracy:** The electron temperature and density at the location of the light intensity maximum have in principle\* a significant impact on the evaluation of the  $H_\alpha$  light due to the dependence of the  $S_{XB}$  value on these two quantities. The  $n_e$  and  $T_e$  profiles are usually obtained from one of the helium beam diagnostics, which have statistical errors of  $\pm 13\%$  for  $n_e$  and  $\pm 5\%$  for  $T_e$  (typical errorbars of the SHE diagnostic) and  $\pm 18\%$  for  $n_e$  and  $\pm 7\%$  for  $T_e$  (for the thermal He beam diagnostic) at the radial positions where the LIDS light typically appears. Additionally, the underlying collisional-radiative model of these diagnostics has systematic errors of  $\pm 10\%$  for  $n_e$  and  $\pm 30\%$  for  $T_e$  [Stoschus11, p.33]. Thus, in total the uncertainty of the edge plasma parameters is  $\pm 23\text{-}28\%$  for  $n_e$  and  $\pm 35\text{-}37\%$  for  $T_e$ . As mainly SHE values were used in the present work, its uncertainties are used further, i.e. the lower error

---

\*The reason for this restriction will be explained further below in "position of LIDS light intensity maximum".



estimates. The density error is rather a statistical error because its statistical error is larger than its systematic error, thus it is treated like a statistical error in the further error propagation. Hence, it would be added quadratically (according to Gaussian error propagation) to other statistical errors, but linearly (simply arithmetically) to systematic errors. On the contrary, the temperature error is predominantly of systematic nature and thus underlined in the error overview in table 7.2 on page 207 to mark this. It will be treated as a systematic error, i.e. added quadratically to further systematic errors and linearly to statistical errors.

Although the plasma is very well characterised at the position of the edge diagnostics, the transformation of the local plasma parameters from the edge diagnostic position to the LIDS position leads to two additional uncertainties.

**Torus asymmetry error:** There is no measurement of the plasma parameters in the region of a few centimetres above the sample holder. Thus the assumption is utilised, that the plasma parameters on the same isobar surface are constant. In an ideal tokamak this should be valid. In reality the transformation of plasma properties from one toroidal position to another bears a number of uncertainties, originating from inaccuracies in plasma position, magnetic ripple effects and limiter imperfections. Limiters present different materials, surface roughnesses and geometries to the plasma at different toroidal and poloidal positions, which cause plasma-wall interactions that do not only modify the limiters but can also influence the local plasma parameters. Therefore, working with the above mentioned assumption plasma parameter measurements closer to the LIDS position will probably be more accurate than those further away. In this sense the thermal helium beam diagnostic is favoured over the supersonic helium beam.

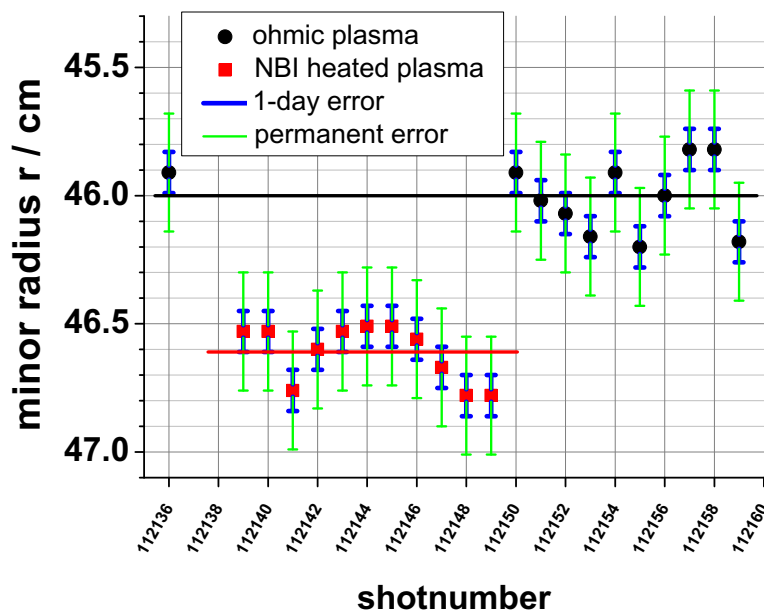
**Position assignment error:** Except these imperfections there is the problem that data of different diagnostics in a tokamak are usually mapped to each other via the minor plasma radius. This radius is derived from the geometrical centre of the torus, which not necessarily is the centre of the magnetic or flux tori. Thus the radial position scales of many diagnostics are fixed in space. But the plasma together with the flux surfaces can shift due to technical imperfections of the positioning systems or due to intrinsic physical effects or plasma drifts. Despite sophisticated positioning systems like the magnetic or optical plasma stabilisation [Mitr9] the plasma can shift. Moreover, physical effects like the Shafranov shift move the flux surfaces to the LFS. As a result, the same space-bound radial position of different diagnostics can refer to different flux surfaces. A re-mapping from the space-bound system to the flux surfaces is a difficult task that needs a lot of detailed information, measurements and calculations. Attempts to do so between different edge diagnostics in the same radial range have lead to agreements of measurements within the same order of magnitude. In the case of LIDS at the bottom of the TEXTOR plasma and plasma parameters from the SHE beam at the top of the plasma on the opposite side of the torus, a plasma shift in horizontal direction introduces only a small misassignment. But a vertical plasma shift e.g. upwards causes a twofold error because it increases densities and temperatures at the SHE position while at the same time it reduces them at the LIDS position. In case of the thermal helium beam this asymmetry is not existing, since it is located on the equatorial plane of the torus and thus the assignment of radial positions is equally sensitive to horizontal and vertical plasma shifts.

The uncertainties evoked by the torus asymmetry and the position assignment have to be added when transferring the  $n_e$  and  $T_e$  values from the edge diagnostic position to the LIDS position. The combination of these uncertainties can only be guessed to cause an additional error of maybe  $\pm 20\%$ . This error is expected to be equally large for density and temperature because the discussed uncertainties are mainly spatial shifts. In total, the uncertainty of the plasma parameters at the LIDS position results in  $\pm 43\%$  for  $n_e$  and  $\pm 41\%$  for  $T_e$  based on the above considerations for the SHE edge diagnostic.

**Position of LIDS light intensity maximum:**

The determination of the position of the light intensity maximum is deduced from the position of the limiter tip, which depends on the following factors:

- The accuracy of the measurement of the limiter height, which is 0.1 mm. This value is the input for the adaptation of the limiter position for different limiters. The accuracy of the limiter position of the lock system [Schweer5] is given by an electro-mechanical signal (accuracy: 0.38 mm), digitalised (with a maximum resolution of 0.1 mm) and converted to a 3 digit reading in 1 mm steps. Thus the overall accuracy is 1 mm.
- For each experimental day a few bright camera images of the limiter are recorded (often during the plasma switch-off at the very end of the discharge or in a disruption) where its tip is visible very well. On the camera image the pixel position of the tip can be assigned with a high certainty of  $\pm 2$  pixels (0.23 mm/pixel for the AVT camera).



**Figure 7.22.:** Radial position of  $H_{\alpha}$  intensity maximum in the background subtracted LIDS images during desorption of a  $2.5 \mu\text{m}$  a-C:H layer; the 1-day error only includes uncertainties in the maximum search algorithm; for a comparison of different shot days a higher uncertainty is valid due to limiter and camera removal; These radial positions are used in figure 7.17 on page 189.

In total the maximum error of the limiter position based on this consideration is ca.  $\pm 1.5 \text{ mm}$ . The spatial calibration of the camera image is deduced from the limiter position in the way just described. In addition to this accuracy the accuracy of the numeric procedure for the search of the light intensity maximum adds. A study of different smoothing algorithms for the desorption image shows that for desorption signals high above the background light, the strength of smoothing has much smaller influence on the position than for weaker desorption signals. For a good SBR two different smoothings yielded a variation of 7 pixels, which equals 1.6 mm (thus an error of  $\pm 0.8 \text{ mm}$ ). Combined with the spatial calibration accuracy a maximum error of  $\pm 2.3 \text{ mm}$  can occur in the absolute value. Figure 7.22 shows an example of the maximum search (with one algorithm and strong LIDS signals) for the desorption of a homogeneous a-C:H layer. The data scatter gives an accuracy for the reproducibility of the position of the maximum, which is  $2.7 \text{ mm}$  for NBI heated discharges and  $3.8 \text{ mm}$  for ohmic

discharges. Since these measurements have been done on the same day, the same spatial camera calibration is valid, thus its inaccuracy does not have to be taken into account for a relative comparison of the data or for the scatter analysis. Thus only the uncertainty of the maximum search algorithm remains. The error ranges of the two different data scatters,  $(2.7 \pm 0.8)$  mm and  $(3.8 \pm 0.8)$  mm, then still overlap, thus the intuitive explanation for the higher scatter for ohmic plasmas due to flatter ohmic profiles may be drawn only with caution. The second statement of these data is the radial difference of 6 mm between the LIDS intensity maximum for the ohmic and NBI case. This statement is very sure compared to the  $\pm 0.8$  mm uncertainty. Therefore, the shift of the intensity maximum for different plasma profiles is a true effect outside the errorbars. For comparisons between different radial camera calibrations (i.e. after a remounting of the camera, limiter or a mirror tilting) the total error of  $\pm 2.3$  mm would have to be used.

In principle, the total uncertainty in the LIDS radial maximum is important for the choice of the plasma parameters from the profile measurements and thus the selection of the  $S/XB$  value. On the other hand, measurements with different plasma scenarios (like in figure 7.22) show that the  $H_\alpha$  intensity maximum of the desorption image follows the plasma gradient in such a way that it tends to occur at similar plasma parameters:  $(3-5) \cdot 10^{18}/\text{m}^3$  and 55-65 eV. The resulting variation of the  $S/XB$  value is in the range of only few percent and hence negligible. Thus the importance to know the exact radial position of the  $H_\alpha$  intensity maximum reduces.

#### $S/XB$ value:

This is a main component of the light-to-particle conversion factor and is taken from the ADAS database, thus it needs correct  $n_e$  and  $T_e$  parameters as input. The accuracy of the numerical calculations behind the ADAS values can be estimated roughly by comparing calculated energy levels of an atom to measured energy levels. For low-Z atoms, the values are easier to calculate and the discrepancies lie usually in the range of 1%. The cross-sections and rates for ionisation and excitation show errors larger than 10% only for very weak spectral lines and more complicated, high-Z atoms. The ionisation rate calculations are more complicated and thus have higher uncertainty than the excitation rates. For hydrogen the uncertainty of the rates should be very small because of its lightness. They are estimated to be in the range of  $\pm 5-10\%$  for low-Z atoms.

This is valid for the value itself. As mentioned above, the determination of the position of the light intensity maximum and the plasma parameters at this specific position have their own uncertainties of  $\pm 2.3$  mm for the position,  $\pm 43\%$  for  $n_e$  and  $\pm 41\%$  for  $T_e$ . They contribute to the uncertainty of the chosen  $S/XB$  value beside the intrinsic uncertainty of the  $S/XB$  value. To estimate the influence of the plasma parameter errors on the  $S/XB$  value, it has been evaluated for the largest error of the plasma parameters in positive and negative directions. In terms of figure 7.6 on page 177 the error ranges of  $n_e$  and  $T_e$  represent a rectangle around a specific  $S/XB$  value. The maximal and minimal values in this rectangle were used here to calculate the induced error. Due to this error rectangle only values up to 70 eV and  $1.3 \cdot 10^{19}/\text{m}^3$  are accessible. On the other side, only values above 25 eV and  $2 \cdot 10^{18}/\text{m}^3$  are relevant for LIDS. The average error of the  $S/XB$  value is  $\pm 10\%$  in the lower right corner of the graph (at 70 eV;  $2 \cdot 10^{18}/\text{m}^3$ ) and increases towards the upper left corner, for low  $T_e$  and high  $n_e$ , to  $\pm 26\%$  (at 25 eV;  $1.2 \cdot 10^{19}/\text{m}^3$ ). There is an imbalance between the negative and positive deviation, i.e. the lower and upper error boundary. The negative error is always larger than the positive error by a factor of 1.3-1.8. In the LIDS relevant range the largest positive error is +23% and the largest negative error -31%, while for the typical values around  $S/XB = 15$  at 30-60 eV and  $4-6 \cdot 10^{18}/\text{m}^3$  the average error is only  $\pm 15-20\%$ . Thus the upper limit of  $\pm 20\%$  at this typical region of plasma parameters is used for the error of the  $S/XB$  value induced by the uncertainties of the edge plasma parameters.

Additionally the radial position error that was estimated to  $\pm 2.3$  mm further above has an influence on the  $S/XB$  error. Its influence can be judged from the steepness of the  $n_e$  and  $T_e$  gradients (cf. e.g. figure 7.10 on page 182) at the LIDS light intensity maximum. The variation in position yields only a small error of  $\pm 5$ -10% in  $T_e$  but a larger error of  $\pm 13$ -34% in  $n_e$ . Again, the maximum values of these variations can be applied to the  $S/XB$  ( $n_e, T_e$ ) graph applying the same method as for the plasma parameter uncertainties themselves. Compared to the previous execution of this method, the small  $T_e$  uncertainty decreased the imbalance between the slightly larger negative error and the positive error to a maximum of 1.3. The average error values for the same typical region as above yield a maximum error of  $\pm 11\%$ .

The total error for the  $S/XB$  value including the mainly statistical uncertainties in radial position, plasma parameters and the rather systematic uncertainties of the ADAS calculations itself thus combines to  $\pm 33\%$ .

### **Inverse atomic yield factor $Y$ :**

The atomic yield factor is based on the knowledge of the dissociation and ionisation processes in the plasma and the desorbed gas composition determined by LID-QMS. The uncertainties of the second part, namely the QMS measurement of the gas composition are rather easy to determine:

The atomic yield factor is routinely determined for each desorption with the ex situ method and thus its uncertainty is mainly determined by the uncertainties of the mass spectrometry (chapter 5.4 on page 134). As only the amount of desorbed gas is necessary for its determination, the errors due to the desorbed area do not appear. The data for the calculation of the  $Y$  value of a single laser spot are acquired in one desorption process, thus also the long-term statistical error does not occur. Only the one-day statistical error of  $\pm 11\%$  remains as total statistical error (cf. table 5.3 on page 136). The systematic error given for the leak rate of the calibration leak is also not taken into account because it is equal for all gas species and thus cancels in the quotient of sums. As systematic error only the uncertainty of the conversion of the calibration leak rate to the different gas species remains with  $\pm 16\%$ . Hence, the sum of systematic and statistical error yields  $\pm 27\%$  for the error of a QMS measurement of a single gas species for the purpose of measuring  $Y$ .

The combination of all relevant gas species leads to a very small error because they strongly compensate each other in the Gaussian error propagation of the formula for  $Y$  (equations 7.5-7.7 on page 174). For example, for deuterium the error of the inverse atomic yield reads

$$\Delta Y_D = \sqrt{\sum_m \left( \frac{\partial Y_D}{\partial N_m} 27\% N_m \right)^2} = [\dots] = \frac{27\% \sqrt{2.16 N_{CD_4} N_{CD_3H} N_{HD}^2 + 8.64 N_{CD_4} N_{CD_3H} N_{D_2}^2}}{(N_{D_2} + 0.5 N_{HD} + 0.8 N_{CD_4} + 0.6 N_{CD_3H})^2} \cdot \sqrt{(11.52 N_{D_2}^2 + 2.88 N_{HD}^2 + 5.76 N_{D_2} N_{HD}) N_{CD_4}^2 + (6.48 N_{D_2}^2 + 1.62 N_{HD}^2 + 3.24 N_{D_2} N_{HD}) N_{CD_3H}^2} \quad (7.17)$$

including the four main gas species  $N_{D_2}, N_{HD}, N_{CD_4}$  and  $N_{CD_3H}$ . Due to this rather complex expression, this error cannot be specified in a general way – not even in relative terms, because equation 7.17 cannot be easily related to  $Y_D$  or its constituents. Typical values for the relative error of the inverse atomic yield are in the range of only  $\pm 1$ -3% as  $Y$  is mainly based on a quotient with sums of virtually the same constituents in the numerator and denominator.

But this error is only valid within the assumptions made for the plasma reactions, e.g. that a  $D_2$  molecule dissociates into an atom and an ion:  $D + D^+$  after being ionised (reaction A). The dominant plasma processes as described in chapter 7.5.2 are the assumptions for the atomic efficiency factors in the calculation of the atomic yield factor. However, it was also

discussed there that less probable plasma processes can occur under the same plasma parameters. Among those, the one with the highest cross-section is the dissociation of the hydrogen molecule in two atoms (reaction  $\mathbb{B}$ ), which approaches reaction  $\mathbb{A}$  for lower temperatures (cf. figure 7.4 on page 172). Their cross-sections are even equal at ca. 10 eV. This is not the relevant temperature range for LIDS but for this temperature the hydrogen molecule would dissociate with an inverse atomic yield of  $Y = 4/3$  instead of 2. The contributions of the hydrocarbon species would decrease the error, but – excluding them – the maximal error would thus reach  $-50\%$  at 10 eV.

LIDS is typically performed above ca. 25 eV, where the dominant reaction  $\mathbb{A}$  is at least a factor of 2 above the less probable one and thus  $Y \geq 3/2$ . In general, for a pure hydrogen release  $Y = 1 + \frac{1}{1+2/b}$  when the less probable reaction  $\mathbb{B}$  is a factor of  $b = \frac{\langle\sigma_{\mathbb{A}}v_e\rangle}{\langle\sigma_{\mathbb{B}}v_e\rangle}$  below the dominant reaction  $\mathbb{A}$ . For typical LIDS conditions with  $T_e = 55$  eV where  $b = 4.3$  and the inverse atomic yield is therefore  $Y = 1.68$ , the systematic error due to the activity of the less probable plasma process is  $-19\%$ .

In the quadratic sum of both error sources, the very small two-sided error due to the QMS measurements raises the sum only by one percentage point and thus its positive branch is neglected here for simplicity. The total combined uncertainty thus amounts to ca.  $-20\%$  for the inverse atomic yield  $Y$  neglecting the very small positive error.

#### **Uncaptured light:**

The amount of light that is induced by the desorption process but not captured by the detection system is in principle very large, since only a small solid angle is covered by the detection. As described in the calibration section, this loss due to the solid angle is already accounted for and thus corrected completely by the way the calibration is performed. If the LIDS light came from a punctiform source, no further correction would be necessary. But due to the extended shape of the LIDS light, some fraction of this light source can be out of the field of view (FoV) of the various detection systems. This is especially problematic when only spatially integrating detectors are used like diodes or spectrometers as no direct estimation of the lost light fraction can be done. Here, camera images (cf. figures 7.7 and 7.9a) and the deduced profiles (cf. figure 7.12) are very helpful. For the desorptions without considerable carbon evaporation the LIDS light shape is not elongated toroidally but quite hemispheric in the far-field. This is indicated also by the exponential decay length of the profiles with ca. 17-24 mm decay length in toroidal and ca. 18-21 mm in radial direction for the standard desorption at 48 cm minor radius. Few such desorptions were performed close to the centre of the circular FoV of the HO and are thus suited very well for an estimation of the uncaptured light outside this circle with radius of ca. 5 cm =  $r_{FoV}$ . The integrated signal of the captured light can be compared to an extrapolation of the exponential decay for a toroidal profile at the plasma radius of the LIDS light maximum. This choice certainly yields the highest values for the lost light and thus an upper error estimation because the small elongation in toroidal direction is strongest at this radial position. Assuming a hemispherically homogeneous distribution of the LIDS light, the exponential decay was multiplied by  $\pi r_{FoV}$  and integrated for  $r_{FoV} \gtrsim 5$  cm. The integration was stopped where the light intensity dropped below 0.01% of the maximum intensity of the smoothed profile maximum. This end of integration is located ca. 15 cm outside the FoV. At such a large distance from the light emission centre the LIDS light would probably be hardly distinguishable from the  $H_\alpha$  background. But this integration of the extrapolated exponential function is only a theoretical estimation to obtain a numerical value for the LIDS light outside the FoV. This estimated uncaptured light within the half-sphere outside the FoV represents ca. 20-27% of the total emitted light. This fraction increases fast for increased limiter distances from the LCFS and decreases at closer approach, however not many good data points are available for these situations. The FoV error for a standard desorption close to the centre of the FoV with a circular FoV of nearly 10 cm diameter as at TEXTOR is thus estimated to

+27% if no FoV correction is applied.

The CLIO setup with its FoV of 23 cm diameter (cf. chapter 7.2) virtually captures the complete LIDS light (97.6% according to the theoretical extrapolation). This is only fully valid for desorptions in the centre of the limiter since the port duct restricts the FoV for desorptions further outside (cf. chapter 7.2 and 7.5.4).

### **Overall uncertainty:**

The overall summary of all these errors is given in table 7.2. According to equation 7.16 on page 179, the final value for the amount of desorbed hydrogen atoms is calculated by the multiplication of the five main values marked in bold type: the measured photon amount of the captured light  $N_{ph}$ , the  $S/XB$  value, the inverse atomic yield  $Y$ , the FoV correction  $V$  for the uncaptured light and additionally – as in LID-QMS – the desorbed area  $A$ . The total uncertainty of the LIDS measurement is thus determined by the Gaussian error propagation of these five factors. For the horizontal observation (HO) with the camera, an uncertainty range of **-55% to +53%** for ohmic plasmas and **-60% to +58%** for NBI heated plasmas results. For the coaxial observation (CLIO) with the spectrometer the uncertainty ranges are **-47% to +43%** for ohmic and **-52% to +48%** for NBI heated plasmas. Thus, the smallest uncertainty for LIDS was achieved for the coaxial observation during ohmic plasmas with less than 50% in positive and negative direction. It is above this value for NBI plasmas due to the higher  $H_\alpha$  background fluctuations and even higher for the horizontal observation mainly because of the higher fraction of uncaptured light due to the restricted FoV.

This discussion of uncertainties shows which the important points for improvement are. On the measurement side especially a larger FoV, the usage of a more narrow and exactly tailored  $H_\alpha$  filter for a camera observation at HO would be very helpful as well as a permanently mounted calibration light source.

The uncertainties in the choice of the  $S/XB$  value could be reduced with a local plasma parameter measurement on the same position as LIDS. Such a measurement could be integrated into the LIDS diagnostic system for example by measurement of several H-Balmer lines with a suitable spectrometer directed at the centre of the LIDS light.

The atomic yield is mainly necessary if hydrocarbons are desorbed and thus less important for desorption from W or other metal surfaces, if it is not covered with a carbon layer. Still the break-up of the hydrogen molecule with different possible paths remains. The uncertainty in this factor could be reduced by taking the less probable plasma reactions into account as described above, since most of the cross-sections are known.

The problem of uncaptured light can be reduced by the discussed methods like known light patterns and extrapolation, and probably solved by a larger FoV. The exponential extrapolation shows that a FoV of 16 cm diameter would reduce the uncaptured light fraction below 10% and 20 cm below 5%. However, the FoV increase is a trade-off with the background subtraction issue, which becomes more uncertain in the edge of a bigger FoV and the SBR drops strongly for an increased FoV.

In the case of a series measurement under identical or very similar conditions, the statistical errors do not have to be estimated as above, but can be calculated statistically, as discussed already for the accuracy of LID-QMS (cf. end of chapter 5.4). For LIDS, identical conditions means not only a homogeneously hydrogen loaded sample and identical laser parameters but additionally also the same plasma conditions and distance of the desorption spot to the plasma. Of the many plasma parameters, for LIDS especially the  $n_e$  and  $T_e$  values in the volume of the LIDS light should be identical and the fraction of charge-exchange hydrogen particles. Such a case was used in the reproducibility study in chapter 7.7 especially for the NBI heated plasmas (N° #112139-47). In such a measurement series the systematic errors have to be summed separately as they are added to the calculated statistical error for the final result.

origin of uncertainty	importance for LIDS	timescale	relative error
<b>photon amount <math>N_{ph}</math> (at HO)</b>	main measurement		<b>-37%...+30% (ohm)</b>
consists of ...			<b>-44%...+37% (NBI)</b>
... first window/first mirror	transmission of optics	years	+5%
... grey filters error	photon count	permanent	<u>±9%</u>
... spectral filter width	isolation of $H_\alpha$ line	permanent	-15%
... camera/detection path error	photon count	various	<u>±18%</u>
... background subtraction	background $H_\alpha$ value	pl. fluctuation	±3%, <u>±18%</u>
<b>photon amount <math>N_{ph}</math> (CLIO)</b>	main measurement		<b>±24% (ohm), ±33% (NBI)</b>
... grey filters error	photon count	permanent	<u>±9%</u>
... notch filter error	photon count	1 day	<u>±4%</u>
... spectrometer/fibre error	photon count	various	<u>±13%</u>
... background subtraction	background $H_\alpha$ value	pl. fluctuation	±3%, <u>±18%</u>
$n_e, T_e$ at LIDS light maximum	choice of $S/XB$ -value	plasma shifts	±43%, <u>±41%</u>
... edge diagnostics error (SHE)	choice of $S/XB$ -value		±23%, <u>±35%</u>
... edge diag. statistical error	choice of $S/XB$ -value		±13%, <u>±5%</u>
... edge diag. systematic error	choice of $S/XB$ -value		<u>±10%</u> , <u>±30%</u>
... transfer to LIDS position	choice of $S/XB$ -value	plasma shifts	<u>±20%</u>
position of LIDS light maximum	choice of $S/XB$ -value	1 day	±2.3 mm
... position of limiter	spatial calibration	1 day	±1.5 mm
... search algorithm	search for maximum	permanent	<u>±0.8 mm</u>
$S/XB$ value	main conversion factor	plasma shifts	<b>±33%</b>
... $n_e, T_e$ at LIDS light maximum	main conversion factor	plasma shifts	<u>±20%</u>
... pos. of LIDS light maximum	main conversion factor	1 day	<u>±11%</u>
... value from ADAS database	main conversion factor	ADAS updates	<u>±10%</u>
<b>atomic yield factor <math>Y</math></b>	gas composition	spot-to-spot	<b>-20%</b>
... QMS combined measurement	$Y$ value	1 day	<u>±3%</u>
... one-mass measurement	gas amount desorbed	1 day	<u>±27%</u>
... species specific leak rate	QMS calibration	permanent	<u>±16%</u>
... daily statistical error	measure.&calibration	1 day	<u>±11%</u>
... assumption of plasma process	formula for $Y$	permanent	-19%
<b>uncaptured light <math>V</math> at HO</b>	amount of $H_\alpha$ photons	FoV, spot shift	<b>+27%</b>
<b>uncaptured light <math>V</math> with CLIO</b>	amount of $H_\alpha$ photons	FoV, spot shift	<b>+3%</b>
<b>desorbed area <math>A</math> (for <math>\varnothing 3</math> mm)</b>	areal H concentration	permanent	<b>±10%</b>
total error for ohmic plasma	HO: -55%...+53%	CLIO: -47%...+43%	
<b>total error for NBI heated plasma</b>	<b>HO: -60%...+58%</b>	<b>CLIO: -52%...+48%</b>	

**Table 7.2.:** Error estimations for a single LIDS measurement; errors for NBI heated plasmas are marked in **red**; systematic errors are underlined

## 7. *In situ* Laser Induced Desorption Spectroscopy (LIDS)

---

The purely systematic error for the photon amount  $N_{ph}$  is thus  $-18\%$  to  $+11\%$  (for the HO) and  $\pm 10\%$  (for CLIO). The uncertainties of  $Y$ ,  $V$  and  $A$  are nearly completely systematic except the statistical error of the QMS measurement for  $Y$ , which has a very small influence on the final error of  $Y$ . Thus all these uncertainties are used as given in table 7.2. The estimation of the systematic error of the  $S/XB$  value is not as simple since two of the three contributors (the plasma parameters and the position of the light intensity maximum) have similarly large systematic errors as statistical errors. To estimate the systematic part of the plasma parameters errors on the  $S/XB$  error, their purely systematic errors of  $\pm 23\%$  (for  $n_e$ ) and  $\pm 36\%$  (for  $T_e$ ) are applied with the same method as for the combined error described above. In the typical region of plasma parameters the induced  $S/XB$  error is  $\pm 10$ - **$14\%$** .

The systematic contribution of the position uncertainty of the light intensity maximum is  $\pm 0.8$  mm, which induces an uncertainty of  $\pm 9\%$  for  $n_e$  and  $\pm 3\%$  for  $T_e$  for the steepest plasma profiles used. Those lead to an error of only  $\pm 3\%$  for the  $S/XB$  value in the typical parameter region. Combined with the ADAS uncertainty of  $\pm 10\%$  a total systematic error of  $\pm 18\%$  for the  $S/XB$  value results.

The combination of all five uncertainty values according to the Gaussian error propagation yields a total systematic error range of  **$-34\%$  to  $+36\%$**  for the HO and  **$-31\%$  to  $+23\%$**  for CLIO.



## 8. Applications of Laser Induced Desorption Spectroscopy

The development of Laser Induced Desorption Spectroscopy and its subsidiary method with mass spectrometric detection was furthered in the recent decade by the need to analyse the fuel-rich co-deposited carbon layers deposited by plasma-wall interactions. In that times carbon (graphite, CFCs, etc) was approved as first wall material and assumed to be used also in the future as PFCs because of its low Z-value, lack of melting and thus shape stability etc. Due to C erosion and deposition, within one experimental day C layers of up to 500 nm thickness can grow for example in TEXTOR within 30 to 50 plasma discharges of 5-6 s discharge duration. Hence, the development and application of LID has begun on such thin a-C:D layers on graphite. These applications will be mentioned briefly at the end of this introduction and in the introduction of the second section of the present chapter.

Post-mortem analysis on many tokamaks, measurements by LIDS and dedicated gas injection experiments, provided large amounts of data, that lead to a model for hydrogen retention which showed an overwhelming domination of retention by co-deposition. The amounts of fuel stored in the hydrocarbon layers extrapolated by the models to long-term fusion operation led to an unsatisfactory short plasma time until the safety limit for tritium would be reached. As a first means of retention reduction the use of carbon material was proposed to be limited to high power loaded areas like the limiters or divertor strike points and to use Be and W for the main chamber and the remaining divertor parts. This increased the predicted plasma time until the ca. 1 kg T limit would be reached from 10 to ca. 50 h [Brezinsek13]. This corresponds to ca. 450 standard ITER discharges of 400 s duration, but the uncertainties in the prediction would also allow a pessimistic result of ca. 260 discharges. This is not satisfactory, since it could result in only one year of experimental operation before extensive detritation would become necessary. Since the co-deposition of T with C is a factor of 3-10 larger than co-deposition with Be and about two orders of magnitude larger than co-deposition with W [Lipschultz10, p.7], carbon was excluded as first-wall material. With this fully metallic first wall of Be in the main chamber and W in the divertor the predictions increased to a plasma time of at least ca. 250 h corresponding to more than 2200 standard discharges [Brezinsek13, p.18]. For the fusion reactor design (like DEMO) the material choice is – at the moment – even a full W first wall. An extensive part of the present LID work is therefore its application to bulk W, which introduces a qualitative change in the hydrogen release (as described in chapter 4) compared to carbon dominated material. This qualitative change modified the operation modes of LID in order to adapt. Examples from very different W exposure conditions reaching from low flux laboratory devices, over tokamak exposure, up to plasma simulators that reproduce conditions as expected at the ITER divertor targets were discussed in chapter 6.2. The maximum H or D concentration of these W samples in the present work is below the lowest LIDS detection limit of  $8 \cdot 10^{20} / \text{m}^2$  as can be seen in the overview figure 6.14 on page 153. Thus carbon samples have to be used as hydrogen sources for the following LIDS applications.

Nevertheless, the formation of carbon layers from unavoidable carbon sources cannot be fully excluded in future fusion devices and applications of LID on carbon materials outside

nuclear fusion are conceivable. Therefore, the first extension of the LID technique from pure C materials was the application to hydrocarbon layers on W. Thin amorphous hydrocarbon layers (a-C:H or a-C:D) on carbon materials had several advantages in the early development stage of laser induced desorption methods. For instance, the laser light reflexion is only changed in acceptable and known ranges by the thin layer (cf. chapter 2.3). The optical layer properties in general are beneficial because the low extinction coefficient makes the layers nearly transparent for the laser. Thus the laser heating process and the resulting temperature distribution is not influenced strongly by these thin layers of several hundred nanometres. The heating process is therefore well defined, to a large extent analytically describable (cf. chapter 2.4.1) and proved to be in agreement with measured surface temperatures, while the depth distribution is only known from model calculations. The hydrogen release from these layers is prompt and nearly complete after one laser pulse (cf. chapter 4). The desorption process is only dependent on the surface temperature and follows the same physics as in the well known slow TDS heating, only faster [Irrek8, p.52]. The optical property of these layers to change their colour characteristics dependent on the temperature, is helpful in the identification of the desorbed area and analysis of partial or complete desorption. Moreover their good adhesion and heat conductivity to the carbon substrate offer a temperature regime of complete hydrogen desorption without significant surface modifications (cf. chapter 3.1). Therefore, two applications of LIDS will be presented in the following two sections on such amorphous hydrocarbon layers.

The first measurement series demonstrates LIDS on an a-C:H layer that predominantly retains protium, while the second layer is an a-C:D layer containing mainly deuterium. Both layers provide a constant source of hydrogen for the desorption process and show the ability to quantify both hydrogen isotopes. Thus, also the absolute values are compared with ex situ methods like LID-QMS and TDS. Exemplarily, the experience gained in these two measurement series can give hints and guidelines for a routinely application of LIDS. These examples were also selected as they were performed in the late stages of the present work, where all the previously introduced detection methods like the coaxial observation were available. Thus, results of three different observation angles can be shown, which can characterise a single LIDS process simultaneously from three views. These provide spatially resolved data of the LIDS light distribution and spectra at the same time.

### 8.1. Laser Desorption of a-C:H Layers

The Balinit<sup>®</sup> layer on W has already been investigated several times in the present work. In chapter 7.7 a hydrogen concentration of  $(6.7 \pm 2.6) \cdot 10^{22} \text{ H\&D/m}^2$  was obtained from LIDS data and  $(6.8 \pm 2.8) \cdot 10^{22} \text{ H\&D/m}^2$  by LID-QMS measurements. Up to now the first Balinit<sup>®</sup> coating has been analysed.

Now W samples with a second Balinit<sup>®</sup> coating are used, which were produced in the same way in a second coating procedure. As W substrate again rolled tungsten plates of 2 mm thickness and 99.95 wt% purity were used, provided by Negele Hartmetall-Technik GmbH (cf. appendix A on page 232 for details). Some specimens were squares of  $25 \times 25 \text{ mm}^2$  (samples B5n, B6n), others were circles with  $\varnothing 25 \text{ mm}$  (B1n, B2n). First, the samples were annealed at 1273 K for more than one hour in vacuum and send to oerlikon balzers Coating Germany GmbH for the Balinit<sup>®</sup> DLC STAR coating. Afterwards the surface roughness of the samples was  $R_a = (1.22 \pm 0.13) \mu\text{m}$  as measured on several 1 mm long line scans on the surface with the stylus profiler. The new Balinit<sup>®</sup> coating has a thickness of ca. 2  $\mu\text{m}$  (including the CrN interlayer) and is thus thinner than the first coating (cf. figure 3.7 on page 81). Hence, the hydrocarbon layer alone has probably only a thickness of ca. 1.5  $\mu\text{m}$  assuming that the

interlayer is similarly thick as in the first coating. This is consistent with a similar volumetric hydrogen concentration because the layer contains about a factor of 1.6 less hydrogen than the previous layer, which agrees quite well with the ratio of the old and new DLC layer thickness, excluding the interlayer.

This reduction of the areal hydrogen concentration was measured ex situ by LID-QMS ca. 1 month before the samples were first exposed in TEXTOR and about 3 months before the last LIDS measurement were performed on them. In the LID-QMS analysis the 3.0 mm laser beam diameter was used at a small angle incidence of ca.  $5^\circ$  which results in an irradiated area of  $7.1 \text{ mm}^2$ . Since the applicable laser power for the later in situ measurements by LIDS would be limited by higher losses due to the CLIO system, different laser pulses were used in LID-QMS to have comparable pulse properties ex situ and in situ. A weak laser heating was used with  $450 \text{ MW/m}^2$  of absorbed laser intensity for 1.5 ms which yields a heat flux factor of  $17.5 \text{ MW} \sqrt{\text{s}/\text{m}^2}$  and a strong pulse with  $850 \text{ MW/m}^2$ , 3.0 ms and  $\text{HFF} = 46.6 \text{ MW} \sqrt{\text{s}/\text{m}^2}$ . The weaker heating led to measured maximal surface temperatures of  $T_{surf} = (1510 \pm 40) \text{ K}$  on average, while the strong heating reached  $(2030 \pm 50) \text{ K}$ . The given error is the error of the measurement series. These temperatures were measured by the one wavelength point pyrometer with the surface emissivity  $\varepsilon = 0.9$  which is the closest setting to the layer emissivity which was measured in advance (14% reflectivity within 1.58-1.8  $\mu\text{m}$  cf. chapter 2.3). The analytically expected temperatures (cf. chapter 2.4) for the weak laser pulse are 1350-1400 K depending on the choice of heat parameters, either for graphite or W. The measured values are in agreement to these values with only a factor of 1.08 increase, which can be explained by the additional heat contact and heat transfer coefficients at the interfaces of layer, interlayer and substrate. Their influence is indicated by the heat offset effect that appears in the beginning of the heating phase (cf. chapter 2.4.3). The maximal temperature is reached at the end of the laser pulse unlike in the case of the strong laser pulses. There, a first temperature maximum is reached at about 0.5 ms and after a decrease a second maximum with similar temperatures at 1.5 ms before the temperature drops to a lower level for the second half of the pulse. These probably unreal temperature drops point to emissivity changes towards lower values like those of the metals of the interlayer and substrate. Hence, the measured values underestimate the temperature and strongly deviate from the analytical expectations of 3110-3220 K. In the evaluation of the areal hydrogen concentration, the desorbed area is used as discussed in chapter 3.1. As described there, the area approaches the laser irradiated area with increasing HFF. For the weak laser pulse it covers 89% and for the strong pulse 98 % of the laser irradiated area on average.

The results of the LID-QMS measurements are summarised in figure 8.3 on page 220 with the individual error bars representing the errors of a single measurement. The reduced error due to repetition of the measurements within one measurement series with identical experimental conditions, is shown by the horizontal dashed lines. The average values of the hydrogen concentration are indicated by the full thick lines and by the triangles at the y-axis, which are repeated in figure 8.3b to compare with the LIDS results later on. The average value for the high HFF reaches  $(4.2 \pm 1.1) \cdot 10^{22} \text{ H\&D}/\text{m}^2$ , which is the already mentioned factor of 1.6 lower than for the first Balinit<sup>®</sup> DLC coating, when desorbed with the same settings. For the weak laser heating a factor of 1.45 lower average value results already including the smaller area of desorption. This lower hydrogen concentration is quite significant as all values of the high HFF series are outside the uncertainty interval of the low HFF series and vice versa. However, the difference between the two average values is not very large since the two uncertainty intervals still overlap rather strongly. Nevertheless, possible explanations for the reduced hydrogen concentration should be shortly discussed.

- One reason might be a discrepancy between the visibly modified area and the real desorption area. Areas that have changed in optical appearance might still be (mainly)

undesorbed or, oppositely, areas which appear to be not modified by the laser may be (partly) desorbed. Such a discrepancy can only be verified by a hydrogen detection method with a high spatial resolution that can resolve the laser spot area, like  $\mu$ -NRA (cf. chapter 6.2). However, for the factor of 1.45 difference, a difference in the desorbed area of ca. 2.1-3.0 mm<sup>2</sup> would be necessary, depending on which of the spot sizes the estimation is based on. This would result in a spot diameter increase of 0.4-0.6 mm, which is not fully unrealistic.

- **a)** The second explanation might be an incomplete desorption, although such an effect has not been observed for a-C:H layers, even on much thicker layers from TEXTOR (cf. figure 4.9 on page 123). There, the values for D and H from LID-QMS are very close to those measured by TDS, except the much higher H value in the erosion dominated area which has been explained with H from the substrate. To exclude such a substrate effect here, laser melting was performed on positions which were not coated by the Balinit<sup>®</sup> layer as they were covered during coating. The standard LIM pulse was used on the minimal laser spot size as discussed in chapter 3.3 which melts the W substrate ca. 30  $\mu$ m deep. As these LIM pulses only desorb  $4.7 \cdot 10^{20}$  H&D/m<sup>2</sup> and thus two orders of magnitude less than the LID pulses, bulk-H desorption can be excluded as an explanation.

However, the comparison of LID and TDS values for the first Balinit<sup>®</sup> layer showed a factor of 1.2-1.5 lower desorption by TDS (cf. chapter 7.7). This deviation is in the opposite direction than for the TEXTOR samples and might indicate that complete desorption for Balinit<sup>®</sup> requires higher temperatures. A fraction of the hydrogen might be desorbed only above the 1273 K of TDS and even above the 1500 K of the weak laser pulses. Only the stronger pulses reaching 2000-3000 K might release this hydrogen fraction. Such strongly bound components can not be completely excluded and could be investigated further with TDS devices that reach such high temperatures.

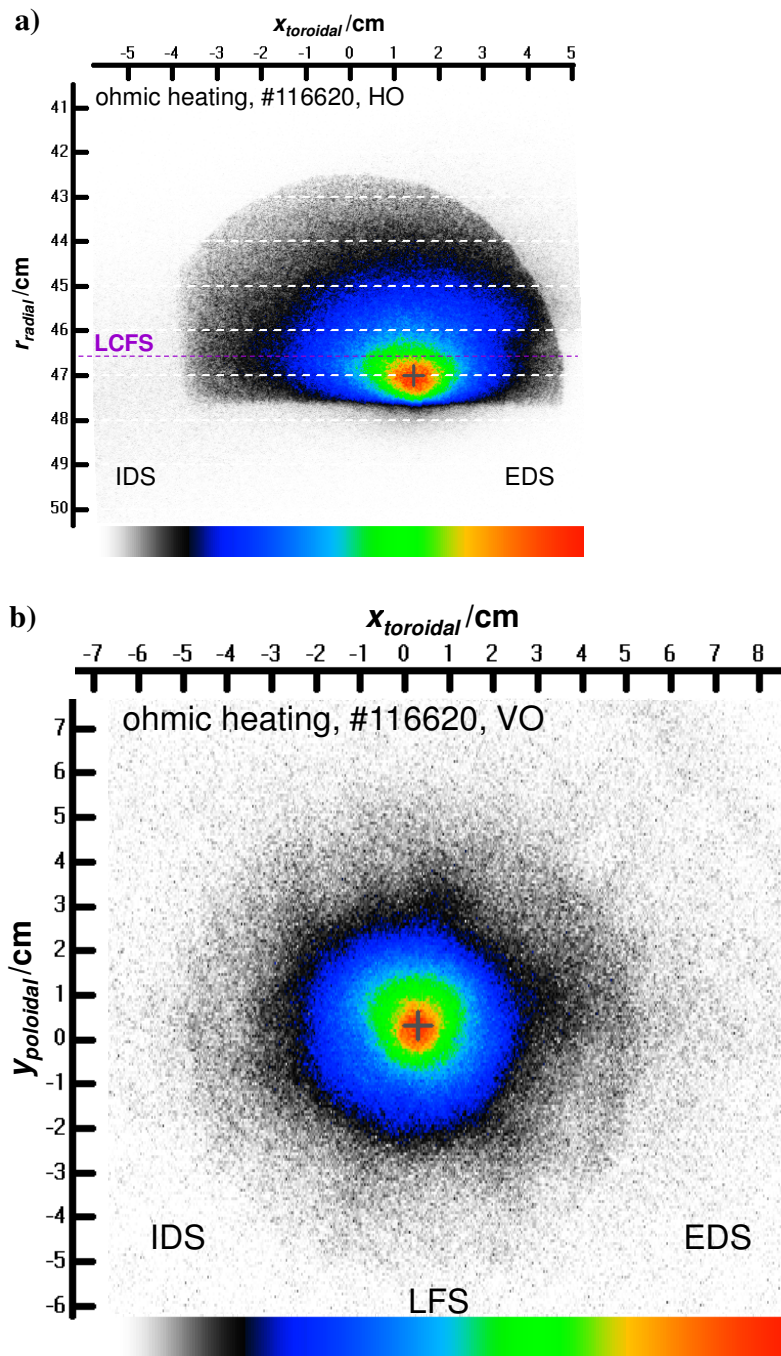
**b)** Instead of the insufficient temperature, a second reason for such an incomplete desorption appeals more to the experiences during the present work, especially those made with W materials. The Balinit<sup>®</sup> layer might be less porous than the tokamak DLC layers, thus providing more resistance to the hydrogen during the migration to the surface (cf. figure 7.3 on page 165 and its discussion). For the even thicker tokamak layers their stratified layer structure and extremely high roughness might provide the necessary desorption paths towards the surface. The only homogeneous DLC layers investigated – except Balinit<sup>®</sup> – were thin (i.e. below 500 nm) thus obviously not thick enough to show such a hindered migration towards the surface. The Balinit<sup>®</sup> layer is such a homogeneous layer but several times thicker and the pores in DLC layers are only few nanometres wide (cf. chapter 4.3), here maybe even less due to a possibly more compact structure. As a consequence, the locally released hydrogen might not be able to migrate towards the surface completely, especially from greater depths. This hindered migration could then be overcome for the strong heating due to the onset of surface modifications that destroy the homogeneity of the layer such as cracking and blistering. Such modifications were observed to occur at ca. 1500 K calculated surface temperature on the Balinit<sup>®</sup> layer (cf. figure 3.5 on page 80). They probably provide the necessary migration paths for the desorbed hydrogen to reach the surface. Hence, for homogeneous a-C:H layers with thicknesses in the micrometre range or thicker, such laser induced modifications might be necessary to reach complete desorption. To verify this explanation a decoupling of the surface modifications and heating would be needed, e.g. heating to 2500 K without producing cracks, which is difficult. The opposite approach with the weak heating and artificially generating the surface modifications e.g. by mechanically induced cracking could provide a proof.

Whether the first or second explanation or a combination of both apply cannot be answered here. Nevertheless, the sample shall serve as a homogeneous and constant hydrogen source for LIDS, which is the case when always the same laser pulses are used. To verify the absolute value of the LIDS data both average values of the two ex situ series shall be used as limits because the LIDS series is performed with a HFF of  $31.5 \text{ MW} \sqrt{\text{s}}/\text{m}^2$ . This is quite in the middle between the HFF values applied in LID-QMS and was achieved by an absorbed laser intensity of  $820 \text{ MW}/\text{m}^2$  for 1.5 ms. In LIDS the laser modified area showed a distinctive spot centre surrounded by a ring as already observed several times (cf. chapter 3.1), which was not observed on the ex situ spots. Probably the higher amount of optical components or a particular component in the coaxial beam path (CLIO) lead to this ring structure. Hence, the desorbed area was determined as the average of the outer diameter of the ring and the diameter of the inner spot centre. During this in situ measurement series two of the already ex situ analysed sample were used (B5n and B6n) and the LIDS light was observed from three directions (for details cf. chapter 7.2):

- At the horizontal observation (**HO**) the fast digital camera with image intensifier, which was actively gated for 5 ms synchronised with the laser pulse recorded full images every 10 ms behind the wide (FWHM=3 nm)  $\text{H}_\alpha$  filter.
- From the top view coaxially (using **CLIO**) along the laser beam the high-resolution spectrometer observed the LIDS light through the hole in the last laser mirror, shielded by a 1064 nm notch filter from the laser light. A spectrum was recorded every 0.5 s with 10 ms integration time each, also synchronised with the laser pulse, hence obtaining a background spectrum and a LIDS spectrum alternately as the laser frequency was 1 Hz.
- The third observation was also from top with the same inclination of  $7^\circ$  but on the LFS instead of the HFS of the tokamak (cam11, cf. figure 7.1 on page 161). This vertical observation (**VO**) was equipped with an analogue camera with a permanently active image intensifier behind a narrower (FWHM=1.5 nm)  $\text{H}_\alpha$  filter. This camera was not absolutely calibrated, but was used to obtain a top-view image of the shape and distribution of the LIDS light. The camera recorded half-images every 20 ms which were stretched by a factor of 2 to obtain quasi full frame images. As this camera was not synchronised with the laser pulses, the LIDS light sometimes occurred on two consecutive images. Then the background subtraction had to be changed from the simple method described in chapter 7.5.1 for the HO to the following. The background subtracted image was obtained as the pixelwise sum of the two images with the LIDS light subtracted by the image before them and the image just after them. Additionally, also a new process was needed to obtain the LIDS image with background by summing the two images with the LIDS light and subtracting half of the image before them and half of the image after them. This is necessary as the sum of the LIDS images alone yields an image including a double background.

First, the HO and VO are discussed as the HO contains the information about the position of the maximum of the LIDS light intensity on which the evaluation of all views is based. The ohmic discharge during which the first example was performed was a standard PWW discharge, whose global parameters are given in the caption of figure 8.1.

The LIDS images of the two observation directions are adjusted in size to be in the same scale and they are positioned in such a way that the maximum of the LIDS light appears at the same position. However, the toroidal scales do not match in absolute numbers. In the vertical view the whole circular sample holder is visible and even its surrounding up to 10 cm from its centre is visible in two of the four directions (towards the high field side HFS and



**Figure 8.1.:** LIDS of a ca. 2  $\mu\text{m}$  thick a-C:H layer on W (Balinit<sup>®</sup> B6n); 810  $\text{MW}/\text{m}^2$  absorbed laser intensity for 1.5 ms; background subtracted images; TEXTOR discharge #116620 with  $I_p = 350$  kA,  $B_t = 2.25$  T,  $n_{e,la} = 2.5 \cdot 10^{19}/\text{m}^3$   
a) horizontal observation; 5 ms image intensifier gate;  $H_\alpha$  filter with 3 nm FWHM  
b) vertical observation; 20 ms integration time;  $H_\alpha$  filter with 1.5 nm FWHM

EDS). Therefore, the origin of the images is chosen at the centre of the sample holder, which corresponds roughly to the centre of the limiter lock duct, disregarding the  $7^\circ$  tilting of the view angle. In the horizontal view the smaller observation volume of slightly less than 10 cm in diameter does not allow to see the whole sample holder as it is ca. 11 cm in diameter. Hence, the centre of the sample holder cannot be identified accurately, therefore the origin of the toroidal scale is chosen at the centre of the observation volume.

The position of the light intensity maximum on the toroidal scale of the VO shows that the desorption took place very close to the sample holder centre. At the HO the LIDS light maximum is slightly more than 1 cm away from the origin of the toroidal axis which means that it is recorded nearly in its full extent and not much LIDS light is uncaptured.

Both images are coded in the same false colour scale and the brightest pixels were scaled to the maximum of the colour scale (i.e. to red). Hence, the shape and extent of the LIDS light can be roughly compared and with both views combined the LIDS light pattern can be discussed in 3D. In general its shape can be described as a hemisphere in the outer, i.e. darker parts. In the top view the areas of similar brightness form concentric circles with some small deformations like the broadening of the green region towards the HFS, especially on the IDS, which can also be seen in the side view. The blue circle is also slightly shifted to the IDS but rather towards the LFS. This slightly larger extend of the blue region is even more pronounced in the HO, where it reaches up to 2.8-3 cm left of the LIDS maximum but only ca. 2.5 cm to the right, on the EDS. This shows that small asymmetries in the LIDS light distribution sometimes occur, when in general its shape is rather symmetric.

The side view from the HO shows more complex shapes of the individual regions from the brightest parts at the light intensity maximum towards the darker parts outside. The small inner regions are quite circular (red region), then become rather elliptical (green region) and finally hemispherical in the far field (blue and black regions). The size of the different regions is very similar in both views. A small bump of the blue region can be seen on the EDS of the side view between  $r = 45$ -46 cm. This is an untypical irregularity in the shape of the LIDS light, which is not observed repeatedly at the same position. In the top view it can hardly be seen as it overlaps with the lower bump at  $r = 47$  cm. Only in a smoothed image with contour lines it is visible and thus confirmed to be a real light emission and not an artefact e.g. due to a reflexion on an optical component. This example shows the worth of two views of the same event as they can help in the mutual interpretation.

Further LIDS measurements were done on another sample (B6n) which was identical but located further outside on the sample holder. Consequently also the LIDS light was located further outside. Therefore, these desorption images were cut vertically at the position of the LIDS intensity maximum and the left part, which contains half of the LIDS light was integrated. The integral was doubled to obtain the value for the total LIDS light. An example of this procedure will be depicted in the next section on desorption of a-C:D layers. In these cases the fraction of lost light is probably even lower because the toroidal light decay on the left side is recorded further away from the laser spot than in the case of LIDS in the centre of the FoV. On the other side, a symmetric light pattern is assumed as generally seen in LIDS.

In the ohmic plasma shown above, the sample was located at 47.9 cm minor plasma radius about 2 mm below the top of the sample holder which is the lower boundary of the LIDS light. In the following LIDS measurements on the same layer but on a different sample always an NBI heated plasmas is used and the sample is at  $r = 48.2$  cm. From the HO view the radial position of the light intensity maximum is determined to ca.  $r = 47.0$  cm minor plasma radius for the ohmic and ca. 47.5 cm for NBI heated discharges. These values are about 1 cm less deep in the plasma than for the previous measurement series on the old Balinit<sup>®</sup> layer (c.f. figure 7.22 on page 202). Since no updated plasma edge profiles were evaluated for the new

LIDS measurement series, it is assumed that the whole plasma was shifted by 1 cm downwards compared to the earlier LIDS measurements. Therefore, the plasma edge parameters at the LIDS light maximum are assumed to be comparable to those of the previous measurement series. This is justified by the previous observation that the LIDS light maximum tends to follow the specific plasma region with  $k_B T_e \approx 55\text{-}60$  eV and  $n_e \approx 4\text{-}5 \cdot 10^{18}/\text{m}^3$ . Consequently, a similar value for the  $S/X_B$  of 15 is used as in the previous measurement series. A further justification is the comparable amount of desorbed hydrogen atoms since the areal H concentration of the new layer is lower by nearly the same factor as the desorbed area increased.

For the second quantification quantity, namely the inverse atomic yield factor  $Y$ , the contribution of desorbed hydrocarbons is used as obtained during LID-QMS (cf. blue diamonds  $\blacklozenge$  and right scale in figure 8.3a). As practically all the desorbed hydrogen is protium,  $Y_H$  is used as defined in equation 7.5 on page 173, which nearly always is just below 2.1, hence this value is used in the HO and CLIO evaluation.

With these two values the conversion of the photon amount into hydrogen amount is done and the areal hydrogen concentration is calculated using the laser spot area determined post-mortem as described above. For the HO the resulting values for the combined H&D concentration are shown as green points ( $\bullet$ ) for each laser pulse in figure 8.3b). Always three laser pulses with a frequency of 1 Hz are fired in each plasma discharge before the desorption position is changed between the discharges. The corresponding TEXTOR shot number for each discharge is given on the x-axis left of the results of each discharge. Only two times no position change is done, namely between the discharges #116809-#116810 and between #116812-#116813, which is indicated by the connecting line between the data points. In these cases all six laser pulses are directed at the same position. Additionally, for the discharge #116815 the same laser spot position was selected as in #116808 as noted in the figure. Although the targeting position of the laser injection system was not moved during the discharge, sometimes the laser beam has desorbed a slightly different position. Thus, in the post-mortem analysis the laser spots sometimes show the shape of two or three overlapping circles that are not perfectly concentric. This is probably caused by the movement of the sample holder or the laser injection due to vibrations originating from the TEXTOR operation itself. Therefore, the combined area of all laser pulses has to be used as desorbed area that refers to the desorbed hydrogen amount of all pulses on this position. Hence, the sum of all laser pulses on one position – the "spot sum" – is shown in the figure by plus signs in circles ( $\oplus$ ) at the end of the pulse series of each spot. Only here the areal hydrogen concentration is referenced to the correct spot area, while the values for the individual laser pulses are too low as they are also calculated with the same combined area. This is done because the desorbed area of the individual spots is not known especially of the 2<sup>nd</sup> and further pulses that heat only small undesorbed areas as they mainly heat the desorbed area of the 1<sup>st</sup> pulse. The advantage of this representation is that the areal concentration of the sum equals the sum of the values of the individual laser pulses. Their contribution to the spot sum can thus be seen. The error of a single LIDS measurement is shown by the error bars on the spot sum and is omitted for the individual laser pulses for the sake of clarity. The average of all spot sums is  $(3.7 \pm 1.6) \cdot 10^{22}$  H&D/m<sup>2</sup> which is marked by the horizontal green line. The corresponding error range of this measurement series is indicated by the dashed green lines. All HO spot sums lie between or very close to the two average values from LID-QMS which are marked on the y-axis by the blue and orange triangles for the pulses with lower and higher HFF than in LIDS, respectively.

Due to the relatively wide  $H_\alpha$  filter at the HO, minor components of light emitted by singly ionised carbon  $C^+$  on the three spectral CII lines shown in figure 7.21 on page 197 can contribute. The high peaks shown there are an extreme case of strong carbon release. A more typical case is shown in the spectra from the CLIO view for the present sample (cf. figure 8.2) where these spectral lines are quite weak. To quantify the carbon contribution in the HO images,

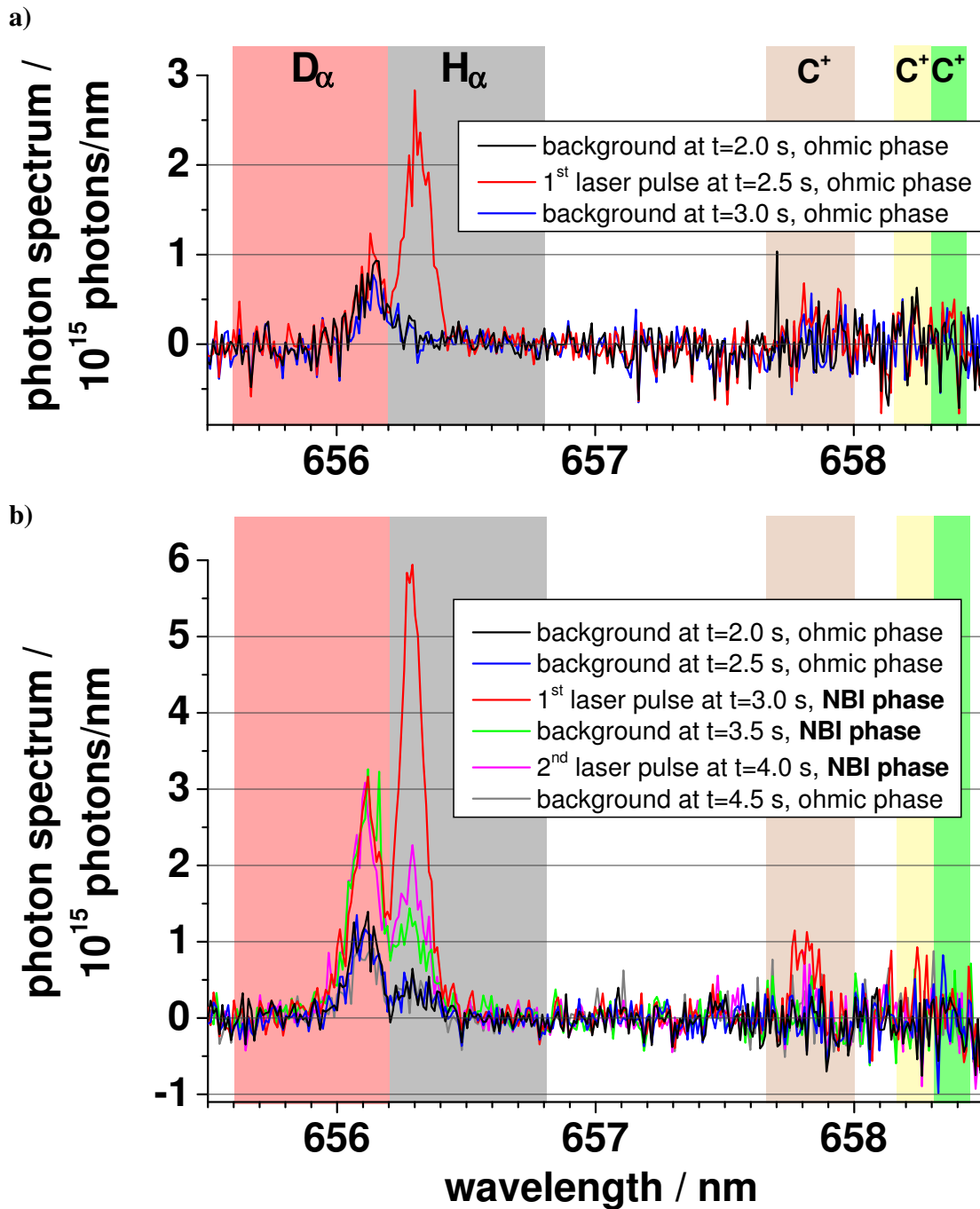


the three lines were evaluated in the marked regions in the figure separately for each line and multiplied by the known filter transmission at the three wavelengths. The sum of these values in relation to the sum of the total light transmitted through the  $H_\alpha$  filter, which includes them and the  $H_\alpha$  and  $D_\alpha$  lines, gives the carbon contribution in the camera signal. For the 2  $\mu\text{m}$  DLC layer discussed here, the carbon contribution is on average 12% for the 1<sup>st</sup> laser pulse, 8% for the 2<sup>nd</sup> and 9% for the further pulses. This means that the contribution of the  $C^+$  light recorded in the HO images is typically low. However, sometimes the values can be significantly higher especially for the second and third laser pulse, as the hydrogen signal is much lower then and maximum values of 19% for the 2<sup>nd</sup> and 42% for the further pulses were obtained here. But many laser pulses also show no carbon contribution at all or have values below the mentioned averages. Especially for the first laser pulse the carbon contribution is always smaller than 19% for the 2  $\mu\text{m}$  DLC layer.

These carbon contribution values obtained from the CLIO spectrometer are used to reduce the photon amount recorded by the HO camera and thus to eliminate the  $C^+$  contribution. The HO image integrals then only contain the combined  $H_\alpha$  and  $D_\alpha$  light, but the light distribution pattern still contains the carbon contribution as the spectrum gives no spatial information. But this contribution is known to form a light band in the outer plasma region which is toroidally elongated much more than the hydrogen light. Thus, for cases with a high carbon contribution, the shape of the LIDS light is not hemispherical as typically in the far field but strongly elongated and hence already hints at the presence of the  $C^+$  light.

The quantification of all spectral lines is performed in two main steps. First, the recorded data (in counts) are multiplied point by point with the calibration curve (in photons/counts/nm), which was obtained during calibration at the same spectral positions. The calibration curve contains the information about the dispersion of the spectrometer, i.e. the wavelength interval  $d\lambda$  (in nm) of each data point, since they are not constant. The result of the multiplication is the shown photon spectrum (in photons/nm). In the second evaluation step, the analysed spectral line is integrated in the marked spectral regions of the photon spectrum (cf. figure 8.2). This area under the spectral line is equal to the amount of photons emitted by LIDS in the integrated wavelength interval. As can be seen in the spectra, the separation is not complete for the hydrogen lines due to the line width of ca. 0.1 nm FWHM. Hence, the integration intervals of the two lines are chosen such that they merge at the minimum between the peaks. As the wings of the peaks extend into the interval of the other line, the obtained individual amount of  $H_\alpha$  and  $D_\alpha$  photons is influenced by the neighbouring line. Probably the larger peak leads to a slight overestimation in the evaluation of the smaller peak and the smaller peak leads to an underestimation of the larger peak. Here the larger peak is  $H_\alpha$  during the 1<sup>st</sup> laser pulse and  $D_\alpha$  is larger for the background and subsequent pulses. Only when both peaks are similarly high it is expected that the mutual influence is also similar and the effect vanishes. However, the sum of both lines always yields the correct combined amount of all  $H_\alpha$  and  $D_\alpha$  photons. Therefore, these combined H&D values will be compared further below to the values from the HO, which anyway only yields the combined values.

To obtain the photon amount induced by the laser, the integrated photon amounts during the background plasma are subtracted from those obtained during the laser pulse. Typically the value from the background spectrum before the laser pulse and the background after the laser pulse are averaged like for the camera observations. But as the time between two acquisitions of a spectrum is half a second, it sometimes occurred that one of this backgrounds is taken during different plasma parameters than were present during LIDS. For example in figure 8.2b) the first two backgrounds (at 2.0 s and 2.5 s after the plasma ignition) were recorded during the initial ohmic phase of the plasma and are thus quite identical. Then the plasma was NBI-heated and the first two laser pulses and one background inbetween them were recorded during this NBI phase. Clearly, the increased plasma background in both hydrogen lines is



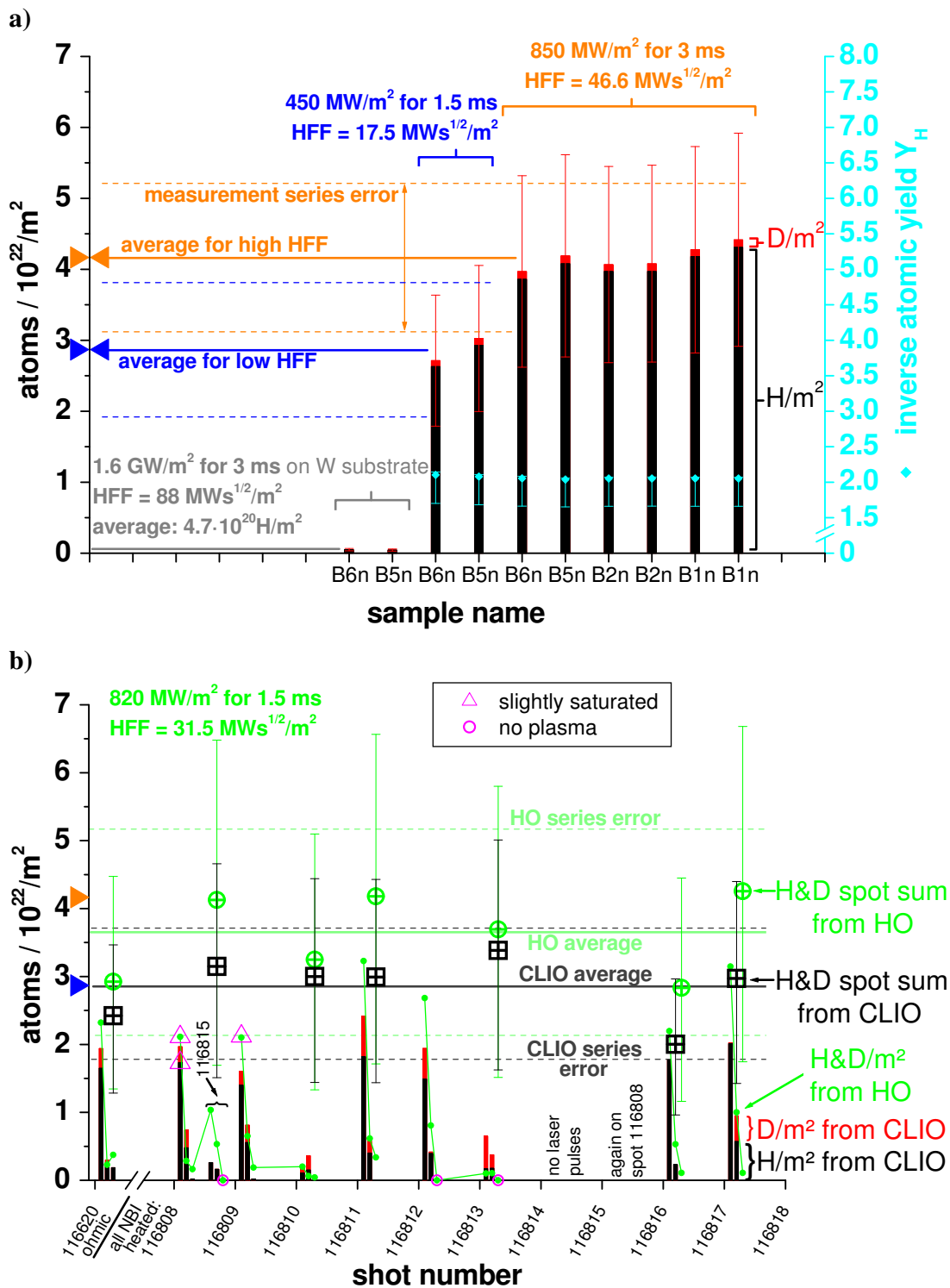
**Figure 8.2.:** LIDS of a ca. 2  $\mu\text{m}$  thick a-C:H layer on W observed through CLIO; 10 ms integration time; 820  $\text{MW}/\text{m}^2$  absorbed laser intensity for 1.5 ms  
 a) during ohmic plasma heating (TEXTOR #116020, sample: Balinit<sup>®</sup> B6n)  
 b) during an NBI heated plasma (TEXTOR #116816, sample: Balinit<sup>®</sup> B5n) with a factor of 2 more transparent neutral density filter than a)

seen and the additional LIDS light at the  $H_{\alpha}$  line. Finally, a last background was acquired in the ohmic phase after the NBI heating was switched off and the background is again very similar to those in the first ohmic phase. In such a case the sensible background for the 1<sup>st</sup> laser pulse is the background during the NBI phase (at 3.5 s) and not an average of this and the previous background as this was in the ohmic phase. For the 2<sup>nd</sup> laser pulse also the background during the NBI phase has to be used instead of an average of two backgrounds. The choice of the most sensible background or average of backgrounds is done for each laser pulse individually depending on the timing and characteristics of each plasma discharge as shown here exemplarily.

The scattering of the spectrum data around the zero line is quite small in the vicinity of the hydrogen lines and increases towards the carbon lines which is not the case in the raw data. This is due to the alternating notch filter transmission which has a local maximum (with 63% transmission) at the hydrogen lines and the next local minimum (with 22%) at the last carbon line. Therefore, the combined sensitivity of the spectrometer and notch filter is almost a factor of 3 higher at the hydrogen lines than at the carbon lines. As this effect is included in the calibration curve, the noise around the carbon lines is amplified by this factor of nearly 3.

The background subtracted photon amounts evaluated from the spectra are divided by the laser spot area obtained by post-mortem analysis. The resulting areal hydrogen concentration related to the combined spot area of all pulses on one spot is shown as bar chart in figure 8.3b for each laser pulse with stacked black and red bars for H and D, respectively. All three laser pulses per discharge were recorded and evaluated except for the discharges after #116814 where the third pulse was not recorded. Additionally, the laser pulses without plasma are marked in which the plasma operation ended before the third laser pulse, e.g. due to a disruption. The sum of all laser pulses on one spot are shown by the black plus signs in squares ( $\boxplus$ ) as the spot sum. Like for the HO the average of these spot sums is marked with a horizontal line and the uncertainty of the CLIO series by the dashed grey lines. The average value of  $2.9_{-1.1}^{+0.9} \cdot 10^{22}$  H&D/m<sup>2</sup> matches almost exactly the lower LID-QMS value obtained with the lower HFF. The CLIO values are somewhat too low since the HFF in LIDS was higher. Hence, the average value should be between the two LID-QMS values like it is for the HO. Nevertheless, only two of the CLIO spot sums lie outside the interval of the LID-QMS average values and the majority is well within the expected interval.

Comparing the results from the HO and CLIO a general tendency to lower values from the coaxial observation is seen especially in the combined H&D spot sums and in the 1<sup>st</sup> pulses. Only in three of the 2<sup>nd</sup> laser pulses and some of the subsequent pulses the CLIO values are higher than the HO values. For the spot sums the difference between the CLIO and HO values is only low when more than 3 pulses are summed like for the spot in #116809+#116810 and the spot in #116812+#116813. But even then it is lower than the values from the horizontal observation. The mismatch between the CLIO and HO data might be also due to some calibration issue, especially for the spectrometer calibration (cf. chapter 7.4) as it had to be done ex situ. In contrast to the HO camera, the spectrometer calibration had to be done outside the tokamak with a shorter working distance than during the experiment. As described in the calibration chapter this introduced some additional correction factors. For most of these factors an error estimation was done in the previous chapter (cf. chapter 7.10) except for the mentioned ratio of the two solid angles as they rely on simple geometrical distances. However, the fact that the CLIO spot sum is always lower than the corresponding HO value hints at a systematic error source, which might have still remained. But this error must be rather low as the HO and CLIO spot sums are always within the error range of each other, which is valid for every laser spot and for the average values. The deviation can be quantified by the quotient of the HO average and CLIO average to a factor of 1.27. This is a rather small deviation, which is also shown by the fact that the two series error ranges overlap strongly.



**Figure 8.3.:** a) LID-QMS on 2  $\mu\text{m}$  a-C:H layer (Balinit<sup>®</sup> B1n, B2n, B5n and B6n)  
 b) LIDS on 2  $\mu\text{m}$  a-C:H layer (Balinit<sup>®</sup> B6n in one ohmic discharge and B5n in 9 NBI2-heated discharges) viewed from the Horizontal Observation (HO) and from top via the Coaxial Laser Injection and Observation (CLIO)

## 8.2. Laser Desorption of a-C:D Layers

In earlier works, experiments with a-C:D layers grown outside the tokamak in the PADOS device, pre-characterised and desorbed in TDS, have proved the basic quantitative abilities of LID-QMS and LIDS [Irrek8]. In situ experiments on the same substrate (unannealed and annealed pyrolytic fine grain graphite EK98 from Ringsdorff and R6650 from Kornmeyer Carbon Group) have shown a satisfactory accuracy of fuel quantification in tokamak grown layers in TEXTOR [Irrek8], [Schweer9]. An in situ live monitoring of the fuel content increase (due to co-deposition) and decrease (due to heating by a plasma disruption) in the main net-deposition area ( $48.2 \text{ cm} < r < 50.5 \text{ cm}$ ) and in the erosion dominated area was demonstrated [Schweer9]. However, these earlier LIDS measurements were performed only at the HO with camera detectors equipped with the mentioned  $H_\alpha$ -filter (FWHM = 3 nm) and thus could not separate H and D. Additionally, a possible carbon contribution was always included in the data. To demonstrate the ability of LIDS to discriminate the hydrogen isotopes the previously discussed desorption of a-C:H is complemented by the desorption of a-C:D layers here.

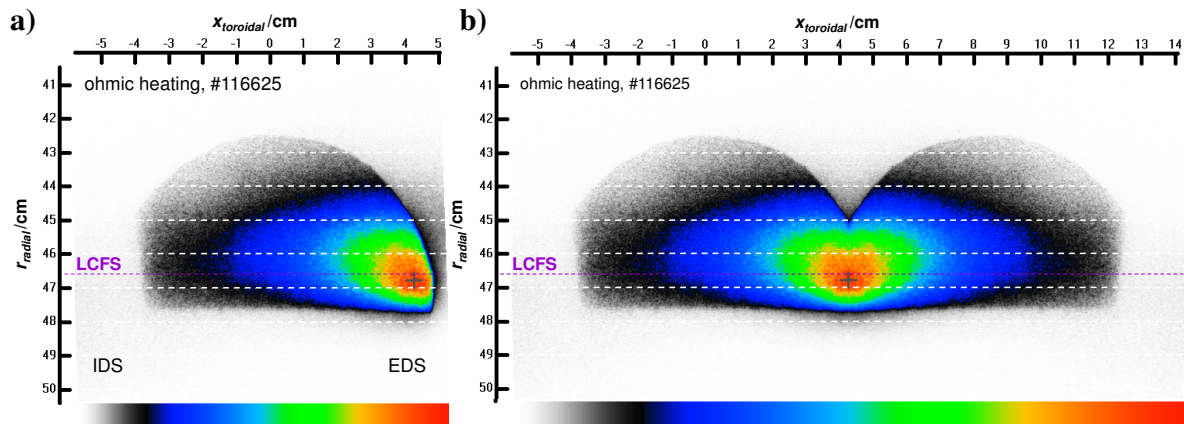
Samples of pyrolytic fine-grain graphite (Ringsdorff EK98) of  $25 \times 25 \times 2 \text{ mm}^3$  were annealed at 1273 K and then coated with an a-C:D layer in the PADOS chamber of the IEK-4 institute. The coating was applied by a glow discharge in  $CD_4$  at 0.5-6 Pa within 3 h under an accelerating DC voltage between 170-390 V and roughly 340 K sample temperature or higher. During the coating process thin Si samples with a mirror polished surface were located on top of the graphite substrates as witness samples and partly covered. In contrast to the rough graphite surface, the layer thickness can be measured very accurately with a stylus profiler by measuring the height step that occurs on the partly covered Si samples. Nearly all measurements on these witness samples showed a sharp height increase by 550 nm. However, due to the roughness of the graphite the layer may be thicker on rough surfaces. Using the same profilometric technique also the roughness of the coated graphite was measured to be  $R_a \approx 1.0 \mu\text{m}$  directly after the coating.

Two of these samples (PADOS GII and GIV) were used for LIDS in TEXTOR on a horizontal sample holder in limiter lock 1. The plasma discharge parameters were set to the standard PWW settings defined earlier. All discharges were heated ohmically and had a line-averaged density of  $n_{e,la} = 2.5 \cdot 10^{19} / \text{m}^3$  except for the last discharge which had the maximal feasible density of  $n_{e,la} = 3.0 \cdot 10^{19} / \text{m}^3$ . In the overview figure 8.6 on page 225 some discharges are missing due to unstable plasma conditions, no plasma ignition or disruptions. Some laser spots ended up only partly on the sample and partly on the stainless steel sample holder due to bad laser targeting and are thus omitted, too. For the first discharge only data from the horizontal observation are shown as the spectrum from the coaxial observation is strongly saturated in  $D_\alpha$ .

The laser pulse settings and timing are equal as in the previous section but due to the lower total reflectivity of the sample, the absorbed laser intensity is higher. The reflectivity of the sample was measured in the spectrophotometer to 8% at the laser wavelength. Thus, the absorbed laser intensity is ca.  $880 \text{ MW}/\text{m}^2$  during the 1.5 ms laser pulse, which yields a HFF of  $34 \text{ MW} \sqrt{\text{s}}/\text{m}^2$ . A laser irradiated area of  $7.7 \text{ mm}^2$  was used which corresponds to a laser beam diameter of 3.1 mm. The spot size determined photographically is 4.7-5.1 mm in diameter. This is due to an increased lateral heat propagation and not to a defocussed laser beam as the desorption of the a-C:H Balinit<sup>®</sup> layer on the same day showed a spot diameter of 3.28 mm. The small increase of the spot size is probably due to the interlayer of the Balinit<sup>®</sup> sample. Although the a-C:D layer is 5 times thinner, it seems to have a worse heat contact between layer and substrate and thus stronger lateral heat diffusion. The analytically calculated temperature increase amount to  $\Delta T \approx 2060 \text{ K}$  and thus the final temperature reaches ca.  $T_{surf} \approx 2500 \text{ K}$ .

## 8. Applications of Laser Induced Desorption Spectroscopy

At first the HO data are discussed exemplarily, then the CLIO spectra and finally the quantitative comparison with the TDS results for this layer. As the top surface of the sample holder was located at a minor plasma radius of  $r_{lim} = 47.7$  cm and the sample surface retracted by 2 mm, the LIDS light starts at  $r_{lim}$  (cf. figure 8.4a). As both samples were positioned in the outer ring of the sample holder, the LIDS light is shifted to the side of the FoV. This is beneficial when the symmetry of the LIDS light is utilised. The modified evaluation procedure is shown here in figure 8.4b where the LIDS light pattern is cut at the toroidal position of the light intensity maximum marked by the plus sign and then mirrored horizontally while the right part of the image is neglected. The combined image 8.4b contains a major fraction of the LIDS light except for the central part 2 cm above the light intensity maximum, which is missing due to the circular shape of the FoV. The integral in the LIDS evaluation is performed on the combined image and hence roughly twice the integral of the unmirrored image. The quotient of the integrals lies between 1.6 and 1.9 depending on the actual toroidal position of the laser spot. The quotient is smaller for the desorptions that are closer to the centre of the FoV. In contrast to the previous section, all LIDS images had to be evaluated in this way due to the toroidal location of the sample. The radial position of the LIDS maximum is similar as in the previous section – only few millimetres deeper in the plasma, still close to the LCFS. Thus, for the photon-to-particle conversion the same  $S/X_B = 15$  value was used.

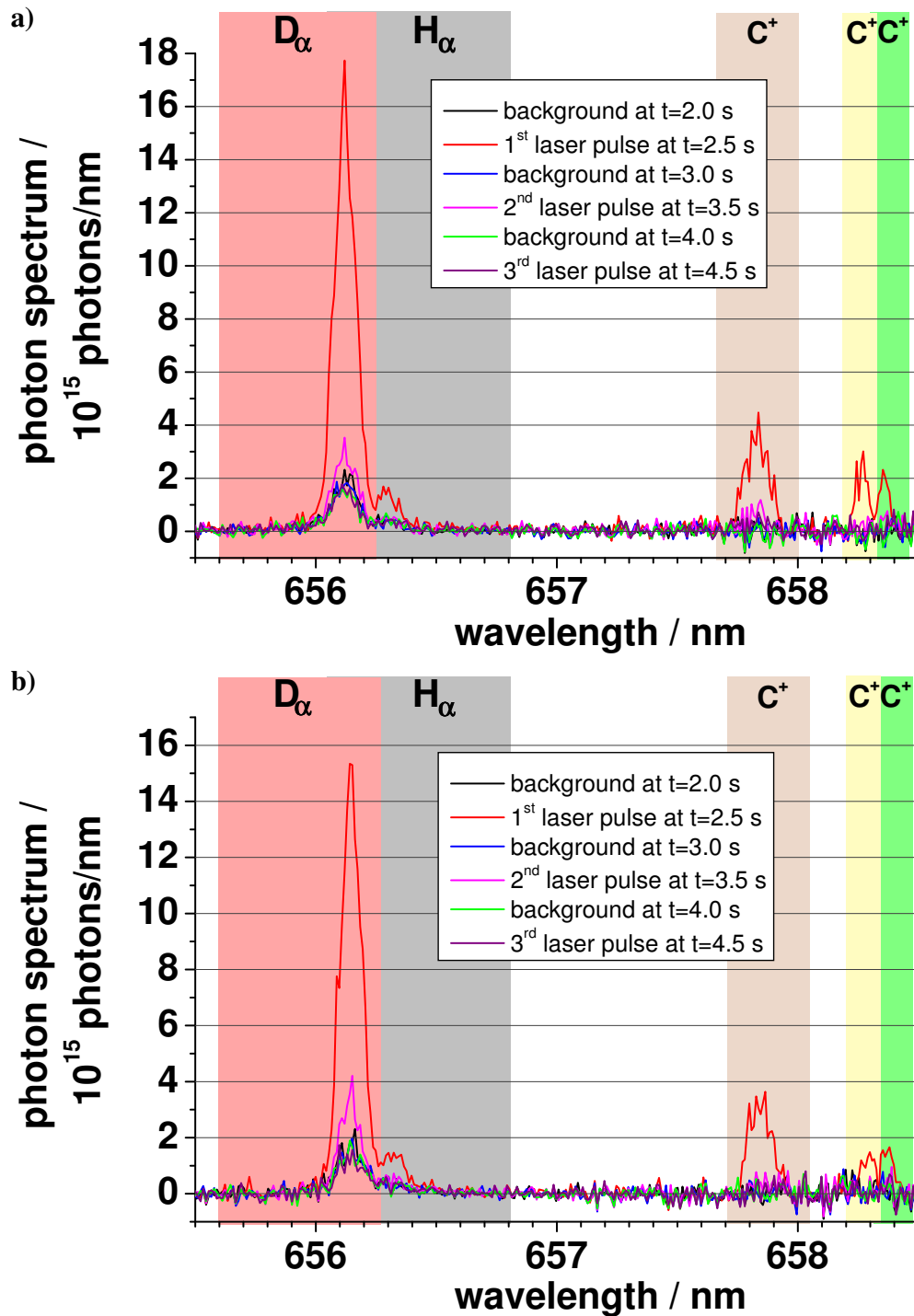


**Figure 8.4.:** LIDS of a 550 nm thick a-C:D layer on graphite (sample PADOS GIV)

- a)  $H_{\alpha}$  light intensity; background subtracted image at the horizontal observation
- b) image a) mirrored horizontally at light intensity maximum (indicated by "+")

For the second quantification factor the inverse atomic yield factor for deuterium (cf. equation 7.6 on page 174) was used, because deuterium is the dominant hydrogen isotope here. The typical value of  $Y_D = 2.4$  for a-C:D layers produced in the PADOS glow discharge plasma is chosen. However, the TDS analysis of the GIV sample provides a value of 2.6 but the  $Y_D$  values are typically lower in LID-QMS, which may be due to a slightly different desorption behaviour due to the rapid heating. TDS typically shows slightly higher hydrocarbon contribution (cf. figure 6.5 on page 141).

The evaluated H&D photon amount obtained from the HO images is again reduced by the fraction of  $C^+$  light that is transmitted parasitically through the  $H_{\alpha}$  filter of the camera detector. Its fraction is obtained from the spectra of the CLIO observation. The minimum fraction of the carbon contribution is 16%, 18% and 41% of the total light recorded in the 1<sup>st</sup>, 2<sup>nd</sup> and 3<sup>rd</sup> laser pulse, respectively. The average carbon contribution is 18%, 28% and 72% and the maximal contribution is 21%, 39% and 100% for the 1<sup>st</sup>, 2<sup>nd</sup> and 3<sup>rd</sup> laser pulse, respectively. The last value means that all the light that passes the  $H_{\alpha}$  filter of the HO during LIDS is CII



**Figure 8.5.:** LIDS of a ca. 550 nm thick a-C:D layer on graphite observed through CLIO; 10 ms integration time;  $880 \text{ MW/m}^2$  absorbed laser intensity for 1.5 ms; ohmic plasma heating; a) TEXTOR #116625, sample: PADOS GIV  
b) LIDS with low  $C^{+}$  contribution (TEXTOR #116617, sample: PADOS GII)

light from  $C^+$  ions, which occurred in a case where no  $H_\alpha$  and  $D_\alpha$  light was detected simultaneously. For the first discharge discussed here, the average values are assumed since the CLIO spectrum was saturated in  $D_\alpha$  and thus the carbon contribution could not be evaluated. In all further cases the carbon contribution obtained for each laser pulse individually is used for the reduction of the HO signal of each laser pulse. In figure 8.5a) a typical spectrum obtained by the coaxial observation is shown with an average H&D amount and a moderate carbon contribution of 18%, 27% and 85% for the 1<sup>st</sup>, 2<sup>nd</sup> and 3<sup>rd</sup> laser pulse, respectively. In this discharge 90% of the total desorbed H&D atoms are released in the first pulse and the remaining 10% in the second pulse. In the whole measurement series on average 88%, 11% and 1% are released in the 1<sup>st</sup>, 2<sup>nd</sup> and 3<sup>rd</sup> pulse, respectively with a minimum of 82%, 7%, 0% and a maximum of 92%, 17% and 3%. The corresponding values for the HO are very similar with only one remarkable deviation that the maximum value for the first laser pulse reaches even 95% of the spot sum.

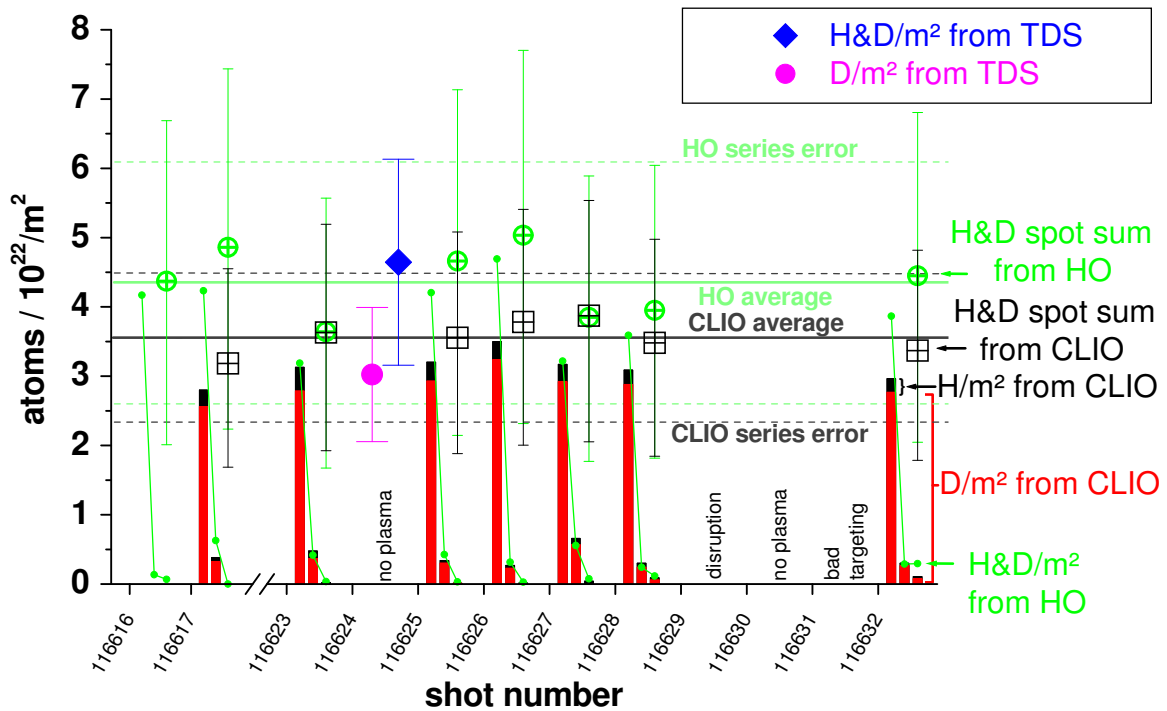
The high carbon contribution for the 2<sup>nd</sup> and 3<sup>rd</sup> pulse are thus not due to an increased carbon release but a consequence of the strong reduction of H&D desorption in the subsequent pulses. The reduction of the hydrogen light is stronger than the reduction of the  $C^+$  light in the subsequent laser pulses, thus the carbon contribution increases. In figure 8.5a the integral of the carbon line at 657.8 nm in the 2<sup>nd</sup> pulse amounts to 17% of the integral of the first laser pulse. The highest value within this measurement series is 35% for #116623 and the lowest 15% for the spectra in figure 8.5b). Laser induced evaporation or sublimation of carbon can most probably be excluded as an explanation for the carbon light in the first laser pulse, since it should occur in the subsequent pulses in similar strength. Unfortunately, it was not possible to analyse more relevant lines like the CD line at 431 nm as the notch filter had many regions with very low or no light transmission like for this spectral line. The observation of such a molecular line could support the more likely interpretation that the  $C^+$  light originates from desorption of hydrocarbons and not from carbon sublimation.

An important finding in the coaxially obtained LIDS spectra is that the two hydrogen lines can still be observed individually even when one line is much larger than the other. Although there is no perfect separation of the lines as discussed in the previous section, the large  $D_\alpha$  line obviously does not influence or overlap the small  $H_\alpha$  line stronger than before. The local minimum between them still exists and thus they can still be evaluated separately. This becomes more complicated for the tritium line  $T_\alpha$ , since its peak is at 656.03-656.05 nm [NIST15], which is in the wing of the  $D_\alpha$  line. Its evaluation would require a more sophisticated procedure including spectral line deconvolution by a line shape fitting.

The  $D_\alpha$  and  $H_\alpha$  line were integrated in the marked wavelength ranges as discussed above. The end of the integral for  $D_\alpha$ , which is the begin of the integral for  $H_\alpha$ , was always chosen in the local minimum between the lines in the first laser pulse, where it is most prominent. After the conversion to H and D atoms those were related to the desorbed area to obtain the surface concentration. Complications with the spot area like in the previous section did not occur as the spots are all fairly circular. Obviously, the laser beam has always heated the same area on each spot position. This is probably the reason, why the 2<sup>nd</sup> and 3<sup>rd</sup> pulse contribute only very little to the spot sum of each spot and hence the values of the 1<sup>st</sup> pulse is very close to the spot sum (cf. figure 8.6). Nevertheless, the subsequent pulses are also shown for a better comparison to the a-C:H layer results of the previous section.

Like for the a-C:H layer the results from the two observations are within the error ranges of each other for each spot except in one case. For two discharges the HO and CLIO results are even equal. The general trend that the HO yields higher values than the CLIO remains. The HO average of the series is a factor of 1.23 larger than the CLIO average, which is nearly the same deviation as in the previous section. This further supports a systematic reason for this deviation as it is quantitatively similar here despite the main hydrogen isotope in the





**Figure 8.6.:** LIDS of a 550 nm a-C:D layer on graphite (PADOS GII and GIV after #116622) viewed from the Horizontal Observation (HO) and from top via the Coaxial Laser Injection and Observation (CLIO); TDS results of sample GIV are added

desorptions has changed from protium to deuterium. There is also not much change in the relative positions of the error ranges of the HO and CLIO series as they still strongly overlap and include the average value of the other series. But the data scatter of the spot sums – or first pulses, which is quite the same here – has considerably reduced. For the a-C:H layer the standard deviation of the spot sums was 17% of the average value for the HO and CLIO. The desorption of the a-C:D layers shows only a standard deviation of 12% for the HO data and even 7% for the CLIO data. This might be due to the following reason. All except one desorption of the a-C:H layer were performed in NBI heated plasmas which have much higher fluctuations of the hydrogen light background by nearly an order of magnitude (cf. chapter 7.7). This introduces more uncertainty in the background subtraction and increases the data scatter compared to the ohmic discharges here.

A small piece of 25 mm<sup>2</sup> was cut out of the sample GIV, which was used in the figure on the right hand side of the x-axis break, and analysed by TDS five months after LIDS. The whole sample was heated to 1273 K and the desorbed gas species were quantified by QMS. In the evaluation of the desorbed D atoms, the molecules of HD (mass 3), D<sub>2</sub> (mass 4), CD<sub>3</sub>H (mass 19) and CD<sub>4</sub> (mass 20) were included, which resulted in  $(3.0 \pm 1.0) \cdot 10^{22}$  D/m<sup>2</sup> (marked in the figure by ●). Comparing this to the deuterium spot sums from CLIO, which result in an average of  $3.2^{+0.9}_{-1.1} \cdot 10^{22}$  D/m<sup>2</sup> shows a very satisfactory agreement within a factor of 1.07. For the protium atoms only the unambiguous mass species of mass 2 (H<sub>2</sub>), 3 (HD) and 19 (CD<sub>3</sub>H) were taken into account, which already showed a high result. In total the hydrogen retention measured by TDS results in  $(4.6 \pm 1.5) \cdot 10^{22}$  H&D/m<sup>2</sup> as marked in the figure (by ◆), which is close to the HO average of  $(4.4 \pm 1.8) \cdot 10^{22}$  H&D/m<sup>2</sup>. All H&D spot sums of the HO and CLIO are within the TDS error range of the combined H&D concentration.

The lessons learned from these and similar measurements can be a guideline for LID applications in other devices. For example a reduced signal scatter can be achieved when LIDS

is performed during quiet and stable plasma phases such as ohmically heated plasmas without additional heating. When the desorption is located in an area which is expected to be deposition dominated, the desorption should be performed repetitively to avoid desorption of very thick layers. The time interval between the desorptions should be chosen such that the newly deposited layer is not larger than a micrometre as the lateral heat propagation starts to be significant then. For thicker layers a precise quantification of the areal hydrogen concentration requires additional knowledge about the desorbed area through close optical inspection or preferentially imaging thermography during LID. In this thickness range nearly all the retained hydrogen can be desorbed in the first pulse, for thicker and more compact layers two laser pulses may be necessary. However, a limit for the layer thickness is also set by the onset of local plasma cooling (cf. chapter 7.9), which should be avoided.

To distinguish different hydrogen isotopes, a high-resolution spectrometer or cameras with narrower or sharper spectral filters than used in the present work are necessary, which should also have no transmission in the IR. The FoV of the not spatially resolving detectors has to be a balanced trade-off between a low background and low uncaptured LIDS light. For conditions like in TEXTOR a FoV of at least 16 cm in diameter should be used to capture ca. 90% of the LIDS light (cf. chapter 7.10). For spatially resolving detectors a larger FoV is preferable as a smaller area of interest can always be defined artificially. For the hydrogen quantification the local plasma density and temperature in the region around the light intensity maximum should be known from measurements or reconstruction. However, if possible a reference sample with known hydrogen content should be placed at a plasma shadowed position for verification of the photon-to-particle conversion factors.

## 9. Summary

Laser induced desorption spectroscopy has been analysed with the main emphasis to develop an in situ method to detect the hydrogen isotope retention in the walls of fusion devices. To qualify laser desorption for this purpose, a number of basic processes have been analysed:

- The laser induced heating process
- The hydrogen desorption and release process
- The surface modifications of laser treated surfaces
- The detection of released hydrogen by quadrupole mass spectrometry (LID-QMS)
- The detection of hydrogen by spectroscopy (LIDS) in the edge plasma of TEXTOR

The work encompassed graphite based solid materials, amorphous hydrogen rich C layers (a-C:H layers), mixed C/W deposits, solid W materials and W fuzz. C deposits and mixed C/W deposits have been produced both in TEXTOR and in laboratory devices.

### Laser heating process

For Laser Induced Desorption (LID) a spatially homogeneous laser beam is essential. In the present work a Nd:YAG laser beam at 1064 nm wavelength with a top-hat shape of 2-3 mm diameter shaped by transmission through fibre optics is used to obtain homogeneous heating. For controlled heating a spike-free temporal and spatial laser power distribution is essential. In the present work the homogenisation of the laser beam is obtained by the use of fibre optics and the appropriate focal length of the coupling lens for the fibre optics. The retained hydrogen of a-C:H layers is released by rapid heating to 1800-2000 K with a 1.5 ms laser pulse of  $700 \text{ MW/m}^2$  absorbed intensity. The temperature for complete desorption reaches ca. 100  $\mu\text{m}$  into the depth.

To reach the desired temperature, the **reflexion** of the laser beam on the materials was measured to determine the absorbed laser intensity. The materials used in the present work can be divided in three groups of low reflectivity below 30% (C based materials), medium reflectivity around 50% (W based materials) and high reflectivity above 80% (Al, Ag, Au) which are not suited for laser heating at the wavelength used here (1064 nm).

For homogeneous materials (graphite, W without layers) the resulting **temperature distribution** was calculated analytically. For anisotropic materials (CFCs) with and without W coatings (JET ITER-like wall coating) numerical calculations (ANSYS code) have been used. The calculations showed a good agreement with time-resolved temperature measurements on the surface. Also for thin C layers the agreement was good, except for the thin mixed C/W layer grown in TEXTOR, where the surface temperature was underestimated. This could not be fully resolved.

For **thick layers** (> 500 nm) with bad heat contact to the substrate, the heat propagation is no longer directed mainly into the depth, but significant lateral propagation can occur. This heat propagation is difficult to calculate, due to the unknown and very low heat conductivity of such layers. A conductivity of  $0.67 \text{ W/mK}$  has been determined by flash laser heating for a thick carbon layer grown on the ALT-II tile of TEXTOR. Such low heat conductivities hamper a controlled heating and the desorbed area is not well defined like for thin layers or bulk

material. For thick deposits with bad heat contact, the desorption area can thus be several times larger than the laser irradiated area, depending on the local thermal contact to the substrate and the heat conductivity of the layer. The size of the desorbed area should then be determined by a fast IR-camera observation during LID or close visual inspection of the laser spot afterwards. Among the thick carbon layers only one layer with a special Cr interlayer for improvement of the contact to the W substrate did not show significant lateral heat propagation. Hence, for in situ grown layers a repetitive LID measurement on the same positions is preferable before the layer thickness increases such that the lateral heat propagation becomes significant.

### Surface modification

Without special interlayers, already few micrometre thick C layers have a strongly reduced destruction threshold. This makes a separation of desorption and destruction very difficult for any laser intensity. For such C layers, complete desorption is reached already with low laser intensities, but always leads to evaporation or delamination of the layer. Fortunately this does not disturb the quantification of the released hydrogen, but produces dust and surface damage.

For thin C deposits the surface modifications are moderate and smaller for thin layers and lower desorption temperatures. The carbon layer detaches locally on the scale of 10  $\mu\text{m}$  from the substrate (C or W) and local cracks in layer and substrate form at the desired temperature of 1800 K, but appear already at 850 K on C. The detached parts can easily overheat and evaporate. But this material losses are small because Nuclear Reaction Analysis (NRA) inside the laser spots of C deposits on W showed that LID does not remove carbon significantly from the deposits, while nearly the complete deuterium inventory ( $> 90\%$ ) is desorbed.

The surface modifications on W were also studied, showing mainly an increase in roughness ( $R_a > 0.2 \mu\text{m}$ ) due to the thermal expansion of the W grains during laser heating leading to plastic deformation. This occurred already for low laser intensities ( $190 \text{ MW/m}^2$  for 1 ms, 670 K). The roughness increases exponentially with laser intensity. For solid W, laser induced melting (LIM) has been applied. The resulting craters have been analysed by optical microscopy, profilometry and cross-section investigations. A several micrometre high circle surrounding the molten spot has been found, while the spot centre is slightly below the initial surface. In total, an increase in the volume is observed. This apparent volume increase is explained by the appearance of large, nearly spherical voids ( $\varnothing \leq 20 \mu\text{m}$ ) at 30-50  $\mu\text{m}$  depth, appearing at the contact zone of melt and solid. During the fast cooling (up to 5000  $\text{K/ms}$ ) thermo-mechanical stresses occur that create a characteristic rapid solidification pattern (RSP) of cellular and cellular-dendritic structures on the surface. The cross-sections of the molten region show relaxation of stresses within the W grains, but no significant increase in grain size. On some samples cracks appear across heated or molten spots and sometimes also circularly outside the laser irradiated area.

### Hydrogen release process

For carbon based materials, the desorption process is determined by the thermally activated release of the hydrogen from a C:H bonding, thus by a single step process. The transport of the hydrogen through the porous C bulk or C layer is not determining the release rate. It has been shown in earlier works that laser induced desorption occurs at similar temperatures as in slow heating by Thermal Desorption Spectrometry (TDS), thus complete desorption is achieved for  $T > 1300 \text{ K}$ . In the present work this behaviour could be confirmed also for a-C:H layers on W and mixed layers (C/W/H/D with 10 at% W).

For laser desorption on bulk tungsten the desorption process has been found to be qualitatively different, because the release process is dominated by the diffusion of the hydrogen. A main result is that LID in tungsten leads only to a partly release of the hydrogen, whereby the fraction of release depends mainly on the surface temperature during plasma exposure.

---

Even a prolongation of the laser pulse to 3 ms at  $500 \text{ MW/m}^2$  – keeping the 1800 K surface temperature – or increase of laser intensity and maximum temperature cannot completely release the retained hydrogen from tungsten in most cases. Numerical calculations with the TMAP7 code show that LID pulses reduce the maximum value of the hydrogen concentration by 1-3 orders of magnitude. This could be confirmed by depth-resolved NRA measurements. But simultaneously the hydrogen diffuses also several tenths of micrometres into the depth, where it establishes a low concentration but over a large volume. Further heating pulses release only small amounts of this hydrogen, which diffuse from the depth and laterally from outside the laser spot. The desorption fraction in the first pulse is determined by the loading conditions during plasma exposure. A low surface temperature ( $T \leq 380 \text{ K}$ ) during exposure leads to a desorption fraction above 90%, which reduces continuously, until at high temperatures ( $T > 800 \text{ K}$ ) less than 20% of the hydrogen desorbs. This is due to a shallow hydrogen depth profile after plasma exposure in the cold case due to a short diffusion length while deep diffusion occurs in the hot case. However, an increase of the binding energy of the hydrogen traps or a higher trap concentrations at higher temperatures could also explain the reduced desorption fraction, as shown by the simulations. In order to fully desorb all the hydrogen isotopes from W materials, the tungsten in the laser spot was molten on the first 30-50  $\mu\text{m}$ . This is deep enough for all plasma exposure conditions used here to obtain complete desorption. Consequently, for longer or hotter plasma exposures, desorption by LIM should be done regularly on the same positions before the hydrogen can diffuse deeper.

By LID-QMS the behavior of hydrogen retention in tungsten has been studied under various exposure conditions. Bulk W was exposed in TEXTOR, PSI-2, Pilot-PSI, PADOS and PlaQ under different plasma fluxes, surface temperatures, exposure times and impact energies. For similar fluences, the data indicate that the amount of retention scales only marginally with the square root of plasma fluence as often reported in the literature but rather with exposure time. In several exposures at similar fluences the retention was much higher for long, low flux exposures than for short, high flux exposures. However, the present data are obtained also under non-uniform surface temperature conditions. Due to this fact and the limited number of data a better analysis of the retention dependence has not been attempted. A second remarkable behavior of hydrogen retention in W was found for W fuzz structures that might occur in plasmas which contain helium ions. W fuzz exposed in erosion dominated areas in TEXTOR showed more than 20 times higher retention than a simultaneously exposed W material with polished surface.

### **Hydrogen quantification**

For ex situ quantification of the released hydrogen in a laboratory device, Quadrupole Mass Spectrometry (QMS) has been optimised in a small vacuum chamber for this particular purpose. A fast mass spectrum is repeated, while the pumping of the chamber is interrupted. Then the laser heating is done and the increase of all masses due to the laser desorption is evaluated automatically by regression analysis of the peak values of all masses at the time of the laser pulse. The accuracy of this method is estimated to roughly  $\pm 35\%$  depending slightly on the laser spot size. The error is mainly determined by systematic uncertainties in the conversion of calibration leak rates to the quantified molecules  $\text{H}_2$ , HD,  $\text{D}_2$  and hydrocarbons in the appropriate pressure regime. The statistical errors are small (ca. 12%). Several improvements in the setup and measurement procedure were introduced, that are vital for a safe and accurate LID-QMS measurement, such as proper treatment of the laser light reflected by the vacuum windows and sample. This is especially important for medium and high reflective samples to prevent desorption of the chamber walls which can otherwise considerably increase the signal background to unacceptable levels.

The in situ quantification method of retained hydrogen (LIDS) operates during plasma operation and without tile removal. It is based on passive spectroscopy of the Balmer- $\alpha$  light from the hydrogen atoms. The hydrogen, which is released from the surface predominantly as molecule, is ionised and dissociated by impact of electrons from the plasma. The dominant reactions in the temperature range of the TEXTOR edge plasma ( $k_B T_e = 25\text{-}100$  eV) yield one ion, which does not emit line radiation, and one atom. Thus for pure  $\text{H}_2$ , HD or  $\text{D}_2$  release (e.g. from W) the two atoms of the molecule yield only one atom after dissociation, i.e. the inverse atomic yield is  $Y = 2$ . If hydrocarbons also desorb (e.g. from a-C:H, DLC layers) typically 10-20% of the total hydrogen is released in hydrocarbons, which increases the factor to  $Y = 2.0\text{-}2.6$ .

Then the atoms are excited by electron impact from the plasma and emit light during relaxation before they are finally ionised. The ratio of excitation and ionisation rate ( $S/X_B$  value) determines the amount of emitted photons and is different for different local electron temperature  $T_e$  and density  $n_e$ . In the evaluation of LIDS images obtained by a camera with gated image intensifier and  $\text{H}_\alpha$  filters, the background subtracted, integrated amount of photons was converted to the amount of atoms by a simplified choice of the  $S/X_B$  value: The  $n_e, T_e$ -values at the position of the  $\text{H}_\alpha$  intensity maximum were chosen based on plasma profile measurements by other diagnostics and the corresponding  $S/X_B$  value was taken from the ADAS database. This simple method was compared with a full consideration of the light emitted for a given plasma profile by numerical simulations (ERO code), which resulted in a deviation of only few percent to the simplified method. It was also found experimentally, that different plasma profiles do not change the chosen  $S/X_B$  value significantly, because the position of the light intensity maximum tends to shift to positions with similar  $n_e, T_e$ -values of ca.  $(4\text{-}5) \cdot 10^{18} / \text{m}^3$  and 50-60 eV.

The numerical simulations with ERO showed that the **shape of the emission light cloud** is sensitive to moderate changes (by factor 1.5 in absolute values and factor 2.3 in decay length) of the  $n_e$  and  $T_e$  profiles, while the total photon amount is practically constant. The simulations also reproduced the measured toroidal and poloidal extent of the  $\text{H}_\alpha$  light shape (30-40 mm FWHM for 2 cm distance to the LCFS) and the e-folding decay length in radial direction (15-20 mm). However, the radial light shape could not be reproduced as perfectly as the toroidal and poloidal shape. With larger distance of the desorption positions from the LCFS, mainly the toroidal and poloidal size increase. Knowing the experimentally obtained light pattern at different distances of the sample to the plasma, a visibility factor  $V$  for invisible fractions of the LIDS light can be applied for cases, where the light is not fully measured. For most cases this correction could be omitted, when the light was centred in the TEXTOR port, since its full diameter (ca. 10 cm) was within the observation volume. However, for LIDS on samples that are more than 3 cm outside the LCFS, a stronger reduction of the emission signal has been observed that could not be explained fully by the visibility correction. The complete **conversion factor**  $C$  for the evaluation of the hydrogen atom amount from the photon amount consists of the three parts:  $C = Y S/X_B V$ . With  $V = 1$ , typically conversion factors of  $C_{EXP} = 28.6\text{-}31$  and  $C_{ERO} = 29\text{-}32$  are obtained.

The statistical **error** of LIDS has been determined with a series of 22 desorptions on a sample with homogeneous hydrogen concentration under two different plasma profiles, laser intensities and three distances from the plasma. The standard deviation was  $\pm 13\%$  showing the good reproducibility of LIDS. The systematic errors are higher, mainly due to the uncertainties in the transfer of the plasma parameters from the remote measurement position to the LIDS position. In the best setup used here, the total measurement uncertainty range of a single measurement is therefore estimated to  $-47\%$  to  $+43\%$  for ohmic and  $-52\%$  to  $+48\%$  for NBI heated plasmas due to stronger  $\text{H}_\alpha$  background fluctuations. Instead, for a series measurement a total systematic error range of  $-31\%$  to  $+23\%$  has to be used for this setup.

---

The **lower detection limit** is determined mainly by the  $H_{\alpha}$  background fluctuations. For ohmic phases of a TEXTOR discharges the detection limit corresponds to a surface concentration of  $8 \cdot 10^{20} \text{ H/m}^2$  ( $\cong 4.3 \cdot 10^{15}$  desorbed H atoms). For NBI heated plasmas the limit increases to  $5 \cdot 10^{21} \text{ H/m}^2$  ( $\cong 2.7 \cdot 10^{16}$  H atoms) due to stronger background fluctuations.

An **upper limit** is given by the onset of local cooling of the plasma by too many desorbed atoms, which are cold compared to the plasma. For TEXTOR-like plasmas the desorption flux should be therefore below  $3 \cdot 10^{20} \text{ H/s}$  as found by earlier gas-puffing experiments. For LID this corresponds to a release of ca.  $3 \cdot 10^{17}$  H atoms, corresponding to an areal hydrogen concentration of ca.  $6 \cdot 10^{22} \text{ H/m}^2$ . It was shown that the presence of plasma cooling during LIDS can be easily recognised by the strong shift of the  $H_{\alpha}$  intensity maximum towards the plasma centre. Solutions to prevent plasma cooling were proposed and partly demonstrated.

At the later stage of the work, a high-resolution spectrometer was used which could separate the spectral  $H_{\alpha}$  and  $D_{\alpha}$  lines of protium and deuterium. In the latest LIDS setup this detection was combined with a **coaxial laser injection and observation**, which complies in many aspects with the conditions in a fusion reactor like ITER by using curved metallic mirrors instead of lenses. It has the additional advantage to move the laser beam and the detection optics simultaneously, and thus assures that the LIDS light is always in the centre of the observation. The retention measured with this system was nearly in agreement with the observation perpendicular to the laser beam within a factor of less than 1.3. The latter observation needs a second access ports to the plasma in addition to the laser injection port, while the coaxial setup occupies only one port.

The agreement of the hydrogen retention measured by LIDS and LID-QMS was usually better than 10%. The comparison with NRA analyses are similarly good, if the deuterium retention is completely within the NRA detection depth (ca.  $3 \mu\text{m}$  from the surface) like in carbon and C layers. For D retention in the bulk of W, underestimation of retention by NRA occurs and increases with higher exposure temperature, which is attributed to deeper D diffusion. This inward diffusion can lead to incomplete desorption, if the laser spot is not heated up to the melting point or if the diffusion length is larger than the melting depth. Including Laser Induced Melting (LIM), the agreement of laser desorption and TDS has been found to be good. This is due to the fact that TDS desorbs the hydrogen completely despite the lower temperature of 1273 K due to the long heating duration ( $> 40 \text{ min}$ ), which increases the diffusion length by three orders of magnitude compared to LID laser pulses.

# A. Appendix: Tungsten Grade Details

- **Goodfellow W**

provider: Goodfellow GmbH

address: Kurstrasse 13, 61231 Bad Nauheim, Germany, [www.goodfellow.com](http://www.goodfellow.com)

purity: 99.95 wt% W

manufacturing: rolled (typically used in the present work: 2 mm thickness)

grain orientation: parallel to the surface

impurities:

typical analysis: (ppm) Ca <20, Cu <20, Fe 20, Mg <10, Mo 150, Ni <20, Pb <50, Si <50, Sn <30, Ti <20, C 30, H 6, N 10, O 30

- **Negele W**

provider: Negele Hartmetall-Technik GmbH

address: Löwenstr. 94, 70597 Stuttgart, Germany, [www.negele-hartmetall.de](http://www.negele-hartmetall.de)

purity: 99.95 wt% W

manufacturing: powder metallurgy, rolled W

- **Plansee UHP-W**

provider: Plansee

address: [www.plansee.com](http://www.plansee.com)

ultra high purity (UHP): 99.9999 wt% W

manufacturing: single forged

grain orientation: parallel to the surface

- **MG Sanders W**

provider: MG Sanders, MGS Precision

address: [www.mgsprecision.co.uk](http://www.mgsprecision.co.uk)

grain orientation: perpendicular to the surface



## B. Appendix: TMAP7 Input File Example

```

1 title input ;scenario: D profile until 10 μm depth with...
2 Sample Problem #2 - LID on Tungsten ;exponential decay length of 3 μm
3 end of title input
4 $
5 $
6 main input
7 dspcnme=d,end ;diffusing species is "d" (= D)
8 espcnme=d2,end ;external species outside the material is "d2" (= D2)
9 segnds=1000,end ;spatial discretisation: ca. 5 mm in 1000 nodes or "segments"
10 nbrencl=2,end ;number of enclosures
11 end of main input
12 $
13 $
14 enclosure input
15 start bdry,1,end
16 etemp=300.,end ;enclosure temperature = 300 K
17 esppres=d2,const,0.0,end ;enclosure species pressure  $p_{D_2} = 0$ 
18 $
19 start bdry,2,end
20 etemp=300.0,end ;enclosure temperature = 300 K
21 esppres=d2,const,0.0,end ;enclosure species pressure  $p_{D_2} = 0$ 
22 end of enclosure input
23 $
24 $
25 thermal input
26 start thermseg,end ;spatial resolution: 100 nm (in the first 50 μm), then...
27 delx=0.0,500*1e-7,498*1.e-5,0.0,end ;... 10 μm until the end at ca. 5 mm
28 tempd=1000*300.0,end ;initially, the temperature is set to 300 K everywhere
29 tcon,const,170.0,end ;heat conductivity  $K = 170 \text{ W/mK}$ 
30 rhocp,const,2.5e6,end ;W density times heat capacity  $\rho c = 2.5 \cdot 10^6 \text{ J/m}^3 \text{ K}$ 
31 hsrc,const,0.0,srcpf,1000*0.0,end ;no internal heat source in the bulk
32 htrbcl,sflux,tabl,1,end ;laser heat flux to the surface in table 1 (line 81-82)
33 htrbcr,adiab,end ;rear side of the W sample is thermally isolated
34 end of thermal input
35 $
36 $
37 diffusion input
38 start diffseg,end
39 nbrden=6.3e28,end ;number density of W atoms per m3 (= lattice density)
40 concd=d,0.0,7.18e26,6.94e26,6.71e26,6.49e26,6.28e26 ;D con-
41 6.08e26,5.88e26,5.68e26,5.50e26,5.32e26,5.14e26,4.97e26 ;centra-

```

## B. Appendix: TMAP7 Input File Example

```

42 4.81e26,4.65e26,4.50e26,4.35e26,4.21e26,4.07e26,3.94e26 ;tion
43 3.81e26,3.69e26,3.56e26,3.45e26,3.33e26,3.23e26,3.12e26 ;depth
44 3.02e26,2.92e26,2.82e26,2.73e26,2.64e26,2.55e26,2.47e26 ;profile
45 2.39e26,2.31e26,2.24e26,2.16e26,2.09e26,2.02e26,1.96e26
46 1.89e26,1.83e26,1.77e26,1.71e26,1.66e26,1.60e26,1.55e26
47 1.50e26,1.45e26,1.40e26,1.36e26,1.31e26,1.27e26,1.23e26
48 1.19e26,1.15e26,1.11e26,1.07e26,1.04e26,1.00e26,9.71e25
49 9.40e25,9.09e25,8.79e25,8.50e25,8.22e25,7.95e25,7.69e25
50 7.44e25,7.20e25,6.96e25,6.73e25,6.51e25,6.30e25,6.09e25
51 5.89e25,5.70e25,5.51e25,5.33e25,5.16e25,4.99e25,4.82e25
52 4.67e25,4.51e25,4.36e25,4.22e25,4.08e25,3.95e25,3.82e25
53 3.69e25,3.57e25,3.46e25,3.34e25,3.23e25,3.13e25,3.02e25
54 2.93e25,2.83e25,2.74e25,2.65e25,898*0.0,0.0, end
55 trapping=ttyp,1,tconc, const,0.01,tspc,d,alphr,equ,3 ;for trap type 1:
trap concentration is 1% of lattice density, release rate  $\alpha_r$  cf. equation 3 (line 73-74)
56   alpht,equ,4,ctrap,const,0.0, end ;trapping rate  $\alpha_t$  cf. equation 4 (1.75-76)
57   dcoef=d,equ,1, end ;D diffusion coefficient cf. equation 1 (line 69-70)
58   qstrdr=d,const,0.0, end
59   srcsd=d,const,0.0,srcpf,const,0.0, end
60   difbcl=ratedep,encl,1,spc,d ;recombination of D to D2 cf. equation 2...
61   exch,d2,ksubd,const,0.0,d,ksubr,equ,2, end ; (line 71-72)
62   difbcr=ratedep,encl,2,spc,d
63   exch,d2,ksubd,const,0.0,d,ksubr,equ,2, end
64   surfa=1.0, end
65 end of diffusion input
66 $
67 $
68 equation input
69 $ (1) Diffusion coefficient (m2/s) ;for D in W
70 y= 4.1e-7*exp(-0.39/8.625e-5/temp),end
71 $ (2) Recombination constant (m4/s) ;from D to D2 on the W surface
72 y= 3.2e-15*exp(-1.16/8.625e-5/temp),end
73 $ (3) alpha_r for trap1 ;release rate  $\alpha_r$  from trap 1
74 y= 1.0e13*exp(-1.45/8.625e-5/temp),end ;in Hz
75 $ (4) alpha_t for trap1 ;trapping rate  $\alpha_t$  for trap 1
76 y= 4.1e-7*exp(-0.39/8.625e-5/temp)/((3.0e-10)**2),end ;in Hz
77 end of equation input
78 $
79 $
80 table input
81 $ (1) heat flux (W/m2) ;absorbed laser intensity  $I(t)$ ...
82 0.0,5.0e8,0.003,5.0e8,0.0031,0.0,60.0,0.0, end ;from 0-3 ms: 500 MW/m2
83 $ (2) Implantation Flux (d/m2.s) ;unused for LID simulation....
84 0.0,1.0e16,5.0,1.e16,5.1,0.0,60.0,0.0, end ;used for code tests with PERI
85 end of table input
86 $
87 $
88 control input
89   time=0.0, end ;starting time  $t = 0$ 
90   timestep=1.0e-6, end ;initial time step  $\Delta t = 1 \mu\text{s}$ 

```

---

```
91 timend=1.0,end ;end of simulation at  $t = 1.0$  s
92 nprint=100,end ;100 calculation cycles are skipped between printing output
93 itermx=9000,end ;iteration maximum
94 delcmx=1.0e-7,end ;convergence limit  $\epsilon$ 
95 bump=1.e-2,end ;fractional change of Newton-Raphson convergence
96 bound=2.0,end ;limitation of Newton-Raphson step change
97 omega=1.3,end ;de- and acceleration of convergence in the diffusion calculation
98 end of control input
99 $
100 $
101 plot input ;control commands for the output file
102 nplot=10,end
103 plotseg=1,end
104 plotencl=1,2,end
105 dname=d,end
106 ename=d2,end
107 dplot=sconc,moblinv,sflux,trapinv,end
108 eplot=end
109 end of plot input
110 $
111 end of data
```

# List of Tables

2.1.	a) Beam convergence for coupling into fibre (geometrical optic approximation) and b) measured beam divergence for coupling out of the fibre for different focal lengths of the lens before the fibre; the corresponding numerical aperture and half-angle are given accordingly; * = values from [Irrek8, p.69]	35
2.2.	Optical distances for imaging the fibre end (object size $G = 400 \mu\text{m}$ ) with an achromatic lens of $f_{out} = 60 \text{ mm}$ to the image size $B$ on the target; $d$ : fibre-target distance for the heating laser (Nd:YAG) and the pilot laser (HeNe)	39
2.3.	Heat properties of tungsten and graphite at temperatures relevant for LID	54
2.4.	Maximum temperature for CFC (DMS 780): measured temperatures with statistical one-sigma deviation; analytic 1D calculation; numeric 3D calculation with temperature dependent, anisotropic heat parameters and heat radiation	58
2.5.	Maximum temperature on CFC (DMS780) with $3 \mu\text{m Mo}$ , $12 \mu\text{m W}$ and a thin a-C:H/D TEXTOR layer on top: measured temperatures with statistical one-sigma deviation; numeric 3D calculation (CFC+Mo+W) with temperature dependent, anisotropic heat parameters and heat radiation	62
4.1.	Desorption fraction after an LID pulse ( $500 \text{ MW/m}^2$ , 3 ms, 1800 K) for different trap types and different initial deuterium profiles; calculated by TMAP7	121
5.1.	Gas flow rates used for QMS calibration leaks in different flow regimes relative to helium; * = The same viscosity was used for $\text{CD}_4$ as for $\text{CH}_4$ since no literature value has been found and the viscosity of $\text{C}_2\text{H}_4$ and $\text{C}_2\text{H}_2$ are similar ( $10.4 \mu\text{Pa s}$ ).	131
5.2.	Masses included in the evaluation of LID-QMS spectra ( <b>in bold type</b> ) and their corresponding gas species, cracking origin and sources; $k_{QMS}$ : example values of calibration factors	133
5.3.	Error estimations for LID-QMS: determination of the average error of desorbed H (or D or $\text{CD}_4$ etc.) per unit area for a single measurement. Systematic errors are <u>underlined</u> . For the QMS it is added to its statistical error. The total errors for QMS and desorbed area are combined by Gaussian error propagation.	136
6.1.	Overview of exposure conditions and D retention results for the position of highest retention in each discussed example; the order is according to surface temperature; parts of the table are published in [Z13]	154
7.1.	Plasma profile parameters and light-to-particle conversion factor $C$ calculated by ERO simulations of the LIDS light and corresponding values from ADAS for $n_e$ , $T_e$ and $S/XB$ at light intensity maximum and in experiment; source at $r = 48.0 \text{ cm}$	183
7.2.	Error estimations for a single LIDS measurement; errors for NBI heated plasmas are marked in <b>red</b> ; systematic errors are <u>underlined</u>	207

# List of Figures

1.1. Tritium emission rates and amounts of natural and anthropogenic T sources on Earth [Sültenfuß98, p.1-7], [Milch2, p.31f], [Tanabe13] . . . . .	26
2.1. General optical setup of the LID experiments; detailed setups for LID-QMS in figure 5.1 on page 126 and for LIDS in figures 7.1, 7.2 on pages 161–162 .	32
2.2. Cross-section of the laser fibre optics (Ceramoptec® WF 400/440 T); white: inner fibre core ( $n_1$ , silica, $\varnothing 400 \mu\text{m}$ ); red: cladding ( $n_2$ , fluorine silica, $\varnothing 440 \mu\text{m}$ ); Only these 2 parts of the fibre are remaining for the coupling-in of the laser light. cyan: silicone buffer ( $\varnothing 530 \mu\text{m}$ ); green: Tefzel coating ( $\varnothing 850 \mu\text{m}$ ); fibre embedded in two-component glue (dark blue circle, with air enclosures) and steel cylinder ( $\varnothing 3 \text{ mm}$ ); $N_A = 0.22$ ; attenuation $< 1 \text{ dB/km}$ @ $1064 \text{ nm}$ . . . . .	33
2.3. Optimised spatial distribution (left) and temporal development (right) of the intensity of a 3 ms, $\varnothing 3 \text{ mm}$ Nd:YAG laser pulse after transmission through a 35 m long optical fibre of $400 \mu\text{m}$ core diameter, imaged by a lens onto a CCD camera chip; The spatial distribution is normalised to the average value of the plateau region. figure already published in [Z13] . . . . .	36
2.4. Dependence of normalised spatial laser profile on lens-fibre distance $l$ , CCD data (2D images) and smoothed 3D side views, $h = \overline{I_{peak}/I_{total}}$ , $T = E_{target}/E_{laser} = E_1/E_0$ , $f_{in} = 60 \text{ mm}$ achromatic lens optimised for HeNe+Nd:YAG with AR 0.5% . . . . .	37
2.5. Spatial laser profile optimisation, dependence on focal position at the fibre entrance, coupling lens with $f_{in} = 80 \text{ mm}$ ; legend: cf. figure 2.4 . . . . .	38
2.6. Spatial laser profile optimisation, dependence on focal length of the coupling lens $f_{in}$ , legend: cf. figure 2.4 . . . . .	39
2.7. Dependence of spatial laser profile on fibre-target distance $d$ ; achromatic lens $f_{in} = 30 \text{ mm}$ , $\varnothing 20 \text{ mm}$ ; colour scale like in previous figure; legend: cf. figure 2.4 . . . . .	40
2.8. a) Temporal laser pulse form at the laser and target (up-scaled) for energies of $E_0 = 7\text{-}40 \text{ J}$ . In the marked regions the standard deviation $\sigma$ of the fluctuations, the slopes (normalised to the laser power) and Fourier transformations (b) are calculated. . . . .	41
2.9. Reflectivity of materials used for LID; measured with a spectrophotometer; a) polished surfaces; b) rough surfaces with considerable fraction of diffuse reflectivity; different W grades have been measured . . . . .	43
2.10. Laser light absorption (at $\lambda_0 = 1064 \text{ nm}$ ) according to Lambert-Beer's law based on measurements of the complex refraction index by ellipsometry (for carbon layers) and interpolated data from [Palik98, vol.1, p.366], [Palik98, vol.2, p.458], [Lide94, p.12/137] for bulk C and W. . . . .	46
2.11. Temperature distribution at the end of the laser pulse; finite element calculation (ANSYS); one forth of an LID laser spot is simulated to reduce calculation time; 3 mm laser spot diameter; 3 ms heating time; $500 \text{ MW/m}^2$ absorbed laser intensity . . . . .	49

2.12. Heat properties of tungsten with data from NIST [Chase98], [Samsonov68] and Institute of Energy Research Jülich [Rödig3] (unlabeled data); lines are only guidelines . . . . .	50
2.13. Temporal development of the W surface temperature in the centre of the laser spot for 2 different laser pulses with the standard LID heat flux factor $27 \text{ MW} \sqrt{\text{s}}/\text{m}^2$	51
2.14. Spatial temperature profiles in depth (a) and radial direction (b) at the end of the same laser pulses as in figure 2.13; 3.0 mm laser diameter . . . . .	52
2.15. Temperature distribution in W after two different laser pulses; 3.0 mm laser beam diameter; left: $700 \text{ MW}/\text{m}^2$ for 1.5 ms; right: $500 \text{ MW}/\text{m}^2$ for 3 ms . . . . .	52
2.16. Temporal development of isotherms on the W surface for two different laser pulses; left: $700 \text{ MW}/\text{m}^2$ for 1.5 ms; right: $500 \text{ MW}/\text{m}^2$ for 3 ms . . . . .	53
2.17. Temporal development of isotherms on W in depth for two different laser pulses; left: $700 \text{ MW}/\text{m}^2$ for 1.5 ms; right: $500 \text{ MW}/\text{m}^2$ for 3 ms . . . . .	54
2.18. Surface temperature and derivative during laser melting of pure tungsten with melting pulse ( $1.5 \text{ GW}/\text{m}^2$ absorbed intensity, 3 ms): rapid solidification processes appear due to the high cooling rate and temperature gradients . . . . .	55
2.19. Heat properties of the two-directional Dunlop DMS780 ("JET CFC"); lines are only guidelines; label "low" marks the direction of low heat conductivity; "high" marks the other two directions . . . . .	56
2.20. Laser heating of a two-directional CFC (Dunlop DMS780) with $2.5 \mu\text{m}$ Mo interlayer and $12.5 \mu\text{m}$ W layer; perpendicular CFC fibre orientation; $500 \text{ MW}/\text{m}^2$ absorbed intensity; 3 ms; circular $\varnothing 3 \text{ mm}$ laser spot; numeric simulation with ANSYS . . . . .	57
2.21. Heat curvature effect: surface temperature evolution for CFC (DMS 780) in perpendicular (a) and parallel (b) fibre orientation; both covered with a thin a-C:H/D layer from TEXTOR; measured with a point pyrometer . . . . .	59
2.22. Heat offset effect: surface temperature evolution for a) CFC (DMS 780) in parallel fibre orientation $3 \mu\text{m}$ Mo, $12 \mu\text{m}$ W and a $280 \text{ nm}$ a-C:H/D layer; b) pure W with $40 \text{ nm}$ a-C:H/D layer; both measured with a point pyrometer . . . . .	61
2.23. Laser power scan on parallel CFC (DMS 780) with $3 \mu\text{m}$ Mo, $12 \mu\text{m}$ W and a thin a-C:H/D TEXTOR layer on top. The data show a power dependent temperature offset in the early phase of the heat pulse. . . . .	62
2.24. Measured thermal diffusivity of graphite with a thick a-C:H/D layer (TEXTOR ALT-II N° 2/19) and a reference sample without layer; deduced heat conductivities and used heat capacity; lines are only guidelines . . . . .	63
2.25. Surface temperature evolution on a C/W/H/D mixed layer grown in TEXTOR on unpolished graphite; measured with a point pyrometer . . . . .	65
3.1. Bulk W with a-C:H/D layer grown in TEXTOR (1 <sup>st</sup> exposure) and analyzed with LIDS ( $\blacktriangle$ , $\blacklozenge$ in 2 <sup>nd</sup> exposure by heating to ca. 2600 K), LID-QMS ( $\blacksquare$ , $\bullet$ ) at different temperatures between 570 and 2700 K), single-point NRA ( $\text{\textcircled{a}}$ - $\text{\textcircled{c}}$ ) and NRA inside and outside the laser spot ( $\square$ 1-5); NRA data and photography already published in [Rubel12] in simplified form; graph: laser spot size vs. HFF . . . . .	69
3.2. a) LID on $2.5 \mu\text{m}$ a-C:H layer (Balinit <sup>®</sup> 3a) with different laser pulse settings; b) laser desorbed area vs. heat flux factor on this and an identical sample . . . . .	74
3.3. LIDS spots on ALT-II tile N° 6/19 and their size vs. HFF; The laser pulse parameters are shown in figure 3.4. . . . .	75

3.4. Laser heating of a thick a-C:H/D layer from TEXTOR on graphite (ALT-II tile N° 6/19); 7° laser incidence; 1.5 ms nominal pulse duration, actual pulse duration and heat flux factor are given below the images; photography; all images adjusted to the same scale . . . . .	76
3.5. LID-QMS spots on 2.5 μm a-C:H layer (Balinit® 2a, 3a) show spot size growth, colour change, blistering, evaporation and cracking (red arrows); one laser pulse; pulse duration, absorbed laser intensity, HFF, calculated and measured maximal temperature are given; tilted photography; all in identical horizontal scale . . . . .	80
3.6. LID spots on 2.5 μm a-C:H layer (Balinit® 3a) showing increasing layer removal from a) to d); each laser pulse with 3 ms pulse duration; the amount of laser pulses, absorbed laser intensity and calculated maximal surface temperature are given; optical bright field microscopy; all images in identical scale . . . . .	81
3.7. right: Balinit® layer scheme; left: surface after 4 laser pulses of 850 MW/m <sup>2</sup> absorbed power for 3 ms each; top: optical microscopy, zoom of green frame in figure 3.6d; bottom: confocal profilometry of the same position . . . . .	81
3.8. Blister cap removal on 2.5 μm a-C:H layer (Balinit® 3a) after 4 laser pulses of 850 MW/m <sup>2</sup> absorbed power for 3 ms each; zoom of red frame in figure 3.6d; confocal profilometry: a,b) stereoscopic* 3D view, c) top view with contour lines every 0.5 μm in altitude, d) profile along the white line marked in c) . . . . .	83
3.9. LID spots on ALT-II tile (N° 2/19) show sharp laser spot edges that clearly define the desorbed area (grey) in contrast to the ca. 15 μm thick a-C:H/D layer (multicoloured); left: edge of one laser spot; right: undesorbed area between two LID spots; optical bright field microscopy . . . . .	84
3.10. Laser heating of a 200 nm mixed C/W/H/D layer from TEXTOR on polished graphite (except a: unpolished graphite); left column: laser spot diameter in mm; right value: absorbed laser intensity in MW/m <sup>2</sup> ; 23° incidence; photography . . . . .	86
3.11. Laser spot edge on a 200 nm C/W/H/D layer from TEXTOR; ∅3.0 mm, 1.5 ms, 700 MW/m <sup>2</sup> absorbed laser intensity, 2600 K; optical bright field microscopy . . . . .	86
3.12. Mixed C/W/H/D layer (10 at% W) on polished graphite; LID pulses: 1.5 ms with 700 MW/m <sup>2</sup> on ∅3.0 mm and 3 ms with 2 GW/m <sup>2</sup> on ∅2.0 mm; optical microscopy . . . . .	88
3.13. Magnification of laser spot border of figure 3.12a (optical bright field microscopy). The letters indicate the same regions as in figure 3.12f. . . . .	89
3.14. Surface roughness increase of tungsten due to laser heating a) surface profile across a laser spot (100 pulses of 1 ms, 470 MW/m <sup>2</sup> ) b) roughness increase with laser intensity (each point: 100 pulses, 1 ms) . . . . .	91
3.15. Growth of deuterium blisters due to laser heating: a) the blisters inside the laser spot (circle) appear darker after a single 3 ms LID pulse of 555 MW/m <sup>2</sup> (optical microscopy, bright field); b) unheated blisters outside laser spot; c) blisters inside laser spot heated with 2×522 MW/m <sup>2</sup> (b and c: optical microscopy, DIC) . . . . .	93
3.16. Laser induced melting on W with 1.3 GW/m <sup>2</sup> , 3 ms, laser ∅2 mm; 1 laser pulse; a) 1D profiles on polished W (optical confocal profilometry); b) LIM with 5° incidence on rough W (optical microscopy) . . . . .	94
3.17. Polished tungsten surface after laser induced melting with 1.7 GW/m <sup>2</sup> , 1 ms pulses; optical confocal profilometry: a) 1D profiles; c) 3D view after 1 laser pulse; optical confocal profilometry . . . . .	94

3.18. Cross-section of a molten laser spot, $1.3 \text{ GW/m}^2$ absorbed laser intensity, 3 ms pulse duration, 1 laser shot, optical microscopy a) polished tungsten 99.95 wt% pure W (from MG Sanders), $6^\circ$ laser incidence b) rough tungsten 99.9999 wt% UHP W (from Plansee), $23^\circ$ incidence . . . . .	96
3.19. Edge of a laser melting spot of $\varnothing 2 \text{ mm}$ , $1.5 \text{ GW/m}^2$ absorbed intensity for 3 ms after one laser pulse on polished Goodfellow W; optical microscopy with DIC contrast . . . . .	98
3.20. a) RSP microstructure in molten tungsten (optical microscopy with DIC filter); b) 3D surface profile of area around a large hill; c) line profiles of RSP microstructure; d) line profile across large hill in b); (b-d: optical confocal profilometry) . . . . .	99
3.21. a) Different RSP microstructures can form depending on: $G_L$ = temperature gradient at solidification front, $R$ = velocity of solidification front; combined information from [Clark88, p.15] and [Giamei85, p.205]; b-d) examples of these structures from the present work . . . . .	100
3.22. FIB cross-section of a surface hill with crater after laser melting of W with $1.3 \text{ GW/m}^2$ , 3 ms, $6^\circ$ incidence; a) large bubble in $13 \mu\text{m}$ depth below the surface hill; b) magnification of the bubble shell of the image a) . . . . .	101
3.23. a) SEM image of a surface crack, 100 heating pulses, $760 \text{ MW/m}^2$ , 1 ms per pulse; ultra high purity W from Plansee, unannealed b) surface crack after one melting pulse (optical microscopy), $1.3 \text{ GW/m}^2$ , 3 ms, W from MG Sanders with elongated grains perpendicular to the surface, annealed, exposed to D plasma in PSI-2 (cf. chapter 6.2) . . . . .	102
3.24. SEM images of W fuzz after TEXTOR exposure (left) and after one standard LID heating pulse (right); a, b) top view, a) and b) are in the same scale; c, d) FIB cross-section, c) and d) are in the same scale but different to a) and b) . .	103
3.25. LID on CFC (DMS780) after exposure in TEXTOR under erosion dominated conditions (a-f) and with 100-250 nm a-C:H/D layer (g-r); left value: absorbed laser intensity in $\text{MW/m}^2$ ; right value: measured maximal temperature in K; the W layer is applied on a $2.5 \mu\text{m}$ Mo interlayer; all images in identical scale . .	105
3.26. Laser heating of a $25 \mu\text{m}$ thick W-Mo-W-Mo double layer on CFC (DMS780) with 100 pulses of $610 \text{ MW/m}^2$ , 1 ms, 0.5 Hz, $16 \text{ mm}^2$ laser irradiated area (red circle); $2^\circ$ incidence; perpendicular fibre orientation $K_{low} \uparrow$ ; optical bright field microscopy of the surface . . . . .	108
3.27. CFC (DMS780) with $25 \mu\text{m}$ W-Mo-W-Mo double layer after deuterium plasma exposure in Pilot-PSI and LID-QMS, 3 ms laser pulse duration, $22^\circ$ incidence; a) $500 \text{ MW/m}^2$ on $\varnothing 2 \text{ mm}$ ; b) $500 \text{ MW/m}^2$ on $\varnothing 3 \text{ mm}$ and $2.2 \text{ GW/m}^2$ on $\varnothing 2 \text{ mm}$ . . . . .	109
4.1. Tetrahedral and octahedral interstitial sites for hydrogen in a bcc crystal like tungsten; adapted from [Heitjans5, p.23,116] . . . . .	111
4.2. Sketch of energetic potential for hydrogen in the lattice of tungsten in the presence of deeper traps with two different binding energies . . . . .	112
4.3. Diffusion coefficient of hydrogen in tungsten according to [Frauenfelder69] .	113
4.4. Trapped and mobile deuterium inventory in tungsten and desorption flux during a standard LID pulse of $500 \text{ MW/m}^2$ absorbed power for 3 ms; numerical simulation with TMAP7; a) traps of 0.85 eV; b) traps of 1.45 eV binding energy . . . . .	117
4.5. Deuterium depth profiles from [Alimov8] measured by NRA in W exposed to a "clean" D plasma (a) and a D plasma with added C impurity (b) at different sample exposure temperatures; planar DC magnetron plasma; $200 \text{ eV/D}$ . . . .	118



4.6.	Deuterium depth profiles in W before and after one 3 ms LID pulse to 1800 K with exponential (a) and constant (b) initial D profile; calculation by TMAP7; a) similarly published in [Z13] . . . . .	119
4.7.	Deuterium depth profiles in W before and after one 3 ms LID pulse to 1800 K; effect of different initial D depths and trap binding energies; calculation by TMAP7 . . . . .	120
4.8.	left: Scheme of hydrogen desorption from amorphous hydrocarbon layers and hydrogen-implanted graphite (a-C:H network adapted from [Küppers95, p.290]) right: local release of molecules and radicals (adapted from [Philipps87])	122
4.9.	Retention in ALT-II (N° 2/19) graphite limiter of TEXTOR a) TDS delta-spectrum in the deposition dominated area; heating rate: 0.136 K/s b) spatially resolved H and D retention measured with 3 methods (positions in d) c) molecular origin of desorbed D atoms during TDS of position a) Figure b) and d) are similarly published in [Z11]. . . . .	123
5.1.	Setup of the Laser Induced Desorption with Quadrupole Mass Spectrometry detection (LID-QMS) for hydrogen retention analysis . . . . .	126
5.2.	Illustration of evaluation procedure for one LID-QMS measurement spot on a deuterium loaded tungsten sample: a) all QMS spectra in two alternating amplification ranges (highest sensitivity and factor 100 lower); time direction: black before red spectra; blue: peak search area b) and c): time evolution of mass peak maxima for mass HD and D <sub>2</sub> (crosses); line: two automatically fitted exponential functions per mass are extrapolated to the time of the laser pulse (vertical line) . . . . .	128
5.3.	LID-QMS spectrum of a typical 15 μm ALT-II layer after subtraction of chamber rest gas background; unambiguously identified masses are marked in red (D containing: 3, 4, 19, 20) and black (H containing: 2, 3, 16, 19); already published in [Z11] . . . . .	130
5.4.	Example spectrum of an annealed 99.95 wt% W loaded with D in an erosion dominated area of TEXTOR; desorption with 500 MW/m <sup>2</sup> in 3 ms; top: weak amplification only necessary for evaluation of masses 2 and 28; bottom: the same desorption with 10× higher QMS-electronics amplification for better accuracy in the low partial pressures . . . . .	134
6.1.	Limiter designed for growth of mixed material layers in TEXTOR . . . . .	138
6.2.	"Mixed material limiter" or "big-gap limiter" after 3 min exposure to TEXTOR plasma, a 200 nm fuel enriched C/W layer has grown . . . . .	139
6.3.	Allocation of different diagnostic applications on a mixed C/W/H/D layer grown in TEXTOR: LID for surface H and D contents; TDS for total H and D contents; NRA for surface D and W; EPMA for surface B, C, O and W; SIMS for depth profiles of all mentioned elements . . . . .	139
6.4.	Deuterium and tungsten concentrations in a C/W/H/D mixed material layer grown in TEXTOR; result comparison of LID, NRA, TDS and EPMA; a) deposition on rough graphite; b) simultaneous deposition on polished graphite	140
6.5.	Fraction of deuterium retained in different desorbing molecules during desorption of a mixed C/W/H/D layer grown in TEXTOR; left: TDS; right: LID-QMS . . . . .	141
6.6.	SIMS depth profile of the mixed material layer in its thickest part (cf. marking "SIMS" in figure 6.3); some signals are scaled to fit the range (see legend) . .	141
6.7.	Composition of a mixed material layer grown in TEXTOR on a dedicated limiter . . . . .	142

6.8.	Optimisation of laser pulse duration on homogeneously D loaded bulk tungsten; LID-QMS with constant heat flux factor; The bars show the minimal and maximal values of a series of 4-8 desorbed positions. The values show their average. . . . .	144
6.9.	Left axis: Laser Induced Desorption (LID) and Melting (LIM) on bulk W after deuterium plasma exposure in TEXTOR; Nuclear Reaction Analysis (NRA) data of retained D for comparison; right axis: plasma flux during exposure; figure similarly published in [Z13] . . . . .	146
6.10.	Radial profile of exposure conditions and LID-QMS results on a tungsten sample exposed to deuterium plasma in Pilot-PSI; data partly published in [Z13] . . . . .	149
6.11.	Repetitive LID pulses for 3 ms each on a W sample exposed to an ECR D plasma illustrate D diffusion into the laser heated volume; the values are absorbed laser intensities; figure similarly published in [Z13] . . . . .	151
6.12.	NRA profiles of D concentration in a W sample exposed in an ECR discharge; a) qualitative D depletion after LID; b) (already published in [Z13]): quantitative depth profiles inside and outside the LID spot as marked in figure a) . . . . .	151
6.13.	Laser Induced Desorption (LID) and Melting (LIM) on a bulk W sample exposed to deuterium plasma in PSI-2 . . . . .	152
6.14.	a) D retention overview after [Lipschultz10] with added results from this chapter ( $\oplus$ ); b) desorbed D fraction of discussed samples by LID at 1800-2000 K depending on the sample surface temperature during plasma exposure . . . . .	153
6.15.	Deuterium desorbed by LID-QMS on a simultaneously exposed W fuzz (left) and a polished W reference sample (right) in the erosion dominated area of the TEXTOR SOL plasma; D content detected by NRA is shown for comparison . . . . .	155
7.1.	Poloidal cross-section of TEXTOR with the LIDS setup in the coaxial version; for a 3D view of this position with an earlier laser setup cf. [Brezinsek5, Fig. 16] . . . . .	161
7.2.	Scheme of the coaxial laser injection and observation system CLIO . . . . .	162
7.3.	Temporal evolution of the LIDS signal at horizontal observation; recorded by a fast diode equipped with an $H_\alpha$ filter, that integrates the LIDS signal in space . . . . .	165
7.4.	Reactions of the hydrogen molecule by electron impact; reaction coefficients for proton impact are at least one order of magnitude lower; marked area shows the $T_e$ range for the desorption spectroscopy in the edge plasma of TEXTOR (data source: [AMJuel12]) . . . . .	172
7.5.	$H_2$ break-up reactions due to ionisation and dissociation processes by electron impact in a plasma of $k_B T_e = 25-120$ eV. Arrow thickness indicates cross-section rate: the two-step ionisation/dissociation into $H^+$ and H is the dominant reaction channel. . . . .	173
7.6.	$S_{XB}$ value dependence on electron temperature and density in the plasma for conditions of the edge plasma, theoretical calculations from [ADAS] . . . . .	177
7.7.	LIDS on 2.5 $\mu\text{m}$ thick a-C:H layers (Balinit <sup>®</sup> B3a); background-free $H_\alpha$ images, all in the same colour scale; effect of laser power, wall-to-plasma distance and plasma heating effect; already published in [Z11b] . . . . .	179
7.8.	LIDS on 2.5 $\mu\text{m}$ thick a-C:H layers (Balinit <sup>®</sup> B3a), profile through light maximum of background free $H_\alpha$ camera images, desorption at 48 cm minor radius . . . . .	180
7.9.	Comparison of (a) measured LIDS $H_\alpha$ light distribution from a 3 $\mu\text{m}$ a-C:H layer and (b) numerical simulation of a comparable hydrogen gas puff with adapted NBI heated plasma conditions (plasma profile for "best fit") . . . . .	181

7.10. Plasma profiles used in the ERO simulations; LCFS at $r = 46$ cm . . . . .	182
7.11. Strong variation of $H_\alpha$ light pattern for the identical $D_2$ gas release under modest variations of plasma temperature, density and their decay lengths, while the total amount of $H_\alpha$ photons is nearly constant (numerical simulations with ERO); a): plasma parameters as measured for figure 7.9a, 7.7a and 7.7b b), c), d): plasma parameters as shown in figure 7.10 for profile b, c and d . . . . .	183
7.12. Comparison of measured LIDS profiles with numerical calculations for the images in figure 7.9 on page 181 . . . . .	184
7.13. Numerical ERO simulation of $H_\alpha$ light from (a) pure $CD_4$ injection and (b) pure atomic deuterium injection under the same plasma conditions as in figure 7.9b . . . . .	185
7.14. LIDS on a sample with homogeneous hydrogen content (Balinit <sup>®</sup> B3a) with variation of plasma properties, laser energy and desorption position shows small standard deviations: $\pm 13\%$ (for all data), $\pm 9\%$ (only NBI heated plasmas) and $\pm 7.2\%$ (for NBI except low laser energy); black/red error bars = errors of a single LIDS measurement; green error bars = error of the measurement series; similarly published in [Z11b] . . . . .	186
7.15. Typical $H_\alpha$ light trace of the LIDS diagnostic recorded by the 14-bit digital AVT camera and integrated on the whole image; desorption of a $2.5 \mu\text{m}$ thick a-C:H layer (Balinit <sup>®</sup> B3a); laser pulses at 2.5, 3.5, 4.5 s; TEXTOR discharge #112139; for zoom cf. figure 7.19 on page 191; similarly published in [Z11b] . . . . .	187
7.16. 2 mm thick W with a $2.5 \mu\text{m}$ a-C:H layer on a Cr interlayer (Balinit <sup>®</sup> B3a) after TDS with two possible choices for the attached layer area (red or green area); optical bright field microscopy (mosaic mode) . . . . .	188
7.17. Plasma parameters during LIDS as measured by the supersonic helium beam diagnostic; #112136 at 2.38 s; $I_p = 350$ kA, $n_{e,la} = 2.5 \cdot 10^{19}/\text{m}^3$ , $B_t = 2.25$ T and #112142 at 2.78 s additionally with NBI( $H_2$ ) at 50 kV and 150 mm V-target The marked regions are the positions of the LIDS light intensity maxima of the measurements in figure 7.14 which are also shown in figure 7.22 on page 202. The error bands of the SHE diagnostic show only its statistical errors; cf. chapter 7.10 for further details on these errors. . . . .	189
7.18. Two TEXTOR limiters with the identical toroidal cross-section (bottom) but with a factor of 3 difference in poloidal cross-section for reduction of hydrogen recycling fluxes in the SOL . . . . .	191
7.19. Zoom of figure 7.15 on page 187: The detection limit of LIDS is determined by the $H_\alpha$ background fluctuation amplitude (blue lines). grey: $H_\alpha$ signals converted to the equivalent hydrogen inventory which would yield this signal; <b>black</b> : definition of smallest detectable signal (fictitious data point); laser pulses at 2.5, 3.5, 4.5 s; a) NBI phase; b) ohmic phase . . . . .	191
7.20. LIDS causes plasma cooling by fuel and impurity injection only for high desorption fluxes. Thick a-C:H layer on ALT-II (N <sup>o</sup> 6/19) tile desorbed with 1.2-1.4 ms pulses, observed with an $H_\alpha$ filter. Energy and intensity are absorbed values. Plasma heating by NBI reduces the cooling and the associated inward movement of the light. The numbers in boxes are the image integrals. . . . .	193
7.21. Three different spectral filter transmissions: Accurate tailoring of narrow-band interference filters adapted for exact selection of hydrogen spectroscopic lines, while excluding undesired line radiation, is essential for LIDS measurement when using a camera or diode. . . . .	197

7.22.	Radial position of $H_{\alpha}$ intensity maximum in the background subtracted LIDS images during desorption of a 2.5 $\mu\text{m}$ a-C:H layer; the 1-day error only includes uncertainties in the maximum search algorithm; for a comparison of different shot days a higher uncertainty is valid due to limiter and camera removal; These radial positions are used in figure 7.17 on page 189. . . . .	202
8.1.	LIDS of a ca. 2 $\mu\text{m}$ thick a-C:H layer on W (Balinit <sup>®</sup> B6n); 810 $\text{MW}/\text{m}^2$ absorbed laser intensity for 1.5 ms; background subtracted images; TEXTOR discharge #116620 with $I_p = 350$ kA, $B_t = 2.25$ T, $n_{e,la} = 2.5 \cdot 10^{19}/\text{m}^3$ a) horizontal observation; 5 ms image intensifier gate; $H_{\alpha}$ filter with 3 nm FWHM b) vertical observation; 20 ms integration time; $H_{\alpha}$ filter with 1.5 nm FWHM . . .	214
8.2.	LIDS of a ca. 2 $\mu\text{m}$ thick a-C:H layer on W observed through CLIO; 10 ms integration time; 820 $\text{MW}/\text{m}^2$ absorbed laser intensity for 1.5 ms a) during ohmic plasma heating (TEXTOR #116020, sample: Balinit <sup>®</sup> B6n) b) during an NBI heated plasma (TEXTOR #116816, sample: Balinit <sup>®</sup> B5n) with a factor of 2 more transparent neutral density filter than a) . . . . .	218
8.3.	a) LID-QMS on 2 $\mu\text{m}$ a-C:H layer (Balinit <sup>®</sup> B1n, B2n, B5n and B6n) b) LIDS on 2 $\mu\text{m}$ a-C:H layer (Balinit <sup>®</sup> B6n in one ohmic discharge and B5n in 9 NBI2-heated discharges) viewed from the Horizontal Observation (HO) and from top via the Coaxial Laser Injection and Observation (CLIO) . . . . .	220
8.4.	LIDS of a 550 nm thick a-C:D layer on graphite (sample PADOS GIV) a) $H_{\alpha}$ light intensity; background subtracted image at the horizontal observation b) image a) mirrored horizontally at light intensity maximum (indicated by "+")	222
8.5.	LIDS of a ca. 550 nm thick a-C:D layer on graphite observed through CLIO; 10 ms integration time; 880 $\text{MW}/\text{m}^2$ absorbed laser intensity for 1.5 ms; ohmic plasma heating; a) TEXTOR #116625, sample: PADOS GIV b) LIDS with low $\text{C}^+$ contribution (TEXTOR #116617, sample: PADOS GII) . . . . .	223
8.6.	LIDS of a 550 nm a-C:D layer on graphite (PADOS GII and GIV after #116622) viewed from the Horizontal Observation (HO) and from top via the Coaxial Laser Injection and Observation (CLIO); TDS results of sample GIV are added . . . . .	225

# Bibliography

## [@] **Link abbreviations in the bibliography:**

arXiv: = <http://arxiv.org/abs/> (online archive "arXive" of the Cornell University Library)

doi: = <http://dx.doi.org/> (digital object identifier = doi®)

handle: = <http://hdl.handle.net/> (Handle System®)

- [ADAS] *Atomic Data and Analysis Structure*, [www.adas.ac.uk](http://www.adas.ac.uk),  
H.P. Summers, *Atomic Data and Analysis Structure - User manual*, 2<sup>nd</sup> edition - version  
2.7 (2004), University of Strathclyde, [www.adas.ac.uk/manual.php](http://www.adas.ac.uk/manual.php)  
Description of ADAS available in: R.E.H. Clark, D.H. Reiter (editors), *Nuclear Fusion  
Research - Understanding Plasma-Surface Interactions*, Springer Series in Chemical  
Physics, Volume 78 (2005) p.399-413, ISBN: 978-3-540-23038-0 (print), 978-3-540-  
27362-2 (online) ..... 176, 177, 180, 242
- [Alimov8] V.Kh. Alimov, J. Roth, R.A. Causey, D.A. Komarov, Ch. Linsmeier, A. Wiltner,  
F. Kost, S. Lindig, *Deuterium retention in tungsten exposed to low-energy, high-flux,  
clean and carbon-seeded deuterium plasmas*, *Journal of Nuclear Materials* 375 (2008)  
192-201, doi: 10.1016/j.jnucmat.2008.01.008 ..... 118, 240
- [Ambrosek8] J. Ambrosek, G.R. Longhurst, *Verification and Validation of TMAP7*, Rev. 2,  
Idaho National Engineering and Environmental Laboratory (2008) INEEL/EXT-04-  
01657, [www.inl.gov/technicalpublications/Documents/4215153.pdf](http://www.inl.gov/technicalpublications/Documents/4215153.pdf) ..... 115
- [AMJuel12] Atomic and Molecular Database for EIRENE (29.8.2012),  
[www.eirene.de/html/amjuel.html](http://www.eirene.de/html/amjuel.html) ..... 172, 242
- [Anderl92] R.A. Anderl, D.F. Holland, G.R. Longhurst, R.J. Pawelko, C.L. Trybus,  
C.H. Sellers, *Deuterium transport and trapping in polycrystalline tungsten*, *Fusion  
Technology* 21 (1992) 745-752, ISSN: 0748-1896 ..... 114
- [Angerer9] G. Angerer, F. Marscheider-Weidemann, M. Wendl, M. Wietschel, *Lithium für  
Zukunftstechnologien - Nachfrage und Angebot unter besonderer Berücksichtigung  
der Elektromobilität*, Fraunhofer-Institut für System- und Innovationsforschung ISI  
Karlsruhe (2009), [www.isi.fraunhofer.de/isi-wAssets/docs/n/de/publikationen/Lithium  
\\_fuer\\_Zukunftstechnologien.pdf](http://www.isi.fraunhofer.de/isi-wAssets/docs/n/de/publikationen/Lithium_fuer_Zukunftstechnologien.pdf),  
english presentation: [www.isi.fraunhofer.de/isi-wAssets/docs/n/de/publikationen/pre-  
sentation\\_lithium\\_angerer.pdf](http://www.isi.fraunhofer.de/isi-wAssets/docs/n/de/publikationen/presentation_lithium_angerer.pdf) ..... 15
- [Ansys12] ANSYS Academic Research - Mechanical, ANSYS Workbench Version 12 and  
13, [www.ansys.com](http://www.ansys.com) ..... 48
- [Baeslack86] W.A. Baeslack III, S. Krishnamurthy, F.H. Froes, *Solidification Characterist-  
ics of Laser Surface Melts in Advanced Titanium Alloys* in F.H. Froes, D. Eylon (edi-  
tors), *Titanium - Rapid Solidification Technology*, Proceedings for the four session sym-  
posium, New Orleans, Metallurgical Society (1986) 97-110, ISBN-10: 0873390504,  
ISBN-13: 9780873390507 ..... 101
- [Baldwin8] M.J. Baldwin, R.P. Doerner, *Helium induced nanoscopic morphology on tung-  
sten under fusion relevant plasma conditions*, *Nuclear Fusion* 48 (2008) 035001,  
doi: 10.1088/0029-5515/48/3/035001 ..... 103

- [Balzers12] OC Oerlikon Balzers AG, Iramali 18, P.O. Box 1000, 9496 Balzers, Liechtenstein  
[www.oerlikon.com/balzers/en/products-services/balinit-coatings/](http://www.oerlikon.com/balzers/en/products-services/balinit-coatings/) . . . . . 45
- [BMW14] Bundesministerium für Wirtschaft und Energie (BMWi), Projektträger Jülich (PtJ), <http://kraftwerkforschung.info/quickinfo/energieversorgung/solange-reichen-die-nicht-erneuerbaren-energieeraeger-angabe-in-jahren/> (22.10.2014) . . . . . 15, 16
- [BP14] British Petroleum (BP),  
<http://mazamascience.com/OilExport/data.html> (24.10.2014) . . . . . 15, 17
- [Brezinsek2] S. Brezinsek, *Untersuchung von atomarem und molekularem Wasserstoff vor einer Graphitoberfläche in einem Hochtemperatur-Randschichtplasma*, Dissertation, Universität Düsseldorf, Forschungszentrum Jülich GmbH · Zentralbibliothek, Jül-3962 (2002), ISSN: 0944-2952, handle: 2128/244 . . . . . 175
- [Brezinsek5] S. Brezinsek, A. Huber, S. Jachmich, A. Pospieszczyk, B. Schweer, G. Sergienko, *Plasma Edge Diagnostics for TEXTOR*, Fusion Science and Technology 47 (2005) 209-219, handle: 2128/2732 . . . . . 161, 242
- [Brezinsek7] S. Brezinsek, A. Pospieszczyk, D. Borodin, M.F. Stamp, R. Pugno, A.G. McLean, U. Fantz, A. Manhard, A. Kallenbach, N.H. Brooks, M. Groth, Ph. Mertens, V. Philipps, U. Samm, TEXTOR, ASDEX Upgrade, DIII-D Teams and JET-EFDA Contributors, *Hydrocarbon injection for quantification of chemical erosion yields in tokamaks*, Journal of Nuclear Materials 363-365 (2007) 1119-1128, doi: 10.1016/j.jnucmat.2007.01.190 . . . . . 173
- [Brezinsek13] S. Brezinsek, T. Loarer, V. Philipps, H.G. Esser, S. Grünhagen, R. Smith, R. Felton, J. Banks, P. Belo, A. Boboc, J. Bucalossi, M. Clever, J.W. Coenen, I. Coffey, S. Devaux, D. Douai, M. Freisinger, D. Frigione, M. Groth, A. Huber, J. Hobirk, S. Jachmich, S. Knipe, K. Krieger, U. Kruezi, S. Marsen, G.F. Matthews, A.G. Meigs, F. Nave, I. Nunes, R. Neu, J. Roth, M.F. Stamp, S. Vartanian, U. Samm and JET EFDA contributors, *Fuel Retention Studies with the ITER-like Wall in JET*, Nuclear Fusion 53(8) 083023 (2013), doi: 10.1088/0029-5515/53/8/083023, handle: 2128/7814 . . 209
- [Bridges7] B.A. Bridges, A.T. Elliott, M.A. Hill, B.E. Lambert, M.P. Little, R. Waters, *Review of Risks from Tritium - Report of the independent Advisory Group on Ionising Radiation*, Health Protection Agency, RCE-4 (2007), Chilton, Didcot (UK), ISBN 978-0-85951-610-5, [www.researchgate.net/profile/Mark\\_Little/publication/254258196\\_Review\\_of\\_risks\\_from\\_tritium\\_Subgroup\\_on\\_Tritium\\_internal\\_dosimetry\\_of\\_the\\_Advisory\\_Group\\_on\\_Ionising\\_Radiation/links/0c96051fc3e4716c6f000000](http://www.researchgate.net/profile/Mark_Little/publication/254258196_Review_of_risks_from_tritium_Subgroup_on_Tritium_internal_dosimetry_of_the_Advisory_Group_on_Ionising_Radiation/links/0c96051fc3e4716c6f000000) . . . . . 24, 25
- [Carslaw59] H.S. Carslaw, J.C. Jaeger, *Conduction of Heat in Solids* (second edition), Oxford University Press, Clarendon Press (1959), ISBN: 0198533683 . . . . . 47, 48
- [Causey2] R.A. Causey, *Hydrogen isotope retention and recycling in fusion reactor plasma-facing components* (Review), Journal of Nuclear Materials 300 (2002) 91-117, doi: 10.1016/S0022-3115(01)00732-2 . . . . . 110
- [Chase98] M.W. Chase, *NIST-JANAF Thermochemical Tables* (Fourth Edition), Journal of Physical and Chemical Reference Data 9, American Chemical Society and the American Institute of Physics for the National Institute of Standards and Technology (1998), <http://kinetics.nist.gov/janaf/janaf4pdf.html> . . . . . 50, 238
- [Clark88] D.E. Clark, G.E. Kroth, *The Weldability of Consolidated Rapidly Solidified Type 304 SS Powders*, in P.W. Lee, J.H. Moll (editors), *Rapidly Solidified Materials - Properties and Processing*,

- Proceedings of the 2<sup>nd</sup> International Conference on Rapidly Solidified Materials, San Diego (1988) 9-17, [www.osti.gov/scitech/biblio/5452407](http://www.osti.gov/scitech/biblio/5452407) ..... 98, 100, 240
- [Cowin78] J.P. Cowin, D.J. Auerbach, C. Becker, L. Wharton, *Measurement of Fast Desorption Kinetics of D<sub>2</sub> from Tungsten by Laser Induced Thermal Desorption*, Surface Science 78 (1978) 545-564, doi: 10.1016/0039-6028(78)90232-7, <http://phdtree.org/pdf/58061846-measurement-of-fast-desorption-kinetics-of-d2-from-tungsten-by-laser-induced-thermal-desorption/> ..... 125
- [Das85] S.K. Das, B.H. Kear, C.M. Adams (editors), *Rapidly Solidified Crystalline Alloys*, Proceedings of a TMS-AIME Northeast Regional Meeting, Morristown, Metallurgical Society (1985), ISBN: 9780873390095 ..... 98, 247
- [Delone93] N.B. Delone, *Basics of Interaction of Laser Radiation with Matter*, Editions Frontières (1993), ISBN: 2-86332-127-7 ..... 47
- [Doyle80] B.L. Doyle, W.R. Wampler, D.K. Brice, S.T. Picraux, *Saturation and Isotopic Replacement of Deuterium in Low-Z Materials*, Journal of Nuclear Materials 93 & 94 (1980) 551-557, doi: 10.1016/0022-3115(80)90173-7 ..... 21
- [Diarc12] DIARC-Technology Inc., Kattilalaaksontie 1, FIN-02330 Espoo, Finland, [www.diarc.fi/energy.html](http://www.diarc.fi/energy.html) ..... 44, 45
- [Finken5] K.H. Finken, D. Reiter, T. Denner, K.H. Dippel, J. Hobirk, G. Mank, H. Keuer, G.H. Wolf, N. Noda, A. Miyahara, T. Shoji, K.N. Sato, K. Akaishi, J.A. Boedo, J.N. Brooks, R.W. Conn, W.J. Corbett, R.P. Doerner, D. Goebel, D.S. Gray, D.L. Hillis, J. Hogan, R.T. McGrath, M. Matsunaga, R. Moyer, R.E. Nygren, J. Watkins, *The Toroidal Pump Limiter ALT-II in TEXTOR*, Fusion Science and Technology 47 (2005) 126-137, handle: 2128/2740 ..... 44, 158
- [Frauenfelder69] R. Frauenfelder, *Solution and Diffusion of Hydrogen in Tungsten*, Journal of Vacuum Science and Technology 6 (1969) 388-397, ISSN: 0022-5355, doi: 10.1116/1.1492699 ..... 112, 113, 240
- [Geier2] A. Geier, H. Maier, R. Neu, K. Krieger and the ASDEX Upgrade Team, *Determination of the tungsten divertor retention at ASDEX Upgrade using a sublimation probe* Plasma Physics and Controlled Fusion 44 (2002) 2091-2100, doi: 10.1088/0741-3335/44/10/302 ..... 138
- [Giamei85] A.F. Giamei, *On the Role of Molybdenum in Rapidly Solidified Nickel-Base Alloys* in [Das85] (1985) 203-217 ..... 98, 99, 100, 240
- [Gierse11] N. Gierse, B. Schweer, A. Huber, O. Karger, V. Philipps, U. Samm, G. Sergienko, *In situ characterisation of hydrocarbon layers in TEXTOR by laser induced ablation and laser induced breakdown spectroscopy*, Journal of Nuclear Materials 415 (2011) 1195-1198, doi: 10.1016/j.jnucmat.2010.11.055 ..... 28
- [Gierse11b] N. Gierse, S. Brezinsek, T.F. Giesen, A. Huber, M. Laengner, R. Leyte-Gonzales, L. Marot, E. Meyer, S. Möller, M. Naim-Habib, V. Philipps, A. Pospieszczyk, B. Schweer, G. Sergienko, M. Zlobinski, U. Samm and the TEXTOR team, *Characterization of hydrocarbon and mixed layers in TEXTOR by laser induced ablation spectroscopy*, Physica Scripta T145 (2011) 014026, doi: 10.1088/0031-8949/2011/T145/014026 ..... 25
- [Gierse14] N. Gierse, *Assessment of Laser Induced Ablation Spectroscopy (LIAS) as a method for quantitative in situ surface diagnostic in plasma environments*, Dissertation Universität Köln (2014), ISBN: 978-3-89336-994-2,

- URN: <http://nbn-resolving.de/urn:nbn:de:hbz:38-57719>,  
URI: <http://kups.ub.uni-koeln.de/id/eprint/5771> ..... 28
- [Gierse14b] N. Gierse, S. Brezinsek, J.W. Coenen, T.F. Giesen, A. Huber, M. Laengner, S. Möller, M. Nonhoff, V. Philipps, A. Pospieszczyk, B. Schweer, G. Sergienko, Q. Xiao, M. Zlobinski, U. Samm and the TEXTOR Team, *In situ deuterium inventory measurements of a-C:D layers on tungsten in TEXTOR by laser induced ablation spectroscopy*, Physica Scripta T159 (2014) 014054,  
doi: 10.1088/0031-8949/2014/T159/014054 ..... 25
- [Haasz94] A.A. Haasz, J.W. Davis, *Fluence dependence of deuterium trapping in graphite*, Journal of Nuclear Materials 209 (1994) 155-160, ISSN: 0022-3115,  
doi: 10.1016/0022-3115(94)90290-9 ..... 21
- [Hartwig78] H. Hartwig, P. Mioduszewski, *Untersuchungen zur laserinduzierten thermischen Desorption*, Zentralbibliothek der Kernforschungsanlage Jülich GmbH (1978), Jül-1530, ISSN: 0366-0885 ..... 42, 125
- [Herrmann4] A. Herrmann, M. Balden, W. Bohmeyer, D. Hildebrandt, *Investigation of Infrared Emission from Carbon Microstructure on a 30 Micron Spatial Scale*, Physica Scripta T111 (2004) 98-100, doi: 10.1238/Physica.Topical.111a00098 ..... 58, 62
- [Herrmann7] A. Herrmann, *Surface temperature measurement and heat load estimation for carbon targets with plasma contact and machine protection*, Physica Scripta T128 (2007) 234-238, doi: 10.1088/0031-8949/2007/T128/045 ..... 60, 61
- [Heitjans5] P. Heitjans, J. Kärger, *Diffusion in Condensed Matter*, Springer (2005), ISBN-13: 978-3-540-20043-7 ..... 110, 111, 113, 240
- [Huber11] A. Huber, B. Schweer, V. Philipps, N. Gierse, M. Zlobinski, S. Brezinsek, W. Biel, V. Kotov, R. Leyte-Gonzales, Ph. Mertens, U. Samm, *Development of laser-based diagnostics for surface characterisation of wall components in fusion devices*, Fusion Engineering and Design 86 (2011) 1336-1340,  
doi: 10.1016/j.fusengdes.2011.01.090 ..... 28, 162, 163
- [Ihde1] J. Ihde, *Untersuchungen zur Wandkonditionierung mit mikrowellenerzeugten Plasmen in einem toroidalen Magnetfeld*, Forschungszentrum Jülich GmbH · Zentralbibliothek, Jül-3935 (2001), Dissertation, Universität Bochum, ISSN: 0944-2952,  
<http://nbn-resolving.de/urn/resolver.pl?urn=urn:nbn:de:hbz:294-2957> p. 54f ..... 22
- [Irrek4] F. Irrek, *Laserinduzierte thermische Desorption von a-C:D-Schichten auf Graphit*, Diplomarbeit, Universität Rostock - Fachbereich Physik (2004) ..... 28, 126
- [Irrek8] F. Irrek, *Entwicklung einer In-situ-Meßmethode zur Bestimmung des Wasserstoffgehalts amorpher Kohlenwasserstoffschichten in Fusionsanlagen*, Forschungszentrum Jülich GmbH · Zentralbibliothek, Jül-4279 (2008), ISSN: 0944-2952, handle: 2128/3621 ..... 28, 32, 35, 41, 48, 52, 68, 71, 78, 123, 125, 129, 135, 160, 164, 173, 175, 180, 184, 190, 196, 197, 210, 221, 236
- [Ivanova11] D. Ivanova, M. Rubel, V. Philipps, B. Schweer, M. Freisinger, A. Huber, N. Gierse, H. Penkalla, P. Petersson, T. Dittmar, *Laser-based and thermal methods for fuel removal and cleaning of plasma-facing components*, Journal of Nuclear Materials 415 (2011) S801-S804, doi: 10.1016/j.jnucmat.2011.01.119 ..... 127
- [Janev3] R.K. Janev, D. Reiter, U. Samm, *Collision Processes in Low-Temperature Hydrogen Plasmas*, Forschungszentrum Jülich GmbH · Zentralbibliothek, Jül-4105 (2003), ISSN: 0944-2952, handle: 2128/249 ..... 172, 174, 175



- [Jaskula14] B.W. Jaskula, *Lithium*, U.S. Geological Survey, Mineral Commodity Summaries 703 (2014) 648-4908, <http://minerals.usgs.gov/minerals/pubs/commodity/lithium/mcs-2014-lithi.pdf> and  
D. Bradley, B. Jaskula, *Lithium-For harnessing renewable energy*, U.S. Geological Survey Fact Sheet 2014-3035 (2014), ISSN: 2327-6932, doi: 10.3133/fs20143035 . 15, 16
- [Johnson10] D. F. Johnson, E. A. Carter, *Hydrogen in tungsten: Absorption, diffusion, vacancy trapping, and decohesion*, Journal of Materials Research 25, No. 2 (2010), doi: 10.1557/JMR.2010.0036. . . . . 111, 114
- [Kirschner11] A. Kirschner, A. Kreter, P. Wienhold, S. Brezinsek, J.W. Coenen, H.G. Esser, A. Pospieszczyk, Ch. Schulz, U. Breuer, D. Borodin, M. Clever, R. Ding, A. Galonska, A. Huber, A. Litnovsky, D. Matveev, K. Ohya, V. Philipps, U. Samm, O. Schmitz, B. Schweer, H. Stoschus, TEXTOR team, *Deposition and re-erosion studies by means of local impurity injection in TEXTOR*, Journal of Nuclear Materials 415 (2011) S239-S245, doi: 10.1016/j.jnucmat.2010.10.058 . . . . . 138
- [Koch4] B. Koch, *Angular Resolved Measurements of Particle and Energy Fluxes to Surfaces in Magnetized Plasmas*, Dissertation, Humboldt-Universität Berlin (2004)  
<http://nbn-resolving.de/urn:nbn:de:kobv:11-10034619>. . . . . 152
- [Kornmeyer11] Kornmeyer Carbongroup, Carbon Holding GmbH (10.10.2011)  
[www.carbongroup.de](http://www.carbongroup.de) . . . . . 121
- [Krieger99] K. Krieger, H. Maier, R. Neu, ASDEX Upgrade Team, *Conclusions about the use of tungsten in the divertor of ASDEX Upgrade*, Journal of Nuclear Materials 266-269 (1999) 207-216, doi: 10.1016/S0022-3115(98)00890-3 . . . . . 138
- [Küppers95] J. Küppers, *The Hydrogen Surface Chemistry of Carbon as a Plasma Facing Material*, Surface Science Reports 22 (1995) 249-321,  
doi: 10.1016/0167-5729(96)80002-1 . . . . . 122, 241
- [Lide94] D.R. Lide, *CRC Handbook of Chemistry and Physics*, 75<sup>th</sup> edition, CRC Press, (1994-1995) . . . . . 42, 46, 237
- [Lide5] D.R. Lide, *CRC Handbook of Chemistry and Physics*, 86<sup>th</sup> edition, CRC Press, Taylor & Francis (2005-2006), page "6-174" . . . . . 131
- [Lipschultz10] B. Lipschultz, J. Roth, J.W. Davis, R.P. Doerner, A.A. Haasz, A. Kalenbach, A. Kirschner, R.D. Kolasinski, A. Loarte, V. Philipps, K. Schmid, W.R. Wampler, G.M. Wright, D.G. Whyte, *An Assessment of the Current Data Affecting Tritium Retention and its Use to Project Towards T Retention in ITER*, PSFC/RR-10-4 (2010),  
[http://www-internal.psfc.mit.edu/library1/catalog/reports/2010/10rr/10rr004/10rr004\\_abs.html](http://www-internal.psfc.mit.edu/library1/catalog/reports/2010/10rr/10rr004/10rr004_abs.html). . . . . 21, 22, 24, 153, 209, 242
- [Litnovsky10] A. Litnovsky, V. Voitsenya, D. Thomas, M. Rubel, G. De Temmerman, L. Marot, K. Yu. Vukolov, I. Orlovskiy, W. Vliegthart, Ch. Skinner, D. Johnson, V. Kotov, J.P.Coad, A. Widdowson, G. Vayakis, R. Boivin, T. Akiyama, N. Yoshida, M. Joanny and the members of the ITPA Specialists Working Group on First Mirrors, *Mirrors for ITER diagnostics: new R&D developments, assessment of the mirror lifetime and impact of the mirror failure on ITER performance*, International Atomic Energy Agency (2010) 522,  
[http://www-naweb.iaea.org/napc/physics/FEC/FEC2010/papers/itr\\_p1-05.pdf](http://www-naweb.iaea.org/napc/physics/FEC/FEC2010/papers/itr_p1-05.pdf). . . . 196
- [Longhurst8] G.R. Longhurst, *TMAP7 User Manual*, Rev. 2, Idaho National Engineering and Environmental Laboratory (2008) INEEL/EXT-04-02352  
[www.inl.gov/technicalpublications/Documents/4215154.pdf](http://www.inl.gov/technicalpublications/Documents/4215154.pdf) . . . . . 114

- [Maisonnier5] D. Maisonnier, I. Cook, P. Sardain, R. Andreani, L. Di Pace, R. Forrest, L. Giancarli, S. Hermsmeyer, P. Norajitra, N. Taylor, D. Ward and contributors, *A Conceptual Study of Commercial Fusion Power Plants - Final Report of the European Fusion Power Plant Conceptual Study (PPCS)*, European Fusion Development Agreement (EFDA), EFDA(05)-27/4.10 revision 1 (revision 0: STAC 10/4.1) (2005) EFDA-RP-RE-5.0, [https://www.euro-fusion.org/wpcms/wp-content/uploads/2012/01/PPCS\\_overall\\_report\\_final-with\\_annexes.pdf](https://www.euro-fusion.org/wpcms/wp-content/uploads/2012/01/PPCS_overall_report_final-with_annexes.pdf) . . . . . 16, 18, 27
- [Markwardt9] C.B. Markwardt, *Non-linear Least Squares Fitting in IDL with MPFIT* in D. Bohlender, P. Dowler, D. Durand (editors), *Astronomical Data Analysis Software and Systems XVII*, ASP Conference Series 411 (2009) 251, arXiv:0902.2850v1 [astro-ph.IM] . . . . . 129
- [Matyja85] H. Matyja, P.G. Zieliński, *Summer School on Amorphous Metals*, Wilga, World Scientific (1985), ISBN-10: 9971501090, ISBN-13: 978-9971501099 . . . . . 98
- [manual94] *TL4, TL6 Testlecks - Calibrated leaks - Fuites calibrées - Gebrauchsanleitung - Operating Instructions - Mode d'emploi*, Leybold AG Vakuumtechnik, Köln (1994) . . . . . 131, 132
- [Manhard11a] A. Manhard, T. Schwarz-Selinger, W. Jacob, *Quantification of the deuterium ion fluxes from a plasma source*, *Plasma Sources Science and Technology* 20 (2011) 015010, doi: 10.1088/0963-0252/20/1/015010 . . . . . 145, 150
- [Manhard11b] A. Manhard, U. v. Toussaint, T. Dürbeck, K. Schmid, W. Jacob, *Statistical analysis of blister bursts during temperature-programmed desorption of deuterium-implanted polycrystalline tungsten*, *Physica Scripta T145* (2011) 014038, doi: 10.1088/0031-8949/2011/T145/014038 . . . . . 22, 92, 93, 123, 150
- [Mayer9] M. Mayer, E. Gauthier, K. Sugiyama, U. von Toussaint, *Quantitative depth profiling of deuterium up to very large depths*, *Nuclear Instruments and Methods in Physics Research B* 267 (2009) 506-512, doi: 10.1016/j.nimb.2008.11.033 . . . . . 150
- [Milch2] I. Milch, *Kernfusion - Berichte aus der Forschung - Folge 2*, Max-Planck-Institut für Plasmaphysik, Garching und Greifswald (2002), ISSN 0172-8482, [www.ipp.mpg.de/46732/3\\_berichte](http://www.ipp.mpg.de/46732/3_berichte) , [www.ipp.mpg.de/47334/berichte.pdf](http://www.ipp.mpg.de/47334/berichte.pdf) . . . . . 25, 26, 27, 237
- [Miller98] J. C. Miller, R. F. Haglund Jr. (editors), *Laser Ablation and Desorption*, Academic Press Limited, London (1998), ISBN 0-12-475975-0 . . . . . 28
- [Mitri9] M. Mitri, D. Nicolai, O. Neubauer, H.T. Lambertz, I. Schmidt, A. Khilchenko, B. Schweer, U. Maier, U. Samm, *Optimised plasma stabilisation at TEXTOR with an advanced, real-time digital control scheme*, *Fusion Engineering and Design* 84 (2009) 1329-1332, doi: 10.1016/j.fusengdes.2009.02.039 . . . . . 201
- [Möller87] W. Möller, P. Børgesen, B.M.U. Scherzer, *Thermal and Ion-induced Release of Hydrogen Atoms Implanted into Graphite*, *Nuclear Instruments and Methods in Physics Research B* 19/20 (1987) 826-831, doi: 10.1016/S0168-583X(87)80165-9 . . . . . 121
- [Neubauer5] O. Neubauer, G. Czymek, B. Giesen, P.W. Hüttemann, M. Sauer, W. Schalt, J. Shruff, *Design Features of the Tokamak TEXTOR*, *Fusion Science and Technology* 47 (2005) 76, handle: 2128/2735 . . . . . 158
- [Neumann73] M. Neumann, *Laserinduzierte thermische Desorption von Festkörper-Oberflächen*, Dissertation, Technische Universität Hannover (1973) . . . . . 127
- [NIST15] A. Kramida, Yu. Ralchenko, J. Reader and NIST ASD Team (2014), *NIST Atomic Spectra Database (ver. 5.2)*, available online: <http://physics.nist.gov/asd>, National Institute of Standards and Technology, Gaithersburg, MD, USA. (29.7.2015) . . . . . 224

- [Ogorodnikova3] O.V. Ogorodnikova, J. Roth, M. Mayer, *Deuterium retention in tungsten in dependence of the surface conditions*, Journal of Nuclear Materials 313-316 (2003) 469-477, doi: 10.1016/S0022-3115(02)01375-2..... 21
- [Ogorodnikova8] O.V. Ogorodnikova, J. Roth, M. Mayer, *Ion-driven deuterium retention in tungsten*, Journal of Applied Physics 103 (2008) 034902, doi: 10.1063/1.2828139..... 21, 112
- [Ohno1] N. Ohno, D. Nishijima, S. Takamura, Y. Uesugi, M. Motoyama, N. Hattori, H. Arakawa, N. Ezumi, S. Krasheninnikov, A. Pigarov, U. Wenzel, *Static and dynamic behaviour of plasma detachment in the divertor simulator experiment NAGDIS-II*, Nuclear Fusion 41 (2001) 1055, doi:10.1088/0029-5515/41/8/309..... 154
- [PSI14] Paul Scherrer Institut (PSI), Villigen, Switzerland, www.psi.ch/media/die-vermessung-des-oekologischen-fussbadrucks, also: K. Treyer, Ch. Bauer, *Life cycle inventories of electricity generation and power supply in version 3 of the ecoinvent database part I:electricity generation*, doi: 10.1007/s11367-013-0665-2 and *part II:electricity markets*, doi: 10.1007/s11367-013-0694-x ..... 17
- [Palik98] E.D. Palik (editor), *Handbook of optical constants of solids*, Academic Press (1998), ISBN-10: 0125444230, ISBN-13: 9780125444231 ..... 46, 237
- [Philipps87] V. Philipps, E. Vietzke, M. Erdweg, K. Flaskamp, *Thermal Desorption of Hydrogen and Various Hydrocarbons from Graphite Bombarded with Thermal and Energetic Hydrogen*, Journal of Nuclear Materials 145-147 (1987) 292-296, doi: 10.1016/0022-3115(87)90346-1 ..... 21, 121, 122, 241
- [Philipps13] V. Philipps, A. Malaquias, A. Hakola, J. Karhunen, G. Maddaluno, S. Almaviva, L. Caneve, F. Colao, E. Fortuna, P. Gasior, M. Kubkowska, A. Czarnecka, M. Laan, A. Lissovski, P. Paris, H.J. van der Meiden, P. Petersson, M. Rubel, A. Huber, M. Zlobinski, B. Schweer, N. Gierse, Q. Xiao, G. Sergienko, *Development of laser-based techniques for in situ characterization of the first wall in ITER and future fusion devices*, Nuclear Fusion 53 (2013) 093002, doi: 10.1088/0029-5515/53/9/093002 .. 28
- [Pintsuk8] G. Pintsuk, J. Compan, D. Pitzer, *Measurement of thermo-physical and mechanical properties of CFC delivered by SNECMA*, Forschungszentrum Jülich GmbH, Final Report EFDA Task TW5-TVM-CFC2Q (2008)..... 55
- [Pospieszczyk80] A. Pospieszczyk, P. Bogen, H. Hartwig, Y.T. Lie, *Determination of Low Surface Coverages of H<sub>2</sub> and CO by Vacuum UV-Resonance Fluorescence Spectroscopy of Laser Desorbed Particles*, Journal of Nuclear Materials 93-94 (1980) 368-376, doi: 10.1016/0022-3115(80)90350-5 ..... 125
- [Quastel6] A.D. Quastel, J.W. Davis, A.A. Haasz, R.G. Macaulay-Newcombe, *Effect of post-D<sup>+</sup>-irradiation time delay and pre-TDS heating on D retention in single crystal tungsten*, Journal of Nuclear Materials 359 (2006) 8-16, ISSN: 0022-3115, doi: 10.1016/j.jnucmat.2006.07.012 ..... 22
- [Ready71] J.F. Ready, *Effects of High-Power Laser Radiation*, Academic Press (1971), ISBN-10: 0125839502, ISBN-13: 978-0125839501..... 46
- [Reiter92] D. Reiter, *The EIRENE code*, Forschungszentrum Jülich (1992), Jül-2599, also: D. Reiter, M. Baelmans, P. Börner, *The EIRENE and B2-EIRENE codes*, Fusion Science and Technology 47 (2005) 172, ISSN: 1536-1055, handle: 2128/2743

- also: D. Reiter, *The EIRENE code User Manual* (2009),  
www.eirene.de/manuals/eirene/eirene.pdf ..... 180
- [Rödig3] M. Rödig, D. Pitzer, *Thermal Conductivities of Tungsten Materials After Neutron Irradiation*, Forschungszentrum Jülich (2003), Final Report EFDA Task TW1-TVP/TU1 ..... 50, 238
- [Rubel12] M. Rubel, D. Ivanova, V. Philipps, M. Zlobinski, A. Huber, P. Petersson, B. Schweer, *Efficiency of fuel removal techniques tested on plasma-facing components from the TEXTOR tokamak*, Fusion Engineering and Design 87 (2012) 935-940, doi: 10.1016/j.fusengdes.2012.02.054 ..... 61, 69, 238, 257
- [Rudakov9] D.L. Rudakov, A. Litnovsky, W.P. West, J.H. Yu, J.A. Boedo, B.D. Bray, S. Brezinsek, N.H. Brooks, M.E. Fenstermacher, M. Groth, E.M. Hollmann, A. Huber, A.W. Hyatt, S.I. Krasheninnikov, C.J. Lasnier, A.G. McLean, R.A. Moyer, A.Yu. Pigarov, V. Philipps, A. Pospieszczyk, R.D. Smirnov, J.P. Sharpe, W.M. Solomon, J.G. Watkins, C.P.C. Wong, *Dust studies in DIII-D and TEXTOR*, Nuclear Fusion 49 (2009) 085022, doi: 10.1088/0029-5515/49/8/085022 ..... 90
- [Samm5] U. Samm, *TEXTOR: A Pioneering Device for New Concepts in Plasma-Wall Interaction, Exhaust, and Confinement*, Fusion Science and Technology 47 (2005) 73-75, handle: 2128/2734 ..... 28
- [Samsonov68] G.V. Samsonov (editor), *Handbook of the Physicochemical Properties of the Elements*, IFI/Plenum Data Corporation (1968), ISBN: 978-1-4684-6068-1 (print) 978-1-4684-6066-7 (online), doi: 10.1063/1.3035172 ..... 42, 50, 238
- [Scherzer90] B.M.U. Scherzer, J. Wang, W. Möller, *Trapping and release of D from "saturated" implants in graphite*, Journal of Nuclear Materials 176 & 177 (1990) 208-212, doi: 10.1016/0022-3115(90)90047-Q ..... 21
- [Schmid12] K. Schmid, U. von Toussaint, *Statistically sound evaluation of trace element depth profiles by ion beam analysis*, Nuclear Instruments and Methods in Physics Research B 281 (2012) 64-71, doi: 10.1016/j.nimb.2012.03.024 ..... 150
- [Schwarz99] T. Schwarz-Selinger, A. von Keudell, W. Jacob, *Plasma chemical vapor deposition of hydrocarbon films: The influence of hydrocarbon source gas on the film properties*, Journal of Applied Physics 86 (1999) 3988, doi: 10.1063/1.371318 ..... 60
- [Schweer4] B. Schweer, A. Huber, G. Sergienko, V. Philipps, F. Irrek, H.G. Esser, U. Samm, M. Kempnaars, M. Stamp, C. Gowers, D. Richards, *Laser desorption of deuterium retained in re-deposited carbon layers at TEXTOR and JET*, Journal of Nuclear Materials 337-339 (2005) 570-574, doi: 10.1016/j.jnucmat.2004.10.156 ..... 28, 37, 40
- [Schweer5] B. Schweer, S. Brezinsek, H.G. Esser, A. Huber, Ph. Mertens, S. Musso, V. Musso, V. Philipps, A. Pospieszczyk, U. Samm, G. Sergienko, P. Wienhold, *Limiter Lock Systems at TEXTOR: Flexible Tools for Plasma-Wall Investigation*, Fusion Science and Technology 47 (2005) 138-145, ISSN: 1536-1055, handle: 2128/2741 ..... 158, 160, 202
- [Schweer7] B. Schweer, F. Irrek, G. Sergienko, V. Philipps, U. Samm, *In situ diagnostic for monitoring of deuterium and tritium in re-deposited carbon layers by laser induced desorption*, Journal of Nuclear Materials 363-365 (2007) 1375-1379, doi: 10.1016/j.jnucmat.2007.01.247 ..... 125
- [Schweer9] B. Schweer, F. Irrek, M. Zlobinski, A. Huber, G. Sergienko, S. Brezinsek, V. Philipps, U. Samm, *In situ detection of hydrogen retention in TEXTOR by laser*

- induced desorption*, Journal of Nuclear Materials 390-391 (2009) 576-580,  
doi: 10.1016/j.jnucmat.2009.01.108 ..... 28, 221
- [Shimada12] M. Shimada, Y. Hatano, Y. Oya, T. Oda, M. Hara, G. Cao, M. Kobayashi, M. Sokolov, H. Watanabe, B. Tyburska-Püschel, Y. Ueda, P. Calderoni, K. Okuno, *Overview of the US–Japan collaborative investigation on hydrogen isotope retention in neutron-irradiated and ion-damaged tungsten*, Fusion Engineering and Design 87 (2012) 1166-1170, doi: 10.1016/j.fusengdes.2012.02.103 ..... 23
- [Sobol95] E.N. Sobol, *Phase transformations and ablation in laser-treated solids*, Wiley-Interscience publication, New York (1995), ISBN 0-471-59899-2 ..... 95
- [SRIM] *The Stopping and Range of Ions in Matter*, www.srim.org, (Attention: The term "Ion" is misleading as it is defined here as "The moving atom, whether it is charged or neutral.") J.F. Ziegler, J.P. Biersack, M.D. Ziegler, *SRIM - The Stopping and Range of Ions in Matter*, Lulu Press Co. (2008), ISBN-13: 978-0-9654207-1-6, ISBN: 0-9654207-1-X, EAN: 9780965420716 ..... 20, 180
- [Stangeby0] P.C. Stangeby, *The Plasma Boundary of Magnetic Fusion Devices*, IOP Publishing (2000), ISBN: 0 7503 0559 2, [http://physics.technion.ac.il/~plasma/publications/ebooks/books2/djvu\\_library/Plasma/General courses/The Plasma Boundary of Magnetic Fusion Devices \(Stangeby, 2000\).pdf](http://physics.technion.ac.il/~plasma/publications/ebooks/books2/djvu_library/Plasma/General%20courses/The%20Plasma%20Boundary%20of%20Magnetic%20Fusion%20Devices%20(Stangeby,%202000).pdf) ..... 172
- [Stoschus11] H. Stoschus, *Electron Transport in the Plasma Edge with Rotating Resonant Magnetic Perturbations at the TEXTOR Tokamak*, Forschungszentrum Jülich GmbH · Zentralbibliothek (2011), ISSN: 1866-1793, ISBN: 978-3-89336-718-4, handle: 2128/4442 ..... 177, 200
- [Sültenfuß98] J. Sültenfuß, *Das Radionuklid Tritium im Ozean: Meßverfahren und Verteilung von Tritium im Südatlantik und im Weddellmeer = The radionuclide Tritium in the ocean: measurement and distribution of Tritium in the South Atlantic and the Weddell Sea*, Institut für Umwelphysik, Berichte zur Polarforschung (Reports on Polar Research) 256, Alfred Wegener Institute for Polar and Marine Research, Bremerhaven (1998), ISSN 0176-5027, handle: 10013/epic.10259  
also published as : *Tritium-Untersuchungen im Südatlantik*, Dissertation, Universität Bremen (1997) ..... 25, 26, 237
- [Tagle83] J.A. Tagle, A. Pospieszczyk, *Measurement of Desorption Energies of H<sub>2</sub> and CO from SS-304 LN and INCONEL 625 Surfaces by Laser Induced Thermal Desorption*, Applications of Surface Science 17 (1983) 189-206,  
doi: 10.1016/0378-5963(83)90033-8 ..... 125
- [Tanabe13] T. Tanabe, *Tritium fuel cycle in ITER and DEMO: Issues in handling large amount of fuel*, Journal of Nuclear Materials 438 (2013) S19-S26,  
doi:10.1016/j.jnucmat.2013.01.284 ..... 26, 237
- [Tanabe14] T. Tanabe, *Review of hydrogen retention in tungsten*, Physica Scripta T159 (2014) 014044, doi: 10.1088/0031-8949/2014/T159/014044 ..... 25, 26
- [tHoen14] M.H.J. 't Hoen, *Deuterium retention in radiation damaged tungsten exposed to high-flux plasma*, Dissertation, Universiteit van Amsterdam (2014), ISBN: 978-94-6259-130-1, handle: 11245/1.417321 ..... 22, 23
- [Thomser12] C. Thomser, V. Bailescu, S. Brezinsek, J.W. Coenen, H. Greuner, T. Hirai, J. Linke, C.P. Lungu, H. Maier, G. Matthews, Ph. Mertens, R. Neu, V. Philipps, V. Riccardo, M. Rubel, C. Ruset, A. Schmidt, I. Uytendhouwen, JET EFDA Con-

- tributors, *Plasma Facing Materials for the JET ITER-Like Wall*, Fusion Science and Technology 62 (2012) 1-8, preprint: [www.iop.org/Jet/fulltext/EFDP11063.pdf](http://www.iop.org/Jet/fulltext/EFDP11063.pdf) . . . . . 108
- [Tokar93] M.Z. Tokar, *The possible nature of the localized recycling effect on the plasma edge in tokamaks*, Plasma Physics of Controlled Fusion 35 (1993) 1119-1135, doi: 10.1088/0741-3335/35/9/004 . . . . . 192
- [Toussaint11] U. von Toussaint, S. Gori, A. Manhard, T. Höschen, C. Höschen, *Molecular dynamics study of grain boundary diffusion of hydrogen in tungsten*, Physica Scripta T145 (2011) 014036, doi: 10.1088/0031-8949/2011/T145/014036 . . . . . 113
- [TriDyn] W. Möller, W. Eckstein, J.P. Biersack, *Tridyn-binary collision simulation of atomic collisions and dynamic composition changes in solids*, Computer Physics Communications 51 (1988) 355-368, doi: 10.1016/0010-4655(88)90148-8 . . . . . 20
- [Ueda11] Y. Ueda, K. Miyata, Y. Ohtsuka, H.T. Lee, M. Fukumoto, S. Brezinsek, J.W. Coenen, A. Kreter, A. Litnovsky, V. Philipps, B. Schweer, G. Sergienko, T. Hirai, A. Taguchi, Y. Torikai, K. Sugiyama, T. Tanabe, S. Kajita, N. Ohno, The TEXTOR team, *Exposure of tungsten nano-structure to TEXTOR edge plasma*, Journal of Nuclear Materials 415 (2011) 92-95, doi: 10.1016/j.jnucmat.2010.08.019 . . . . . 103
- [Umrath97] W. Umrath, H. Adam, A. Bolz, H. Boy, H. Dohmen, K. Gogol, W. Jorisch, W. Mönning, H.J. Mundinger, H.D. Otten, W. Scheer, H. Seiger, W. Schwarz, K. Stepputat, D. Urban, H.J. Wirtzfeld, H.J. Zenker, *Grundlagen der Vakuumtechnik*, Leybold (1997), <http://www-ekp.physik.uni-karlsruhe.de/~simonis/praktikum/p2/p2-versuchsanleitungen/VakuumGrundlagen.pdf>  
also in English: *Fundamentals of Vacuum Technology*, Leybold Vacuum Products and Reference Book (2001/2002), p. 96ff, [www.yumpu.com/en/document/view/20590981/fundamentals-of-vacuum-technology/3](http://www.yumpu.com/en/document/view/20590981/fundamentals-of-vacuum-technology/3) . . . . . 133
- [Unterberg5] B. Unterberg, S. Brezinsek, G. Sergienko, C.C. Chu, P. Dumortier, J.D. Hey, D. Kalupin, A. Kreter, M. Lehnen, A.M. Messiaen, Ph. Mertens, A. Pospieszczyk, U. Samm, B. Schweer, M.Z. Tokar, G. Van Wassenhove, the TEXTOR-team, *Local effects of gas fuelling and their impact on transport processes in the plasma edge of the tokamak TEXTOR*, Journal of Nuclear Materials 337-339 (2005) 515-519, doi: 10.1016/j.jnucmat.2004.09.041 . . . . . 193
- [vac] L. Holland, W. Steckelmacher, J. Yarwood, *Vacuum Manual*, E. & F.N. SPON London, John Wiley & Sons New York (1974), ISBN: 0 419 10740 1, table 1.26 on page 54 and explanations on page 16 . . . . . 131
- [vanHoey11] O. Van Hoey, A. Kirschner, I. Uytdenhouten, G. Van Oost, R. Chaouadi, *Tracing of hydrogen isotopes with the ERO code*, 13<sup>th</sup> International Workshop on Plasma-Facing Materials and Components for Fusion Applications (PFMC 2011), poster P33A, [www.ipp.mpg.de/1530412/Book\\_of\\_Abstacts\\_vers\\_1\\_1\\_-\\_2011-05-03.pdf](http://www.ipp.mpg.de/1530412/Book_of_Abstacts_vers_1_1_-_2011-05-03.pdf) , p.119 . . . . . 180
- [Vietzke87] E. Vietzke, V. Philipps, *Surface Modification due to Hydrogen-Graphite Interaction*, Nuclear Instruments and Methods in Physics Research B23 (1987) 449-457, doi: 10.1016/0168-583X(87)90470-8 . . . . . 60, 105, 121, 122
- [Wienhold83] P. Wienhold, M. Profant, F. Waelbroeck, J. Winter, *Rechencode PERI - Permeation von Wasserstoff durch Metallmembranen, Freisetzung aus Metalloberflächen und Inventar in Metallwänden*, Zentralbibliothek der Kernforschungsanlage Jülich GmbH, Jül-1825 (1983), ISSN: 0366-0885, <http://dmssrv.zb.kfa-juelich.de/w2p2/autologin1.asp?action=ExpDownload&Path=%5CPublic+FZJ%5CPublikationen%5CJUEL%2DBerichte%5CJ%FC1%5F1825%5FWienhold%2Epdf> . . . . . 115

- [Wirtz12] O.M. Wirtz, *Thermal Shock Behaviour of Different Tungsten Grades under Varying Conditions*, Dissertation, RWTH Aachen (2012),  
<http://nbn-resolving.de/urn/resolver.pl?urn=urn:nbn:de:hbz:82-opus-43140>,  
<http://darwin.bth.rwth-aachen.de/opus3/volltexte/2012/4314/> ..... 102
- [Wirtz13] M. Wirtz, J. Linke, G. Pintsuk, L. Singheiser, M. Zlobinski, *Comparison of thermal shock damages induced by different simulation methods on tungsten*, *Journal of Nuclear Materials* 438 (2013) S833-S836, doi: 10.1016/j.jnucmat.2013.01.180 ..... 102
- [Zayachuk13] Y. Zayachuk, *Deuterium Retention in Tungsten and Tungsten-Tantalum Alloys under High Flux Plasma Exposure*, Dissertation, Universiteit Gent (2013-2014), ISBN: 978-90-8578-635-1, <http://lib.ugent.be/catalog/rug01:002052815>,  
handle: 1854/LU-4337237 ..... 22
- [Z9] M. Zlobinski, *Laserinduzierte Desorption an plasmaerzeugten Wandbeschichtungen*, Diplomarbeit, Universität Düsseldorf (2009) ..... 55, 71, 124, 125, 197
- [Z11] M. Zlobinski, V. Philipps, B. Schweer, A. Huber, S. Brezinsek, Ch. Schulz, S. Möller, U. Samm, the TEXTOR Team, *Laser induced desorption as tritium retention diagnostic method in ITER*, *Fusion Engineering and Design* 86 (2011) 1332-1335,  
doi: 10.1016/j.fusengdes.2011.02.030 ..... 27, 28, 80, 123, 124, 125, 127, 129, 130, 163, 164, 171, 177, 241, 256
- [Z11b] M. Zlobinski, V. Philipps, B. Schweer, A. Huber, H. Stoschus, S. Brezinsek, U. Samm and the TEXTOR Team, *In situ measurements of fuel retention by laser induced desorption spectroscopy in TEXTOR*, *Physica Scripta* T145 (2011) 014027,  
doi: 10.1088/0031-8949/2011/T145/014027 ..... 28, 80, 159, 168, 170, 177, 179, 185, 186, 187, 188, 192, 242, 243, 256
- [Z13] M. Zlobinski, V. Philipps, B. Schweer, A. Huber, M. Reinhart, S. Möller, G. Sergienko, U. Samm, M.H.J. 't Hoen, A. Manhard, K. Schmid, the TEXTOR Team, *Hydrogen retention in tungsten materials studied by Laser Induced Desorption*, *Journal of Nuclear Materials* 438 (2013) 1155-1159, doi: 10.1016/j.jnucmat.2013.01.255 ..... 36, 110, 114, 119, 121, 143, 145, 146, 147, 149, 150, 151, 154, 236, 237, 241, 242, 256, 257

# Erklärung

Die oben aufgeführten Veröffentlichungen [Z11], [Z11b] und [Z13] wurden in dieser Dissertation in Auszügen teils wörtlich, teils inhaltlich benutzt. Die entsprechenden Textstellen und Abbildungen sind als wörtliches Zitat gekennzeichnet oder als inhaltliche Quelle genannt, da an ihnen Koautoren beteiligt waren. Der Eigenanteil an den Veröffentlichungen ergibt sich wie folgt:

**Thema:** Der Themenschwerpunkt liegt bei allen Veröffentlichungen auf der laserinduzierten Desorption sowie den damit durchgeführten Messungen der Wasserstoffrückhaltung. Daher behandeln sie Aspekte, die zum Kern des Dissertationsthemas gehören und somit ursprünglich von den Dissertationsbetreuern als Arbeitsrahmen vorgegebenen wurden. Die konkreten Fragestellungen und Probenauswahl, die in den Veröffentlichungen behandelt werden, wurden teils selbständig (z.B. Reproduzierbarkeit, Messungen auf plasmaabgewandten Flächen) und teils unter Mitwirkung von Betreuern und Mitarbeitern (z.B. Nachweisgrenzen, Konversionsfaktoren, Modellierung der Desorption, Vergleich mit anderen Messmethoden) als Themen gewählt.

**Infrastruktur und Kooperation:** Alle Veröffentlichungen enthalten Messungen an TEXTOR oder an Proben, die in TEXTOR exponiert wurden, woran eine Vielzahl der Mitarbeiter des TEXTOR-Teams beteiligt war. Ebenso wurden alle TEXTOR-Experimente mit den Leitern des TEXTOR-Teams und weiteren Wissenschaftlern vor- und nachbesprochen, sodass ursprüngliche Planungen und Interpretationen abgeändert wurden. Die Experimente an Pilot-PSI in Nieuwegein und der Glimmentladung an PADOS in Jülich (in [Z13]) wurden nach Einweisung unter Anleitung und Assistenz eines mit den Anlagen vertrauten Mitarbeiters durchgeführt. Die Experimente am ECR Plasma im MPI Garching wurden vollständig von den Mitarbeitern vor Ort durchgeführt und die exponierte Probe anschließend nach Jülich gebracht, wo die Laserdesorptionsexperimente selbständig durchgeführt und ausgewertet wurden.

**Messungen:** Die ex situ Messungen mittels Laserdesorption wurden stets selbständig durchgeführt und ausgewertet; die in situ Messungen mit Unterstützung des TEXTOR-Teams. Der Aufbau, Ablauf und die Auswertung beider Methoden wurde mehrfach nach eigenen Vorstellungen mit Hilfe von Mitarbeitern umgebaut, verbessert und erweitert. Dies schließt insbesondere die Installation einer ferngesteuerten Laserpositionierung, verbesserter Kamerasysteme, stabilere Quadrupolmessungen mit genauerer Kalibrierung, Untergrundreduktion sowie Funktionserweiterungen der Auswerterroutinen ein.

**Weitere Messmethoden:** Vergleichsmessungen mit anderen Messmethoden (TDS, NRA) wurden von den für die jeweilige Methode zuständigen Mitarbeitern und Doktoranden des FZ Jülich (in [Z11], [Z13]) bzw. des MPI Garching (in [Z13]) durchgeführt und ausgewertet, jedoch selbständig in Diagrammen und im Text zusammengefasst und dargestellt. Die Messpositionen und konkreten Messaufträge wurden meist selbständig oder in Absprache mit Betreuern gewählt.

Unterstützende Messmethoden zur Plasmacharakterisierung (Heliumdiagnostiken an TEXTOR, Plasmafluss am ALT-II, Thomsonstreuung an Pilot-PSI etc.) wurden von den zuständigen Mitarbeitern durchgeführt und ausgewertet. Die Darstellung der Ergebnisse erfolgten wiederum selbständig.



**Simulationen:** Die numerischen Simulationen in [Z13] zur Wärme- und Wasserstoffdiffusion in Wolfram mit dem Code TMAP7 wurden mit einem bereits vorhanden Code, dessen Handbuch und Unterstützung durch einen Mitarbeiter aus der numerischen Abteilung der PWW-Gruppe des FZ Jülich durchgeführt. Die Anpassung an die Parameter und Bedingungen bei der Laserdesorption wurden so erstellt. Nach dieser Einarbeitung wurden weitere Variationen der Simulation selbständig programmiert und Simulationsrechnungen selbst durchgeführt. Dabei flossen auch hilfreiche Diskussionen mit anderen Nutzern von TMAP7 innerhalb des Arbeitsverbundes des Trilateralen Euregio Clusters in Nieuwegein und Mol ein. Die veröffentlichten Ergebnisse wurden selbständig in Diagrammen und Beschreibungen dargestellt.

**Interpretation:** Die Interpretation der Messergebnisse der Laserdesorption erfolgte unter Mitwirkung der Betreuer und weiterer Mitarbeiter. Bei den Ergebnissen der anderen Messmethoden waren zusätzlich die sie durchführenden Mitarbeiter beteiligt.

**Schriftliche Arbeit:** Die Artikeltexte basieren auf eigenen Formulierungen, die von den Dissertationsbetreuern und einigen der Koautoren in mehrfacher Iteration verändert, ergänzt und korrigiert wurden.

**Referenzen:** Literaturquellen und weitere Referenzen in den Veröffentlichungen wurden für alle bereits vorher bekannten Erkenntnisse und Sachverhalte angegeben, soweit es sich nicht um in diesem Fachgebiet allgemein Bekanntes handelt.

Ein Teilergebnis der vorliegenden Dissertation wurde in [Rubel12] vorveröffentlicht: Dafür erfolgten die Planung, Messungen, Auswertungen und Ergebnisse bezüglich der Experimente an TEXTOR und der Laserdesorption wie oben beschrieben in Jülich größtenteils in Eigenarbeit. Dagegen erfolgten die Messungen, Auswertung und Interpretation der NRA Ergebnisse und die Anfertigung des Textes durch den Erstautor der Vorveröffentlichung.

Ich versichere an Eides Statt, dass die Dissertation von mir selbständig und ohne unzulässige fremde Hilfe unter Beachtung der „Grundsätze zur Sicherung guter wissenschaftlicher Praxis an der Heinrich-Heine-Universität Düsseldorf“ erstellt worden ist.

Die Dissertation wurde in dieser oder ähnlicher Form noch nie bei einer anderen Institution vorgelegt.

Ich habe vorher noch keine erfolglosen oder erfolgreichen Promotionsversuche unternommen.

# Danksagung

## Danke an ...

Prof. Ulrich Samm für seine interessante Fusionsvorlesung an der Universität Düsseldorf, die mich überhaupt erst nach Jülich brachte, Erklärungen, Unterstützung und viel Geduld.

Prof. Georg Pretzler für das Korreferat, für andere Perspektiven als sie bei der Nähe zur Arbeit möglich sind und Unterstützung bei Satz und Layout.

Dr. Volker Philipps für die enge und freundliche Betreuung der täglichen Arbeit vor Ort, Nutzung seiner guten Kontakte in die Fusionsgemeinschaft, Literaturhinweise, gute Ideen, anschauliche Interpretationen, äußerst ergiebige Korrekturlesen und Durchhaltevermögen.

Dr. Bernd Schwer für die hervorragende Betreuung besonders während meiner Diplomarbeit, die mir zusammen mit der guten Einarbeitung durch Dr. Florian Irrek, dem hier ebenfalls gedankt sei, einen guten Einstieg in das Thema und die praktische Arbeit ermöglichte.

Klaus Klören für den erstklassigen Laserservice, unermüdlicher Sorge um die Lasersicherheit, schnelles Umsetzen neuer Auf- und Umbauten und nahezu unerschöpfliche Hilfsbereitschaft.

Michaele Freisinger für unzähliges Probenausheizen, TDS Messungen und Diskussion, sowie die immer freundliche und kompetente Hilfe und Wartung rund um QMS, QME, QMG & Co.

Dr. Günter Esser, Christian Schulz und Harry Reimer für alle Arbeiten an PADOS und nochmal großen Dank an Harry Reimer für sehr viele Photographien, auch in dieser Arbeit.

Dr. Meike Clever, Dr. Bernd Schwer und Dr. Alexander Huber für Hilfe mit den digitalen AVT-Kameras und Rahim Allahyari für deren Softwareverbesserung.

Dr. Gennady Sergienko for a lot of tips, tricks and hints from his huge toolbox of knowledge.

Klaus Dieter Schüller, Thorsten Tietz und Michael Vogel für "physikersichere" Elektronik und andere Hardware auch mit ungewöhnlichen Sonderwünschen.

Dr. Jan Coenen und Nadine Hartmann für Temperaturmessungen mit IR-Kameras und mehr.

Alexis Terra für die Hilfe beim Einstieg in ANSYS und einen Hauch französischen Flairs.

Ingo Lassive und Werner Müller für Probenherstellung, Polieren, Schneiden und Präparieren.

Dr. Sören Möller und Christian Schulz für NRA-Messungen in Jülich und Dr. Klaus Schmid vom Max-Planck-Institut für Plasmaphysik in Garching für NRA-Tiefenprofile.

Dr. Per Petersson, Dr. Darya Ivanova and Prof. Marek Rubel at the KTH Royal Institute of Technology in Stockholm, Sweden for NRA and  $\mu$ -NRA measurements and interesting questions, explanations, lectures and information.

Das IEK-2 Team des FZ Jülich für diverse Materialdaten, Querschleife, SEM, FIB, eine Probe ultrareinen Wolframs, Erklärungen und sehr kollegiale, unbürokratische Zusammenarbeit speziell an Dr. Marius Wirtz, Dr. Thorsten Loewenhoff, Dr. Corinna Thomser, Dr. Jochen Linke, Dr. Gerald Pintsuk und Dr. Egbert Wessel.

Dr. Albrecht Pospieszczyk, Dr. Dmitriy Borodin und Dr. Sebastijan Brezinsek für Einblicke in ADAS und allerlei Hilfe in der Spektroskopie.

Dr. Andreas Kirschner für die ERO Simulationen und Einführung in TMAP7 sowie gute Erklärungen der physikalisch-chemischen PWW-Vorgänge.

Dr. Henning Stoschus und Prof. Oliver Schmitz für Messungen der Plasmarandparameter.

Prof. Bernhard Unterberg für konkrete, wichtige Fragestellungen und Aspekte der LID.

Prof. Mikhail Tokar for explanations on the effects of plasma cooling and distortion.

Prof. Detlev Reiter für die interessante Fusionsvorlesung, gute Hinweise und Prüferfunktion.

Dr. Armin Manhard vom Max-Planck-Institut für Plasmaphysik in Garching für die Wolframprobe aus PlaQ und fachliche Hinweise.

Dr. Philippe Mertens für eine Probe ITER-ähnlichen Wolframs und die Longman-Lektüren.

Dr. Arkadi Kreter für Informationen zu CFCs und Graphit und seinen guten Humor.

Dr. Peter Wienhold für die Einführung in die Colorimetrie und Dünnschichtphysik und die Organisation der EPMA Messungen, für die Dr. Silvia Richter (RWTH Aachen) gedankt sei.

Das Mirrorlab-Team speziell Dr. Maria Matveeva, Dr. Sören Möller, Marko Laengner und Christian Schulz und die Einrichtung des Spiegellabors unter der Leitung von Dr. Andrey Litnovsky, für die gute Geräteausstattung und die Möglichkeit sie jederzeit nutzen zu können.

Herrn Klaus Watermeyer aus der Technologieabteilung des FZJ fürs Aushelfen beim Polieren.

Die PC-Gruppe speziell Horst Lambertz, Thorsten Gürth und Martina Mangels für schnelle Lösung akuter Computerprobleme und Kooperation bei größeren IT-Projekten.

Luxherta Buzi, PhD for the best talks about everything and a bit of fun beside the work.

Dr. Michael Reinhart und Dr. Niels Gierse für die Bürogesellschaft, gemeinsames Messen und Niels besonders für kreative Ideen zu unterschiedlichen Themen sowie moralische und pragmatische Unterstützung beim Schreiben dieser Arbeit.

Angelika Hallmanns für gute organisatorische und administrative Unterstützung.

Allen weiteren Mitarbeitern des IEK-2, deren Beitrag ich hier vielleicht vergessen habe zu erwähnen und speziell allen Doktoranden für die kollegiale Arbeitsatmosphäre besonders auch Dr. Maren Hellwig und Dr. Dmitry Matveev.

Danke an das Graduiertenkolleg 1203 in Zusammenarbeit mit der Heinrich-Heine-Universität Düsseldorf für einige interessante Fortbildungen, Seminare und Finanzierung.

Thanks to our Japanese cooperation partners especially Prof. Yuji Torikai from the Hydrogen Isotope Research Center, University of Toyama and Prof. Yoshio Ueda from the University of Osaka for providing the W fuzz sample and many helpful thoughts.

Thanks to Dr. Christian Ruset from the National Institute for Laser, Plasma and Radiation Physics in Bucharest, Romania for providing the JET ITER-like wall W-Mo coatings on CFC.

Thanks to the unofficial "Tritium Team" of the TEC cooperation with Dr. Rianne 't Hoen (who worked at the DIFFER Institute in the Netherlands) and Dr. Yevhen Zayachuk (who worked at SCK-CEN in Mol, Belgium) for helpful discussions on hydrogen retention and a good time at conferences.

Thanks to the whole DIFFER team (at that time FOM Institute Rijnhuizen in Nieuwegein) for a warm welcome for experiments especially Dr. Jürgen Rapp and Dr. Hennie van der Meiden also for his hints on LIM.

And the TEXTOR Team: Alle weiteren Mitarbeiter, die zum Betrieb von TEXTOR beigetragen haben, speziell Dirk Nicolai und Manfred Sauer für schöne Plasmen, Interesse an den Messzielen und Geduld bei zahlreichen Bunkersperrungen für Lasertests.

Vielen Dank meiner Familie für die Unterstützung vor allem während der Schreibphase.

Kontakt zum Autor: [LID@GMX-TOPMAIL.DE](mailto:LID@GMX-TOPMAIL.DE)

Jül-4396  
September 2016  
ISSN 0944-2952

